Beyond Elemental Fluorine:

Investigations of High Potential Oxidizers,

Non-Classical Fluorine Complexes and the Simons Process

Inaugural-Dissertation

to obtain the academic degree

Doctor rerum naturalium (Dr. rer. nat.)

submitted to the

Department of Biology, Chemistry, Pharmacy

of Freie Universität Berlin

by

Gene Senges

2023

The work for the present dissertation has been conducted between May 2018 and April 2023 under the guidance of Prof. Dr. Sebastian Hasenstab-Riedel at the Institute of Chemistry and Biochemistry (Department of Biology, Chemistry and Pharmacy) of Freie Universität Berlin.

1st reviewer:	Prof. Dr. Sebastian Hasenstab-Riedel
2nd reviewer:	Prof. Dr. Beate Paulus
Date of defense:	15.09.2023

Acknowledgments

First, I want to thank my supervisor Prof. Dr. Sebastian Riedel for the opportunity and the support to follow my interest in fundamental research on a variety of different topics of the fascinating fluorine chemistry.

I want to thank Prof. Dr. Beate Paulus for offering and accepting the position as the second referee.

I am very grateful for all scientific discussions, accompanied by many new insights, with Dr. habil. Helmut Beckers, Dr. Yetsedaw A. Tsegaw, Dr. Simon Steinhauer and Dr. Ana Guilherme Buzanich. For further helpful discussions, I additionally want to thank Dr. habil. Franziska Emmerling and Dr. Nikolai V. Ignat'ev. For an inspiring talk and debate I thank Prof. em. Dr. Antonio Togni.

To my colleagues and friends Marlon Winter, Patrick Voßnacker, Dr. Tyler A. Gully, Dr. Merlin Kleoff, Thomas Drews, Friederike Fuß, Paul Golz, Dr. Benjamin Schmidt, Dr. Jan H. Nissen, Dr. Günther Thiele, Dr. Moritz Malischewski, Jonas R. Schmid, Holger Pernice, Dr. Karsten Sonnenberg, Dr. Sebastian Hämmerling, Maite Nößler and Clara A. von Randow I owe special thanks for offering a helping hand and an open ear whenever needed. I want to express my gratitude to my matrix colleagues Dr. Tony Stüker, Dr. Frenio A. Redeker, Yan Lu, Dr. Lin Li and Mei Wen for the support, cooperation and many joint matrix sessions. For further support beyond the institute, I additionally want to thank Jennifer Anders, Hendrik Ronneburg, Dr. Stefanie Kieninger, Rebekka Trenkle, Teresa Lobkowicz, Dennis Schulze, Dr. Wenjamin Moschkowitsch and Dr. Wiebke Riedel.

For manufacturing tailor-made equipment and providing technical drawings of the corresponding constructions Horst Binkowski, Frank Totzauer, Bettina Röder, Peter Schwartze, Karina Hille, Ayhan Dede, Jesse Holloway and Dirk Busold are gratefully acknowledged. I thank the *Zentraleinrichtung für Datenverarbeitung* (ZEDAT) for providing computational resources and Dr. Michaël Kulka for recording SEM images of a nickel anode.

I want to thank Dr. Julia Bader, Dr. Yetsedaw A. Tsegaw, Dr. Merlin Kleoff, Dr. Ana Guilherme Buzanich, Jennifer Anders and Marlon Winter for proofreading the manuscript of this work.

Moreover, the support of the former and present permanent staff in the inorganic department (AC) Dr. Rainer Kickbusch, Dr. Johann Spandl, Daniela Doppelstein, Marie Nickel, Inge Kanakaris-Wirtl, Lamis Sires, Jaqueline Grewe and Dr. Adelheid Hagenbach is gratefully acknowledged.

For their support and many insightful discussions especially during my studies I am very thankful to my friends from the ‘AK Hack’, Dr. Stefanie Fritz, Dr. Juliane Krüger, Philip Schweighöfer, Dr. Darina Heinrich, Dr. Heike Haller, Dr. Alexander Higelin, Martin Wozniak and Dr. Felix Brosi.

For their friendship I want to thank my parents, grandparents and my extrauniversity friends Marcus Hoffmann, Leroy Hawelky, Martin Winkler, Timo Lieben, Thomas Hansen, Andreas J. Hick, Toni R. Werner, Simon Recla, Vincent M. Heppner, Martin Ehrenberger, Ramon Angelow, Mathias Neupötsch, Pascal Voigt, Jana Kemmer, Christian Hennemann, Benedikt Rumpf, Yves Borgwardt, Saskia Schmidt, Manuela Winter, Bernd Benecke and Beate Haubrock.

My deepest thanks go to Michael Flach and Caroline Winkler for never letting me down and always cheering me up even during tough times.

Declaration of Independence

Herewith I certify that I have prepared and written my thesis independently and that I have not used any sources and aids other than those indicated by me. The present thesis is free of plagiarism. I have marked as such all statements that are taken literally or in content from other writings. I also declare that I have not applied for an examination procedure at any other institution and that this dissertation has not been submitted in the same or similar form in any previous doctoral procedure.

List of Abbreviations

*a*HF	anhydrous hydrogen fluoride
aq	aqueous
ax	axial
B3LYP	Becke 3-parameter Lee-Yang-Parr
BDE	bond dissociation energy
BP86	Becke 1988 and Perdew 1986
br	broad
CA	chronoamperometry
CV	cyclic voltammetry
δ	deformation mode
D4	Grimme's dispersion correction 4
def2-TZVPP	Karlsruhe default-2 triple-ζ basis set with a larger polarization set
DFT	density functional theory
EA	electron affinity
ECF	electrochemical fluorination
ECP	effective core potential
EPR	electron paramagnetic resonance
eq	equatorial
EXAFS	extended X-ray absorption fine structure
$F_{2,i}$	molecular fluorine isolated in noble gas matrices
$F_{2,s}$	solid fluorine phase in noble gas matrices
FEP	fluorinated ethylene-propylene copolymer
FIA	fluoride ion affinity
FIR	far-infrared
FKM	fluorocarbon-based fluoroelastomer materials
FWHM	full width at half maximum
FTIR	Fourier-transform infrared (spectrum)
GGA	generalized gradient approximation
IE	ionization energy

ip	in phase
IR	infrared
LA	Lewis acid
LB	Lewis base
LED	light emitting diode
LPBWE	lone pair bond weakening effect
MCT	mercury cadmium telluride (mid-infrared detector)
MIR	mid-infrared
MW	microwave
v	stretching mode
$\tilde{\nu}$	wavenumber
Nd:YAG	neodymium-doped yttrium aluminum garnet (laser medium)
Ng	noble gas
NPA	natural population analysis
OCV	open circuit voltage
oop	out of phase
PBE	Perdew-Burke-Ernzerhof
PCTFE	polychlorotrifluoroethylene
PFA	(poly-)perfluoroether-tetrafluoroethylene
PTFE	polytetrafluoroethylene
PXRD	powder X-ray diffraction
RI	resolution of identity
r_W	van der Waals radius
SCS-MP2	spin-component scaled second-order Møller-Plesset perturbation theory
SEM	scanning electron microscopy
sh	shoulder
um	umbrella / out-of-plane deformation mode ({EF_3} or {EF_4} moieties)
UV	ultraviolet
UV/Vis	ultraviolet/visible regime
WCA	weakly coordinating anion
XANES	X-ray absorption near-edge structure

XAFS	X-ray absorption fine structure
ZPE	zero-point energy

Abstract

Fluorine oxidizes xenon when externally activated by photolysis, heat or electrical discharge. Alternatively, the oxidation of Xe can be mediated by liquid Lewis acids such as AsF_5 or SbF_5 in the dark. In order to elucidate the role of the Lewis acids in suspected Lewis acid-fluorine adducts (non-classical fluoro complexes) the reactions of F_2 with BF_3, AsF_5, SbF_5, and $Cs[AuF_6]$ as a potential source for AuF_5 were studied under matrix isolation conditions supported by quantum-chemical calculations. The F−F stretching mode of F_2 is usually IR inactive but found slightly activated by self-aggregation of F_2 or Lewis acidic or Lewis basic species in solid Ne or Ar environment. It served as an indicator for the influence of the different Lewis acids and was monitored during deposition and the subsequent annealing and photolysis experiments.

The fluorine-rich precursor PtF_6, which is known to selectively yield the lower platinum fluorides PtF_n (n = 3–5) and fluorine atoms upon photolysis under matrix isolation conditions, was studied in combination with co-deposited laser-ablated metals and metal fluorides. The corresponding deposits contained large amounts of matrix-isolated ion pairs of the type $M[PtF_6]$ (M = Na, K, Cs) and free $[PtF_6]^-$, and allowed the investigation of these species under these conditions for the first time. The photolysis with UV light of the free hexafluoridoplatinate(V) ion yielded a band in the IR spectrum that is characteristic of a polarized $[F_2]^-$, representing the first experimental indication for a non-classical fluoro complex.

Earlier findings from our group – the end-on $[(\eta^1\text{-OO})Mn^{IV}OF]$ and side-on $[(\eta^2\text{-OO})Mn^{V}OF]$ complexes derived from the photolysis of matrix-isolated MnO_3F – were extended by newly recorded IR and UV/Vis spectra of highly pure MnO_3F and its photolysis products isolated in solid Ne, Ar, and N_2. The investigation yielded a robust experimental base for the ongoing in-depth high-level quantum-chemical investigation.

The industrially very important Simons process is used for the electrochemical fluorination of organic molecules. Its underlying mechanisms are part of a controversial debate ever since its invention about a century ago. This method, which uses nickel electrodes and anhydrous hydrogen fluoride, is thought to proceed either via a purely electrochemical pathway, or via a mechanism that is mediated by a strong oxidizer such as NiF_3 that is produced electrochemically. An unprecedented electrochemical in-situ XAFS approach allowed to investigate the elusive species that are present in the black film formed on the anodes under conditions closely matching the industrial ones. The obtained results represent the first experimental evidence for nickel centers in an oxidation state higher than +II under the conditions of the Simons process.

Kurzzusammenfassung

Die Oxidation von Xenon mit elementarem Fluor gelingt durch Aktivierung mittels Bestrahlung, Erhitzen oder elektrischer Entladung. Alternativ kann die Oxidation von Xenon auch in Gegenwart flüssiger Lewissäuren wie AsF_5 oder SbF_5 unter Lichtausschluss herbeigeführt werden. Um die Rolle der Lewissäuren in den vermuteten Lewissäure-Fluor-Addukten (nicht-klassische Fluor-Komplexe) aufzuklären, wurden die Reaktionen von F_2 mit BF_3, AsF_5 und SbF_5 sowie $Cs[AuF_6]$ als möglicher Quelle für AuF_5 unter Matrixisolationsbedingungen, gestützt von quantenchemischen Berechnungen, untersucht. Die F−F-Streckschwingung von F_2 ist üblicherweise IR-inaktiv, aber kann durch Selbstaggregation von F_2 oder durch Lewis-saure oder Lewis-basische Spezies in fester Ne- oder Ar-Umgebung geringfügig aktiviert werden. Sie diente als Indikator für den Einfluss der unterschiedlichen Lewissäuren und wurde während der Co-Kondensation und den nachfolgenden Erwärmungs- und Bestrahlungsexperimenten überwacht.

Das fluorreiche PtF_6, das durch gezielte Bestrahlung unter Matrixisolationsbedingungen selektiv zu den niederen Platinfluoriden PtF_n (n = 3–5) und Fluorradikalen reagiert, wurde in Kombination mit co-kondensierten laserablatierten Metallatomen und Metallfluoriden untersucht. Die erhaltenen matrix-isolierten Proben enthielten zu großen Anteilen Ionenpaare des Typs $M[PtF_6]$ (M = Na, K, Cs) sowie freies $[PtF_6]^-$, wodurch die Untersuchung dieser Spezies unter diesen Bedingungen zum ersten Mal möglich wurde. Die Bestrahlung des freien Hexafluoridoplatinat(V)-Ions ergab eine Bande im IR-Spektrum, die charakteristisch für ein polarisiertes $[F_2]^-$ ist und damit den ersten experimentellen Hinweis auf einen nicht-klassischen Fluor-Komplex darstellt.

Zuvor wurden in unserer Gruppe durch Bestrahlung von matrix-isoliertem MnO_3F Ergebnisse zu den end-on bzw. side-on koordinierten O_2-Komplexen $[(\eta^1\text{-OO})Mn^{IV}OF]$ und $[(\eta^2\text{-OO})Mn^{V}OF]$ erhalten. Diese wurden durch neu aufgenommene IR- und UV/Vis-Spektren von hoch-reinem MnO_3F und seinen Photolyse-Produkten isoliert in festem Ne, Ar und N_2 ergänzt. Diese weiterführende Untersuchung lieferte verlässliche Daten, die aktuell im Zusammenhang mit Ergebnissen hochpräziser quantenchemischer Berechnungen diskutiert werden.

Der industriell häufig angewendete Simons-Prozess ist ein Verfahren zur elektrochemischen Fluorierung von organischen Molekülen. Hierfür kommen Nickelelektroden und wasserfreier Fluorwasserstoff zum Einsatz. Die zugrundeliegenden Mechanismen werden seit seiner Erfindung vor rund einem Jahrhundert kontrovers diskutiert: Der Simons-Prozess läuft entweder nach einem rein elektrochemischen Mechanismus ab oder wird durch ein starkes Oxidationsmittel wie NiF_3 vermittelt, das elektrochemisch gebildet wird. Durch einen nie zuvor dagewesenen in-situ XAFS-

Ansatz wurde die Untersuchung der schwer fassbaren Spezies in dem schwarzen Film möglich, der sich auf der Anode unter industrienahen Bedingungen bildet. Die dabei erhaltenen Ergebnisse stellen den ersten experimentellen Beweis für die Existenz von Nickel-Zentren in höheren Oxidationszuständen als +II unter den Bedingungen des Simons-Prozesses dar.

Table of Contents

"The study of hydrogen fluoride is beset with difficulties and dangers,
but the valuable results obtained compensate for the obstacles
that must be overcome."

– Joseph H. Simons[1]

1 Introduction

1.1 The Element Fluorine

With a 0.027 w% in the earth's crust, fluorine is an abundant, mononuclidic (100 % ^{19}F) element that features the highest electronegativity among all elements on the Pauling scale.[2–4] The lightest halogen is almost exclusively found in its reduced form in fluoride containing minerals like fluorspar (CaF_2), cryolite ($Na_3[AlF_6]$) and fluorapatite ($Ca_5(PO_4)_3F$).[3,5] Elemental fluorine, however, is present in the mineral antozonite or "stinkspar", a dark purple to black fluorspar contaminated with uranium or thorium.[2,6,7] Radiation emitted upon nuclear decay causes radiolysis of CaF_2, and diffusion enables the separation of the elements in the inert CaF_2 matrix, which are subsequently trapped as F_2 molecules and Ca clusters, the latter causing the dark color of the ore.[6,7] F_2 was studied in gaseous,[8,9] liquid[10] or solid state[11–13] by methods such as electron diffraction,[14] (matrix) IR,[10,12] (matrix) Raman,[10,12,14] UV/Vis,[8,9] and NMR spectroscopy[6] as well as X-ray[15] and neutron diffraction.[16] In addition to numerous experimental studies, molecular fluorine has also been extensively investigated computationally at various levels of theory.[13,17–19]

The first synthesis of elemental fluorine, a pale-yellow gas, was achieved by Henri Moissan in 1886 by the electrolysis of KF dissolved in anhydrous HF (*a*HF) in a platinum apparatus.[2,5] Elemental F_2 is produced industrially, adapting the method developed by Moissan,[20] via the electrolysis of hydrogen fluoride obtained by the reaction of sulfuric acid with CaF_2, as depicted in Scheme 1.[2,4,21]

$$CaF_2 + H_2SO_4 \xrightarrow{\Delta T} 2\,HF + CaSO_4$$

Scheme 1: Industrial production of hydrogen fluoride.

In order to increase the efficiency of the process and lower the energy demand, KF is added as a conducting salt.[5] By the subsequent formation of bifluoride ions $[F{-}H{-}F]^-$,[4] the vapor pressure of the system is lowered at a higher melting point.[5] The electrolysis of the regularly used KF·2HF melt (HF content 39–42 %) is commonly conducted in a temperature range of 80–100 °C, at voltages of 8.5–10.5 V and at current densities of 12 $A{\cdot}dm^{-2}$.[5] The high potential used for the electrolysis mainly accounts for the high anodic overpotential, since the potential of HF decomposition is calculated to be about 2.9 V in a KF·2HF melt at 85 °C.[5] A common industrial electrolysis cell consists of a mild steel or Monel housing and comprises cathodes made from mild steel or iron (the cell walls might act as a cathode as well) and an anode made from carbon (ungraphitized, amorphous, or porous).[5] The gas-filled compartments over the anode and

cathode are separated to prevent the formation of explosive H_2/F_2 mixtures.[3,5,22] The raw fluorine can be purified from HF by passage of the gas over NaF pellets.[23] Pure F_2 can also be obtained via heating the fluorine-rich solids MnF_4 (or mixtures with MnF_3)[5,24] or $K_2[NiF_6]$,[5,25,26] while both materials can be regenerated upon F_2 exposure at higher temperatures.

Once produced, F_2 is an extreme oxidizer and reacts with virtually every element in the periodic table, except for He, Ne and Ar (irrespective of the HArF[27] molecule).[3] It reacts violently with organic molecules and water.[28] Fluorine owes its oxidation power to the resulting strong element−fluorine bonds and its very weak F−F bond (Table 1),[29–31] which can be described as a charge-shift bond.[32,33] Due to the missing radial nodes of the 2p orbitals, they are very compact and close to the core.[4] The binding event of two fluorine atoms leads to the repulsion of the 2p orbitals of the bonding partners, the so-called lone pair bond weakening effect (LPBWE).[30,33,34] Due to the coincidentally low positive or even negative deformation densities in the bonding region, the F−F bond is only stabilized by the ionic-covalent resonance energy (charge-shift bond), which also applies, for example, to H−F, C−F and Si−F bonds.[4,19,33]

Table 1: Properties of the halogens X_2 (X = F, Cl, Br, I) featuring bond distances (*d*) given in Å, electronegativities (*EN*, Pauling scale), bonding dissociation energies (*BDE*) of the diatomic molecules and electron affinities (*EA*) given in $kJ \cdot mol^{-1}$, as well as melting and boiling points given in K.

X_2	*d*(X–X)	*BDE*	*EN*	*EA*	*m.p.*	*b.p.*
F_2	1.41[a,b,e]	158.78[a]	3.98[b,d]	328.16[a,b,d]	53.53[a,c]	85.03[a,b]
Cl_2	1.99[a]	242.58[a]	3.16[d]	348.57[a,d]	171.7[a]	239.11[a]
Br_2	2.28[a]	192.81[a]	2.96[d]	324.54[a,d]	201.2[a]	332.0[a]
I_2	2.67[a]	151.08[a]	2.66[d]	295.15[a,d]	386.85[a]	457.55[a]

Values were taken from [a] ref. [29], [b] ref. [5], [c] ref. [16], [d] ref. [4]; [e] depending on the state or the applied level of theory there is a deviation in the F−F bond distance 1.404(12) (α-F_2, 10 K),[7] 1.411 (calc., gas, 0 K),[18] 1.4177(15) (gas, 1 atm, r.t.),[35] 1.4168(5) (gas),[36] 1.4076 (SCS-MP2)[37] and as discussed in reference [7].

With an increasing mass and correspondingly higher van der Waals interaction, the melting and boiling points of the group 17 elements increase from fluorine to iodine. This trend is also attributed to the phenomenon of the halogen bond.[7] The halogen bond and its influence on the chemistry of fluorine is described in detail in Section 1.9.[38] In accordance with its smaller size and the faster saturation, F_2 has a lower electron affinity than chlorine.[4]

In contrast to the heavier halogens, higher oxidation states of fluorine than ±0 could not be accessed by usage of purely chemical methods.[3,30] The radical cation $[F_2]^{\bullet+}$ was first characterized by its electron emission spectrum in a supersonic beam and later generated during Fourier transform ion cyclotron resonance experiments by an external ion source.[30,39,40] The reaction with H_2 provided evidence for the $[F_2H]^+$ cation in the gas phase.[39]

1.1.1 Products from Industrial Processes Involving Elemental Fluorine

There is a range of industrially manufactured products that essentially rely on the use of elemental fluorine (Figure 1).[5] A number of publications has already been devoted to these processes and a selection is discussed in the following sections.[2,5,21,41,42]

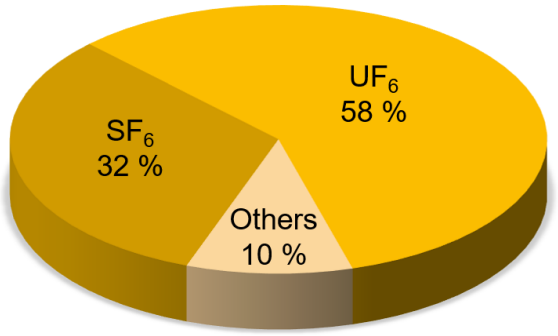

Figure 1: Industrial use of elemental fluorine. The fraction of "Others" contains compounds such as IF_5, CF_4, COF_2, and MoF_6. The compounds and estimated data were taken from reference [5].

Since fluorine is a mononuclidic element, it is used for the enrichment of the uranium isotope ^{235}U (0.72 %[29] in natural uranium) and 58 % of the industrially produced fluorine is used for the UF_6 production.[5] First, U_3O_8 is converted in a multistep process to UO_2, upon exposure to hydrofluoric acid to UF_4 and subsequently oxidized by elemental F_2 to UF_6 (Scheme 2). The mixed isotopologues $^{235}UF_6$ and $^{238}UF_6$ are then separated for example by gas centrifugation or by gas diffusion.[4,5]

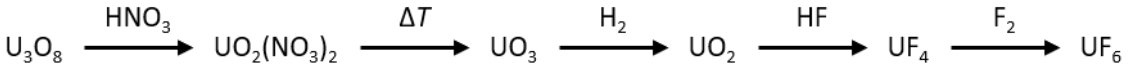

Scheme 2: Production of uranium hexafluoride.[4]

About 32 % of the industrially produced fluorine is directly used to produce the inert gas sulfur hexafluoride (SF_6) via the direct fluorination of sulfur with elemental F_2 (burning sulfur in an F_2 stream).[5,21] SF_6 is mainly used as an insulating and quenching gas in low-maintenance gas-insulated high-voltage systems, such as transformers, switchgears, circuit breakers and lines.[43,44] Although SF_6 has a global warming potential of 22200,[2] it is still used since it currently is hardly replaceable for these purposes.[21,43] Diluted gas mixtures of F_2 are used as etching gases for microelectronics and in the automotive industry for conditioning the inner surface of plastic fuel tanks to reach a lower permeability for e.g. hydrocarbons and thus reduce their emission in the environment.[45] Polycyclic aromatics can be poly- or fully fluorinated using CoF_3. The reduced by-product, CoF_2, is then regenerated upon exposure to elemental fluorine.[42]

Incomparable in production volume but highly important, the proton bombardment of $^{18}O_2$ or $H_2{}^{18}O$ using a cyclotron source yields ^{18}F as difluorine or fluoride.[46] The latter process is preferred since a higher activity is obtained.[46] The $^{18}F^-$ is separated via the deposition on an anion-exchange resin and eluted as a suitable precursor like tetrabutylammonium fluoride (TBAF) for the synthesis of ^{18}F-labeled radiopharmaceuticals such as [^{18}F]fluorodeoxyglucose for positron emission tomography imaging (^{18}F-PET).[46–48]

In the light of the highly energy demanding production of F_2, industrial processes involving it are comparably expensive.[49] Where possible, different pathways using HF,[50] $H[BF_4]$[49] or alkali metal fluorides (best reactivity/cost ratio for KF)[42] are chosen depending on the starting material.

1.1.2 Hydrogen Fluoride

Besides the high toxicity of hydrogen fluoride (HF) and the consequently high demand on safety equipment and experience in its handling to prevent severe consequences,[51] it represents the "[...] *life blood of the fluorochemicals industry*".[52] Like NH_3 and H_2O,[53] also hydrogen fluoride exhibits strong hydrogen bonds and has, compared to the higher homologues, anomalously high melting and boiling points at −83.36 and +19.51 °C,[2,3] respectively. HF forms hydrogen-bridged oligomeric zig-zag chains $(HF)_n$ in the solid,[2,21,54,55] mostly unbranched chains of n = 6,7 members in the liquid, and oligomers depending on pressure and temperature in the gas phase.[2,21,55,56] In the presence of fluoride anions, HF forms the bifluoride anion $[F{-}H{-}F]^-$ with one of the strongest known hydrogen bonds, which is endothermic by about 163 $kJ{\cdot}mol^{-1}$.[57]

Anhydrous hydrogen fluoride (*a*HF) was first obtained in 1856 by Fremy by heating KF·HF.[2,21] Commercially available hydrogen fluoride contains a certain amount of water.[58] Storing HF over $K_2[NiF_6]$, or better, electrochemically drying[50,59] lowers the amount of H_2O. Although aqueous solutions of HF react only weakly acidic, the pure *a*HF represents a superacid (see Section 1.7.1).[60] Acting as both the reactant and the solvent, *a*HF serves as the medium for the electrochemical fluorination after Simons.[61–65]

The reaction of *a*HF with strong Lewis acids like BF_3, AsF_5, and SbF_5 yields even more acidic media (see Section 1.7.1)[2,60,66] that provide access to a large variety of unusual chemical systems including carbocations[60] and high potential oxidizers,[67] and allows for catalysis by means of, for example, Friedel-Crafts reactions.[60,68]

1.2 Fluorinated Materials

Fluorine is an element of the extremes and so are many compounds derived from it. They range from the most reactive transition metal fluorides like AuF_5[69] and PtF_6[70,71] to the inert and persistent compounds like perfluorooctane sulfonic acid (PFOS)[50,72] and SF_6.[2,43]

The range of possible oxidation states of fluorine from ±0 in elemental F_2 and its complexes (Section 1.8)[73] to −I in compounds such as NaF, HF, or polytetrafluoroethylene (PTFE) is reflected in its high electronegativity and position in the periodic table. Intermediate oxidation states (mean values) are also accessible for example in $Cs^+[F_2]^-$ (−½),[74] $Cs^+[F_3]^-$ (−⅓),[75,76] $[F_5]^-$ (−⅕),[77] which are discussed in Section 1.9. Even in formally positively charged fluoronium species like the double-norbornyl type fluoronium $[C{-}F{-}C]^+$ cation, the fluorine atom has a negative atomic charge at the most of the levels of theory featured in reference [78].

Whether a fluorinated compound is reactive or inert depends not only on the degree of fluorination, but also on the efficiency of the steric shielding by the fluorine atoms. The diameter of the central atom is also crucial in terms of the accessibility for a nucleophilic attack: the chalcogen hexafluorides SF_6, SeF_6 and TeF_6 rise in their reactivity from very inert to very reactive.[79] Whereas it is hard to degrade or decompose SF_6,[80] SeF_6 can be reduced easier and represents a viable oxidizer,[79] and TeF_6 features a rich chemistry,[79,81] also with respect to its 'career' as a weakly coordinating fluorine analogue in the form of the $-OTeF_5$ group.[81–83]

Even the addition of a single fluorine atom might make a difference, as seen upon the comparison of acetic and fluoroacetic acid. The former is, with a pK_a value of 4.76,[2] a household chemical used for cooking and cleaning and is - besides an unpleasant smell - harmless to humans, while the latter molecule is a very toxic substance impairing the citric acid cycle after Krebs.[84,85] The further substitution of hydrogen by fluorine atoms at the aliphatic carbon leads to trifluoroacetic acid, which has a remarkably increased acidity (pK_a = 0.52).[2] This trend is based on the negative inductive effect of the fluorine substituent which usually increases the acidity and lowers the basicity of aliphatic and aromatic hydrocarbons and alcohols.[2,86] The substitution of hydrogen by fluorine atoms in an organic molecule can have an influence on its conformation,[87] which forces the perfluorinated alkanes in a helical structure, whereas the non-fluorinated analogues represent a zig-zag chain.[2] Especially important for drug design, a conformational influence is originated by the *gauche* interaction of two vicinal fluorine atoms caused by a hyperconjugation.[46] Thereby the σ orbitals of C−H bonds donate electron density into the σ* orbital of the adjacent C−F bond.[46] Drug properties like solubility, lipophilicity and metabolic stability can be adjusted via the fluorine substitution pattern.[88,89] In recent years, more than half of the agrochemicals contained fluorine,

acting more specific, being more tolerated by crops and less problematic to the environment at a low acute toxicity to humans.[84]

While the peroxide $(H_3CO)_2$ is explosive, its fluorinated analogue $(F_3CO)_2$ is relatively inert.[90] $(F_3CO)_2$ is even suitable for the controlled introduction of an $-OCF_3$ group into aromatic compounds.[91] Perfluorinated molecules comprising organic ligands like in $B(C_6F_5)_3$ and $[Al(OR^F)_4]^-$ ($R^F = C(CF_3)_3$) or purely inorganic compounds bearing the $-OTeF_5$ group are useful as very strong Lewis acids or the corresponding weakly coordinating anions (WCAs).[82,83,92–94] WCAs are also present in the electrolyte of Li-ion batteries in the form of lithium bis(trifluoromethanesulfonyl)imide (LiTFSI).[92,95–97] The popular Nafion® membrane is a copolymer comprising a PTFE backbone and sulfonic acid functional groups, and is highly proton conducting.[98,99] Thus, this membrane is not limiting the performance in terms of current density in suitable systems.[99] Experiments employing *a*HF can be performed in containers made from perfluorinated plastics such as PTFE, PFA, and FEP, which are known to well resist this strong acid.[21,100] However, these materials are slightly permeable for HF, which necessitates a certain wall-thickness of reactors, especially for long term experiments.[21,100]

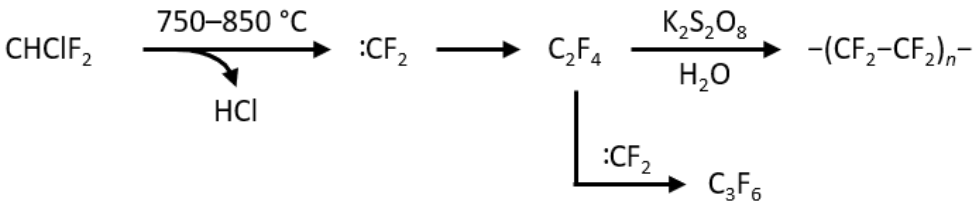

Scheme 3: Industrial production of PTFE according to reference [2]. Chlorodifluoromethane is pyrolyzed, the formed difluorocarbene dimerizes to tetrafluoroethylene, which is subsequently subjected to a radical polymerization with $K_2S_2O_8$ emulsified in water as a starter. Hexafluoropropylene is formed as a side product.

Next to fundamental research and industrial applications, PTFE, which is produced from the radical polymerization of tetrafluoroethylene (Scheme 3), is also used as an everyday-life material. It acts as a non-sticky coating for cookware, while stretched PTFE material is part of the Gore-Tex fabrics of outdoor apparel.[2]

Besides the favorable properties of these functional materials, it must be noted that (fully) fluorinated materials are highly persistent in the environment and bioaccumulative, depending on their carbon chain length.[72,101–106] Many of these compounds have therefore been phased out and substituted, where replaceable;[102,104,105,107,108] however, a detailed discussion on the environmental impact of perfluorinated materials is beyond the scope of this work.[72,101,106,109,110]

1.3 Methods of Fluorination

The introduction of fluorine to a molecule has the potential to either increase its reactivity or impart specific inertness, resulting in exceptional properties in the resulting material.[2] Several pathways (as cited in the subsequent discussion) can be utilized to introduce fluorine into a molecule:

- introduction of a fluorine-containing building block
- ligand exchange (e.g. halogen exchange, nucleophilic substitution)
- fluorination with HF (gas, solution, electrochemically)
- fluorination by a high-valent transition metal fluoride (e.g. CoF_3, NiF_3)
- direct fluorination with elemental fluorine (if necessary: additional external activation)

These general fluorination methods differ in their ability to result in the desired product and the corresponding yield, and thus, every method has its own value for specific applications.[28,42,50,111,112]

More recently, fluorinated groups have received considerable attention due to their ability to fine-tune the properties such as acidity, polarity and the lipophilicity of organic molecules.[89] This is particularly useful for drug design, therefore selective methods for the introduction of $-CF_3$,[89,113] $-OCF_3$,[114] and $-SCF_3$[115] groups have been developed.

The nucleophilic substitution of a leaving group (e.g. tosylate or halogenides) by a fluoride ion by means of a halogen exchange reaction ('halex')[52] can for instance be facilitated by TBAF,[116] KF[48] or via a Swarts reaction with SbF_3.[52] Other nucleophilic sources of fluoride are HF in the form of complexes such as pyridine/HF (Olah's reagent)[117,118] or DMPU/HF (DMPU = *N*,*N*'-dimethylpropyleneurea).[118] For the synthesis of aryl fluorides, the Wallach and Balz-Schiemann reactions are commonly employed.[42,49,119] However, as these reactions involve potentially explosive diazonium salts, for industrial large scale processes nucleophilic aromatic substitution (S_NAr) or transition metal catalyzed fluorination reactions are employed instead.[47,120]

Fluorination reactions can be conducted using HF as a gas or as an aqueous solution.[3,121,122] Depending on the (HF containing) solvent, electrode material and starting material, the electrochemical fluorination, which is discussed in detail in Section 1.4, facilitates the fluorination of a broad range of organic molecules on an industrial scale, ranging from rather mild to harsh conditions.[50,112,123]

The introduction of larger amounts of fluorine into an organic molecule can be facilitated by the fluorination with high-valent metal fluorides such as CoF_3, which is still a fairly mild reagent.[42,124,125] The results obtained by fluorination with the strong oxidizer NiF_3 are comparable with those of the electrochemical fluorination after Simons.[61–65,111,126] By increasing the fluorine content of metal fluorides, extremely high potential oxidizers such as PtF_6, capable of oxidizing even oxygen and xenon, are obtained.[70,71,127]

The fluorination with elemental fluorine is primarily of use for reactions that are not feasible with the abovementioned methods. This method is of little avail for the synthesis of functionalized organic molecules, since they are known to react violently with F_2.[28] On the other hand, the oxidation power of fluorine opens the gate for accessing high or highest oxidation states of non-metals (e.g. SF_6),[5] metalloids (e.g. AsF_5)[128] and metals (e.g. OsF_6, IrF_6).[127] In some cases, the oxidation power of F_2 needs to be further enhanced by an external activation such as electric discharge, UV light, heat, or even the addition of a Lewis acid like for the oxidation of Xe.[129–132] Similarly, PtF_6 can be obtained in low yields from the fluorination of Pt with elemental fluorine alone but is obtained in higher yields by electrically heating a Pt wire in a fluorine atmosphere for instance by the use of a car battery (see also Section 4.1.3.1).[79,127]

There are different specific strategies for the synthesis of solid phases with high fluorine amounts including flux methods and solid state reactions at low or high pressure, which are thoroughly reviewed in reference [122].

Many of these reactions are understood also with respect to their underlying mechanisms,[133] such as nucleophilic substitution reactions[47] or fluorination reactions with fluorine atoms.[129,134] However, there are simple-looking reactions that do not allow for a conclusion on a distinct mechanism.[134] The oxidation of xenon, which normally requires an external activation,[129] also proceeds in the dark at low temperatures in liquid Lewis acids.[130–132] The latter phenomenon as well as the mechanisms of the industrially important Simons process pose mysteries to many fluorine chemists.[50,123,130,135]

1.4 Electrochemical Fluorination

Fluorination reactions with elemental fluorine and often with metal fluorides are harsh (vide supra) and the mild fluorinating reagent CoF_3 relies on elemental F_2 to regain the catalyst.[28,42,126] Given the facts that these methods are not suitable for all substrates and that the costly production of F_2 is energy demanding,[2,42,61] energy efficient and safer ways were necessary to obtain the desired fluorinated organic products on an industrial scale.[2,50,136,137] Meeting both demands simultaneously, electrochemical methods using hydrogen fluoride in its pure form or as part of different molten salts such as KF·[NH_4]F·1.7HF, [NEt_4]F·4HF or even aprotic [NEt_4]F/MeCN were developed.[50,138–140] Besides the mild or selective fluorination on Pt electrodes using molten organic salt electrolytes bearing certain amounts of HF[112,140,141] and the Philips/CAVE process (CAVE = **C**arbon **A**node **V**apor phase **E**lectrochemical fluorination)[123] using KF·2HF melts as the electrolyte, the Simons process is a commonly used method for the large scale fluorination of organic molecules.[50,123,136,137] The former two methods are described in detail in the references [112,123,140], while the following discussion will focus on the Simons process and the underlying mechanisms.

1.4.1 The Simons Process

The electrochemical fluorination (ECF) after Simons is a method for the syntheses of (mostly fully) fluorinated organic substances containing functional groups, such as perfluorooctane sulfonic acid (PFOS), perfluorobutane sulfonic acid (PFBS) or trifluoromethanesulfonic acid (triflic acid) from the corresponding non-fluorinated starting compounds.[50,61,102,112,123,142–144] The substances derived from the Simons process were used in a large variety of applications such as surfactants for paints or fire extinguishing foams. Some derivatives were even of biomedical interest as blood substitutes for the ability of compounds like perfluorooctyl bromide (PFOB) to dissolve oxygen in high amounts.[50,123,145] PFOS was applied as a soil-resistant and water-repellant coating[50,102,123] and had been produced at up to 4500 $t \cdot a^{-1}$[108] until it was phased out and restricted in use.[146] It was replaced by the lighter and potentially less toxic and less bioaccumulative PFBS,[102,104] which has been regarded as a substance of very high concern (SVHC) by the European Chemical Agency (ECHA) as of 2020.[147] Nevertheless, lithium bis(trifluoromethanesulfonyl)imide (LiTFSI), derived from the widely used triflic acid, acts as an indispensable part of electrolytes of modern Li-ion batteries.[95–97,148]

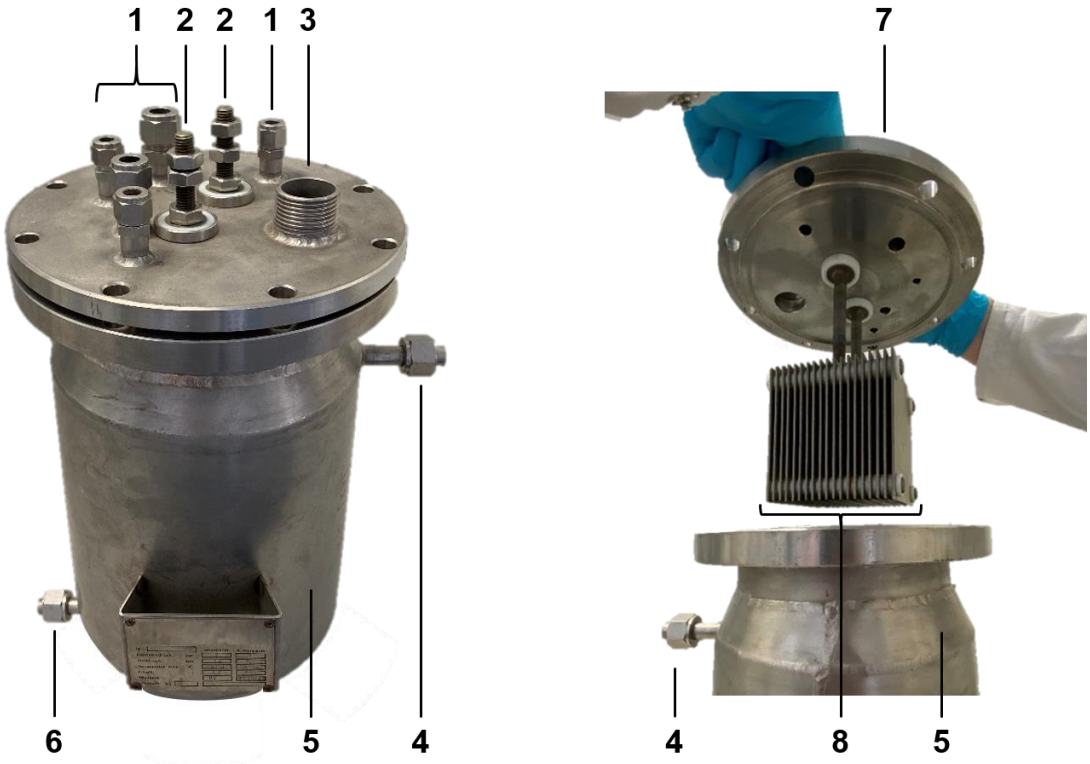

Figure 2: Electrochemical cell (left: closed, right: open) with an inner volume of 4.7 l for the performance of Simons type ECF at normal pressure and in an approved temperature range from −20 °C to +20 °C. The cell consists of **1**) connectors for the supply of *a*HF, organic starting material and inert gas, **2**) electrical feedthroughs (PTFE-insulated), **3**) connector for a reflux condenser, **4**) outlet of coolant (methanol), **5**) double-walled vessel with cooling jacket (stainless-steel), **6**) inlet of coolant (methanol), **7**) flange connector cell top (PTFE seal not shown), **8**) array of nickel anodes and cathodes. The photos were taken by the author.

Highly valuable fluorinated products are obtained by the Simons process,[50,102,123,136,137,144,149] which employs inexpensive resources, i.e. simple organic starting materials, nickel electrodes, *a*HF acting as both the medium and the fluoride source, and electricity.[50,61–65,123,150] The Simons type ECF is most commonly performed in stainless steel reactors with arrays of polarized nickel anodes and cathodes (Figure 2), in a temperature range of 0 to 15 °C, at cell voltages of 4.5 to 7.0 V and at current densities of 0.5 to 3.0 $A \cdot dm^{-2}$.[50,123,149,150] Elemental fluorine is not produced under these conditions and not employed in this process.[61]

1.4.1.1 Proposed Reaction Mechanisms

After Simons published his method of electrofluorination in 1949,[61–65,150] which was based on his findings in the 1920s,[151] the optimum in operating conditions was found by continuous development.[50,58,112,123,136,137] A typical Simons type ECF run consists of two steps, which are I) a conditioning or induction phase, where residual water in the *a*HF is oxidized and an anodic film is formed,[58,123] and II) the addition to and the subsequent fluorination of the organic molecule in

the pre-conditioned cell.[58] It must be noted that the addition of the organic molecules has an impact on the anodic film that is hardly reproducible und could thus not be clarified, as outlined by Alsmeyer et al.[123] as well as by Dimitrov et al.[152]

Conclusions about the mechanisms of the Simons process were mostly drawn from the outcome of the experiments,[123] i.e. the products and their corresponding ratio under the harsh conditions of this process (vide supra).

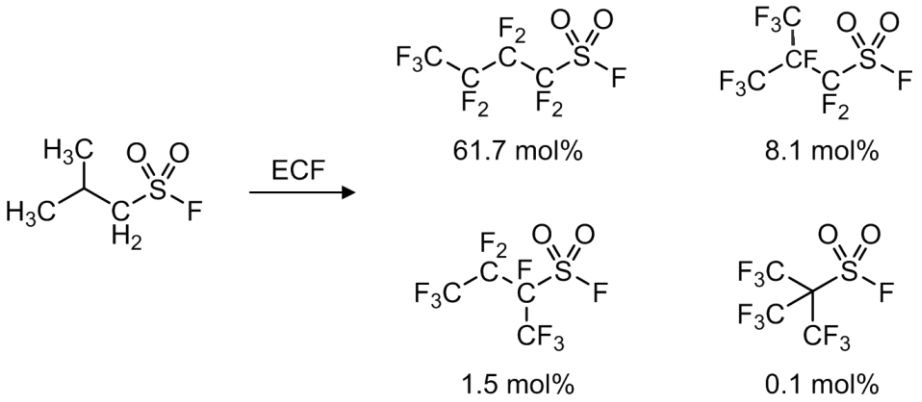

Figure 3: Carbon chain isomerization during Simons type ECF of i-butylsulfonyl fluoride. The (selected) rearranged compounds and the product ratio were taken from reference [142].

However, difficulties in the interpretation of these results arise, since not only the desired completely fluorinated[112] but also fragmented (e.g. OF_2, NF_3, CF_4, C_2F_6, SO_2F_2),[111,142,143,152,153] rearranged[123,142,153] (Figure 3) and partially fluorinated products[153,154] (Figure 4) as well as radical species[152,155] are obtained at an overall low reproducibility.[58,123,152]

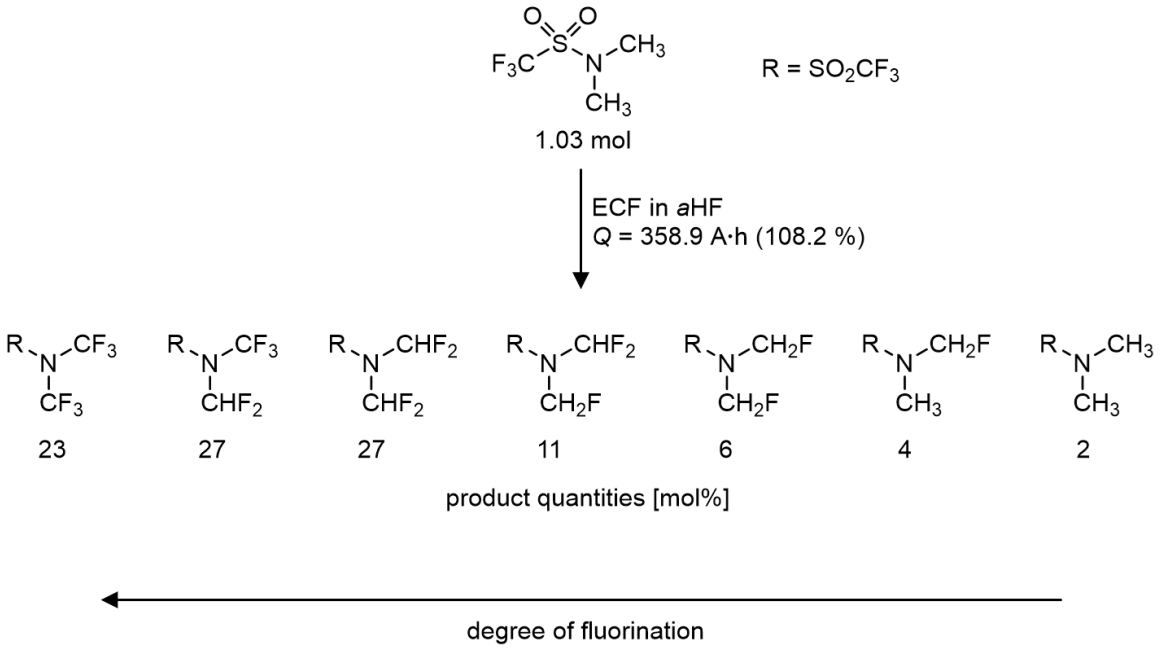

Figure 4: Fluorinated products obtained after a Simons ECF run after passage of 108 % of the calculated charge required for the complete fluorination of the starting material. Correspondingly, fragmented products were also reported. The compounds and values were taken from reference [143].

The question after the mechanism accounting for the formation of all the different products observed in the Simons process "... *is an old question, and usually, old questions are hard to answer*", as stated by Krossing,[156] in the sense that it has been the subject of controversy since its invention about a century ago.[50,123,125,135,139,142,151,152,157–159]

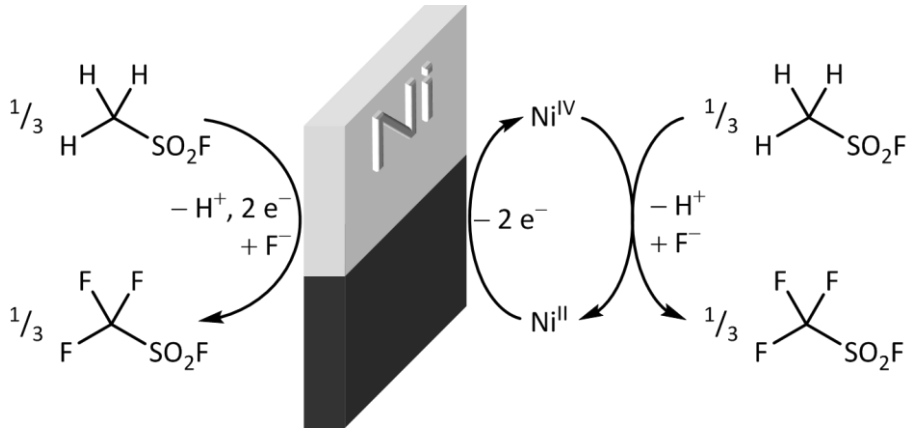

Figure 5: Schematic overview of the different proposed mechanisms for the synthesis of trifluoromethyl sulfonic acid fluoride in liquid *a*HF on nickel electrodes in the Simons process. Either the starting material undergoes direct electrochemical oxidation on the anodic surface according to the EC_bEC_N mechanism (depicted left),[123,125,135,139,148,157,158,160] or the reaction proceeds via the electrochemical generation of Ni^{III}/Ni^{IV} which mediates the fluorination of the organic compound (depicted right).[50,142,143,148,152,154,155,159,161,162]

Accordingly, much effort has been made to elucidate the underlying chemistry of the Simons process. The proposed mechanisms (illustrated in Figure 5) can be principally divided into two

groups: I) The direct electrochemical oxidation of the organic starting material on the anode following the EC_bEC_N mechanism, a four-step process with two electrochemical (E) oxidation steps and two chemical steps – proton abstraction (C_b) and fluoride addition (C_N), as depicted in Scheme 4.[123,125,135,139,148,157,158,160]

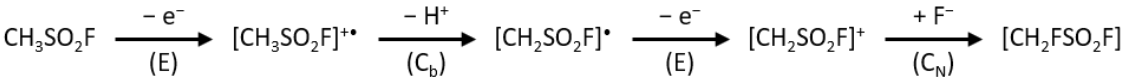

Scheme 4: Proposed EC_bEC_N[123,125,135,139,148,157,158,160] mechanism for a single H/F exchange. The perfluorination proceeds via the repetition of these steps. The scheme was adapted from references [123,125].

II) High potential oxidizing agents are electrochemically formed on the surface of the anode, i.e. NiF_4, NiF_3, $[NiF_2{\cdot}F_2]$ or $F^\bullet$ atoms, which subsequently oxidize and fluorinate the organic starting material. Thus, the second group of mechanisms becomes purely chemical in nature with respect to the conversion of the organic compounds. Depending on the substrates used in the Simons process, indications were found for both types of mechanisms.[50,123,135,155,159]

The first type of mechanism was introduced by Meinert[158,160] and refined and coined as "EC_bEC_N" by Burdon et al.,[125] Rozhkov,[139] and Gambaretto and coworkers.[135,157] However, Rozhkov used platinum as the anode material and aprotic solvents, a method later called mild or selective fluorination (vide supra).[112,139,141] The conditions of the actual Simons method (Section 1.4.1) are different from those used by Rozhkov.[123,135,139,157,160] In the EC_bEC_N mechanism, the appearance of per- and non-fluorinated (starting material) compounds after a Simons ECF run is explained in a 'zipper-like' fashion.[123] Thereby, the substrate is adsorbed on the anode's surface, the hydrogen atoms are subsequently and sequentially replaced by fluorine atoms, and afterwards the perfluorinated molecule desorbs from the anode. The basicity of the organic substrate decreases with every H/F exchange. Therefore, the desorption of the less basic partially fluorinated organic molecules competes with their perfluorination, which explains the occurence of the former.[135] Cationic intermediates might explain the observation of rearranged and cyclized products.[123,135,142,157,163]

Despite the proposed EC_bEC_N mechanism being a catchy and easily comprehended explanation for a broad variety of substances,[123,135] it does not cover all phenomena, and alternative explanations are possible, such that the formation of cyclized products might also follow a radical mechanism.[142] As the Simons process is also suitable for the fluorination of cationic species like the $[NMe_4]^+$ cation, a single H/F exchange following the EC_bEC_N mechanism would require an intermediary dication that most likely does not exist.[152] A study of Groß et al. featuring EPR data

revealed that the fluorination of the hexafluoropropene derivative depicted in Scheme 5 via ECF or F_2 yielded the same stable radical.[155] A comparability of Simons type ECF with the fluorination with elemental fluorine was likewise pointed out by Dimitrov et al.[152,164]

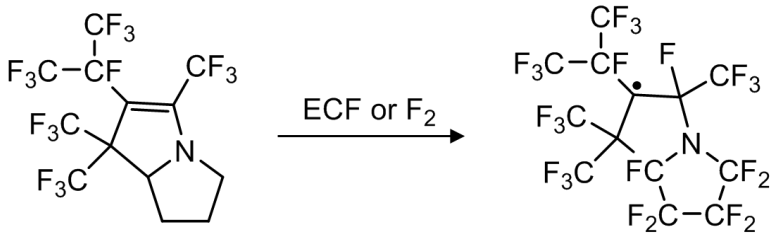

Scheme 5: Free radical pathway during Simons ECF in accordance with reference [155].

If the initial oxidation was electrochemical in nature, no fluorinated products should be observable when no electrical potential is applied. Indeed, Sartori and coworkers obtained fluorinated compounds in a well-conditioned Simons ECF cell with previously anodized nickel electrodes that had been disconnected from the energy source before the addition of the non-fluorinated starting material.[50,142,154,159] This suggests the presence of a nickel-based oxidizing agent that facilitates the chemical fluorination of the substrate.[50,142,154,159] In accordance with these results Bartlett and coworkers showed that the fluorination of CH_3CN employing the black *R*-NiF_3 (cf. Section 1.5.1) or the conversion in a Simons ECF lead to similar products.[50,111,142,165] Supporting this correlation, Ignat'ev and coworkers observed a black film on the anodes upon the emersion of an array of electrodes (cf. Figure 2) instantly after a Simons ECF experiment. They suggested the black film was NiF_3, which decomposed via a slightly brownish film to yellowish green NiF_2 in air within minutes.[50,126,142,165,166]

Scherson and coworkers studied nickel surfaces that have been subjected to Simons ECF or solely exposed to gaseous or liquid hydrogen fluoride ex-situ by X-ray photoelectron spectroscopy (XPS). Thereby the highest detected fluoride of Ni was NiF_2 due to the loss of potential control when emerged from the HF solution, and the necessary exposure to ultrahigh vacuum during XPS measurements.[167,168] From the work of Stein et al. it is known that nickel in a higher oxidation state than +II, i.e. $[NiF_6]^{3-}$ and $[NiF_6]^{2-}$, can be prepared electrochemically from solutions of $[NH_4]F$ or KF in HF on nickel anodes.[169] Many further electrochemical investigations of the anodic behavior of nickel, using a large variety of hydrogen fluoride-based media, have been reported during the last decades. However, none of the studies comprised an in-situ characterization of the anode's surface, which leaves the question of the possible participation of nickel in an oxidation state higher than +II in the Simons process unanswered.[50,58,138,162,167,169,170,171,172] The (anodic)

behavior of nickel towards HF recently received attention from the theoretical perspective,[173] and a combined theoretical and electrochemical investigation is found in reference [174].

As it is described above, not necessarily a singular mechanism accounts for all the observations in the Simons type ECF. This is in line with the statement of Simons: "*Any postulation may contain a small element of truth for some minor part of the total chemical changes but be completely in error if employed to explain the entire process*."[151]

However, experimental evidence by means of physical methods for the in-situ existence of nickel in an oxidation state higher than +II in the black film formed under the conditions of the Simons process has not yet been reported.

1.4.1.2 X-ray Absorption Fine Structure Spectroscopy

X-ray based techniques deliver information on the properties of materials such as catalytically active species.[175–178] X-ray absorption fine structure (XAFS) spectroscopy is an element-specific method that can be used to draw conclusions about oxidation states, coordination environment and bond distances of the elements of interest.[179] In the broad scope of applications of this technique ranging from materials science and catalysts research over (inert) matrix isolation investigations to even biological systems, it is of particular interest for the investigation of electrochemical in-situ and in-operando systems, such as fuel cells.[177,179–181] This method can be routinely applied but it relies on a tunable and brilliant X-ray source, which is generally provided by a synchrotron source.[179]

The irradiation of an atom with X-rays at an energy sufficiently high to excite e.g. a 1s electron into the continuum results in a jump in the spectrum that correlates to the absorption K-edge of the selected element. The lifetime of the excited state comprising a core-hole corresponds to spectral broadening in the sense of the energy-time uncertainty (eqn. 1).[178]

$$\Delta E \Delta t \geq \hbar \tag{1}$$

This means that the shorter-lived the excited state is, the broader the observed features become.[175] Upon absorption there are principally two ways of decay to the created 1s hole: X-ray fluorescence and the Auger effect. Both enable the indirect determination of the linear absorption coefficient $\mu(E)$ by measuring the X-ray fluorescence (XRF) signal emitted with the variation of the incident X-ray energy. In addition XRF allows the identification and quantification

of the atoms in the sample system. X-ray fluorescence is the predominant process at photon energies higher than 2000 eV.[179]

XAFS spectra can be measured either in transmission or in fluorescence modes. For transmission measurements, the sample is positioned between two ionization chambers that measure the intensities of the incident (I_0) and transmitted X-rays (I). This method follows the Beer-Lambert law (eqn. 2), where σ is the cross section, ρ the density and t the thickness of the sample.[175,179,182] The product of σ and ρ equals the linear absorption coefficient $\mu(E)$.[175]

$$I = I_0 e^{-\sigma \rho t} \tag{2}$$

The measurement in fluorescence is usually performed in a right angular arrangement of incident beam and detector with the sample at 45°, minimizing the inelastic scattering from the sample. Alternatively, in grazing exit geometry, the sample can be positioned normal to the incident beam.[179] The latter allows to obtain surface sensitive data and to reduce self-absorption effects, which are hard to correct.[183] These effects are based on the following facts: The incident X-rays penetrate the sample material to a certain depth and the fluorescence X-rays must travel the same way back. Thereby, the fluorescence X-rays are partially absorbed by the material, which is the so-called self-absorption (SA). The measurement of XAFS spectra in fluorescence $\mu(E)$ follow the simplified equation 3, I_f being the intensity of the fluorescence X-rays:[179]

$$\mu(E) \propto \frac{I_f}{I_0} \tag{3}$$

In cases where the sample cannot be prepared with a proper thickness for measurements in transmission, these must be performed in fluorescence mode. The linear absorption coefficient $\mu(E)$ can be approximated for a material with more than one component. It equals the total density ρ_{tot} (eqn. 4), where ρ_i represents the density and σ_i the cross section of the component i and φ_i the mass fraction of component i of the molecular weight of the material (M) M_i/M.[175]

$$\mu = \sum_i \rho_i \sigma_i = \rho_{\mathrm{tot}} \sum_i \phi_i \sigma_i \tag{4}$$

While neglecting the interactions between different atoms,[175] equation 4 allows an approximate calculation of the linear (μ) or linear mass absorption coefficients ($\mu \cdot \rho^{-1}$). The reciprocal μ^{-1} represents the absorption length, which specifies the thickness of the material to attenuate the beam of X-rays to $1 \cdot e^{-1}$ of its incident intensity.[175]

The obtained XAFS spectra can be divided into the X-ray absorption near-edge structure (XANES) and extended X-ray absorption fine structure (EXAFS) regions, which are exemplified at the Ni K-edge spectrum of elemental nickel measured in transmission (Figure 6).

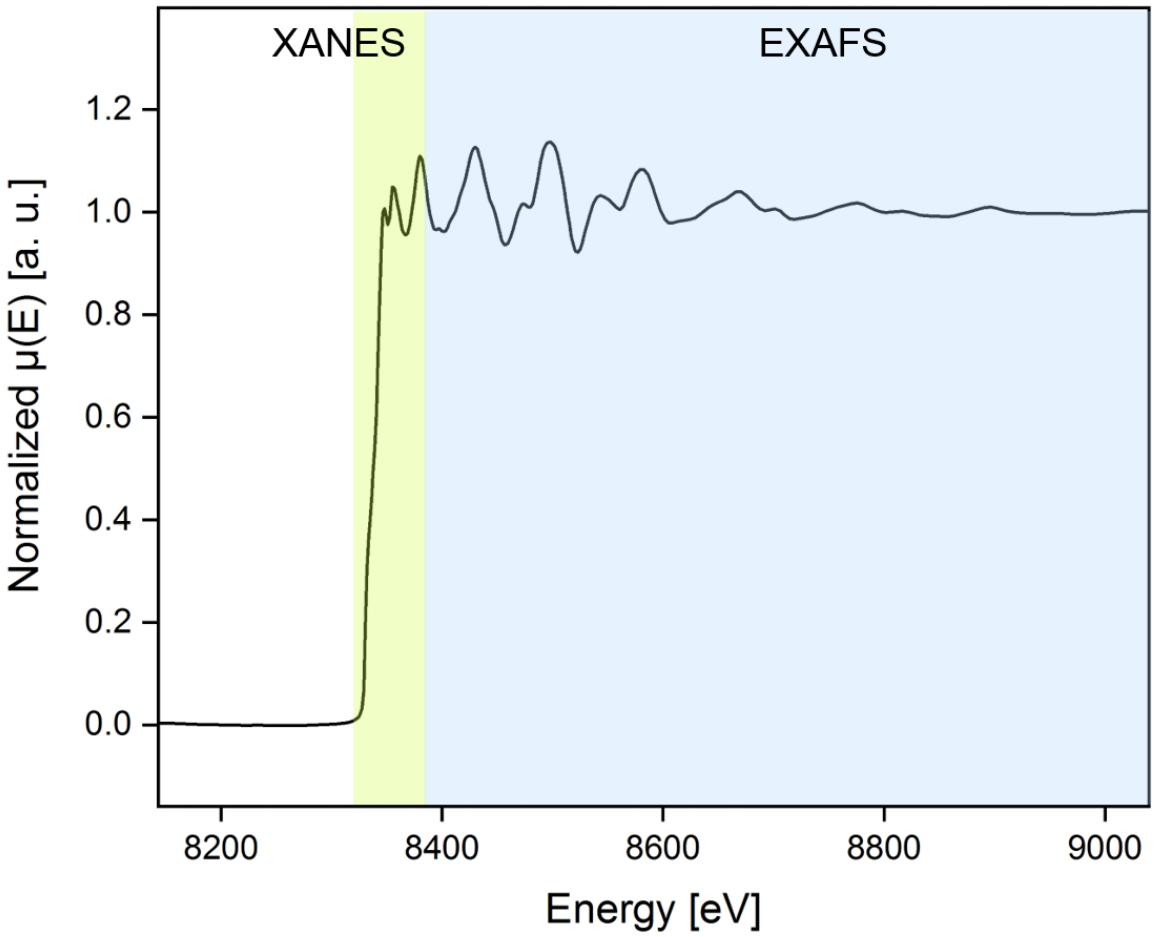

Figure 6: Ni K-edge spectrum of elemental nickel (2 µm foil) measured in transmission in the XANES and EXAFS regions (highlighted). The spectrum was plotted by using data from reference [184].

Crucially depending on a homogenous sample and flux of the X-ray source, the EXAFS region can be analyzed and interpreted after processing the spectra. Thereby the X-ray energy is converted into *k* (i.e. the wavenumber of the photoelectron), which is subsequently '*k*-weighted' (usually multiplied with k^2 or k^3) and subjected to a Fourier transformation afterwards.[175,179] This region is therefore sensitive to distances to and the nature of the neighboring atoms. The XANES region, which is indicative for the oxidation state, is more challenging to interpret. However, based on spectra of reference standards, the XANES region can be interpreted for example by linear combination fitting of the spectra, and is somewhat more robust in terms of the sample quality.[179] The exact position of the K-edge can be determined for instance by the first derivative of $\mu(E)$. Depending on the coordination environment, the pre-edge region might also feature peaks that correspond to s-d transitions, which are forbidden due to the selection rules of $\Delta l = \pm 1$ for dipole transitions.[175] However, these transitions are allowed after p-d hybridization for quadrupole transitions ($\Delta l = \pm 2, 0$) and are relatively strong for non-centrosymmetric coordination environments.[175] Consequently, strong pre-edge features are observed for tetrahedral (allow p-d mixing) and weak ones for octahedral (no p-d mixing) symmetries.[179]

1.5 Transition Metals in High(est) Oxidation States

Coming from the Simons process, an application decisively depending on nickel[50,67] in assumed higher oxidation states, the question arises how the thermally labile higher nickel fluorides NiF_3 and NiF_4[126,185] can be filed within the trend of the highest oxidation state in the periodic table. While oxidation states well exceed +IV even for lighter transition metals than Ni (cf. Figure 7), no higher nickel fluoride than NiF_4 is known.[50,126,186–188] Following the trend of the highest oxidation state of the elements at some point the highest achievable oxidation state does no longer correspond to the group number, as visualized in Figure 7. Note that this subchapter mainly focusses on the reported results on oxido and fluorido compounds and does not include organometallic compounds, where non-innocent ligands play a major role in the redoxactivity.[189]

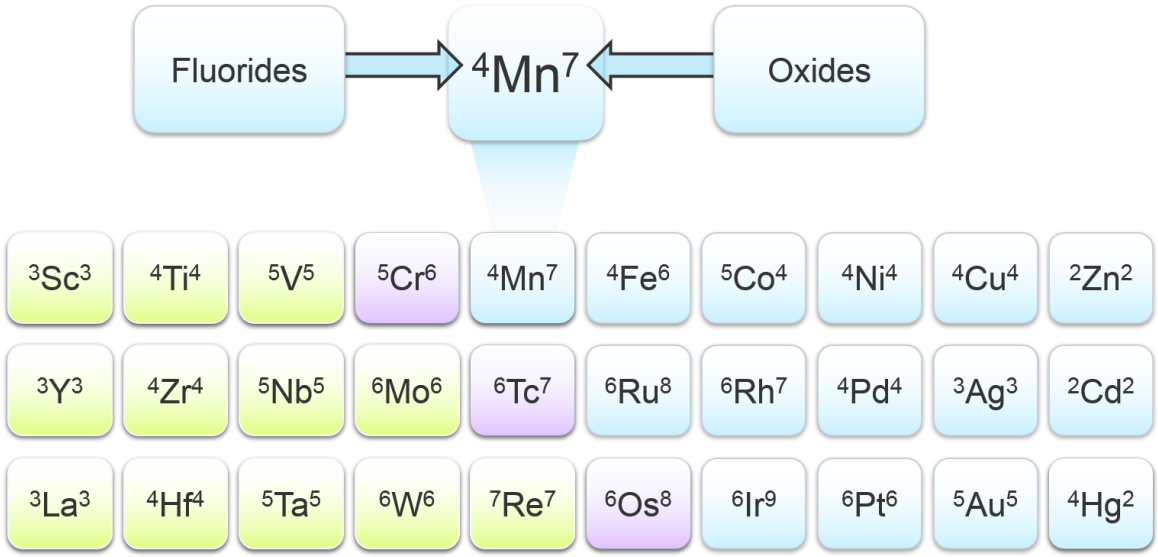

Figure 7: Highest known oxidation states of the elements of the d-block in homoleptic fluorides (superscript left) and oxides (superscript right) in accordance with references [30,188,190]. Elements following the periodic trend in both fluorides and oxides are highlighted green, the first elements featuring discrepancies are highlighted purple, the others blue.[191]

The highest oxidation states are generally obtained for compounds with oxido or fluorido ligands or both.[30,188,192–194] Due to its small size fluorine allows for high coordination numbers.[4] In the formal concept of the oxidation states,[53] the bonding electrons are fully assigned to the more electronegative bonding partner and the resulting ionic charge is determined accordingly. Despite this concept being easy, it must not be directly related to the exact electronic situation at the center and ligands,[195,196] but can be compared for the most strongly ionic systems.[30,188] In this sense, quantum-chemical calculations do not reflect the formal oxidation state but result in a description of the charge distribution at the involved atoms (partial charges) for example via natural population analysis (NPA).[195,196,197] The sometimes large discrepancy between the highest oxidation state in fluorides and oxides (e.g. for Mn) can be explained with the missing radial nodes

of the very compact 3d orbitals, which cause increased steric crowding of the ligands.[193] The overlap with bonding partners is only possible with the radial 3d probability density decreasing slower than that of the semi-core shells (3s, 3p), and results in weak and elongated bonds due to Pauli repulsion of the ligand's orbitals with the metal's 3s and 3p orbitals.[4,198] This phenomenon is the strongest for 3d metals but also applies for the 4d and 5d elements.[4,198] As shown by the periodic trends for the d-block in Figure 7, the highest oxidation state for the elements increases in the order 3d < 4d < 5d metals. Correspondingly, the 4d orbitals are bigger compared to the semi-core orbitals due to the radial node and allow for better overlapping with the orbitals of the bonding partner. Due to a relativistic expansion of the d orbitals, overlapping and bonding is even stronger for the 5d elements and their compounds.[4] In other words, relativity opens the gate to higher oxidation states, since the 3rd row transition metals are thus enabled to bind more electronegative partners.[188]

The border, where the elements stop following the described trend or where discrepancies between the maximum oxidation states in oxides and fluorides appear, received attention from both theoretical and experimental perspectives. Concerning the isolated molecules CrF_6,[199,200] TcF_7[201] and OsF_8,[192,193] only TcF_7 was calculated to be stable, while the others, in contrast, feature at least one exothermic pathway of unimolecular F_2 elimination. In the case of CrF_6, a spin forbidden singlet-triplet transition for CrF_6 to CrF_4 in their respective ground states necessitates the incorporation of the singlet-singlet transition, for which the F_2 elimination is endothermic.[199] On the other hand OsF_8 was calculated to have a substantial barrier of 203.9 kJ·mol^{-1} (B3LYP) for a concerted F_2 elimination.[192] The thermodynamic instability can be generally explained by steric crowding of the fluorine ligands at higher coordination numbers for both OsF_8 and CrF_6, while the missing radial nodes aggravate the 'situation' for the latter.[4,198] Recently reported data on calculated high-pressure phases of CrF_6,[202] TcF_7[203] and OsF_8[203] show that these high oxidation states could exist, but compelling experimental evidence for these molecular species is missing to date.[10,193] Once the elements do not longer follow the described trend, the highest achievable oxidation state with regard to the group number does not automatically become unreachable (cf. $[IrO_4]^+$).[190] The maximum oxidation state becomes less predictable and particularly interesting.[191,204–206] This is especially true for mercury, for which the highest oxidation state +IV became evident with neon matrix-isolated HgF_4 molecules, rendering Hg a transition metal.[207]

When aiming for high(est) oxidation states, lowering the formal oxidation state of the electronegative ligand from −I in fluorides to −II in oxides reduces the steric crowding due to a lowered number of ligands.[208] This is reflected in the above described trend (Figure 7). The combination of both oxygen and fluorine ligands leads to oxo-fluorides with interesting

properties, which are exemplified in the following. OMF and OMF_2 molecules (M = Sc, Ti, V, Cr, Mn, Fe, Co, Ni, Cu, Pd, Ag, Pt, Au)[209–211] and OHgF[212] show an anomaly, which is called the "oxo-wall"[211,213] and roughly sets a border between group 8 and 9.[209,214] This phenomenon describes that the early transition metals form oxo-complexes with double bonded oxide (O^{2-}) ligands, whereas the compounds of the late transition metals feature singly bonded oxyl ($O^{\bullet-}$) ligands with a radical character accompanied by oxidation states +III and +II of the metal center, respectively.[209,214] Due to the number of valence electrons of Sc, $OScF_2$ as well contains an oxyl ligand and the metal is in the oxidation state +III.[209] Next to the mentioned compounds, also oxo-fluorides with the metal in high(est) oxidation states like OMF_3 (M = V, Mn, Fe, Pt)[209,211] and MO_2F_2 (M = Cr, Mo, W),[215,216] MOF_4 (M = Cr, Mo, W)[217] are known and of synthetical use, and compounds like OsO_2F_4 and OsO_3F_2 have been reported as well.[193] Oxofluorides such as $ReOF_5$ and $OsOF_5$ are (very) strong oxidizers, in the same range as MoF_6 (the former) or surpassing OsF_6 (the latter) in oxidative strength.[193,218] Transition metals are known to form η^1-O_2 and η^2-O_2 complexes, while an assignment to superoxo (the former) and peroxo (the latter) ligands essentially depends on the exact charge transfer from the metal to the ligand.[219] Therefore, the nature of these species can hardly be elucidated by experiments only, and the compounds are classified by the aid of calculated data.[219] Together with oxides and ozonide complexes (η^2-O_3), these compounds have been collectively reviewed in reference [219].

Within the 3d transition metals, manganese, together with chromium, has the widest range of oxidation states from −III to +VII.[4] This broad redox chemistry renders Mn useful in a large variety of catalytical systems: from Mn as a part of the photosystem II, where it represents the active site of the water-oxidizing complex Mn_4CaO_5, over $La_{0.5}Ca_{0.5}MnO_3$ nanowires, to manganate based anodes for a proton-conducting solid oxide steam electrolyzer.[220] Manganese in its highest oxidation state +VII in the well-known permanganate ion $[MnO_4]^-$ has made history.[4,188,221–224] However, the highest oxidation state of binary manganese fluorides known experimentally to date is +IV in MnF_4.[188] Its existence in molecular form, however, could not be unequivocally proven so far.[193,223] A fluoride with manganese in an even higher oxidation state, i.e. +V in MnF_5, was calculated to be thermochemically stable but matrix isolation experiments, where an excess of F_2 was reacted with laser-ablated manganese atoms, did not yield such species.[223] On the other hand, a higher formal oxidation state of Mn in manganese fluorides could be achieved by bonding the metal center to additional oxide ligands.[211]

Regarding oxo-fluorides in the highest oxidation states, the group 7 members Mn, Tc and Re all form MO_3F,[187,215,225,226] while only technetium and rhenium form MO_2F_3 and MOF_5 (see reference [201] and references therein). DFT calculations predicted that manganese oxo-fluorides MnO_xF_y

($x + y = 1–4$; x, $y = 0–4$) except for OMnF exceed the electron affinities of the halogens[227,228] and thermochemical information on OMnF, $OMnF_2$ and their cationic analogues was reported.[229] At higher oxygen contents also complexes such as $(O)_2MnF$, $[(\eta^1\text{-}O_2)_2MnF_2]$ and $[(\eta^2\text{-}O_3)MnF_2]$ were recently characterized.[230,231] These oxo-fluorides rather resemble the chemistry of binary compounds of oxygen and transition metals like $[(\eta^1\text{-}O_2)MO_2]$ and $[(\eta^2\text{-}O_2)MO_2]$ (M = Rh, Ir), or $[OSc(\eta^2\text{-}O_3)]$.[219,232,233] Before this very recent interest from the theoretical and matrix isolation perspectives,[209,221,226,230] surprisingly little was known about oxo-fluorides of manganese and permanganyl fluoride remained rather a lone wolf. Since the first synthesis by Friedrich Wöhler in 1828,[234] MnO_3F can be synthesized in large quantities.[187,215,221,235,236] Thus, numerous investigations using matrix isolation IR[187,237–240] and UV/Vis[187,241–243], gas phase IR,[224,241,244] and microwave spectroscopy,[245] He(I)-PES,[246] single crystal XRD[236] as well as EXAFS spectroscopy[237] and quantum-chemical studies[226,227,241,247] are well documented. However, a study featuring the photochemical behavior of permanganyl fluoride, isolated in inert matrices, as a potential precursor of new oxo-fluoride species of manganese, has not been reported yet.

1.5.1 Selected Fluorides

As outlined in the previous subchapter, the highest oxidation states can be achieved with oxo ligands. In contrast, and in accordance with Higelin and Riedel, "[...] *the most extreme oxidation states* [...]" are stabilized by fluoride ligands.[193] High potential oxidizers such as NiF_4[126] were, together with fluoro-oxidizers such as $[KrF]^+[PtF_6]^-$,[248] thoroughly reviewed.[30,188,193] The focus of the following considerations is on the former type with the most relevant examples for the present work.

Christe reported a purely chemical route for synthesizing F_2 (Scheme 6) a century after Moissan had first synthesized elemental fluorine electrochemically.[20,121]

$$2\ K[MnO_4] + 2\ KF + 10\ HF + 3\ H_2O_2 \xrightarrow{HF_{aq}\ (50\ \%)} 2\ K_2[MnF_6]\downarrow + 8\ H_2O + 3\ O_2$$

$$SbCl_5 + 5\ HF \longrightarrow SbF_5 + 5\ HCl$$

$$K_2[MnF_6] + 2\ SbF_5 \xrightarrow[-\ 2\ K[SbF_6]]{} MnF_4 \longrightarrow MnF_3 + ½\ F_2$$

Scheme 6: Christe's chemical route to yield elemental fluorine with the decomposition of the postulated in-situ generated, thermodynamically unstable MnF_4.[121]

A possible explanation for the evolution of fluorine from the reaction mixture of $K_2[MnF_6]$ and SbF_5 could be the decomposition of a thermodynamically unstable MnF_4.[121] Christe contended as the basis for his approach – putting the cart before the horse – that hexafluoridometallates(IV) of Mn, Ni, Cu represented the stabilized forms of the respective neutral tetrafluorides.[121] In the sense that the stronger acid displaces the weaker from its salt,[121] the $[MnF_6]^{2-}$ is deprived of the protective fluoride shell or 'activated' by the fluoride abstraction by the very strong Lewis acid antimony pentafluoride,[249] and MnF_4 is thought to be generated in-situ and subsequently decomposed to MnF_3 and molecular F_2.

Besides ternary phases such as $Na_3[NiF_6]$,[250] $K_3[NiF_6]$,[251,252] $K_2[NiF_6]$[253,254] and $Li_2[NiF_6]$[67,255] with nickel in higher oxidation states than +II, the only known room temperature stable binary nickel fluoride was NiF_2,[256,257] until 1989.[126,258] The late discovery of higher nickel fluorides[126,258] can be explained by the general rule that binary systems of higher oxidation states can be stabilized upon complex formation, as pointed out by Biltz in 1927.[253,259] Christe's fundamental and elegant approach of the fluoride abstraction by Lewis acids was then applied to a larger range of systems.[258] This route paved the way for higher binary nickel fluorides, the unstable tan/brown colored NiF_4 and the meta-stable black NiF_3 that were accomplished in a modified approach (Scheme 7) by Bartlett and coworkers.[126,166,258,260,261]

$$K_2[NiF_6] + 2\,BF_3 \xrightarrow[T = -65\,^\circ C]{a\mathrm{HF}} K[BF_4]_{solv.} + NiF_4\downarrow$$

$$NiF_4 \xrightarrow{T > -55\,^\circ C} NiF_3 + \tfrac{1}{2}\,F_2$$

$$NiF_3 \xrightarrow{T > 39\,^\circ C} NiF_2 + \tfrac{1}{2}\,F_2$$

Scheme 7: Synthesis of tan/brown colored NiF_4 and its thermolysis to black NiF_3. The decomposition temperatures refer to the quantitative decomposition. The reported NiF_2 had a yellow/brownish color. All data were taken from references [126,258].

NiF_3 is known to form three different solid phases with increasingly thermally stable *R*- (rhombohedral), *P*- (pyrochlore) and *H*-forms (hexagonal tungsten bronze), respectively, with *R*-NiF_3 being the purest form. With the stability, the contamination with potassium increases, which is in accordance with the synthetic procedure. The samples are purified by decanting the supernatant solution of $K[BF_4]$ in *a*HF in the second leg of a double-leg reactor and NiF_3 is washed with the back-distilled *a*HF at 0 °C for seven times.[126] The solid state structure of crystalline *R*-NiF_3 of the $Li[SbF_6]$ type in the space group $R\bar{3}$ was determined via neutron diffraction at 2 K and

features two different Ni–F distances of 1.959(3) and 1.811(3) Å, which were assigned to Ni^{II}–F and Ni^{IV}–F, respectively.[166]

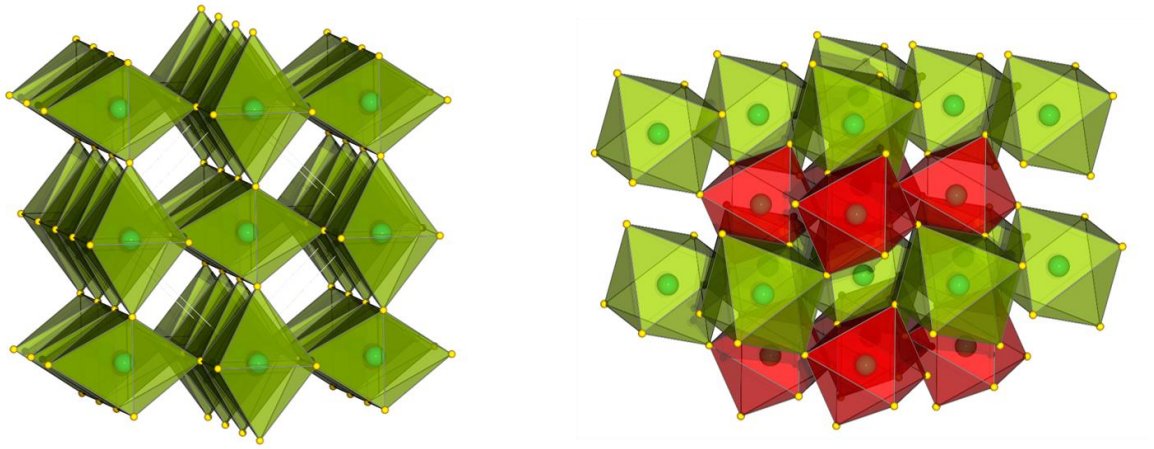

Figure 8: Solid state structures of NiF_2 (rutile type, *P*4_2*/mnm*, left) and mixed-valent *R*-NiF_3 ($Ni^{II}[Ni^{IV}F_6]$, $Li[SbF_6]$ type, $R\bar{3}$, right) with Ni centers (green) and F corners (yellow). The structures feature all-corner linked octahedra, while those with the longer Ni^{II}–F distances are highlighted green, those with shorter Ni^{IV}–F distances red. The structural data were taken from references [256] and [166], respectively.

This mixed-valent structure $Ni^{II}[Ni^{IV}F_6]$[166,262] is in agreement with the reported EXAFS data of Hector et al. The corresponding UV/Vis spectra featured an absorption throughout the visible region corresponding to the dark brown/nearly black color[126] of the substance and led to the exclusion of the presence of nickel in an oxidation state of +III.[251,262] Comparable structures were reported for the mixed-valent $Pd^{II}[Pd^{IV}F_6]$[262] and the platinum analogue $Pt^{II}[Pt^{IV}F_6]$.[263] Tramšek et al. later reported another mixed-valent nickel fluoride, i.e. Ni_2F_5 or $[Ni^{II}_3Ni^{IV}F_{10}]$ that can be obtained upon thermal decomposition of *R*-NiF_3 at 100 °C.[264] Ni_2F_5 can be re-oxidized to *R*-NiF_3 by KrF_2 in *a*HF at 0 °C.[264] The thermal stabilities $NiF_4 < NiF_3 < Ni_2F_5$ suggest that the respective binary Ni–F phase is the more stable the lower the concentration of Ni^{IV} is.[126,264] As pointed out by Bartlett and coworkers, Ni^{IV} and Ag^{III}, in their cationic forms dissolved in *a*HF acidified with AsF_5, SbF_5 or BiF_5, represent the strongest oxidizers presently known.[67,193,265,266] It is therefore understandable that the reaction of NiF_3 with CH_3CN was reported to be violent at temperatures as low as −40 °C.[126] Although both Ag^{III} and Ni^{IV} are able to oxidize $[PtF_6]^-$ to the neutral hexafluoride,[266] neither of them was found to oxidize $[AuF_6]^-$.[67,193,267] However, besides a recent matrix isolation study on molecular nickel fluorides NiF_x (x = 1–4)[268] and very recent quantum-chemical results on hypothetical crystal structures of NiF_4,[269] the high potential oxidizers NiF_4 and AgF_3 have not been structurally characterized as bulk materials so far.[193]

1.6 Molecular Hexafluorides and Related Compounds

As outlined in the previous subchapter, fluoride ligands stabilize high and extreme oxidation states.[193] Due to its small size, fluorine also allows for high coordination numbers,[4,79] which is reflected by 16 known homoleptic hexafluorides and one heptafluoride (ReF_7),[270] see also reference [271]. These molecules, which range from (rather) unreactive (SF_6, SeF_6) to extremely reactive (RuF_6, PtF_6),[79] are highlighted in the following sections with the focus on the transition metal hexafluorides with the highest electron affinities, and their related anions. The oxidative behavior of the hexafluorides (one-electron oxidizers such as PtF_6) must be discriminated from the fluoro-oxidizers (e.g. $[KrF]^+$) as they differ in their oxidation mechanisms,[218,272] with respect to a simple electron transfer (the former) and a formal F^+ transfer (the latter).

The oxidation 'power' of a chemical species, may it be an atom or a molecule, is correlated to its electron affinity (EA),[79] which is defined as the amount of energy that is released when this species binds an electron and, at the extreme, forms an anion.[4] As ionization potentials always exceed the electron affinities, the latter is no stand-alone criterion in determining the oxidative strength of a chemical species.[4] The EA must be discussed when referring to other magnitudes such as the atomization energies (if it applies) and the lattice energy in the sense of a Born-Haber cycle (see Scheme 8).[4]

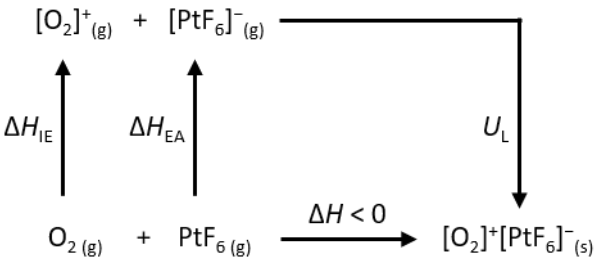

Scheme 8: Born-Haber cycle of the spontaneous and exothermic reaction of O_2 with PtF_6, featuring ionization energy (ΔH_{IE}), electron affinity (ΔH_{EA}) and lattice energy (U_L).[4,218,272]

Since the potential window of most electrolytes is too small to obtain electrochemical data, the strength of highly potent one-electron oxidizers is typically evaluated through the oxidation of a specific target atom or molecule (see also Section 1.5.1).[272] Since the lattice energy does not differ much within a given compound class such as the transition metal hexafluorides and their $[O_2]^+$ salts,[4,79] reactions with weak reducing agents like O_2 or Xe allow a conclusion on the oxidizing abilities of the former.[79,193,218,272] Table 2 features a compilation of experimental and calculated electron affinities of selected hexafluorides, which are close to or well beyond the electron affinities of the halogens (3.0–3.6 eV).[228,273] Electron affinities can be determined by the photodetachment of electrons with a (tunable) laser arranged perpendicular to a negative ion

beam.[274] Another experimental possibility to (roughly) determine the electron affinity is the collisional ionization of the oxidizer of interest with an alkali metal.[275] Thereby, negative molecular ions are produced in the cross section of perpendicular beams of a molecular hexafluoride and an alkali metal that is thermally evaporated and accelerated with an adjustable voltage, and the ion current is subsequently measured. Given the high EA of IrF_6 and PtF_6,[79] they readily react with thermal (non-accelerated) sodium atoms.[275] The electron affinities can also be obtained by the flowing afterglow Langmuir probe technique (FALP), where thermalized electrons are attached to the molecule in a plasma flow and the anions are additionally detected by a coupled mass spectrometer.[276,277]

Table 2: Experimental (index exp) and calculated (index calc) electron affinities given in eV. Experimental uncertainties are given in the references (see the footnotes).

Species	**EA_{exp}**	**EA_{calc}**
Pt	2.13[a]	1.85[h]
Au	2.31[a]	
PtF_2		2.86[h]
F_2	3.0[a]	3.08[k]
$F^{\bullet}$	3.4[a]	3.23[h]
WF_6	3.36[b]	3.16[b,c]
ReF_6	< 3.8[b,e], < 5.14[b,f]	4.58[b,c]
PtF_4	5.50[g]	5.29[h]
OsF_6	5.93[b]	5.92[b,c]
IrF_6	6.50[b]	5.99[b,c]
PtF_6	7.00[b,d]	7.09[b,c]
RuF_6	7.5[b,d]	6.98[b]
PtF_7		7.68[j]
$AsF_6^{\bullet}$		7.78[k]
$SbF_6^{\bullet}$		8.06[k]
AuF_6		8.20[c]

The values were taken from [a] ref. [274], [b] ref. [79], [c] ref. [273], [d] ref. [278], [e] ref. [277], [f] ref. [275], [g] ref. [279]. CCSD(T) values (adiabatic EA) from [h] ref. [280], [j] ref. [281]. [k] Values at the Feller-Peterson-Dixon (FPD) level of theory from ref. [282]. The complete set of electron affinities of the 2nd row transition metal hexafluorides are found in references [79] and [283]. Explorative, calculated data on 1st row transition metal hexafluorides are found in references [284] and [202].

The transition metal hexafluorides of 4d and 5d metals show the trend of increasing electron affinities when going from left to right,[275] which leads to the fact that the strongest oxidizers are

found with RuF_6, RhF_6 and PtF_6.[79] The hexafluorides of Ru, Rh and Pt are all able to oxidize O_2 and Xe (see for instance the reaction with PtF_6 in Scheme 9), while xenon is also oxidized by IrF_6 when heated.[79,285]

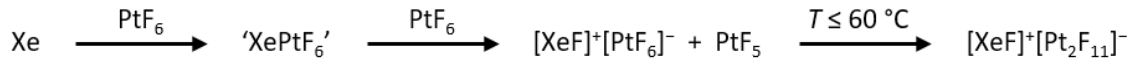

Scheme 9: Oxidation of Xe with excess PtF_6 according to reference [286].

With respect to this trend in reactivity and as depicted in Figure 7, the hexafluorides of Pd and Au were not experimentally observed, and the highest oxidation states in fluorides of these elements are +IV[287] and +V,[69] respectively. AuF_5 itself is an extraordinarily strong Lewis acid and is only observed in the dimeric form $(AuF_5)_2$, even in the gas phase,[69] but its room temperature-stable $[AuF_6]^-$ salts are well known.[69,288–291] A compound of the composition AuF_7 was later found to be better described as the non-classical complex $[AuF_5{\cdot}F_2]$[195,292,293] that could not be experimentally proven to date.[10,208] In the sense that higher oxidation states can be stabilized by the formation of anions (vide supra),[4,121,126,253,259] and that MoF_6, TcF_6, WF_6 and ReF_6 represent viable fluoride ion acceptors, corresponding hepta- and octafluorido-metalates(VI) were observed.[79] $[RhF_7]^-$ is calculated to form a classical anionic complex as well, but was not observed yet.[79,283] Although the heavier MF_6 were calculated to exhibit comparably large fluoride ion affinities,[273,283] higher coordination numbers than six in homoleptic fluorido-complexes of Ru, Os, Ir and Pt are not known. Instead, non-classical anionic complexes like $[MF_5{\cdot}F_2]^-$/$[MF_6{\cdot}F]^-$ were calculated to be more stable for Ru and Pt.[79,273,283]

PtF_6 (*m.p.* = 61.3 °C),[294] first synthesized in 1957,[295] is historically important to facilitate the oxidation of oxygen ($[O_2]^+[PtF_6]^-$)[71,296] and xenon ($[XeF]^+[PtF_6]^-$/$[XeF]^+[Pt_2F_{11}]^-$)[70,286] and thereby generate the first noble gas compound.[4,193] It loses F_2 upon heating above 100 °C.[193] PtF_6 was characterized by (matrix) IR,[297–299] (matrix) Raman,[297,299–301] and (matrix) UV/Vis spectroscopy,[298,299,302] as well as electron[303] and X-ray diffraction.[127] The increasing electron affinity of the metal hexafluorides (from left to right) is also reflected in the ligand to metal charge transfer bands that are correspondingly shifted from the UV into the visible regime when going from colorless WF_6 to deeply red colored PtF_6.[79,300] Next to the fundamental investigation of the matrix-isolated transition metal hexafluorides in terms of their IR and UV/Vis spectra,[298] a systematic study of the photochemistry of PtF_6 was not available in advance of the present work.[304]

Besides the platinum compounds already mentioned, the $[PtF_6]^-$ anion is also suitable to stabilize other reactive cations such as $[NF_4]^+$,[305] $[ClF_6]^+$,[306] $[AsF_4]^+$[307] and $[KrF]^+$.[248] Corresponding

hexafluoridoplatinate(V) and -(IV) salts of the alkali metals, i.e. M[PtF_6] (M = K, Rb, Cs)[218,286,308,309] and M_2[PtF_6] (M = Li, Na, K, Rb, Cs),[122,310,311] were characterized as well, including EXAFS data of K[PtF_6] and K_2[PtF_6].[312] The [PtF_6]$^-$ salts were investigated by IR and Raman spectroscopy as well as XRD.[286,308] However, although the hexafluoridometalates Cs[UF_6] and Cs[NbF_6] were studied by matrix isolation techniques (see also Section 1.10.1, Section 3.2.2),[313–315] corresponding ionic derivatives of PtF_6 in matrix isolation approaches were not reported. Due to the high electron affinity of PtF_6, it can spontaneously react with reducing agents in the gas phase (vide supra), making it an ideal candidate to study its molecular anion employing the laser ablation technique for metals and metal salts (see Section 1.10.1.1).

Tetrameric PtF_5 (*cis*-F-bridged octahedra) is known to disproportionate into PtF_4 and PtF_6 at higher temperatures.[30,316,317] PtF_5 is formed together with F_2 and Kr upon the decomposition of [KrF]$^+$[PtF_6]$^-$.[30,248] It forms complexes with ClF_3 and IF_5,[309,317] and is known to form salts like [AsF_4]$^+$[PtF_6]$^-$[307] and [NO]$^+$[PtF_6]$^-$,[318] which renders PtF_5 a Lewis superacid.[273,318–321] Together with Xe and F_2, PtF_5 forms the [XeF_5]$^+$[PtF_6]$^-$ salt.[321] A predicted non-classical complex of the type [$PtF_5{\cdot}F_2$]$^-$/[$PtF_6{\cdot}F$]$^-$[273] could not yet be proven experimentally.[79] The tetrafluoride of Pt is a light-brown solid[322,323] that is known in several sixfold coordinated complex salts [PtF_6]$^{2-}$ with alkali metal and nitrosyl counter ions,[310,318,324] and as the bromine trifluoride adduct [$PtF_4(BrF_3)_2$].[322,325] As it is typical for group 10 metals (see Section 1.5.1), also PtF_3 is known as a mixed-valent fluoride, i.e. $Pt^{II}[Pt^{IV}F_6]$.[263]

Using Knudsen cell mass spectrometry, the lower fluorides PtF_4, PtF_3 and PtF_2 were studied with regard to their thermochemical properties,[326] while IR frequencies were reported for both the mono- and difluoride in matrix-isolated samples.[211] However, a thorough investigation comprising spectroscopic evidence for all the platinum fluorides PtF_n (n = 1–6) had not been reported prior to the present work and is featured in reference [304] (cf. Section 3.2). Analogous matrix isolation studies of iridium fluorides IrF_n (n = 1–6)[327] and a comparable study on MoF_n (n = 1–6)[328] were published very recently.

After Au with 2.31 eV, Pt has the second highest electron affinity of the metals with 2.13 eV.[274] This is even more pronounced upon the addition of fluorido ligands and increases with the fluorine content (Table 2).[281,293] In the case of Pt, the calculated maximum EA in fluorido complexes is reached in PtF_7 with 7.68 eV.[281] As reported by Riedel, any fluorides higher than PtF_6, i.e. PtF_7 or PtF_8, are unlikely to form, since all decomposition pathways yielding PtF_5 or PtF_6 are (strongly) exothermic.[281]

A precise quantum-chemical description of compounds containing 5d metals requires the treatment of relativistic effects,[208] which are outlined briefly in accordance with reference [4]. These effects are highly important from the 6th row of the periodic table on and divide into scalar-relativistic and spin-orbit coupling effects. The former ones are subsequently split into direct and indirect effects. The 6s electrons, despite their small probability density close to the core, are contracted and consequently stabilized, which is considered a direct scalar-relativistic effect. This leads to the inert-pair effect, which stabilizes for example Pb^{II} over Pb^{IV}. On the other hand, the contracted 6s orbital better shields the nuclear charge and – indirectly – leads to the expansion of the 5d orbitals, which cause better overlap with ligand orbitals and increase bond strengths (cf. Section 1.5). Noteworthy, the direct effects account for p, d and f orbitals as well, but less, and the direct and indirect scalar-relativistic effect are mutually dependent and reinforce each other. This "cooperative" effect also causes the yellow color of gold,[329] for which the relativistic effects are the strongest in the so-called "gold maximum". The spin-orbit coupling causes the splitting of orbitals with $l > 0$.[4]

A recent publication on the $[NF_4]^+$ formation mechanism revealed calculated data on high-valent fluorine radical compounds of main group Lewis acids and others, which should fairly surpass the oxidative power of PtF_6, such as $AsF_6^\bullet$ and $SbF_6^\bullet$, and even that of speculative AuF_6, with $Sb_2F_{11}^\bullet$.[282] This study thereby also made clear that the oxidative power of elemental fluorine can be further enhanced by strong Lewis acids, especially in the presence of an external activation source (heat, glow discharge, γ irradiation or UV irradiation). Recently, quantum-chemical calculations predicted a high-pressure stabilized phase of AuF_6[330] and an oxidation state of +X in $[PtO_4]^{2+}$.[204,205]

1.7 Lewis Acid-Lewis Base Interactions

Numerous strong oxidizers can only be generated and controlled by the use of (conjugated) superacidic media (see the previous sections), which are obtained by the combination of strong Lewis and Brønsted acids, where the latter acts as a Lewis base.[60] The interactions in these systems are highlighted in the following.

The behavior of acids and bases was described in two fundamental definitions by I) Brønsted and Lowry[331,332] and by II) Lewis.[333] Brønsted defined acids as proton donors and bases as proton acceptors, and both exist in chemical equilibrium with the resulting second acid-base pair (Scheme 10).[53]

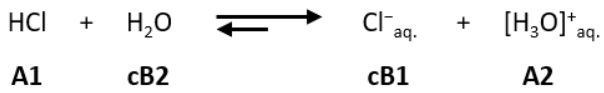

Scheme 10: Reaction of HCl (acid **A1**) with H_2O (conjugated base **cB2**) to Cl^- (conjugated base **cB1**) and $[H_3O]^+$ (acid **A2**) exemplifying the acid-base definition of Brønsted and Lowry.[331,332]

According to the definition by Lewis,[333] an acid is a molecule or atom (ion) with a deficiency of electrons (e. g. H^+, Mg^{2+}, BF_3) and acts as an electron acceptor, while a species with an excess of electrons (e. g. F^-, CO, NH_3) represents a base and acts as an electron donor. Due to the broader range of the definition, a combination of a Lewis acid and a Lewis base does not necessarily lead to a proton transfer like in the Brønsted concept, but to the formation of a dative bond by means of a donor-acceptor complex in a Lewis acid-base adduct (Scheme 11).[53]

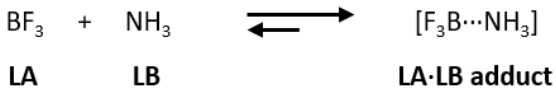

Scheme 11: Formation of an adduct of the Lewis acid (**LA**) BF_3 and the Lewis base (**LB**) NH_3 exemplifying the acid-base definition of Lewis.[73,333]

Since the latter concept holds as an explanation for many reactions, it is applied to a huge variety of chemical systems, especially in organic synthesis. Among many other homogenously catalyzed reactions, the Lewis acid BF_3 mediates reactions such as cyclization and Diels-Alder types and rearrangements.[334] The demand to replace (very toxic) oxidizers like CrO_3, which was, for example, used in stoichiometric amounts in the homogenous industrial production of menadione (Scheme 12), urged the development of Lewis acid catalysts aided by environmentally friendly oxidizers like H_2O_2 in the light of green(er) chemistry.[335,336]

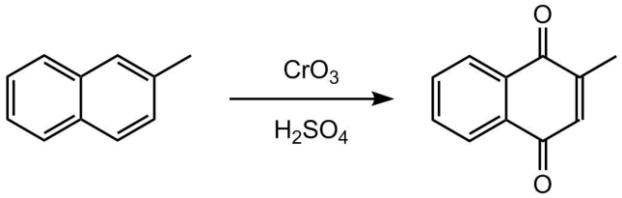

Scheme 12: Industrial production of menadione via the CrO_3/H_2SO_4 route.[336]

An oxidation leading to the same product as featured in Scheme 12 can be facilitated using a Pd^{II} catalyst (polystyrenesulfonic acid resin exchanged with Pd^{II}) and an aqueous solution of H_2O_2.[336] Heterogenous (Lewis acid) catalysts allow for their regeneration and reuse at an overall eased product separation.[335] The use of spatially demanding groups around Lewis acidic and basic centers leads to *frustrated Lewis pairs* (FLP), which can be realized either as an intermolecular interaction in separated molecules or as an intramolecular interaction on a shared backbone. Sterically hindered and thus not able to form a stable adduct, FLPs allow for the activation of small molecules like H_2 or CO_2.[4,337]

Lewis acids can be differentiated by their effect on a corresponding base and subsequently characterized by their strength (acidity). Since the influence of the group bonded to the Lewis acidic center is not only steric but also electronic in nature, the Lewis acids are affected by the hard-soft acid-base (HSAB) principle.[338,339] There are different (standard) methods[340] to characterize and scale Lewis acids, which are categorized as I) global (thermodynamic aspects of the LA·LB adduct), II) effective (change in structure or other physicochemical properties) and III) intrinsic (e.g. EA, LUMO energy).[339] Base specific affinities like the *fluoride ion affinity* (FIA, see Section 1.7.1) scale represent global scales of the Lewis acidity.[339] Spectroscopic methods like NMR and IR spectroscopy provide insight into the effect of a Lewis acid on a selected base.[339] The Gutmann-Beckett method regards the chemical shift $\Delta\delta$ of $OPEt_3$ in the ^{31}P NMR upon coordination to a Lewis acid.[341] Similarly, a characteristic frequency shift $\Delta\tilde{\nu}$ of the ν(CN) of CH_3CN can be observed under the influence of a Lewis acid.[339,342] However, as pointed out by Erdmann and Greb, different acidity scales must be compared cautiously, since the observed trends might differ with respect to the HSAB principle.[339]

1.7.1 Superacids

As outlined in Section 1.1.2, HF reacts as a weak Brønsted acid in aqueous solution, but by adding boron trifluoride, the acidity is remarkably increased from a pK_a value of 3.2 (HF) to 0.5 ($H[BF_4]$),[29] as shown in Scheme 13. Thereby a fluoride ion coordinates a BF_3 molecule (LA) and forms a stable

adduct, the tetrahedral tetrafluoridoborate(III) anion $[BF_4]^-$,[3,53] one of the smallest weakly coordinating anions.[4,343]

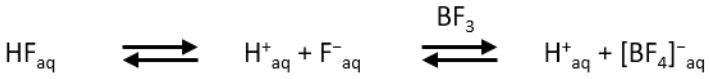

Scheme 13: Formation of tetrafluoroboric acid with pre-equilibrium of HF dissociation in an aqueous medium.[3]

The charge in the tetrahedral $[BF_4]^-$ is delocalized over four uniform fluorido ligands and all possible coordination sites only have a fraction of a fluoride ion's charge, thus lowering the coordination of a proton and eventually leading to a less basic anion.[92] This reactivity principle is exploited for (conjugated) superacidic systems, which are described in the following.[60]

According to Olah,[60] superacids can be categorized as follows:

- Primary superacids of Brønsted (e.g. HSO_3F) or Lewis type (e.g. $B(OTeF_5)_3$)[249]
- Binary Brønsted (e.g. $HF–HSO_3F$) or conjugated Brønsted/Lewis systems (e.g. $HF–SbF_5$)
- Ternary systems (e.g. $HSO_3F–SbF_5–SO_3$)
- Solid systems (e.g. Nafion, zeolithic acids, graphite intercalated superacids)

A Brønsted acid that exceeds the acidity of pure H_2SO_4 with an H_0 value lower than −12 resulting from the acidity function defined by Hammett and Deyrup[344] is called a Brønsted superacid.[60] The acidity using the Hammett acidity function (eqn. 5)[4,60,344] is determined by adding a weak base like 4-nitro-aniline to the superacidic system. The change in color upon protonation is analyzed spectrophotometrically and the ratio of the concentration of protonated $[BH^+]$ and non-protonated base [B] derived accordingly.

$$H_0 = \mathrm{p}K'_{\mathrm{BH^+}} - \log\frac{[\mathrm{BH^+}]}{[\mathrm{B}]} \qquad (5)$$

In contrast to its low acidity in aqueous media, neat anhydrous HF itself represents a superacid (H_0 = −15.1).[60] Its sensitivity towards impurities like water even in smallest quantities leads to higher values of up to H_0 = −11.[60] In analogy to aqueous media,[53] the addition of a Lewis acid remarkably increases the acidity of HF, but only an anhydrous environment allows for the use of the even stronger Lewis acids AsF_5 and SbF_5, since both readily hydrolyze in the presence of water. Conjugated systems of Lewis and Brønsted acids result in extremely strong acids with $H_0 \leq -24$ for magic acid ($HSO_3F–SbF_5$) and fluoroantimonic acid ($HF–SbF_5$), while the latter is more sensitive towards the addition of SbF_5 and thus regarded the strongest superacidic system presently known in bulk.[60]

For the purpose to distinguish between and scale strong fluoro-acids, the concept of the *fluoride ion affinity* (FIA) was developed.[66,343,345] A quantitative scale was introduced by Christe and coworkers about 20 years ago,[66] based on the preliminary work of Bartlett and coworkers.[345] The FIA corresponds to the negative amount of energy that is released when a fluoride ion is bound to a Lewis acid. As defined by Krossing, a Lewis superacid represents a species with a higher FIA than gaseous SbF_5.[249] Table 3 contains a compilation of selected Lewis acids and their corresponding FIA upon binding a fluoride ion.

Table 3: Fluoride ion affinities of selected gaseous Lewis acids given in kJ·mol^{-1}. Species in italics are based on calculated data.

Lewis acid / anion	**FIA**
$BF_3/[BF_4]^-$	338[a]
$AsF_5/[AsF_6]^-$	426[a]
$B(C_6F_5)_3/[FB(C_6F_5)_3]^-$	444[a]
$SbF_5/[SbF_6]^-$	489[a] (434)[a,b]
$Al(O^tBu^F)_3/[FAl(O^tBu^F)_3]^-$	537[a]
PtF_5/[PtF_6]$^-$	(547)[c]
AuF_5/$[AuF_6]^-$	556[a]
$As(OTeF_5)_5/[FAs(OTeF_5)_5]^-$	593[a]
$CB_{11}F_{11}$/$[CB_{11}F_{12}]^-$	716[a]

[a] value taken from ref. [249], calculated at the MP2/def2-TZVPP level of theory using the $COF_2/[COF_3]^-$ reference system; [b] the value in parentheses represents the FIA of liquid SbF_5 (see also ref. [346]); [c] value taken from ref. [273] calculated at the CCSD(T)/CBS level of theory with ZPE, core-valence and scalar relativistic corrections.

All the featured complex anions, even $[BF_4]^-$, the anion of the weakest representative BF_3, belong to the so-called weakly coordinating anions (WCA). In these anions, the charge is distributed over many atoms, which leads to a low charge per atom. Consequently, the lower the charge per (surface) atom, the lower the coordination ability towards a counter-cation and the less basic these WCAs are, which renders for example the abovementioned Lewis acid−HF systems extremely acidic.[4,343] Next to superacids the use of WCAs is widespread and they are applied for instance as components of electrolytes in ionic liquids, for electrodeposition, or in batteries, and play a substantial role in polymer chemistry as well, and therefore represent a research field on their own.[92,93,347]

Owing to the extremely high acidity, the systems comprising AsF_5 and SbF_5 are somewhat indispensable for the synthesis of fluorido compounds of elements in high oxidation states such as $[NiF_3]^+$ or $[AgF_2]^+$ (see also Section 1.5.1).[67] Moreover they stabilize reactive species like $[ClF_2]^+$

in the salt $[ClF_2][AsF_6]$[348] and facilitate the synthesis of unusual compounds like $[AuXe_4][Sb_2F_{11}]_2$[349] or non-classical structural motifs like a sixfold coordinated carbon in $[C_6(CH_3)_6]^{2+}$.[350] Depending on the concentration SbF_5 in *a*HF, oligomeric forms $[Sb_nF_{5n+1}]^-$ (n = 1–4)[60] are formed upon self-aggregation and result in a more acidic HF−SbF_5 system, which corresponds to higher FIA values of the neutral $[Sb_nF_{5n}]$.[4,343,346]

Although the compounds AsF_5 and SbF_5 are very useful for preparative chemistry, they have been less investigated in matrix isolation studies. Be it the high toxicity, reactivity, or the associated complicated handling, these acids were rarely seen in publications after the fundamental work of Aljibury and Redington, who investigated neon and argon matrix-isolated as well as thin film (only SbF_5) samples of these pentafluorides.[73,351]

1.7.2 Van der Waals Complexes

The interaction of weak bases with acidic molecules was considered decades ago from the matrix isolation perspective and will be explained in the following based on the well-established reactivity of BF_3,[73,352–355] with respect to the lack of comparable matrix data for AsF_5 and SbF_5 adducts.[73,351] Generally, complexes with binding energies in the range of 100–200 kJ·mol^{-1} are considered as strongly interacting, while those in the range of 20–40 kJ·mol^{-1} are weakly interacting and denoted van der Waals complexes.[73,356]

Three different formation processes of complexes under matrix isolation conditions are possible:[73]

1) formation in the gas phase ($\Delta H > T\Delta S$)
2) formation upon condensation ($\Delta H < T\Delta S$)
3) location of LA and LB in the same matrix cavity

In principle, the enthalpies of [LA·LB] complexes compete with the entropy. When the enthalpy is high enough (1), a formation in the gas phase is possible. In the condensed state (generally applies to matrix isolation experiments) the temperature is low enough for the entropy term of the Gibbs-Helmholtz equation to become negligible (2), and even a low binding energy leads to the formation of these complexes. If even the enthalpy is not sufficiently high (3), the two binding partners can be trapped in the same matrix cage.[73]

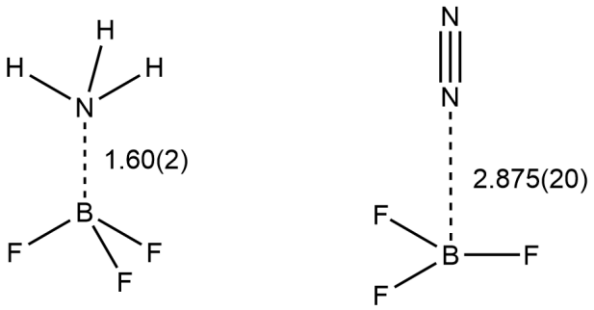

Figure 9: Schematic BF_3 complexes of NH_3 and N_2 with close-to-tetrahedral and planar {BF_3} units, respectively. The experimental B–N distances are given in Å and the structures were adapted from references [73,357–359].

A complex of ammonia and BF_3, which was described as an "archetypal"[73] Lewis acid-Lewis base complex features the boron center in almost tetrahedral local symmetry, while a complex with N_2 represents a van der Waals complex comprising an almost planar {BF_3} moiety, with respective binding energies of about 80[357,360] and 17 kJ·mol^{-1}[358] (Figure 9). Microwave spectra reveal that the van der Waals complexes [BF_3·CO] and [BF_3·Ar] feature a planar {BF_3} unit, too.[358] Thus, the degree of deformation becomes a criterion for the strength of the interaction. The investigation of loosely bound complexes is principally best performed using a tracer moiety that is IR active (favorably used spectroscopic technique in matrix isolation investigations, see Section 1.10.2) in both its coordinated and isolated forms, for example {CO} or {CN} moieties.[73] Consequently, the 'best' conditions are when the Lewis acid and Lewis base are IR active and when both are deformed upon coordination, which has an impact on the IR spectrum.

Table 4: Gas phase basicities (given in kJ·mol^{-1}) of selected fluorinated and non-fluorinated molecules including common impurities in matrix investigations of fluorinated molecules. All values were taken from references [73,361].

Base	Gas phase basicity
NH_3	819.0
H_2O	660.0
AsF_3	604.2
CO_2	515.8
CF_4	503.7
SiF_4	476.6
N_2	464.5
HF	456.7
O_2	396.3
Ar	346.3
F	315.1
F_2	305.5
Ne	174.4

Table 4 features gas phase basicities of selected Lewis bases, which are relevant for the experiments potentially leading to the adducts [LA·F_2] of Lewis acids and molecular fluorine. In accordance with the examples of the complexes mentioned above, the interaction of a Lewis acid like BF_3 with a base and the probability to observe a complex is correlated to the base strength, i.e. the gas phase basicity. Consequently, each of the common impurities[180,362–365] such as CO_2, SiF_4, HF and even Ar might represent a competing base to F_2 and makes the study of [LA·F_2] complexes (Section 3.1) challenging. Noteworthy, a complex is geometrically well-defined accompanied by sharp bands in the IR spectrum if its binding energy exceeds a threshold of about −10 kJ·mol^{-1}, as given by Ault.[73,354]

1.8 Lewis Acid-Mediated Fluorination Reactions

It is indisputable that molecules such as BF_3, AsF_5, and SbF_5 act as electron-pair acceptors and exhibit an increasing FIA in the given order,[66] yield the stable $[BF_4]^-$, $[AsF_6]^-$ and $[SbF_6]^-$ salts or compounds with molecular or ionic fluorides, and increase the acidity of *a*HF.[4,130,131,366]

The oxidation of Xe with elemental F_2 aided by AsF_5, SbF_5 and even *a*HF yielding $[XeF]^+[AsF_6]^-$, $[XeF]^+[SbF_6]^-$ and XeF_2, respectively,[130–132,367] takes place in the dark and at temperatures where the respective acid is liquid (Scheme 14), although the reaction of only the elements Xe and F_2 does not proceed without an external activation by photolysis, heating or electrical discharge.[129]

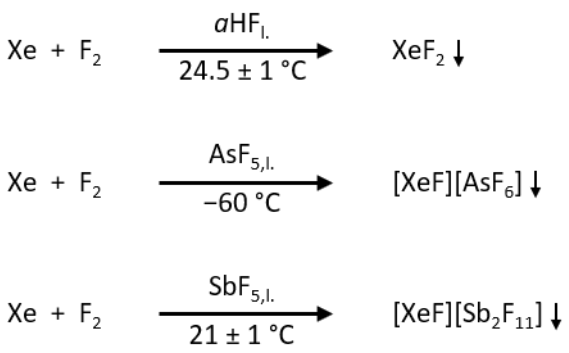

Scheme 14: Liquid Lewis acid-mediated oxidation of xenon with fluorine in the dark.[130–132]

These reported observations lead to the questions how the system Xe/F_2 is activated and what the exact role of the added Lewis acid is. Principally, two different roles of the Lewis acid are conceivable:

- activation of F_2 by the formation of an $[LA{\cdot}F_2]$ adduct as a stable intermediate[195]
- formation of a transient $[LA{\cdot}F_2]$ adduct and product stabilization by a WCA[368]

The second point explains the products obtained for the AsF_5 and SbF_5 mediated reactions (Scheme 14). However, it does not explain the low temperatures at which the reactions occur (especially in liquid AsF_5), nor the activation by *a*HF. To shed light into these reactions, one must control the reaction conditions by means of concentration of the reactants and the energy input. This could be achieved by the matrix isolation method, which is portrayed in Section 1.10. An outline of the known complexes of F_2 is featured in the following Section 1.9.

1.9 Complexes of Molecular Fluorine

Due to the high reactivity of elemental fluorine (cf. Section 1.1, Section 1.3), complexes containing {F_2} units are rarely seen in the literature[73,110] and will be highlighted in the following, beginning with the fundamental concept of halogen bonding.[38,110,369,370]

The halogen molecules X_2 (X = F, Cl, Br, I) are characterized by an anisotropic electrostatic potential,[38,110,369,370] with a torus of a more negative electrostatic potential around each atom perpendicular to the bonding axis and a terminal σ-hole with a more positive electrostatic potential along the bond axis on each end of the molecule (Figure 10).

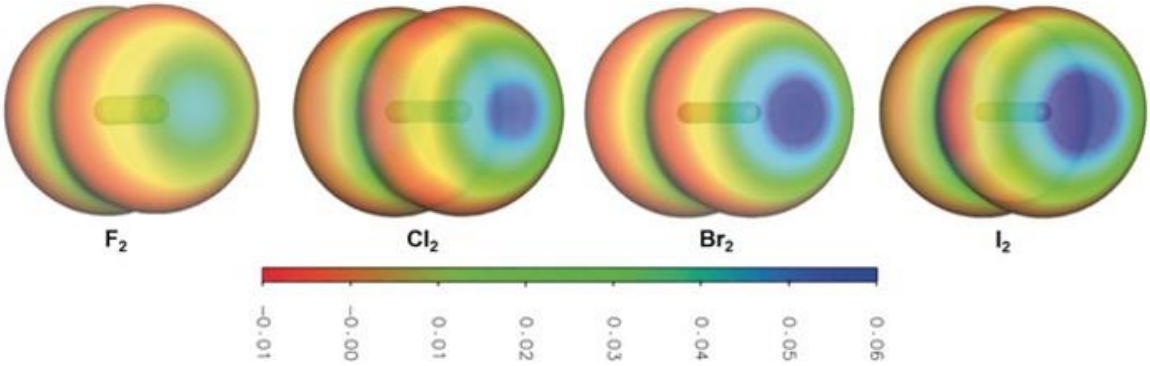

Figure 10: Mapping of the electrostatic potentials of the dihalogen molecules F_2, Cl_2, Br_2 and I_2 (ranging from −0.01 (red) to +0.06 a.u. (blue)) onto their electron densities at an isosurface value of 0.0035 a.u. obtained at the B3LYP-D3/def2-TZVPP level of theory. The figure was extracted from reference [110] and reprinted with the permission of Wiley.

This anisotropic distribution of the electron density defines the possibilities of orientation of the halogens towards both Lewis acids and bases. In the presence of a base the halogens are coordinated linearly, with the σ-hole pointing towards the nucleophilic center, which is reflected for example in the polyhalogen anions and F_2-Lewis base complexes (vide infra).

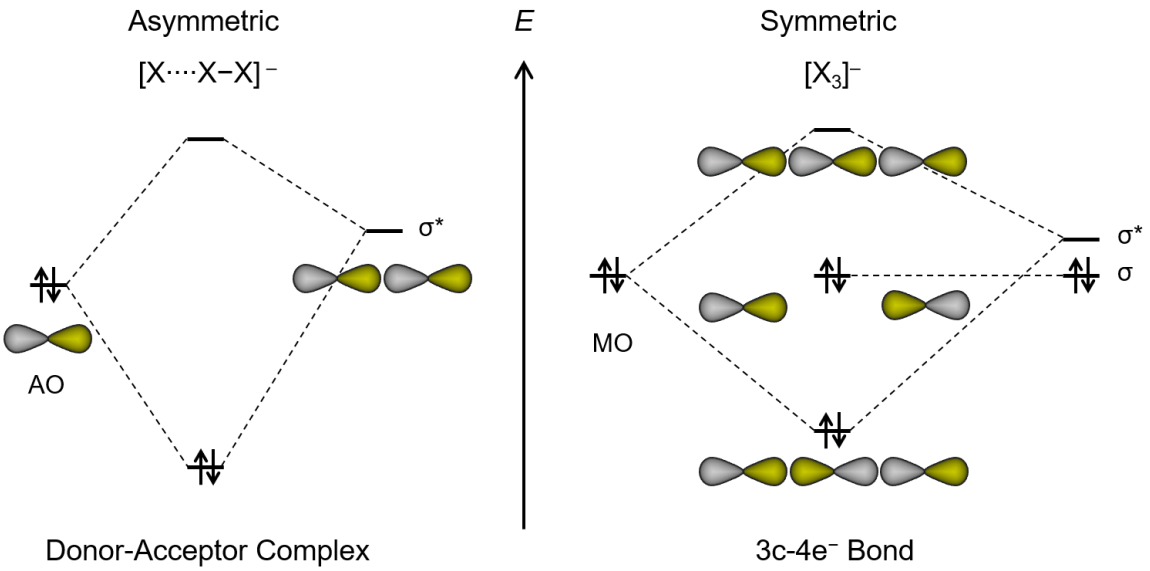

Figure 11: Molecular orbital schemes for asymmetric ($[X\cdots X{-}X]^-$) and symmetric ($[X_3]^-$) trihalogen monoanions (X = F, Cl, Br, I) adapted from references [110,371].

Taking trihalogen monoanions as an example (Figure 11), asymmetric representatives are regarded as donor-acceptor complexes of a Lewis base X^- and an acid X_2 (X = F, Cl, Br, I), while symmetric species are best described with a 3c-4e⁻ bond, mirroring the higher negative charges of the terminal atoms compared to the central one.[110] By choosing the right cation and the right stoichiometry, even large anions like $[Cl_{13}]^-$ with six coordinated Cl_2 molecules and large networks like $[I_{26}]^{4-}$ and $[Br_{20}]^{2-}$ can be obtained.[369,370,372] This concept also applies to polyinterhalogens and poly-pseudointerhalogens and has led to a large variety of new compounds like the octahedral $[Cl(BrCl)_6]^-$ and the distorted pyramidal $[Br(BrCN)_3]^-$ monoanions.[373]

In contrast, the halogens coordinate an acidic center in an end-on fashion but in angular geometry, with the torus of higher electron density pointing towards the electronegative center of the Lewis acid, as featured for instance in $[AuF_5{\cdot}F_2]$.[195] This continues in side-on coordination with the smallest polyfluorine anion, the difluorine radical monoanion $[F_2]^{\bullet-}$ (in the following $[F_2]^-$)[110], as depicted for selected $M^+[F_2]^-$ ion pairs in Figure 12.

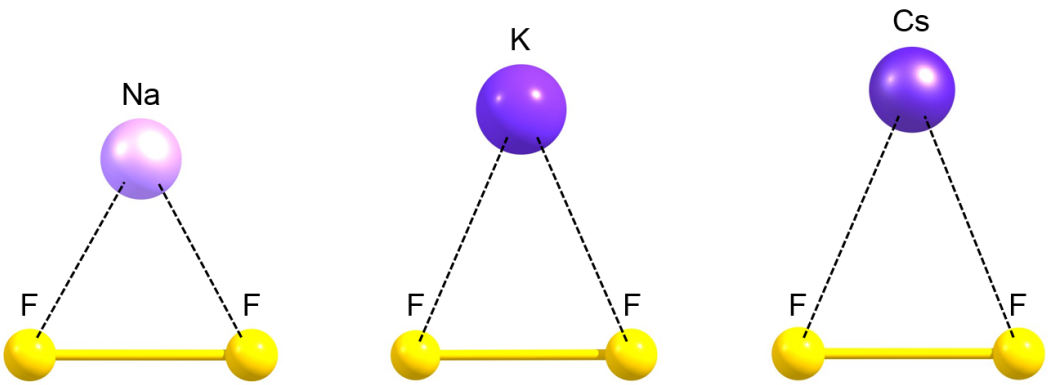

Figure 12: Minimum structures of Na[F_2], K[F_2] and Cs[F_2] calculated at the RI-B3LYP-D4/def2-TZVPP level of theory.

Although there is a large variety of ionic polyhalogen compounds for the heavier homologues Cl, Br and I, the polyfluorine anions seem to be strictly limited to the $[F_5]^-$, $[F_3]^-$ and $[F_2]^-$ species.[110] All of them have been observed under matrix isolation conditions.[110] The difluorine monoanion $[F_2]^-$ was solely observed in the form of ion pairs[74,374,375] (except for the free form in mass-spectrometric measurements),[376] while $[F_3]^-$ is known in ion pairs and its free form,[10,18,75–77,377,378] and $[F_5]^-$ was exclusively observed in its free form under matrix isolation conditions.[10,77,378]

Table 5: Experimental vibrational frequencies (given in cm^{-1}) and absorption maxima (given in nm) of argon matrix-isolated M[F_2] (M =Li, Na, K, Rb, Cs).

Species	Medium	$\tilde{\nu}_{IR}$(ν(M–F_2))	$\tilde{\nu}_{Raman}$(ν(F–F))	λ_{max}
Li[F_2]	Ar	708[a,b]	452±1[a,d]	300±3[e]
Na[F_2]	Ar	454[a]	475±1[a,d]	310±1[e]
K[F_2]	Ar	342[a]	464±1[a,d]	294±1[e]
Rb[F_2]	Ar	266[a,c]	462±1[a,d]	288±1[e]
Cs[F_2]	Ar	248[a,c]	459±1[a,d]	284±1[e]

[a] values taken from ref. [374]; [b] only for ^{6}Li[F_2], no corresponding band was reported for ^{7}Li[F_2]; [c] assignment to $(MF)_2$ could not be ruled out; [d] values taken from ref. [74]; [e] values taken from ref. [375].

Regarding Table 5, the Raman bands of the M[F_2] species are assigned to ν(F–F) modes (small metal-dependent shift), the IR bands to symmetric M–F_2 stretching modes (strong metal dependent shift) but a corresponding antisymmetric ν_{as}(F–M–F) had not been observed by Andrews and coworkers and reported to be of very low IR intensity by Gutsev et al.[110,374,379] However, in IR experiments, the ν(F–F) had been exclusively observed as a weak band in the sodium case.[374] The absorption maxima of the different M[F_2] only slightly differ from the one of fluorine (λ_{max} = 283 nm).[8,9] The $[F_2]^-$ anion was first observed in EPR studies after X-ray irradiation of an LiF sample at −180 °C,[375,380] and also after the electron bombardment of potassium bifluoride K[HF_2] single crystals,[381] and the X-ray irradiation of $KMgF_3$ single crystals,[382] each at

77 K (see the references).[110] When F_2 was employed as an electron acceptor to probe radical anions next to radical cations in neon matrices, also $[F_2]^-$ was observed in EPR experiments.[383,384]

Table 6: Experimental IR frequencies of $M[F_3]$ and the free $[F_3]^-$ given in cm^{-1} (n.o. = not observed). If more than one value for a specific band position was reported, the most accurate one is given.

Species	***ṽ*(Ne)**	***ṽ*(Ar)**	**Assignment**
$Li[F_3]$	n.o.[a]	n.o.[a]	ν_3 (ν_{as})
$Na[F_3]$	n.o.[a]	n.o.[a,e]	
$K[F_3]$	561.2[a]	549[e,f]	
$Rb[F_3]$	561.2[a]	549.2[a,e,f]	
$Cs[F_3]$	561.3[a,b]	549.9[a,c,e,f]	
$[F_3]^-$	524.7[b,c]	510.6[a,c]	
$[F_5]^-$	850.7[b]		
$Li[F_3]$			$\nu_1 + \nu_3$ ($\nu_s + \nu_{as}$)
$Na[F_3]$			
$K[F_3]$	946[d]		
$Rb[F_3]$	944[d]		
$Cs[F_3]$	941[d]	923.4[a]	
$[F_3]^-$	914[d]	892.0[a]	

[a] values were taken from ref. [377], the free $[F_3]^-$ was only observed when the corresponding MF_3 was observed; values were taken from [b] ref. [10,77], [c] ref. [18], [d] ref. [378], [e] ref. [76], [f] ref. [75].

In the early matrix isolation studies of polyfluorine monoanions by Ault and Andrews,[75,76] when the laser ablation of metals and metal salts had not been developed yet,[385,386] they used Knudsen cells for the evaporation of alkali metal fluorides at 490 (CsF) to 750 °C (NaF).[75,76,387] Since no plasma is created by the thermal evaporation of the metal fluorides, a free $[F_3]^-$ cannot be produced from F–F bond cleavage and subsequent electron capturing processes,[10,18,378,388] and a co-deposit of MF and F_2 leads to the corresponding $M[F_3]$ ion pairs.[75,76]

Upon the laser ablation of metals and metal fluorides (see Figure 17), also the free trifluorine monoanion is achievable,[18,377,378] while higher concentrations of fluorine additionally allow for the formation of the free pentafluorine monoanion $[F_5]^-$.[10,77] The experimental MIR frequencies of the species $M[F_3]$ and free $[F_3]^-$ are compiled in Table 6. The latter species as well as $[F_5]^-$ are proposed to form upon the reactions of F_2 enabled by the plasma formed upon pulsed laser ablation (see Scheme 15).

(1) $M \xrightarrow{h\nu} M^+ + e^-$

(2) $F_2 \xrightarrow{h\nu} 2\,F^\bullet$

(3) $F^\bullet + e^- \longrightarrow F^-$

(4) $F^- + F_2 \longrightarrow [F_3]^-$

(5) $[F_3]^- + F_2 \longrightarrow [F_5]^-$

Scheme 15: Mechanism for the formation of polyfluorine monoanions with laser-ablated metals as proposed in reference [10].

Upon the impact of a laser pulse on a metal target (cf. Scheme 15), a plasma containing cations and electrons is formed (1). The light emitted by the plasma lies also in the UV region and leads to the homolytic bond cleavage of the F–F molecules (λ_{max} = 283 nm[8,9], (2)). Fluorine atoms ($F^\bullet$) further react with electrons in the gas phase to form the corresponding F^- anion (3), which can then coordinate to an F_2 molecule to form $[F_3]^-$ (4). The pentafluorine monoanion is thought to be formed upon the coordination of a second F_2 molecule, according to (5).[10]

That the species $M[F_3]$ was observed for the Cs, Rb and K cases but not for the lighter alkali metals Na and Li was explained by a higher coulombic interaction of the latter two with the fluoride ions.[377]

The heavier halogens as well as interhalogens were investigated regarding their reactivity towards different Lewis bases.[73] Molecular ClF features a permanent dipole and is therefore IR active and suitable for studying interactions with coordinating molecules, as has been reviewed by Young.[73] In accordance with the gas phase basicities of the N donor bases,[361] the contribution of the ionic form $[LB{\cdot}Cl]^+F^-$ in the $[H_3N{\cdot}ClF]$ and $[(CH_3)_3N{\cdot}ClF]$ complexes increases with the stabilization energy, while the Cl–F bond is elongated.[73,389] The higher polarizability of Cl_2 allows for an easier activation of the ν(Cl–Cl) mode compared to the difluorine molecule. The observability of the X–X stretching (X = halogen) mode of the respective complex is directly correlated to the strength of interaction.[73] In contrast to that, F_2 as a part of complexes has been studied for fewer examples and, of those rarities, the reactivity was studied in the presence of NH_3[390] or SeCO (ν(F–F) at 851.7 cm^{-1}),[391] depicting rather electron-donating basic but not acidic molecules.[73]

Table 7: Reported matrix-isolated and gas phase difluorine complexes with band positions of F–F stretching vibrations given in cm^{-1}. The complexes are still featured, even when the ν(F–F) was not observed (n.o.) and the assignment solely based on the shifted modes of the counter-moiety (compared to the parent species). Complexes found in the gas phase with exclusively microwave data available are featured with "MW". The reaction of HCN and F_2 was studied in solid argon, but a complex was only found in the gas phase. Calculated interaction energy values (ΔE_{int}) are given $kJ \cdot mol^{-1}$ and at the respectively highest level of theory in the references.

Complex	**Medium**	$\tilde{\nu}$**(ν(F–F))**	ΔE_{int}	**References**
F_2	Ar	892	–	[74,180]
$[FH \cdot F_2]$	Ne	892[a]	−6.27	[364,392]
$[Hg \cdot F_2]$	Ar	877.7	–	[180]
$[H_2O \cdot F_2]$	Ar	877.5[b]	−1.6	[393,394]
$[OCSe \cdot F_2]$	Ar	851.7	−34.16	[391]
$[H_3N \cdot F_2]$	Ar	781	−3.6	[355,390,395,396,397]
$[H_2S \cdot F_2]$	Ar, gas	n.o., MW	–	[398,399]
$[(H_2S)_2 \cdot F_2]$	Ar	n.o.	–	[398]
$[CH_3CN \cdot F_2]$	gas	MW	–	[400]
$[HCN \cdot F_2]$	Ar, gas	MW	–	[401]
$[(CH_2)_2O \cdot F_2]$	gas	MW	–	[402]
$[MF_2 \cdot F_2]$ (M = B, Al, Ga, In, Tl)	Ne, Ar	n.o.	−518[c]	[403]

[a] The band was reported to not be shifted from the F_2 fundamental and not be observed in argon, while the bands of the {HF} moiety are reportedly shifted by only 4 cm^{-1} (see ref. [364,393]). The given isomer is in accordance with calculated data in references [364,392,404]. [b] The band was reportedly not shifted for different isotopomers of the complex (ref. [393]). [c] value for $[BF_2 \cdot F_2]$, the interaction energies of the other $[MF_2 \cdot F_2]$ are comparable and found in reference [403].

Keeping the strong dependence on the interaction in mind, with similar polarizabilities of Ar and F_2 (same number of electrons),[402] it is not surprising that the ν(F−F) was not observed for all reported F_2 complexes compiled in Table 7.[405] As pointed out by Karpfen, the $[H_3N \cdot F_2]$[395] complex "[...] *constitutes an instance of a very weak interaction, dominated by a dispersion distribution* [...]".[38] This is in line with the interaction energies of the other complexes, which are very low for $[H_2O \cdot F_2]$[393] or even not reported for most of the F_2 complexes (cf. Table 7). Some of these complexes were only observed in the gas phase.[405] In contrast, the interaction in $[OCSe \cdot F_2]$[391] (explicit feature below) and $[MF_2 \cdot F_2]$[403] is exceptionally strong. Although the latter was reported to contain a discrete $\{F_2\}$ unit, no ν(F−F) was observed.[403]

The $[OCSe \cdot F_2]$ complex reported by Della Védova and coworkers is a 'textbook' example of an F_2 complex and will be briefly highlighted in the following:[391] The OCSe molecule contains two possible binding sites O and Se, the former binding to F_2 with −0.11 $kJ \cdot mol^{-1}$ in linear conformation

(d_{F-F}= 1.412) and the latter one with −34.16 kJ·mol^{-1} in angular conformation (d_{F-F}= 1.553) at the B3LYP/6-31+G* level of theory. The elongation of the F−F bond distance is caused by the donation of electron density of the Se lone pair into the antibonding σ* orbital of F_2. This weakening of the bond is reflected in a redshift of the ν(F−F) by remarkable 40 cm^{-1} with reference to elemental fluorine.[74,180,391,406] This also perturbs the other vibrations in the molecule, with the result that also the strong ν(C=O) is blue-shifted but only by 2.4 cm^{-1}.[391] If the ν(F−F) is not observable due to a small activation as for example the O-donor in the described [SeCO·F_2] example,[391] one principally can only rely on the shifted features of the other parent molecule supported by quantum-chemical results, as it was shown for the side-on complexes [MF_2·F_2] (M = B, Al, Ga, In, Tl) by Wang et al.[403]

This principally defines the criteria for revealing a complex comprising an {F_2} moiety in accordance with references [10,73,77,195]: I) Activation of the {F_2} moiety should lead to a gain in IR intensity and shift of the ν(F−F) accompanied by an elongation of the F−F distance. II) The vibrational band(s) of the coordinating moiety are shifted as well but should be found in close vicinity to the parent bands. A clear assignment of these bands must be supported by computed structural and spectral data.

A translation of the $[F_3]^-$ into preparative chemistry was attempted by the synthesis $[N(CH_3)_4]^+[F_3]^-$ in low temperature solutions of $[N(CH_3)_4]F$ in acetonitrile or fluoromethane but was unsuccessful due to the inherent instability of this trifluorine monoanion salt.[407] The anionic species F^-, $[F_2]^-$ and $[F_3]^-$ were observed in the gas phase after initial electron capturing by F_2 in mass spectrometric experiments[376] and CsF is known to catalyze the oxidation of CO_2 leading to $CF_2(OF)_2$ with elemental fluorine.[408,409] It should be noted that the ion pair Cs[F_3] does not rearrange to produce higher oxidation states than +I under matrix isolation conditions.[77] DFT calculations show that at sufficiently high pressures (30 GPa) the rearrangement should be enabled to yield $Cs^{III}F_3$,[77,410,411] which was reviewed and discussed as solid phases with a higher fluorine content at even higher pressures in the literature.[122,410] Within the debate about the mechanisms of the Simons process, only speculations about a [NiF_2·F_2] complex as a mediator appeared.[50,162,171,172]

1.10 The Matrix Isolation Technique

The direct monitoring of chemical reactions, which are taking place on the time scale of picoseconds,[178] is simply impossible under conditions achievable in a common chemical laboratory. Yet, there are principally two ways to provide access to the investigations of these ultrafast processes: looking fast, or stopping motion.[178,412,413] The first possibility is the direct observation of chemical reactions via pump-probe processes using femtosecond lasers,[178] which is a broad field on its own.[414] The second method is perturbing the chemical system by freezing out nuclear motion and trapping species quantitatively in an inert environment and is called matrix isolation.[412,415–417] The method will be explained mainly focused on the working techniques and common experimental parameters used at Freie Universität Berlin for conciseness, while many other options are possible and will only be mentioned briefly.[412,415,418–420]

The fundamental principle of matrix isolation is the deposition of a reactive species (guest) diluted in an inert gas (host) onto a spectroscopically suitable support (a window or a mirror), which is positioned in a high vacuum chamber and cooled to sufficiently low temperatures, where the host gas is solid and has no significant vapor pressure.[412,415,421,422] Its development is dated back to the fundamental work of Whittle, Dows and Pimentel in 1954,[415] as well as to contributions of other groups.[416,417,423,424] The isolation under cryogenic conditions features two advantages: First, the reactive species (usually diluted to 0.1–1.0 %) is statistically distributed in the solid matrix and therefore well separated from their next neighboring molecule, thus intermolecular interactions are largely inhibited. The matrix-isolated system can therefore be investigated for an indefinite amount of time. Second, the temperature of usually 5 K in neon is low enough to preclude molecular decomposition and hamper particle diffusion.[384,388,415,422] With the low temperature the entropic term of the Gibbs-Helmholtz equation becomes negligible, which enables the formation of transient species such as weakly bound van der Waals complexes.[73,352,354,355,388]

A matrix isolation system consists of a cold head, which represents the heat sink for the mounted matrix support and is pivoted in a high vacuum chamber (‘matrix chamber’). The chamber holds ports for one or more gas inlets and for windows, which are optically transparent for the chosen spectroscopic method or irradiation processes.[354,355,421,425,426] An electrical resistance heater with a thermocouple is mounted on the cryostat close to the matrix support to allow for annealing of the matrix. The high vacuum of the system can be maintained below $1 \cdot 10^{-6}$ mbar by an oil diffusion pump pre-pumped by a rotary pump.[421] The development of durable closed-cycle helium cryostats (taking the places of liquid H_2 or liquid He cryocoolers) and commercially available FTIR spectrometers were the gamechangers that made the matrix isolation technique applicable for a

larger community.[412,421] An example of the functional principle of a matrix isolation system comprising a deposition unit for laser ablation and multiple windows for irradiation as well as the simultaneous IR and UV/Vis investigation of a sample is shown in Figure 13.

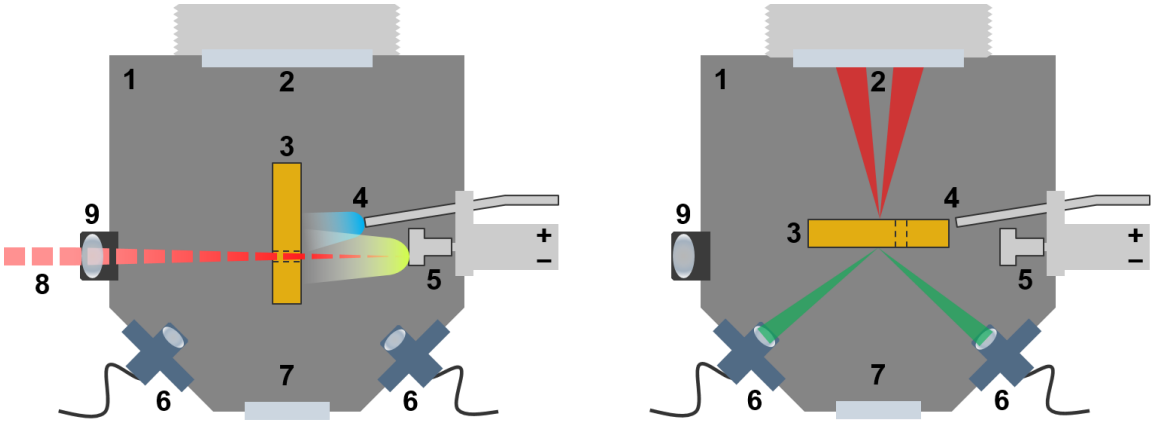

Figure 13: Schematic of a matrix isolation setup for the co-deposition of a reactive gas mixture with laser-ablated metals or metal salts (left) and measurement of IR and UV/Vis spectra in reflection (right), with the following components: **1**) high vacuum chamber maintained at $p \leq 10^{-6}$ mbar by an oil diffusion pump coupled to a rotary pump (pre-pump); **2**) CsI window for the measurement of IR spectra in reflection (spectrometer and transfer optics were omitted for clarity); **3**) rotatable gold-plated copper mirror (matrix support) cooled to 5 K; **4**) gas inlet for reactive gas mixture (blue plume); **5**) metal/metal salt target on a rotatable target holder (yellow plume, detailed view in Figure 16); **6**) connector for fiber optics for the measurement of UV/Vis spectra; **7**) SiO_2 or Al_2O_3 windows for photolysis experiments; **8**) incident pulsed laser light; **9**) focusing lens.

With the availability of this versatile method with adaptable systems, creativity emerged and researchers in many different fields made use of it. Matrix isolation studies range from fundamental research of purely inorganic compounds,[77,355,427] over the study of reaction intermediates,[388] such as organic radicals,[412,428] and mechanistic aspects of industrial processes by means of metal clusters[429] to atmospheric[430] and even astrochemistry.[431,432] In the light of many fluorinated inorganic compounds being highly toxic, these species and novel derivatives thereof are ideal to be studied in matrix isolation experiments, since only small amounts of substance must be produced and handled for this purpose.[27,422,433] The isolating conditions offer the opportunity to study extreme systems in (extraordinarily) high[186,268,434] and unusually low oxidation states.[223,268]

1.10.1 Methods for Generating Matrix-Isolated Samples

As it is already evident from the discussion above (Section 1.10), the matrix isolation techniques can be employed to investigate a wide range of systems, and thus the species under investigation may not be generated in identical ways. Many different sample generation procedures are

documented, notably in reference [435]. Briefly, molecular cations can be generated by microwave discharge or photoionization,[384,388] molecular anions by electron bombardment or the laser ablation of metals,[10,384,388] and metal atoms and clusters by for instance the use of effusive Knudsen cells with subsequent annealing.[420] The focus of this work lies on the deposition and photochemistry of reactive volatiles[436] with or without co-deposited laser-ablated metal atoms.[73,419] Accordingly, the following options are representatives for the preparation of matrix-isolated species:[412]

(1) deposition of a pre-mixed gas mixture of a reactive gas diluted in the host gas
(2) deposition of the host gas passed over a solid sample of the reactive species
(3) combination of a reactive gas mixture and laser-ablated metals or metal salts
(4) photolysis of a matrix-isolated precursor

If the reactive gas is stable and unreactive with respect to the sample vessel, i.e. storable at room temperature for the duration of the experiments (up to several hours), such as F_2 diluted in Ne in an F_2-passivated stainless-steel vessel, option (1) is the method of choice with the advantage of the best control of the reactant concentration. For this reason option (1) is also applicable for mixtures of more than one reactive component diluted in the host and may still be a good choice if the starting material only slightly reacts with the walls of the storage container.[420] If decomposition of the starting material during storage of the gas mixture at room temperature plays a major role, the host gas can alternatively be passed over a solid sample of the reactive species (2).[351] This method can be used for samples with a sufficiently high vapor pressure at lower temperatures (e.g. SbF_5[351], PtF_6[304], MnO_3F[187]), which can be controlled by appropriate cooling baths.[412] Method (2) allows the positioning of the sample very close to the matrix chamber[214] and thus the matrix support, without impairing the experiment due to excessive sample loss upon reaction with the walls of the deposition device. In addition to the simple deposition of gas mixtures, the laser ablation of metals and metal salts (3) increases the number of examinable systems by a cornucopia of reactants, such as excited metal atoms, cations, anions, as well as free electrons, which allow for electron capturing processes (see also Section 1.10.1.1).[18,377,388,425,437] The radiation caused by the plasma, respectively, might impair the experiment by decomposition of the starting material and/or formation of unwanted side products. In the same way, the irradiation with an exciting laser for Raman experiments might lead to eventual decomposition of the matrix sample in terms of wavelength and intensity (Figure 14, b).[73] Alternatively, or additionally, the species of interest can be generated by the photolysis of a precursor via irradiation with light at a suitable wavelength,[27,419,424,433,436,438] preferably in accordance with its electron absorption spectrum.[436]

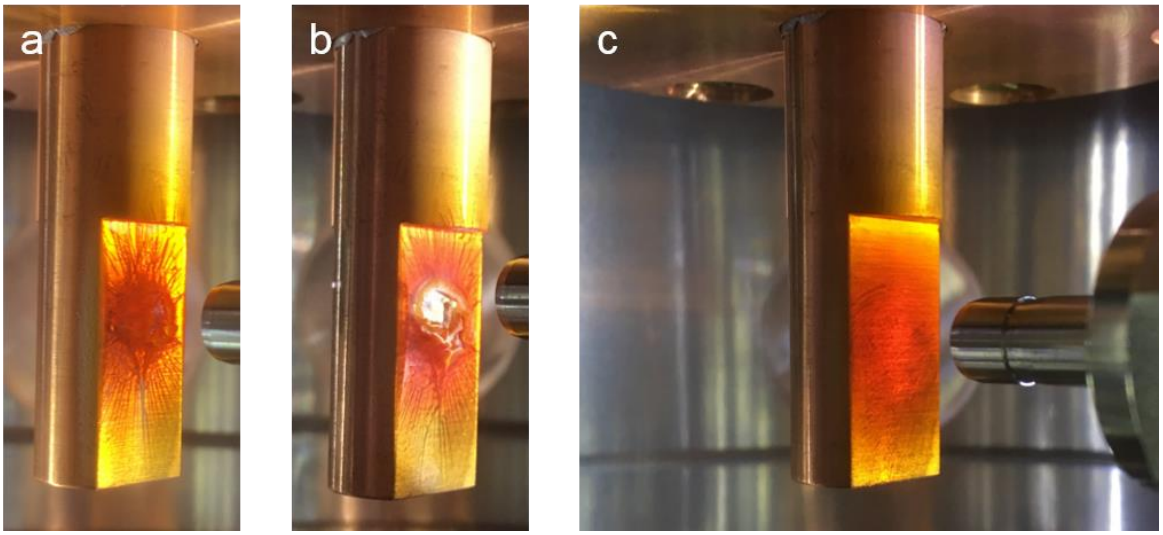

Figure 14: The photos were taken after a) the deposition of PtF_6 in Ar at $T \leq 20$ K, b) the measurement of Raman spectra of this deposit with a green light laser (λ = 532 nm, P = 1000 mW), and c) the deposition of PtF_6 in Ar at T = 22.5 K in an independent experiment.

Besides the possibility of a faster deposition (10–20 min), which reduces impurities and is therefore favored for laser-induced fluorescence investigations, a slow deposition of 1–2 mmol·h^{-1} (0.4–0.7 mbar·l·min^{-1}) for several hours at an appropriate temperature leads to a better optical and thus optimized spectral quality for IR, Raman, and UV/Vis spectroscopy.[420] Moreover, chipping or cracking of the deposited matrix is prevented,[355,420,429] as seen upon comparison of Figure 14 a and c. Impurities are not necessarily part of the sample but might result from its reaction with the walls of the container and the deposition line.[420]

On the subject of suitable matrix hosts, there is a wide range of conceivable matrix host materials available: from (rather) inert (Ne, Ar, N_2, Kr, Xe) to reactive (H_2O, CO, CO_2, cyclohexane, CCl_4, CH_4, H_2, O_2, F_2, and even ammonia).[10,73,313,415,431,439,440] The inert noble gases can be additionally doped with reactants such as N_2,[436] F_2[223] or Xe[441] to study specific reactions. According to an investigation of Beattie and Millington, the perturbing effect is increasing in the order Ne < Ar < $O_2 \approx F_2$ < Kr < Xe < N_2 < CO.[313] An article specifically dealing with host-guest interactions employing FIR, MIR, UV/Vis and XAFS spectroscopy was recently published by Young et al. and gave a comparable order of the hosts.[439] Different splitting patterns were reported on alkali metal hexafluoridouranates in argon and nitrogen matrices.[314] The overall smallest shifts compared to the gas phase values are observed in neon matrices.[73,388,439]

After the deposition of the matrix, the embedded species can be manipulated in a way that unimolecular processes of isolated molecules can be triggered by irradiation of the deposit at a suitable wavelength.[419,436] Alternatively, the matrix can be subjected to annealing to allow for

diffusion of certain species and enable bimolecular reactions.[377,426] Both processes are illustrated in Figure 15 at the example of the decomposition and (re-)formation of the $Cs^+[F_3]^-$ ion pair.

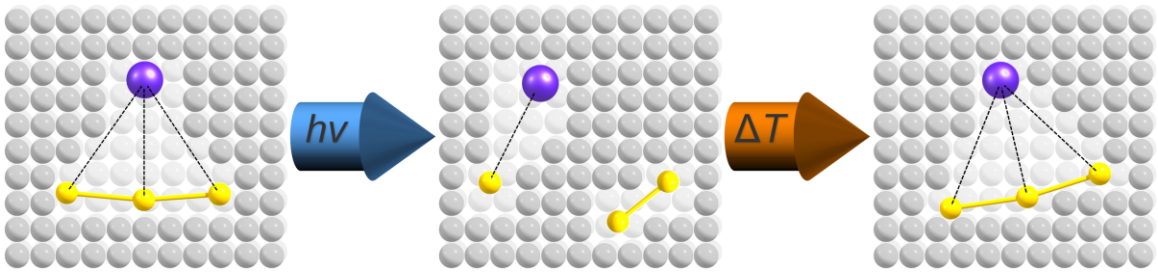

Figure 15: Schematic illustration of the decomposition upon blue light photolysis and the formation of the $Cs^+[F_3]^-$ ion pair upon annealing, in accordance with the observations in Figure 49 and references [10,77,377,378]. The yellow spheres represent fluorine, the purple spheres cesium and the grey spheres argon atoms.

Since the matrix host forms a rigid cage around the embedded species, smaller atoms such as hydrogen and fluorine atoms have a larger mobility than heavier atoms or small molecules.[418,420,422,442,443] In the sense of the 'cage effect' two distinct particles formed upon decomposition by irradiation but trapped in the same matrix site likely recombine to the starting material or rearrange.[420] If one of the fragments diffuses, the recombination is precluded.[422] On the other hand, weakly bonded complexes can be observed when the parent molecules are trapped adjacent in the same matrix site as a cage pair.[73]

1.10.1.1 Laser Ablation of Metals and Metal Salts

The laser ablation of metals[18,385,386,388,437] and metal salts[377,378] largely extends the possibilities of examinable systems under matrix isolation conditions with ionic species[18,388,441] and metal centers in unusually low[210,268] and high[10,186,434] oxidation states. The operating principle is shown by the example of the co-deposition of platinum hexafluoride with laser-ablated metals and metal salts in Figure 16.

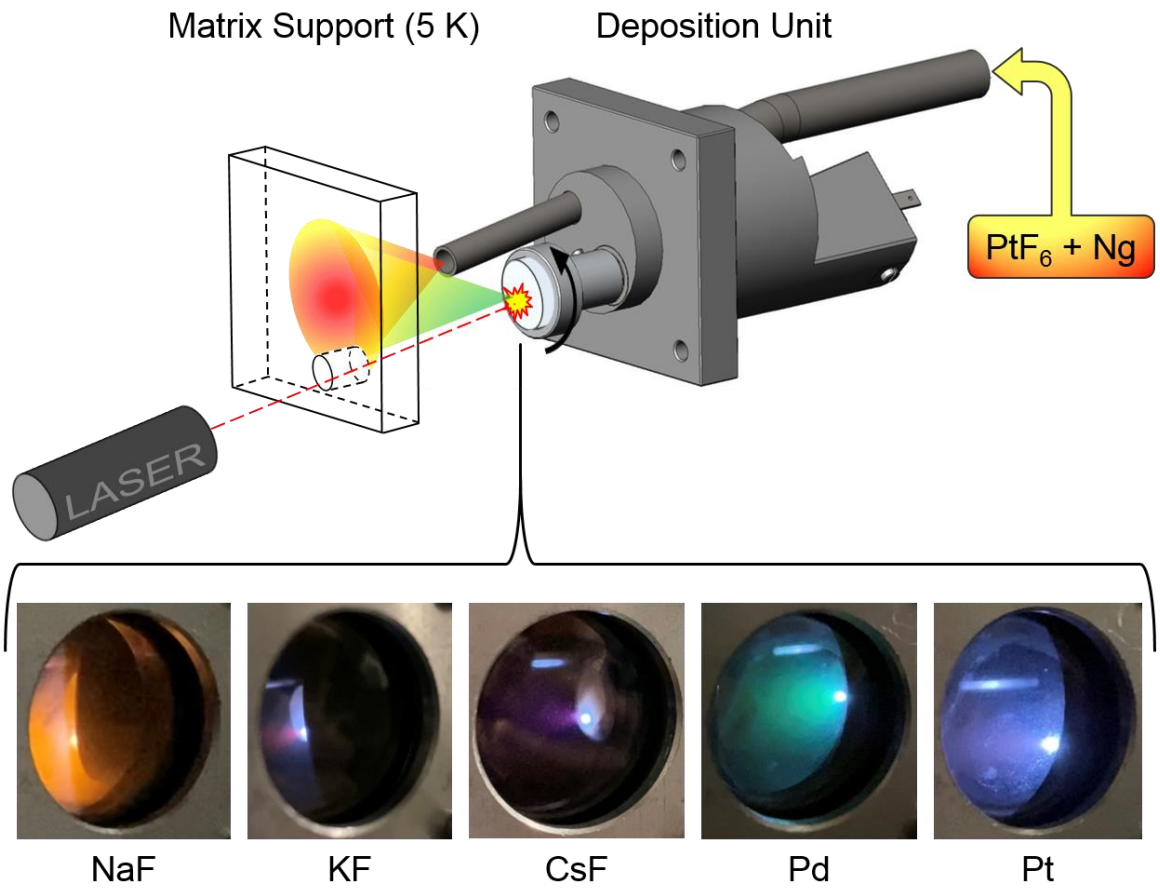

Figure 16: Functional principle of the co-deposition of PtF_6 and laser-ablated metals and metal fluorides (detailed process in Figure 17) as well as photographs of the plasma plumes during the laser ablation of NaF, KF, CsF, Pd and Pt. The pulsed laser in the operating setup is guided into the high-vacuum chamber onto the rotating target via a mirror and additionally focused with a focusing lens, while the latter two were omitted for clarity. The radially decreasing PtF_6 density (as seen in Figure 14 and ref. [304]) of a deposited matrix is highlighted red to yellow. A top view and a cutaway drawing with a detailed description of the deposition unit are found in Figure 99 and Figure 100, respectively.[444]

The process of laser ablation with respect to the events taking place upon the impact of a laser pulse on a target starts with the liberation of electrons. They leave positively charged metal centers in place, which are then expelled from the target due to Coulomb repulsion in a so-called 'Coulomb explosion'. Subsequently, further matrix material is evaporated thermally.[378] The whole process is taking place on a nanosecond time scale and is described in detail in reference [378]. Time-resolved photographs of the pressure-dependent expansion of a plasma-plume are found in reference [445]. The species formed upon the laser ablation of a metal target are illustrated in Figure 17.

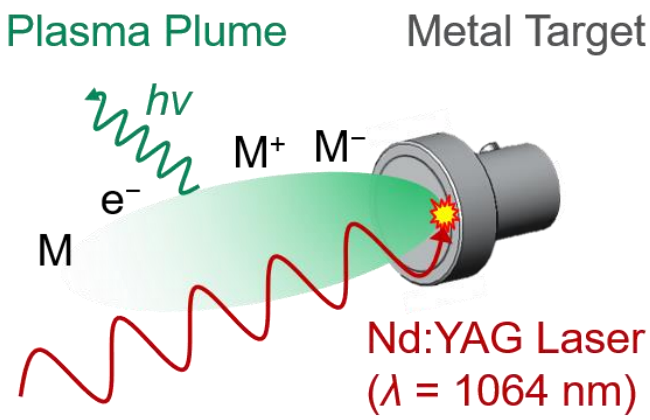

Figure 17: Laser ablation of a metal target. The formed plasma contains free electrons as well as metal cations, atoms, and anions, in accordance with reference [10].

Although the alkali metal fluorides are transparent for the light at λ = 1064 nm (Nd:YAG laser), their laser ablation is still possible (except for monocrystals) due to color centers caused by defective sites in the crystal, which works especially well for pressed targets made from pestled salts.[377] The electrons formed during the laser ablation of elemental metals[388] allowed for the formation of the free $[F_3]^-$ and $[F_5]^-$ anions and also for a conclusion on the mechanism of their formation (cf. Section 1.9 and Scheme 15 therein).[10]

1.10.2 Characterization of Matrix-Isolated Species

As only small amounts of substance including matrix host and reactive species are deposited, which are in the order of 4 mmol for long-term deposited matrices (this work), the applied characterization method(s) must be very sensitive and tailored to the chemical problem.[435] Thus, matrix-isolated samples have been investigated by FTIR,[421] Raman,[74,75,446] UV/Vis,[298,375] EPR,[384,397] Mössbauer,[73,447] and XAFS spectroscopy,[439,448] and also other methods.[73,435]

The most common method is the Fourier transform infrared spectroscopy (FTIR).[388,412,421,426] IR spectra can be measured in transmission or reflection. For the measurement in transmission the vacuum chamber is equipped with IR-transparent windows, usually made from cesium iodide, and positioned directly in the beam path of the spectrometer. In the setup used in this work, this method needs permanent flushing of the beam path with dry air to suppress atmospheric H_2O. For the measurement in reflection the light is coupled in via transfer optics and the matrix support is a mirror (e.g. gold-plated copper support, cf. Section 4.1.2).[412] The measurement in reflection has the advantages that the IR light passes the sample twice, which doubles the signal-to-noise ratio, and that UV/Vis spectra can be obtained from the same sample (Figure 13).

Besides a possibly useful host-specific shift (Section 1.10.1), isotopic labelling of the starting material could clarify some difficult cases.[186,393,449] The larger the relative mass difference, the stronger the respective shifts in the vibrational spectra, the strongest effect being observed for a H/D exchange.[393] As fluorine is a mononuclidic element and the lighter ^{18}F isotope has a half-life of 109.7 min, fluorine-centered isotopically labelled experiments exceed the range of feasibility.[2] However, the experimental strategy can be projected on other tracers such as different alkali metals or alkali metal salts,[313,374,377] which can cause a shift of the resulting species due to different metal-dependent coulomb interactions.[377]

1.10.3 The Role of Quantum-Chemical Calculations

Besides the costly option of multiple setups allowing for different spectroscopic techniques, a usual matrix isolation setup is limited by up to two characterization methods at a time. Although the comparison with experimental gas phase data of the species of interest is possible and generally used,[388] computational chemistry can improve the assignment of absorption bands or even make it possible in the first place.[421]

The first-principles methods based on density functional theory (DFT) give reliable results and are able to describe systems at low computational cost to obtain the ground states of molecular systems. They will be portrayed briefly in accordance with reference [450]. At the outset, DFT is based on the two Hohenberg-Kohn theorems.[451] The first theorem states that for any interacting particle system the electron density is defined by a unique external potential. The ground state electron density specifies molecular properties. The second theorem states that the variational principle applies for DFT. Using the Kohn-Sham formalism, the electron density of the interacting system can be calculated based on the exactly known non-interacting system. The remaining electron density is treated by the exchange-correlation functional (E_{XC}). The challenging part, the approximate description of E_{XC}, is done in increasing accuracy in the order of local density approximation (LDA), generalized gradient approximation (GGA, e.g. PBE, BP86) or hybrid functionals. The latter, such as the commonly used and generally well-performing B3LYP functional, besides DFT exchange, also contain exact Hartree Fock exchange.[37,450]

Accurate results at a comparable computational effort, but wavefunction-based, can be obtained with a low-level correlation method like the spin-component-scaled 2nd order Møller-Plesset perturbation theory (SCS-MP2).[37] Depending on the chemical question, more sophisticated but also much more expensive coupled-cluster (e.g. CCSD(T)) and configuration-interaction (e.g. QCISD) methods may be necessary.[450]

The accuracy of the results obtained by any of the mentioned methods strongly depends on the set of basis functions supplied. Basis sets are categorized by their quality, i.e. by how many basis functions the orbitals are approximated. Double-, triple- and quadruple-ζ basis sets use two, three, and four functions per orbital, respectively. Within the split valence basis sets ζ applies only to the valence orbitals. Beyond the so-called basis set limit the further addition of more basis functions (larger basis set) has no effect and better results with a particular method cannot be obtained. For the B3LYP functional, which was mainly used in this work, the basis set def2-TZVPP of triple-ζ quality was found to be close enough to the basis set limit.[450,452]

2 Objectives

AuF_5, an extremely strong Lewis acid, is predicted to form a non-classical complex with elemental fluorine comprising a discrete strongly polarized $\{F_2\}$ moiety with an elongated F–F bond.[195,273] A similar but gradually decreasing behavior is assumed for the Lewis acids SbF_5, AsF_5, and BF_3. This activation of F_2 could explain the reported reactivity of F_2 towards Xe in the dark at low temperatures in the presence of Lewis acids (cf. Section 1.8).[130–132] To research the reactivity of the Lewis acids BF_3, AsF_5, SbF_5, and AuF_5 towards fluorine, these species will be investigated by matrix isolation techniques supported by quantum-chemical calculations. For this purpose, the Lewis acids and fluorine will be diluted in noble gases, co-deposited at different concentrations, and then subjected to annealing and photolysis experiments. AuF_5 will potentially be produced in-situ from laser-ablated $Cs[AuF_6]$ at higher fluorine concentrations.

The fluorine-rich photo-labile precursor PtF_6 represents a source of both the Lewis acid and F_2 and thus potentially of non-classical F_2 complexes. Multiple bands throughout the UV/Vis region stand for a rich photochemistry of PtF_6. A detailed study was recently published[304] and will serve as a 'toolbox' for the combination of PtF_6 with the simultaneously laser-ablated metals Pd, Pt, or metal fluorides NaF, KF, and CsF. Thereby, the behaviour of PtF_6 will be investigated in terms of the products formed after I) the co-deposition and II) the subsequent photolysis in solid neon and argon matrices.

The photo-decomposable precursor permanganyl fluoride (MnO_3F) is a source of the novel manganese oxofluorides $[(\eta^2\text{-}OO)Mn^{V}OF]$ and $[(\eta^1\text{-}OO)Mn^{IV}OF]$ as discovered by Li et al.[453] Using highly pure MnO_3F, these species will be further investigated in the inert matrix hosts Ne, Ar, and N_2 by IR and UV/Vis spectroscopy to obtain reliable reference data and verify the previous band assignments.

The Simons process is an industrially important electrochemical fluorination method to produce partially and fully fluorinated organic molecules on nickel electrodes in anhydrous hydrogen fluoride. Its mechanism, however, has been controversially debated since its invention about a century ago (cf. Section 1.4.1, Section 1.4.1.1). A black film is formed upon polarization on the anode and is thought to comprise an active species – nickel in an oxidation state higher than +II – to facilitate the fluorination. To elucidate the nature of this anodic film, ex-situ as well as in-situ investigations with specifically designed XAFS cells will be conducted.

3 Results and Discussion

3.1 Lewis Acid-Fluorine Interactions

The oxidation of Xe by elemental F_2 in the dark mediated by liquid Lewis acids gave rise to the question of the distinct effect of the Lewis acid (cf. Section 1.8).[130–132] It must be noted that the reaction of the system AsF_5–F_2–Xe in the dark leads to $[XeF][AsF_6]$, but only when AsF_5 was in the liquid state at −60 °C and not at +20 °C in the gaseous state.[130] The systems were thoroughly investigated in terms of the conditions including a thermochemical assessment with virtually no barrier for the product formation, being the thermal energy below 1.76 kJ·mol^{-1} (RT at 213 K), and a possible $[LA{\cdot}F_2]$ intermediate stayed elusive.[130] In order to shed light into a possible mechanism, the reaction must be 'paused' in the moment when a potential $[LA{\cdot}F_2]$ adduct is formed, while its decomposition must be suppressed. This could be facilitated under matrix isolation conditions.

Known for their high fluoride ion affinities BF_3, AsF_5 and SbF_5 have long been used in inorganic syntheses to stabilize uncommon cations or to obtain metal fluorides in high oxidation states by fluoride abstraction and concomitant formation of their fluorido anions $[BF_4]^-$, $[AsF_6]^-$, and $[SbF_6]^-$.[121,126,261,454] In addition, the reactivity of matrix-isolated boron trifluoride towards many different bases, ranging from the strong NH_3 and CH_3CN over medium H_2O to weak ones such as CO and N_2, has been extensively studied. Upon strongly binding to strong bases, BF_3 is deformed to almost tetrahedral local symmetry indicated by large redshifts of the antisymmetric and the symmetric stretching modes. On the contrary, BF_3 keeps its planarity when only weakly bound to a weak base and the corresponding vibrational bands only shift marginally (cf. Section 1.5, Section 1.7).[73] However, besides the IR spectra of the pure Lewis acids, AsF_5 and SbF_5 were not investigated seeking for Lewis acid-base complexes under matrix isolation conditions.[73,351] In search for gold in an oxidation state higher than +V, it was found that "AuF_7" is best described as a non-classical F_2 complex $[AuF_5{\cdot}F_2]$, bearing a discrete $\{F_2\}$ unit with a strongly polarized and elongated F–F bond.[195,273] Correlated with the strong acidity of AuF_5,[69] the reports about the Lewis superacid AuF_5 are rare.[10,69,249,455]

The following considerations are based on references [10,77,195]. If a complex consisting of the strong Lewis acid AsF_5 and the (very weak) Lewis base F_2[73,361] forms a stable intermediate, it should be observable under matrix isolation conditions by means of its IR spectrum. The F–F stretching mode of elemental fluorine is IR inactive, but polarized F_2 molecules show a very weak IR band around 890 cm^{-1} under matrix isolation conditions (cf. Table 14 in Section 3.1.2.1). Accordingly, the ν(F–F) should be polarized more strongly by a Lewis acid in a Lewis acid-fluorine

[LA·F_2] complex and thus should gather a higher IR intensity. Moreover, the F−F bond should be weakened, and the ν(F−F) band should consequently be red-shifted, allowing for a discrimination of coordinated and free F_2 species. Developing these thoughts further, the intensity and the position of the ν(F−F) should depend on the acidity of the added Lewis acid, suggesting that the intensity should rise in the order BF_3 < AsF_5 < SbF_5 < AuF_5,[66,69,249] and that the magnitude of the redshift rises in the same way, as illustrated for the latter three in Figure 18.

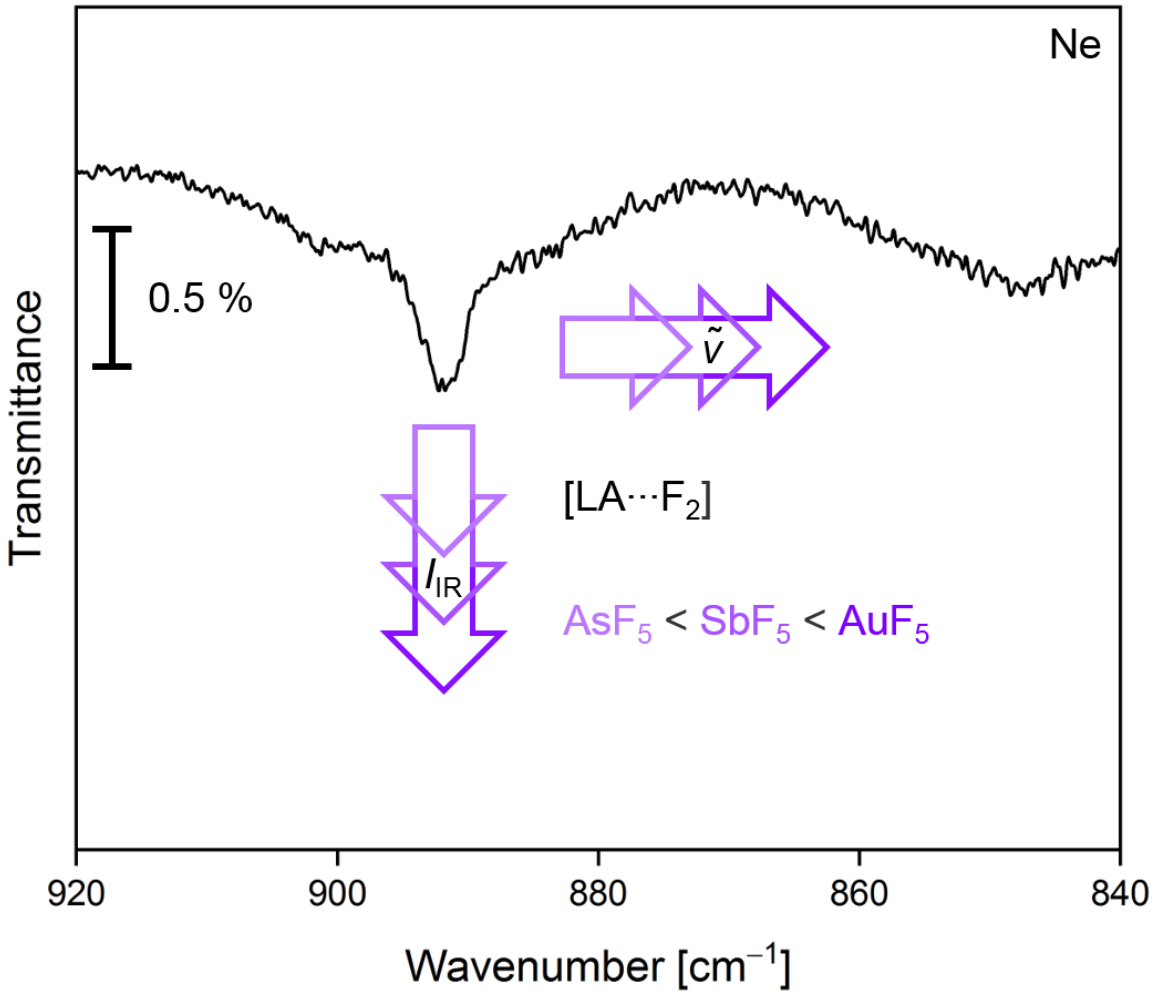

Figure 18: IR spectrum recorded after the deposition of F_2 (3 % in Ne) for 60 min and a schematic trend for the suspected development of the ν(F−F) band of a [LA·F_2] complex in terms of intensity and position upon addition of different Lewis acids with respect to their fluoride ion affinities [73,195,249].

In order to study the interaction of F_2 with a Lewis acid (LA) in the sense of an [LA·F_2] complex isolated in noble gas (Ng) matrices, three generally different experimental pathways are conceivable:

- condensation of a premixed gas mixture LA/F_2/Ng (see the following chapters)
- co-deposition of a laser-ablated 'fluorine-rich' precursor (e.g. Cs[AuF_6]) with F_2/Ng (Section 3.1.2.5)
- photolysis of a pre-deposited 'fluorine-rich' precursor (e.g. PtF_6) in Ng or F_2/Ng (Section 3.2)

These approaches represent constrained versions of the abovementioned Lewis acid mediated oxidation of Xe by F_2. They principally allow for a specific investigation of the interaction of F_2 with different Lewis acids, without impairing the potentially formed non-classical F_2 complexes[79,195,273,283] with an additional electron donor like Xe. In an F_2-passivated and inert environment (BF_3, F_2, Ne/Ar), only the formation of coordination compounds should be possible, since the Lewis acids BF_3, AsF_5, and SbF_5 reportedly do not react with F_2 at ambient temperatures.[282] Neglecting impurities, either the formation of oligomers[73,456] or an [LA·F_2] complex are left, as exemplified for BF_3 in Scheme 16.

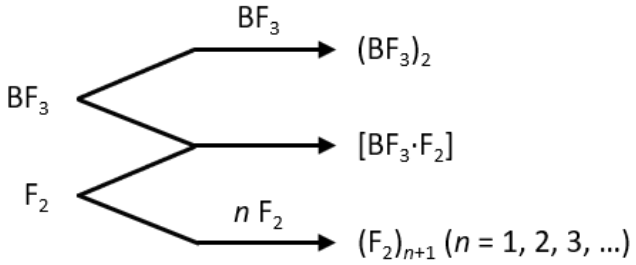

Scheme 16: Conceivable products formed from BF_3 and F_2 simultaneously diluted in Ne or Ar.

Although the Lewis acid BF_3 played a tangential role in the work of Bartlett's group,[130] it is a gaseous, strong Lewis acid[29,66] that was studied in detail in terms of Lewis acid-Lewis base interactions, as featured in a comprehensive review one decade ago.[73] BF_3 is therefore well suited to be studied for the interaction with F_2 under matrix isolation conditions (Section 3.1.2.2). Analogous experiments were performed with AsF_5 (Section 3.1.2.3), SbF_5 (Section 3.1.2.4), and laser-ablated Cs[AuF_6] (Section 3.1.2.5), the latter being a potential source for superacidic AuF_5.[195,249] PtF_6 was investigated as a precursor for non-classical F_2 complexes as described in Section 3.2. All experimental data are supported by quantum-chemical calculations (Section 3.1.1).

3.1.1 Quantum-Chemical Description of [LA·F_2] Complexes

The study of weakly or in this work very weakly bound complexes is always confronted with the problem that the quantum-chemical description strongly depends on the methods and basis sets employed.[73] Thus, the Lewis acids BF_3, AsF_5, SbF_5 and AuF_5 and their respective adduct with fluorine, which acts as a very weak Lewis base,[73,361] have been subjected to structure optimizations and frequency calculations at different levels of theory (SCS-MP2, B3LYP, PBE and BP86 using the def2-TZVPP basis set) employing the *Turbomole* software package (for details see Section 4.2). Since the program *Turbomole* is limited in its molecular symmetry options by a maximum of a sixfold rotation axis, molecular fluorine was calculated in C_1 and not $D_{\infty h}$ symmetry. The calculated minimum structures of the free Lewis acids were obtained in their expected geometries (BF_3, AsF_5, SbF_5: D_{3h}; AuF_5: C_{4v}). Regarding AuF_5, symmetry-reduced structures were energetically slightly favored over C_{4v} using the GGA functionals PBE and BP86 by −1.70 (C_s) and −1.78 kJ·mol^{-1} (C_1), respectively. The optimized structures of the Lewis acids BF_3, AsF_5, SbF_5 and AuF_5 and the respective F_2 complexes at all levels of theory are compiled in Section 6.1.1 in the appendix. The RI-B3LYP-D4/def2-TZVPP optimized structures are depicted in Figure 19, covering the most important structural features such as the closest intermolecular contacts and the F−F bond distances. Reflecting the anisotropic electrostatic potentials characteristic of all halogens,[110] fluorine binds in a linear fashion towards bases and in an angular geometry to acids with the torus of a more negative electrostatic potential pointing towards the electrophilic center of the acid.

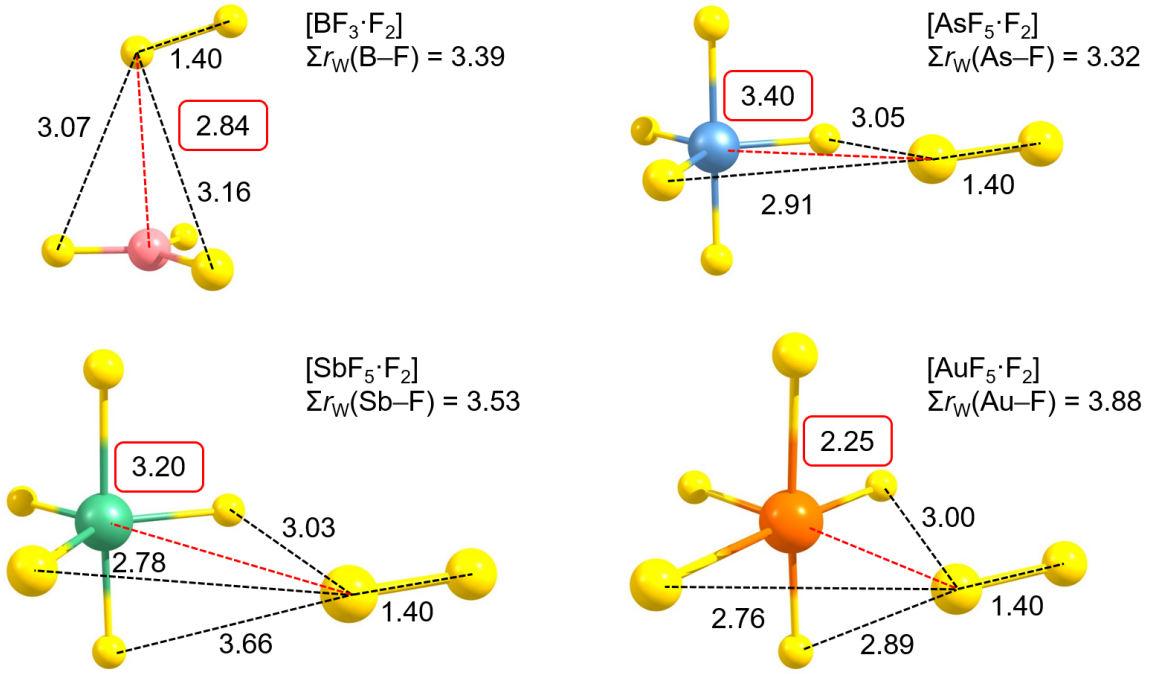

Figure 19: Structures of the Lewis acid-fluorine adducts C_s-[BF_3·F_2], C_1-[AsF_5·F_2] (see the text for details), C_s-[SbF_5·F_2], and C_s-[AuF_5·F_2] optimized at the RI-B3LYP-D4/def2-TZVPP level of theory. The E–F (E = B, As, Sb, Au) contacts are highlighted in red and the closest F_2–F contacts are given in black. The sums of the van der Waals-radii Σr_W(E–F) are given for comparison. The van der Waals radius of a fluorine atom is 1.47 Å.[457–459] All bond distances are given in Å. The E–F–F angles are 104.5° for B, 110.5° for As, 114.5° for Sb and 113.7° for Au.

All studied [LA·F_2] complexes feature the {F_2} moiety (LB) end-on coordinated in an angular fashion with respect to the anisotropic charge distribution of the halogens[110] (cf. Figure 10 in Section 1.9). They all have a C_s-symmetric global minimum structure at all applied methods, except for [AsF_5·F_2]. For the latter, a C_s-symmetric minimum was found as well (PBE), but at the other levels of theory a C_1-symmetric global minimum was obtained, with a C_s-symmetric structure lying 0.2 (B3LYP, BP86) or 0.5 kJ·mol^{-1} (SCS-MP2) higher in energy. [AuF_5·F_2] was calculated to have C_s symmetry at all levels of theory, however, the C_1-symmetric states were calculated as little as −0.018 kJ·mol^{-1} lower in energy (B3LYP), which is somewhat neglectable given the method-inherent errors of about 4.6 kJ·mol^{-1}.[460] Since the computed [LA·F_2] adducts virtually have the same structure for all the methods used, the discussion of the structural features will be solely based on the B3LYP results. Table 8 comprises the calculated energies of the formation of the [LA·F_2] adducts. Since the matrix measurements are performed at 4–5 K, the entropic term and the temperature contribution to the enthalpic term of the actual heat of formation can be neglected because the vibrational and rotational levels are not significantly populated.[73]

Table 8: Calculated ZPE-corrected electronic contributions to the energy of formation ΔE_f of the Lewis acid-fluorine adducts $[BF_3 \cdot F_2]$, $[AsF_5 \cdot F_2]$, $[SbF_5 \cdot F_2]$, and $[AuF_5 \cdot F_2]$. The ΔE_f values are given in $kJ \cdot mol^{-1}$.

Complex	SCS-MP2-ΔE_f	B3LYP-ΔE_f	BP86-ΔE_f	PBE-ΔE_f
C_s-$[BF_3 \cdot F_2]$	+0.54	–3.84	–1.34	–5.04
C_1-$[AsF_5 \cdot F_2]$	+1.33	–3.67	–1.13	–4.61(C_s)
C_s-$[SbF_5 \cdot F_2]$	–0.32	–5.44	–2.04	–6.92
C_s-$[AuF_5 \cdot F_2]$	–31.98	–34.09	–31.13	–35.28

With respect to the results featured in Table 8, the adducts $[BF_3 \cdot F_2]$, $[AsF_5 \cdot F_2]$ and $[SbF_5 \cdot F_2]$ generally represent very weakly bound, or – considering the SCS-MP2 values of the former two – even slightly unbound systems. With $[AuF_5 \cdot F_2]$ being calculated as a comparably strongly bound adduct at all applied levels of theory, the binding energy develops in the order $[BF_3 \cdot F_2] \approx [AsF_5 \cdot F_2] < [SbF_5 \cdot F_2] << [AuF_5 \cdot F_2]$. These low binding energies are not unexpected in the light of a reported calculated value of about 6 $kJ \cdot mol^{-1}$ (MP2/6-31G) for an $[FH \cdot F_2]$ complex.[392] With respect to this trend, a small influence of the Lewis acid on the F−F distance of the $\{F_2\}$ moiety is expected (Figure 19, Table 9). The small polarizability of F_2 compared to higher halogens and interhalogens renders these data even comparable to the results regarding the $[LB \cdot F_2]$ adducts described in the literature (cf. Table 7 in Section 1.9 and the references therein).

Table 9: Calculated F−F bond distances of the minimum structures of the Lewis acid-fluorine adducts $[BF_3 \cdot F_2]$, $[AsF_5 \cdot F_2]$, $[SbF_5 \cdot F_2]$, and $[AuF_5 \cdot F_2]$.

d(F−F)	SCS-MP2 [Å]	B3LYP [Å]	BP86 [Å]	PBE [Å]
F_2	1.409	1.397	1.415	1.413
$[BF_3 \cdot F_2]$	1.410	1.397	1.415	1.414
$[AsF_5 \cdot F_2]$	1.409	1.397	1.415	1.414
$[SbF_5 \cdot F_2]$	1.410	1.397	1.419	1.419
$[AuF_5 \cdot F_2]$	1.412	1.401	1.446	1.443

The computed F−F bond distances are comparable with the reported calculated values[7,13,195] (see also Table 1 in Section 1.1). Since the F−F bond distance is not or only marginally elongated, it can hardly be used as a measure for the interaction, particularly in the very weakly bound systems $[BF_3 \cdot F_2]$, $[AsF_5 \cdot F_2]$, and $[SbF_5 \cdot F_2]$. As the $\{F_2\}$ moiety coordinates end-on towards the central atom of all the Lewis acids discussed here, the distance E−F_2 (E = B, As, Sb, Au) becomes particularly important as a criterion for the strength of interaction with respect to the sum of the van der Waals radii (Σr_W). The Σr_W(E−F) of the contacts E−F_2 (E = B, As, Sb, Au) is slightly exceeded in the

arsenic case, while the distances are found well below the Σr_W(E−F) in the other [LA·F_2] complexes (Figure 19). These results agree with the expectations raised by microwave data for weakly bound F_2 complexes of for example NH_3, H_2O and H_2S, in which the E−F_2 (E = N, O, S) distances resemble the Σr_W(E−F),[405] and are reflected in the BF_3, AsF_5 and SbF_5 cases of the present work. A strongly bound [AuF_5·F_2] with a strongly perturbed {F_2} moiety was described more than a decade ago.[195] The computed results of the present work agree with these data and show a comparably weaker impact by the weaker Lewis acids SbF_5, AsF_5 and BF_3.

Table 10: Selected calculated bond angles of the {BF_3}, {AsF_5}, {SbF_5} and {AuF_5} moieties in the [LA·F_2] adducts given in °. The subscript 'um' refers to the umbrella angle of the {BF_3} moiety and the subscript 'ax' and 'eq' to the axial and equatorial fluorido ligands of the {EF_5} (E = As, Sb, Au) moieties, respectively. The angles refer to the fluorido ligands at the F_2 coordination sites.

[LA·F_2]	Moiety	SCS-MP2 [°]	B3LYP [°]	BP86 [°]	PBE [°]
[BF_3·F_2]	$BF_{3,um}$	179.1	179.1	179.2	178.9
[AsF_5·F_2]	F_{ax}–As–F_{ax}	179.4	179.3	179.5	179.3
	F_{eq}–As–F_{eq}	121.7	122.0	121.4	122.1
[SbF_5·F_2]	F_{ax}–Sb–F_{ax}	173.7	176.8	168.9	168.5
	F_{eq}–Sb–F_{eq}	133.4	127.8	143.0	143.5
[AuF_5·F_2]	F_{ax}–Au–F_{ax}	177.1	175.9	175.8	175.7
	F_{eq}–Au–F_{eq}	176.8	175.1	173.9	173.6

The [BF_3·F_2] adduct comprises a comparably short B−F_2 contact (Figure 19), while the {BF_3} moiety is only marginally distorted with the boron atom being slightly elevated from the BF_3 plane (Table 10). The system is slightly stronger bound than [AsF_5·F_2], although AsF_5 is a stronger Lewis acid than BF_3.[249] This could be explained by less steric crowding of only three ligands in BF_3 compared to the five fluorido ligands of AsF_5, which also holds for all F_2−F distances exceeding twice the van der Waals radius of a fluorine atom (2.94 pm)[457] in [BF_3·F_2] in contrast to the [EF_5·F_2] adducts. For SbF_5, the deviation from the original D_{3h} symmetry is stronger than for AsF_5 (cf. Table 10), which is expected due to its higher acidity. As free AuF_5 has a C_{4v}-symmetric ground state geometry, it naturally features a free coordination site. Therefore, the F_2 adduct hardly differs in the F−Au−F angles compared to free AuF_5 with F_{eq}–Au–F_{eq} angles of 174.8° (SCS-MP2), 172.7° (B3LYP), 168.0° and 167.3° (BP86), and 168.0° (PBE). Given that the contacts of the E−F_2 distances scale with the strength of interaction within these adducts, this trend is well reflected in the vibrational frequencies of the {F_2} moiety of these species. Table 11 contains the calculated band positions and Table 12 covers the relative band shifts upon the influence of the specific Lewis acids, while both tables comprise the same IR intensities.

Table 11: Calculated F–F stretching frequencies $\tilde{\nu}$(ν(F–F)) of molecular F_2 and the Lewis acid-fluorine adducts $[BF_3{\cdot}F_2]$, $[AsF_5{\cdot}F_2]$, $[SbF_5{\cdot}F_2]$, and $[AuF_5{\cdot}F_2]$ given in cm^{-1} and IR intensities I_{IR} in $km{\cdot}mol^{-1}$.

Species	SCS-MP2		B3LYP		BP86		PBE	
	$\tilde{\nu}$(ν(F–F))	I_{IR}	$\tilde{\nu}$(ν(F–F))	I_{IR}	$\tilde{\nu}$(ν(F–F))	I_{IR}	$\tilde{\nu}$(ν(F–F))	I_{IR}
F_2	983.8	0	1048.0	0	996.4	0	997.0	0
$[BF_3{\cdot}F_2]$	980.8	0.38	1046.4	0.18	994.6	0.08	993.6	0.10
$[AsF_5{\cdot}F_2]$	982.2	0.11	1046.9	0.02	995.4	0.01	993.5 (C_s)	0.03
$[SbF_5{\cdot}F_2]$	979.8	1.35	1043.1	0.06	961.1	3.70	956.5	4.73
$[AuF_5{\cdot}F_2]$	964.4	24.83	1003.0	0.67	770.4	109.74	776.7	102.86

The absolute position of the F−F stretching band is strongly overestimated by all methods used compared to experimental findings (Section 3.1.2, e.g. Figure 22, see also Table 14). A full set of the band positions and the corresponding vibrational modes of both the free Lewis acid and the $[LA{\cdot}F_2]$ complexes of BF_3 (Table 37), AsF_5 (Table 38), SbF_5 (Table 39) and AuF_5 (Table 40) are found in the appendix. By contrast, IR intensities together with the relative shifts of the ν(F−F) (Table 12) well reflect the small structural deviations of {LA} and $\{F_2\}$ moieties upon adduct formation.

Table 12: Calculated shifts $\Delta\tilde{\nu}$(ν(F–F)) of the Lewis acid-fluorine adducts $[BF_3{\cdot}F_2]$, $[AsF_5{\cdot}F_2]$, $[SbF_5{\cdot}F_2]$, and $[AuF_5{\cdot}F_2]$ relative to molecular F_2 given in cm^{-1} and IR intensities I_{IR} in $km{\cdot}mol^{-1}$.

Species	SCS-MP2		B3LYP		BP86		PBE	
	$\Delta\tilde{\nu}$(ν(F–F))	I_{IR}	$\Delta\tilde{\nu}$(ν(F–F))	I_{IR}	$\Delta\tilde{\nu}$(ν(F–F))	I_{IR}	$\Delta\tilde{\nu}$(ν(F–F))	I_{IR}
F_2	0	0	0	0	0	0	0	0
$[BF_3{\cdot}F_2]$	−3.0	0.38	−1.6	0.18	−1.8	0.08	−3.4	0.10
$[AsF_5{\cdot}F_2]$	−1.6	0.11	−1.1	0.02	−1.0	0.01	−3.5 (C_s)	0.03
$[SbF_5{\cdot}F_2]$	−4.0	1.35	−4.9	0.06	−35.3	3.70	−40.5	4.73
$[AuF_5{\cdot}F_2]$	−19.4	24.83	−45.0	0.67	−226.0	109.74	−220.3	102.86

Although the GGA functionals render the ν(F−F) the strongest band in the respective IR spectra of the gold-centered adduct, which seems by far overshot, $[AuF_5{\cdot}F_2]$ depicts a propitious system to be experimentally studied with respect to the more realistic SCS-MP2 and B3LYP results.

In accordance with the structures of the $[LA{\cdot}F_2]$ adducts depicted in Figure 19, also the NPA charges featured in Table 13 reflect the extremely small structural changes of the complexes compared to the free parent molecules, with the consecutive polarization of one coordinated F_2

molecule in the order $[BF_3 \cdot F_2] \approx [AsF_5 \cdot F_2] < [SbF_5 \cdot F_2] << [AuF_5 \cdot F_2]$. The full set of NPA charges of the $[LA \cdot F_2]$ adducts are found in Section 6.1.2 in the appendix.

Table 13: NPA charges (in e) of the fluorine atoms of the coordinated $\{F_2\}$ moieties in the Lewis acid-fluorine adducts $[BF_3 \cdot F_2]$, $[AsF_5 \cdot F_2]$, $[SbF_5 \cdot F_2]$ and $[AuF_5 \cdot F_2]$. Consistent with the structures in Figure 19 the terminal fluorine atoms are labelled 'term' and the fluorine atoms at the coordinated site 'coord', respectively.

$[LA \cdot F_2]$	**Atom**	**SCS-MP2**	**B3LYP**	**BP86**	**PBE**
$[BF_3 \cdot F_2]$	F_{term}	0.009	0.011	0.008	0.010
	F_{coord}	−0.004	−0.007	−0.005	−0.005
$[AsF_5 \cdot F_2]$	F_{term}	0.006	0.008	0.005	0.006
	F_{coord}	−0.005	−0.007	−0.004	−0.006
$[SbF_5 \cdot F_2]$	F_{term}	0.018	0.017	0.028	0.029
	F_{coord}	−0.010	−0.013	−0.012	−0.012
$[AuF_5 \cdot F_2]$	F_{term}	0.067	0.088	0.063	0.062
	F_{coord}	0.020	0.006	0.006	0.007

The polarization and elongation of the F−F bond is extremely low at all applied levels of theory (except for the $[AuF_5 \cdot F_2]$ cases). However, these values did not significantly change for F_2 in the presence of two AsF_5 molecules (see Table 53 and Figure 103 in the appendix). A weak ν(F−F) band caused by polarized F_2 is expected under matrix isolation conditions, whether F_2 coordinates a Lewis acid or not.[10,195] This could necessitate an alternative indicator to experimentally verify a Lewis acid-fluorine interaction.

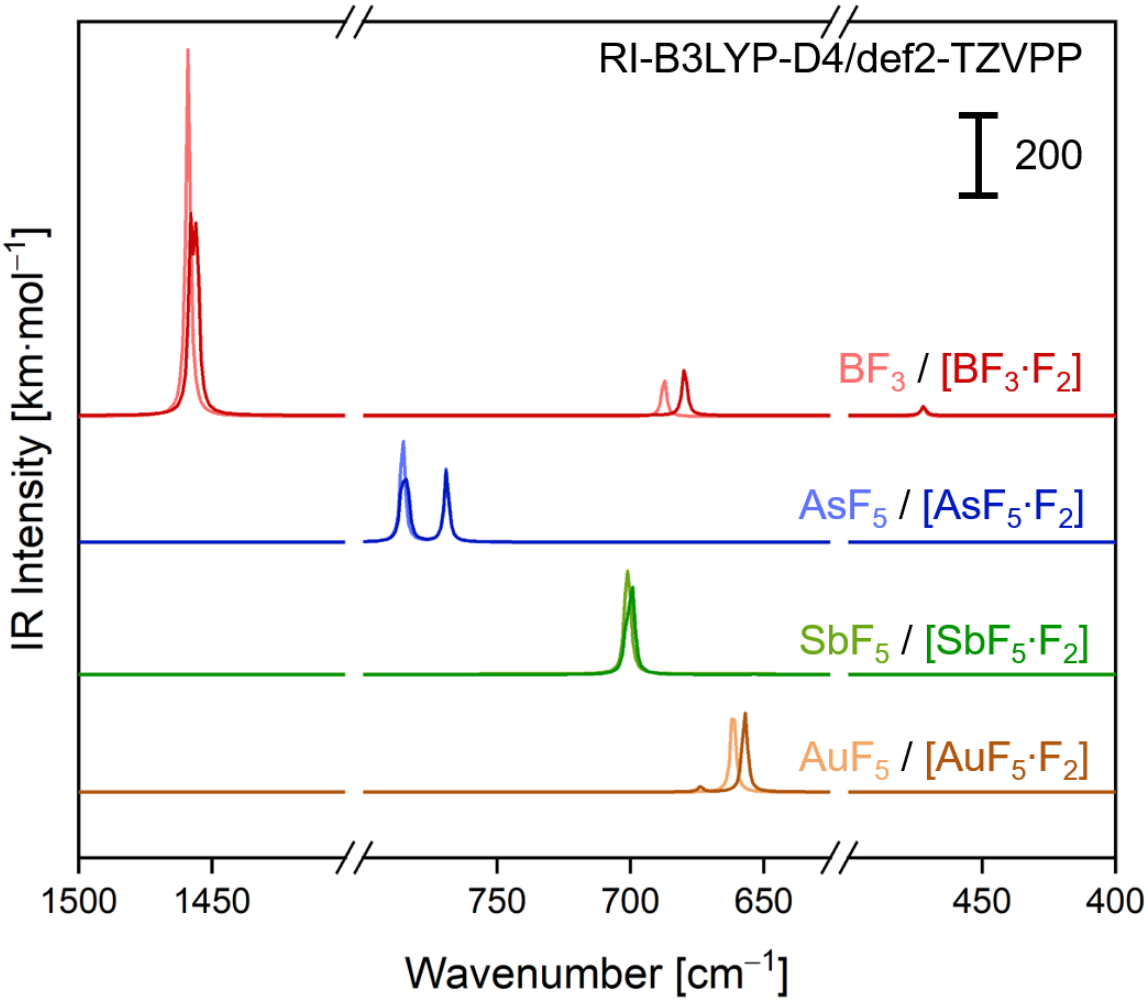

Figure 20: IR spectra (FWHM = 1 cm^{-1}) of the Lewis acids BF_3 (red traces), AsF_5 (blue traces), SbF_5 (green traces), AuF_5 (brown traces), and the corresponding F_2 adducts computed at the RI-B3LYP-D4/def2-TZVPP level of theory. The more deeply colored spectra represent the F_2 adducts, the lighter ones the free Lewis acids.

The highly IR active vibrational modes of the Lewis acids (see Section 3.1.2) are expected to be influenced by the coordinated F_2 molecules[73] in the [LA·F_2] adducts. Regarding the computed IR spectra (Figure 20), the adducts show intense and characteristic features in the E–F stretching region and, in the case of BF_3, also the deformation modes reportedly lie in the MIR region[461] (see also Section 3.1.2). Generally, the bands of the D_{3h}- or C_{4v}-symmetric parent molecules split or lose degeneracy due to the lowered symmetry of the [LA·F_2] adducts. As a result of the weak interaction with fluorine, the bands split only marginally and the relative shifts are small, in particular for the stretching modes. The effect of the coordination of an F_2 molecule is comparably larger for the deformation modes, as can be seen in Figure 21.

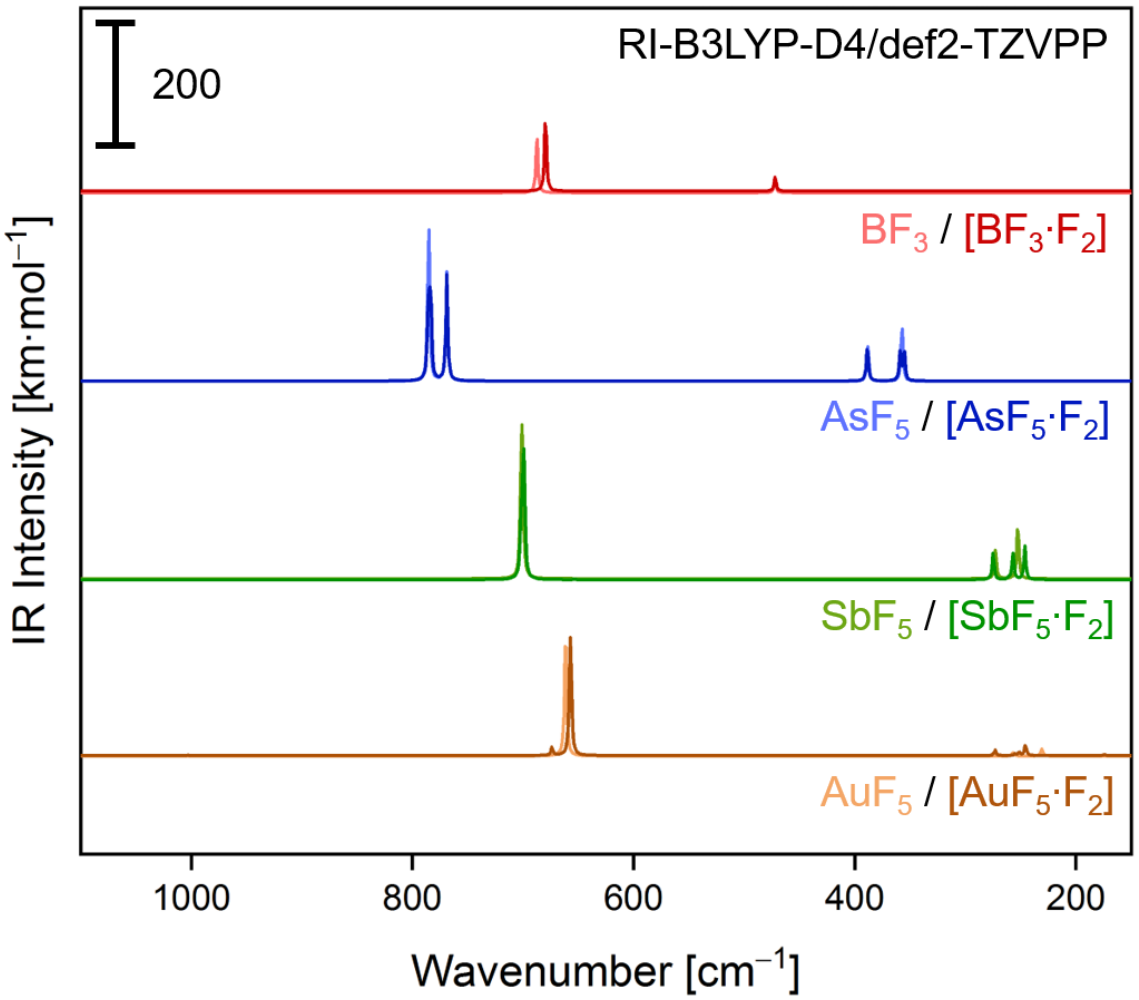

Figure 21: IR spectra (FWHM = 1 cm^{-1}) in the low frequency region of the Lewis acids BF_3 (red traces), AsF_5 (blue traces), SbF_5 (green traces), AuF_5 (brown traces), and the corresponding F_2 adducts computed at the RI-B3LYP-D4/def2-TZVPP level of theory. The more deeply colored spectra represent the F_2 adducts, the lighter ones the free Lewis acids.

Due to the expected low concentration of the desired adducts in matrix isolation experiments, the bands characteristic of [LA·F_2] could end up in a shoulder of the stronger bands of the parent Lewis acids or be obscured by an oligomeric band of the latter, which cannot be completely avoided. Given the low binding energies, it must be noted that the quantum-chemical data only describe the free complexes, while stabilizing effects of a surrounding matrix, such as cage pairing of the reactants,[73,462] are not considered.

3.1.2 Experimental Results

The experimental study primarily focuses on the polarization of the F_2 molecule and the resulting shift of the fluorine fundamental stretching mode in the corresponding IR spectra. In accordance with the results obtained by quantum-chemical calculations, the fluorine fundamental is expected to be polarized in the presence of a Lewis acid. This means that the more acidic the Lewis acid is, the more intense and more strongly shifted the F−F stretching band is expected.[73,195,249] Among the discussed Lewis acid-fluorine adducts of BF_3, AsF_5, SbF_5 and AuF_5 (Section 3.1.1), $[AuF_5{\cdot}F_2]$[195] is the most promising system to study. Yet, the former three Lewis acids are available in large quantities as monomeric gases (BF_3, AsF_5) or as an oligomeric, viscous liquid (SbF_5) with an appreciable vapor pressure and are much easier to control for an efficient deposition.[3,29,351,463] Since fluorine (^{19}F), like arsenic (^{75}As) and gold (^{197}Au), is a mononuclidic element and the relative mass difference of the stable antimony isotopes ^{121}Sb and ^{123}Sb is very small, no isotopically labelled experiments were performed.[29] All experiments employing BF_3, AsF_5, SbF_5 and $Cs[AuF_6]$ (diluted in a CsF target and subjected to laser ablation) and molecular F_2 were performed using a so-called single jet setup,[73,464] where the gases are premixed (see the experimental details in Section 4.1). This is possible because BF_3, AsF_5 and SbF_5 do not react with F_2 at ambient temperatures.[282]

3.1.2.1 F_2 in Noble Gas Matrices

Elemental fluorine is IR inactive, because it does not contain a permanent dipole corresponding to its $D_{\infty h}$ symmetry, and weakly Raman active,[13,74] due to the small changes in polarizability in its 18-electron system.[402] Accordingly, isolated F_2 needs to be externally activated (even self-aggregation in solid F_2) to give measurable bands in the vibrational spectra.[10,13] Although the molecules are isolated in inert noble gases, the F_2 molecules weakly interact with the host and are thus slightly polarized by the noble gas atoms.[74,180,393]

As an overview, the newly observed F_2 bands in neon and argon matrices are compiled together with literature-known F−F stretching frequencies observed in the matrix hosts related to the objective of this work in Table 14. A clear-cut definition of isolated and ‘solid’ fluorine by means of their vibrational spectra cannot be given but, where applicable, fluorine is arbitrarily considered as isolated when the band appears lower than 895 cm^{-1} and referred to as a solid phase for band positions higher than this value.

Table 14: Experimental vibrational frequencies (IR and Raman) of isolated F_2 molecules ($F_{2,i}$) and a solid F_2 phase ($F_{2,s}$) in different media given in cm^{-1}. Matrix sites and shoulders are given in parentheses. Concerning the data for liquid F_2, higher frequency bands around 900 cm^{-1} are considered as a higher aggregate and correlated with $F_{2,s}$, the lower frequencies around 890 cm^{-1} correspondingly with $F_{2,i}$.

Medium	$\tilde{\nu}$ (ν(F–F), $F_{2,i}$)		$\tilde{\nu}$ (ν(F–F), $F_{2,s}$)	
	IR	Raman	IR	Raman
Ne (matrix)	(892.3)[a], 892[i], 891.7[a], (891.0)[a], 884.4[b,k]		901.3[a]	
Ar (matrix)	(894.8)[a], (892.3)[a], 892.1[h], 891.8[a]	892±1[d]	(899.3)[a], 898.2[a], (896.9)[a]	
F_2 (solid)			898[b]	896[c], 895[j], 894[c], 887[c]
F_2 (liquid)		894[b], 888[f]	897.5[f]	
F_2 (gaseous)		893.9418(16)[g], 892.1±2[e]		891.85[f]

[a] this work; [b] ref. [10]; [c] ref. [13]; [d] ref. [74]; [e] ref. [406]; [f] ref. [465]; [g] ref. [466]; [h] ref. [180], the F_2 fundamental is thought to be activated by an impurity; [i] ref. [364], the F_2 fundamental is activated by HF; [j] ref. [12]; [k] ref. [10], the band was observed in a mixture of 6 % F_2 and 6 % Cl_2 simultaneously embedded in excess neon.

However, for solid fluorine also a low frequency Raman band at 887 cm^{-1} was reported by Mattsson et al.[13] This band was formed together with α-F_2 upon annealing of amorphous fluorine, but its nature could not be elucidated. Brosi et al. observed a band at 884.4 cm^{-1} in a matrix sample of 6 % F_2 and 6 % Cl_2 simultaneously embedded in excess neon and assigned it to the fundamental of F_2.[10] However, they did not address the unexpectedly low frequency of this ν(F−F), which could principally stem from F_2 polarized by Cl_2, with respect to the high concentrations. Both bands are seen to be caused by F_2 with a weakened bond.[13] Noteworthy, the band of β-F_2 experiences a pressure and temperature dependent shift from ca. 901 (1.3 GPa, 150 K) to ca. 920 cm^{-1} (5.4 GPa, 300 K).[467]

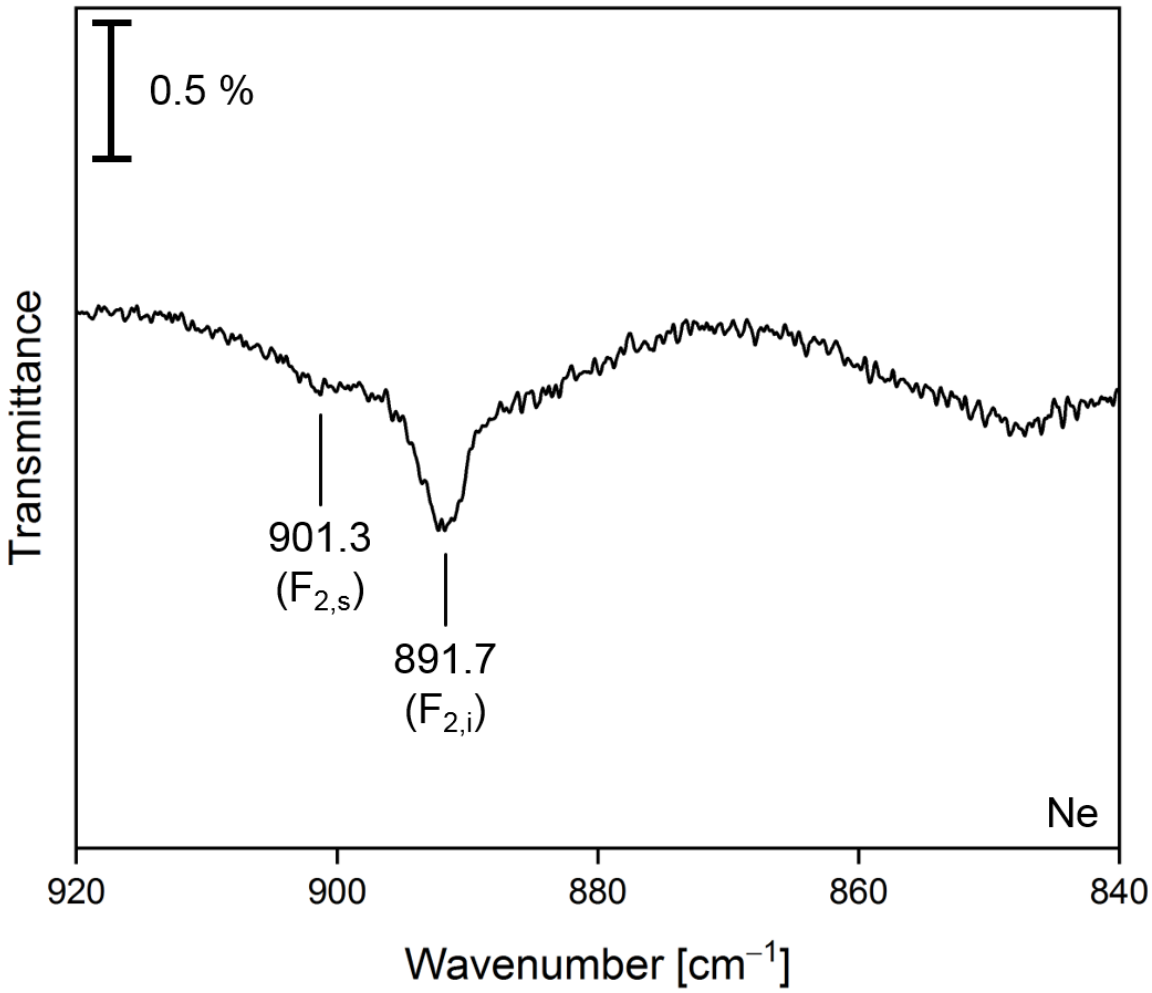

Figure 22: The IR spectrum was recorded after the deposition of molecular fluorine (3 % diluted in Ne) onto a CsI window at 4 K for 60 min at a deposition rate of 0.6 mbar·l·min^{-1}. The bands of solid ($F_{2,s}$) and matrix-isolated F_2 ($F_{2,i}$) are indicated.

As depicted in Figure 22, the matrix IR spectrum of fluorine at a concentration of 3 % diluted in neon features a shoulder at 901.3 and a weak, broad band at 891.7 cm^{-1} (FWHM = 4 cm^{-1}), which agree with the literature values compiled in Table 14.

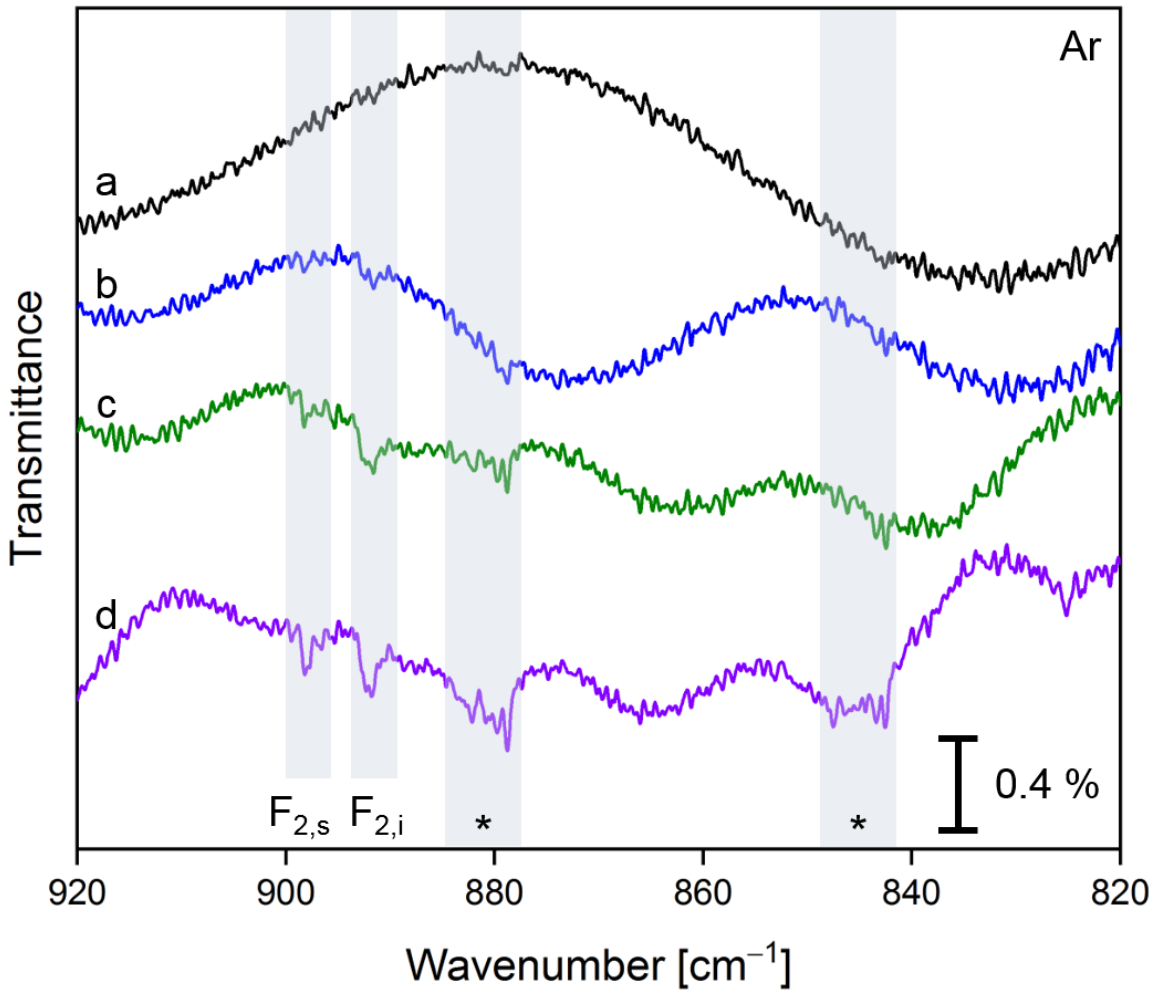

Figure 23: The IR spectra were recorded after the deposition of a) pure argon for 25 min, and after the subsequent deposition of F_2 (3 % diluted in Ar) for b) 30 min, c) 70 min, and d) 100 min onto a CsI window at 4 K at a deposition rate of 0.5 mbar·l·min^{-1}. Features that are associated with AsF_5 are marked with an asterisk (see the text below and Section 3.1.2.3 for more details).

In contrast to neon, the deposition of F_2 in excess argon resulted in two weak bands at 891.8 (matrix-isolated, in the following referred to as $F_{2,i}$)[74] and 898.2 cm^{-1} (solid, in the following referred to as $F_{2,s}$)[10] with an approximate ratio of 1:1, as depicted in Figure 23. With respect to the deposited amount of the F_2 gas mixture, the fluorine-associated bands should rise more uniformly within time. As it is apparent, the deposition of fluorine is not taking place at a constant rate. In the first 30 min no F_2, during consecutive 40 min small amounts of F_2 accompanied by small amounts of impurities and during the following 30 min larger amounts of F_2 and larger amounts of impurities are deposited. A contamination of the gas mixture in the sample compartment can be excluded, because the latter features should have uniformly increased upon deposition, which was not observed. As discussed in Section 3.1.2.3, these impurities are associated with AsF_5.

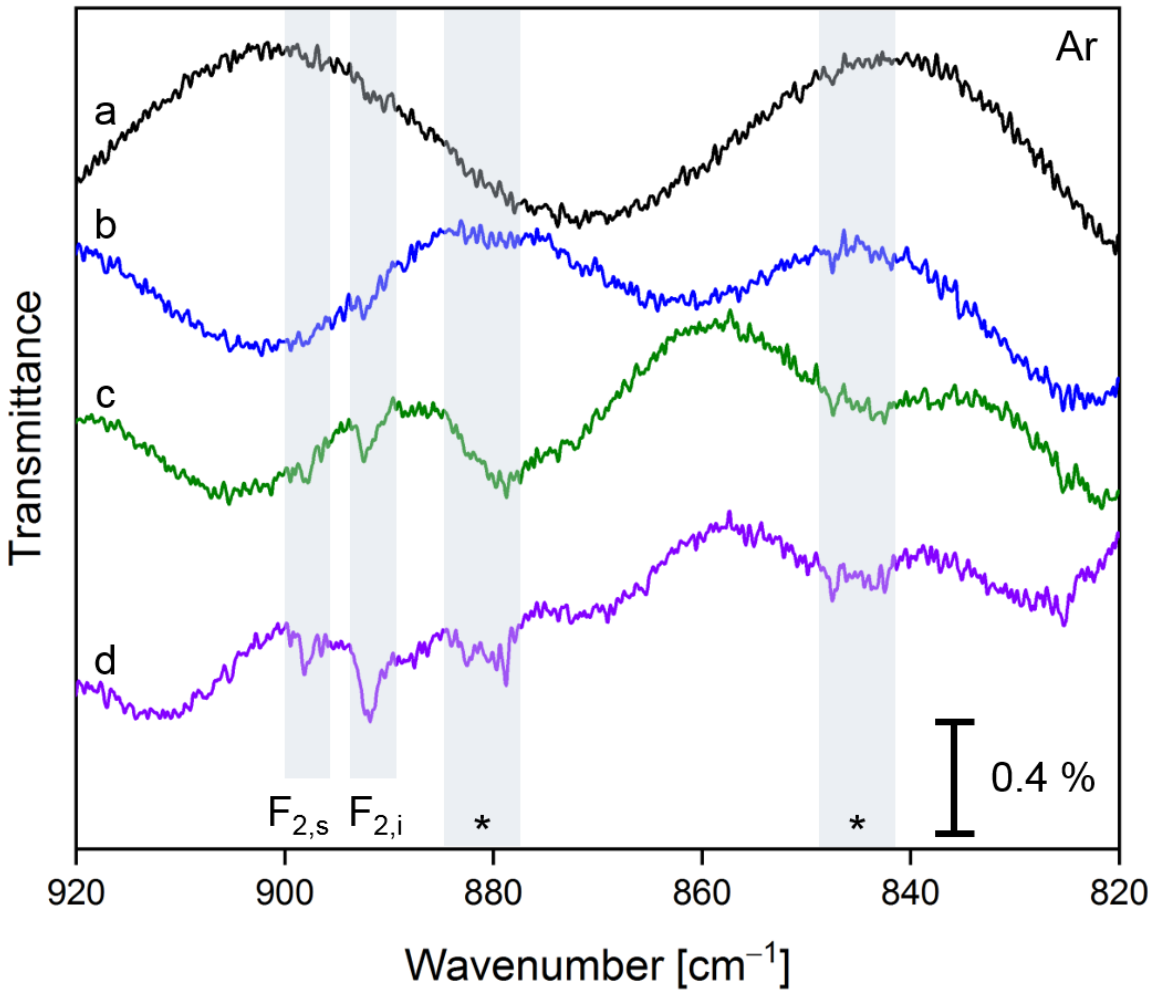

Figure 24: The IR spectra were recorded after the deposition of F_2 (3 % diluted in Ar) onto a CsI window at 4 K for a) 10 min, b) 30 min, c) 55 min, and d) 86 min at a deposition rate of 0.5 mbar·l·min^{-1}. Features that are associated with AsF_5 are marked with an asterisk. The spectrum of a pre-deposited argon layer did not show any absorption bands in this region and was omitted for clarity.

Exchanging the gas mixture, a second set of experiments (Figure 24) revealed that the AsF_5 associated species can be partially 'eluted' from the deposition line and the ν(F–F) increased correlated to the amount of the gas mixture deposited, while the ratio $F_{2,s}$:$F_{2,i}$ decreased to about 0.5:1.

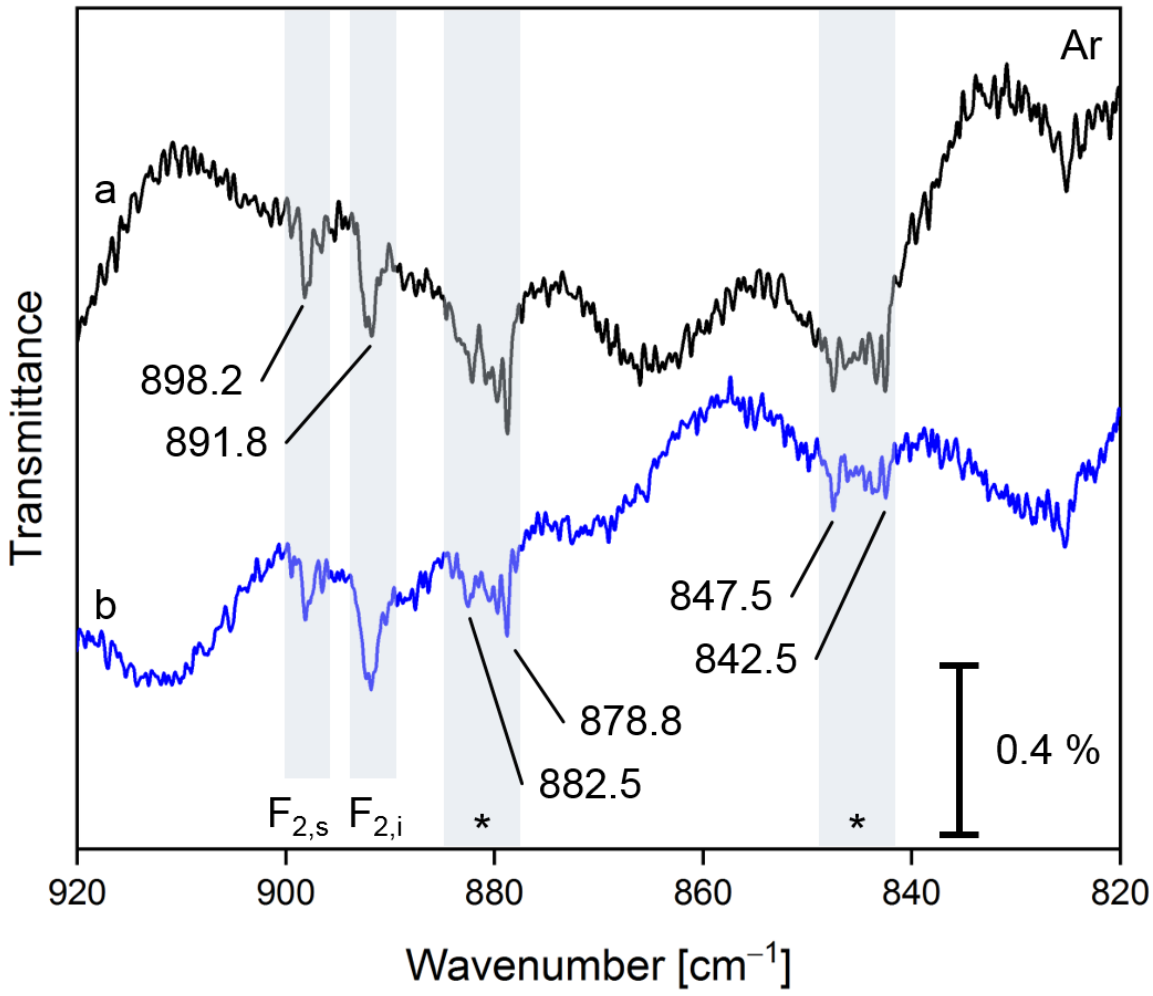

Figure 25: The IR spectra were recorded after depositing exactly 48 mbar·l of F_2 (3 % diluted in Ar) onto a CsI window at 4 K within a) 100 min (identical with trace d in Figure 23), and b) 86 min (identical with trace d in Figure 24) in two independent but subsequent experiments. Features that are associated with AsF_5 are marked with an asterisk.

Apparently, the amounts of $F_{2,s}$, $F_{2,i}$ and the AsF_5 associated features, one at 878.8 cm^{-1} (matrix site at 882.5 cm^{-1}) and another one at 847.5 cm^{-1} (matrix site at 842.5 cm^{-1}), differ during these two independent experiments, depicted in Figure 23 and Figure 24. Upon comparison of the final spectra of these experiments in Figure 25, a correlation between the bands becomes apparent: A lower intensity of the AsF_5 associated bands corresponds to a lower intensity of the $F_{2,s}$ band and a higher intensity of the $F_{2,i}$ band. This might be explained by the former species slowing down the crystallization process of argon, which stays liquid for a longer period and allows for a higher aggregation of the fluorine molecules rather than isolating them by a quick solidification. Due to the low intensity of the discussed features, the step-by-step difference spectra of the two sets of experiments were found not to be indicative for the processes and are not presented.

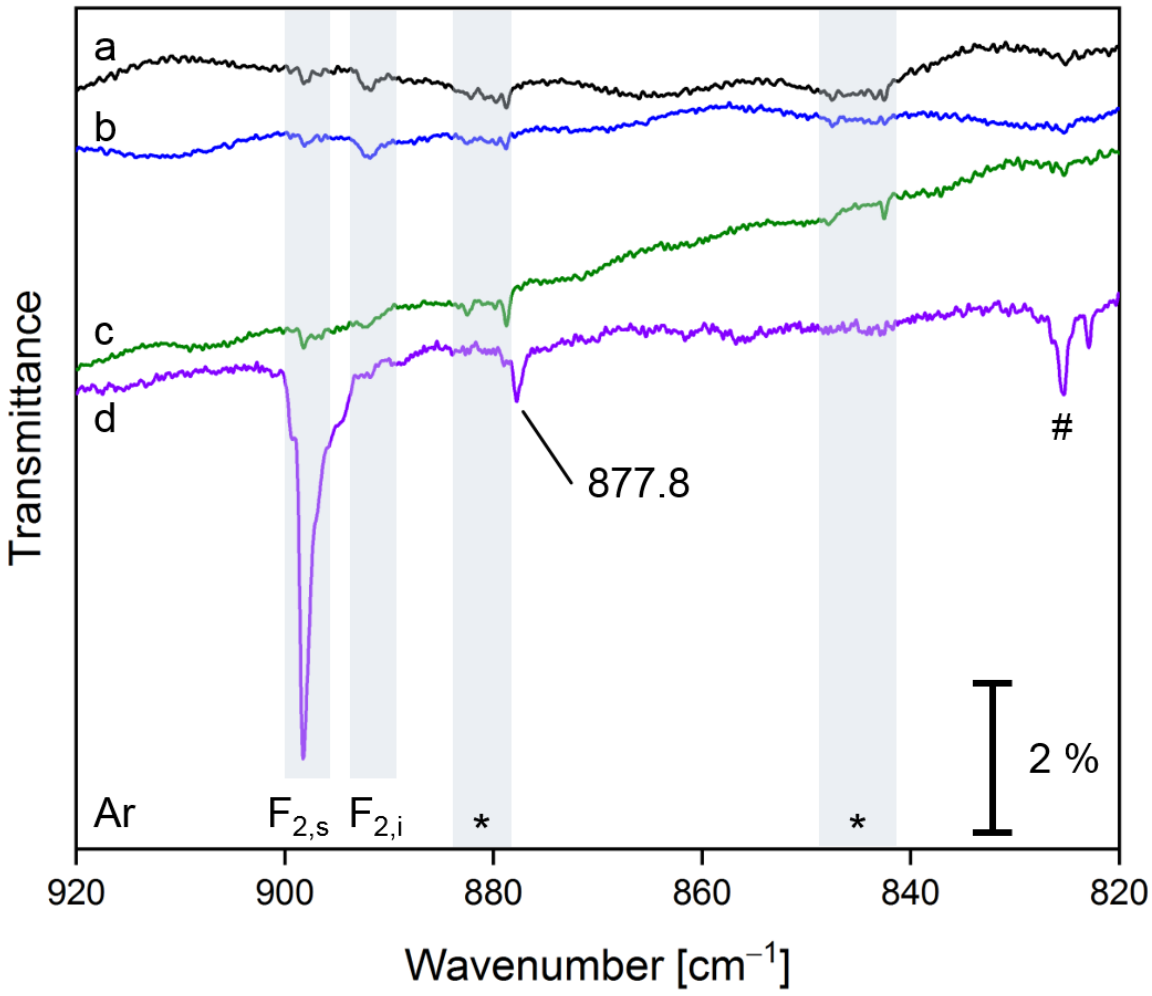

Figure 26: The IR spectra were recorded after depositing exactly 48 mbar·l of F_2 (3 % diluted in Ar) during a) 96 min, and b) 100 min in two independent but subsequent experiments, and c) after deposition of F_2 (1 % diluted in Ar) at a deposition rate of 0.5 mbar·l·min^{-1} for 180 min onto a CsI window at 4 K, and d) after deposition of F_2 (3 % diluted in Ar) at a deposition rate of 0.5 mbar·l·min^{-1} for 60 min onto a gold-plated copper support at 5 K. AsF_5 associated bands (spectra a)-c) are marked with an asterisk. Spectra a)-c) were measured in transmission, spectrum d) in reflection, where the light passes the sample twice and the band intensities are consequently increased. A weak band caused by traces of OF_2[393] is marked with a hash.

A reference experiment at a lower F_2 concentration of 1 % in argon resulted in a higher contamination and an increased $F_{2,s}$:$F_{2,i}$ ratio of 2:1 (spectrum c in Figure 26), with the $F_{2,i}$ band lying only slightly above the noise level. A similar experiment was performed at an independent matrix isolation setup, where AsF_5 had never been used, to circumvent the AsF_5 associated features. The obtained spectrum (spectrum d in Figure 26) contains a very intense $F_{2,s}$ band next to a very weak $F_{2,i}$ band ($F_{2,s}$:$F_{2,i}$ ratio of 25:1), a band at 877.8 cm^{-1}, indicative for a polarized {F_2} unit,[180,393] but no band associated with AsF_5. Moreover, this spectrum was found to be heavily contaminated with HF (A = 16 %), CO_2 (A = 47 %) and SiF_4 (A = 15 %) and additionally contained OCF_2 (A = 30 %) and CF_4 (A = 25 %), determined at the absorbance (A) of the strongest feature of the respective impurity.[180,362–365] Quite the reverse to a failed experiment, this spectrum reveals two important things about the F_2 bands: I) The impurities were available in sufficiently high

amounts to potentially enable a complex formation with F_2, but no new absorption band accounting for an F_2 complex was observed. F_2 complexes of these compounds are either not known or do not shift the F–F stretching band (see Table 7). This indicates that the exact nature of these contaminants does not influence the formation of the $F_{2,s}$ band. II) The large amount of impurities has an influence on the intensity of the $F_{2,s}$ band and subsequently on the $F_{2,s}$:$F_{2,i}$ ratio. Note that in a regular 'clean' experiment employing only F_2 diluted in Ng the intensity of for example SiF_4 at 1023.1 cm^{-1}[365] was in the range of 1–2 %, even after longer deposition times than in the abovementioned case. For the assignment of the band at 877.8 cm^{-1} [Hg·F_2] and [H_2O·F_2], which were reported at 877.7[180] and 877.5 cm^{-1},[393] respectively, come into question. However, no water[468] was present in the spectrum, and Hg had only been used in the form of laser-ablated silver-amalgam prior to these experiments. These facts leave the band at 877.8 cm^{-1} unassigned.

In conclusion, noble gas matrix-isolated fluorine primarily forms two phases. The first accounts for isolated F_2 molecules[74,180] and is found at 891.7 cm^{-1} in Ne and at 891.8 cm^{-1} in Ar at a low impurity level. The second one is found at 901.3 cm^{-1} in Ne and at 898.2 cm^{-1} in Ar and accounts for a solid fluorine phase,[10] which is preferably formed in perturbed matrices at a higher impurity level. Lower frequency vibrational bands of F_2 have been reported for complexes (see Table 7) and in perturbed matrices at 887 cm^{-1} (annealed matrix of amorphous F_2)[13] and at 884.4 cm^{-1} (6 % F_2 and 6 % Cl_2 embedded in Ne),[10] which all account for more strongly polarized {F_2} moieties or F_2 molecules, correspondingly.

It is worth noting that the recently recorded spectra of long-term (180 min) deposition of 3 % fluorine in neon in well-passivated systems showed a consistently high level of impurities in independent experiments (Figure 110 in the appendix). It was found that, although the gas mixture was exchanged in between two consecutive sets of experiments, the level of contaminants could not be efficiently lowered. Virtually the same results were obtained using an independent matrix isolation setup at the same experimental conditions. The cooling of a gas mixture of 3 % F_2 in Ne to 77 K during deposition was not advantageous towards 'cleaner' spectra (see also Section 4.1.3.5 and Figure 111 in the appendix). Note that these facts only effected the experiments employing SbF_5 and laser-ablated Cs[AuF_6], and the experiments using BF_3 and AsF_5 are unaffected. Accordingly, the spectrum shown in Figure 22 serves as the main reference for the band of isolated fluorine $F_{2,i}$.

3.1.2.2 BF_3 and F_2 in Noble Gas Matrices

Among the studied Lewis acids with their respective ability to polarize the F_2 molecule, BF_3 is the smallest and weakest representative in the series BF_3, AsF_5, SbF_5 and AuF_5.[66,69,249] Nevertheless, BF_3 is a strongly IR active molecule that provides detectable bands even at low concentrations that should shift considerably upon complex formation.[73]

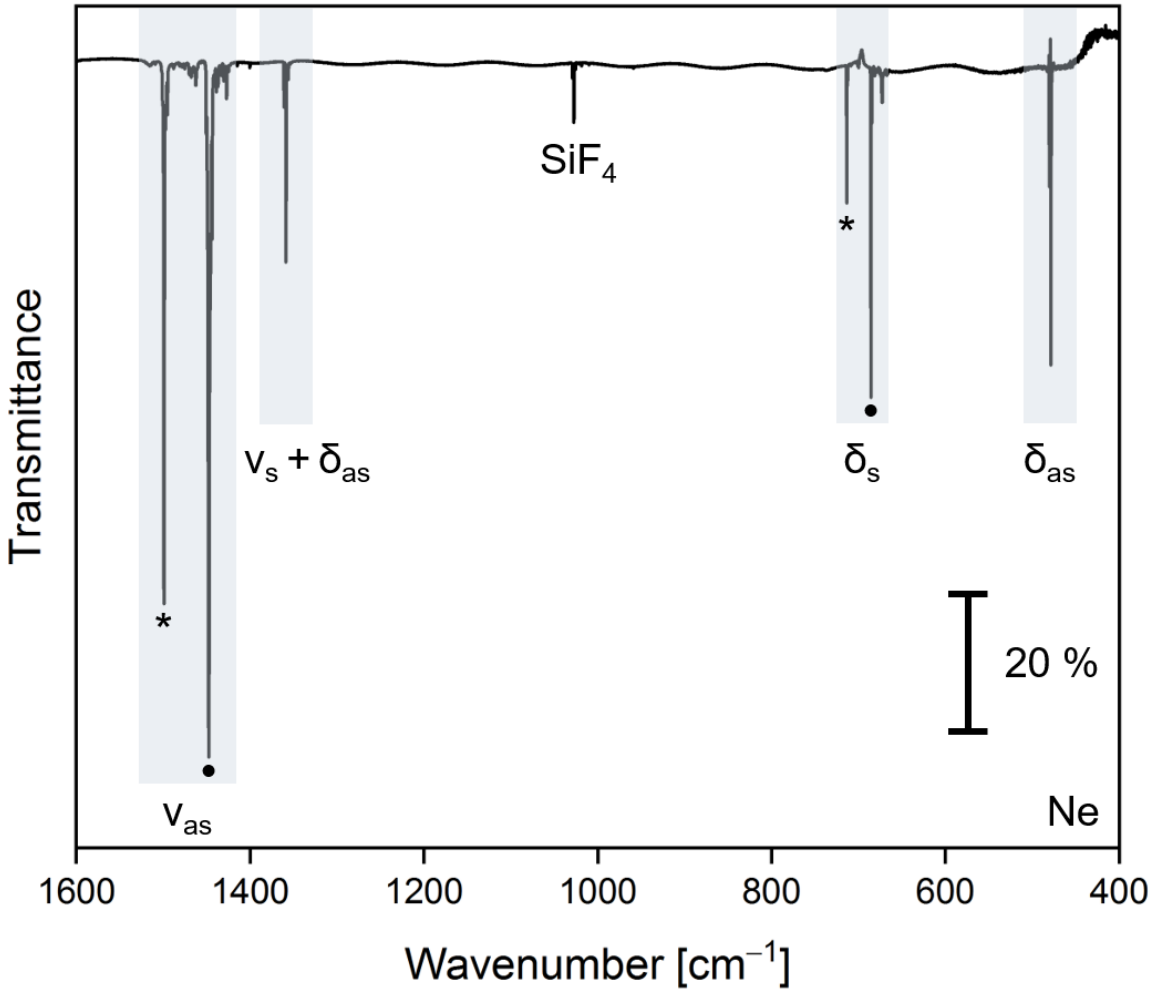

Figure 27: IR spectrum of the fundamentals of BF_3 and a combination band in solid neon. The isotopomers $^{10}BF_3$ and $^{11}BF_3$ are marked by asterisks and dots, respectively. The isotopic splittings of the antisymmetric deformation mode and the combination band are 2 cm^{-1}. The IR spectrum was recorded after the deposition of BF_3 (0.1 % in Ne) onto a CsI window at 4 K for 17 min at a deposition rate of 0.6 $mbar \cdot l \cdot min^{-1}$. The bands were found to match the reported literature values.[469] A weak band caused by SiF_4 is indicated.[470]

In order to prevent saturation of the spectra at prolonged deposition, the concentration of BF_3 was chosen to be very low (0.02 % in Ar, 0.1 % in Ne). A spectrum showing the fundamentals of BF_3 embedded in neon is depicted in Figure 27, while a corresponding spectrum in argon is depicted in Figure 104 in the appendix. The main observations during the experiments employing BF_3 and F_2 are also summarized in Table 15.

Table 15: IR band positions (given in cm^{-1}) of the main features observed in the BF_3/F_2 experiments in neon and argon. The band maxima of the ν(F−F) are bold and only the most prominent matrix sites are given. The band positions of the BF_3 and F_2 fundamentals agree with the literature values.[10,13,180,456,461,469] Band positions in italics were only observed after annealing.

Assignment	Ne	Ar
$\nu_{as}(BF_3)$	1499.1[a], 1447.6[b]	1498.2[a], 1447.1[b]
$\nu_s + \delta_{as}(BF_3)$	1361.1[a], 1358.8[b]	1364.3[c]
ν(F−F), $F_{2,s}$	902.3 sh, **901.2**, 900.3 sh	**898.1**, 897.1 sh, 896.3 sh
ν(F−F), $F_{2,i}$	**892.4** br, 891.4 sh, 890.4 sh	892.9 sh, **892.4**, 891.5 sh
$\nu_{as}(AsF_{3,eq})$, $[AsF_5{\cdot}F_2]$*[,d]	886.3, 884.7, **883.0**, 881.6, *880.6* br	882.4, 880.5, 879.8, **878.8**
$\nu_{as}(AsF_{2,ax})$, $[AsF_5{\cdot}F_2]$*[,d]	*852.7* br, *848.3*, 847.2, **846.0**	847.6, 843.6, **842.5**
$\delta_s(BF_3)$	713.4[a], 685.6[b]	703.0[a], 675.7[b]
$\delta_s((BF_3)_2)$	*662.6*, *659.6*, *652.3*	*655.2* (*+ sites*)
$\delta_{as}(BF_3)$	480.5[a], 478.7[b]	479.2[c]

[a] $^{10}BF_3$, [b] $^{11}BF_3$., [c] only one maximum could be assigned clearly in this region due to the extended site structure, [d] tentative assignment of an assumed cage pair (marked uniformly by an asterisk throughout the figures) in comparison with the corresponding modes of the parent bands, [d] no definite vibrational mode could be assigned; sh = shoulder; br = broad.

Clear evidence for the formation of a discrete $[BF_3{\cdot}F_2]$ complex upon co-condensation of BF_3 and F_2 was found neither in argon nor in neon, but indications will be briefly discussed in the following. The non-appearance of a $[BF_3{\cdot}F_2]$ adduct might be explained with the extremely low basicity of F_2 (305.5 $kJ{\cdot}mol^{-1}$),[73,361] when considering that even N_2 features a higher basicity of 464.5 $kJ{\cdot}mol^{-1}$[73,361] and only forms a van der Waals complex with BF_3, which is calculated to be endothermic by −2.27 $kJ{\cdot}mol^{-1}$.[73,471] On the other hand, even though the coordination of N_2 does not lead to a deformation of the planar $\{BF_3\}$ moiety[73,357] in this loosely bound $[BF_3{\cdot}N_2]$ complex, the $\delta_s(BF_3)$ is perturbed and red-shifted by 23 cm^{-1}.[73,472] In contrast, the corresponding $\nu_{as}(BF_3)$ is only shifted by 4 cm^{-1},[73,472] making the B−F stretching region less indicative for loosely bound complexes. A similar behavior was observed for a $[BF_3{\cdot}CO]$ complex,[473] featuring a gas phase basicity of 562.8 $kJ{\cdot}mol^{-1}$ of CO (carbon side),[73,361] a planar $\{BF_3\}$ moiety in the complex, an experimental complex binding energy of 7.5 $kJ{\cdot}mol^{-1}$[73,474] (calculated 4–10 $kJ{\cdot}mol^{-1}$)[73,473,475] and corresponding shifts of $\nu_{as}(BF_3)$ and $\delta_s(BF_3)$ of 9 and 40 cm^{-1},[73,472] respectively. That the interaction energy of the $[BF_3{\cdot}N_2]$ adduct lies in the same range as the $[BF_3{\cdot}F_2]$ adduct in the present work indicates that a perturbed out-of-plane deformation mode $\delta_s(BF_3)$ might be observable.

The detailed observations in the individual experiments in argon and neon are presented in the following two subchapters, especially regarding the IR active features in the F–F stretching region.

3.1.2.2.1 BF_3 and F_2 in Ar

Besides the BF_3 fundamentals (Figure 104 in the appendix), the deposition of a gas mixture of BF_3 (0.02 %) and F_2 (1 %) diluted in argon gave rise to bands at 892.4 and 898.1 cm^{-1}, assigned as matrix-isolated (denoted $F_{2,i}$) and solid F_2 (denoted $F_{2,s}$), as depicted in Figure 28. The development in the BF_3 stretching and deformation regions upon deposition and annealing processes is depicted in Figure 112, which is found in the appendix.

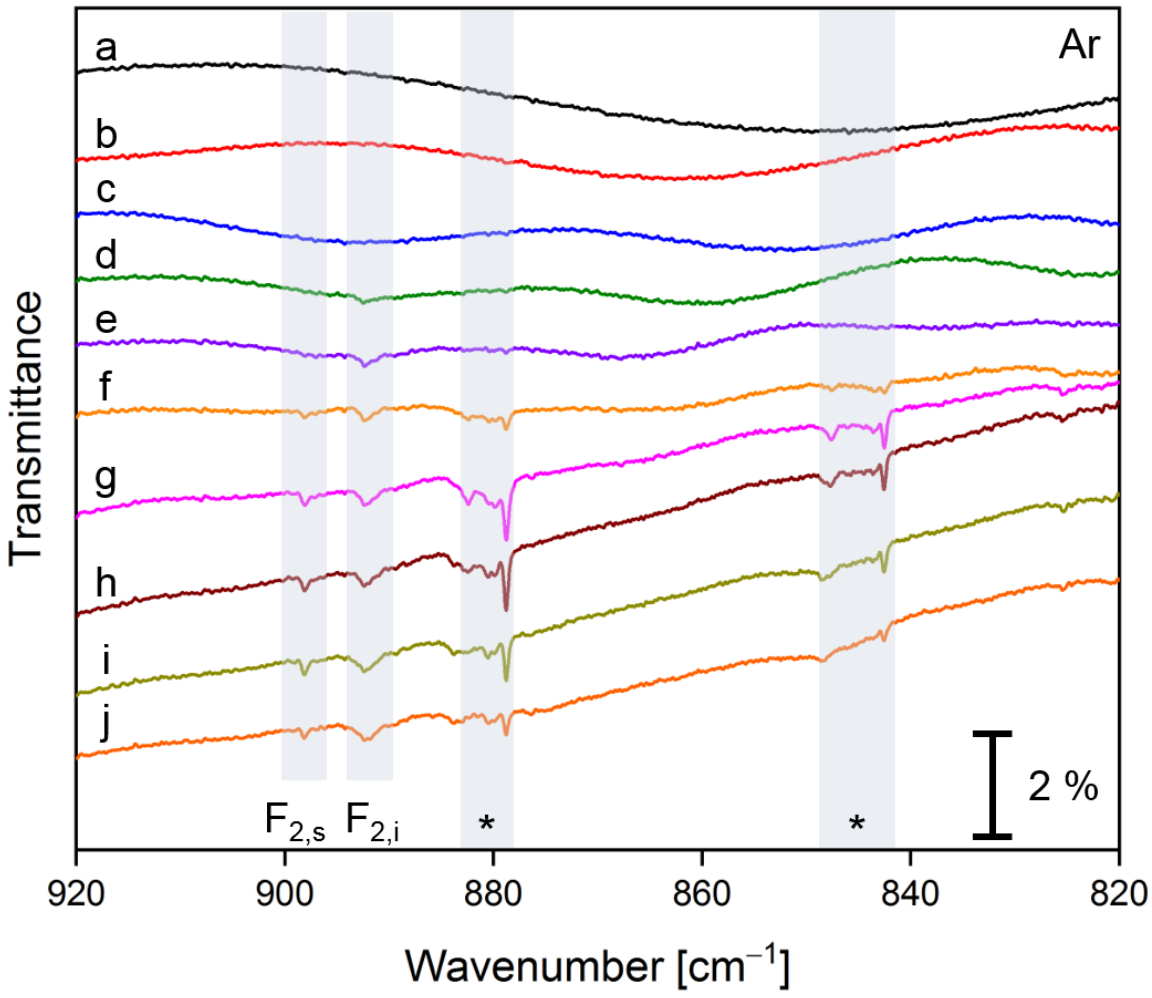

Figure 28: The IR spectra were recorded after the deposition of a) argon for 18 min, b) subsequently BF_3 (0.1 % in excess argon) for 15 min, c) subsequently BF_3 (0.02 % in excess argon) for 16 min, and after the subsequent deposition of BF_3 (0.02 %) and F_2 (1 %) diluted in argon for d) 16 min, e) 32 min, f) 62 min, and g) 122 min onto a CsI window at 4 K at a deposition rate of 0.5 mbar·l·min^{-1}, and after annealing of the matrix to h) 22 K, i) 30 K, and j) 35 K. IR active features caused by traces of AsF_5 in combination with F_2 are marked by an asterisk.

As a consequence of an arsenic contamination of the deposition line (see Section 3.1.2.3), the spectra contained IR active features with maxima at 878.8 and 842.5 cm^{-1} associated with AsF_5 in combination with F_2, which are marked by an asterisk in Figure 28. Apparently, these bands formed upon prolonged deposition and, with them, the absorption of solid fluorine and also the ratio $F_{2,s}$:$F_{2,i}$ increased. Note that the latter information is important, because of the low signal-to-noise ratio especially in the beginning of the deposition, when the additional $F_{2,s}$ band could be hidden. This indicates that the formation of a separated phase of solid fluorine favorably takes place together with the appearance of an impurity, in accordance with the discussion in Section 3.1.2.1. Other than that, the AsF_5/F_2 associated bands decrease by 65 % upon annealing, while the $F_{2,i}$ band even slightly increases and a shoulder located at 891.8 cm^{-1} grows out of the $F_{2,i}$ band at 892.4 cm^{-1}. A detailed view of the F−F stretching region is found in the appendix in Figure 113.

Although no new F_2 band position characteristic of [BF_3·F_2] was observed, the formation of an adduct is not necessarily excluded, since the F−F stretching frequency is calculated to be of low intensity (Table 11) and an appreciably shifted BF_3 centered band might be indicative for an adduct formed.

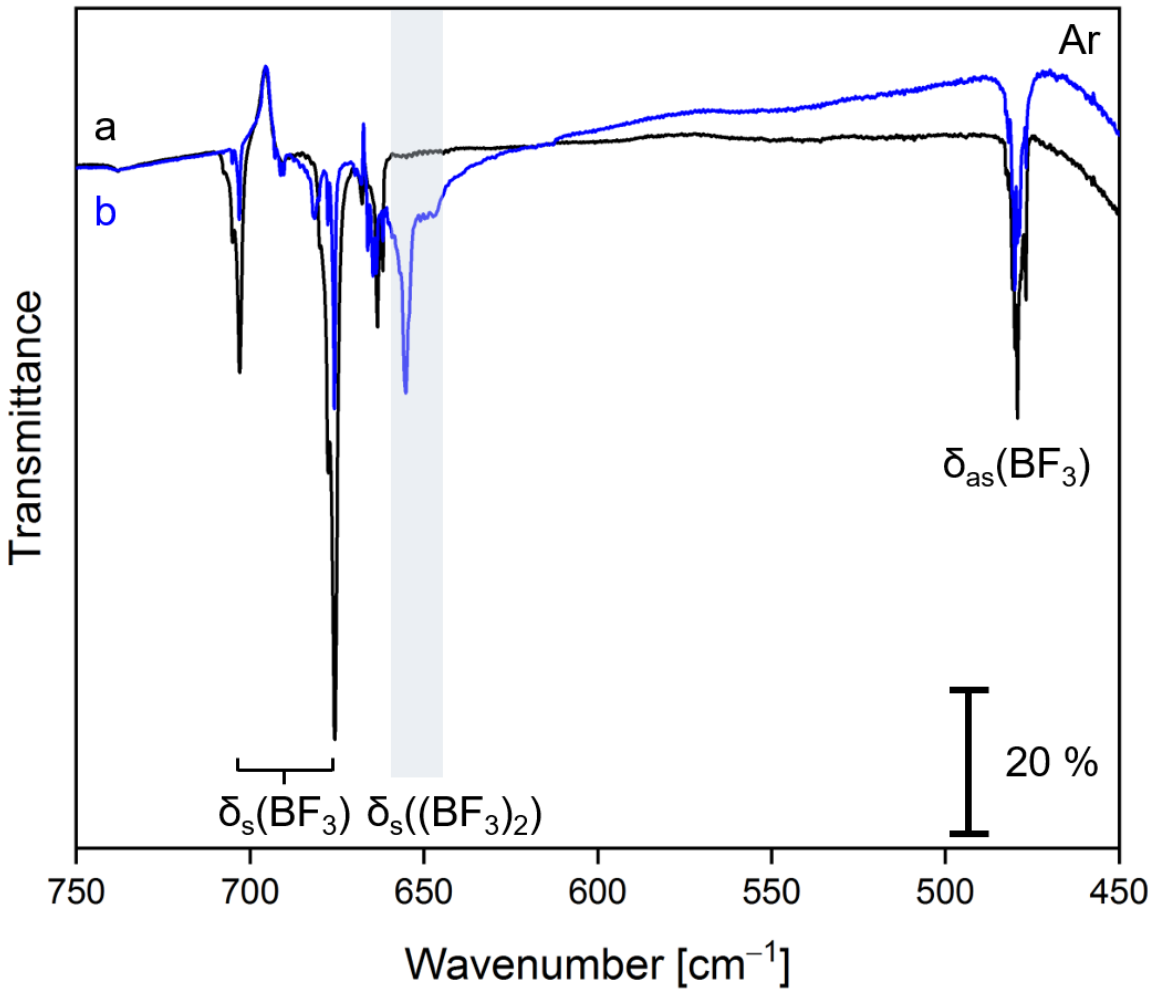

Figure 29: The IR spectra were recorded after the deposition of a) argon for 18 min, subsequently BF_3 (0.1 % in excess argon) for 15 min, subsequently BF_3 (0.02 % in excess argon) for 16 min, and after the subsequent deposition of BF_3 (0.02 %) and F_2 (1 %) diluted in argon onto a CsI window at 4 K for 122 min at a deposition rate of 0.5 mbar·l·min^{-1} and after b) annealing of the matrix to up to 35 K.

With respect to the quantum-chemical results (Table 37 in the appendix), a potential [BF_3·F_2] adduct should lead to a blueshift of the out-of-plane BF_3 deformation by 8 cm^{-1}. Since this mode is calculated to be the only one to significantly shift upon F_2 coordination, the band at 655.2 cm^{-1} despite being red-shifted by 20 cm^{-1} it is the only one to come into consideration. The reported weakly bound [BF_3·N_2] complex features a redshift of 23 cm^{-1} in this region,[73,471,472] suggesting a similar behavior for a [BF_3·F_2] adduct. However, in accordance with Nxumalo et al.,[456] the highlighted bands in Figure 29 are assigned to the BF_3 dimer. In the case that a [BF_3·F_2] complex would be formed upon annealing, it could be obscured by these strong bands. The IR spectra in the B–F stretching region do not feature new bands besides the development of matrix sites of the fundamentals of BF_3 (Figure 114 in the appendix). Generally, the broadening of the bands accompanied by the formation of an extended matrix site structure is known from the literature.[456]

3.1.2.2.2 BF_3 and F_2 in Ne

In order to elucidate the dependency of the potential adduct formation on the matrix host, analogous experiments were performed in neon matrices. Upon the deposition of BF_3 and F_2 in excess neon (Figure 30), the F–F stretching band of matrix-isolated fluorine ($F_{2,i}$) at 891.9 cm^{-1} already appeared at an early stage of the deposition.

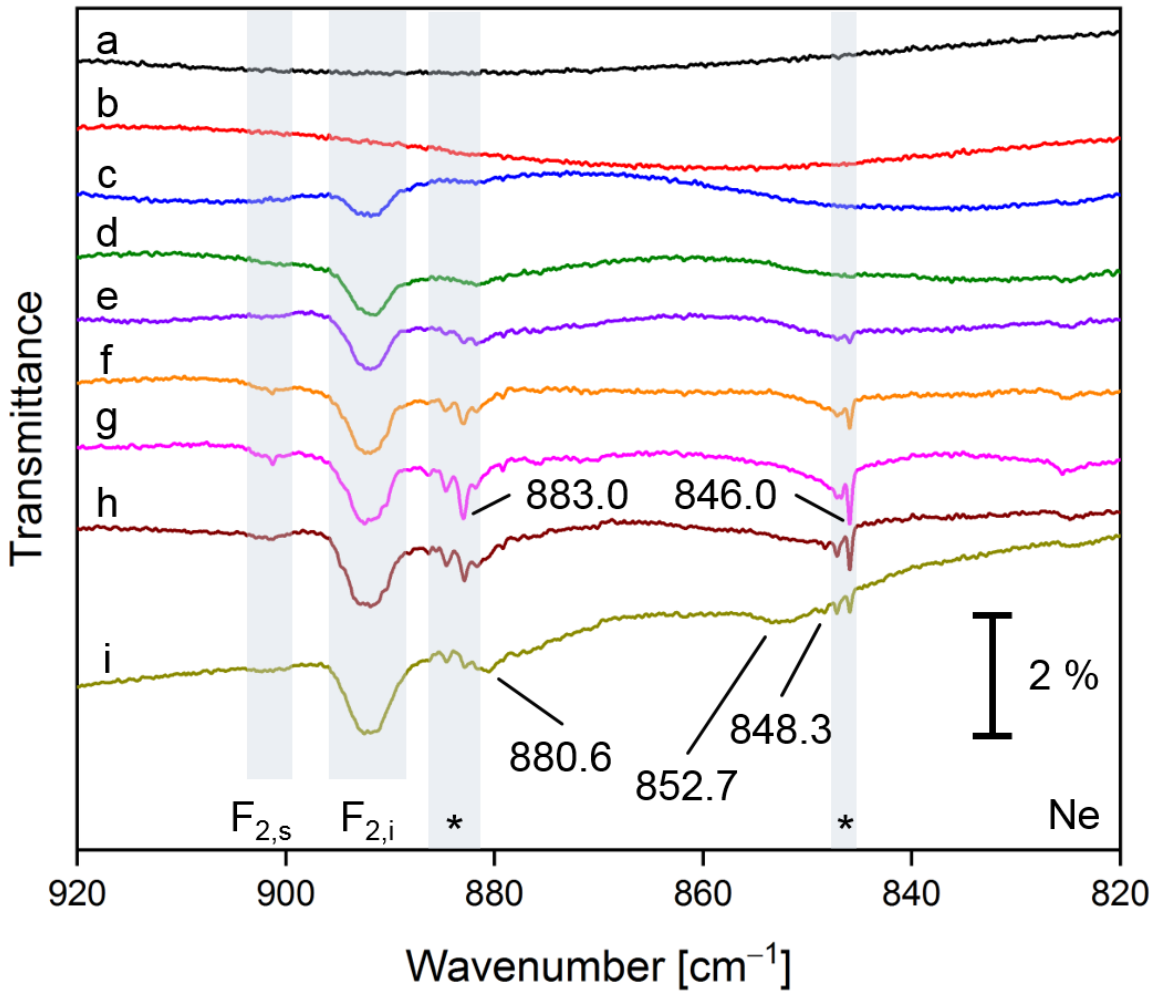

Figure 30: The IR spectra were recorded after the deposition of a) neon for 19 min, b) subsequently BF_3 (0.1 % in excess neon) for 17 min, and after the subsequent deposition of BF_3 (0.1 %) and F_2 (1 %) diluted in neon for c) 16 min, d) 33 min, e) 60 min, f) 91 min and g) 120 min onto a CsI window at 4 K at a deposition rate of 0.6 mbar·l·min^{-1}, and after annealing of the matrix to h) 11 K and i) 13 K. IR active features caused by traces of AsF_5 in combination with F_2 are marked by an asterisk.

The prolonged condensation of the reactants gave rise to two bands stemming from AsF_5 in combination with F_2 (contamination of the deposition line, vide supra) concomitant with the band assigned to solid fluorine ($F_{2,s}$) at 901.3 cm^{-1}. The first of the AsF_5/F_2 associated bands is centered at 883.0 cm^{-1} with matrix sites at 886.3, 884.7 and 881.6 cm^{-1}, and the second at 846.0 with a site at 847.2 cm^{-1}. Coincidentally, a shoulder of the $F_{2,i}$ band became apparent at 890.3 cm^{-1}, which was observed as a distinct band in AsF_5 experiments (Section 3.1.2.3.2, Figure 39). The AsF_5/F_2

associated features diminished upon annealing, which was observed in the $AsF_5/F_2/Ng$ experiments as well (Section 3.1.2.3). During annealing, the $F_{2,s}$ band diminished and the $F_{2,i}$ first intensified and then sharpened up slightly, while this process also gave rise to broad new features at 880.6 and 852.7 cm^{-1} and a weak band at 848.3 cm^{-1}, which could be interpreted as a smearing of the AsF_5/F_2 associated bands in a way that the cage-paired AsF_5 and F_2 slightly diffuse to 'form' geometrically ill-defined complexes, which are known to result in broad bands.[73,354] This could also explain the increasing $F_{2,i}$ band, which was observed in the argon experiments as well (vide supra). A close view on the bands' development upon annealing is featured in Figure 117 in the appendix.

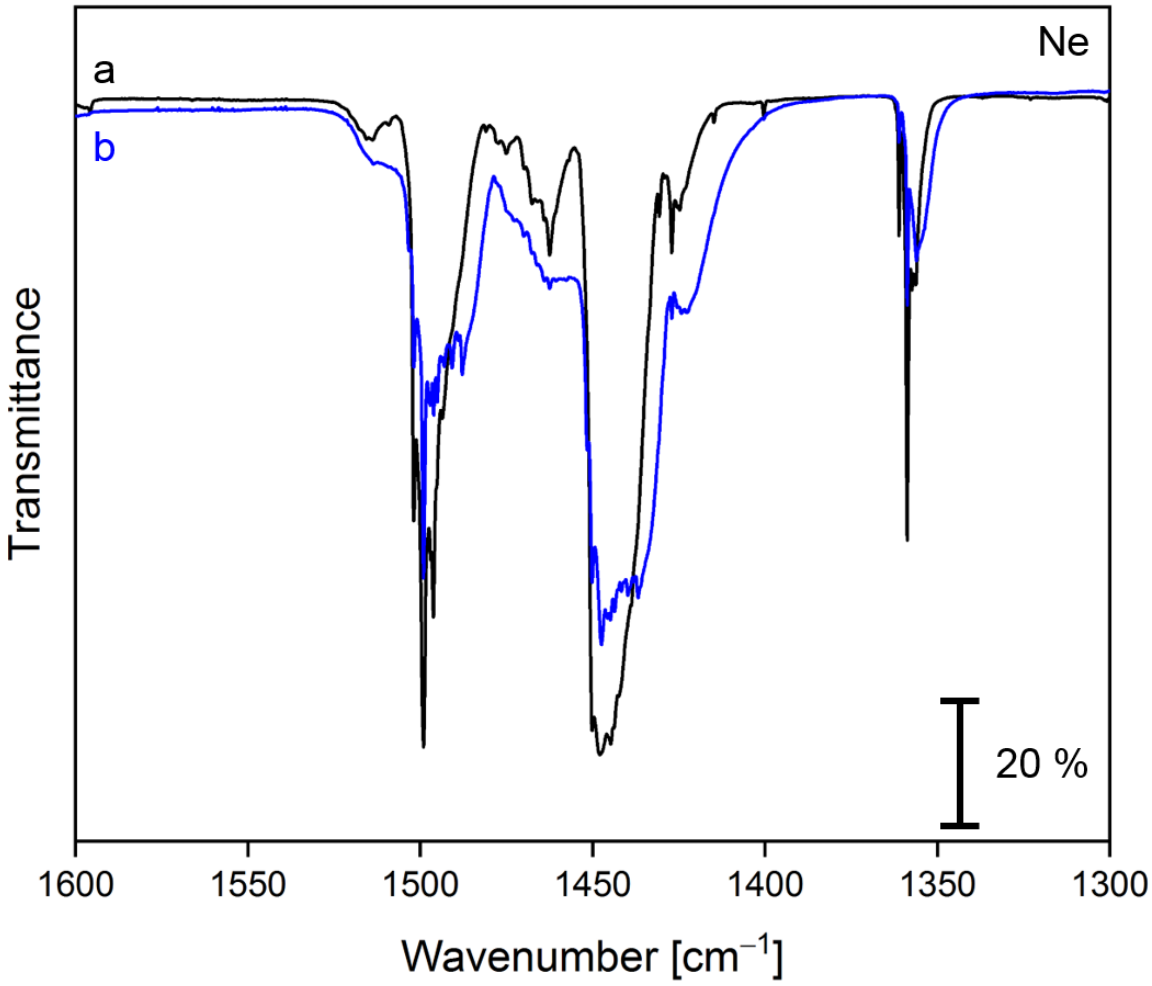

Figure 31: The IR spectra were recorded after the deposition of a) neon for 19 min, subsequently BF_3 (0.1 % in excess neon) for 17 min, and the subsequent deposition of BF_3 (0.1 %) and F_2 (1 %) diluted in neon onto a CsI window at 4 K for 120 min at a deposition rate of 0.6 mbar·l·min^{-1} and b) after annealing of the matrix to up to 13 K.

In the B–F stretching (Figure 31) and deformation regions (Figure 32) blue-shifted bands associated with the discussed behavior of the F_2 bands indicating a distorted $\{BF_3\}$ moiety in a $[BF_3 \cdot F_2]$ adduct were not observed. Although the spectra were found saturated regarding the

fundamentals and matrix sites thereof, the choice of a highly concentrated BF_3 seemed to be justified in order to offer sufficient amounts of the Lewis acid and thereby to provoke a Lewis acid-base interaction with the very weak base F_2.[73,361]

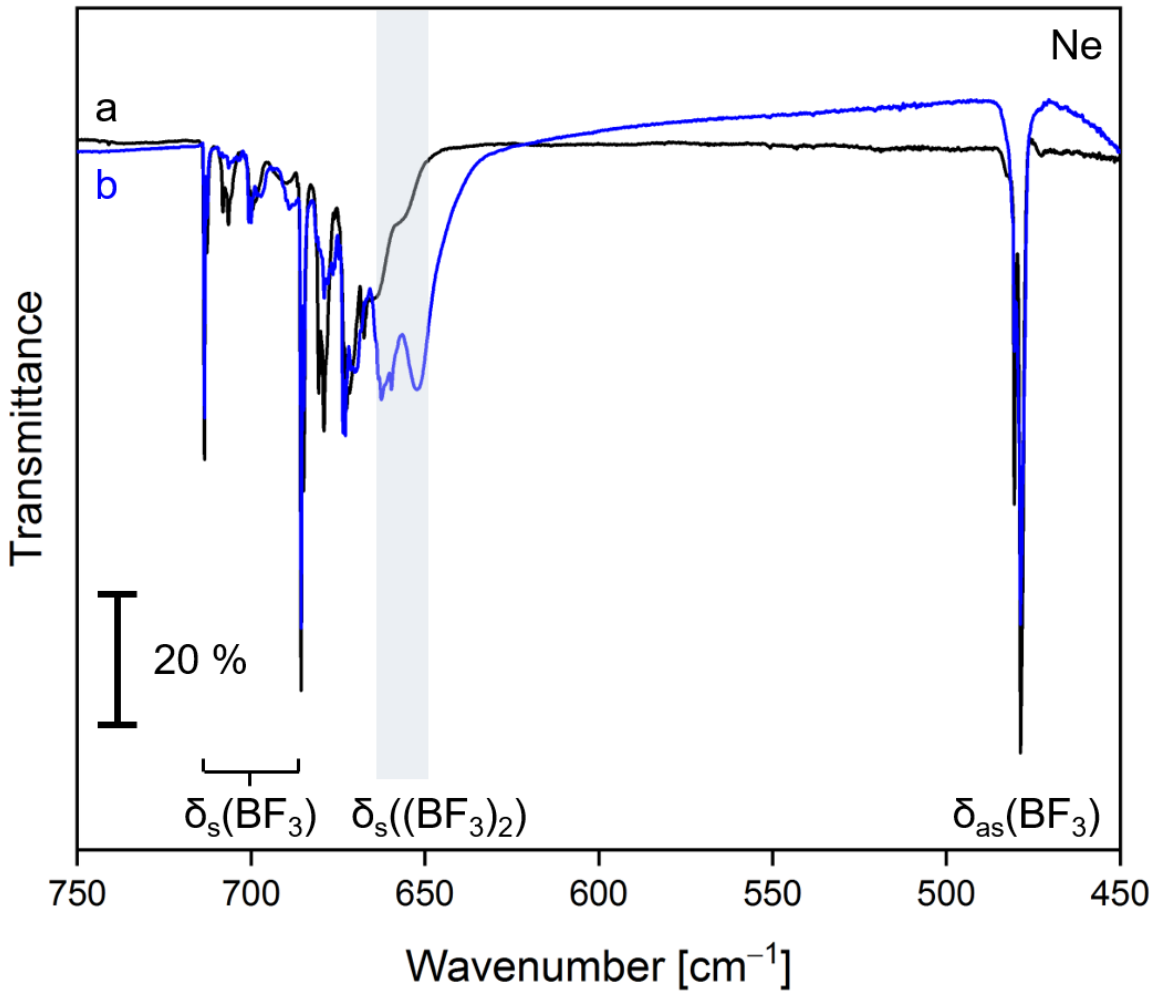

Figure 32: The IR spectra were recorded after the deposition of a) neon for 19 min, subsequently BF_3 (0.1 % in excess neon) for 17 min, and the subsequent deposition of BF_3 (0.1 %) and F_2 (1 %) diluted in neon onto a CsI window at 4 K for 120 min at a deposition rate of 0.6 mbar·l·min^{-1} and b) after annealing of the matrix to up to 13 K.

During the annealing of the matrix to 13 K, the monomeric fundamentals decreased and two bands at 652.3 and 662.6 (site at 659.6) cm^{-1} increased strongly. These were assigned to the symmetric deformation of the BF_3 dimer in accordance with the results in argon and corresponding to reference [456]. Blue-shifted bands (see Table 37 in the appendix), which would be attributable to a fluorine complex or its decomposition upon annealing, were not observed. Next to the formation of the dimeric species, the BF_3 stretching and deformation regions where generally governed by changes in matrix sites upon annealing, which agrees with the literature.[456] The step-by-step spectra in the B−F stretching and deformation regions are depicted in Figure 115

and Figure 116 in the appendix, respectively. The neon results are found to be in line with the obtained argon data.

Concluding the experiments of BF_3 and F_2, evidence for a BF_3-specific F_2 band could not be found, even at high concentrations of the reactants. The BF_3 stretching and deformation regions were governed by site changes of the Lewis acid and the formation of the dimer was observed in both argon and neon matrices. The formation of the $F_{2,i}$ band seemed to be favored for BF_3 during the neon experiments at a lower $F_{2,s}$:$F_{2,i}$ ratio than in argon, where the contamination with AsF_5 was less than in the analogous argon experiments. All 'activity' in the F−F stretching region is made up by matrix-isolated and solid F_2, as well as bands associated with AsF_5 combined with F_2, which were found in experiments explicitly employing AsF_5 too. AsF_5 therefore had a significant impact on the spectra and promoted the formation of the $F_{2,s}$ band as discussed in Section 3.1.2.1. The straightforward assignment to an [AsF_5·F_2] complex is not possible, because it contradicts the quantum-chemical results (Section 3.1.1) in intensity and shift of the ν(F−F) band. This is true especially for the lower frequency band centered at 846.0 cm^{-1}.

3.1.2.3 AsF_5 and F_2 in Noble Gas-Matrices

In contrast to BF_3, only little is known about AsF_5 and SbF_5 under matrix isolation conditions.[30,73] Only the fundamental work of Aljibury and Redington, who measured IR spectra of matrix-isolated and pure thin film samples of arsenic and antimony pentafluorides, has been documented.[351] The reactions of these compounds with Lewis bases under matrix isolation conditions were not studied.[73] In order to compensate for the extremely low basicity of difluorine, AsF_5 and SbF_5 are more promising candidates for the investigation of Lewis acid-fluorine interactions than BF_3 due to their higher acidities.[66]

The experiments using arsenic pentafluoride were performed with pre-mixed AsF_5/Ng and AsF_5/F_2/Ng gas mixtures in an F_2-passivated stainless-steel system to enable the accurate control of the amount of AsF_5 deposited. For pre-conditioning of the system, the deposition was started at a higher concentration of AsF_5 (up to 1 %), since the capillary of 100 cm length leading to the matrix chamber 'consumed' the AsF_5 in the beginning of the deposition with the result that no AsF_5 bands were observed in the matrix IR spectrum. In other words, only when the reaction in the deposition line has ceased the species of interest can be observed. A typical IR spectrum of 0.1 % AsF_5 embedded in excess Ar is depicted in Figure 33.

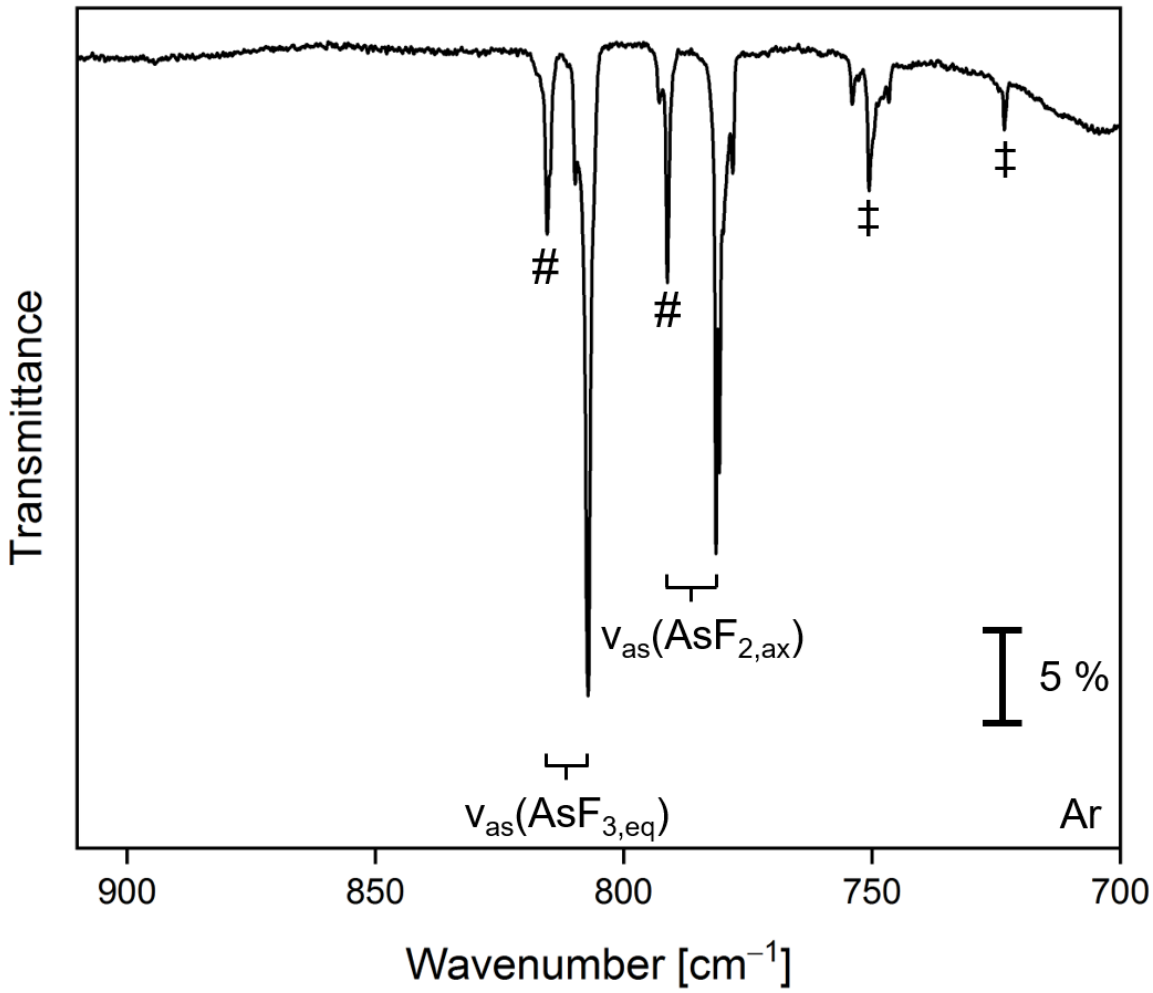

Figure 33: IR spectrum of the IR active fundamentals of AsF_5 in solid argon. Oligomeric absorptions are marked by a hash, unassigned impurity bands by a double dagger. The spectrum was recorded after the deposition of AsF_5 (0.1 % in Ar) onto a CsI window at 4 K for 30 min at a deposition rate of 0.8 mbar·l·min^{-1}. The bands were found to match the reported values.[351,461,476,477]

Although AsF_5 is reportedly monomeric in the gas phase,[463] a non-negligible amount of oligomeric species was found in the matrix (Figure 33), even at very low concentrations as compared to reference [351]. Corresponding data in solid neon, exhibiting an extended site structure, are shown in Figure 105 in the appendix. As an overview, the mainly observed bands in the AsF_5/F_2 experiments are compiled in Table 16.

Table 16: Band positions (given in cm^{-1}) of the main features observed in the AsF_5/F_2 experiments in neon and argon. The band maxima of the ν(F−F) are bold and only the most prominent matrix sites are given. The band positions of AsF_5 and oligomeric absorptions agree with the literature data.[351,461,476,477]

Assignment	Ne	Ar
ν(F−F), $F_{2,s}$	901.2	**898.2**, 896.7 sh
ν(F−F), $F_{2,i}$	892.9 sh, **892.3**[a], 891.3, **891.1**[b], **890.3**[a]	894.5, 892.3, **891.8** sh
$\nu_{as}(AsF_{3,eq})$, $[AsF_5 \cdot F_2]^{*,c}$	884.7, **883.2**	882.5, 879.9 sh, **878.8**
$\nu_{as}(AsF_{2,ax})$, $[AsF_5 \cdot F_2]^{*,c}$	846.7, **845.9**	847.7, 843.5, **842.5**
$[AsF_5 \cdot F_2]^{*,c,d}$	774.1 sh, **773.6**	770.0 sh, **768.9**
$\nu_{as}(AsF_{3,eq})$, oligomeric	820.2, **818.3**	817.3 sh, **815.4**
$\nu_{as}(AsF_{3,eq})$	812.2, **810.6**	809.7 sh, **807.2**
$\nu_{as}(AsF_{2,ax})$, oligomeric	797.2, **795.6**	792.8, **791.2**
$\nu_{as}(AsF_{2,ax})$	**783.8**, 783.1 sh	**781.4**, 780.7

[a] Maxima before annealing; [b] maximum after annealing; [c] tentative assignment of an assumed cage pair upon comparison with the corresponding modes of the parent bands, these bands are marked uniformly by an asterisk throughout the figures; [d] no definite vibrational mode could be assigned; sh = shoulder.

The spectra of AsF_5 in combination with F_2 contained weak signals in the F−F stretching region of an intensity in the order of the $F_{2,s}$ and $F_{2,i}$ bands. The matrix site-splitting of those bands resembled the splitting of about 2 cm^{-1} of the absorptions of mono- and oligomeric AsF_5 in both argon and neon. A correlation between AsF_5 and the co-deposits of AsF_5 and F_2 is thus assumed.

However, the spectra of AsF_5 contained impurity bands at 1112.3, 750.6 and 723.4 cm^{-1} in argon and at 1114.7, 753.3 and 726.4 cm^{-1} in neon of medium (Ar) to high (Ne) intensity. These could not be assigned to arsenic based species like $OAsF_3$ or AsF_3,[461,478–480] which are conceivable decomposition products from AsF_5 upon passage through the stainless-steel deposition line, or to common impurities like OF_2, COF_2, or CF_4.[180,362,363,393] However, the abovementioned impurity bands were not observed in experiments with BF_3 and F_2, where features associated with AsF_5/F_2 were also detected at the same positions in the F−F stretching region (see Section 3.1.2.2). This indicates that the bands rather stem from the combination of AsF_5 and F_2, however, a contribution of the impurity cannot be completely ruled out. As also F_2 complexes with impurities are conceivable even at lower concentrations, the spectra were studied for the correlation of the intensities of impurities' bands and the F_2 bands. Except for the heavily contaminated case (large amounts of multiple impurities) discussed in Section 3.1.2.1, no evidence for a direct correlation of the impurities and the appearance of the F_2 bands was found.

3.1.2.3.1 AsF_5 and F_2 in Ar

Upon the co-condensation of AsF_5 (0.1 %) and F_2 (1 %) simultaneously diluted in Ar with AsF_5 (1 % in Ar) pre-deposited for 15 min, weak fluorine-dependent bands appeared at 898.2 (896.7 sh), 894.2 and 892.4 (891.8 sh) cm^{-1}, as depicted in Figure 34. The former and its shoulder are assigned to solid fluorine ($F_{2,s}$), while the latter three features are considered as isolated fluorine ($F_{2,i}$) in accordance with Table 14 found in Section 3.1.2.1 and Table 16.

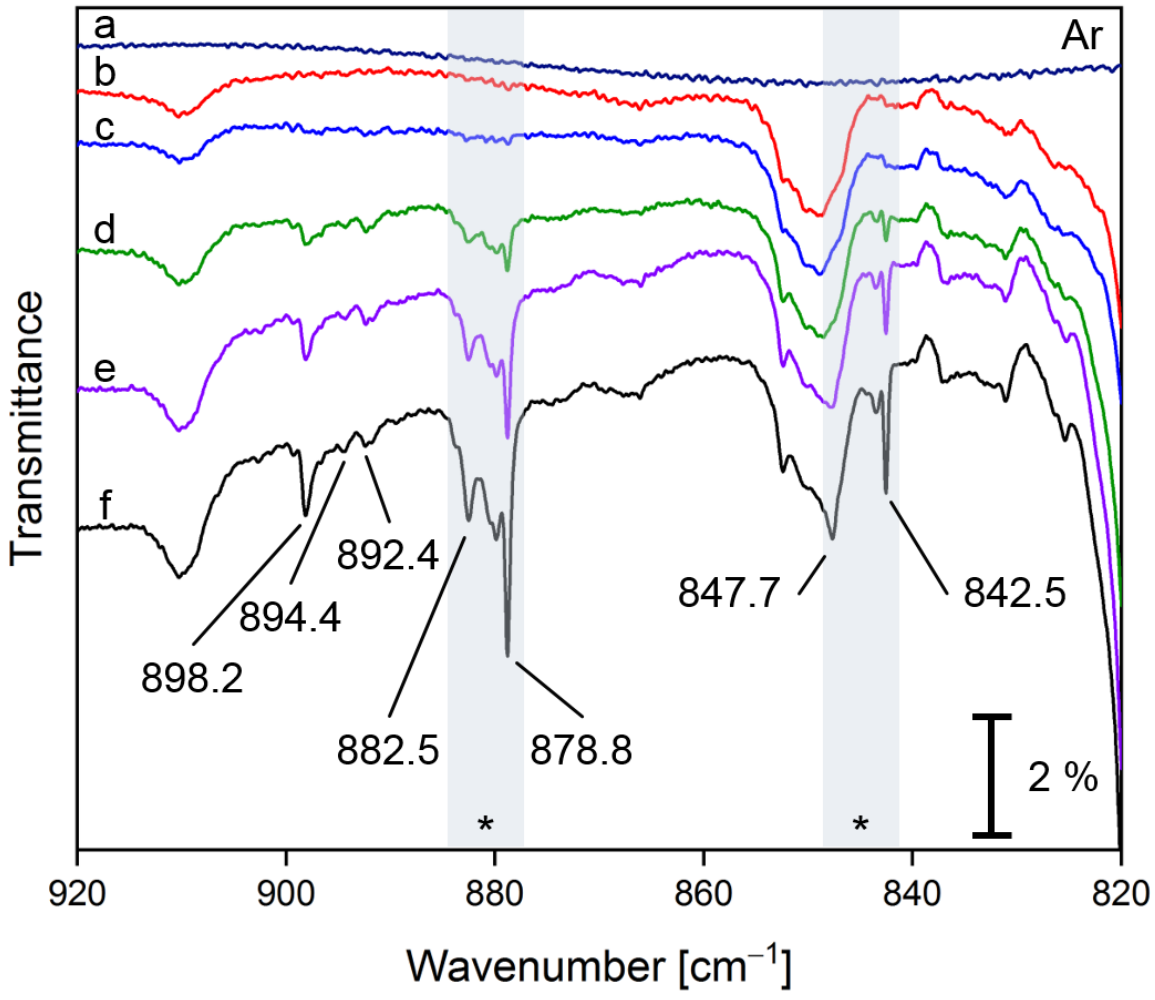

Figure 34: The IR spectra were recorded after the deposition of a) argon for 15 min, b) AsF_5 (1 % in Ar) for 18 min, and the subsequent deposition of a gas mixture of 0.1 % AsF_5 and 1 % F_2 in excess Ar for c) 16 min, d) 76 min, e) 136 min and f) 180 min onto a CsI window at 4 K at a deposition rate of 0.6 mbar·l·min^{-1}. IR active features caused by AsF_5 in combination with F_2 are marked with an asterisk.

Two stronger sets of bands at 882.5, 879.9 and 878.8 cm^{-1}, as well as at 847.7, 843.5 and 842.5 cm^{-1}, also formed during the deposition. While an activation of F_2 by the strong Lewis acid AsF_5[66] with a concomitant, characteristic ν(F–F) is imaginable, the positions and intensities of these bands exceed the calculated shifts of the vibrational bands of an [AsF_5·F_2] complex (Table 12 in Section 3.1.1 and Table 38 in the appendix). Upon the comparison of trace b, where only highly

concentrated AsF_5 (1.0 % in Ar) was deposited, with the subsequent traces (Figure 34), where lower concentrated AsF_5 at 0.1 % and F_2 at 1.0 % in Ar were co-deposited, it becomes evident that the features peaking at 878.8 and 842.5 cm^{-1} stem from the combination of both reactants. This is also reflected in the delayed deposition of these species. Based on the abovementioned 'column'-effect of the stainless-steel deposition capillary, all fluorine bands develop in the same way, slower at the beginning, faster at the end with increasing intensities.

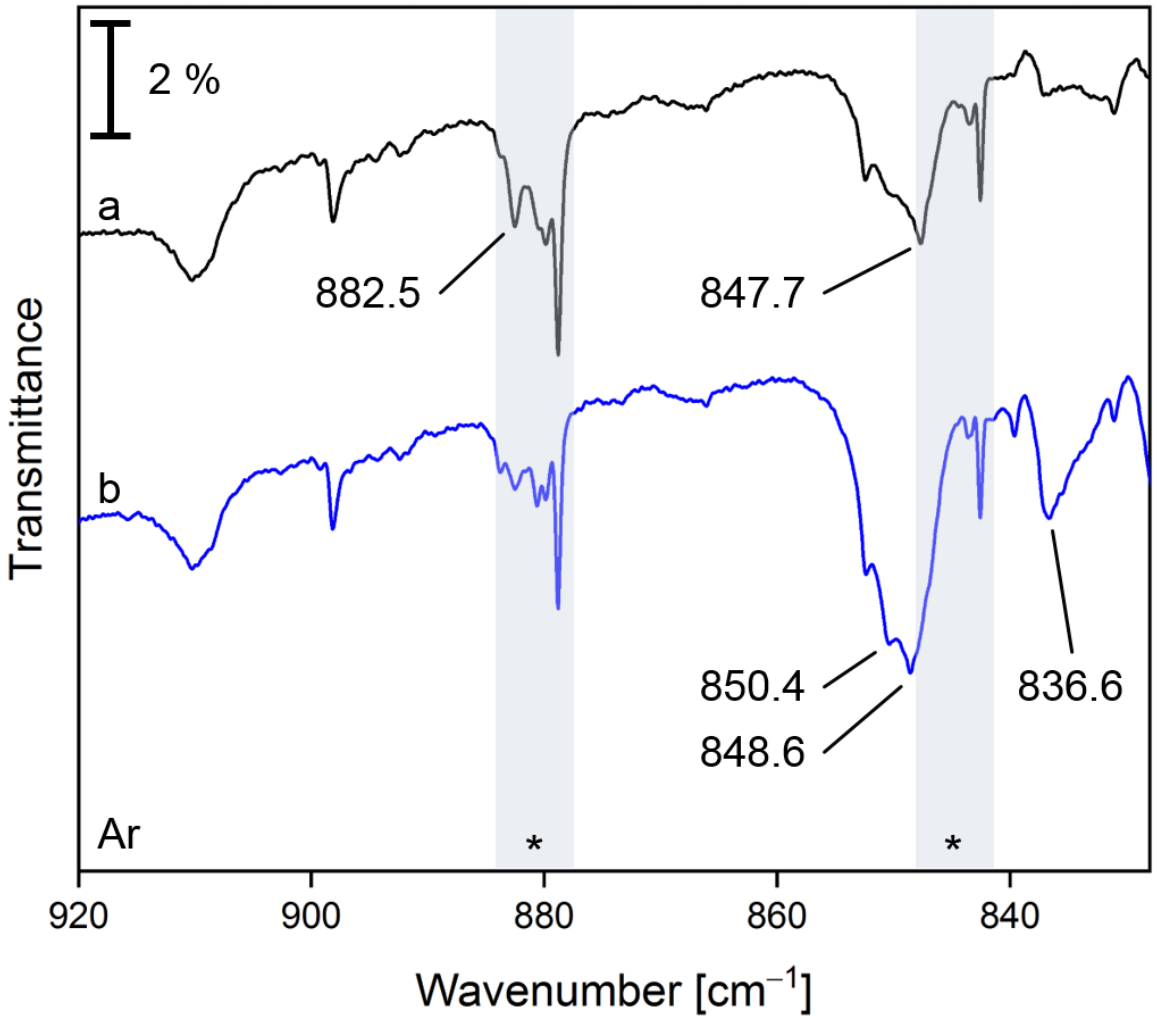

Figure 35: The IR spectra were recorded after a) the deposition of argon for 15 min, AsF_5 (1 % in Ar) for 18 min, and a gas mixture of 0.1 % AsF_5 and 1 % F_2 in excess Ar onto a CsI window at 4 K for 180 min at a deposition rate of 0.6 mbar·l·min^{-1}, and after b) annealing this deposit to 25 K. IR active features caused by AsF_5 in combination with F_2 are marked with an asterisk.

Upon annealing the matrix to 25 K, the recorded spectrum was mainly governed by a broadening of the AsF_5 absorptions (Figure 35, and Figure 118 in the appendix) including the increasing features at 850.4, 848.6 and 836.6 cm^{-1}. While the $F_{2,s}$ and $F_{2,i}$ bands remained almost unchanged, the features at 882.5 and 847.7 cm^{-1} were decreasing, rendering them as matrix sites of the sharp bands at 878.8 and 842.5 cm^{-1}, which were slightly decreasing as well.

The overall very intense bands of arsenic pentafluoride would not allow the discrimination of a coordinated AsF_5 from free (mono- and oligomeric) AsF_5, if the frequency shift was small (Table 38 in the appendix), which corresponds to the calculated small interaction energy of about −4 kJ·mol^{-1} at the RI-B3LYP-D4/def2-TZVPP level of theory (even less stable at the other levels of theory, see Table 8). At these low interaction energies, there is virtually no chance for the Lewis acid and F_2 to form a complex in the gas phase at room temperature, since the entropic term is not frozen out as under matrix isolation conditions.[73] By choosing high concentrations of the starting materials, the probability of forming a matrix cage pair (molecules lying adjacent in the same matrix site)[73] increases. This on the other hand increases the probability of eventually finding evidence for an [LA·F_2] complex. Unfortunately, the cage pair does not necessarily lead to a well-defined geometry of the formed complex, meaning that sharp bands are not guaranteed for adjacent Lewis acid and base molecules.[73,354,481]

In order to further investigate the findings at high concentrations of AsF_5, an experiment employing very dilute AsF_5 was performed. As AsF_5 is monomeric in the gas phase,[463] one would also expect to primarily observe the monomeric absorptions. The contrary is the case, since in an experiment with highly diluted AsF_5, where fluorine at a concentration of 1 % diluted in argon was passed through the deposition capillary and 'eluted' arsenic centers as AsF_5, it became apparent that the oligomeric absorptions are predominant. The oligomeric bands are located at 815.4 and 791.1 cm^{-1} (Figure 36) and are blue-shifted by 4 cm^{-1} each from the reported gas phase values,[461,476,477] and agree with the reported matrix results.[351]

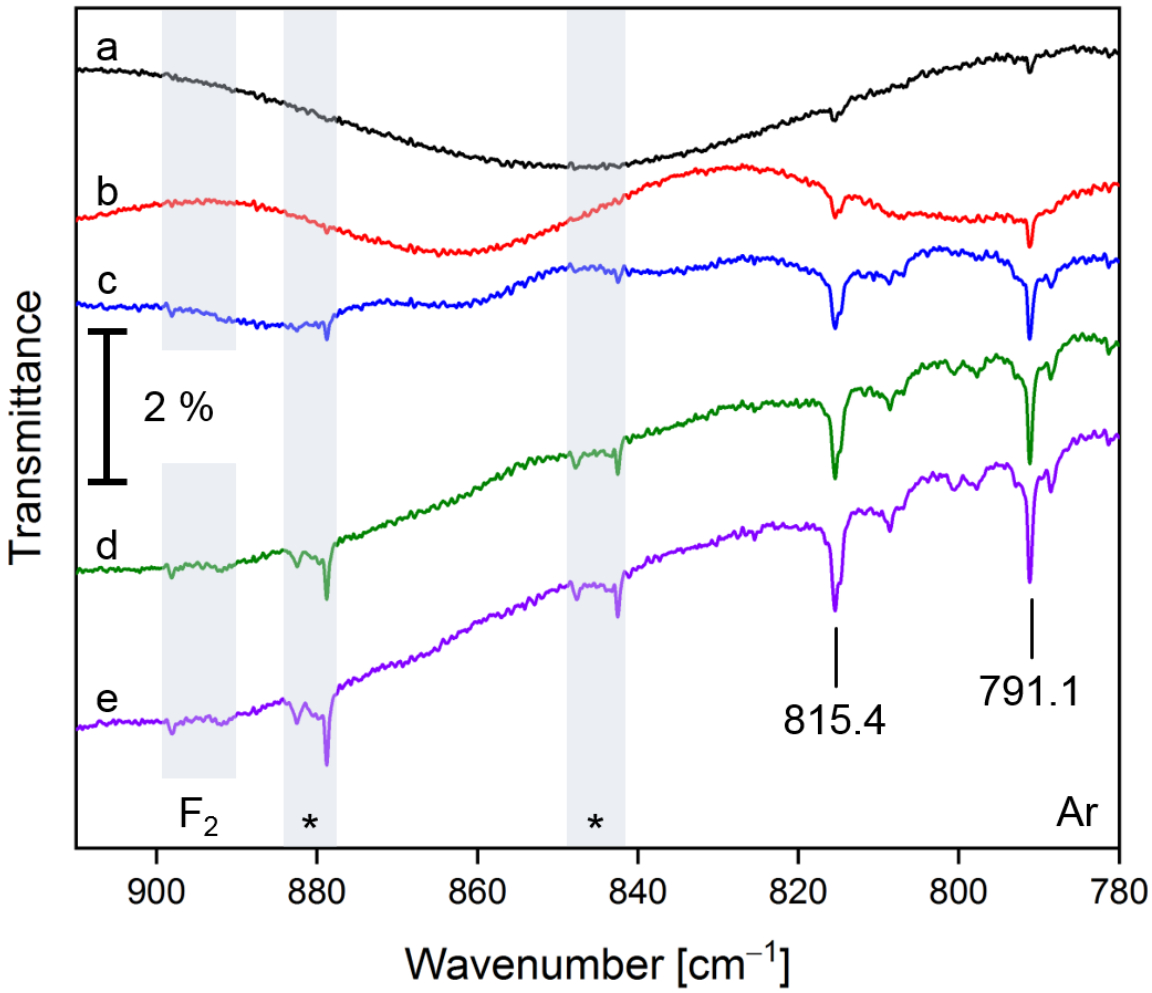

Figure 36: IR spectra recorded after the deposition of a) argon for 20 min, and fluorine (1 % in excess argon, accompanied by highly diluted AsF_5) for b) 15 min, c) 75 min, d) 150 min and e) 180 min onto a CsI window at 4 K at a deposition rate of 0.6 mbar·l·min^{-1}. Absorptions of monomeric AsF_5 and molecular fluorine were highlighted. IR active features caused by traces of AsF_5 in combination with F_2 are marked with an asterisk.

Note that traces of AsF_5 were already observed in the argon spectrum (Figure 36, trace a). It was somewhat unexpected that the features characteristic of deposits of AsF_5/F_2 with maxima at 878.8 and 842.5 cm^{-1} would still form in measurable quantity at this low concentration. The assignment to the vibrational modes originated at the {AsF_5} moiety of an [LA·F_2] adduct is only reasonable with the assumption of cage pairing but not concerning the calculated spectra (Table 38 in the appendix). In the calculated case, the Lewis acid-centered bands only shift marginally up to 2 cm^{-1} upon complexation, while experimental shifts versus the parent bands are +72 and +61 cm^{-1} for the corresponding antisymmetric stretching modes $\nu_{as}(AsF_{3,eq})$ and $\nu_{as}(AsF_{2,ax})$, respectively. In addition, only the bands of solid and isolated fluorine were observed, but none of the shoulders of $F_{2,s}$ and $F_{2,i}$ nor the band around 894 cm^{-1} (vide supra). Those are therefore regarded as concentration-dependent, which leads to the assignment of sites of molecular fluorine (solid/isolated).

Noteworthy, the bands of the species AsF_3 and $OAsF_3$, which are conceivable in the discussed reduction/re-oxidation ('elution') of arsenic centers, are lying well below 800 cm^{-1}.[478–480] Upon annealing of the very diluted matrix to up to 25 K, broadening of the already existing bands and matrix sites changes were observed (Figure 119 in the appendix).

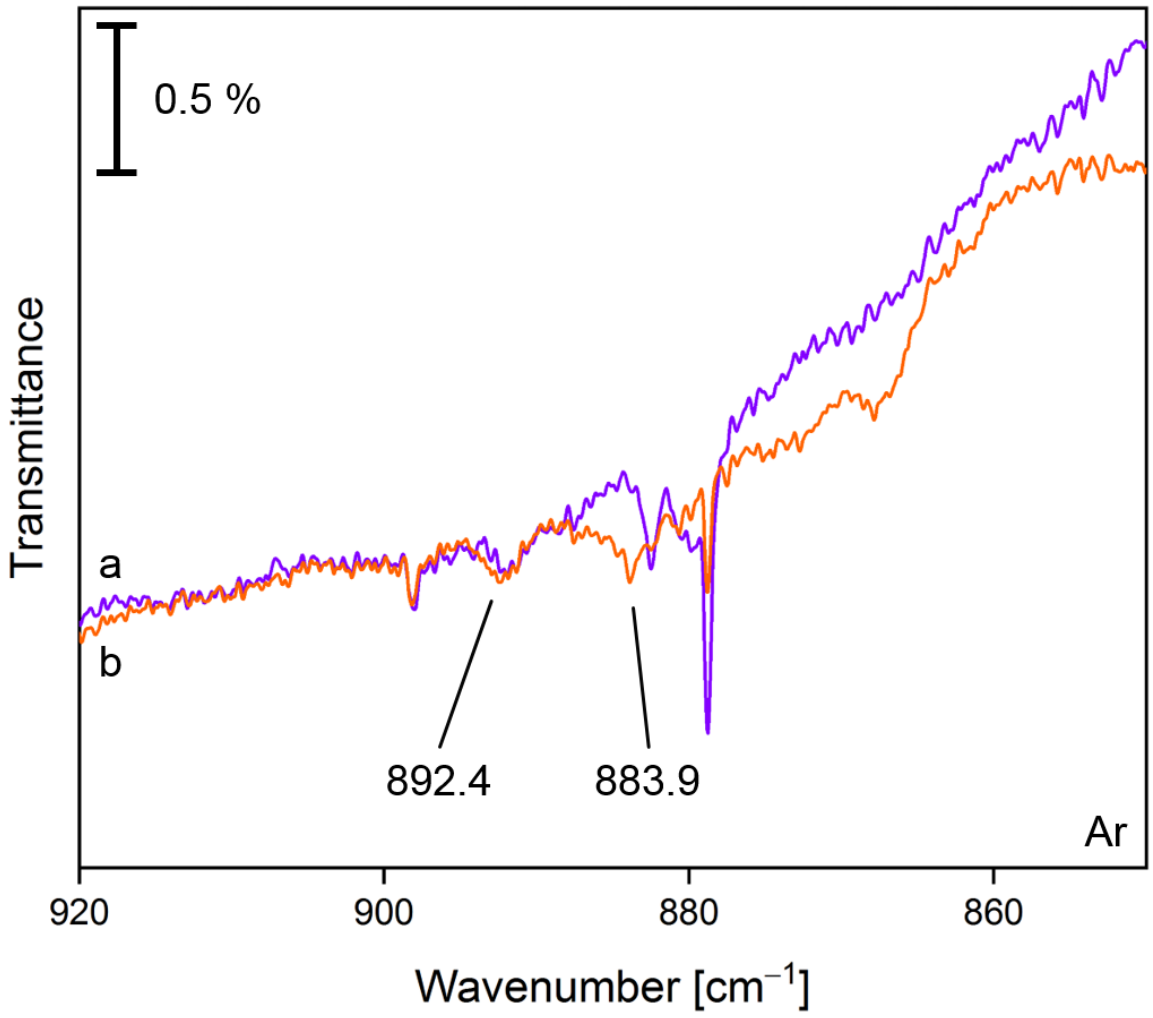

Figure 37: The IR spectra were recorded after the deposition of a) argon for 20 min and fluorine (1 % in excess argon, accompanied by highly diluted AsF_5) onto a CsI window at 4 K for 180 min at a deposition rate of 0.6 mbar·l·min^{-1} (purple trace) and after b) subsequent stepwise annealing to 30 K for 5 min (orange trace). Newly emerging bands are highlighted.

At 30 K, all bands almost diminished, while the $F_{2,i}$ band at 891.9 cm^{-1} was marginally intensified and slightly blue-shifted to 892.4 cm^{-1} (Figure 37). In addition, a very weak band emerged at 883.9 cm^{-1}, which might represent either a site of the F_2-dependent band peaking at 878.8 cm^{-1} or another phase of F_2, which would agree with the value of 884.4 cm^{-1} reported by Brosi et al. from an experiment of Cl_2 (6 %) and F_2 (6 %),[10] simultaneously embedded in neon. This band development reflects the results obtained at a higher concentration and could be interpreted as the decomposition of the cage pair, where the moieties drift apart. In turn, those free F_2 molecules could then contribute to a higher intensity of either the $F_{2,i}$ or the $F_{2,s}$ band.

Additionally, the sharp bands of the AsF_5/F_2 associated features form independently of the concentration and aggregation of AsF_5 in the matrix. They are truly connected to both the Lewis acid and difluorine, since the corresponding bands were not observed in the AsF_5 spectrum at high concentration without added fluorine (Figure 34). Their sharp shape could be attributable to a well-defined geometry in a matrix cage.[73,354,481] However, the bands with maxima at 878.8 and 842.5 cm^{-1} could represent the respective $\nu_{as}(AsF_{3,eq})$ and $\nu_{as}(AsF_{2,ax})$ modes of a coordinated $\{AsF_5\}$ moiety of a 1:1 $[AsF_5 \cdot F_2]$ cage pair, which seems to be justified with respect to a splitting of 36 cm^{-1} of these modes compared to 26 cm^{-1} in free AsF_5. If this is the case, the coordinated $\{F_2\}$ moiety would perturb the $\{AsF_5\}$ moiety but would not be sufficiently polarized in the complex to produce a remarkably shifted band.

3.1.2.3.2 AsF_5 and F_2 in Ne

In order to clarify the results obtained in argon, experiments employing very diluted concentrations of AsF_5 stemming from re-oxidized arsenic species in the deposition capillary (see also the previous Section 3.1.2.3.1) were performed in neon. Upon the condensation of fluorine at a concentration of 1 % diluted in neon, $F_{2,s}$ (very weak) and $F_{2,i}$ bands, the bands associated with the cage pair $[AsF_5 \cdot F_2]$ at 883.2, 845.9 and 773.6 cm^{-1}, and again oligomeric absorptions of AsF_5 emerged at 818.2 and 795.9 cm^{-1} in neon (see Figure 120 in the appendix for a detailed view). All these bands are blue-shifted by 3–5 cm^{-1} from the values obtained in argon. The oligomeric absorptions agree with the reported matrix bands[351] and are accordingly blue-shifted from the gas phase values.[461] Additional matrix sites of the fundamentals were observed in comparable intensity but shifted by some wavenumbers, which could be due to the overall extended site structure in neon (Figure 105 in the appendix).

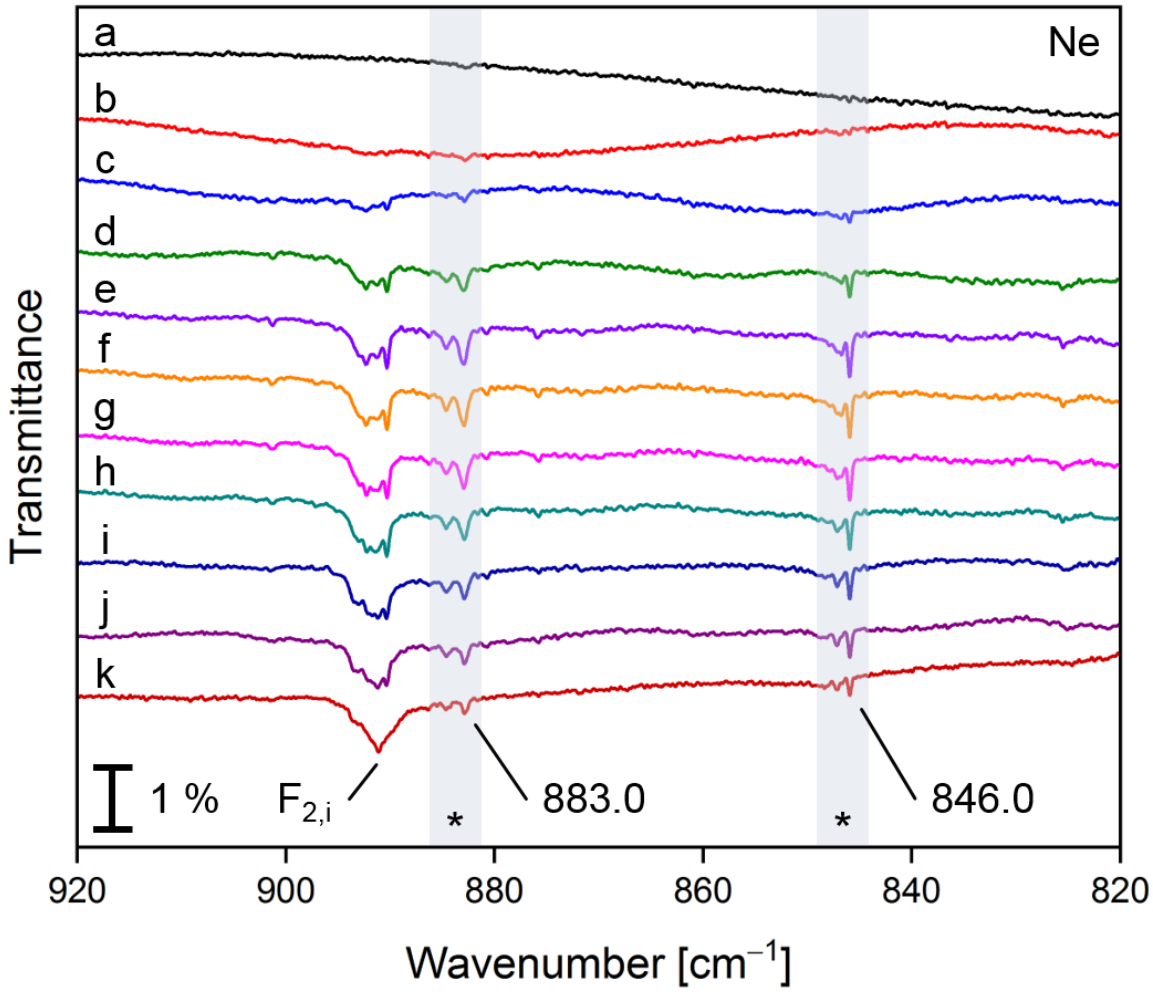

Figure 38: The IR spectra were recorded after the deposition of a) neon for 22 min, and after the subsequent deposition of fluorine (1 % in excess neon, accompanied by highly diluted AsF_5) for b) 20 min, c) 60 min, d) 120 min and e) 180 min onto a CsI window at 4 K at a deposition rate of 0.6 mbar·l·min^{-1} and after annealing of the matrix to f) 8 K, g) 10 K, h) 11 K, i) 11 K (a second time), j) 11.5 K and k) 13 K. IR active features caused by AsF_5 in combination with F_2 are marked by an asterisk.

More remarkable was the observation of two bands at 883.0 (+ site at 884.6) and 846.0 cm^{-1} (+ site at 846.7 cm^{-1}) as depicted in Figure 38, representing the neon analogues of the argon representatives (Figure 34). A more complex band associated with molecular F_2 showcasing distinct maxima at 892.3 and 891.3 and a new red-shifted maximum at 890.3 cm^{-1} (with respect to the band width of the F_2 band in e.g. Figure 22) was formed during the deposition (Figure 39, Figure 121 in the appendix). The described band structure of the multi-component band of matrix-isolated F_2 developed upon the sequential annealing steps (Figure 38, Figure 121 in the appendix) in a way that the central (originally lowest local) maximum of the band at 891.1 cm^{-1} increased, while the other two components decreased and eventually vanished (Figure 39). This process was accompanied by a decreasing or broadening of all AsF_5 related bands (Figure 120 in the appendix). Since the overall intensity of the $F_{2,i}$ band did not decrease even at annealing temperatures of up to 13 K, the major fraction of the matrix was retained. On the other hand, this means that the F_2

molecules changed their chemical environment and might have diffused from a coordination site of AsF_5 to a more isolated Ne cage. Simultaneously, the small amount of the solid F_2 phase fully vanished upon the annealing process.

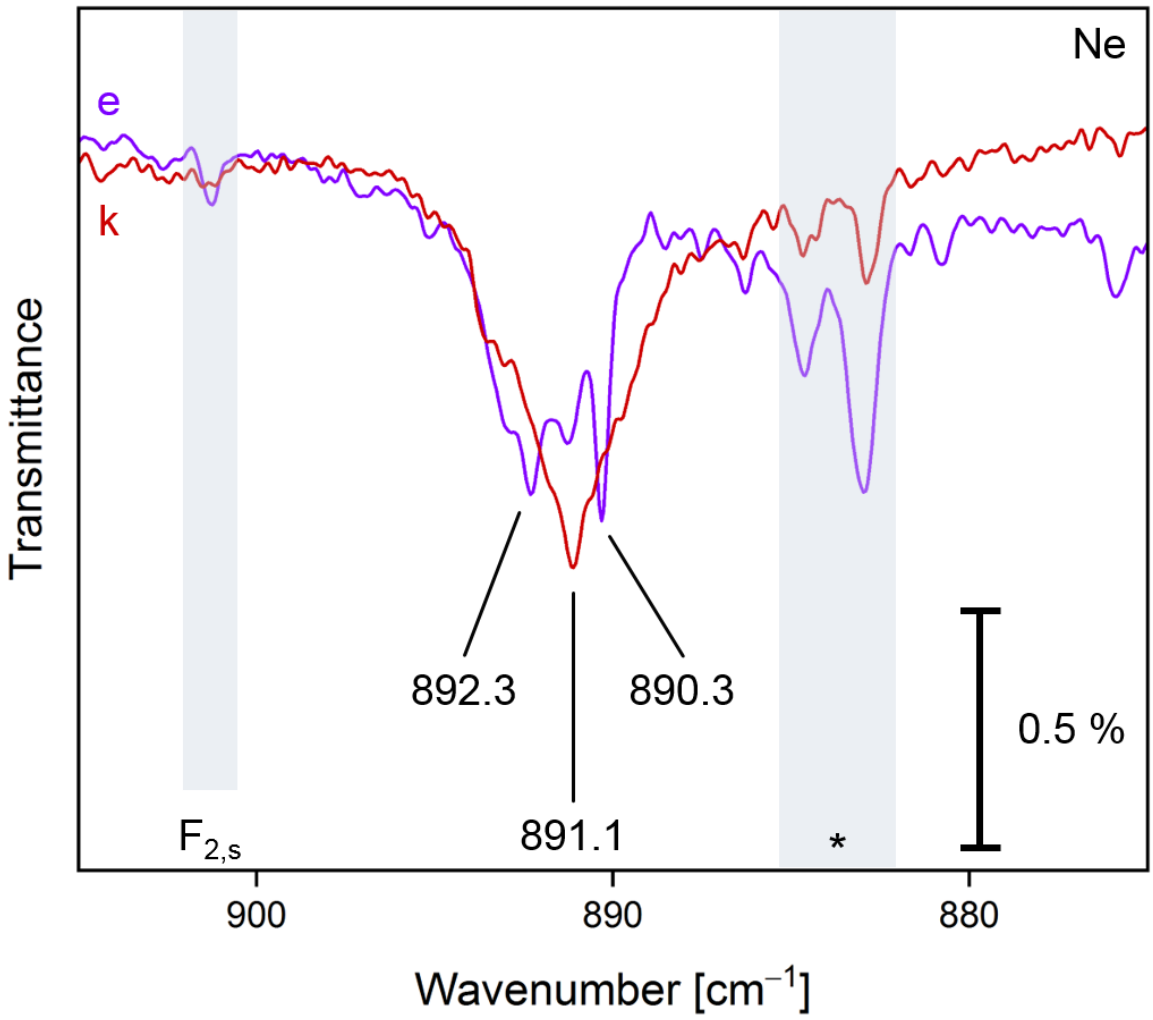

Figure 39: The IR spectra were recorded after e) the deposition of neon for 22 min and the subsequent deposition of fluorine (1 % in excess neon, accompanied by highly diluted AsF_5) onto a CsI window at 4 K for 180 min at a deposition rate of 0.6 mbar·l·min^{-1} (purple trace) and after k) the final annealing of the matrix to 13 K. Both spectra are identical with Figure 38. IR active features caused by AsF_5 in combination with F_2 are marked by an asterisk.

With respect to the quantum-chemical results, a small shift of about 1 cm^{-1} for complex and free F_2 is conceivable (Table 11, Table 12), but the large shift of the tentatively assigned F_2-dependent AsF_5 bands (73 and 62 cm^{-1} for $\nu_{as}(AsF_{3,eq})$ and $\nu_{as}(AsF_{2,ax})$, respectively) seems to be farfetched (Table 38 in the appendix). However, these shifts agree with the observations in argon (see also Table 16).

By any means, the combination of very diluted AsF_5 at a high concentration of elemental fluorine gave rise to a sharp, distinct band at 890.3 cm^{-1} associated with a polarized F_2 molecule in solid

neon, which seems to be correlated to the decomposition of a tentatively assigned [$AsF_5 \cdot F_2$] cage pair.

3.1.2.4 SbF_5 and F_2 in Noble Gas-Matrices

Besides the well-known applications on a preparative scale of the strongest conventional Lewis acid[4,249] and a long dispute[73] on the true molecular structure (D_{3h}) with respect to its tendency to form oligomers even in the gas phase,[463,482] fewer things are known about Lewis acid-base reactivity of SbF_5 under matrix isolation conditions. Since its acidity is even higher than that of the lighter homologue AsF_5,[66] SbF_5 is well suited to be studied regarding its reactivity towards elemental fluorine.

According to the recommendation in the literature[351] and in order to prevent the long-term contamination of the deposition capillary described in Section 3.1.2.3, which was believed to be even more drastic for SbF_5, the deposition was performed by using a cooled glass U-tube (with by-pass) positioned in close proximity to the vacuum chamber (ca. 10 cm glass line-in). A different pathway was chosen for the deposition, employing stainless steel and glass parts that were never in contact with AsF_5. However, a short (ca. 20 cm) piece of stainless-steel tubing is permanently installed to connect the sample line to the individual deposition units, which was used for AsF_5 experiments as well and was thus contaminated. The overall contamination with AsF_5 in the SbF_5 experiments was small compared to the BF_3 experiments (Section 3.1.2.2).

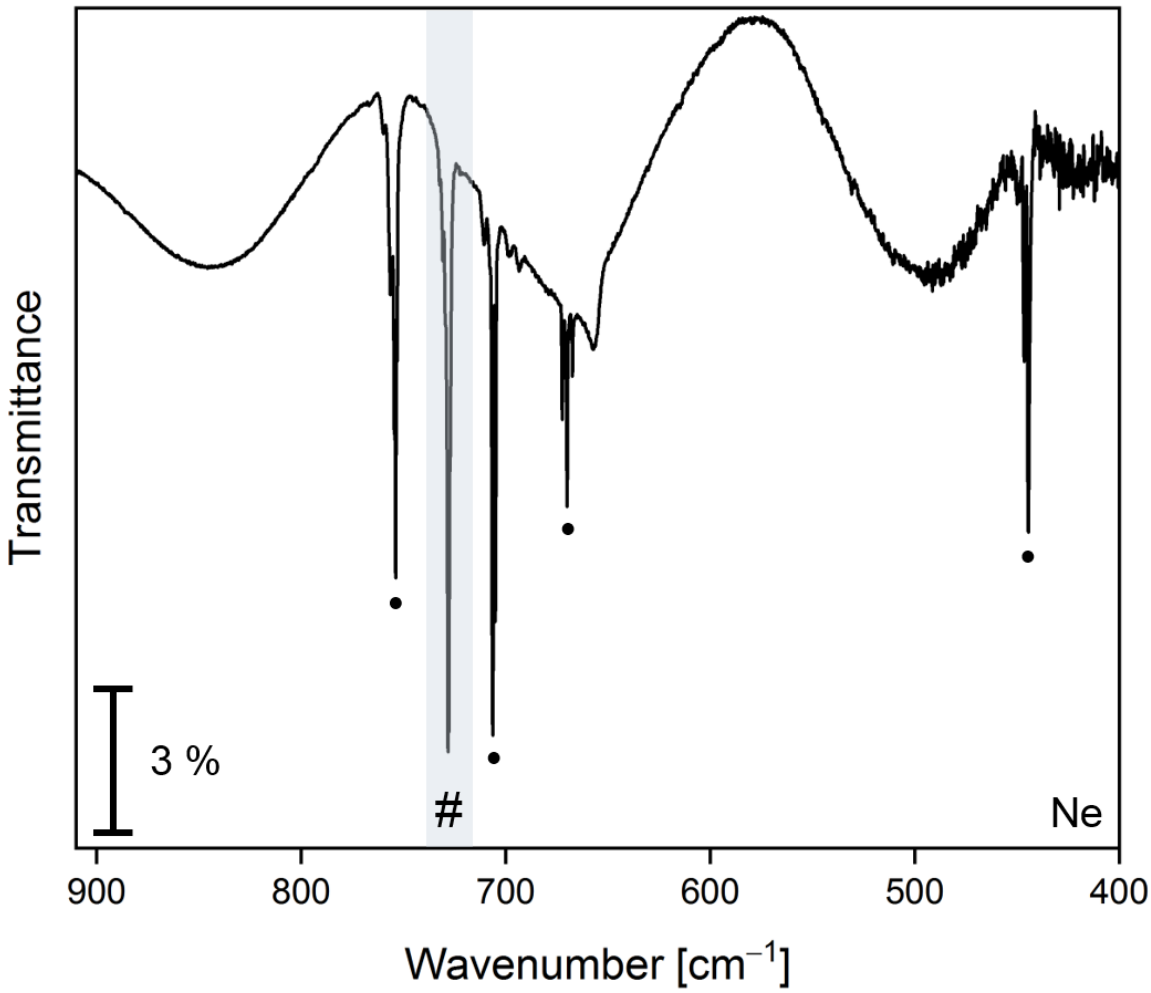

Figure 40: IR spectrum recorded after the deposition of neon passed over a solid sample of SbF_5 maintained at −54.4 to −54.2 °C onto a CsI window at 4 K for 11 min at a deposition rate of 0.6 mbar·l·min^{-1}. The bands were found to match the reported values.[351,483–487] The quasi-degenerate $\nu_{as}(SbF_{3,eq})/\nu_{as}(SbF_{2,ax})$ band(s) of monomeric SbF_5 is marked with a hash, the bands of polymeric SbF_5 by a bullet (cf. Table 17, and Table 39 in the appendix).

Antimony pentafluoride, in contrast to the homologous arsenic compound, is found in oligomeric forms in the gas phase,[463,482] which renders the exclusive deposition of the monomer in noble gas matrices challenging.[351] A spectrum of SbF_5 embedded in solid neon is depicted in Figure 40, a corresponding spectrum in argon in Figure 106 in the appendix. A compilation of the main observations in the course of the experiments employing SbF_5 and F_2 are found in Table 17.

Table 17: Band positions (given in cm^{-1}) of the main features observed in the SbF_5/F_2 experiments in neon and argon. The band maxima of the ν(F−F) are bold and only the most prominent matrix sites are given. The band positions agree with the literature data.[351,483–488]

Assignment	Ne	Ar
ν(F−F), $F_{2,s}$	902.7 sh, **901.5**, 900.4 sh	898.1
ν(F−F), $F_{2,i}$	891.9 br	894.8 sh
$\nu_{as}(AsF_{3,eq})$, $[AsF_5 \cdot F_2]$*,[a]	882.9	878.8 vvw
$\nu_{as}(AsF_{2,ax})$, $[AsF_5 \cdot F_2]$*,[a]	846.0	842.6 vvw
$(SbF_5)_x$[b]	756.5	751.2
$\nu(SbF_{4,term})$, $(SbF_5)_x$[b]	753.9	
$\nu_{as}(SbF_{3,eq})/\nu_{as}(SbF_{2,ax})$, SbF_5[c]	728.3	725.9
$\nu(SbF_{4,term})$, $(SbF_5)_x$[b]	706.4	703.7
$\nu(SbF_{4,term})$, $(SbF_5)_x$[b]	705.1	
$\nu(SbF_{4,term})$, $(SbF_5)_x$[b]	670.0	667.9[d]
ν(Sb−F−Sb), $(SbF_5)_x$[b]	444.5	445.1

[a] tentative assignment of an assumed cage pair upon comparison with the corresponding modes of the parent bands, these bands are marked uniformly by an asterisk throughout the figures; [b] these bands are caused by polymeric SbF_5 ($(SbF_5)_x$ (x is unknown)) and were assigned based on reference [489] with the remark that they were not assigned to singular modes in references [483–485]; [c] the only monomeric absorption in the MIR regime, $\nu_{as}(SbF_{3,eq})$ and $\nu_{as}(SbF_{2,ax})$ are quasi-degenerate (see references [483–485] and Table 39 in the appendix); [d] coincides with gaseous CO_2[10,351,490]; term = terminal, br = broad.

As the fluoride ion affinity increases upon higher aggregation of $(SbF_5)_x$ (x = 1, 2, 3, 4) and is found the highest for the tetrameric species,[346] a higher aggregate of SbF_5 is not necessarily counterproductive in order to polarize F_2 and thereby activate[73] the F−F stretching mode.

3.1.2.4.1 SbF_5 and F_2 in Ne

In order to obtain a better insight into the observations made with F_2 and the weaker[66] Lewis acids BF_3 and AsF_5, neon experiments were similarly conducted for SbF_5 and F_2.

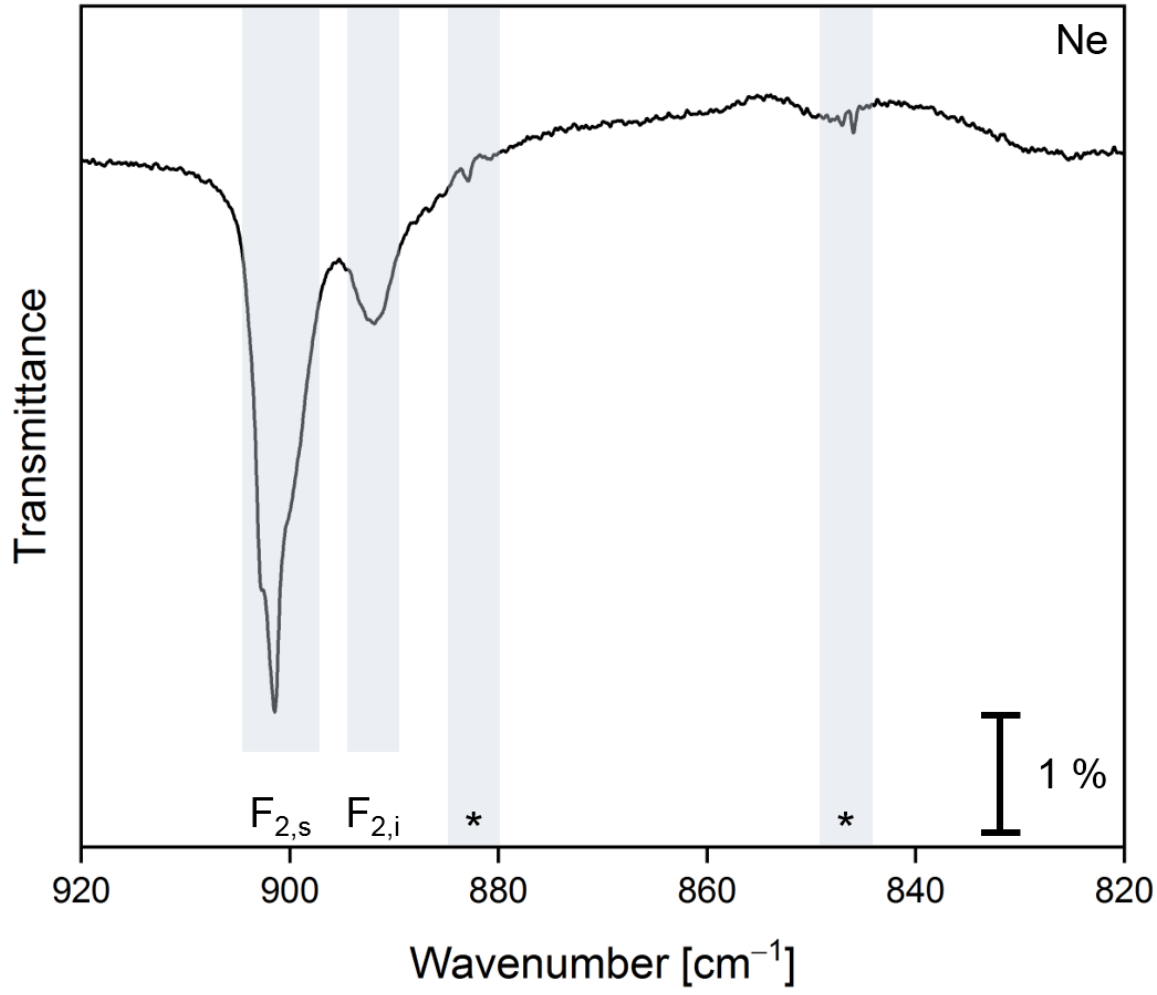

Figure 41: The IR spectrum was recorded after the pre-deposition of neon for 22 min (deposited via a bypass) and the subsequent deposition of fluorine (3 % in excess neon) passed over a solid sample of SbF_5 maintained at −52.3 to −47.8 °C onto a CsI window at 4 K for 211 min at a deposition rate of 0.6 mbar·l·min^{-1}. IR active features caused by traces of AsF_5 in combination with F_2 are marked by an asterisk.

Figure 41 shows the spectrum obtained after the deposition of SbF_5 in an F_2/Ne stream. The deposition took place homogenously, as it can be seen in Figure 122 and Figure 123, which feature the detailed step-by-step spectra in the F_2 and SbF_5 regions and are found in the appendix. An ideal temperature range for reliably increasing the SbF_5 bands was found between −48.9 and −48.5 °C at an average pressure of $1 \cdot 10^{-6}$ mbar in the matrix vacuum chamber. As especially the spectrum of the matrix sample obtained upon passage of a highly concentrated 3 % F_2 in Ne gas mixture over a solid sample of SbF_5 contained the $F_{2,s}$ and $F_{2,i}$ bands in high intensity, the matrix was subjected to a detailed photochemical investigation (Figure 42).

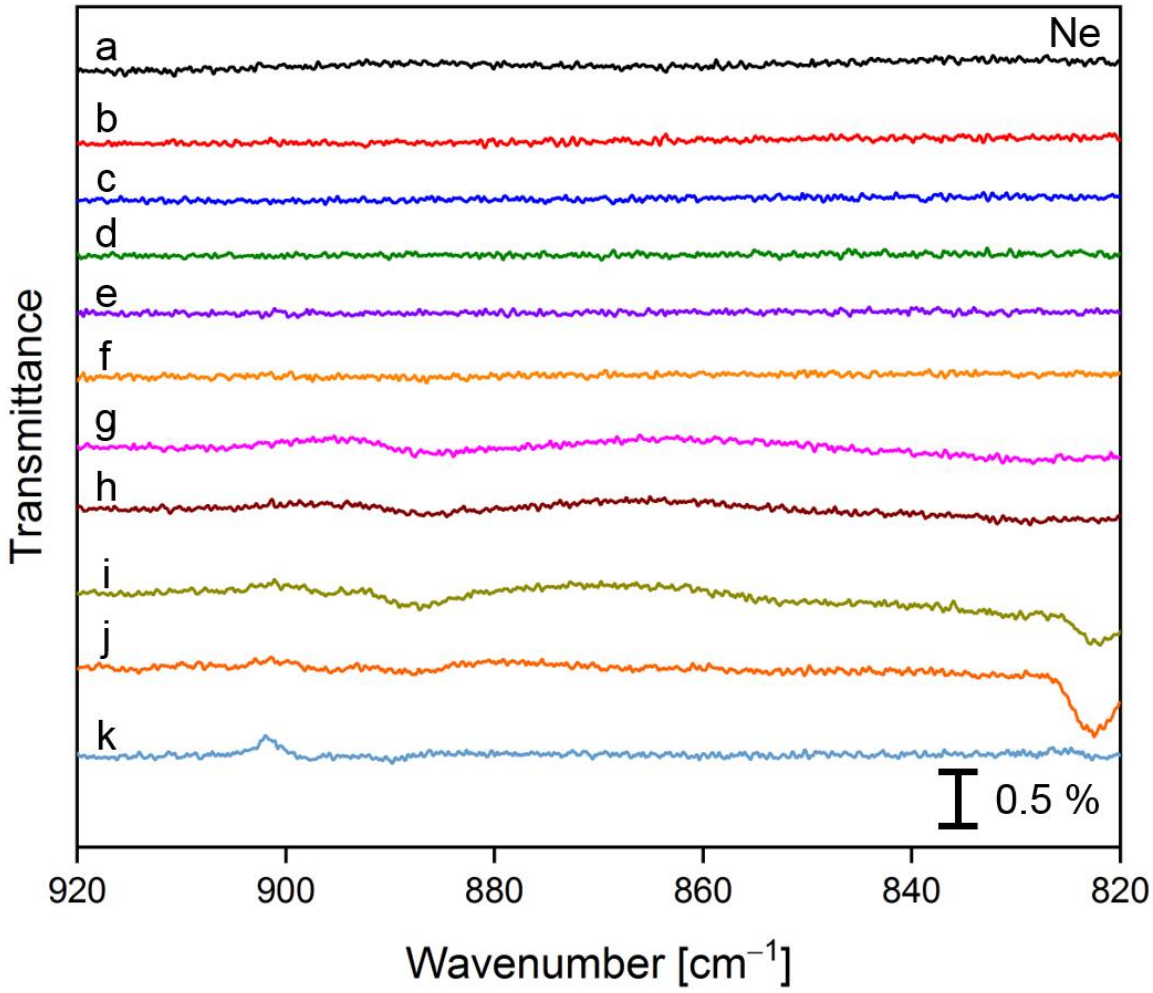

Figure 42: The difference IR spectra show the changes after photolysis and annealing of the initial deposit of neon for 22 min and fluorine (3 % in excess neon) passed over a solid sample of SbF_5 maintained at −52.3 to −47.8 °C onto a CsI window at 4 K for 211 min at a deposition rate of 0.6 mbar·l·min^{-1}. The matrix was subsequently irradiated at a) λ = 730 nm (LED) for 5 min, b) λ = 656 nm (LED) for 5 min, c) λ = 625 nm (LED) for 5 min, d) λ = 596 nm (LED) for 5 min, e) λ = 528 nm (LED) for 5 min, f) λ = 455 nm (LED) for 5 min, g) λ = 278 nm (LED) for 5 min, h) λ = 278 nm (LED) for further 10 min, i) full-arc Hg lamp for 10 min, j) full-arc Hg lamp for further 20 min, and k) annealed to 9 K. Bands pointing downwards are formed at the expense of the bands pointing upwards. The spectral range down to 500 cm^{-1} is shown in Figure 43.

According to the IR spectra, irradiation with visible light did not lead to substantial changes in the F_2 region and only caused changes in the matrix sites of SbF_5 (Figure 43).

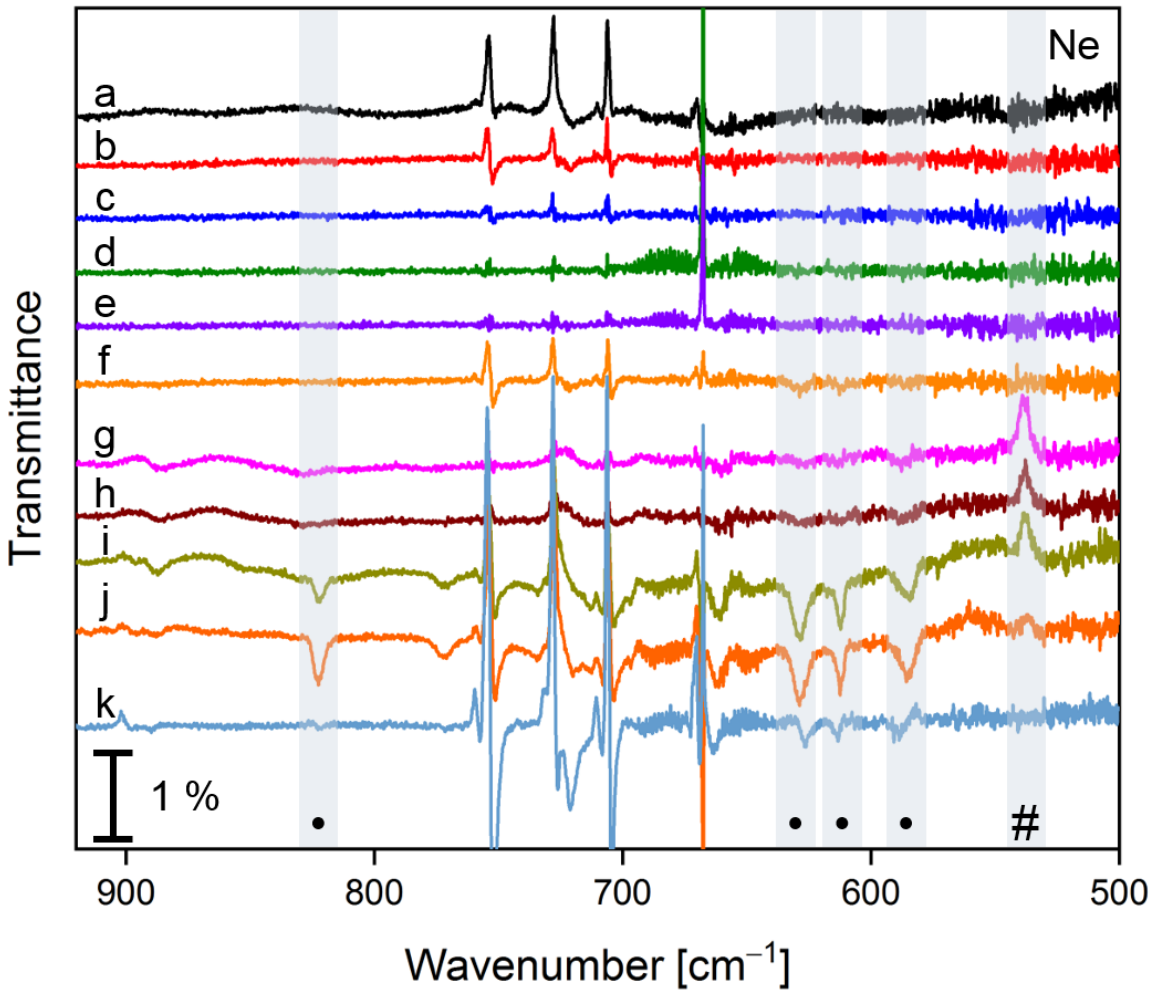

Figure 43: The difference IR spectra show the changes after photolysis and annealing of the initial deposit of neon for 22 min and fluorine (3 % in excess neon) passed over a solid sample of SbF_5 maintained at −52.3 to −47.8 °C onto a CsI window at 4 K for 211 min at a deposition rate of 0.6 mbar·l·min^{-1}. The matrix was subsequently irradiated at a) λ = 730 nm (LED) for 5 min, b) λ = 656 nm (LED) for 5 min, c) λ = 625 nm (LED) for 5 min, d) λ = 596 nm (LED) for 5 min, e) λ = 528 nm (LED) for 5 min, f) λ = 455 nm (LED) for 5 min, g) λ = 278 nm (LED) for 5 min, h) λ = 278 nm (LED) for further 10 min, i) full-arc Hg lamp for 10 min, j) full-arc Hg lamp for further 20 min, and k) annealed to 9 K. New features are marked by a bullet, an impurity of unknown origin by a hash. Bands pointing downwards are formed at the expense of the bands pointing upwards.

Next to marginal changes of the $F_{2,s}$ and $F_{2,i}$ bands upon UV-photolysis, broad features at 822.5, 628.7, 612.4 and 584.2 cm^{-1} appeared at full-arc Hg lamp irradiation and slightly increased upon annealing of the matrix to 9 K. However, these bands do not scale with any other of the decreasing F_2-related bands and are all beyond the expected shifts of a Lewis acid-fluorine adduct (Table 12, and Table 39 in the appendix). Moreover, a corresponding behavior was not observed at the lower fluorine concentration of 1 % in Ne (Figure 126 in the appendix). Note that the features at 628.7, 612.4 cm^{-1} were also observed in almost identical position in experiments using laser-ablated $Cs[AuF_6]$/CsF (cf. Figure 51 in Section 3.1.2.5). A broad, minor feature (with respect to the intensity

of the SbF_5 fundamentals) at 537.8 cm^{-1} diminished at UV-photolysis and could not be assigned, since no other band with comparable behavior was found in the spectra.

Analogous experiments were performed at a concentration of 1 % F_2 and the obtained IR spectra largely revealed the same species upon deposition (Figure 44), which proceeded homogenously (Figure 124, Figure 125 in the appendix). The $F_{2,s}$ band at 901.5 cm^{-1}, comprising two shoulders at 900.3 and 902.7 cm^{-1} (Figure 41) in the experiment with 3 % F_2, was present with two distinct bands at 901.4 and 902.8 cm^{-1} in this set of experiments (1 % F_2). Apparently, the formation of the $F_{2,s}$ band is favored over the $F_{2,i}$ band, the latter being found less prominent in the $SbF_5/F_2/Ne$ experiments.

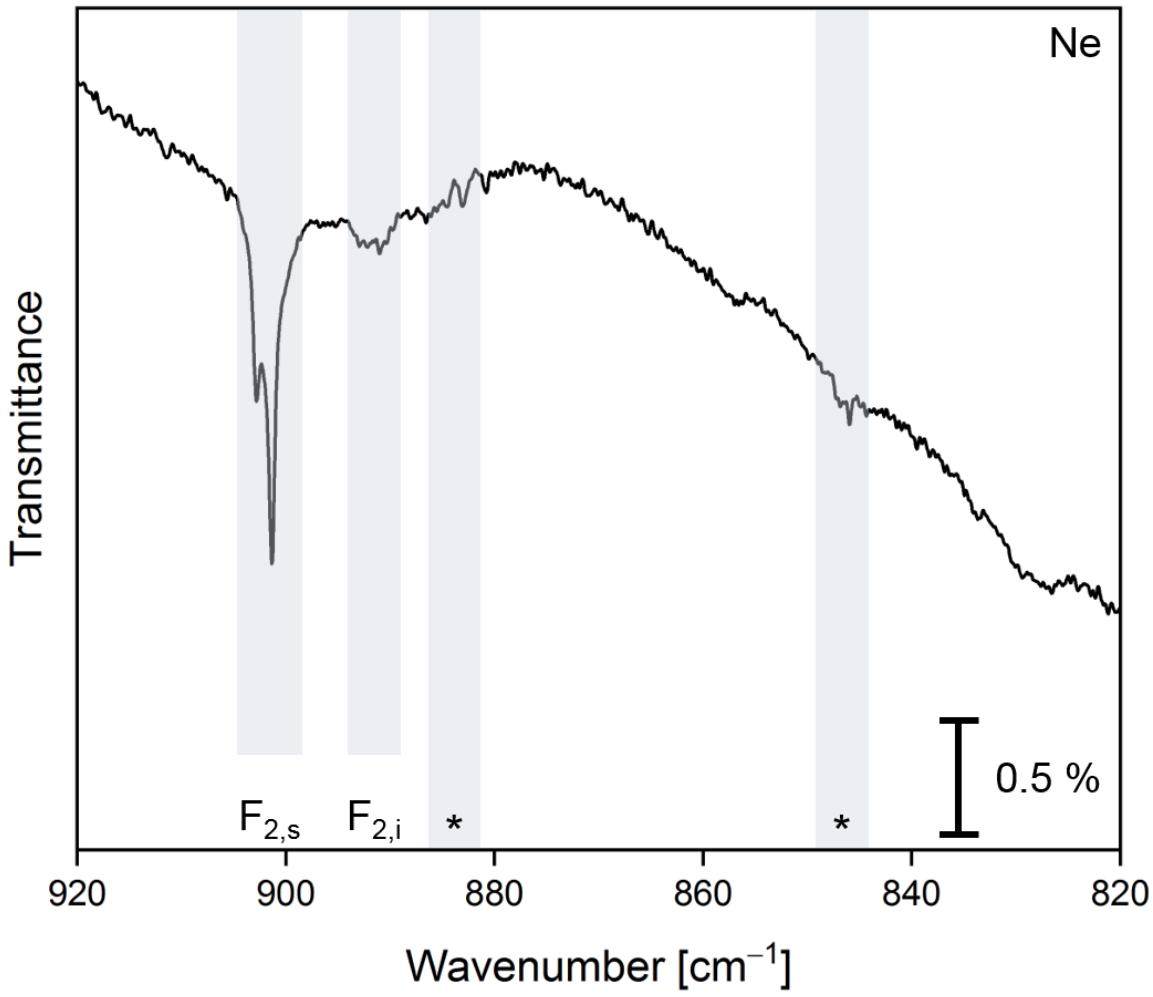

Figure 44: The IR spectrum was recorded after the deposition of neon for 27 min and fluorine (1 % diluted in neon) passed over a solid sample of SbF_5 maintained at −49.1 to −48.1 °C onto a CsI window at 4 K for 180 min at a deposition rate of 0.6 mbar·l·min^{-1}. IR active features caused by traces of AsF_5 in combination with F_2 are marked by an asterisk.

The irradiation of the matrix by a full-arc mercury lamp for 30 min did not lead to changes in the F_2 stretching region and only caused changes of matrix sites of SbF_5. The formation of a band at 822.5 cm^{-1} was not observed, supporting the assumption that this feature does not account for

the ν(F–F) of an [LA·F_2] adduct (vide supra). In addition, the annealing of the matrix to 9 K only induced the $F_{2,s}$ band to slightly decrease – which was found to be comparable to Figure 42 (trace k) – and changes of matrix sites of SbF_5 as well (Figure 126 in the appendix).

3.1.2.4.2 SbF_5 and F_2 in Ar

Substituting the host by argon, the deposition of an analogous SbF_5/F_2 mixture in argon (1 % F_2 in Ar) proceeded homogenously (Figure 128 in the appendix) and exclusively gave rise to the $F_{2,s}$ band at 898.1 cm^{-1}, while in the $F_{2,i}$ region no band lower than the shoulder at 894.8 cm^{-1} was observed (Figure 45).

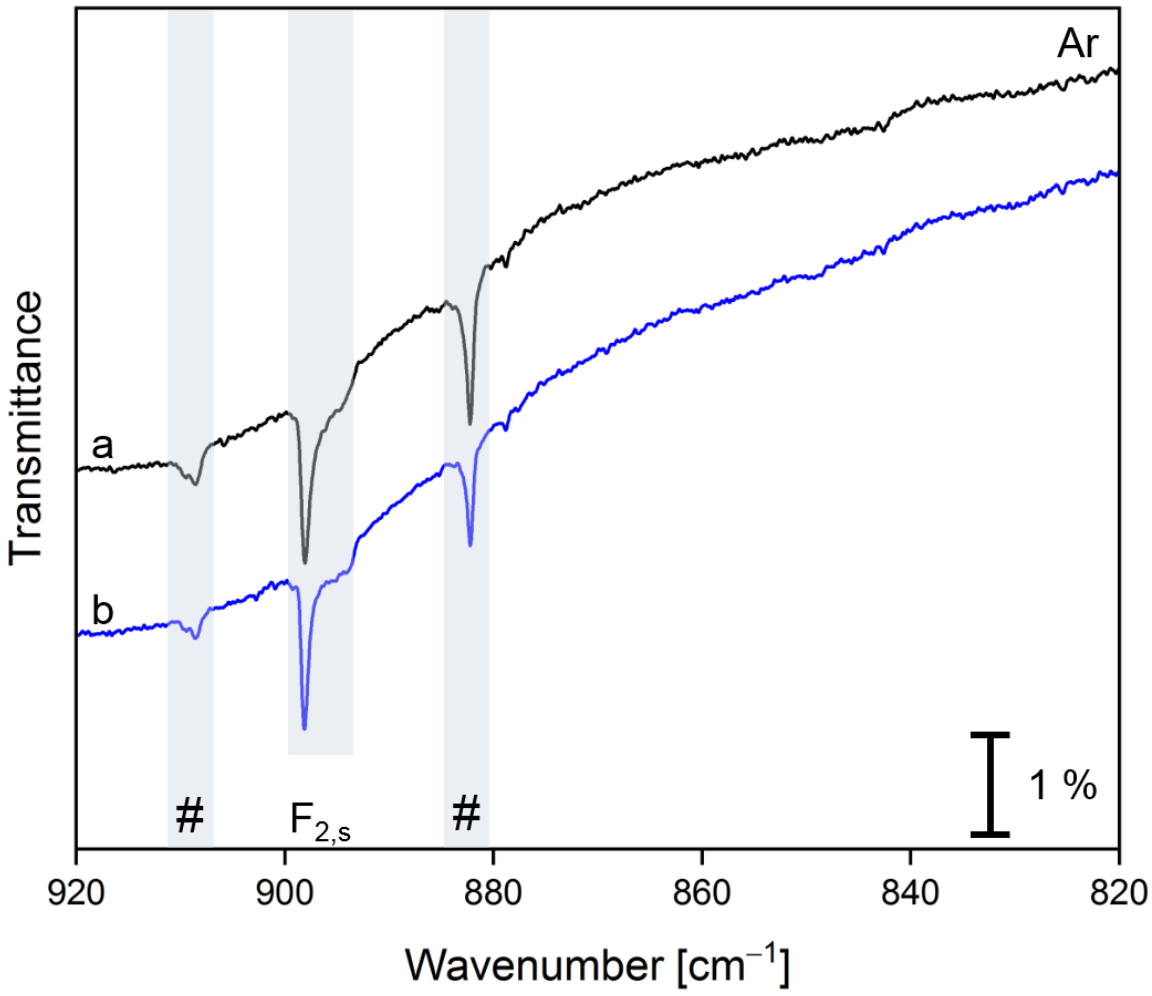

Figure 45: The IR spectra were recorded after a) the deposition of argon for 20 min, and the subsequent deposition of fluorine (1 % diluted in argon) passed over a solid sample of SbF_5 maintained at −49.2 to −48.3 °C onto a CsI window at 4 K for 180 min at a deposition rate of 0.5 mbar·l·min^{-1}, and b) the annealing of the matrix to 25 K. Bands caused by impurities of unknown origin are marked by a hash.

The feature at 882.5 cm^{-1} had been observed in equal position and was also found labile upon annealing to 25 K in experiments with AsF_5 and F_2 in Ar (e.g. Figure 35). As this band was observed

as an impurity in the spectrum of pure argon (Figure 127 in the appendix), it can hardly be correlated to the amount of substance (SbF_5/F_2) deposited or assigned to an F_2-related band or [LA·F_2] adduct. On the contrary, the band position is known from experiments using AsF_5 as a Lewis acid and could principally account for isolated F_2 molecules only formed under the influence of a Lewis acid or other contaminants at sufficient amounts (the appearance of the feature in the Ar spectrum could be explained by the abovementioned 'column' effect of the deposition unit). This would be somehow in line with the band at 884.4 cm^{-1} observed by Brosi et al.[10] The feature at 908.6 with a shoulder at 909.5 cm^{-1} is regarded as an impurity, since it is blue-shifted from the $F_{2,s}$ band and therefore in contradiction to the quantum-chemically expected redshift of ν(F−F) of a polarized {F_2} moiety in an [LA·F_2] adduct (Table 12). Both impurity bands decreased upon annealing to 25 K (Figure 129 in the appendix), which agrees with the observations in the AsF_5 experiments (vide supra), while only changes of matrix sites were observed in the region of the SbF_5 fundamentals (Figure 106, Figure 128 in the appendix).

The experiments employing antimony pentafluoride and various concentrations of fluorine in both neon and argon matrices did not reveal bands which are straightforwardly assignable to the {SbF_5} and fluorine moieties in a discrete [LA·F_2] adduct. The extended investigation of the photochemical reactions of SbF_5 and F_2 (3 %) embedded in solid neon revealed features at 822.5, 628.7, 612.4 and 584.2 cm^{-1}, which did not find correspondence at a lower F_2 concentration of 1 %. A sharp band at 882.5 cm^{-1}, which was found in experiments of both the strong Lewis acids AsF_5 and SbF_5, lies in an acceptable range for a polarized fluorine moiety or phase. However, this band could not be obtained correlated to the amounts of SbF_5 and F_2 deposited and could only be tentatively assigned to F_2 activated by a larger amount of Lewis acid or other contaminants.

In conclusion, the experiments employing SbF_5 and F_2 revealed that both the bands $F_{2,s}$ and $F_{2,i}$ were remarkably increased upon the influence of the very strong Lewis acid SbF_5. These deposits were not photosensitive in the F_2 region. Since SbF_5 forms oligomers in gaseous,[463,482] liquid[4,346,486,491] and solid states,[492] as well as in matrix-isolated systems,[351,483,486] it does not only represent a Lewis superacid[249] in all these systems but somewhat resembles the reaction conditions of the fluoro-oxidation of xenon with F_2 in liquid SbF_5 in the dark[130,131] (Scheme 14). In other words, when the fluorine fundamental is observable and (IR) active, the fluorine molecule is polarized and 'active' for fluorination. This principally answers the initial question if Lewis acids polarize the fluorine moiety and thereby increase its oxidation potential to facilitate the oxidation of for instance Xe[130,131] (Scheme 14). This corresponds to the results of Bartlett and coworkers, where only small interaction energies can play a role in a concerted complex and product formation process, which proceeds at −60 °C in the dark (Scheme 17).[130]

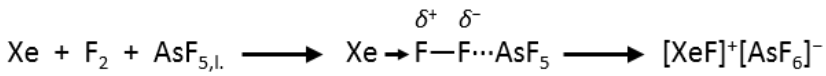

Scheme 17: Concerted complex formation and product formation in the liquid AsF_5 mediated oxidation of xenon in the dark according to reference [130].

Note that the strong visibility of the fluorine fundamental could alternatively or additionally stem from a distorted matrix cage induced by a high amount of perturbing 'impurities', like SbF_5 and its oligomers in this case.

3.1.2.5 Laser-Ablated $Cs[AuF_6]$ and F_2 in Neon Matrices

The most promising adduct according to the literature and the quantum-chemical description in Section 3.1.1 is the fluorine adduct of gold pentafluoride, $[AuF_5 \cdot F_2]$.[69,195,249,292,434] In contrast to the other Lewis acids (vide supra), AuF_5 with a calculated C_{4v} minimum structure[195] is known in its monomeric form only under matrix isolation conditions[10] but, owing to its high Lewis acidity, otherwise as the dimer $(AuF_5)_2$.[69] The latter can be produced from $[KrF][AuF_6]$ or $[O_2][AuF_6]$.[69,290,291] Another room temperature stable gold(V) compound, $Cs[AuF_6]$,[289] can be diluted in 97 % CsF and pressed into a target, and subsequently subjected to laser ablation experiments[455] and co-deposited with F_2/Ng gas mixtures. Principally, the laser ablation of this mixed complex salt target made from $Cs[AuF_6]$/CsF should allow the deposition of conceivable derivatives such as the free ions Cs^+, F^-, and $[AuF_6]^-$, but also decomposition products with reduced gold centers like $[AuF_4]^-$ (Scheme 18).[455] In addition to the free ions, contact ion pairs could be expected as well.[455]

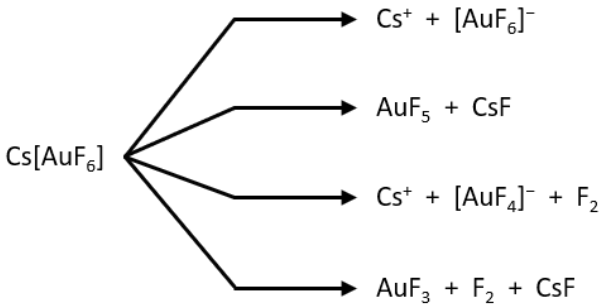

Scheme 18: Conceivable products of laser-ablated $Cs[AuF_6]$.

The ratio of these derivatives should depend on the laser power and on the stability of the target. Small fractions of water potentially causing the reduction of Au^V centers are instantly absorbed by the hygroscopic CsF during transfer to the matrix vacuum chamber. The target 're-dries'

accompanied by surficial crystallite formation in the evacuated chamber after installation upon pumping.

Only the reduced $Cs[AuF_4]$ (bearing an Au^{III} center) had been verified after laser ablation of $Cs[AuF_6]$ containing targets in the literature[455] and in the present work (Figure 108 in the appendix). The additional use of fluorine in higher concentrations should enable the re-oxidation of monomeric gold compounds bearing Au^{III} centers to Au^{V} species in the gas phase or in the short-lived liquid phase. In order to increase the chances to obtain highly oxidized gold species, the use of $Cs[AuF_6]$ was favored over $Cs[AuF_4]$ as a precursor in the mixed salt target.

Therefore, co-deposition experiments employing laser-ablated $Cs[AuF_6]$ (embedded in a CsF matrix in form of a target) and F_2 (diluted in neon at various concentrations) were performed. Prior to a detailed discussion of the different concentrations of fluorine, a compilation of the IR spectra after the deposition of laser-ablated $Cs[AuF_6]$ (3 % in CsF) with fluorine diluted at 0.1, 1.0 and 3.0 % in neon, respectively, is shown in Figure 46.

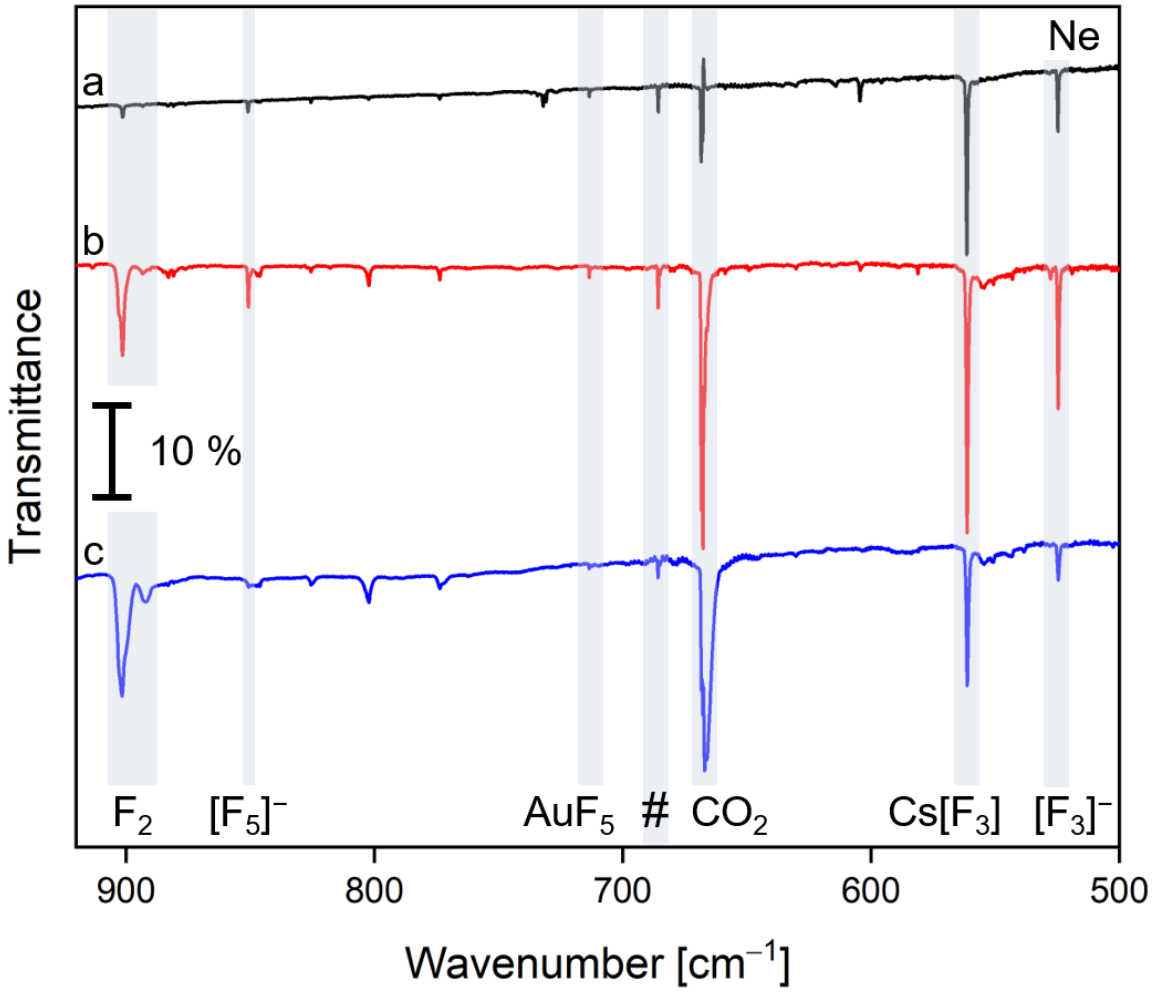

Figure 46: The IR spectra were recorded after the co-deposition of laser-ablated $Cs[AuF_6]$ (3 % in CsF, 3 Hz repetition rate, 30 mJ/pulse) and fluorine with a) 0.1 %, b) 1.0 %, and c) 3.0 % diluted in neon onto a CsI window at 4 K for 180 min each at deposition rates of 0.5 (a, b) and 0.6 mbar·l·min^{-1} (c). The band at 685.7 cm^{-1} is marked with a hash and discussed in the text. The other weak features could not be assigned to the species of interest. The expanded $F_{2,i}$ region is shown in Figure 47.

The spectra revealed the bands of $F_{2,s}$, $F_{2,i}$, $[F_5]^-$, $Cs[F_3]$ and $[F_3]^-$, while only traces of AuF_5, a tentatively assigned very weak band at 713.4 cm^{-1}, were found (cf. Table 18 and references therein). A feature at 685.7 cm^{-1} lies in the region of AuF_3 but is shifted by −7 cm^{-1} compared to the reported value.[434] Note that no other known binary Au−F species or [NgAuF] complexes (see the references [434,493]) were observed but could have also been obscured by the strong CO_2 band structure,[10,490] which was present in all LA/F_2 experiments due to the non-evacuated beam path of the spectrometer. By increasing the concentration of elemental fluorine in neon from 0.1 to 1 % all the mentioned bands in Table 18 gained intensity.

Table 18: Observed species, their band positions (given in cm^{-1}) and their relative band intensities dependent on the concentration of F_2 in neon matrices with reference to the lowest concentration of 0.1 %.

Species	Band position	Relative band intensities	
		F_2 (1.0 % in Ne)	**F_2 (3.0 % in Ne)**
$F_{2,s}$[a]	901.3	+650 %	+896 %
$F_{2,i}$[b]	893.2	+253 %	+863 %
$[F_5]^-$[c]	850.7	+243 %	−30 %
AuF_5[d]	713.4	+49 %	−40 %
$Cs[F_3]$[e]	561.3	+51 %	−21 %
$[F_3]^-$[f]	524.6	+131 %	−44 %

The assignments are in accordance with [a] ref. [10], [b] ref. [74,75,180], [c] ref. [10,77,110,378], [d] ref. [10,434,493] (AuF_5 was independently reported at 711 and 720 cm^{-1} in solid Ne), [e] ref. [10,77,377], [f] ref. [10,18,77].

In contrast, a further increase of the F_2 concentration to 3 % did not lead to higher but even to comparably lower intensities of the polyfluorine monoanion bands, while the intensities of the $F_{2,s}$ and $F_{2,i}$ bands increased remarkably (Figure 46, Figure 47).

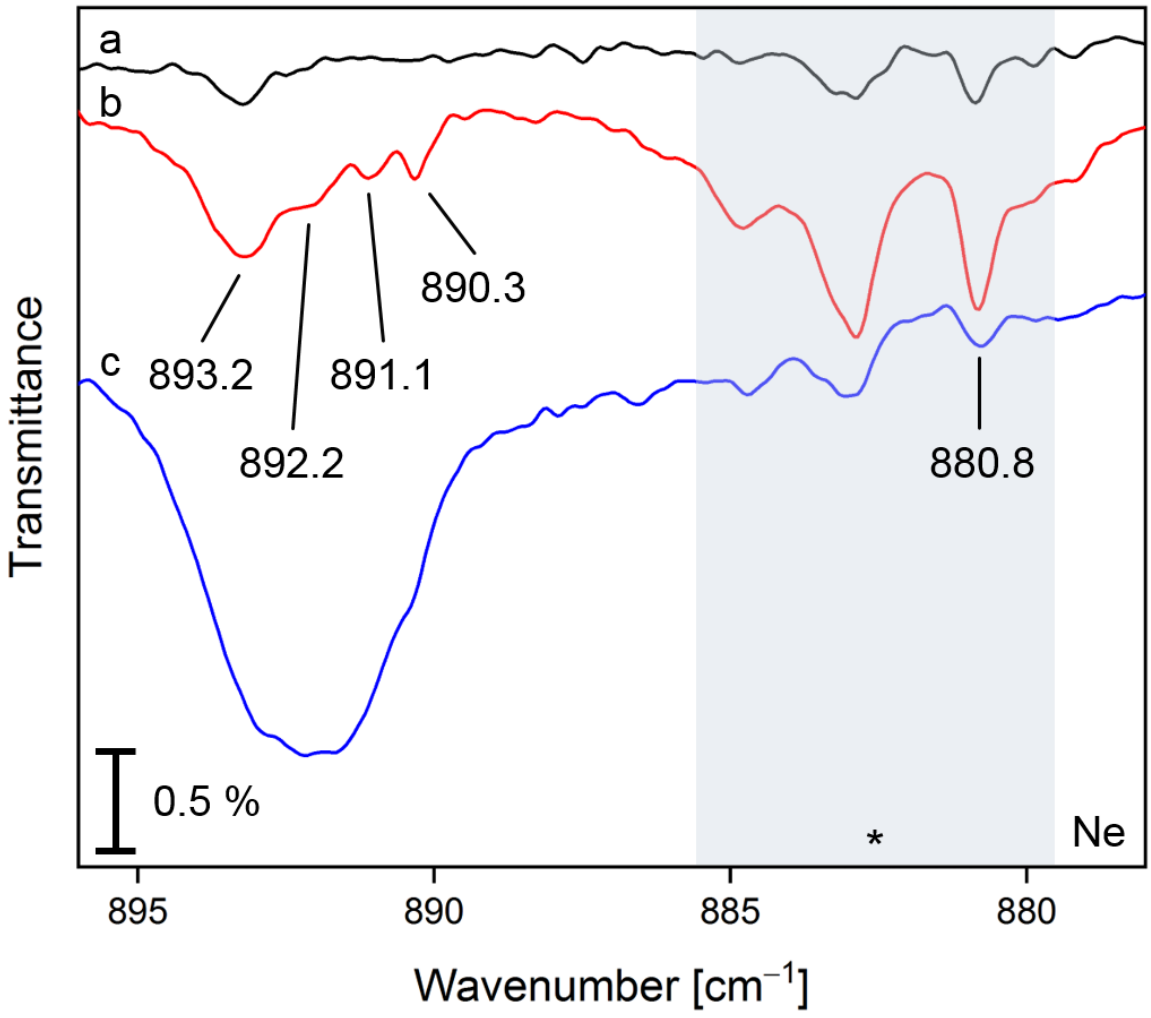

Figure 47: The IR spectra were recorded after the co-deposition of laser-ablated $Cs[AuF_6]$ (3 % in CsF) and fluorine at a) 0.1 %, b) 1.0 %, and c) 3.0 % diluted in neon onto a CsI window at 4 K for 180 min each at deposition rates of 0.5 (a, b) and 0.6 mbar·l·min^{-1} (c). The spectra are identical with Figure 46. IR active features caused by traces of AsF_5 in combination with F_2 are marked by an asterisk.

Interestingly, the maximum of the band indicative for isolated fluorine $F_{2,i}$ at 893.2 cm^{-1} was found blue-shifted compared to the band at 892.3 cm^{-1} in the AsF_5/F_2 experiments (Figure 47, see also Figure 39). In return, the maximum was found red-shifted by 1 cm^{-1} at the high concentration of 3 % F_2 in neon compared to the lower concentrated 1 % mixture. Upon closer inspection, it becomes apparent that this $F_{2,i}$ band represents an envelope of the underlying structure and actually consists of four features at 893.2, 892.2, 891.1 and 890.3 cm^{-1}. The latter three features are comparable to the spectra of an AsF_5/F_2 deposit depicted in Figure 39. In the light of a small fraction of AsF_5 (Figure 48) apparent as an impurity for reasons mentioned above, this band structure is not surprising. More importantly, since the band at 893.2 cm^{-1} is the only $F_{2,i}$ related feature present in the spectrum at 0.1 % F_2 in Ne, it seems to depict the only 'truly' isolated $F_{2,i}$ band in the experiments employing $Cs[AuF_6]/F_2$. The other three components of the $F_{2,i}$ band could depict unspecified higher aggregates thereof, which only allow speculations about their true

nature. Although the band at 880.8 cm^{-1} featured a higher intensity in this set of experiments, the feature was apparent in the AsF_5/F_2 experiments and can thus not be assigned to an AuF_5-specific F_2 band.

The deposit obtained at a concentration of 1 % F_2 in Ne seemingly featured the best isolated system with narrow band widths, while featuring the bands of interest in sufficiently high intensity, and was thus subjected to a detailed investigation of its photochemistry. The IR spectrum of a deposit of $Cs[AuF_6]$ (3 % in CsF) and F_2 (1 % in Ne) after 180 min in the region 820–920 cm^{-1} is featured in Figure 48, while the step-by-step spectra are shown in Figure 130 and Figure 131 in the appendix.

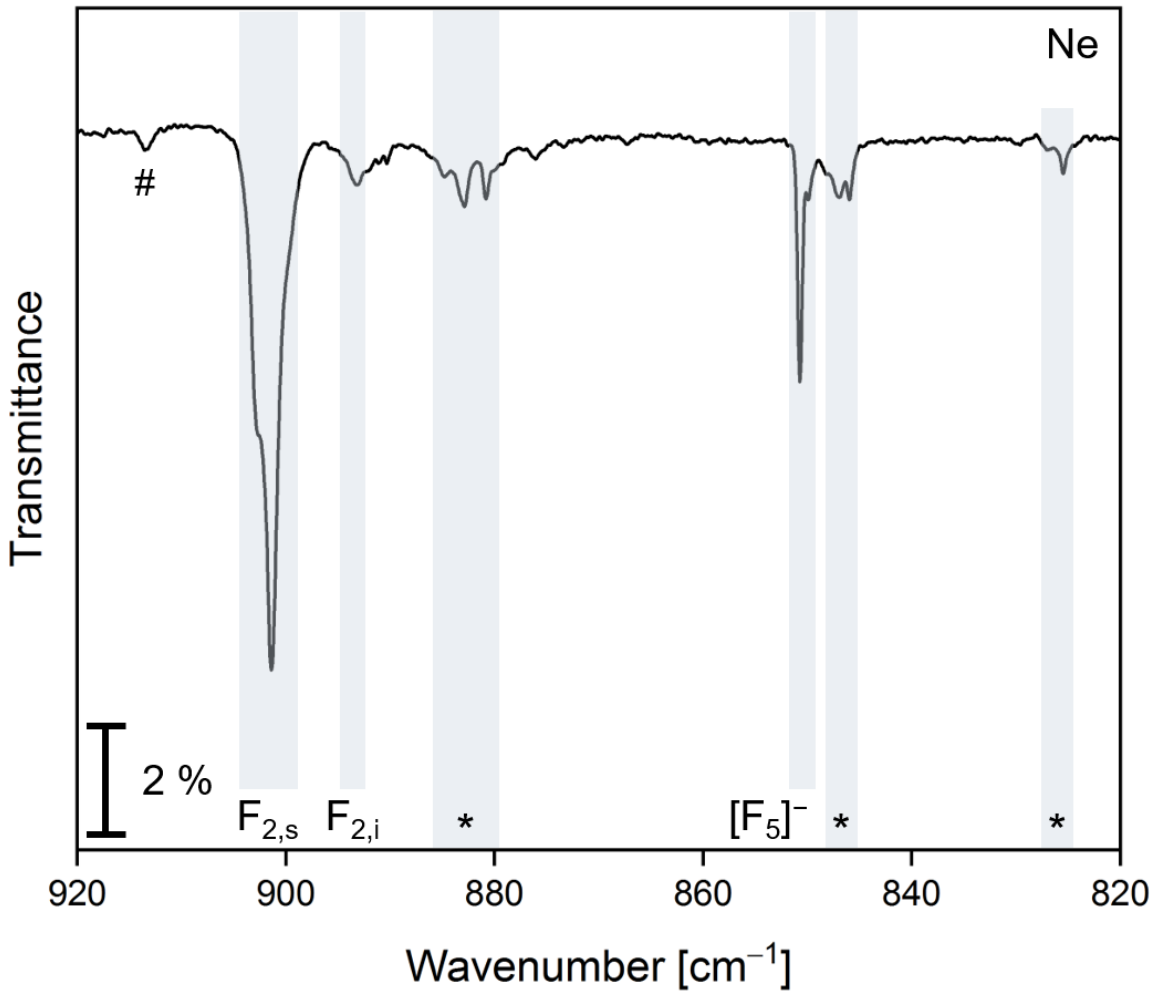

Figure 48: The IR spectrum was recorded after the deposition of neon for 21 min, and the subsequent co-deposition of fluorine (1 % diluted in neon) and laser-ablated $Cs[AuF_6]$ (3 % diluted in a CsF target, 3 Hz repetition rate, 30 mJ/pulse) onto a CsI window at 4 K for 180 min at a deposition rate of 0.5 $mbar \cdot l \cdot min^{-1}$. IR active features caused by traces of AsF_5 in combination with F_2 are marked by an asterisk. A band caused by an unknown impurity that has been discussed in Section 3.1.2.4.2 is marked by a hash.

In addition to the bands of molecular fluorine $F_{2,s}$ and $F_{2,i}$ and small absorptions due to impurities associated with traces of arsenic pentafluoride (vide supra), the IR spectra revealed the bands of

polyfluorine monoanions, i.e. $[F_3]^-$ and $[F_5]^-$, as well as the $Cs[F_3]$ ion pair, which were assigned in accordance with the literature (cf. Table 18). In the light of the rather low intensity of the antisymmetric stretching band ν_3 of $[F_5]^-$ at 850.7 cm^{-1}, the reported IR active combination band ($\nu_1 + \nu_3$) at 1805 cm^{-1}[10,77,378] was not observed in the experiments of the present work.

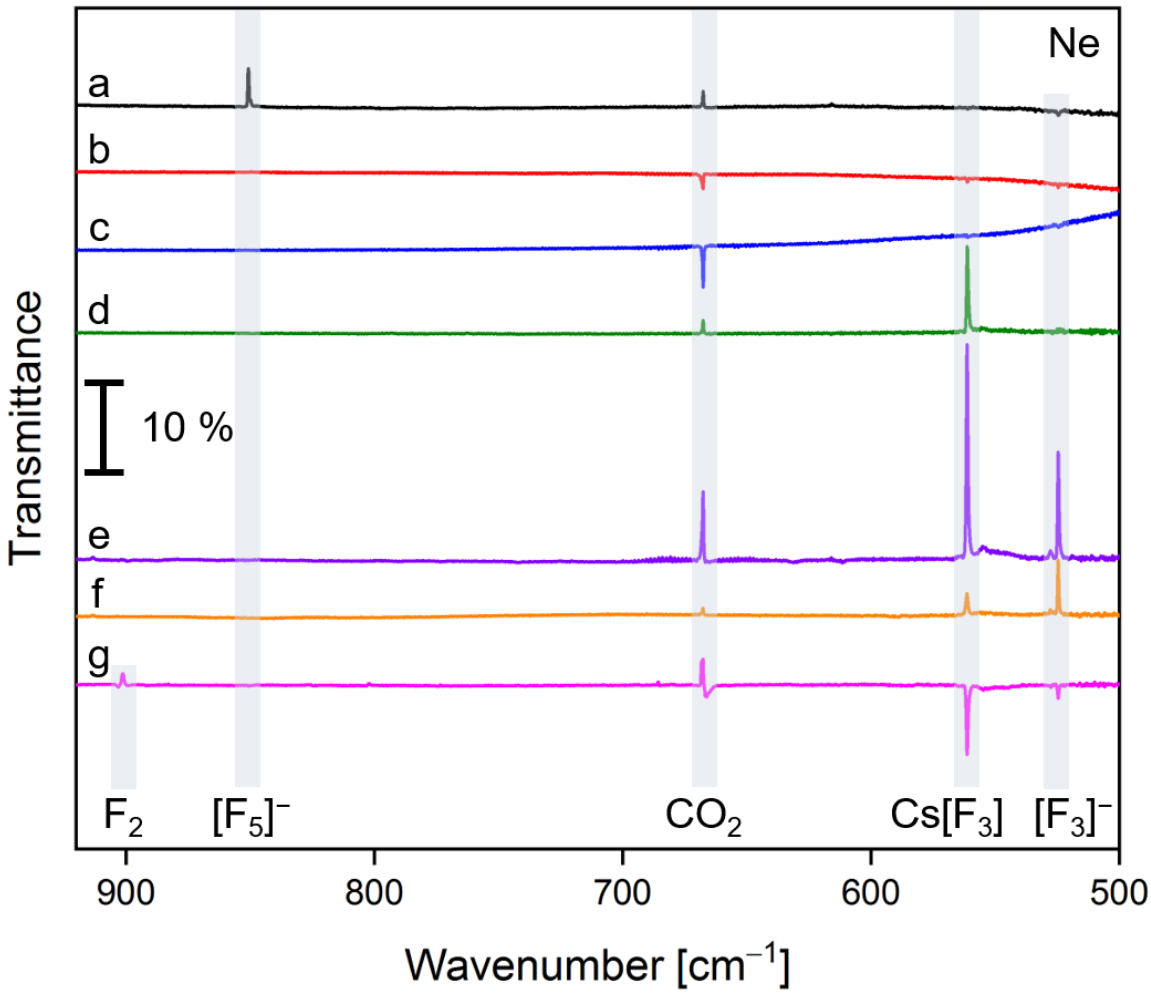

Figure 49: The difference IR spectra show the spectral changes after the irradiation of an initial deposit of fluorine (1 % diluted in neon) and laser-ablated $Cs[AuF_6]$ (3 % diluted in a CsF target, 3 Hz repetition rate, 30 mJ/pulse) deposited for 180 min at a deposition rate of 0.5 mbar·l·min^{-1} at a) λ = 730 nm (LED), b) λ = 625 nm (LED), c) λ = 596 nm (LED), d) λ = 528 nm (LED), e) λ = 455 nm (LED), f) λ = 278 nm (LED), for 12 min each, and after a final annealing step to g) 9 K. The CsI window (matrix support, T = 4 K) was coated with neon for 21 min prior to the deposition of the $Cs[AuF_6]/F_2$ sample. The bands pointing downwards are formed at the expense of the bands pointing upwards.

This deposit (Figure 48) was irradiated with light throughout the visible spectrum and the near-UV (Figure 49). The IR spectra were largely governed by the changes of the features of the polyfluorine monoanions, which are well documented in the literature.[10,77,377,378] However, the F–F stretching region (F_2) was found to be photochemically inactive (Figure 132 in the appendix).

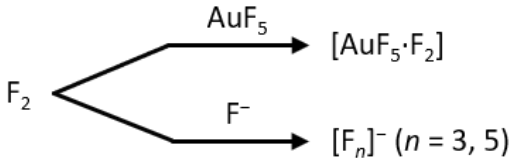

Scheme 19: Oxidation by adduct formation (top) and reduction by polyfluorine monoanion formation (bottom).

According to these results, the adduct formation of the type $[LA{\cdot}F_2]$ and the coordination of a fluoride ion by means of the formation of a polyfluorine mononanion $[F_n]^-$ (n = 3, 5) seem to 'battle' for the F_2 molecule (Scheme 19). The $[F_n]^-$ formation depicts a reduction of F_2 by the electron donor F^-. In contrast, the formation of a Lewis acid-base adduct represents an 'oxidation' by means of a slightly positive polarization of the $\{F_2\}$ moiety (see also Table 13). In this sense the very strong oxidant F_2 is preferentially reduced. The results of Ault and Andrews, who observed the rearrangement of $[Cl{-}F{-}F]^-$ to $[F{-}Cl{-}F]^-$[76] are along the same lines (see Scheme 20).

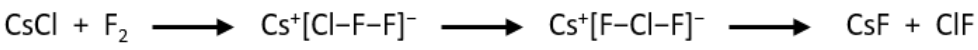

Scheme 20: Cl/F exchange under matrix isolation conditions according to reference [76].

The polyfluorine monoanions $[F_5]^-$ and $[F_3]^-$/$Cs[F_3]$ can be quantitatively decomposed upon irradiation with red light at λ = 730 nm (LED) or blue light at λ = 455 nm (LED), respectively.[10,77,377,378] In order to offer more free fluorine to the gold centers and enable the formation of a potential $[AuF_5{\cdot}F_2]$ complex, the formation of free fluorine from the polyfluorine monoanions was attempted via irradiation and annealing processes.

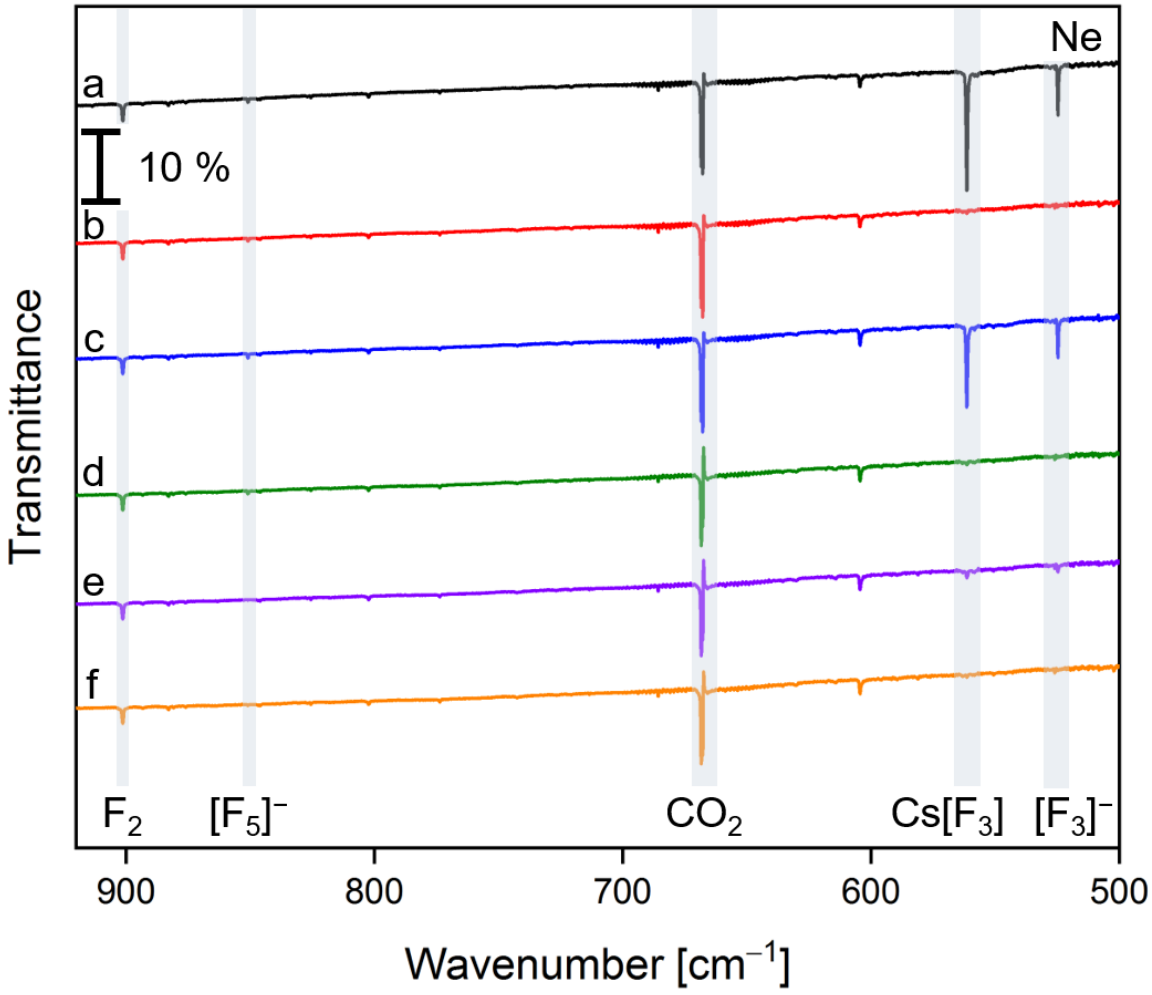

Figure 50: The IR spectra were recorded after a) the deposition of neon for 24 min, and the subsequent co-deposition of fluorine (0.1 % diluted in neon) and laser-ablated $Cs[AuF_6]$ (3 % diluted in a CsF target, 3 Hz repetition rate, 30 mJ/pulse) onto a CsI window at 4 K for 180 min at a deposition rate of 0.5 mbar·l·min^{-1}, b) the irradiation of the initial deposit λ = 278 nm (LED) for 60 min, c) the annealing of the matrix to 9 K, and the subsequent irradiation at d) λ = 278 nm (LED) for 40 min, e) λ = 730 nm (LED) for 5 min, and f) λ = 278 nm (LED) for 20 min.

For this purpose, the polyfluorine monoanions in a deposit of laser-ablated $Cs[AuF_6]$ (3 % in CsF) and F_2 (0.1 % in Ne) were decomposed by irradiating the sample with UV light at λ = 278 nm (LED) for 60 min (Figure 50, trace b). After that, the matrix was annealed to 9 K and the subsequently formed $[F_3]^-$/$Cs[F_3]$ were photolyzed at λ = 278 nm again. Thereby a small amount of $[F_5]^-$ formed, which was decomposed upon photolysis at λ = 730 nm. The matrix was quantitatively free from polyfluorine monoanions after a final irradiation step at λ = 278 nm. The F–F stretching region remained unchanged during these processes (Figure 133 in the appendix) and did moreover not show any photochemical reaction when this matrix was subsequently irradiated at λ = 656, 625, 596, 528 and 455 nm. With respect to the photochemical results of the BF_3, AsF_5 and SbF_5 experiments, this is not surprising.

The results at the lowest concentration of F_2 (0.1 % in Ne) do not necessarily exclude the potential existence of an F_2 adduct of AuF_5 under matrix isolation conditions. If such an adduct could be obtained following the photolysis of the polyfluorine monoanions, then it is assumed that a larger amount would be obtained at a higher concentration of fluorine. Therefore, an experiment was performed with laser-ablated $Cs[AuF_6]$ (3 % in CsF) and F_2 (3 % in Ne) and – to possibly capture an $[AuF_5 \cdot F_2]$ complex – the initial deposit was subjected to irradiation at wavelengths again throughout the visible and near-UV spectrum, and to consecutive annealing steps. Note that the literature-known changes due to transformations of the polyfluorine monoanions[10,77,377,378] in the single steps are discussed above and not explicitly shown in this case. IR spectra were recorded after each step and those featuring significant changes are shown in Figure 134, Figure 135 and Figure 136 in the appendix. The most intense changes were observed after the irradiation with blue light at λ = 455 nm (LED) and the corresponding difference spectrum is depicted in Figure 51 (trace b).

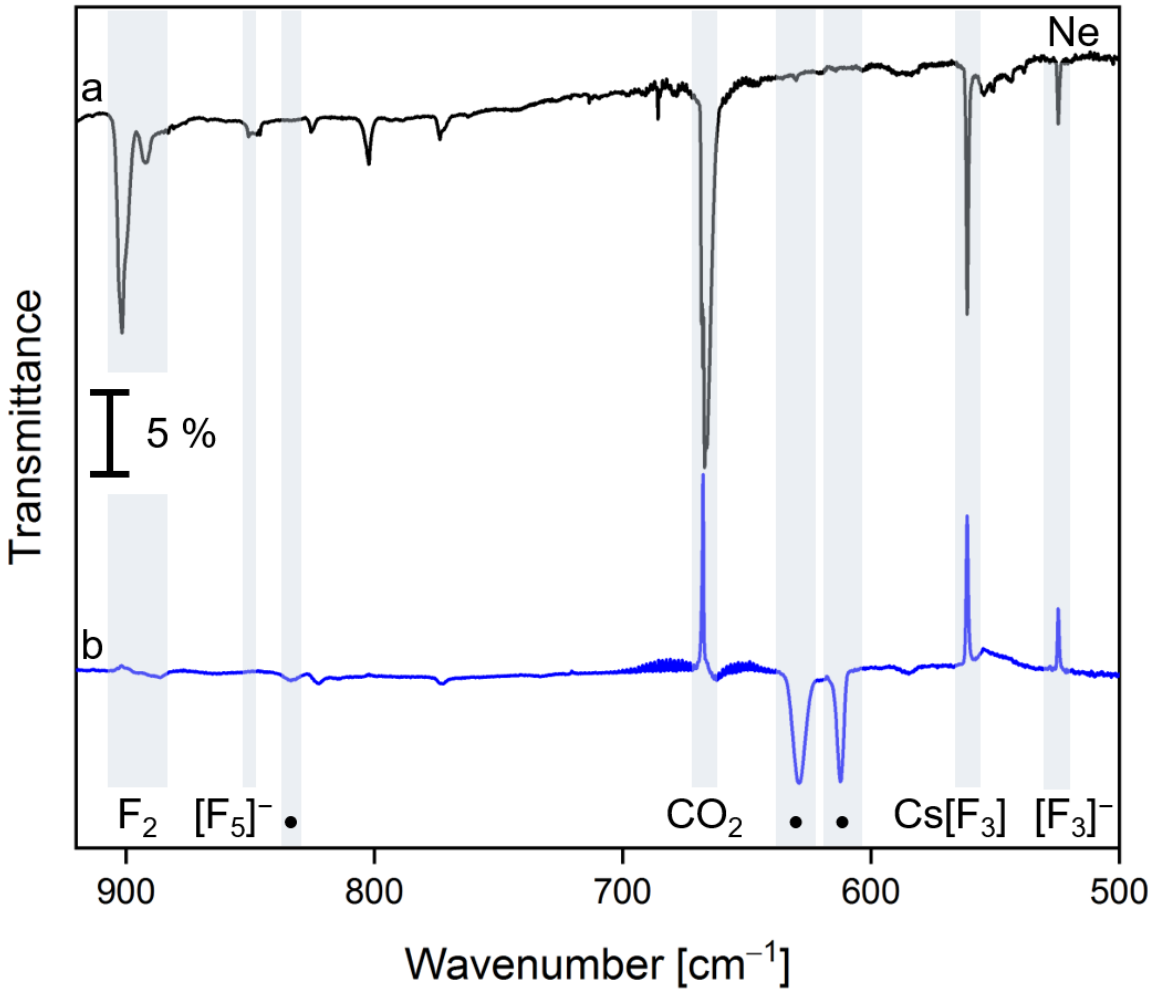

Figure 51: The IR spectrum (a) was recorded after the co-deposition of laser-ablated $Cs[AuF_6]$ (3 % diluted in a CsF target, 3 Hz repetition rate, 30 mJ/pulse) and fluorine at 3 % diluted in neon onto a CsI window at 4 K for 180 min at a deposition rate of 0.6 mbar·l·min^{-1}. The difference spectrum (b) shows the spectral changes after the irradiation of the matrix at λ = 455 nm (LED) for 60 min. Previous irradiation and annealing steps are mentioned in the text. The bands pointing downwards are formed at the expense of the bands pointing upwards. New features are marked by a bullet.

As depicted in Figure 51, small changes in matrix sites around the F_2 fundamental were observed upon blue light photolysis at λ = 455 nm (LED), accompanied by a slightly increased feature/shoulder at 886.3 cm^{-1} (see Figure 135 in the appendix for step-by-step spectra), which is known from experiments employing SbF_5 and F_2 (887.2 cm^{-1}, Figure 43). A weak, broad band at 833.3 cm^{-1} emerged during this process but was found at too low wavenumbers to be assigned to an F_2 adduct. The broad new bands at 628.3 and 612.2 cm^{-1} (see also Figure 134 and Figure 136 in the appendix) are not indicative for an F_2 complex since they should have been observed – to a lesser extent – at lower fluorine concentrations. Moreover, they are found in almost equal position in SbF_5/F_2 experiments, when compared to the IR spectra in Figure 43. Although they do roughly resemble the quantum-chemically predicted positions for an $\{AuF_5\}$ moiety coordinated

by F_2 (see Table 40 in the appendix and reference [195]), only one quasi-degenerate intense band would be expected.

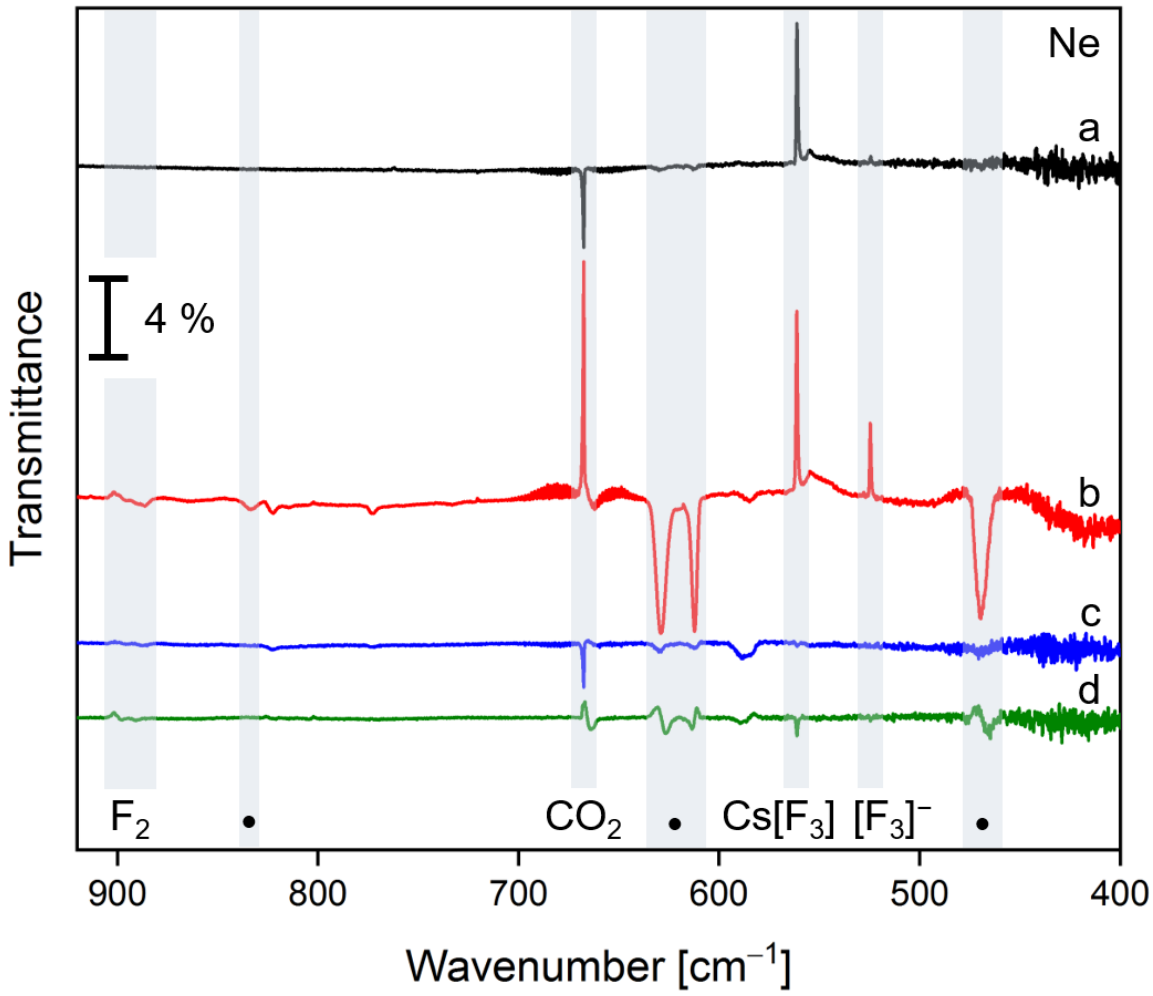

Figure 52: The difference spectra show the spectral changes after the irradiation of an initial deposit of laser-ablated $Cs[AuF_6]$ (3 % diluted in a CsF target, 3 Hz repetition rate, 30 mJ/pulse) and fluorine at 3.0 % diluted in neon onto a CsI window at 4 K for 180 min at a deposition rate of 0.6 mbar·l·min^{-1} at a) λ = 528 nm (LED) for 20 min, b) λ = 455 nm (LED) for 60 min, and c) λ = 375 nm (LED) for 20 min and after d) a final annealing step of the matrix to 9 K. The bands pointing downwards are formed at the expense of the bands pointing upwards. New prominent features are marked by a bullet.

Another broad band at 469.0 cm^{-1} of equal intensity developed simultaneously (Figure 52, Figure 134 and Figure 136 in the appendix) with the broad bands discussed above. No corresponding band was found in SbF_5/F_2 experiments, probably because the spectra were very noisy below 500 cm^{-1}. The band lies principally in the region of the difluorine monoanion/ion pairs ($[F_2^-]$),[74,374] but is found blue-shifted by 10 cm^{-1} from the literature value of $Cs[F_2]$[374] while also being far too intense. Additionally, no development around 700 cm^{-1} was observed, which means that low-valent gold species were not re-oxidized under these conditions.[10,434,493]

Since AuF_5 could not be produced in larger amounts from laser-ablated $Cs[AuF_6]$ and the experiments with fluorine in different concentrations had a comparable outcome as with the other Lewis acids, analogous experiments were not performed in argon.

These results indicate that an F_2 adduct of the type $[AuF_5 \cdot F_2]$ could not be obtained employing $Cs[AuF_6]$ as a starting material and under the chosen conditions. Overall, the quantity of the potentially formed AuF_5 was found to be too low in co-deposition experiments of F_2/Ng gas mixtures and laser-ablated $Cs[AuF_6]$/CsF targets to acquire a corresponding F_2 adduct. Apparently, the re-oxidation of the gold centers is not taking place or not leading to Au^V species in relevant amounts. Experiments with high concentrations of F_2 of up to 3 % only lead to the formation of a very intense band accounting for a polarized solid fluorine phase. The solid F_2 is hardly involved in matrix reactions, indicated by a lower $[F_3]^-$ content at the same laser power and the same repetition rate like in the experiments performed with 1 % fluorine. Regardless of the directly bound $Cs[F_3]$ ion pair, the high intensities of the $F_{2,s}$ and $F_{2,i}$ bands, which were found to be even higher than in the SbF_5 case, indicate a strong influence of CsF (the primarily laser-ablated species), i.e. the polarization of F_2. As analogously outlined for SbF_5, a polarized F_2 molecule is also more IR active than a non-polarized one. Notionally irrespective of their nature – be it Lewis acid or an additional 'impurity' like CsF – a high amount of co-deposited substance(s) leads to a more distorted or non-uniformly crystallized matrix. Consequently, the species are less well isolated and the formation of higher aggregates, in this case those of elemental fluorine, could be favored.

3.1.3 General Discussion and Conclusion of [LA·F_2] Adducts

In summary, in the presented sets of matrix isolation experiments employing the strong Lewis acids BF_3, AsF_5, SbF_5 and 'AuF_5' (attempted generation from laser-ablated $Cs[AuF_6]$, vide supra) with an increasing FIA in this order[249] and different concentrations of elemental fluorine, a direct proof for a 1:1 [LA·F_2] adduct by means of a characteristic ν(F−F) band could not be unequivocally found (Figure 53).

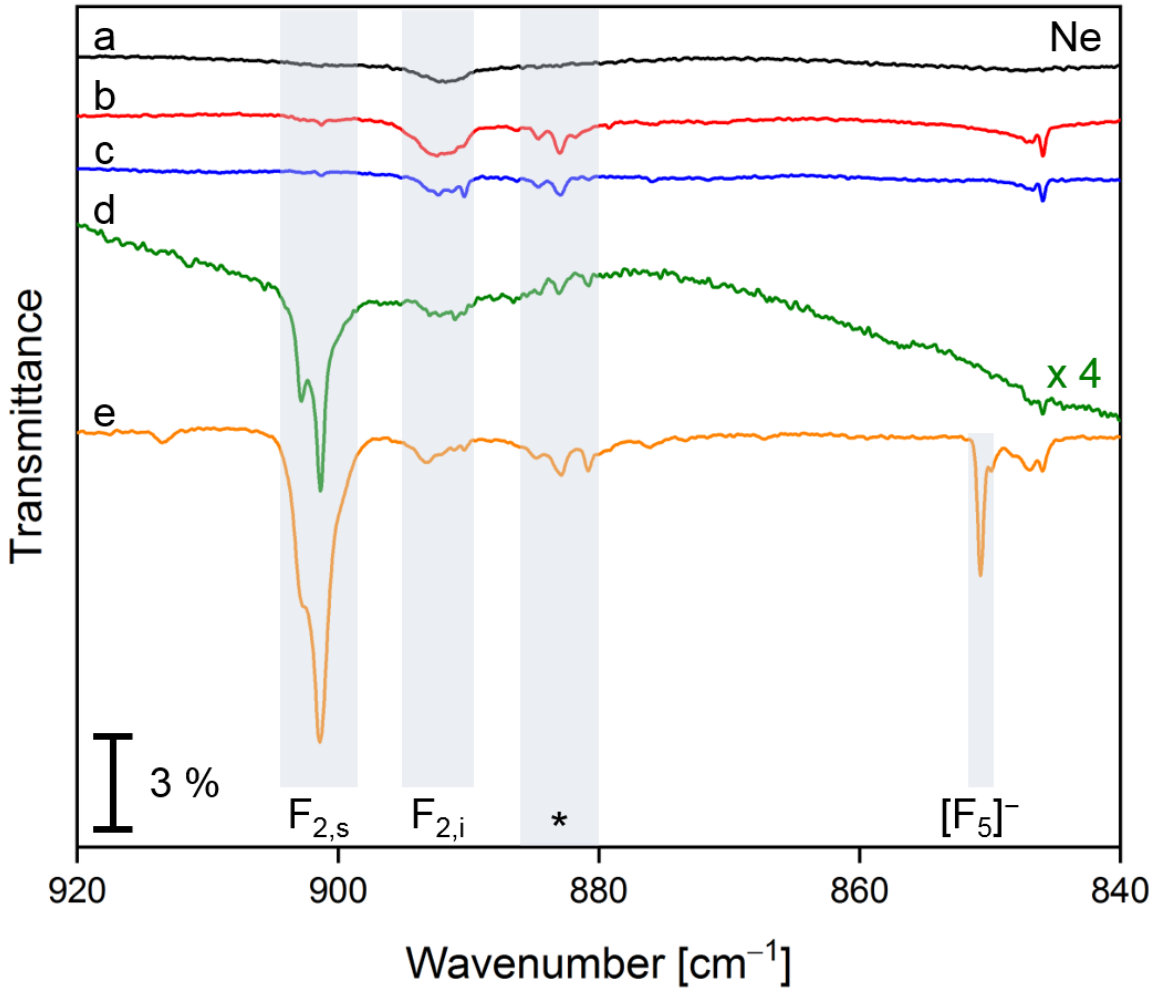

Figure 53: Comparison of matrix IR spectra after long-term co-deposition of different Lewis acids and high concentrations of fluorine diluted in neon. The IR spectra were recorded after the deposition of a) solely F_2 (3 %) for 60 min, b) BF_3 (0.1 %) and F_2 (1 %) for 120 min, c) AsF_5 (highly diluted) and F_2 (1 %) for 180 min, d) SbF_5 ($\vartheta \leq -48.5$ °C) and F_2 (1 %) for 180 min (magnified for clarity), and e) laser-ablated $Cs[AuF_6]$ (3 % in CsF) and F_2 (1 %) for 180 min onto a CsI window at 4 K at deposition rates of 0.5 to 0.6 mbar·l·min^{-1}. IR active features caused by traces of AsF_5 in combination with F_2 are marked by an asterisk.

Upon the comparison of the obtained ν(F−F) bands – of isolated and solid F_2, respectively – in the co-condensation experiments employing different Lewis acids (Figure 53) and fluorine at different concentrations, it becomes evident that the relative intensities of the $F_{2,s}$ and $F_{2,i}$ bands do not

necessarily depend on the fluorine concentration but rather on the nature or amount of the co-deposited species (Table 19).

However, a band indicative for isolated fluorine molecules was only observed as a shoulder in the experiments employing SbF_5 and F_2 in Ar (Figure 45), while generally argon acted as a better carrier gas than neon concerning the overall level of impurities.

At a low impurity level of the matrices, the $F_{2,s}$ band (in these cases of low intensity) and the AsF_5/F_2-dependent bands (assumed cage pair, marked by an asterisk throughout the figures) were reduced or fully vanished upon annealing, as seen for instance in Figure 30, Figure 120 and Figure 121 (the latter two are found in the appendix), while the $F_{2,i}$ band sharpened during this process. Other bands, including the fundamentals of the respective Lewis acid, experienced band broadening and decreasing intensities induced by annealing. In fact, the persistence of the predominant F_2 band in each experiment is rather unexpected, since annealing can be accompanied by the loss of matrix material, especially at high temperatures such as 13 K for neon matrices.

Table 19: Comparison of positions (given in cm^{-1}), relative intensities (approximate ratios) and shapes of the ν(F−F) bands of solid (s) and isolated (i) F_2 in both neon and argon matrices under the influence of different Lewis acids or laser-ablated $Cs[AuF_6]$ (embedded in CsF). The maxima of the bands are bold, values between $F_{2,s}$ and $F_{2,i}$ are given in italics and are assigned to $F_{2,s}$. The underlying spectra were measured at a resolution of 0.2 cm^{-1}.

Deposited species	**Ng**	**$\tilde{\nu}$ (ν(F−F), $F_{2,s}$)**	**$\tilde{\nu}$ (ν(F−F), $F_{2,i}$)**	**$I(F_{2,s}) : I(F_{2,i})$**
F_2[a]	Ne	**901.3**	**891.7**	0.1 : 1
$BF_3 + F_2$[b]	Ne	902.3 sh, **901.2**, 900.3 sh	**892.4** br, 891.4 sh, 890.4 sh	0.2 : 1
$AsF_5 + F_2$[b,c]	Ne	902.6, **901.2**	892.9 sh, 892.3, **891.3**, 890.3[g]	0.2 : 1
$SbF_5 + F_2$	Ne	902.8 sh[a,b], **901.4**[a,b], 900.4 sh[a,b]	892.2 sh[b], **891.0**[b] 894.7 sh[a], **892.1 br**[a]	10 : 1[b] 4 : 1[a]
$Cs[AuF_6] + F_2$	Ne	902.8 sh[a,b,d], **901.3**[a,b,d], 900.3 sh[a], 899.6 sh[b,d]	**893.2**[b,d], 892.5 sh[d], 892.1 sh[b], 891.1 sh[b], 890.3[b] **892.2 br**[a], 890.5 sh[a]	7 : 1[d] 14 : 1[b] 4 : 1[a]
F_2[a]	Ar	899.3 sh[e], **898.2**, 897.0 sh[e], *894.8* sh[e]	**891.8**, 892.3 sh	0.5 : 1 25 : 1[e]
$BF_3 + F_2$[b]	Ar	**898.1**, 897.1 sh, 896.3 sh	892.9 sh, **892.4**, 891.5 sh	1 : 1
$AsF_5 + F_2$	Ar	**898.0**[c] 899.3[f], **898.2**[f], 896.7sh[f], *894.5*[f]	**891.9**[c] **892.4**[f], 891.8[f]	2 : 1[c] 6 : 1[f]
$SbF_5 + F_2$[b]	Ar	**898.1**, 896.3 sh	*894.8* sh	5 : 1[h]
$Cs[AuF_6] + F_2$	Ar	–[i]		

[a] at 3 % F_2; [b] at 1 % F_2; [c] AsF_5 highly diluted; [d] at 0.1 % F_2; [e] only observed at a high impurity level; [f] at 0.1 % (AsF_5); [g] novel feature; [h] this ratio represents an estimation, since intensities of shoulders cannot be counted; [i] experiments were not performed for reasons given in Section 3.1.2.5.

Combined with the absence of a clear indication for a Lewis acid-dependent shifted ν(F−F) band except for one case, it becomes apparent that the lower the impact of the co-deposited species (BF_3, AsF_5, SbF_5, $Cs[AuF_6]$/CsF) towards a uniform formation of a matrix, the higher the relative amount of isolated F_2 molecules and the less intense the $F_{2,s}$ band becomes (Table 19). Vice versa, a larger impact could lead to a more distorted matrix cage or could reduce the rate of solidification/crystallization and thereby elongate the lifetime of the liquid state, which would

promote the self-aggregation of F_2 molecules via halogen bonding[38,110] rather than the isolation. The matrix formation might be impaired by:

- total amount of embedded species (concentration of reactants, laser power)
- nature of the embedded species (neutral, ionic, higher aggregates)
- sizes and shapes of the embedded species (e.g. EF_3 or EF_5 molecules)
- Lewis acid-base reactions of the reactants with impurities

Apparently, these effects cannot always be studied separately. For example, on offering enough AsF_5 to enable the interaction with fluorine, oligomeric species are found to be co-deposited, even at very low concentration of the Lewis acid (vide supra). These higher aggregates could conceivably hamper the formation and isolation of an [LA·F_2] adduct by disturbing the formation of a regular, undistorted matrix, and by less singular Lewis acid molecules available for the coordination of F_2. The impact of two coordinated AsF_5 molecules on one F_2 molecule was found to be insignificant (Table 53 and Figure 103 in the appendix). These cooperative effects then aggravate the interpretation of the resulting spectra.

Reflecting the considerations in Section 3.1.2.1, the exact nature of the species that activates F_2 does not seem to matter. A strong Lewis acid like AsF_5 or SbF_5 or even the very weak one HF, and even a comparably large amount of CsF might participate in or catalyze fluorination reactions with elemental fluorine.[130–132,408,409] This assumption also holds for the outcome of the experiments with AsF_5 in a high dilution in neon, where a new component of the band of isolated fluorine was observed. The possible positions of the F−F stretching bands in the IR regime (IR and Raman) upon the comparison of reported data with results of this work (Table 14) create the following impression: There are the two main bands, one of solid ($F_{2,s}$) and one of isolated fluorine ($F_{2,i}$) centered at 901.3 and 891.7 cm^{-1} (both in neon), respectively, with a more or less continuous 'transition' in between them based on the degree of self-aggregation. This is seen to be influenced by the matrix host, as well as the nature and amount(s) of the co-deposited species (for example also CsF dust that is expelled in the course of the laser ablation of the mixed salt target). The results of this work indicate that the higher the amount of the co-deposited species, the higher the (relative) intensity of the $F_{2,s}$ band observed. Bartlett and coworkers have shown that the oxidation of Xe with F_2 proceeds in the presence of AsF_5 at a temperature of −60 °C, where AsF_5 is a liquid, but not at +20 °C, where AsF_5 is a gas.[130] This indicates that pure liquid AsF_5 itself acts as a solvent and thereby represents a medium that is very disparate of an isolating system (isolated F_2 molecules in the gas phase, gaseous dilutions thereof, matrix-isolated samples). In the sense that also liquid HF catalyzes the oxidation of Xe with F_2 in the dark, as reported by Schrobilgen and

coworkers,[132] it becomes clear that the role of the Lewis acid in these kind of reactions does not exclusively relate to its acidity but – more importantly – to its amount (relative to F_2) and its state of aggregation. Therefore, the existence of Lewis acid-fluorine adducts [LA·F_2] is not excluded under the conditions of matrix isolation but might lie below the detection limit with respect to the predicted extremely low IR activity of these compounds (with respect to their {F_2} moieties, Table 11).

In addition to that, if fluorine shows roughly the same behavior by means of the interaction energy towards different species, it could be possible that a perturbing species, like a Lewis acid, CsF, or higher aggregates thereof (e.g. CsF dust) stabilizes one of the $F_{2,s}$ or $F_{2,i}$ phases instead of an individually shifted one. This means that there would be not necessarily a direct correlation to the acidity of the Lewis acid and different species might activate the same F_2 phase. This could explain that mainly the intensities of the $F_{2,s}$ and $F_{2,i}$ bands vary upon the variation of the Lewis acid. This interpretation makes also sense regarding the expected non-well-defined complex geometries[73,354] at the calculated low binding energies (Section 3.1.1). Moreover, the ν(F−F) modes at 892 cm^{-1} for the weakly bound [FH·F_2] complex[364,392,393,404] was found in identical position with the fundamental of elemental F_2.[74] The ν(F−F) of [H_2O·F_2] was reportedly found in equal position at 877.5 cm^{-1} for different isotopomers, while the H/D and $^{16}O/^{18}O$ exchanges only had an effect on the water centered band positions.[393] A band at almost the same position, 877.7 cm^{-1}, was assigned to a [Hg·F_2] complex by Young and coworkers,[180] while the appearance of the $F_{2,i}$ band at 892.1 cm^{-1} in the latter report was interpreted as impurity-induced, which adds further weight to this argument. In addition to that, the shapes of the $F_{2,s}$ and $F_{2,i}$ bands can be compared. The full width at half maximum is about 2.5 cm^{-1} for the $F_{2,s}$ and 4.0 cm^{-1} for the $F_{2,i}$ band. The $F_{2,s}$ band more likely accounts for a singular species/phase due to the narrower band width that suggests a geometrically better defined species[73,354] and also compares to the band width of α-F_2.[13,467] Conversely, the $F_{2,i}$ band has a comparably broad shape in all cases and the underlying multi-component structure is only revealed in the case of a very low concentrated AsF_5 in neon (Figure 53, Table 19). In the case of laser-ablated Cs[AuF_6] (diluted to 3 % in CsF), the maximum of the $F_{2,i}$ band is found blue-shifted by about 1 cm^{-1} compared to the other cases and an overall higher aggregation of F_2 is observed. This behavior somewhat corresponds to the donor strength of F^- in CsF, which features the lowest coulombic interaction of the alkali metal fluorides,[377] for the formation of polyfluorides, and to the role of CsF as a catalyst in fluorination reactions employing elemental fluorine.[408,409] The results of this work indicate that there is a higher aggregation of fluorine in more distorted matrices, which might not be resembled in the

abovementioned liquid Lewis acid mediated fluorination reactions of elemental Xe[130–132] (see also Scheme 14 in Section 1.8).

Regarding the amount of energies needed for a heterolytic F–F bond cleavage (1510 kJ·mol^{-1}) and the homolytic one (159 kJ·mol^{-1}),[39,494] it becomes apparent that none of the experimentally known Lewis acids to date has the power to substantially polarize F_2 in the direction of the former case. This becomes evident in [AuF_5·F_2], where the heterolytic bond cleavage with the formal product $[AuF_6]^-$ + F^+ was calculated by Himmel and Riedel to be lowered to still about 1000 kJ·mol^{-1}.[195] Regarding these extreme cases, a small shift of the charge is apparently enough to facilitate the Lewis acid mediated fluorination of Xe.[130,131] Monitoring an oxidation with elemental fluorine without the actual presence of a reducing agent seems to be at the limit of experimental feasibility even with Lewis acids as strong as BF_3, AsF_5 and SbF_5 in the light of a very weak ν(F–F) band. Consequently, the adduct formation does not necessarily take place without an electron donor.[130] The presence of a catalytically active [LA·F_2] complex for the oxidation of e.g. Xe upon the addition of AsF_5 is not excluded, since the complex might exist in a transition state, which is consistent with Bartlett's 3-body-approach (Lewis acid-fluorine-xenon interaction).[130] In addition to that, the product $[XeF]^+[AsF_6]^-$ might be strongly stabilized by the hexafluoridoarsenate(V) ion, which might be the driving force of the reaction.[129,348,368]

The reported results on [BF_2·F_2] and [AlF_2·F_2] complexes,[403] for which the {MF_2} units should strongly activate the fluorine fundamental, do not include experimental data accounting for a characteristic ν(F–F) band. Therefore, the 'missing' trend of specifically shifted stretching bands of activated (polarized) fluorine in this work becomes not particularly surprising. Tentatively said, weakly bound systems such as the Lewis acids and CsF in this work and HF[364,392,393,404] favorably promote the $F_{2,s}$ and $F_{2,i}$ bands, while more strongly bound systems, as for example [OCSe·F_2],[391] an individually shifted band position is observed. Therefore, the ν(F–F) is not necessarily specifically shifted for every coordinating species.

Since the assignment of the singular features of the bands $F_{2,s}$ and $F_{2,i}$ to distinct chemical species solely based on experiments is speculative, a future quantum-chemical modelling of F_2 at various concentrations in a neon environment in the solid state could provide a more detailed insight.[495]

3.2 PtF_6 – A Precursor for Neutral and Anionic F_2 Complexes

According to its UV/Vis spectrum,[79,298] platinum hexafluoride exhibits a rich photochemistry, which was studied in a combined matrix isolation (using MIR, FIR, and UV/Vis spectroscopy) and relativistic quantum-chemical investigation within a cooperation with Dr. Lin Li and Dr. habil. Helmut Beckers from the Inorganic Chemistry at the Institute of Chemistry and Biochemistry at the Freie Universität Berlin and Dr. Artur Wodyński, Dr. Robert Müller and Prof. Dr. Martin Kaupp from the Quantum Chemistry at the Institute of Chemistry at the Technische Universität Berlin. This systematic study of the higher and the lower platinum fluorides PtF_n (n = 1–6) and fluorine complexes of the type $[PtF_n \cdot F_2]$ (n = 4, 5) provided detailed insight into the nature of these species and the conditions at which these species are selectively formed. The obtained results were published in:

G. Senges, L. Li, A. Wodyński, H. Beckers, R. Müller, M. Kaupp, S. Riedel, *Chem. Eur. J.* **2021**, 27, 13642.

These results, in conjunction with those obtained from the investigation of the $[LA \cdot F_2]$ complexes (cf. Section 3.1), motivated the approach to use PtF_6 together with laser-ablated metals or metal fluorides as a potential source for anionic non-classical fluoro complexes with a discrete $\{F_2\}$ moiety.[79,195,273]

Knowing the conditions to selectively yield the platinum fluorides PtF_n (n = 1–6), as described in the reference [304], enables a new approach, in which the photochemistry of PtF_6 provides a robust foundation and serves as a 'toolbox'. Neither the Lewis acids BF_3, AsF_5, and SbF_5 in the presence of F_2 (Section 3.1), nor $[PtF_n \cdot F_2]$ (n = 4, 5)[304] or the reported $[MF_2 \cdot F_2]$ (M = B, Al, Ga, In, Tl)[403] showed or were reported to show any band confidently assignable to an F–F stretching mode in the IR spectra. Consequently, these neutral species, independent of their Lewis acidities, only allow for a low or even no (IR) activation of difluorine. F_2 depicts a very strong oxidizer on the one hand but a very poor electron donor and a very weak Lewis base[73,361] on the other hand. When modelling the liquid Lewis acid mediated oxidation of Xe[130–132] (cf. Scheme 14 and discussion in Section 3.1) in a constrained approach, i.e. by solely using the Lewis acid and F_2, an electron donor like xenon[131] to 'fuel' the reduction of fluorine is missing. Considering that cesium fluoride catalyzes direct fluorinations with elemental fluorine,[75,408,409] which binds fluoride from thermally evaporated CsF to form $Cs[F_3]$,[75,76] further points out the necessity of an electron donor. In contrast to the laser ablation of metals or metal salts, which additionally produces free electrons,[18,377,378,388,425] the pivotal reduction of difluorine in the plasma plume is excluded when

thermally evaporated CsF is used.[75,76] This renders both electrons and fluoride ions efficient reducing agents under matrix isolation conditions.[10,377]

In order to compensate for the loose 'fixation' of a fluorine molecule in a cage pair of the type $[LA{\cdot}F_2]$, a photosensitive, fluorine-rich precursor like PtF_6 could be employed. Simultaneously, as no ν(F−F) was observed for $[PtF_n{\cdot}F_2]$ (n = 4, 5),[304] the lack of electrons from a missing reducing agent for an at least partial reduction of $\{F_2\}$ moiety could be compensated by fluoride ions or electrons generated by the laser ablation of metals or metal fluorides.[10,18,388,425] In contrast to F_2 complexes, where a reliable experimental proof remained elusive (vide supra), the existence of the difluorine monoanion $[F_2]^-$ was experimentally proven in the presence of all the (stable) alkali metal cations under matrix isolation conditions.[74,110,374,375]

A newly developed deposition unit, which represents an advancement of the device used for the deposition of solely PtF_6,[214,304] should allow the quantitative deposition of PtF_6 – at a low sample loss due to a high diameter of the deposition line and a high reproducibility[275] – and the simultaneous laser ablation of metals or metal salts (see Figure 16 in Section 1.10.1.1, as well as Figure 99 and Figure 100 in Section 4.5). In this process, PtF_6 should be reduced to $[PtF_6]^-$ or the corresponding ion pairs $M[PtF_6]$ (M = Na, K, Pd, Cs, Pt) by scavenging an electron from the laser-induced plasma, or alternatively, form species like $[PtF_7]^-$ by capturing a fluoride ion. The products after deposition will be subsequently photolyzed by light at a suitable wavelength to potentially yield a complex of the type $[PtF_n{\cdot}F_2]^-$ (n = 3, 4, 5) based on the results in reference [304]. Thereby, a partially reduced and therefore better polarizable $\{F_2\}$ moiety[74] derived from the photodecomposition of the PtF_6-based precursor becomes imaginable.

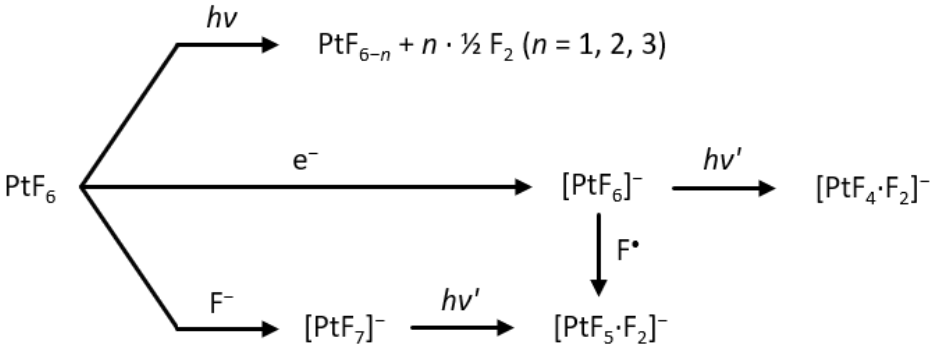

Scheme 21: Conceivable reactions of platinum hexafluoride in the presence of laser-ablated metal fluorides, which are the source[10] of electrons, fluoride ions and photons (*hν*). Subsequent irradiation with light at a specific wavelength of an already existing deposit is referred to as *hν'*. Fluorine atoms (F•) are thought to be produced photochemically and the reaction to occur after diffusion upon annealing. Cations as parts of starting materials and products were omitted for clarity, while also ion pairs are conceivable products.

Generally, the pathways given in Scheme 21 are conceivable with respect to the results already obtained on the neutral platinum fluorides,[304] the reported electron-capturing processes[10,378,388] (cf. Section 1.6) and the coordination of a fluoride ion to PtF_6 in analogy to the polyfluorine monoanions[10,110,378] (cf. Section 1.9). The obtained experimental results are supported by quantum-chemical calculations and are presented in the following subchapters.

3.2.1 Quantum-Chemical Results

The neutral platinum fluorides PtF_n (n = 1–6) and the complexes $[PtF_n \cdot F_2]$ (n = 4, 5) have been characterized both quantum-chemically and experimentally, as reported in reference [304]. In order to obtain a good comparability with the fluoridoplatinate species $[PtF_n]^-$ (n = 5, 6, 7), $M[PtF_6]$ (M = Na, K, Pd, Cs, Pt) and the complexes $[PtF_5 \cdot F_2]^-$ and $[PtF_4 \cdot F_2]^-$, also the neutral PtF_n (n = 3–6) compounds were subjected to structure optimizations and frequency calculations at the RI-B3LYP-D4/def2-TZVPP level of theory. The optimized structures of all these species are found in the form of xyz coordinates in Section 6.2.1, their corresponding NPA charges in Section 6.2.2 and vibrational frequencies in Section 6.2.3 in the appendix. Regarding the experimentally expected large amount of derivatives in high oxidation states obtained from platinum hexafluoride, even under the influence of long-term irradiation with blue and UV light,[304] the quantum-chemical description focusses on binary and ternary ionic and neutral platinum fluoride compounds with platinum in high formal oxidation states ranging from +III to +VI to support the experimental results in Section 3.2.2.

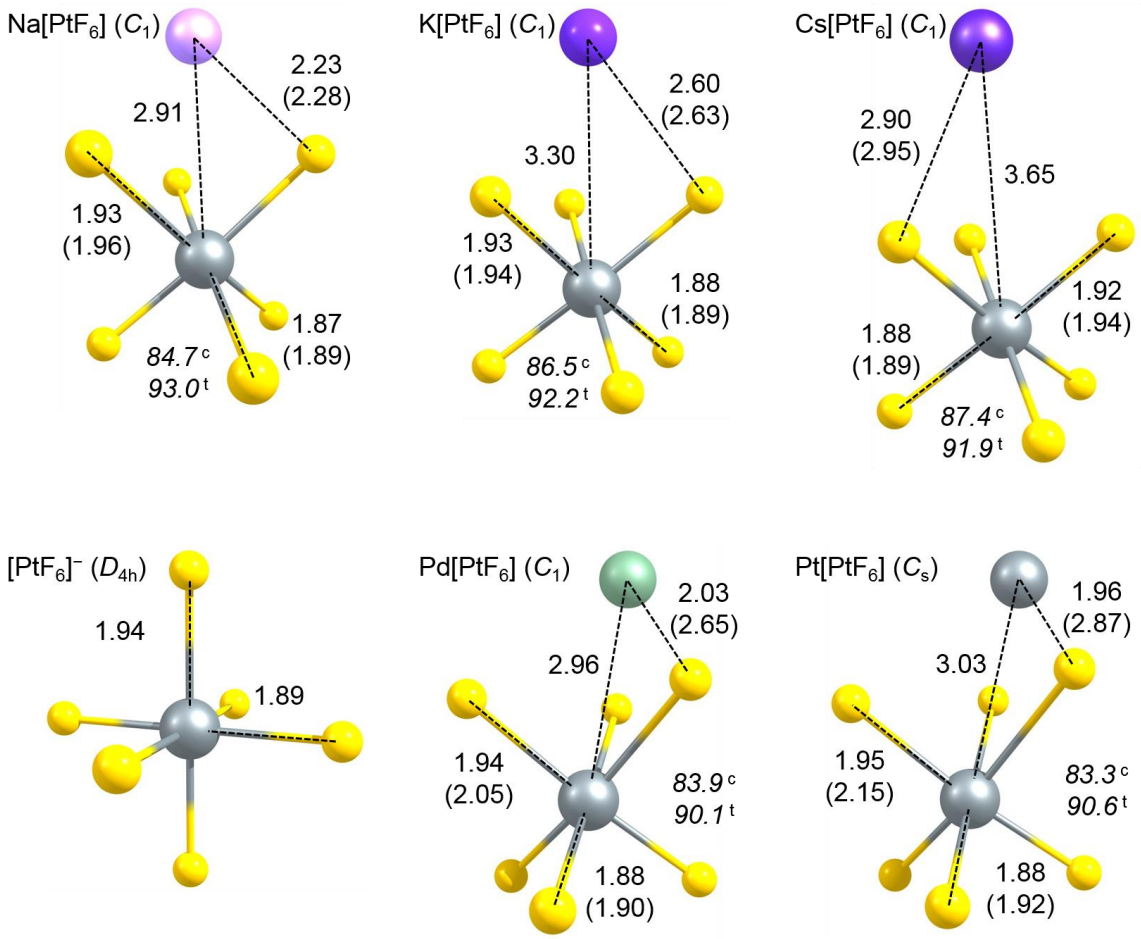

Figure 54: Minimum structures of hexafluoridoplatinate compounds with different cations calculated at the RI-B3LYP-D4/def2-TZVPP level of theory. The six fluorido ligands are divided into two sets of three, referred to as coordinated (superscript c, closer to the counter cation) and terminal (superscript t) $\{PtF_3\}$ moieties. The featured bond distances (in Å) represent the shortest ones within these moieties, while the largest ones are given in parentheses. The largest F–Pt–F bond angles (in °) refer to the central platinum atom and are given in italics for the coordinated and terminal $\{PtF_3\}$ moieties.

The structures of the ion pairs $M[PtF_6]$ (M = Na, K, Pd, Cs, Pt) depicted in Figure 54 have in common that the terminal $\{PtF_3\}$ moieties feature shorter Pt–F bond distances and larger F–Pt–F bond angles than the 'coordinated' $\{PtF_3\}$ moieties (closer to the counter cation). In accordance with the van der Waals radii, the central Pt–M distances increase in the order Na (r_W = 2.4 Å) < K (r_W = 2.8 Å) < Cs (r_W = 3.0 Å).[459] The alkali metal ions Na^+, K^+ and Cs^+ are found in similar positions on one of the faces of the distorted $\{PtF_6\}$ octahedrons with only a small deviation in the top Pt–F bond distances. Similar structures were reported for $M^+[UF_6]^-$ (M = alkali metal) by Arthers et al.[314] and $Cs^+[NbF_6]^-$ by Beattie et al.[313] The Pd (r_W = 2.05 Å)[459] and Pt (r_W = 2.05 Å)[459] atoms are rather located at one of the edges, which is evident from the large deviation in the top Pt–F bond distances and is accompanied by longer distances to the central platinum atom and shorter M–F contacts.

Although PtF_6 and $[PtF_6]^-$ are reportedly octahedral[298,300,321,496] within the accuracy of the experimental method, the quantum-chemical (non-relativistic, scalar-relativistic) calculations result in distorted structures of D_{4h} or D_{3d} symmetry[273,280] due to the impact of Jahn-Teller distortion.[280,300,304,497] Upon inclusion of spin-orbit coupling,[79,304,496,498] relativistic calculations reveal an O_h-symmetric ground state for PtF_6. Consequently, the non-relativistic computations at the RI-B3LYP-D4/def2-TZVPP level of theory in the present work resulted in D_{4h}-symmetric structures for both PtF_6 and $[PtF_6]^-$.

Because of the e_g and b_{2g} levels in the D_{4h}-symmetric PtF_4 lying very close to each other, not only the closed shell singlet (^1E_g) but also the open shell triplet ($^3e_g \times ^1b_{2g}$) are accessible.[304] The latter configuration results in a triplet ($^3B_{2g}$) ground state for PtF_4, which was found in symmetry-reduced D_{2h} conformation, being 56 kJ·mol^{-1} lower in ZPE-corrected energy than the corresponding D_{4h} conformation, with a slightly deviated F−Pt−F angle of 87.6°. In D_{4h} symmetry, a singlet state was found 67 kJ·mol^{-1} higher in energy than the triplet ground state, reflecting the results given in references [280,304]. For PtF_3 as a reported C_{2v}-symmetric molecule,[304] a structure optimization at the RI-B3LYP-D4/def2-TZVPP level of theory resulted in a doublet (^2A) C_1-symmetric structure.

In order to obtain insight into the oxidation states of the different hexafluoridoplatinates, the NPA charges are summarized in Table 20.

Table 20: NPA charges (in e) and electronic ground state (GS) symmetries in $M[PtF_6]$ (M = Na, K, Pd, Cs, Pt) obtained at the RI-B3LYP-D4/def2-TZVPP level of theory. The superscript 'av' refers to the averaged values of the coordinated (lying closer to the counter cation) and terminal fluorine atoms in accordance with the structures shown in Figure 54. The superscripts 'ax' and 'eq' refer to axial and equatorial F ligands in D_{4h}-PtF_6 and D_{4h}-$[PtF_6]^-$.

Compound	**GS**	**$Pt_{central}$**	**$F_{coordinated}^{av}$**	**$F_{terminal}^{av}$**	**M**
D_{4h}-PtF_6	^3E_g	2.315	−0.363^{ax}	−0.397^{eq}	
D_{4h}-$[PtF_6]^-$	$^2B_{1g}$	2.200	−0.594^{ax}	−0.503^{eq}	
C_1-$Na[PtF_6]$	^2A	2.174	−0.600	−0.448	0.971
C_1-$K[PtF_6]$	^2A	2.182	−0.594	−0.460	0.980
C_1-$Cs[PtF_6]$	^2A	2.187	−0.591	−0.466	0.983
C_1-$Pd[PtF_6]$	^1A	2.015	−0.555	−0.472	1.068
C_s-$Pt[PtF_6]$	$^1A''$	1.937	−0.540	−0.485	1.140

Since the 'coordinated' group of F ligands is influenced by a counterion, the averaged NPA values are more negative compared to the terminal group of fluorine atoms in all cases. Owing to the edge position of the counter ion in the $M[PtF_6]$ (M = Pd, Pt) cases, a stronger distortion of the

{PtF_6} moiety leads to a larger deviation of the NPA charges of the fluorine atoms within coordinated/terminal groups. The Pt charges of the alkali metal hexafluoridoplatinates(V) are found to be comparable to the one of isolated $[PtF_6]^-$, thus featuring oxidation states of +V for the central platinum atom and +I for the alkali metal ions in accordance with reference [304]. In contrast to these results, and in comparison with the published data,[304] the NPA charges of Pt[PtF_6] correspond to oxidation states +IV and +II for the central platinum atoms and the counter cations, respectively, rendering the latter compound formally mixed-valent.[263] Due to the similar structure Pd[PtF_6] is seen to be comparable. As in the presence of palladium and platinum cations the {PtF_6} moiety rather resembles $[PtF_6]^{2-}$, the expected IR spectrum strongly deviates from the hexafluoridoplatinate(V) species (Figure 55). The overall intensity of the IR active bands of Pd[PtF_6] and Pt[PtF_6] was found to be lower than those of the free $[PtF_6]^-$ anion and the M[PtF_6] (M = Na, K, Cs) ion pairs.

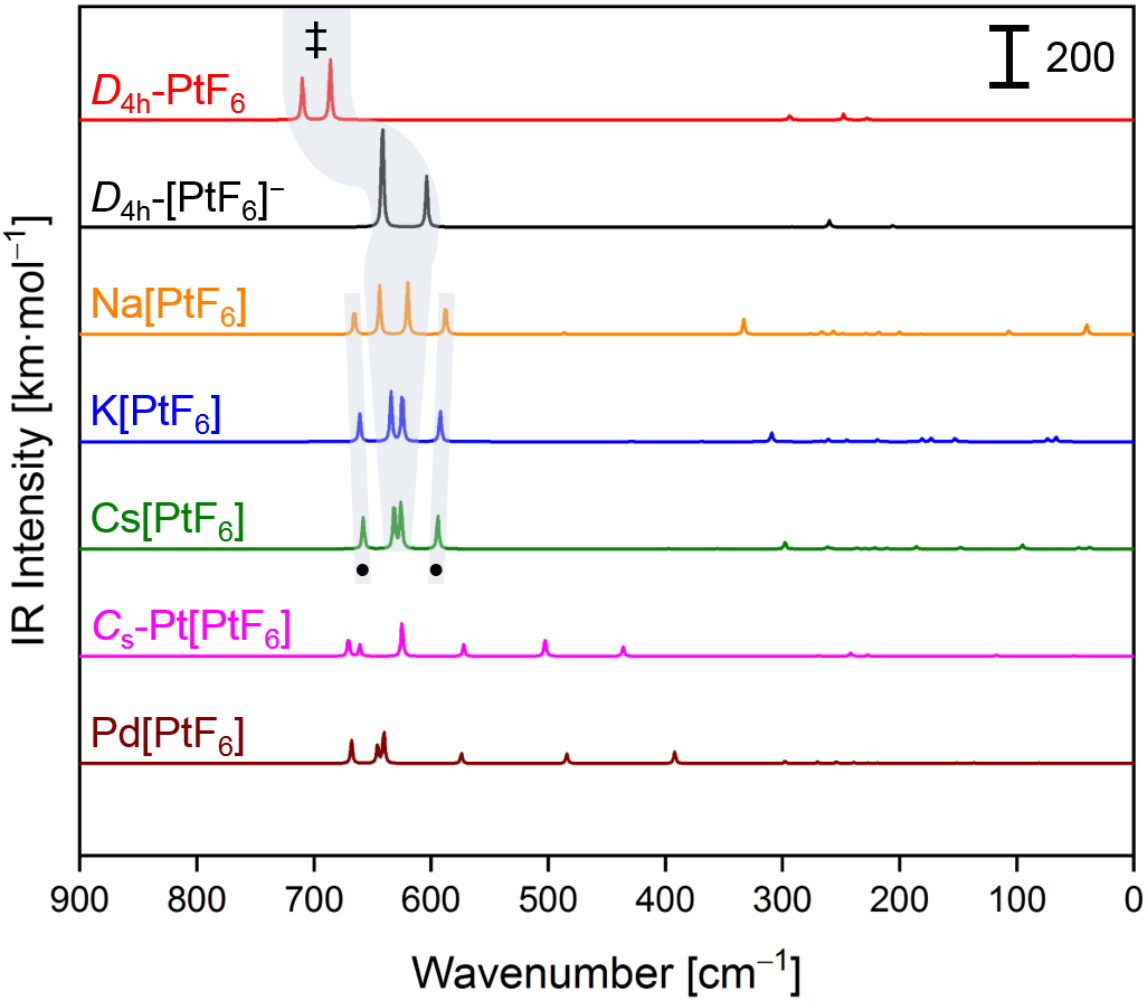

Figure 55: IR spectra of PtF_6, $[PtF_6]^-$ and M[PtF_6] (M = Na, K, Pd, Cs, Pt) compounds obtained at the RI-B3LYP-D4/def2-TZVPP level of theory (FWHM of 1 cm^{-1}). Bands associated with antisymmetric F–Pt–F stretching modes (ligands in *trans* position) are marked by a double dagger, those of the symmetric stretching modes

of coordinated (lower frequencies) and terminal {PtF_3} moieties by a bullet. If not stated differently, the point group of the species is C_1.

The lowered symmetry of D_{4h}-PtF_6 and D_{4h}-$[PtF_6]^-$ leads to a splitting of the $\nu_{as}(PtF_6)$, the only strong IR active fundamental (a T_{1u} mode in O_h symmetry) in the MIR regime,[297,304,321] into E_u and A_{2u} modes. Similarly, the $\nu_{as}(PtF_6)$ splits but not as strong as in the free $[PtF_6]^-$ under the influence of an alkali metal cation in M[PtF_6] (M = Na, K, Cs). Moreover, the IR inactive symmetric A_{1g}[300] splits into two components (coordinated and terminal {PtF_3} moieties, cf. Figure 54) and gains some IR activity in the alkali metal ion pairs (Table 21, Figure 55).

Table 21: Vibrational modes in the MIR region of M[PtF_6] (M = Na, K, Pd, Cs, Pt) in comparison with PtF_6 and $[PtF_6]^-$. The frequencies were obtained at the RI-B3LYP-D4/def2-TZVPP level of theory and are given in cm^{-1}. The symmetries of the vibrational modes are given in parentheses for the compounds optimized in symmetries higher than C_1, i.e. PtF_6 (D_{4h}), $[PtF_6]^-$ (D_{4h}) and Pt[PtF_6] (C_s). The subscripts 'coord' and 'term' refer to coordinated and terminal {PtF_3} units. The intensities of the bands are found in Figure 55.

Mode	PtF_6	$[PtF_6]^-$	Na[PtF_6]	K[PtF_6]	Cs[PtF_6]	Mode	Pd[PtF_6]	Pt[PtF_6]
$\nu_s(PtF_{3,term})$	*663.4* (A_{1g})[b]	*634.2* (A_{1g})[b]	665.5	660.8	657.8	$\nu_s(PtF_2^{central})$	667.9	670.5 (A')
$\nu_{as}(PtF_{2,eq})$[a]	686.1 (E_u)	641.4 (E_u)	643.9	634.2	631.5	$\nu_{as}(PtF_2^{central})$	645.7	660.9 (A'')
$\nu_{as}(PtF_{2,ax})$[a]	709.9 (A_{2u})	603.7 (A_{2u})	620.0	624.5	625.7	$\nu(PtF_{term})$	640.3	624.8 (A')
$\nu_s(PtF_{3,coord})$	*663.4* (A_{1g})[b]	*634.2* (A_{1g})[b]	587.5	592.2	594.2	$\nu(PtF_{coord})$	574.1	572.0 (A')
$\nu_s(PtF_{2,eq,oop})$[a]	632.7 (B_{2g})	581.1 (B_{2g})	486.2	429.2	397.1	$\nu_s(MF_2^{counter})$	484.1	502.6 (A')
$\nu_s(PtF_{2,ax})$[a]	621.7 (A_{1g})	578.0 (A_{1g})	398.6	368.8	355.2	$\nu_{as}(MF_2^{counter})$	392.0	435.9 (A'')

[a] The description of the vibrational modes is based on the D_{4h} symmetry of $[PtF_6]^-$ and accounts for the approximate local D_{4h} symmetry of the alkali metal hexafluoridoplatinates. The missing equatorial in-phase stretching modes and the coordinated/terminal {PtF_3} stretching modes are therefore blending into each other. [b] The bands of PtF_6 and the free $[PtF_6]^-$ that split upon coordination of an alkali metal ion are given in italics and are featured doubly for comparability.

Although the overall metal-dependent shifts of the IR active bands are appreciably well described at the RI-B3LYP-D4/def2-TZVPP level of theory, the splitting of the two central features seems to be the most realistic for the cesium case (Figure 55) in the light of the experimental results (see Section 3.2.2), where only three major bands are observed and the central band is not split. This could be explained by a more C_{3v} type character[314] of the M[PtF_6] (M = Na, K, Cs) ion pairs, for which twofold degenerate antisymmetric stretching modes were obtained in C_{3v} symmetry, leading to a joint central band for these structures. The M[PtF_6] structures optimized in C_{3v} symmetry have approximately the same energies with +1.12, +0.24 and −0.22 $kJ \cdot mol^{-1}$ versus the ZPE-corrected C_1 energies (vide supra), but feature, however, twofold degenerate imaginary frequencies at 318i, 211i and 121i cm^{-1} for Na[PtF_6], K[PtF_6] and Cs[PtF_6], respectively. The symmetric stretching modes are split by 78, 69 and 63 cm^{-1} for Na^+, K^+ and Cs^+, respectively (see

also Figure 140 in the appendix), which correspond to the C_1 results. Corresponding to Table 21, the coordination of the transition metal atoms Pd or Pt leads to species which feature more singular Pt−F bands rather than characteristic group frequencies at overall lower IR intensities. This renders these Pt^{IV} compounds less probable to be experimentally observed, when compared to the alkali metal hexafluoridoplatinates(V).

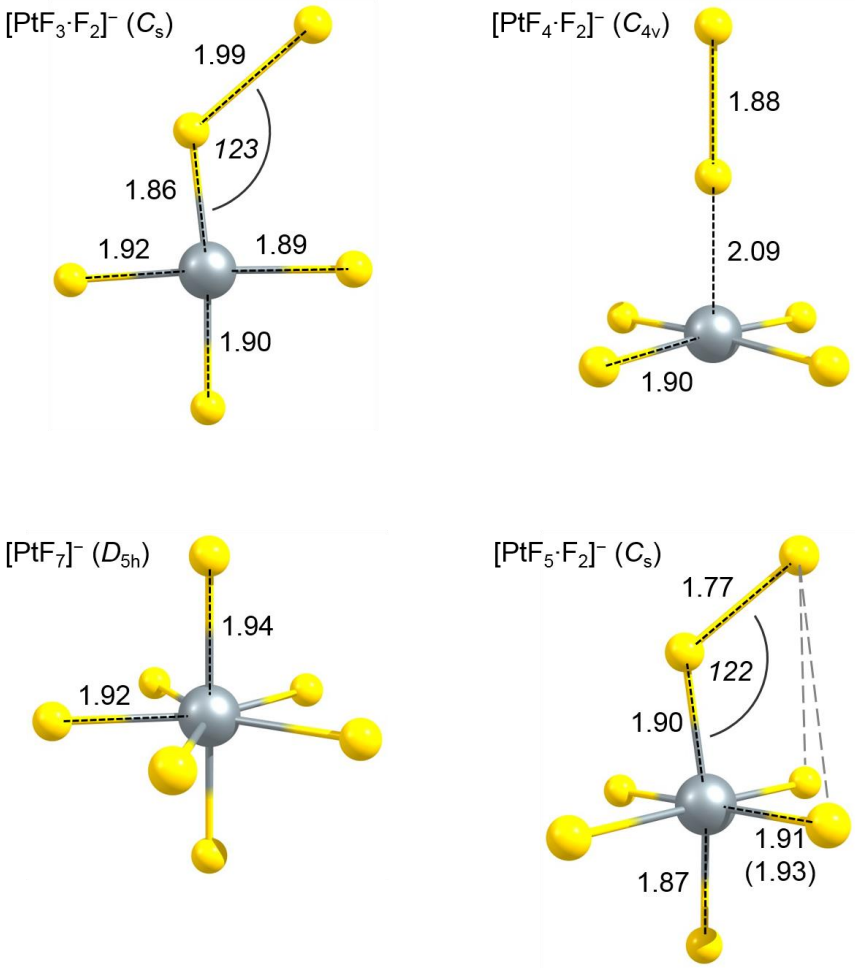

Figure 56: Structures of binary anionic platinum fluorido compounds in oxidation states +III, +IV, +V and +VI computed at the RI-B3LYP-D4/def2-TZVPP level of theory. The *trans*-F−Pt−F angle in the {PtF_4} moiety in C_{4v}-$[PtF_4{\cdot}F_2]^-$ is 176°. An eclipsed C_1-$[PtF_4{\cdot}F_2]^-$ features an F−F bond distance of 2.12 Å, while the one in free $[F_2]^-$ is 2.02 Å. For the equatorial Pt−F distances in $[PtF_5{\cdot}F_2]^-$ slightly differing, the longest one is given in parentheses. Bond distances are given in Å, angles are italicized and given in °.

In accordance with the experimental results (Section 3.2.2), the bands located below 500 cm^{-1} were observed in equal position employing different laser-ablated species and are therefore regarded independent of a counter-ion. Consequently, these band are seen to be exclusively related to mononuclear platinum fluorido compounds. The most relevant minimum structures are depicted in Figure 56 and their NPA charges are featured in Table 22. Minimum structures from reference [273] served as starting structures for PtF_6 and $[PtF_6]^-$. The structure of $[PtF_5{\cdot}F_2]^-$ was

orientated at the non-classical C_s-symmetric $[MF_7]^-$ structure type consisting of an $[MF_6]^-$ and a fluorine atom from the same reference.

For PtF_3 a slightly distorted T-shaped minimum of C_1 symmetry was found, whereas C_s and C_{2v} structures both were 4.6 kJ·mol^{-1} higher in energy and each featured one imaginary frequency of about 115i cm^{-1}, resembling an out-of-plane bending mode. The minimum structures of C_s-$[PtF_3{\cdot}F_2]^-$ and C_1-$[PtF_4{\cdot}F_2]^-$ were found in eclipsed forms with respective dihedral F−Pt−F−F angles of 0° and 0.3°, while the former did not converge in 90° conformation. C_1-$[PtF_4{\cdot}F_2]^-$ appeared in a C_s type fashion but did not converge in C_s symmetry in this conformation. A staggered structure featured an imaginary frequency at 13i cm^{-1}, being only 0.2 kJ·mol^{-1} lower in energy, indicating virtually no barrier for the rotation of $\{F_2\}$ around the Pt−F_2 axis. However, a C_{4v}-$[PtF_4{\cdot}F_2]^-$ was found to be 5.5 kJ·mol^{-1} lower in energy and shifted the ν(F−F) mode from the FIR (206 cm^{-1}, C_1) into the MIR regime (410 cm^{-1}, C_{4v}), thereby raising the calculated IR intensity from 4 to 16 km·mol^{-1}. For $[PtF_5{\cdot}F_2]^-$ a dihedral F−Pt−F−F angle of 45° is preferred, since it featured an imaginary frequency at 68i cm^{-1} in the 0° conformation and rotated towards 45° during a structure optimization in C_1 symmetry starting from the eclipsed conformer. Noteworthy, this is in contrast to the minimum structures of $[LA{\cdot}F_2]$ from reported ($[AuF_5{\cdot}F_2]$)[195] and results from this work ($[EF_5{\cdot}F_2]$ (E = As, Sb, Au), Section 3.1.1), the minimum structures of which correspond to an 'eclipsed' conformer with a dihedral F−E−F−F angle of 0° (2° in the As case).

The structure of C_{4v}-$[PtF_4{\cdot}F_2]^-$ was found to be 255.6 kJ·mol^{-1} higher in energy than D_{4h}-$[PtF_6]^-$. This corresponds to a wavelength of λ = 468 nm, while neglecting the activation barrier for the reaction. Compared to D_{5h}-$[PtF_7]^-$, the sum of the electronic ground state energies of D_{4h}-$[PtF_6]^-$ and a fluorine atom lie only 3.2 kJ·mol^{-1} lower and $[PtF_5{\cdot}F_2]^-$ lies 58.2 kJ·mol^{-1} (λ = 2055 nm) higher in energy. Therefore, these reactions are seen to be potentially initiated via photolysis with even red or near-IR light. With a limited fluorine atom mobility in neon matrices, the formation of a discrete $[PtF_7]^-$ becomes energetically conceivable[304,499,500] but would necessitate a large rearrangement of the fluorido ligands in the matrix cage.

Table 22: NPA charges (in e), electronic ground states (GS) and symmetries of binary neutral platinum fluorides and anionic mononuclear platinum fluorido complexes obtained at the RI-B3LYP-D4/def2-TZVPP level of theory. The subscripts 'ax' and 'eq' refer to axial and equatorial fluorido ligands, and the subscripts 'coord' and 'term' refer to the fluorine atoms coordinated at the central platinum atoms and the fluorine atoms in terminal position, respectively.

Compound	**GS**	**$Pt_{central}$**	**F_{ax}**	**F_{eq}**	**F_{coord} (F_2)**	**F_{term} (F_2)**
D_{4h}-PtF_6	^3E_g	2.315	−0.363	−0.397		
D_{4h}-$[PtF_6]^-$	$^2B_{1g}$	2.200	−0.594	−0.503		
D_{5h}-$[PtF_7]^-$	$^1E_1''$	2.289	−0.563	−0.433		
C_{4v}-PtF_5	$^2B_1$	2.158	−0.324	−0.458		
C_s-$[PtF_5{\cdot}F_2]^-$	$^1A'$	2.134	−0.471	−0.548[av]	−0.222	−0.247
C_{4v}-$[PtF_5]^-$	$^1B_1$	1.937	−0.438	−0.625		
D_{4h}-PtF_4	^1E_g	1.676		−0.419		
D_{2h}-PtF_4	$^3B_{2g}$	1.801		−0.450		
C_{4v}-$[PtF_4{\cdot}F_2]^-$	$^2B_1$	1.889		−0.553	−0.418	−0.261
C_1-$[PtF_4{\cdot}F_2]^-$	^2A	1.967		−0.609[av]	−0.361	−0.172
D_{4h}-$[PtF_4]^-$	$^2B_{1g}$	1.414		−0.604		
C_1-PtF_3	^2A	1.480	−0.512[i]	−0.456[i]		
C_s-$[PtF_3{\cdot}F_2]^-$	$^1A''$	1.450		−0.561[av]	−0.341	−0.424
C_1-$[F_2]^-$	^2A				−0.500	−0.500
C_s-Cs$[F_2]$	$^2A'$				−0.484	−0.483
C_{2v}-K$[F_2]$	$^2B_1$				−0.485	−0.485
C_{2v}-Na$[F_2]$	$^2B_1$				−0.484	−0.484

[i] C_1-PtF_3 was found to slightly distorted from C_{2v} symmetry and the NPA charges account for a T shape with one longer (1.89 Å, labelled 'ax') and two shorter Pt−F bond distances (1.87 Å, labelled 'eq'); [av] averaged values, a full set of NPA charges is supplied in Section 6.2.2 in the appendix.

Upon the comparison of the NPA charges of the neutral PtF_n (n = 3–5) with the $[F_2]^-$ complexes in Table 22, it becomes evident that C_s-$[PtF_3{\cdot}F_2]^-$, C_{4v}-$[PtF_4{\cdot}F_2]^-$ and C_s-$[PtF_5{\cdot}F_2]^-$ indeed contain platinum in a formal oxidation state of +III, +IV and +V, respectively. These findings also agree well with the results of neutral PtF_n (n = 1–6) found in reference [304]. Upon the coordination of $[F_2]^-$ a fraction of its charge is transferred to the Lewis acidic moiety (vide infra) and distributed over the fluorido ligands, while the charge of the central platinum atom is approximately maintained. That the $\{PtF_n\}$ moiety rather resembles its corresponding neutral than its anionic form justifies the description of the $\{F_2\}$ moiety of the non-classical complexes $[PtF_n{\cdot}F_2]^-$ (n = 3–5) as an $[F_2]^-$ ligand. The overall charge transfer from the $[F_2]^-$ ligand to the $\{PtF_n\}$ moiety increases in the order $PtF_3 < PtF_4 < PtF_5$. In contrast to the $[PtF_4{\cdot}F_2]^-$ complexes, the PtF_3 and PtF_5 analogues feature a

different polarization of the fluorine atoms in the $[F_2]^-$ ligand, being the terminal fluorine atom more negatively charged than the coordinated one.

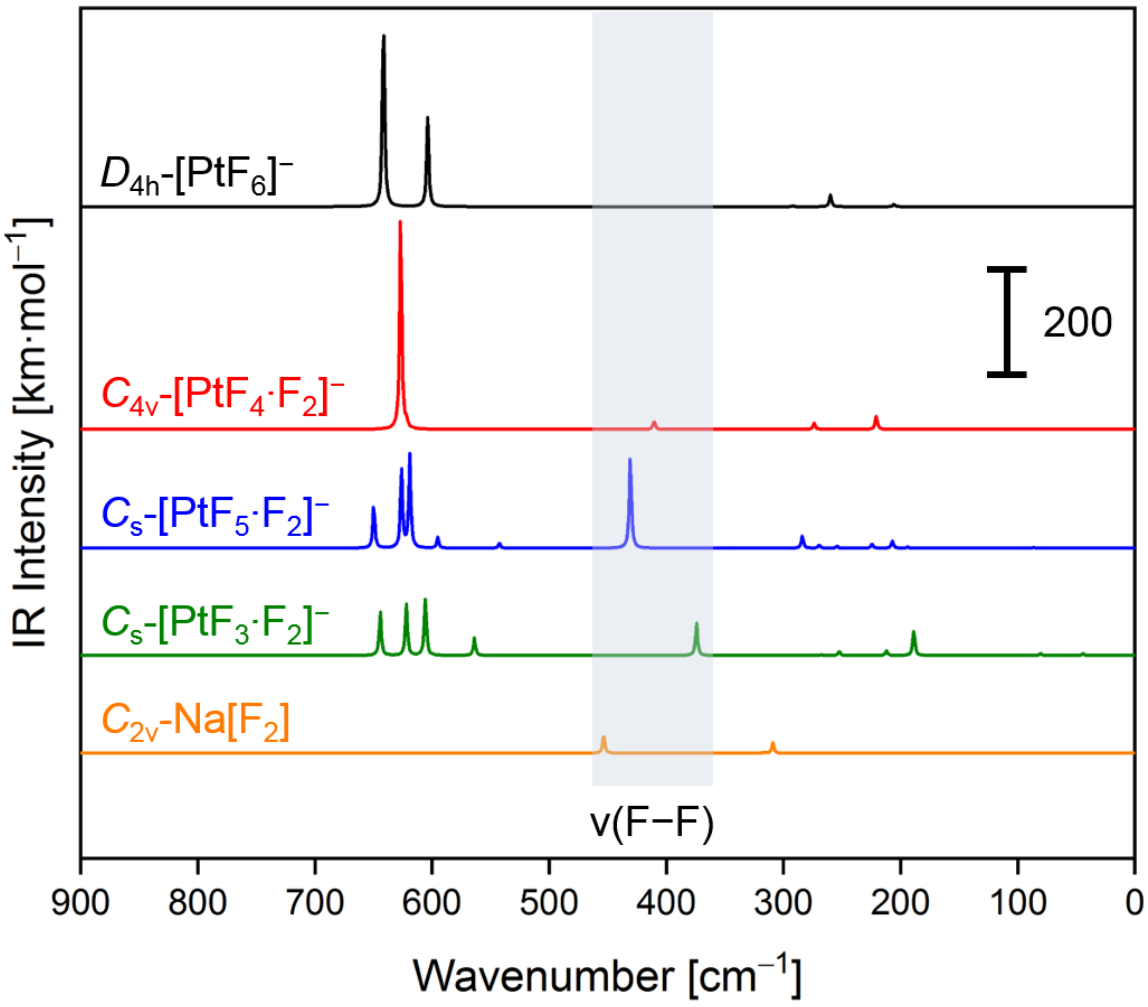

Figure 57: Infrared spectra of $[PtF_6]^-$, $[PtF_4{\cdot}F_2]^-$, $[PtF_5{\cdot}F_2]^-$ and $[PtF_3{\cdot}F_2]^-$ and $Na[F_2]$ calculated at the RI-B3LYP-D4/def2-TZVPP level of theory (FWHM of 1 cm^{-1}) with highlighted F–F stretching bands. The corresponding structures of $[PtF_n{\cdot}F_2]^-$ (n = 3, 4, 5) and $[PtF_6]^-$ are depicted in Figure 56.

The computed IR spectra of the $[PtF_3{\cdot}F_2]^-$, $[PtF_4{\cdot}F_2]^-$ and $[PtF_5{\cdot}F_2]^-$ complexes depicted in comparison with $[PtF_6]^-$ and $Na[F_2]$ in Figure 57 indicate an activation of the ν(F–F) mode, which was found to increase in the order PtF_4, PtF_3 and PtF_5. This could be explained with PtF_5 being a Lewis superacid,[273,318–321] leading to the formation of $[XeF_5]^+[PtF_6]^-$ upon the reaction with Xe and F_2.[273,321] However, besides $[PtF_6]^{2-}$ salts[310,318,324] and the $[(BrF_3)_2PtF_4]$ adduct,[322,325] and PtF_3 being a mixed-valent compound in the bulk,[263] no results explicitly targeting the Lewis acidity of these compounds were reported.[304]

In order to estimate the Lewis acidities of the platinum fluorides, fluoride ion affinity (FIA) values have been calculated based on the ZPE-corrected energies of the obtained minimum structures at the RI-B3LYP-D4/def2-TZVPP level of theory. The absolute FIA values featured in Table 23 were

computed using the $COF_2/[COF_3]^-$ reference system, since it omits the use of a free fluoride ion in the calculation by an isodesmic model reaction.[501,502]

Table 23: FIA values of PtF_3, PtF_4, PtF_5 and PtF_6 at the RI-B3LYP-D4/def2-TZVPP level of theory in $kJ \cdot mol^{-1}$.

Compound	FIA[a]
PtF_3	458
PtF_4	357
PtF_5	523
PtF_6	308

[a] absolute FIA values determined by the $COF_2/[COF_3]^-$ reference system using ZPE-corrected values and an experimental FIA of 208.8 $kJ \cdot mol^{-1}$ for COF_2.[501,502]

The FIA of PtF_5 is in good agreement with the CCSD(T)/CBS value of 546 $kJ \cdot mol^{-1}$ reported by Dixon and coworkers.[273] The value for PtF_3 is very high and hardly corresponds to the comparably low charge of the Pt center (cf. Table 22) but also relates to the strong polarization of the $[F_2]^-$ and the respective ν(F–F) mode. The acidities of PtF_n (n = 3–5) principally reflect the described trends of the NPA charges and the polarization of an $[F_2]^-$ ligand. However, the polarization and IR activation of the $\{[F_2]^-\}$ moiety in $[PtF_n \cdot F_2]^-$ (n = 3–5) with respect to the acidities of the PtF_n (n = 3–5) and the NPA charges cannot be directly correlated to a change in the F–F bond distance (see also Figure 56).

The MIR band positions of $[PtF_n \cdot F_2]^-$ and the neutral PtF_n (n = 3–5) are featured in Table 24. The calculated vibrational spectra of binary neutral and anionic platinum fluorido compounds with platinum in oxidation states +III to +VI are additionally compiled in Figure 139 in the appendix.

Table 24: Vibrational frequencies in the MIR region of $[PtF_5 \cdot F_2]^-$ (C_s), $[PtF_4 \cdot F_2]^-$ (C_{4v}), $[PtF_3 \cdot F_2]^-$ (C_s), PtF_5 (C_{4v}), PtF_4 (D_{4h}), PtF_3 (C_1) and $Na[F_2]$ (C_{2v}) obtained at the RI-B3LYP-D4/def2-TZVPP level of theory. The symmetries of the vibrational modes are given in parentheses. The description of the vibrational modes is based on the C_{4v}-symmetric PtF_5. Vibrational frequencies are given in cm^{-1}.

Mode	$[PtF_5 \cdot F_2]^-$	PtF_5	$[PtF_4 \cdot F_2]^-$	PtF_4	$[PtF_3 \cdot F_2]^-$	PtF_3	$Na[F_2]$
$\nu(PtF_{ax})$	649.7 (A')	686.0 (A_1)					
$\nu_{as}(PtF_{2,eq})$	626.1 (A')	679.3 (E)	626.8 (E)	697.1 (E_u)	644.2 (A')	679.9 (A)	
$\nu_{as}(PtF_{2,eq})$	619.1 (A'')				622.0 (A')		
$\nu_s(PtF_{2,eq,ip})$	595.1 (A')	660.3 (A_1)	621.8 (A_1)	683.7 (A_{1g})	605.7 (A')	664.0 (A)	
$\nu_s(PtF_{2,eq,oop})$	555.2 (A'')	618.3 (B_2)	561.2 (B_2)	615.6 (B_{2g})	563.8 (A')	629.4 (A)	
$\nu(Pt-F_2)$	542.5 (A')						
$\nu(F-F)$	430.7 (A')		410.4[a] (A_1)		374.2 (A')		453.5[b] (A_1)

[a] This can also be interpreted as an antisymmetric Pt−F−F mode, a corresponding symmetric mode is found at 273.73 cm^{-1} but coupled to an out-of-plane PtF_4 bending mode; [b] The ν(F−F) modes of C_1-$[F_2]^-$, C_s-$Cs[F_2]$ and C_{2v}-$K[F_2]$ were computed at 351.57 (A), 384.47 (A') and 391.74 cm^{-1} (A_1), respectively.

3.2.2 Experimental Results

The co-deposition of platinum hexafluoride and the laser-ablated metals Pd and Pt as well as the metal fluorides NaF, KF, and CsF, as illustrated in Figure 16 in Section 1.10.1.1, gave rise to two new sets of bands. One was observed in equal position for different laser-ablated metals/metal fluorides and is thus regarded to be independent of the counterion, while the other set of bands experienced a shift depending on the co-deposited metal center. In accordance with the reported band positions of $[XeF_5]^+[PtF_6]^-$ and $[NO]^+[PtF_6]^-$,[289,321,503] these bands were assigned to matrix-isolated free $[PtF_6]^-$ and the corresponding ion pairs $M[PtF_6]$ (M = Na, K, Cs), respectively. The long-term UV light photolysis at λ = 266 nm (laser) of these deposits revealed the formation of a band accounting for a counterion-independent $[F_2]^-$ – a species that should be IR inactive.

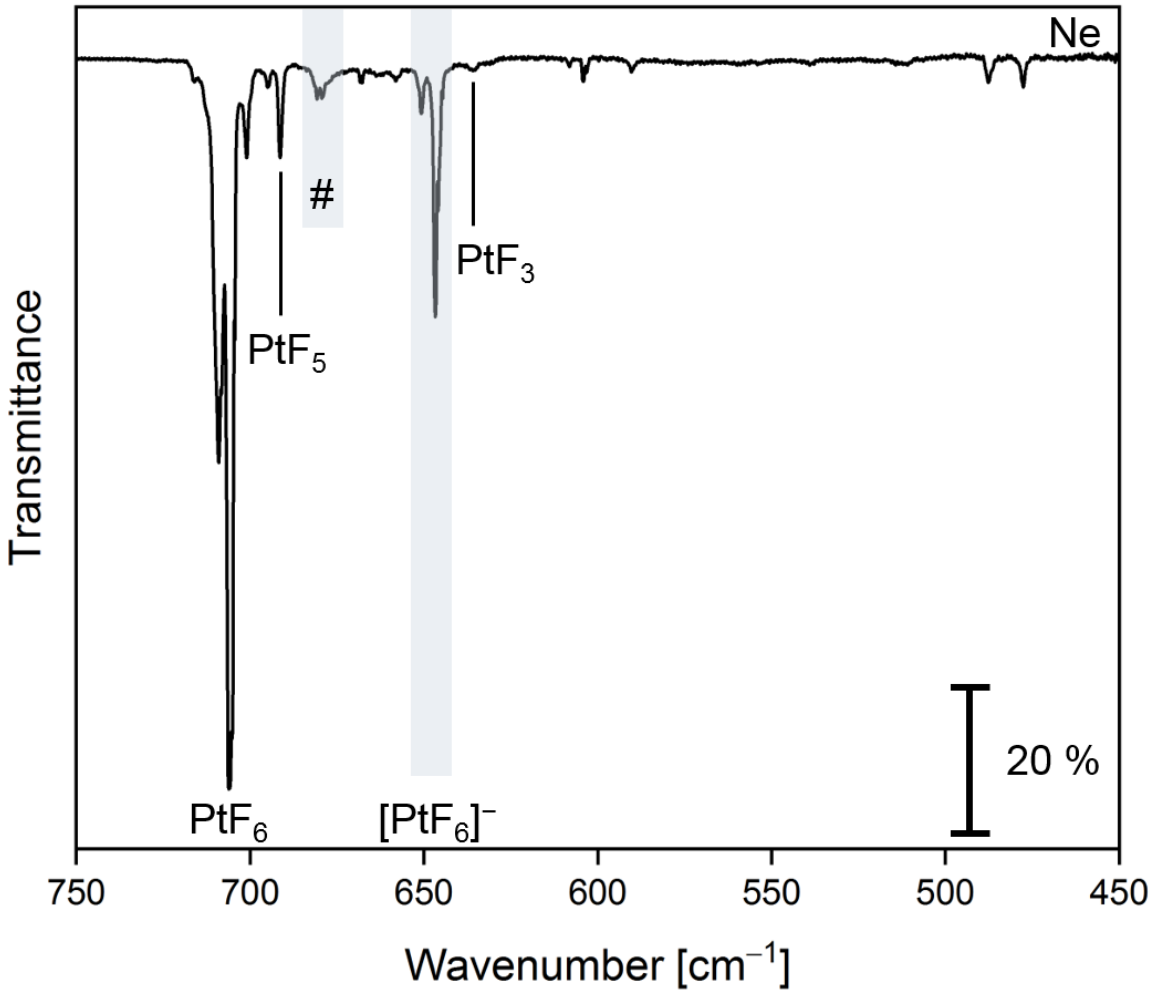

Figure 58: The IR spectrum was recorded after the co-deposition of neon passed over a solid sample of PtF_6 maintained at −79 to −78 °C and laser-ablated platinum atoms (10 Hz repetition rate, 18 mJ/pulse) onto a gold-plated copper mirror at 5 K for 60 min at a deposition rate of 0.5 mbar·l·min^{-1}. The feature marked with a hash contains fractions of both PtF_5 and PtF_3. The matrix support had been coated with pure neon for 20 min prior to the co-deposition and the corresponding spectrum served as the background.

The only IR active T_{1u}-symmetric fundamental of PtF_6 in the mid-infrared region was observed at 706.1 with a site at 709.0 cm^{-1} in neon and 701.7 with a site at 705.4 cm^{-1} in argon and reflects the literature values.[297,304,321] Next to the literature known band positions (see the discussion below), the similar structures of the bands assigned to PtF_6 and $[PtF_6]^-$ (in both Ne and Ar) also indicate a similar, octahedral structure[298,304,321] and thereby supported the assignments. The photochemistry of all these deposits was largely governed by the formation and decomposition of the neutral platinum fluorides,[304] which is not surprising regarding a typically observed $[PtF_6]^-/PtF_6$ ratio of 1:3 in neon as depicted in Figure 58. A ratio of 1:2 was found in argon, as depicted in Figure 141, and is additionally compared with the neon data in Figure 142 in the appendix. As the yields were found to be lower in argon and the corresponding spectra featured broader bands and were rather noisy especially in the region below 500 cm^{-1}, the discussion and the featured spectra mainly focus on the results obtained in neon matrices. A small amount of HF, which is constantly produced from the reaction of PtF_6 with water vapor diffusing through the walls of the evacuated sample container (PFA), a literature-known phenomenon,[100,504] was consequently always present in the IR spectra (despite removal of HF at a sample temperature of −80 °C in dynamic vacuum at $1.5 \cdot 10^{-5}$ mbar for 20 min in advance of the experiments, also see Section 4.1.3.1).

The deposit of PtF_6 and laser-ablated platinum atoms already contains the reduced species PtF_3 and PtF_5,[304] following the photolytic decomposition of the starting material PtF_6. This happens because the laser-induced plasma does not only supply ions and free electrons for the formation of the products but also emits light provoking the decomposition of the precursor and the formation of side products. Analogous experiments were performed by employing the laser-ablated NaF, KF, CsF salts and Pd metal. The spectra after deposition are depicted in Figure 59.

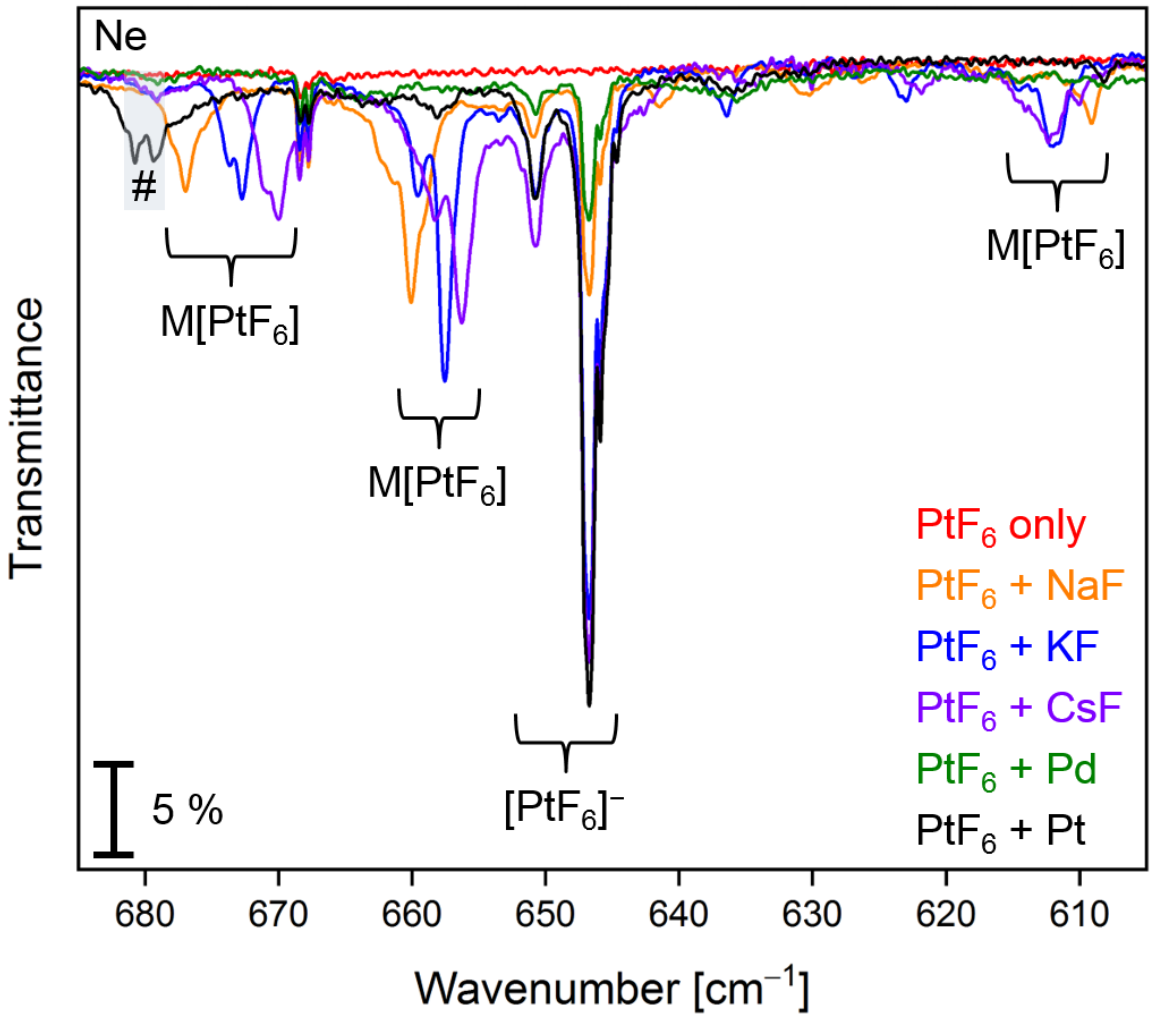

Figure 59: The IR spectra were obtained after the co-deposition of neon passed over a solid sample of PtF_6 maintained at −79 to −78 °C and laser-ablated NaF (orange trace), KF (blue trace) and CsF (purple trace), each at 6 Hz repetition rate and 25 mJ/pulse, and laser-ablated Pd atoms (10 Hz repetition rate, 25 mJ/pulse, green trace) and platinum atoms (10 Hz repetition rate, 18 mJ/pulse, black trace) onto a gold-plated copper mirror at 5 K for 60 min at a deposition rate of 0.5 mbar·l·min^{-1}. The PtF_6 reference spectrum (red trace) was obtained after 45 min and 0.6 mbar·l·min^{-1}. The feature marked with a hash contains fractions of both PtF_5 and PtF_3. The matrix support had been coated with pure neon for 20 min prior to the co-deposition and the corresponding spectrum served as the background.

The IR spectra show a band that was observed in all experiments with a stationary position at 646.7 and a matrix site at 650.8 cm^{-1} in neon (and 642.2 and 647.9 cm^{-1} in argon, respectively). In accordance with the literature-known values of hexafluoridoplatinates(V) this band was assigned to free $[PtF_6]^-$.[289,321,503] Moreover, the spectra revealed an individual set of three discernable bands for each of the metal fluorides co-deposited. These are assigned to the ion pairs of $M[PtF_6]$, since the coordination of a counterion leads to a splitting of the $[PtF_6]^-$-centered bands (see Section 3.2.1). The experimental band positions of the hexafluoridoplatinate species and their assignment to the vibrational modes are compiled in Table 25.

Table 25: Band positions and assignments of hexafluoridoplatinate species in neon matrices (given in cm^{-1}) as well as $M[PtF_6]/[PtF_6]^-$ intensity ratios determined at the ν_{as}(F−Pt−F) bands of the $M[PtF_6]$ species (M = Na, K, Cs). Matrix sites are given in parentheses.

Experiment	$M[PtF_6]$			$M[PtF_6] : [PtF_6]^-$
	$\nu_s(PtF_{3,terminal})$	ν_{as}(F–Pt–F)	$\nu_s(PtF_{3,coordinated})$	
NaF + PtF_6	677.0 (677.8 sh)	660.1 (661.3 sh)	609.1	1 : 1
KF + PtF_6	672.8 (673.7 sh)	657.6 (659.6 sh)	611.9	1 : 2
CsF + PtF_6	670.0 (670.8 sh)	656.3 (658.3 sh)	612.4	1 : 3

The splitting of the symmetric stretching modes of the coordinated and terminal $\{PtF_3\}$ moieties of 68, 60, and 58 cm^{-1} for $Na[PtF_6]$, $K[PtF_6]$ and $Cs[PtF_6]$, respectively, resemble the B3LYP values (based on the C_1 structures) of 78, 69 and 64 cm^{-1} (see Section 3.2.1). Apparently, the central features associated with antisymmetric F−Pt−F stretching modes of the experimentally observed set of absorption bands of the alkali metal hexafluoridoplatinates(V) are not split, in contrast to the quantum-chemical calculations (C_1-symmetric structures, Table 21, Figure 55). This could be explained by a more C_{3v} type character of the $M[PtF_6]$ ion pairs, as discussed in Section 3.2.1 (see also Figure 140 in the appendix), which is known from $Cs[NbF_6]$, with Cs^+ sitting in facial position of the anion in a solid neon environment.[313] However, the IR active antisymmetric stretching band of the isolated octahedron is split into a doublet in a weakly interacting environment (Ne or Ar) and into a triplet in a strongly interacting environment (N_2) for $Cs[NbF_6]$ and $Cs[UF_6]$.[313,314] This enables an alternative explanation of the $M[PtF_6]$ spectra, where the bands around 670 and 660 cm^{-1} both become ν_{as}, leaving the bands around 611 cm^{-1} non-assigned. This better reflects the band structures of the former two bands, which differ from the latter one that is found without an additional shoulder. However, the quantum-chemical results support three bands in this region. Employing laser-ablated palladium and platinum atoms, the major product observed is free $[PtF_6]^-$. Other features in the Pt−F stretching region were very weak and could neither be compared to the absorption bands of the alkali metal species (in terms of their relative intensities) nor to the B3LYP vibrational spectra. The ratios of antisymmetric to symmetric stretching bands, which were the same for all $M[PtF_6]$, support these assignments. The $[PtF_6]^-$ band had the same shape with a varying intensity in all experiments, which implies that no additional (side) product is hidden (e.g. a shoulder) below this very strong band.

The spectra after the co-deposition of PtF_6 with the laser-ablated species are found to be at the border of saturation (except for Pd) after 60 min deposition time in terms of the intensity of the PtF_6 T_{1u}-band (Figure 143 in the appendix). Using the same conditions for the laser ablation (pulse

energy and repetition rate) specific for the metal fluorides and specific for the metals allowed the comparison of the M[PtF_6] and [PtF_6]$^-$ bands' intensity ratios. It was found that the laser ablation of platinum metal had the largest impact on the photodecomposition of the starting material PtF_6 as can be seen from the highest intensity of the PtF_5 band (Figure 143 in the appendix). This might be additionally caused by the increased repetition rate compared to the laser ablation of the metal fluorides. The overall lower intensity of the hexafluoridoplatinate(V) associated bands in the case of NaF can be explained by a higher coulombic interaction of F^- with Na^+ than with the heavier alkali metal cations K^+ and Cs^+ that had been reported in the course of a systematic investigation of the polyfluorine monoanions with different alkali metal salts.[377]

3.2.2.1 Photochemistry

The matrix-isolated hexafluoridoplatinates(V) depicted in Figure 59 were subjected to photolysis experiments in the range from λ = 656–266 nm. The resulting step-by-step IR spectra are explicitly shown for the co-deposit of PtF_6 and laser-ablated CsF in Figure 61, while only the spectra of the largest changes were compiled. A 'full' version of these spectra down to 450 cm^{-1} is found in Figure 144 in the appendix.

Following the results on the photochemistry of PtF_6 and PtF_4, the samples obtained after co-deposition of PtF_6 and laser-ablated NaF, KF, CsF, Pd and Pt were investigated by UV/Vis spectroscopy. As a consequence of the large amount of unreacted PtF_6 deposited, the UV/Vis spectra were mainly governed by the strong absorption bands of PtF_6 and PtF_4[304] (reference data of photolysis experiments of solely PtF_6 embedded in neon are featured in Figure 146 in the appendix). Moreover, the UV/Vis spectra were noisy, as depicted for a co-deposit of PtF_6 and laser-ablated CsF embedded in neon in Figure 147 in the appendix. Therefore, the experimental study could only be focused on the IR data.

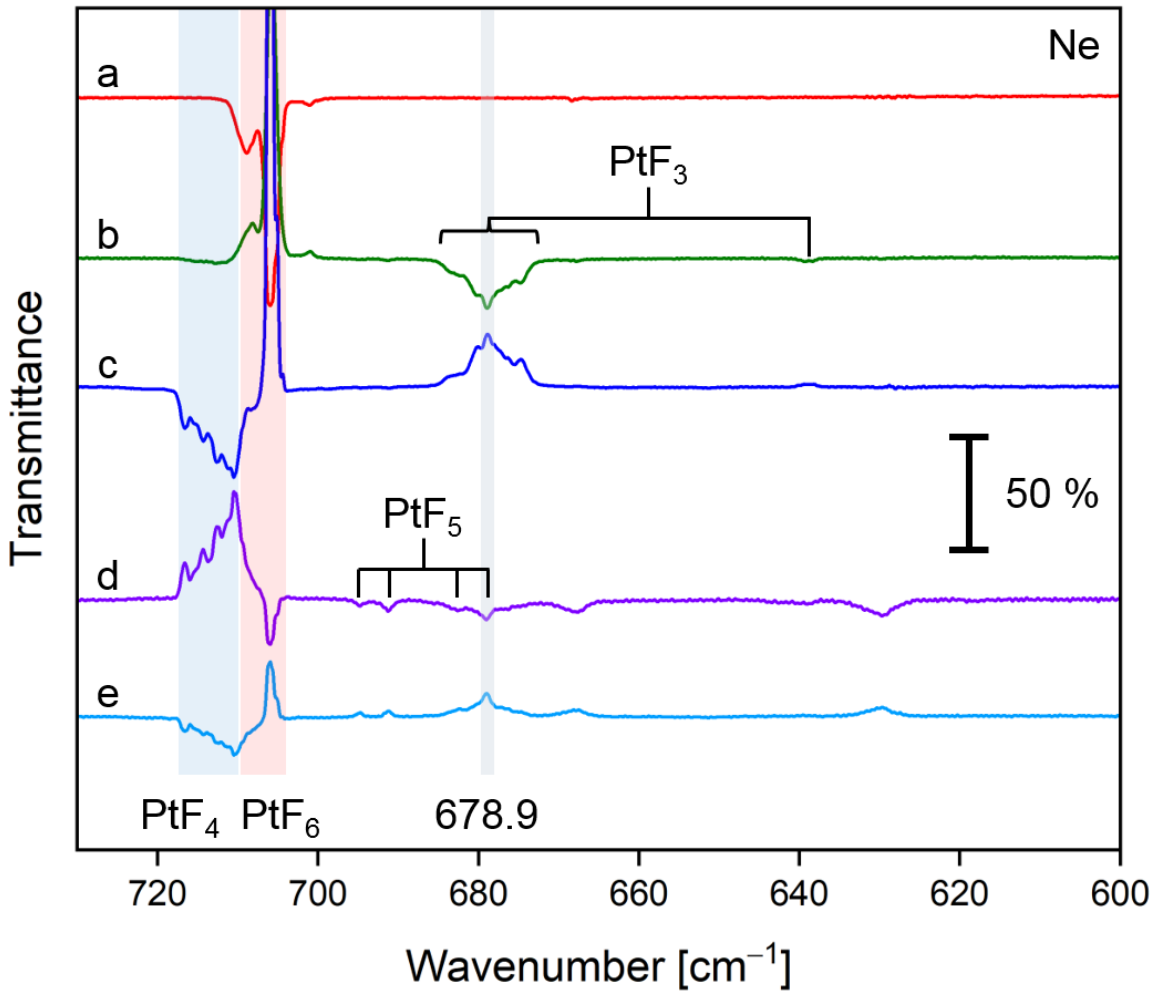

Figure 60: IR spectra were recorded after sequential steps of annealing and irradiation of an initial deposit of a) neon passed over a solid sample of PtF_6 maintained at −79 to −78 °C onto a gold-plated copper mirror at 5 K for 45 min at a deposition rate of 0.6 mbar·l·min^{-1}. The difference IR spectra show the changes after the irradiation of this deposit at b) λ = 528 nm (LED) for 60 min, c) λ = 470 nm (LED) for 20 min, d) λ = 266 nm (laser) for 10 min, and e) λ = 470 nm (LED) for 5 min. The matrix support had been coated with pure neon for 20 min prior to the co-deposition and the corresponding spectrum served as the background. The bands pointing downwards are formed at the expense of the bands pointing upwards.

In order to obtain reference spectra at all the wavelengths applied for the photochemical investigation of the hexafluoridoplatinates(V), solely PtF_6 in Ne was deposited and subjected to a sequence of annealing and irradiation steps at wavelengths throughout the visible and the UV range from λ = 656 nm to λ = 266 nm. The IR spectra featuring the largest changes are depicted in Figure 60 – in accordance with the UV/Vis spectra shown in Figure 146 in the appendix. Next to the reported features of the neutral binary platinum fluorides,[304] these measurements revealed a new intense band at 678.9 cm^{-1} upon the irradiation of a deposit of PtF_6 embedded in neon with green light at λ = 528 nm (LED). This band resembled the shape of a band that had been exclusively observed in argon at 679.8 cm^{-1} and had been assigned to PtF_5 (ν_{as}(Pt−F_4)) earlier.[304] Since this band, however, was observed to be formed/decomposed independently of the ν_{as}(Pt−F_4) of PtF_5 at 691.3 and a matrix site at 694.8 cm^{-1}, the best description of the complex structure of the band

centered at 678.9 cm^{-1} seems to be that it comprises features of both PtF_3 and PtF_5, with the individual amounts depending on the specific photochemical process.

The formation of the higher platinum fluorides PtF_5 and PtF_6 after the quantitative decomposition of the latter upon blue light irradiation is only possible when fluorine atoms are present in the matrix. Fluorine atoms represent highly efficient oxidizers, since they are constrained in their mobility in solid neon matrices.[304,499,500] With the maximum of the UV/Vis spectrum of F_2 at 283 nm,[8,9] the photolysis at λ = 266 nm should yield sufficient amounts of fluorine atoms to enable re-oxidation of the Pt^{III} and Pt^{IV} centers to the abovementioned high-valent fluorides.[304] Fluorine atoms might also be formed from homolytic bond cleavage, which could abstract another fluorine atom from a {PtF_5} moiety leading to PtF_4 and F_2,[304] while the latter could be photolyzed again to give two fluorine atoms.

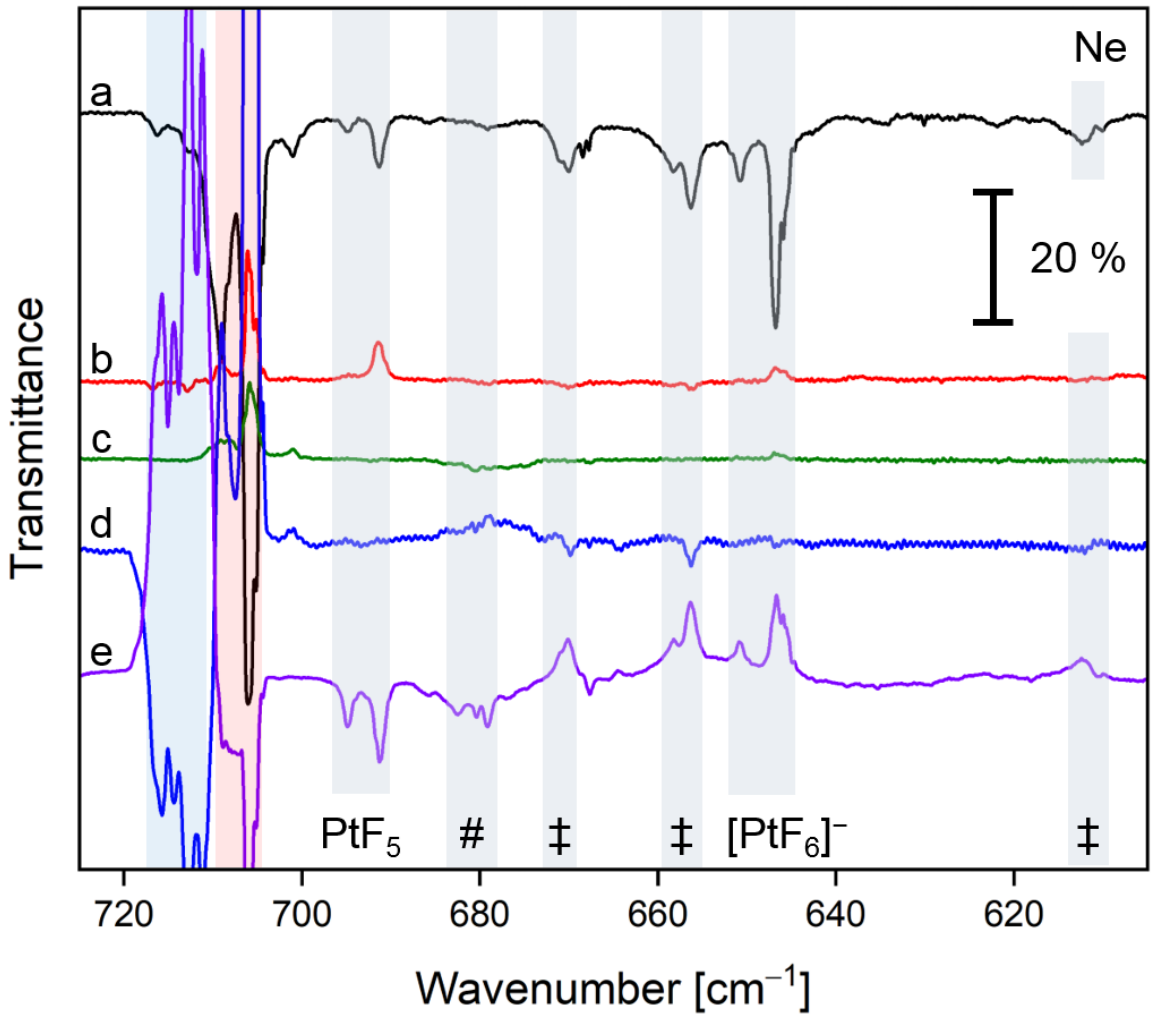

Figure 61: IR spectra were recorded after sequential steps of annealing and irradiation of an initial deposit of a) neon passed over a solid sample of PtF_6 maintained at −79 to −78 °C and laser-ablated CsF (6 Hz repetition rate, 25 mJ/pulse) onto a gold-plated copper mirror at 5 K for 60 min at a deposition rate of 0.5 mbar·l·min^{-1}. The difference IR spectra show the changes after the irradiation of this deposit at b) λ = 656 nm (LED) for 20 min, c) λ = 528 nm (LED) for 8 min, d) λ = 405 nm (LED) for 60 min, and e) λ = 266 nm (laser) for 90 min. The bands of Cs[PtF_6] are marked with a double dagger, those of PtF_4 and PtF_6 are highlighted in light blue and light red, respectively. The region marked with a hash could comprise features of coordinated or free PtF_5, PtF_4 or PtF_3. The matrix support had been coated with pure neon for 20 min prior to the co-deposition and the corresponding spectrum served as the background for spectrum a). The bands pointing downwards are formed at the expense of the bands pointing upwards.

The M[PtF_6] and [PtF_6]$^-$ species were observed to be only slightly photoactive at blue light irradiation (Figure 61, trace d), but were quantitatively decomposed after long-term UV light irradiation. The decomposition of M[PtF_6] and [PtF_6]$^-$ was accompanied by the formation of a weak band at 474.4 cm^{-1} that was assigned to a polarized [F_2]$^-$. The observations indicated a comparable behavior for the co-deposits of PtF_6 with laser-ablated KF, CsF and Pt and are summarized in Figure 62. Caused by the overall lower intensity of the bands associated with [PtF_6]$^-$, a band at 474.4 cm^{-1} was not observed after the UV photolysis at λ = 266 nm of the deposit of PtF_6 and laser-ablated NaF. With respect to the feature at 477.5 cm^{-1}, which was apparent in all experiments at varying

concentrations, the $[F_2]^-$ band at 474.4 cm^{-1} could have been hidden. This is relevant especially at lower concentrations of $[F_2]^-$ in the light of the photo-decomposition of the band at 477.5 cm^{-1} to a certain amount. The nature of this band could not be clarified, since no trends could be found upon comparison of the series of conducted experiments, but it had also been observed in high intensity as an impurity in a deposit of PtF_6 in neon. Using 0.5 % F_2 diluted in neon instead of pure neon in a co-deposition experiment employing PtF_6 and laser-ablated CsF gave comparable results and did not lead to an increase of either of the bands accounting for $Cs[PtF_6]$, $[PtF_6]^-$ or $[F_2]^-$. This indicates an intramolecular process based on $[PtF_6]^-$.

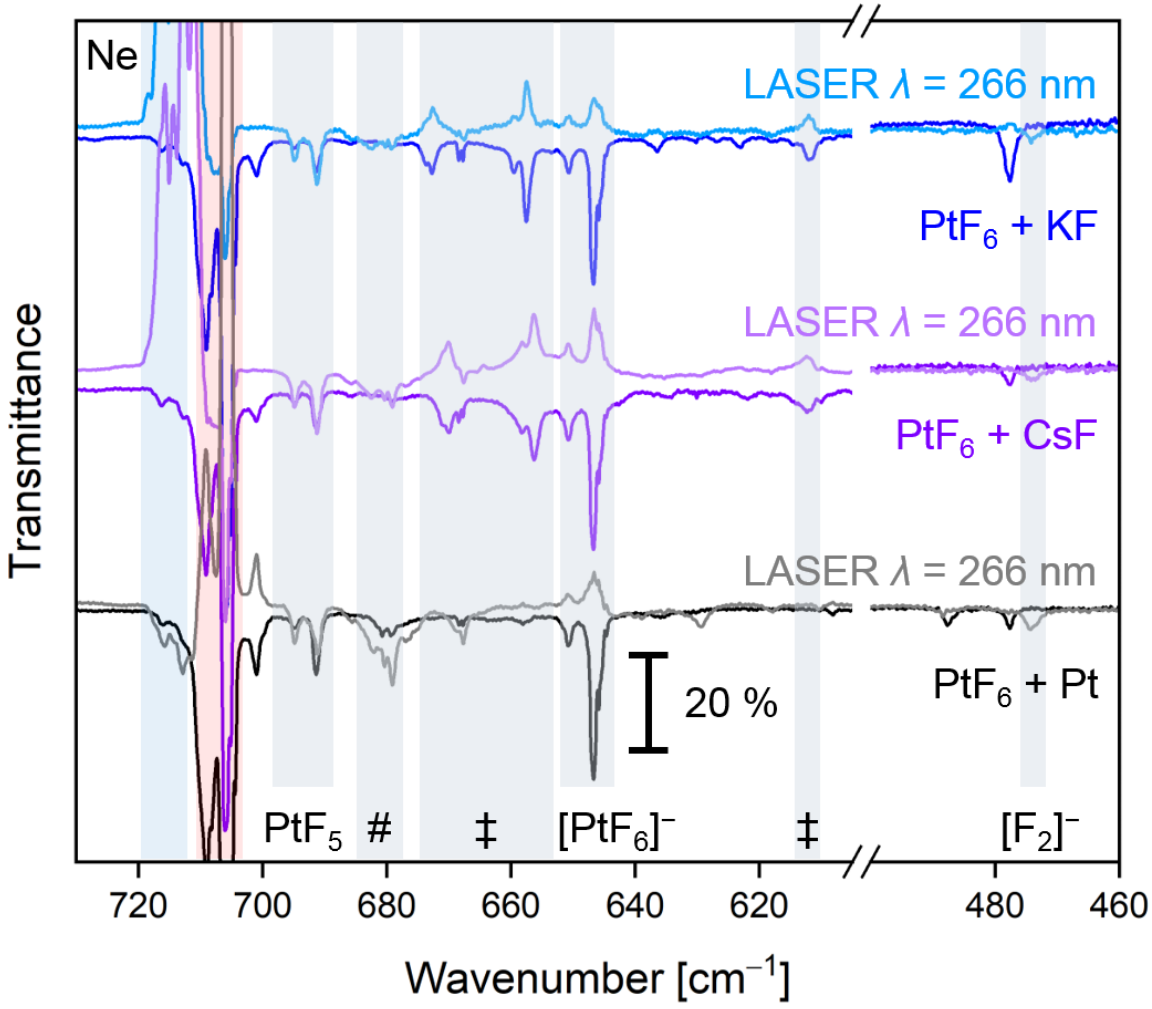

Figure 62: The IR spectra were obtained after the co-deposition of neon passed over a solid sample of PtF_6 maintained at −79 to −78 °C and laser-ablated KF (blue trace) and CsF (purple trace), each at 6 Hz repetition rate and 25 mJ/pulse, and laser-ablated platinum atoms (10 Hz repetition rate, 18 mJ/pulse, black trace) onto a gold-plated copper mirror at 5 K for 60 min at a deposition rate of 0.5 mbar·l·min^{-1}. The difference IR spectra show the changes after the irradiation of these deposits at λ = 266 nm (laser) for 90 min (traces in the respective lighter colors). The bands of $M[PtF_6]$ (M = K, Cs) are marked with a double dagger, those of PtF_4 and PtF_6 are highlighted in light blue and light red, respectively. The region marked with a hash comprises features of PtF_5 and PtF_3. The matrix support had been coated with pure neon for 20 min prior to each co-deposition and the corresponding spectra served as the backgrounds. The bands pointing downwards are formed at the expense of the bands pointing upwards.

The irradiation at λ = 266 nm of the M[PtF_6]/[PtF_6]$^-$ containing matrix samples gave primarily rise to the bands of PtF_5, PtF_3 and the band assigned to a polarized [F_2]$^-$. During this process, a band centered at 678.9 cm^{-1} with an extended structure is formed. This is seen to be primarily caused by PtF_5 and PtF_3 and their respective matrix sites. Additionally, coordinated {PtF_n} moieties as parts of complexes [PtF_n·F_2]$^-$ (n = 3, 4, 5) could be involved with respect to the B3LYP spectra in Figure 57 and Figure 139 in the appendix. This crowded area could not be fully analyzed with respect to all of the components, even at the applied resolution of 0.2 cm^{-1}. As it can be seen from Figure 62, molecular PtF_4 is decomposed (KF and CsF cases) and only slightly formed in the Pt case, while the UV light photolysis promotes the formation of PtF_5 in all these cases, indicating that a high oxidation state of Pt could be assumed in a [PtF_n·F_2]$^-$ complex. As the [F_2]$^-$ band at 474.4 cm^{-1} was found with the highest intensity in the experiments with laser-ablated platinum atoms, the follow-up photochemistry was studied in detail for this case (Figure 63). This is seen to be advantageous in order to eliminate side products and increase the yield of the precursor [PtF_6]$^-$ compared to the experiments employing the alkali metal fluorides. Note that similar experiments were performed with argon serving as the matrix host but did not yield a clear or reproducible [F_2]$^-$ band.

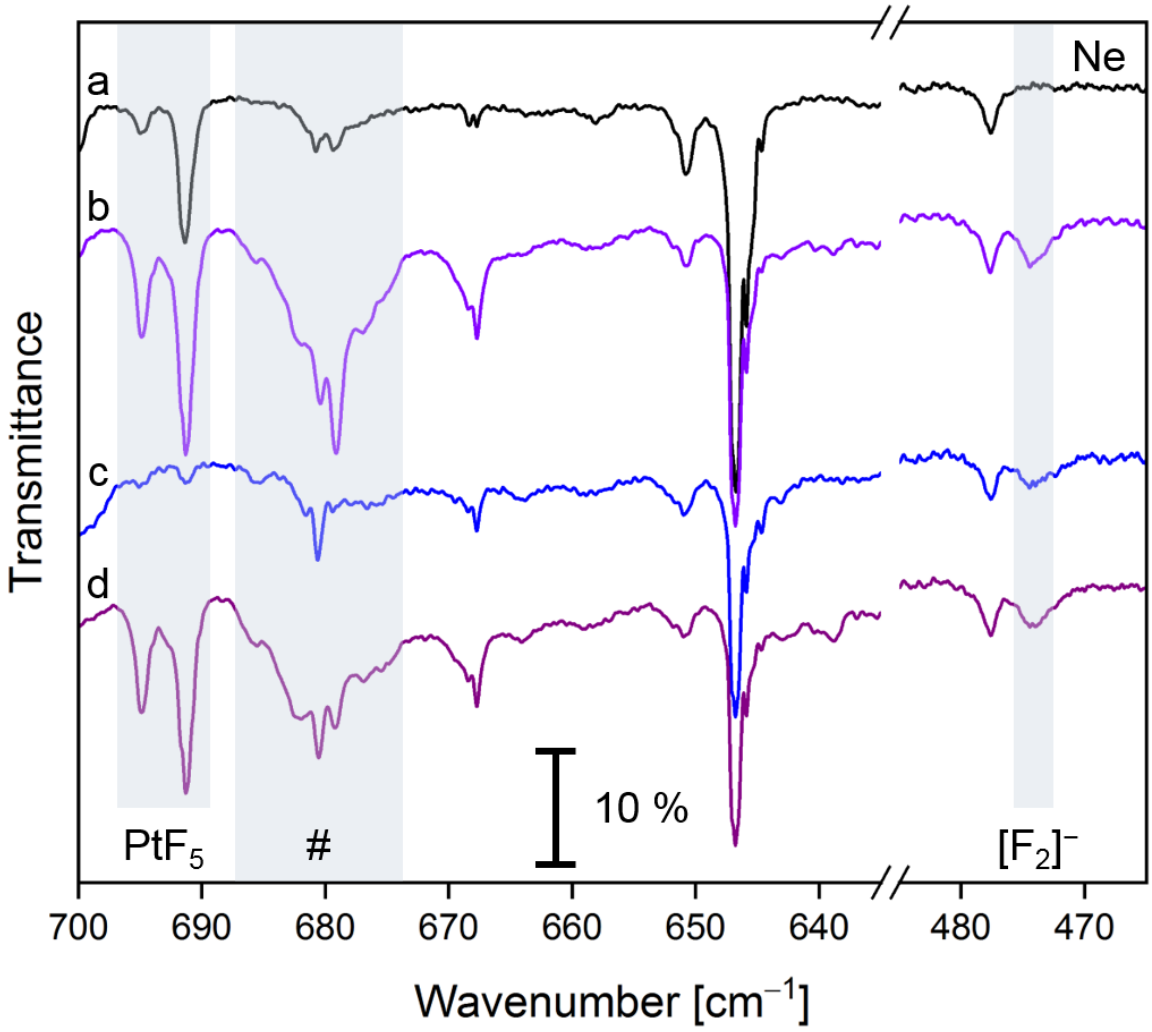

Figure 63: The IR spectra were obtained after a) the co-deposition of neon passed over a solid sample of PtF_6 maintained at −79 to −78 °C and laser-ablated platinum atoms (10 Hz repetition rate, 18 mJ/pulse, black trace) onto a gold-plated copper mirror at 5 K for 60 min at a deposition rate of 0.5 mbar·l·min^{-1}, and after the subsequent irradiation at b) λ = 266 nm (laser) for 90 min, c) λ = 470 nm (LED) for 60 min and d) λ = 266 nm (laser) for 10 min. The region marked with a hash comprises features of both PtF_5 and PtF_3. The matrix support had been coated with pure neon for 20 min prior to the co-deposition and the corresponding spectrum served as the background.

Comparing the spectra after photolysis experiments of PtF_6 with laser-ablated Pt with those obtained from pure PtF_6 embedded in neon (cf. reference [304]), no new characteristic band could be assigned to a coordinated {PtF_n} moiety of a $[PtF_n{\cdot}F_2]^-$-complex (n = 3, 4, 5) in the overall crowded Pt−F stretching region (see also Figure 145 in the appendix). The feature at 667.7 cm^{-1} with a shoulder at 668.6 cm^{-1} shows a photochemical behavior comparable to the $[F_2]^-$ band at 474.4 cm^{-1} and the band at 678.9 cm^{-1}. It can hardly be assigned to a $[PtF_n{\cdot}F_2]^-$ complex, since it depicts a singular band (no additional other bands) and is not red-shifted strongly enough to be comparable to the calculated results (Figure 139 in the appendix). Moreover, it is overlapping with traces of CO_2.[10,490] This leads to an analysis solely based on the development of the parent bands

of isolated PtF_3, PtF_4 and PtF_5. Noteworthy, no other indications for hidden bands such as shoulders were found regarding the strong features of the binary neutral platinum fluorides.

After the UV irradiation of the co-deposits of PtF_6 with laser-ablated KF, CsF and Pt the band accounting for coordinated $[F_2]^-$ and the bands indicative for isolated PtF_3, PtF_4 and PtF_5 were apparent. The assignment of the $[F_2]^-$ band at 474.4 cm^{-1} to one particular species of the type $[PtF_n{\cdot}F_2]^-$ (n = 3, 4, 5) is therefore not unequivocally possible (Figure 63). The amount of $[F_2]^-$ is comparable in KF and CsF cases, but was observed almost doubled in the Pt case. The amount of PtF_5 formed upon UV photolysis at λ = 266 nm (laser) is approximately equal in all cases, only slightly smaller in the Pt case. Upon the irradiation of the PtF_6/Pt deposit with blue light at λ = 470 nm (LED), PtF_5 was almost quantitatively decomposed, while the $[F_2]^-$ band only lost about 25 % of its intensity (see Figure 63 and Figure 64), which does not support a correlation of PtF_5 and $[F_2]^-$.

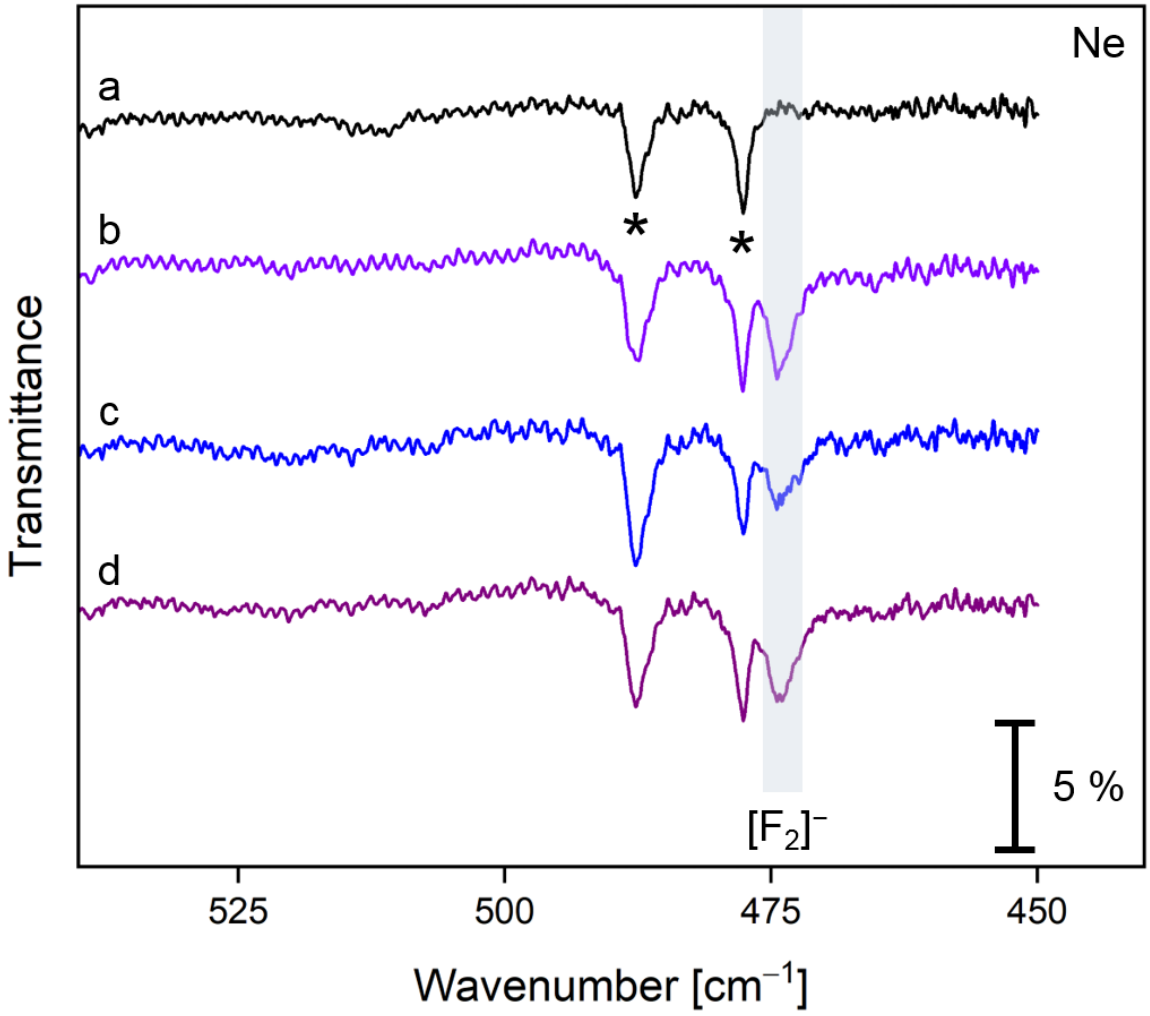

Figure 64: The IR spectra were obtained after a) the co-deposition of neon passed over a solid sample of PtF_6 maintained at −79 to −78 °C and laser-ablated platinum atoms (10 Hz repetition rate, 18 mJ/pulse, black trace) onto a gold-plated copper mirror at 5 K for 60 min at a deposition rate of 0.5 mbar·l·min^{-1}, and after the subsequent irradiation at b) λ = 266 nm (laser) for 90 min, c) λ = 470 nm (LED) for 60 min and d) λ = 266 nm (laser) for 10 min. Impurity bands already apparent after deposition are marked by an asterisk. The matrix support had been coated with pure neon for 20 min prior to the co-deposition and the corresponding spectrum served as the background. The expanded spectra in this figure are identical with the ones shown in Figure 63.

PtF_4 is decomposed upon UV light irradiation in the experiments employing KF and CsF, while being marginally formed in the Pt case. The blue light irradiation at λ = 470 nm leads to the known formation of PtF_4 with remarkably increasing bands, as opposed to the decreasing $[F_2]^-$ band (Figure 65). The latter band only slightly decreases, which is in line with the reported loss of about 75 % of the EPR signal intensity upon the irradiation of free $[F_2]^-$ at λ = 400 nm for 30 min[383,384] and corresponds to the behavior of the reported vibrational spectra.[74,374]

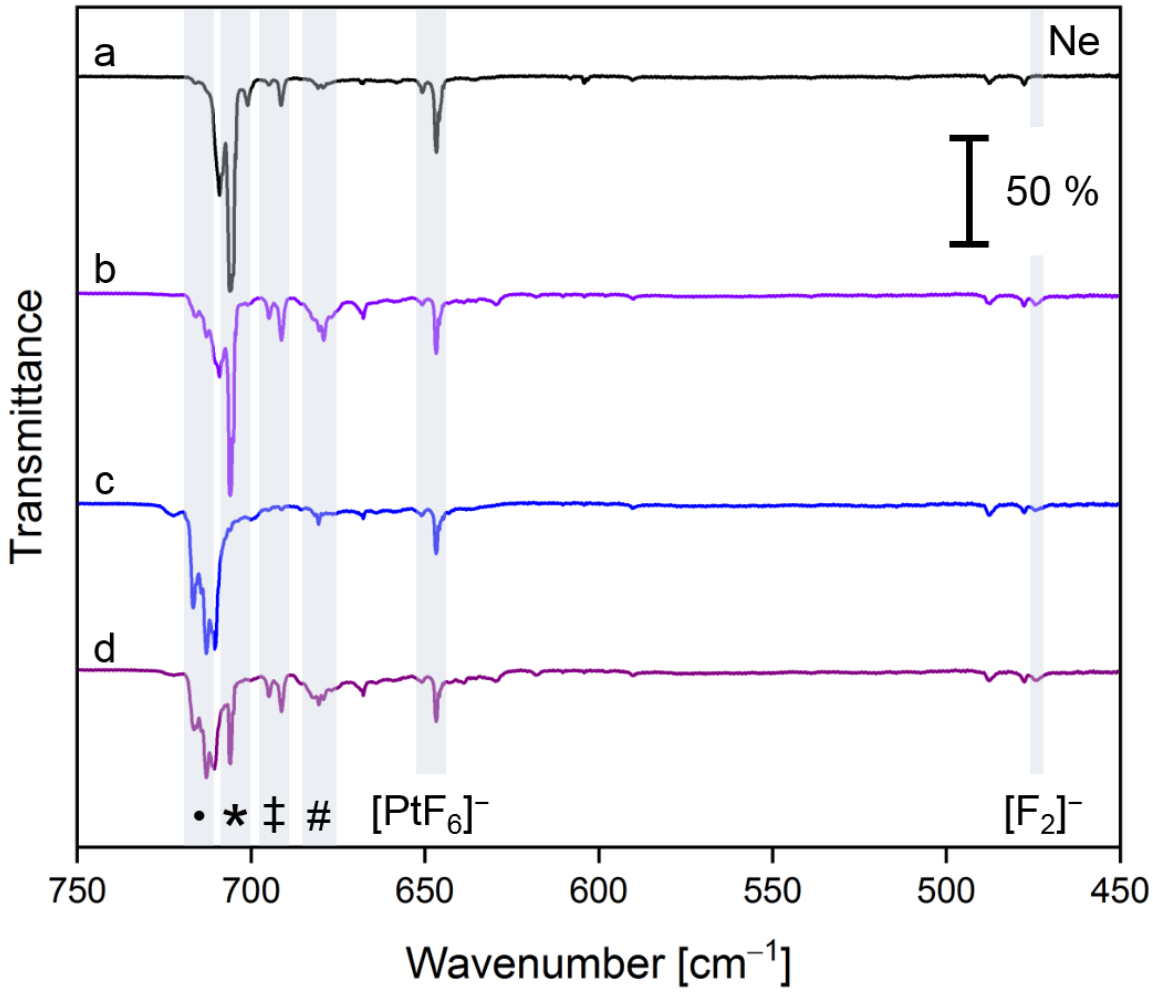

Figure 65: The IR spectra were obtained after a) the co-deposition of neon passed over a solid sample of PtF_6 maintained at −79 to −78 °C and laser-ablated platinum atoms (10 Hz repetition rate, 18 mJ/pulse, black trace) onto a gold-plated copper mirror at 5 K for 60 min at a deposition rate of 0.5 mbar·l·min^{-1}, and after the subsequent irradiation at b) λ = 266 nm (laser) for 90 min, c) λ = 470 nm (LED) for 60 min and d) λ = 266 nm (laser) for 10 min. The compounds PtF_4, PtF_6, PtF_5 and PtF_3 are highlighted with a bullet, an asterisk, a double-dagger and a hash, respectively, while the latter comprises features of both PtF_5 and PtF_3. The matrix support had been coated with pure neon for 20 min prior to the co-deposition and the corresponding spectrum served as the background. The spectra in this figure are identical with the ones shown in Figure 63.

PtF_3 is formed only in negligible amounts during the co-deposition of PtF_6 and all laser-ablated species (see also Figure 59 and Figure 143 in the appendix) but is formed in small amounts upon UV light irradiation of the matrix in all cases, yielding the strongest band in the Pt case, coincidentally with the intensity of the $[F_2]^-$ band. Moreover, PtF_3 was partially decomposed at blue light photolysis and regained intensity upon UV light photolysis for a second time, which was also observed for $[F_2]^-$.

In terms of the photochemical behavior, a $[PtF_3{\cdot}F_2]^-$ complex is favored over the analogous Pt^{IV} and Pt^{V} compounds. Since $[PtF_4{\cdot}F_2]^-$ features the weakest F–F stretching mode and the strongest ν_{as}(Pt–F) stretching band according to the calculated spectra (Figure 57), the experimentally

observed intensity of the $[F_2]^-$ band at 474.4 cm^{-1} would therefore necessitate a very strong and remarkably shifted band in the Pt−F stretching region, which was not observed. Therefore, $[PtF_5 \cdot F_2]^-$ and $[PtF_3 \cdot F_2]^-$ are rather conceivable than $[PtF_4 \cdot F_2]^-$ in the light of an experimentally expected low amount of a non-classical complex. Developing this thought further, the intensity of the $[F_2]^-$ band scales with the intensities of the Pt−F stretching bands of both $[PtF_5 \cdot F_2]^-$ and $[PtF_3 \cdot F_2]^-$ (cf. Figure 57). The low intensity of the $[F_2]^-$ band could thus explain that the Pt−F stretching bands might have comparably low intensities and might be obscured. The calculated F−F stretching modes are red-shifted by 44 and 100 cm^{-1} from the experimental value, respectively. In lieu of meaningful UV/Vis spectra, the true absorption spectra of the potential complexes $[PtF_n \cdot F_2]^-$ remain unknown. Since the photochemistry of the anionic platinum fluoride species is not necessarily directly correlated to the neutral ones, the absorption spectra of PtF_4 and $[PtF_4 \cdot F_2]^-$ could differ. The existence of the latter would not be excluded and might form in an event when PtF_4 itself is decomposed.

In the light of missing characteristic Pt−F stretching band(s), the experimental spectra are not fully conclusive to allow the determination of one distinct chemical species accounting for the $[F_2]^-$ band. $[PtF_5 \cdot F_2]^-$ and $[PtF_3 \cdot F_2]^-$, possibly both at the same time depending on the conditions, are conceivable candidates with respect to the quantum-chemically predicted spectra and the acidities of the parent Lewis acids.

3.2.2.2 Summary and Outlook

The co-deposition of PtF_6 and laser-ablated metals (Pd, Pt) or metal fluorides (NaF, KF, CsF) yielded the free hexafluoridoplatinate(V) anion $[PtF_6]^-$ in both neon and argon matrices as well as the corresponding ion pairs $M[PtF_6]$ (M = Na, K, Cs) in neon matrices. The UV photolysis of these deposits yielded a band accounting for a polarized $[F_2]^-$ anion, originated from $[PtF_6]^-$. The experimental and quantum-chemically predicted band positions are summarized in Table 26.

Table 26: Experimental and calculated (RI-B3LYP-D4/def2-TZVPP) band positions (in cm^{-1}) of the free $[PtF_6]^-$, the ion pairs $M[PtF_6]$ (M = Na, K, Cs) and a polarized $[F_2]^-$ ion in comparison with calculated $[PtF_n{\cdot}F_2]^-$ (n = 3, 4, 5) in the MIR regime. Matrix sites are given in parentheses.

Species	Ne	B3LYP	Description
$[PtF_6]^-$	(650.8) 646.7 (645.9 sh)[a]	641.4	$\nu_{as}(PtF_{2,eq})$
		603.7	$\nu_{as}(PtF_{2,ax})$
$Na[PtF_6]$	677.0 (677.8 sh)	665.5	$\nu_{s}(PtF_{3,terminal})$
	660.1 (661.3 sh)	643.9	$\nu_{as}(PtF_{2,eq})$
		620.0	$\nu_{as}(PtF_{2,ax})$
	609.1	587.5	$\nu_{s}(PtF_{3,coordinated})$
$K[PtF_6]$	672.8 (673.7 sh)	660.8	$\nu_{s}(PtF_{3,terminal})$
	657.6 (659.6 sh)	634.2	$\nu_{as}(PtF_{2,eq})$
		624.5	$\nu_{as}(PtF_{2,ax})$
	611.9	592.2	$\nu_{s}(PtF_{3,coordinated})$
$Cs[PtF_6]$	670.0 (670.8 sh)	657.8	$\nu_{s}(PtF_{3,terminal})$
	656.3 (658.3 sh)	631.5	$\nu_{as}(PtF_{2,eq})$
		625.7	$\nu_{as}(PtF_{2,ax})$
	612.4	594.2	$\nu_{s}(PtF_{3,coordinated})$
$[PtF_3{\cdot}F_2]^-$ [b]	474.4	374.2	ν(F–F)
$[PtF_4{\cdot}F_2]^-$ [b]		410.4	
$[PtF_5{\cdot}F_2]^-$ [b]		430.7	

[a] The band positions in Ar are found at (647.9) 642.2 cm^{-1}. [b] a clear assignment based on the computed and experimental data is not possible.

The $[F_2]^-$ band appears at 474.4 cm^{-1}, independent of the co-deposited metal or metal fluoride, and is therefore constrained in its binding partners to the neutral platinum fluorides. It might be associated with a derivative of free $[PtF_6]^-$ originated from an intramolecular process, since it was not found to be increased by adding 0.5 % F_2 to the neon, which is in line with the constrained mobility of the strongly oxidative fluorine atoms in neon matrices.[304,499,500] Moreover, the

intensity of the $[F_2]^-$ band was found to be the strongest for laser-ablated Pt. The assignment to the coordinating $\{PtF_n\}$ moiety of the $[F_2]^-$ is not straightforward, since no new band attributable to a shifted $\{PtF_n\}$ moiety (n = 3–5) was observed in the Pt−F stretching region with respect to the quantum-chemically expected shifts (Figure 139 in the appendix). The comparison of the photolysis products of a sample of PtF_6 embedded in neon with those of a co-deposit of PtF_6 and laser-ablated platinum atoms in neon revealed that the region around 678.9 cm^{-1} is crowded with bands of PtF_5 and PtF_3, which only leaves room for speculations about additional hidden bands. With respect to the weak observed ν(F−F) band of an $\{[F_2]^-\}$ moiety, the tentative assignment to $[PtF_3{\cdot}F_2]^-$ or $[PtF_5{\cdot}F_2]^-$ complexes with speculatively hidden PtF_n-bands seems to be reasonable, since these complexes show more balanced Pt−F and F−F stretching bands' intensities at the RI-B3LYP-D4/def2-TZVPP level of theory. The alternative assignment to a $[PtF_4{\cdot}F_2]^-$ complex is disfavored, because a comparably stronger ν_{as}(Pt−F) and a less prominent ν(F−F) at the same level of theory are expected as shown in Figure 57, but no corresponding Pt−F stretching band(s) were found in the experimental spectra. This also corresponds to the calculated higher acidities of PtF_3 and PtF_5 (cf. Table 23 in Section 3.2.1) and the correlated stronger activation of the $\{[F_2]^-\}$ unit. However, the tendency of these PtF_6-containing deposits to non-selectively produce the higher platinum fluorides PtF_5 and PtF_6 as well as the lower-valent PtF_3 upon UV light irradiation (vide supra) with fluorine atoms being present in the matrix[304,443] could principally allow for the formation of either of the $[PtF_n{\cdot}F_2]^-$ complexes (n = 3, 4, 5).

An eventual proof of the $[F_2]^-$ could be obtained in future EPR experiments.[383,384] Regarding the results reported by Howard and Andrews, Raman spectra could also provide an answer if the band is rather assigned to the F−F or the $F_nPt{-}F_2$ stretching mode and thereby provide insight into the perturbation of the $[F_2]^-$ by the $\{PtF_n\}$ moiety (see also Table 5 as well as references [74,374,375]).

3.3 Novel Oxofluorides of Manganese Derived from Photolyzed MnO_3F

This subchapter is based on unpublished results of Li et al.,[453] who discovered the new manganese oxofluorides [(η^2-OO)Mn^{V}OF] and [(η^1-OO)Mn^{IV}OF] derived from photolytically decomposed MnO_3F under matrix isolation conditions. They proposed a photochemical mechanism on the formation supported by energy calculations at the CCSD(T)/def2-QZVPP level of theory based on singlet and triplet species optimized at the PBE0-D3(BJ)/def2-QZVPP level of theory (the xyz coordinates of these species are featured in Section 6.3.1 in the appendix). The present work enhances the fundamental work by additionally or newly recorded IR and UV/Vis spectra of highly pure MnO_3F and its photolysis products embedded in neon, argon and nitrogen matrices. The following results and discussion feature content and figures of a corresponding manuscript that is currently in preparation for publication.[505]

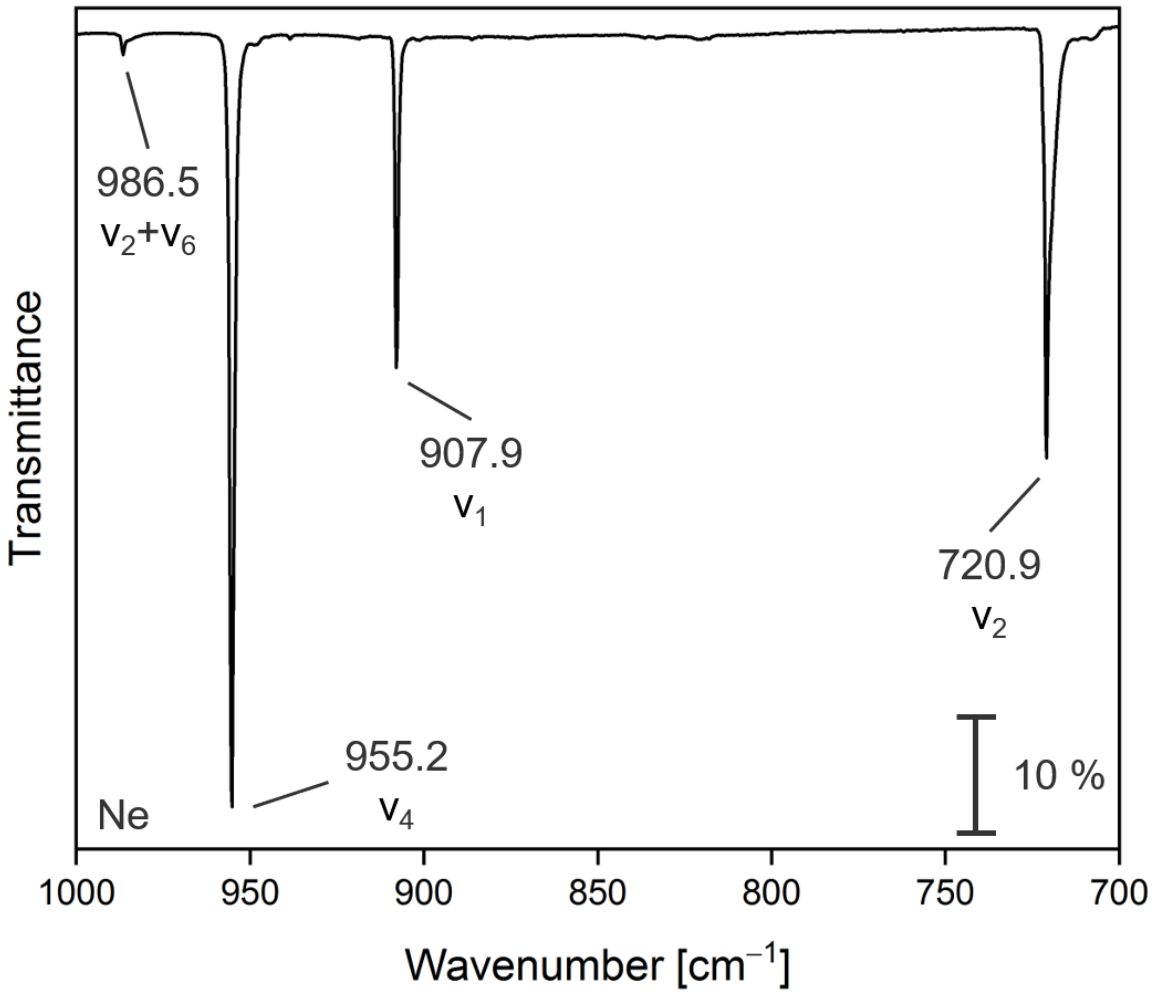

Figure 66: IR spectrum of MnO_3F embedded in solid neon in the Mn–F and Mn=O stretching region. The spectrum was recorded after the deposition of neon passed over a solid sample of MnO_3F maintained at −110.3 to −108.5 °C onto a gold-plated copper mirror at 6 K for 100 min at a deposition rate of 0.6 mbar·l·min^{-1}. A spectrum of pure neon pre-deposited for 42 min (including 20 min when the MnO_3F sample was too cold to be deposited) served as the background. Corresponding spectra in nitrogen (Figure 149) and argon matrices (Figure 152) are found in the appendix.

The synthesis of these novel [(η^2-OO)Mn^{V}OF] (labelled **B**) and [(η^1-OO)Mn^{IV}OF] (labelled **C**) compounds was facilitated by the photodecomposition of MnO_3F (labelled **A**) embedded in inert matrices. The photochemical interconversion between these photoproducts **B** and **C** was studied in detail. An IR spectrum of neon matrix-isolated **A** is found in Figure 66. All reactions were followed by IR and UV/Vis spectroscopy and the observed vibrational frequencies are summarized in Table 27.

Table 27: Experimental and calculated[453] IR frequencies of MnO_3F (**A**), [(η^2-OO)$Mn^{V}OF$] (**B**) and [(η^1-OO)$Mn^{IV}OF$] (**C**) given in cm^{-1}.

Compound	Ne	Ar	N_2	Calc.[a]	Ar (Lit.)	N_2 (Lit.)
A MnO_3F						
$\rho(MnO_3)$ (ν_6)				284.1		264[c]
				369.8		339[c], 340[d]
				405.6		380[c], 380[d]
ν(Mn–F) (ν_2)	720.9 (708.3)	715.6 (705.4)	717.0 (719.7, 708.3)	728.0	715.6[b]	716[c], 717[d]
$\nu_s(MnO_3)$ (ν_1)	907.9 (901.2)	903.6 (905.8 sh)	908.7 (910.6, 907.5 sh)	1016.5	903.7[b]	904[c], 904[d]
$\nu_{as}(MnO_3)$ (ν_4)	955.2 (948.7)	950.6 (953.5 sh)	955.9 (956.6 sh, 953.0)	1053.6	950.6[b]	951[c], 953[d]
$\nu_2+\nu_6$	986.5 (984.4 sh)	978.8 (977.1 sh)	984.6 (986.1, 987.5 sh)			
B [(η^2-OO)MnOF][e]						
ν_s(Mn–O)				515.3		
ν_{as}(Mn–O)				536.7		
ν(Mn–F)	721.1 (725.2)	713.6 (717.5, 709.5)	714.4 (715.8, 713.4)	721.0		
ν(O–O)	926.5 (934.5)	928.7 (925.5, 922.4)	925.3 (926.3 sh)	1001.1		
ν(Mn=O)	955.4 (975.0, 962.2)	956.4 (955.2 sh), 948.7 (950.4 sh)	953.0 (956.2, 950.9)	1028.7		
C [(η^1-OO)MnOF]						
ν(Mn–OO)	671.7 (674.1 sh)	666.1 (664.0)	672.2 (669.0)	564.0		
ν(Mn–F)	684.9 (687.6 sh)	685.2 (681.6, 674.8, 670.5)	695.8 (697.7)	708.7		
ν(Mn=O)	819.5 (810.5, 831.5)	809.6 (822.8, 816.6, 805.2 +sh)	810.8 (813.7 sh, 801.4)	1024.7		
ν(O–O)	1104.7 (1100.1 sh)	1100.8 (1105.4, 1104.0, 1098.4, 1096.2)	1104.7 (1103.0 sh)	1294.1		

[a] Computed harmonic frequencies at PBE0-D3(BJ)/def2-QZVPP level of theory scaled by 0.9573 as recommended in the literature.[506] The band positions in parentheses refer to matrix sites. The experimental values from the literature have been taken from [b] ref. [239], [c] ref. [244], and [d] ref. [187]. [e] The computed frequencies in the table are for the triplet state. The frequencies for the singlet state are 611.8 (ν_{as}(Mn–O)), 641.1 (ν_s(Mn–O)), 752.4 (ν(Mn–F)), 1044.0 (ν(O–O)), and 1108.1 cm^{-1} (ν(Mn=O)).

To correlate the changes in band intensities in the IR and UV/Vis regions and to confirm the band assignment of the newly formed species, a series of IR and UV/Vis spectra from the same neon, argon and nitrogen matrices was recorded. The principal results are identical regardless of the host material used. Therefore the discussion will be mainly focused on the results obtained in neon matrices, while nitrogen and argon data are found in the appendix and referenced in suitable positions.

Table 28: Electronic transitions (absorption maxima) of MnO_3F (**A**), [(η^2-OO)MnOF] (**B**) and [(η^1-OO)MnOF] (**C**) in inert matrices given in nm.

Compound	λ (Ne) [a]	λ (N_2) [a]	λ (Ar) [a]	λ (N_2) [b]	Assignment [b]
A MnO_3F					
	208.5	207.5	211.5	216	–
	261.0	252.5	246.0	250	σ(O)→Mn c. t.
	299.5	299.5	299.5	300	π(F)→Mn c. t.
	444.0	442.5	446.5	448	π(O)→Mn c. t.
	629.0	593.5	708.5	645	π(O)→Mn c. t.
B (η^2-OO)MnOF					
	235.5	n. o.	n. o.		
	370.0	≈ 360	n. o.		
C (η^1-OO)MnOF					
	297.0	278.5 sh	≈ 276 sh		
	359.5	360.5	358.0 sh		

[a] This work; n. o. = not observed; spectral resolution = 0.5 nm; [b] values were taken from ref. [187], c. t. = charge transfer.

The absorption maxima in the UV/Vis spectra of **A**, **B** and **C** in inert solids are summarized in Table 28 and compared to literature values of **A**. The electronic transitions of MnO_3F in Ne (Table 70), N_2 (Table 71, Figure 155), and Ar (Table 72, Figure 156) including their vibrational progressions are found in the appendix.

3.3.1 MnO_3F and its Photolysis Products in Ne

After the co-deposition of MnO_3F (**A**) seeded in excess neon, three fundamentals at 720.9 (ν_2, ν(Mn−F)), 907.9 (ν_1, $\nu_s(MnO_3)$) and 955.2 cm^{-1} (ν_4, $\nu_{as}(MnO_3)$) were observed along with a combination band at 986.5 cm^{-1} ($\nu_2+\nu_6$, ν(Mn−F)+$\rho(MnO_3)$), as depicted in Figure 66. Similar band positions were found in N_2 and Ar matrices with maximum matrix-shifts of 8 cm^{-1} and are compiled in Table 27. The findings are in accordance with previously reported matrix isolation results[187,237–240] and with the scaled harmonic frequencies calculated at the PBE0-D3(BJ)/def2-QZVPP level of theory (Table 27). Although the symmetric and asymmetric MnO_3 stretching frequencies are significantly overestimated, stemming from the use of a global scaling factor of 0.9573,[506] the use of a scaling factor optimized for high frequencies leads to a better agreement between theory and experiment,[507] and the relative band positions are reflected well by the theory.

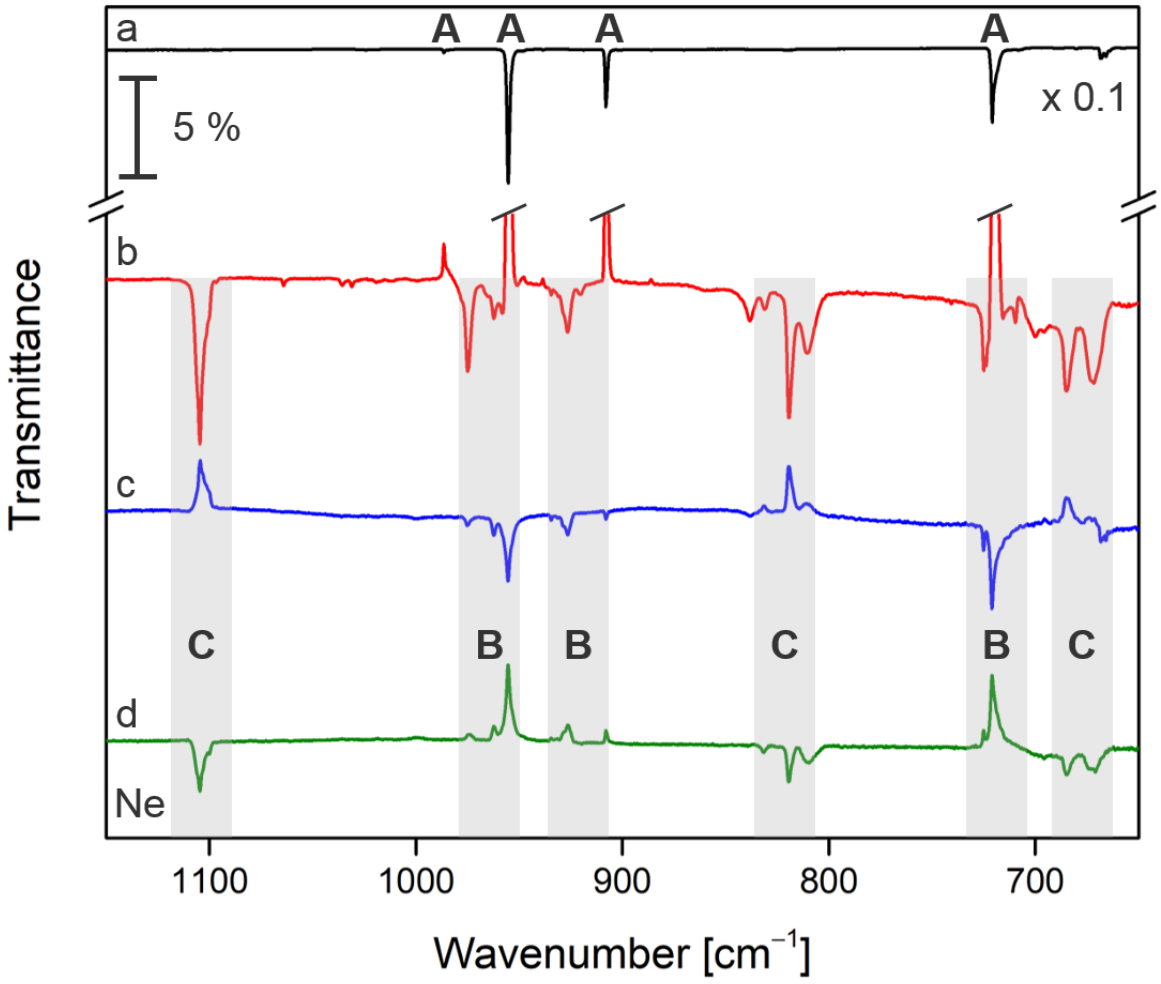

Figure 67: IR (this figure) and UV/Vis spectra (cf. Figure 68) were recorded from the same neon matrix at 6 K showing the photochemistry of MnO_3F (**A**) and the interconversion between species [(η^2-OO)Mn^{V}OF] (**B**) and [(η^1-OO)Mn^{IV}OF] (**C**). The spectra were obtained after a) the deposition of neon passed over a solid sample of MnO_3F maintained at −110.3 to −108.5 °C onto a gold-plated copper mirror at 6 K for 100 min at a deposition rate of 0.6 mbar·l·min^{-1} (black trace), and after the irradiation of this initial deposit at b) λ = 455 nm for 80 min (red trace), c) λ = 365 nm for 40 min (blue trace) and d) again at λ = 455 nm for 40 min (green trace). In the difference spectra a,b and c, the bands pointing downwards are formed at the expense of the bands pointing upwards. Corresponding spectra in nitrogen (Figure 149, Figure 150) and argon matrices (Figure 152, Figure 153) are found in the appendix.

From previous reports[187,241,242] and the UV/Vis spectra that were measured from the same samples as the IR spectra (this work, vide infra) it is known that MnO_3F has a strong absorption band at λ = 444.0 nm (Figure 68). During photolysis with blue light at λ = 455 nm for 80 min all observed bands of **A** (IR, UV/Vis) completely vanished, giving rise to a new set of bands. Upon prolonged photolysis at the same wavelength, a splitting of these new bands into two sets of bands, one of which is characteristic for **B** and one for **C**, was observed. Once formed, the bands of **B** decreased upon prolonged irradiation at λ = 455 nm, while the bands of **C** strongly increased. The four bands at 671.7, 684.9, 819.5 and 1104.7 cm^{-1} (+ matrix sites, Table 27) are characteristic

of species **C**. Consistent with the UV/Vis spectra, no color change of the matrix of diluted reactants/products upon irradiation was observed (Figure 148 in the appendix).

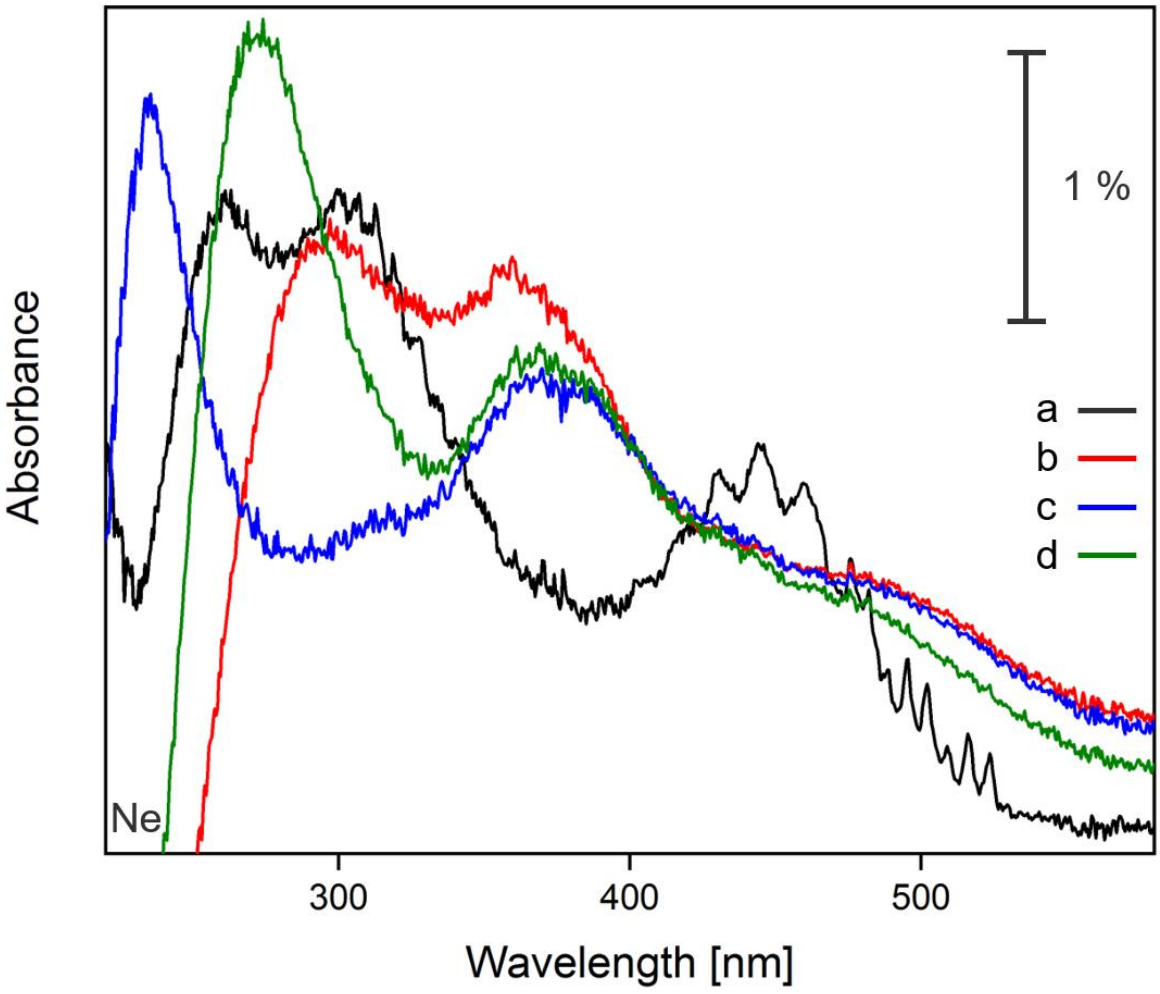

Figure 68: IR (cf. Figure 67) and UV/Vis (this figure) spectra were recorded from the same neon matrix at 6 K showing the photochemistry of MnO_3F (**A**) and the interconversion between species [(η^2-OO)Mn^{V}OF] (**B**) and [(η^1-OO)Mn^{IV}OF] (**C**). The spectra were obtained after a) the deposition of neon passed over a solid sample of MnO_3F maintained at −110.3 to −108.5 °C onto a gold-plated copper mirror at 6 K for 100 min at a deposition rate of 0.6 mbar·l·min^{-1} (black trace), and after the irradiation of this initial deposit at b) λ = 455 nm for 80 min (red trace), c) λ = 365 nm for 40 min (blue trace) and d) again at λ = 455 nm for 40 min (green trace). Corresponding spectra in nitrogen and argon matrices are depicted in Figure 155 and Figure 156, respectively, in the appendix.

Quantum-chemical calculations at the PBE0-D3(BJ)/def2-QZVPP level of theory (Table 27) were performed to assign the newly formed species based on their characteristic vibrational frequencies. The band at 671.7 cm^{-1} obtained in a Ne matrix is assigned to the vibration of an Mn–O single bond calculated at 564.0 cm^{-1}. Similarly, the band at 684.9 cm^{-1} agrees well with the calculated vibration of Mn–F at 708.7 cm^{-1}. Compared to the vibrations of species **A**, the corresponding Mn–F and Mn=O stretching modes of **C** are red-shifted by 36.0 and 135.7 cm^{-1}, respectively. The observed shifts suggest a significant rearrangement of the ligand sphere around the Mn center. This is also confirmed by an additional band observed in the neon matrix at

1104.7 cm^{-1}, which is too high to be assigned to any of the Mn–O vibrations of **A**. Furthermore, this band position is indicative for an O–O stretching vibration in an end-on bonded O_2 complex, which are typically found in the region 1000–1300 cm^{-1}.[219] For example, the end-on bonded O_2 complexes [(η^1-OO)IrO_2] and [(η^1-OO)RhO_2] were reported in Ne matrices and showed O–O stretching modes at 1022.8 and 1108.0 cm^{-1}, respectively.[232,233] The new bands, which were observed after the long-term photolysis of **A** at λ = 455 nm, are accordingly assigned to the novel manganese(IV) oxofluoride O_2 complex [(η^1-OO)$Mn^{IV}OF$] **C**.

The set of bands characteristic of species **B**, initially formed during photolysis at λ = 455 nm, but decomposed upon prolonged irradiation, were found to reappear after photolysis at λ = 365 nm (at the near UV absorption maximum of **C**, Figure 67, Figure 69).

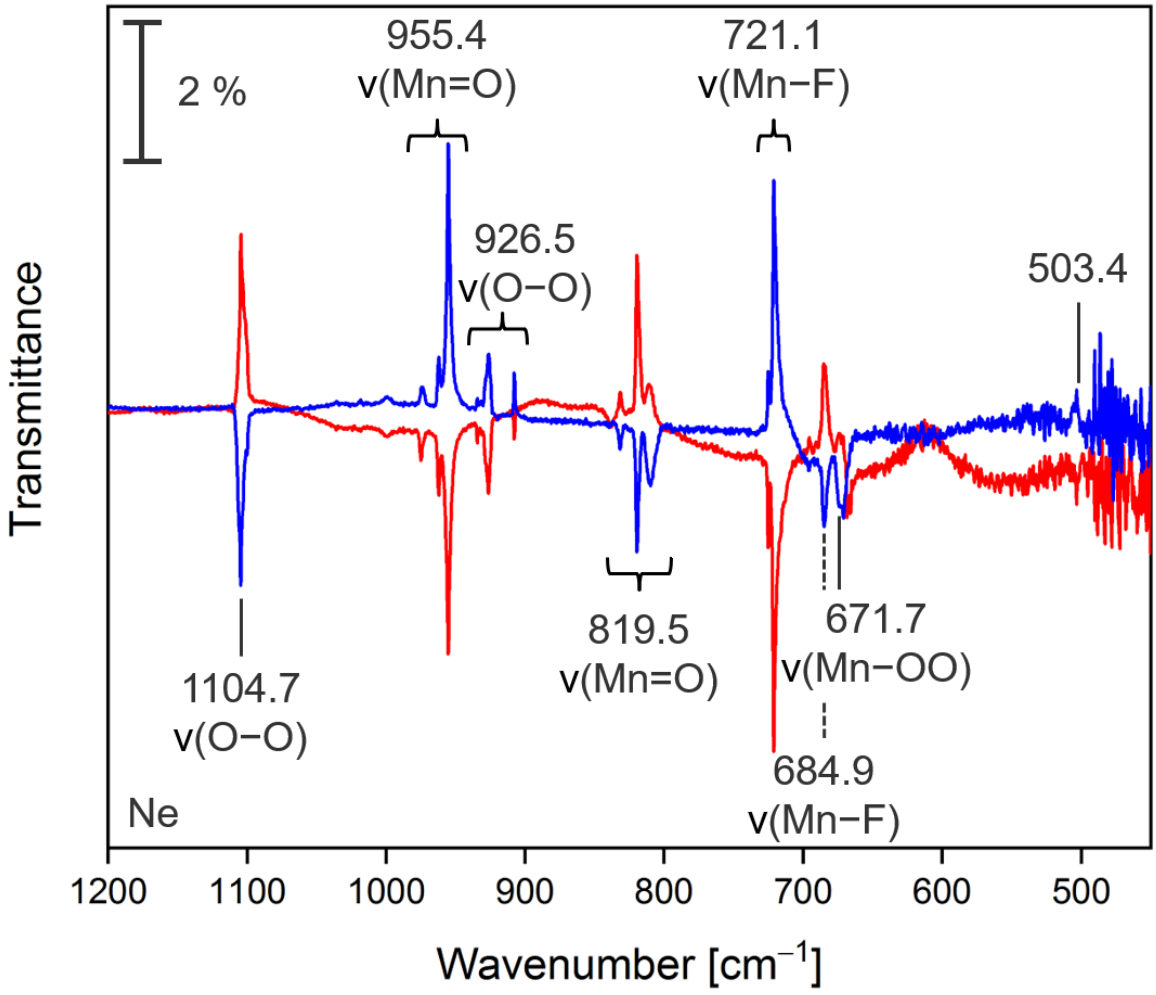

Figure 69: Difference IR spectra of [(η^1-O_2)MnOF] (**C**) and [(η^2-O_2)MnOF] (**B**) in solid Ne displaying the interconversion of **C** to **B** and **B** to **C** after photolysis at λ = 365 nm for 40 min (red trace) and at λ = 455 nm for 40 min for the second time (blue trace), respectively. The spectra in this figure are identical with the spectra c and d in Figure 67. The bands pointing downwards are formed at the expense of bands pointing upwards. Corresponding spectra in solid nitrogen and argon are depicted in Figure 151 and Figure 154, respectively, in the appendix.

The Mn–F and Mn=O stretching modes of **B** are found in almost equal positions with respect to those of MnO_3F (**A**), shifted only by +0.2 and +0.2 cm^{-1} in Ne, by –2.0 and –1.9 cm^{-1} in Ar, and by –2.6 and –2.9 cm^{-1} in N_2 matrices, respectively (Table 27). Compared to the findings for **C**, these shifts are associated with a rather small change in molecular structure, while an additional band at 926.5 cm^{-1} indicates the formation of a side-on O_2 complex. Corresponding O–O stretching bands are typically found between 800 and 930 cm^{-1},[219] for example for [(η^2-OO)IrO_2] at 896.3 cm^{-1} and [(η^2-OO)RhO_2] at 930.4 cm^{-1} in Ne matrices.[232,233] The subsequent photolysis at λ = 455 nm for 40 min for a second time resulted once more in the end-on complex [(η^1-OO)$Mn^{IV}OF$] **C**, while follow-up irradiation at λ = 365 nm yielded species **B** (Figure 69). This behavior was reproducible with repeated irradiation cycles at λ = 455 nm and λ = 365 nm lights. Since the absorption bands of **B** are reversibly converted to bands characteristic of **C** upon photolysis, species **B** is suggested to be a structural isomer of compound **C**. Therefore, the new bands of species **B** were assigned to the side-on bonded O_2 manganese oxofluoride complex [(η^2-OO)$Mn^{V}OF$] with manganese in its formal oxidation state +V.

Analogous to the IR experiments, UV/Vis experiments were performed to elucidate the photochemistry of MnO_3F (**A**), and its derivatives **B** and **C**. The UV/Vis spectra of MnO_3F (**A**) obtained in the Ne matrix are in excellent agreement with the data from the literature both in the gas phase and in the nitrogen matrix (cf. Table 28).[187,241,242] A detailed analysis of all vibrational progressions and electronic transitions has been documented in the literature.[242]

Irradiation into the absorption maximum of **A** in the visible range with blue light at λ = 455 nm for 80 min resulted in the complete disappearance of the features characteristic of **A** and the appearance of two new broad bands at 359.5 and 297.0 nm (Figure 68). Subsequent photolysis near the former absorption maximum of the new species at λ = 365 nm for 40 min revealed new features at 370.0 and 235.5 nm, the latter being more intense, while the bands at 359.5 and 297.0 nm disappeared. Upon further irradiation of the same neon matrix with blue light at λ = 455 nm for a second time for 40 min, the features observed before seemed to be red-shifted but the bands of pure species **B** were not observed. This resulted in a band positioned between the absorption bands of the two species **B** and **C** at about 365.5 and 274.0 nm. The corresponding N_2 and Ar data are found together with the Ne data in Table 28. It should be noted that the UV/Vis spectra of the species **A**, **B** and **C** and their correlation are currently under high-level theoretical investigation. Until finished, the assignment of these species is solely based on their IR spectra, which were measured simultaneously with their UV/Vis spectra of the same samples.

To support the experimental assignments and to provide detailed insights into the reaction mechanism of these products, further calculations using DFT and coupled-cluster methods had been performed previously (see also Section 4.2).[453] As it can be seen in Figure 70, the transformation enthalpy of **A** to **B** at 0 K (ΔH_0) is predicted to be 84.1 kJ mol^{-1}. The side-on bonded O_2 complexes have O–O bond distances of 137.2 and 139.1 pm for the singlet and triplet states, respectively. These bond lengths are comparable to the side-on bonded O_2 complex [(η^2-OO)IrO_2] with a calculated O–O bond distance of 145.1 pm at the CCSD(T)/aug-cc-pVTZ level of theory.[233]

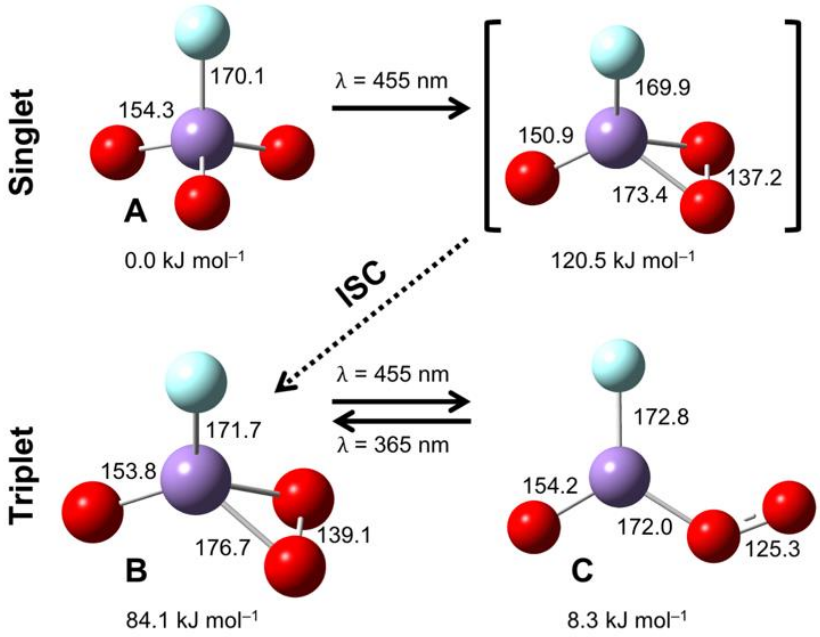

Figure 70: Local minima located along the reaction path for the formation of the end-on [(η^2-OO)MnOF] (**B**) and the side-on coordinated O_2 complex [(η^1-OO)MnOF] (**C**) out of MnO_3F (**A**). The relative enthalpies at 0 K (ΔH_0) calculated at the RO-CCSD(T)/def2-QZVPP level of theory are given in kJ mol^{-1}, and PBE0-D3(BJ)/def2-QZVPP bond distances are given in pm. The brackets indicate an intermediate that is not observed experimentally; color code: Mn (violet), F (turquoise), O (red).[453]

As it is evident from both IR and UV/Vis experiments the bands of complexes **B** and **C** are photoreversible, those of the precursor MnO_3F (**A**) are not (Figure 67, Figure 68, Figure 69). These findings are underlined by quantum-chemical calculations that revealed that MnO_3F (**A**) possesses a singlet ground state. In contrast to the end-on **C** and side-on **B** complexes with triplet ground states, this suggests an intersystem crossing process. Therefore, it is likely that the initial irradiation process leads to a transition from the singlet to the triplet surface via intersystem crossing, which is a non-reversible process (Figure 71).[453]

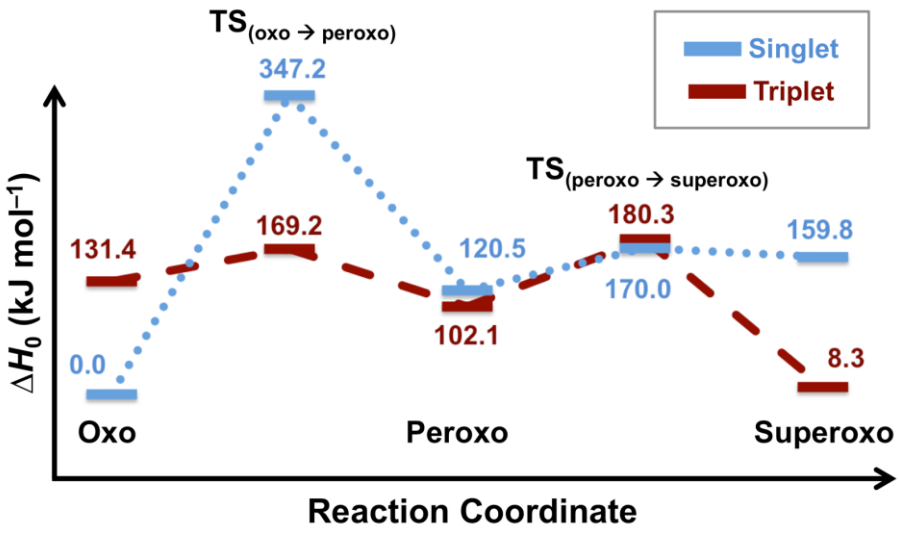

Figure 71: Energy diagram of different electronic configurations of MnO_3F isomers computed at the RO-CCSD(T)/def2-QZVPP level of theory.[453]

3.3.2 Summary

In the light of recently discovered oxofluorides of manganese (cf. Section 1.5), this part of the work features novel oxofluorides of manganese: the end-on [(η^1-OO)Mn^{IV}OF] and side-on [(η^2-OO)Mn^{V}OF] complexes with Mn in an oxidation state lower than +VII. These compounds were prepared by the photolysis of permanganyl fluoride ($Mn^{VII}O_3F$) using lights at appropriate wavelengths and were spectroscopically identified by joint matrix isolation and quantum-chemical studies.[453] The photochemical interconversion between the new complexes embedded in solid neon, argon, and nitrogen was investigated by IR and UV/Vis spectroscopy. Computational studies up to the CCSD(T)/def2-QZVPP level of theory supported the assignment of these previously unknown products and provided detailed insight into their molecular structures based on the characteristic vibrational bands and energy calculations.[453]

3.4 New Insights into the Simons Process

Many different fluorinated products are obtained by the Simons process and different mechanisms could account for their formation, namely the EC_bEC_N and mediated (e.g. via NiF_3/NiF_4) types (cf. Section 1.4.1.1). Nickel fluorides with Ni in a higher oxidation state than +II are thought to be formed within a black film on the anode under the conditions of the Simons process. In order to find experimental proof for the existence of such species the anodic behavior of nickel was investigated in liquid *a*HF by the use of cyclic voltammetry (CV), chronoamperometry (CA), and open circuit voltage measurements (OCV). The electrochemical characteristics served as the fundament for the ex-situ and in-situ characterization of the anodic film by powder X-ray diffraction (PXRD), scanning electron microscopy (SEM) and X-ray absorption fine structure (XAFS) spectroscopy.

The experiments for the investigation of the anodic film were performed without the use of organic starting material for the following reasons: I) Sartori et al. obtained fluorinated compounds from non-fluorinated starting material, even though the (well-conditioned) ECF cell had been disconnected from the power supply before the addition of this substrate. This indicates that an oxidizing agent had been present prior to the addition of the organic molecules.[154] II) Dimitrov et al. observed identical CV scans of nickel anodes in *a*HF and a solution of dibutylmethylamine in *a*HF, further supporting that the anodic process is independent of the substrate.[508] III) The addition of organic starting material after the induction period leads to hardly reproducible changes of the anodic film.[123,152]

In order to correctly mimic the industrial process, the conditions were chosen to fit the industrial ones (*a*HF without additives, Ni anode and cathode, cell potentials of +4.5 up to +7.0 V, current densities of 0.5 to 3.0 $A \cdot dm^{-2}$)[50,61,123,150] as closely as possible. Accordingly, and as outlined in Section 1.4.1.1, the focus of the present work lies in the generation of an anodic black film at high potentials in the induction/conditioning period of the Simons process and the characterization of the nickel fluoride film by ex-situ and in-situ methods.

Joint theoretical and electrochemical perspectives within a cooperation with Dr. Stefan Mattsson and Prof. Dr. Beate Paulus from the Theoretical Chemistry at the Institute of Chemistry and Biochemistry at the Freie Universität Berlin revealed the possibility to stabilize nickel in an oxidation state higher than +II at sufficiently high potentials in *a*HF and the results were published in:

S. Mattsson, G. Senges, S. Riedel, B. Paulus, *Chem. Eur. J.* **2020**, 26, 10781.

This motivated further in-depth investigations of the anodic film under the conditions of the Simons process, since physical evidence for the existence of any Ni^{x+} ($x > 2$) centers in the anodic black film is missing to date.

The results related to the in-situ characterization of the anodic film, i.e. the development and construction of an electrochemical in-situ XAFS cell and the XAFS spectra, were obtained in cooperation with Dr. habil. Franziska Emmerling, Dr. Ana Guilherme Buzanich, Bettina Röder, Dr. Uwe Reinholz and Dr. Martin Radtke from the Division 6.3 (Structure Analysis) at the Bundesanstalt für Materialforschung und -prüfung (BAM).

3.4.1 Ex-situ Characterization of the Anodic Film

The cyclic voltammogram of a nickel anode in a 3-electrode setup with Ni acting as both the working (WE) and the counter electrode (CE) with a platinum quasi reference electrode (Pt QRE) in liquid *a*HF at 0 °C (setup depicted in Figure 157 in the appendix) showed only one distinct oxidation feature at +3.57 V vs. Pt QRE on the forward scan (Figure 72), which was found to agree well with the DFT value of +3.1 V for the oxidation of Ni^{2+} to Ni^{3+}.[174] By this assignment, the possible formation of mixed-valent species like $Ni^{II}[Ni^{IV}F_6]$ or $Ni^{II}_3Ni^{IV}F_{10}$ is formally neglected but is not precluded.[166,262,264] The reduction peak on the backward scan at +1.42 V vs. Pt QRE is assigned to the reduction of electrochemically formed NiF_x ($x > 2$) species.[174] This is in line with the large peak-to-peak separation ($\Delta E_p >> 57$ mV), which indicates two irreversible electrochemical processes.[509] However, according to an earlier report comparable reduction peaks were assigned to the cathodic stripping of elemental fluorine[172] that is reportedly not formed under the applied conditions.[50,61] These basic electrochemical characteristics of Ni anodes in *a*HF have been discussed in reference [174].

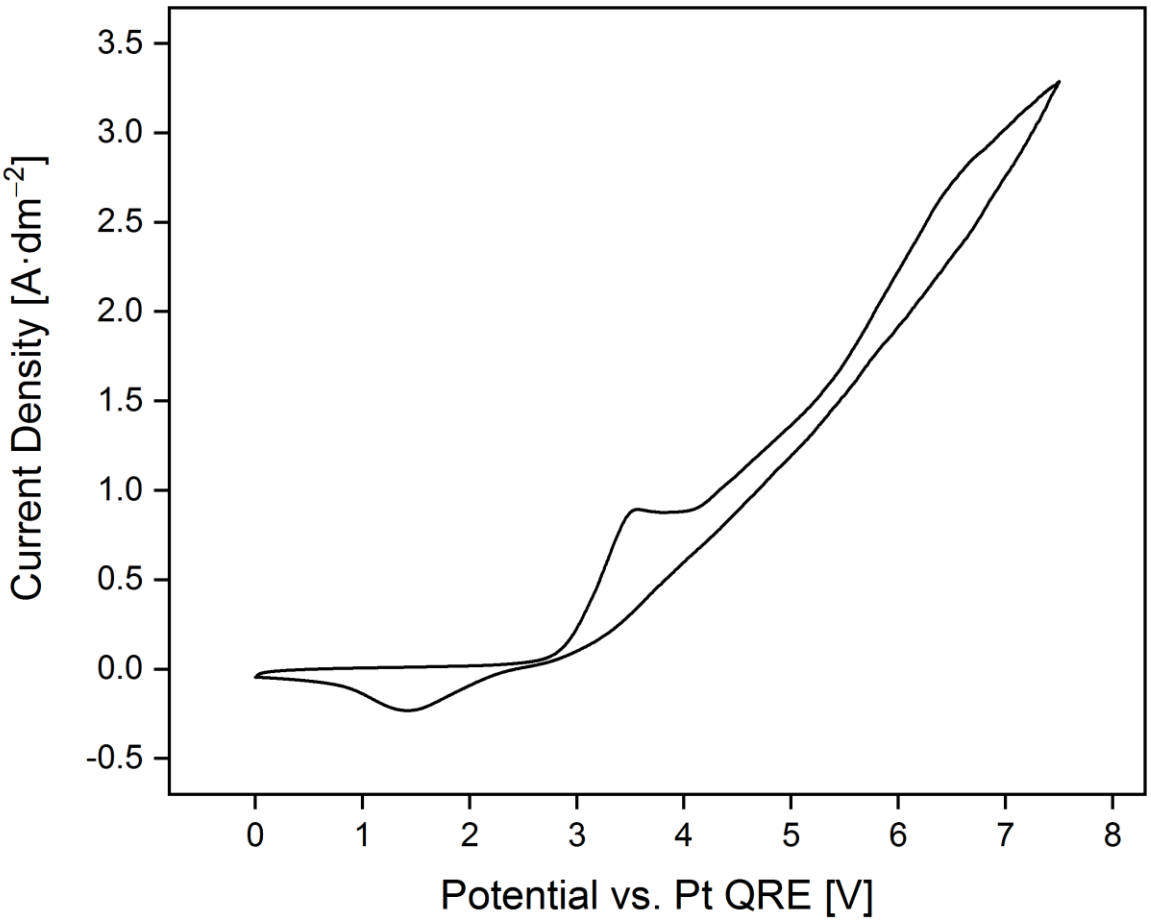

Figure 72: Cyclic voltammogram of the system Ni|NiF_x|HF_l‖HF_l|$H_{2,g}$|Ni ($x \geq 2$) at 0 °C in the potential window from 0.0 V to +7.5 V acquired at a scan rate of 50 mV·s^{-1} using planar electrodes with Ø = 1 mm. The figure was reproduced based on the data from reference [174].

Further investigations of the anodic behavior of nickel was conducted in 2-electrode setups, where two nickel plate electrodes were used, one serving as the anode (WE) and the other one as both the counter and the reference electrode (RE). The omission of the Pt QRE necessitates the oxidation peak to shift from ca. +3.5 V (Figure 72) to about +4.5 V. The latter value represents the cell potential, since the potential between Ni (CE) vs. Pt QRE was measured with ca. 1.0 V (within experimental accuracy) in all experiments and simply adds to the potential of the Ni (WE) vs. Pt QRE. This value matches the minimum potential of the industrial process of +4.5 V.[50,123] In order to obtain the largest effect, i.e. a thick anodic film, +6.0 V, the maximum of the cell potential recommended in reference [50], was applied in the induction phase during the ex-situ studies.

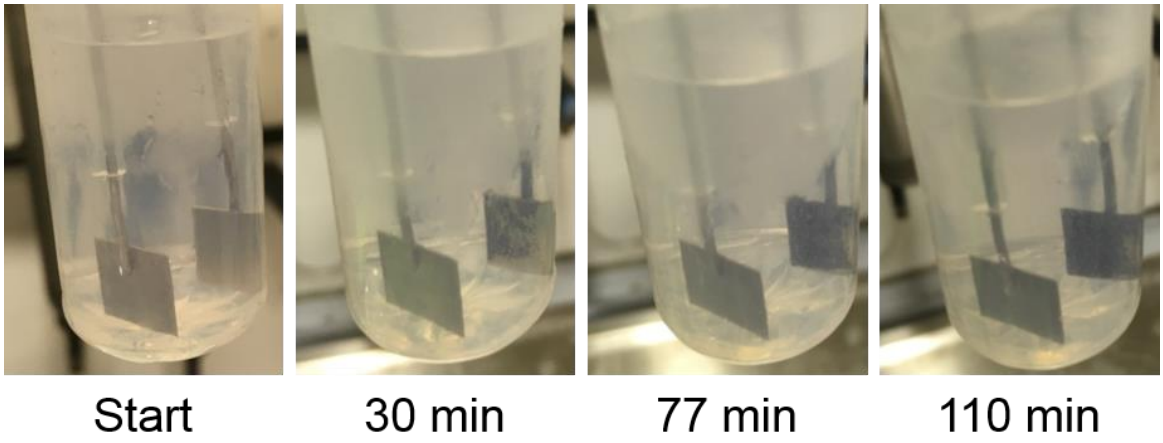

Figure 73: PFA-insulated nickel plate electrodes ($A_{electrode}$ = 2.1 cm^2) in liquid *a*HF at 0 °C (V = 15 ml) subjected to chronoamperometry at a cell potential of +6.0 V vs. Ni for 130 min (cf. CA scan in Figure 74). The formation of a black film on the anode (depicted right) sets in after 30 min closest to the cathode (depicted left) and is almost completed after 77 min, while the cathode (depicted left) turned slightly greyish.

For the polarization experiments using CA, the distance between the electrodes was kept at 15 mm (center-to-center, in all experiments) and – to optimize the photographical documentation – the angle between the electrodes' planes was set around 30°. During CA, constant H_2 evolution was monitored at the cathode, which turned slightly greyish during this process. The formation of a black film on the anode set in at the site closest to the cathode. It was clearly visible 30 min after the start of the CA and was nearly completed after 77 min (Figure 73). This is reflected in the simultaneously recorded chronoamperogram (Figure 74), in which the maximum of current density was reached by the same time.

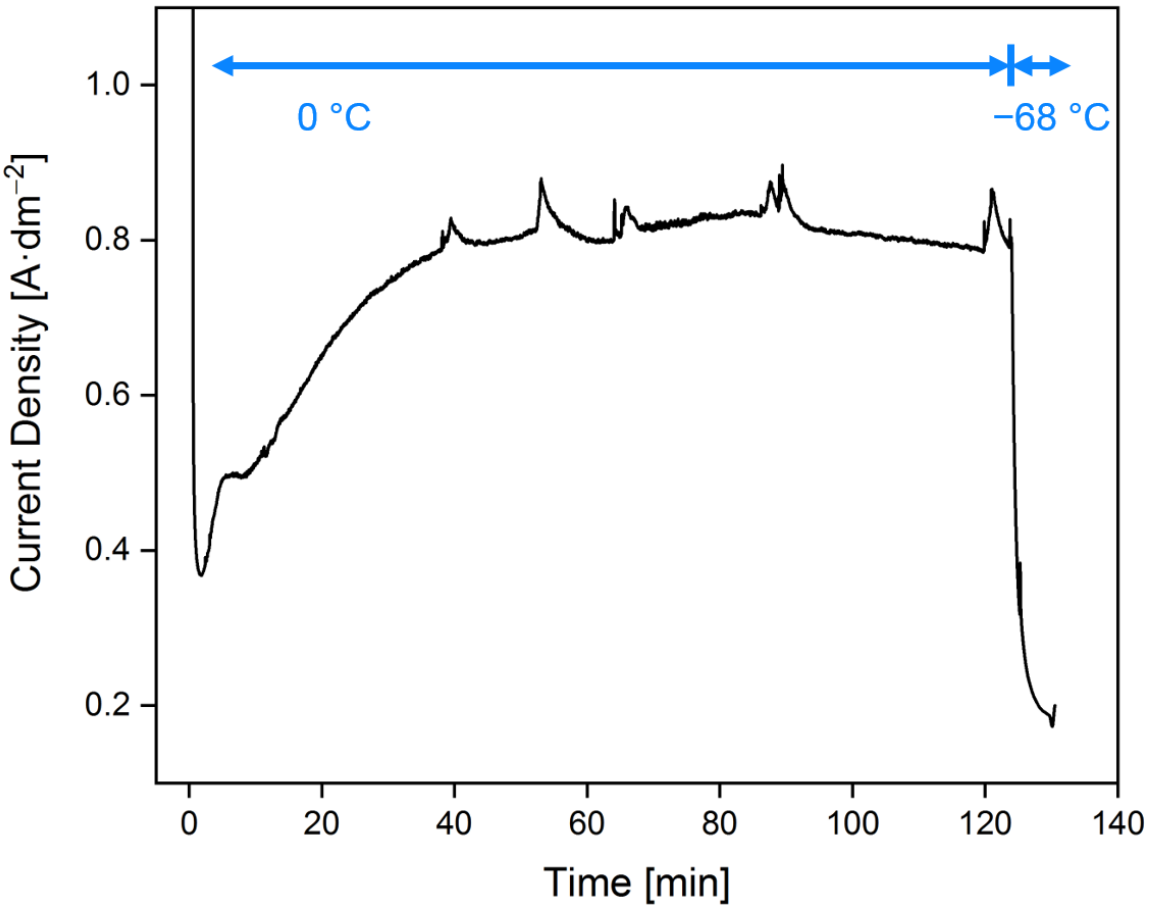

Figure 74: Chronoamperogram of Ni|NiF_x|HF_l‖HF_l|$H_{2,g}$|Ni ($x \geq 2$) at +6.0 V for 120 min at 0 °C and 10 min at –68 °C . The operator-induced spikes in current density are due to vibrations upon the removal of the cooling bath in order to take photographs of the cell (Figure 73).

The behavior upon polarization with respect to the obtained current density-time curve (chronoamperogram) agrees well with the literature data.[58,510] Attempting to stabilize the black film, the CA was continued at –68 °C for 10 min, resulting a steeply decreasing current density. After the CA phase ended, the electrolyte was maintained at –68 °C, a temperature at which both NiF_3 and NiF_4 are reportedly stable.[126] The development of the anodic film was subsequently followed by an open circuit voltage scan (OCV), where the residual cell voltage decreased quickly from ca. +3.4 V to +1.8 V within 1 min and further decreased to +1.6 V during the following 9 min with the tendency to decrease even further (Figure 158 in the appendix). This process was accompanied by the decomposition of the black film (Figure 75) to a brownish film, which matches the color of a decomposed film as reported in reference [142].

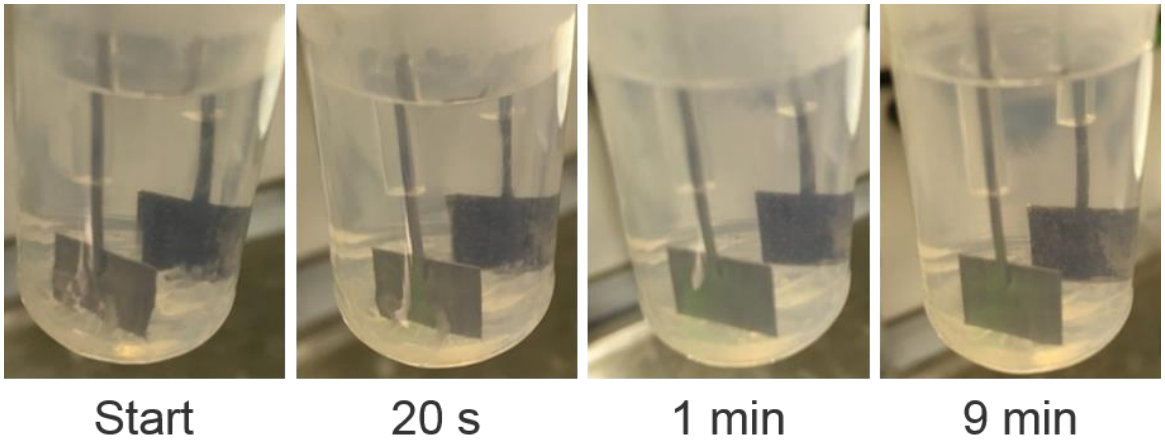

Figure 75: Decomposition of the anodic black film (anode depicted right) that has been formed during CA at +6.0 V vs. Ni for 130 min (Figure 73) under open circuit conditions to a brownish film in *a*HF at −68 °C. The corresponding OCV scan is shown in Figure 158 in the appendix.

After the elaboration of reliable conditions at which a substantial black film forms on a nickel anode in *a*HF, the questions arose how its thickness depends on the potential and what is the lower potential threshold where the black film becomes unstable. Therefore nickel electrodes were polarized in a chronoamperometric experiment at a cell potential of +6.0 V for 60 min. After that, the cell potential was lowered to +5.0 V. In the same experiment the potential was subsequently lowered in consecutive 0.1 V steps every 3 min, while the current density was measured (Figure 76).

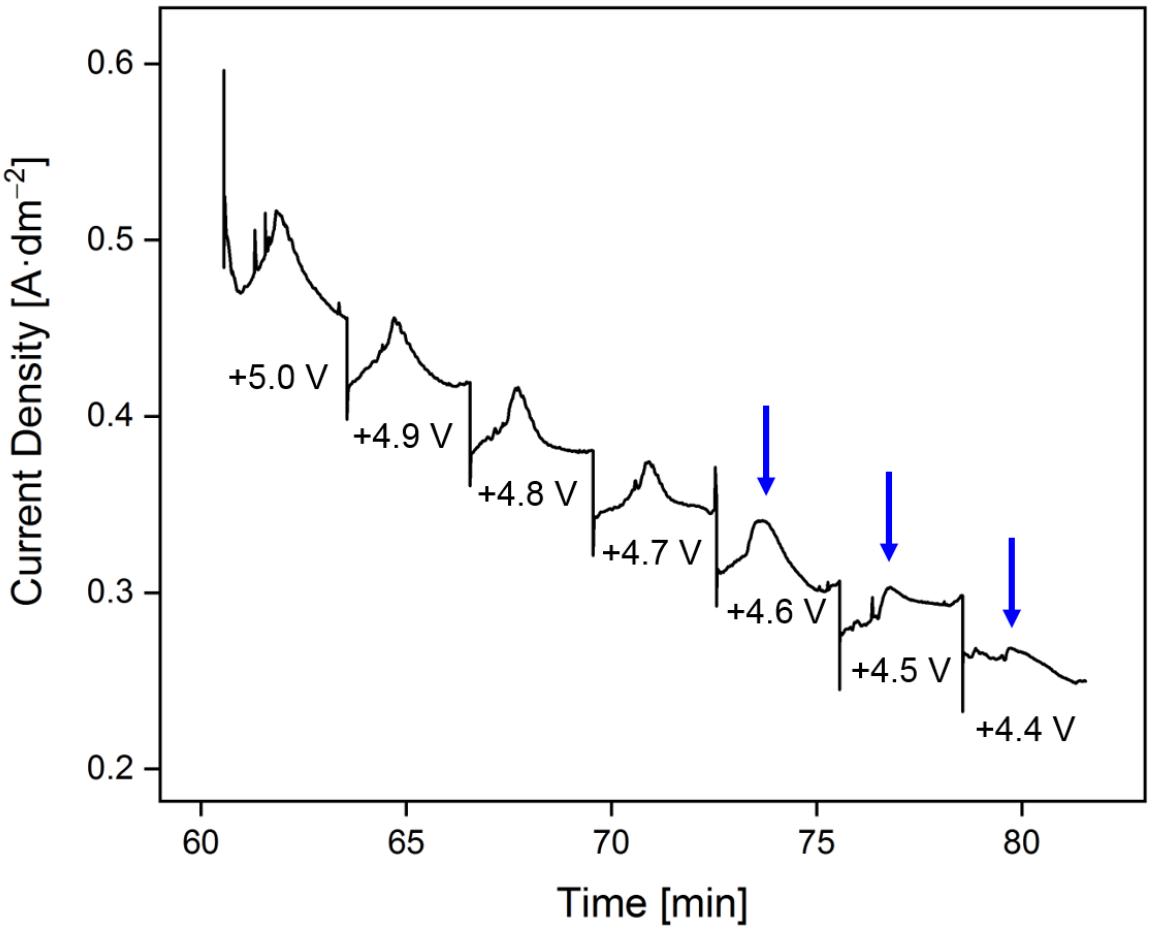

Figure 76: Chronoamperogram with consecutively lowered 0.1 V steps after an initial conditioning phase of a system Ni|NiF_x|HF_l‖HF_l|$H_{2,g}$|Ni ($x \geq 2$) at +6.0 V for 60 min. The time scale refers to the absolute run time of the CA experiment. A maximum in current density indicative for the re-oxidation/stabilization of the black film after a change in potential was not observed below a cell potential of +4.5 V and is highlighted by blue arrows.

At every potential step in the range from +5.0 to +4.5 V, a local maximum in current density was observed, which is interpreted as the re-oxidation of the film upon stabilization of the potential that is intermittently destabilized upon each potential change. The respective height of the maximum corresponds to each potential step, indicating a thinner film at lower potentials and vice versa. The threshold, where no re-oxidation of the black film was observed, was found at +4.4 V. The simultaneous color changes on the anode's surface resemble these observations (Figure 77).

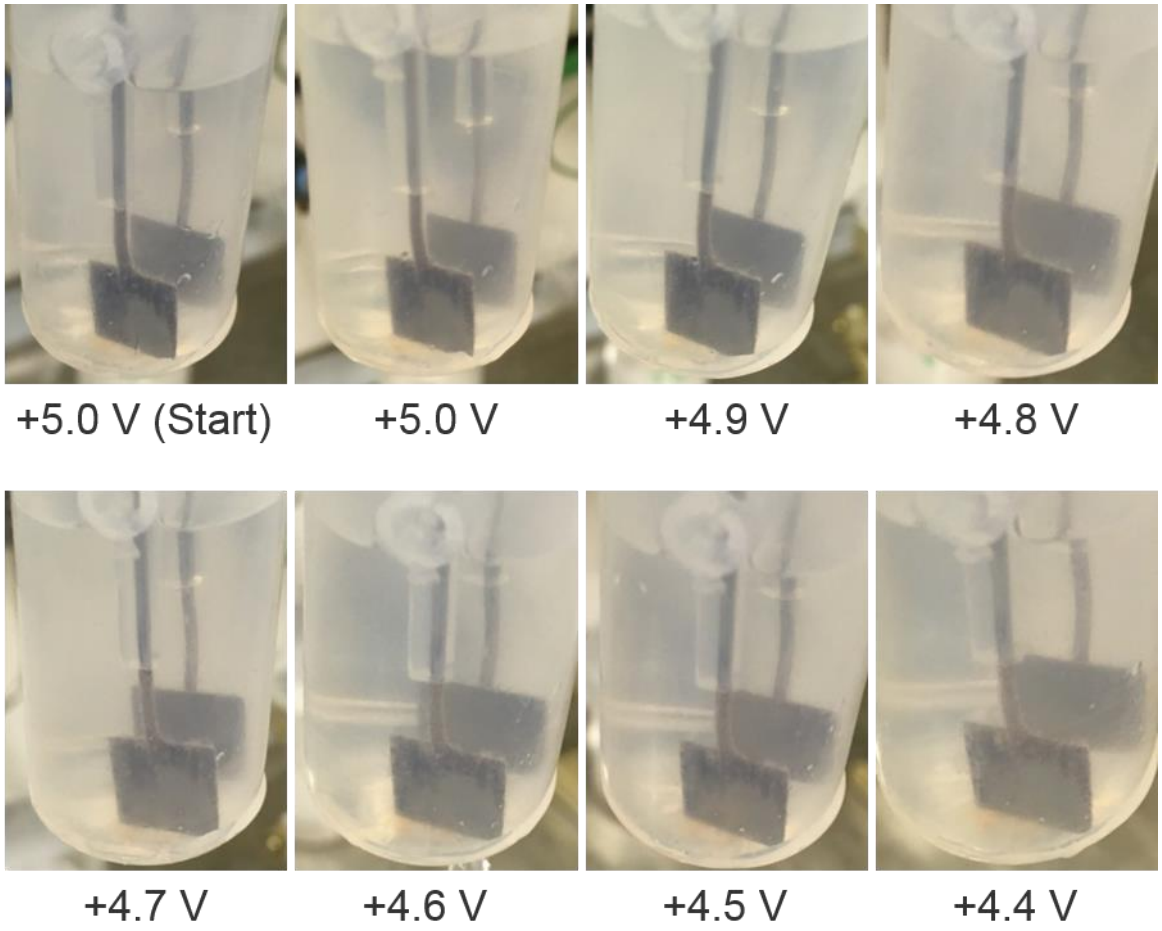

Figure 77: Photos of the backside of the nickel anode (left) and cathode (right) in liquid *a*HF at 0 °C after an initial polarization (CA) at a cell voltage of +6.0 V for 60 min at consecutively lowered potentials (potential change every 3 min). The photos were taken at the beginning of the +5.0 V phase, and afterwards at the end of each potential step, when the potential was found to be stabilized (Figure 76). The black color has been completely vanished at +4.4 V. The backside of the anode was not completely covered with the black film and was thus chosen for a better contrast.

Upon lowering the potential, the black color of the anodic film was found to bleach and to be completely vanished at +4.4 V. This is associated with a decreasing thickness of the black film, which is therefore potential dependent and completely destabilized at potentials below +4.5 V (vide supra). This threshold thus corresponds to the usual cell potential range of the industrial process (+4.5 to +6.0 V).[50]

After the decomposition of the anodic black film in each experiment, especially after an extended decomposition period, non-negligible amounts of a colorless to slightly brownish solid collected at the bottom of the cell, as depicted in Figure 78.

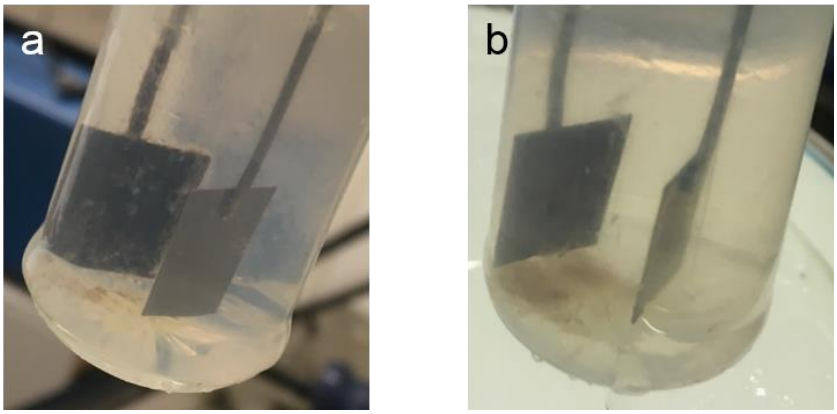

Figure 78: Nickel anode (left) and cathode (right) in liquid *a*HF after a) applying a cell potential of +6.0 V for 120 min and b) the decomposition under open circuit conditions for 60 min accompanied by NiF_2 collecting at the bottom of the cell.

In order to elucidate the species apparent on the anode's surface after decomposition, a sample for powder X-ray diffraction (PXRD) was prepared as follows: A nickel wire (PFA-insulated like the plate electrodes) was polarized at +6.0 V for 120 min in *a*HF at 0 °C, while a black film was formed on the anode. After that, the electrolyte was cooled to −80 °C and the anodic film allowed to decompose within three minutes. The Ni wire was then quickly transferred into a PFA tube filled with perfluorinated ethers (low-melting mixed composition) that was held at −80 °C as well. The hydrolysis of the decomposition products was estimated to be low due to the evolving HF vapor during the transfer of maximal two seconds. Colorless and dark-brownish fragments were subsequently scratched of the wire, conserved in the perfluorinated ether oil and subjected to PXRD measurements. The diffractograms of both samples are featured in Figure 79 in comparison with simulated literature data of Ni (fcc),[511] NiF_2 (rutile)[257] and NiF_3 ($Li[SbF_6]$ type).[166]

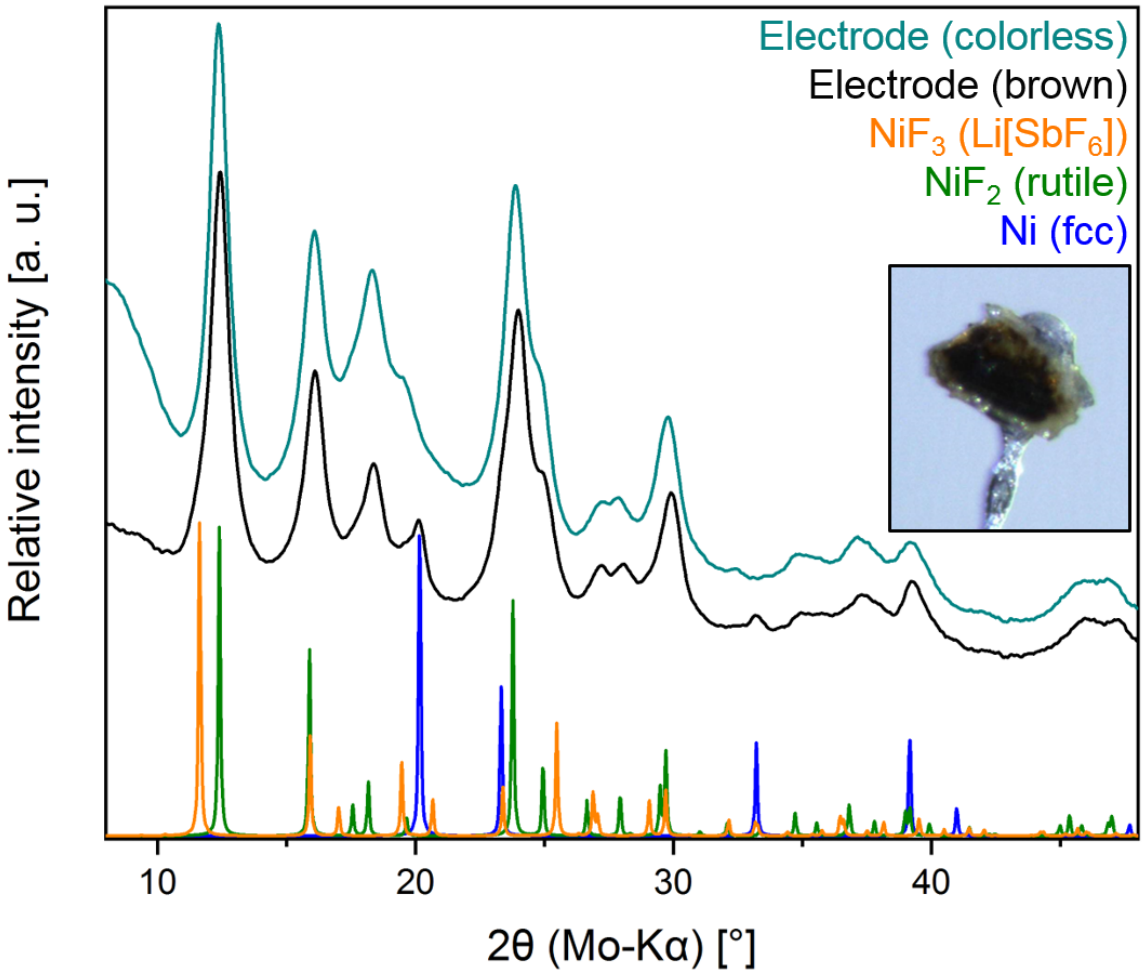

Figure 79: Powder X-ray diffractograms of surficial fragments of a decomposed Ni anode in comparison with simulated diffractograms based on the structures of Ni (fcc),[511] NiF_2 (rutile)[257] and NiF_3 (Li[SbF_6] type).[166] A dark-brown fragment is shown for illustration.

The PXRD data revealed that the dark-brown fragments contained mostly NiF_2 and traces of elemental nickel. The colorless fragments contained NiF_2 with an even smaller fraction of Ni^0, while no indications for NiF_3 were found. A contribution of elemental nickel by scratching the sample off the Ni wire cannot be excluded.

According to these results, the species apparent in the black film most likely cannot be elucidated via ex-situ methods. With the perspective to investigate the anodic processes in-situ via XAFS spectroscopy, the morphology of the surface was studied by SEM, which allowed to estimate the thickness of the film. For this purpose, a sample was generated under analogous conditions (anodization at +6.0 V for 120 min in *a*HF at 0 °C, see also Figure 78), but with half of the anode masked with PTFE tape to create a visible step to enable the estimation of the thickness of the anodic layer. During the conditioning phase at +6.0 V a constant gas evolution was monitored at the masked site, presumably caused by the partial decomposition of PTFE on the anode's surface. This led to a clearly visible step between areas of metallic luster (thin NiF_2 layer) and the strongly

corroded parts (thick NiF_2 layer) of the anode. The anodic film was allowed to decompose under open circuit conditions and the electrode was subsequently subjected to SEM measurements.

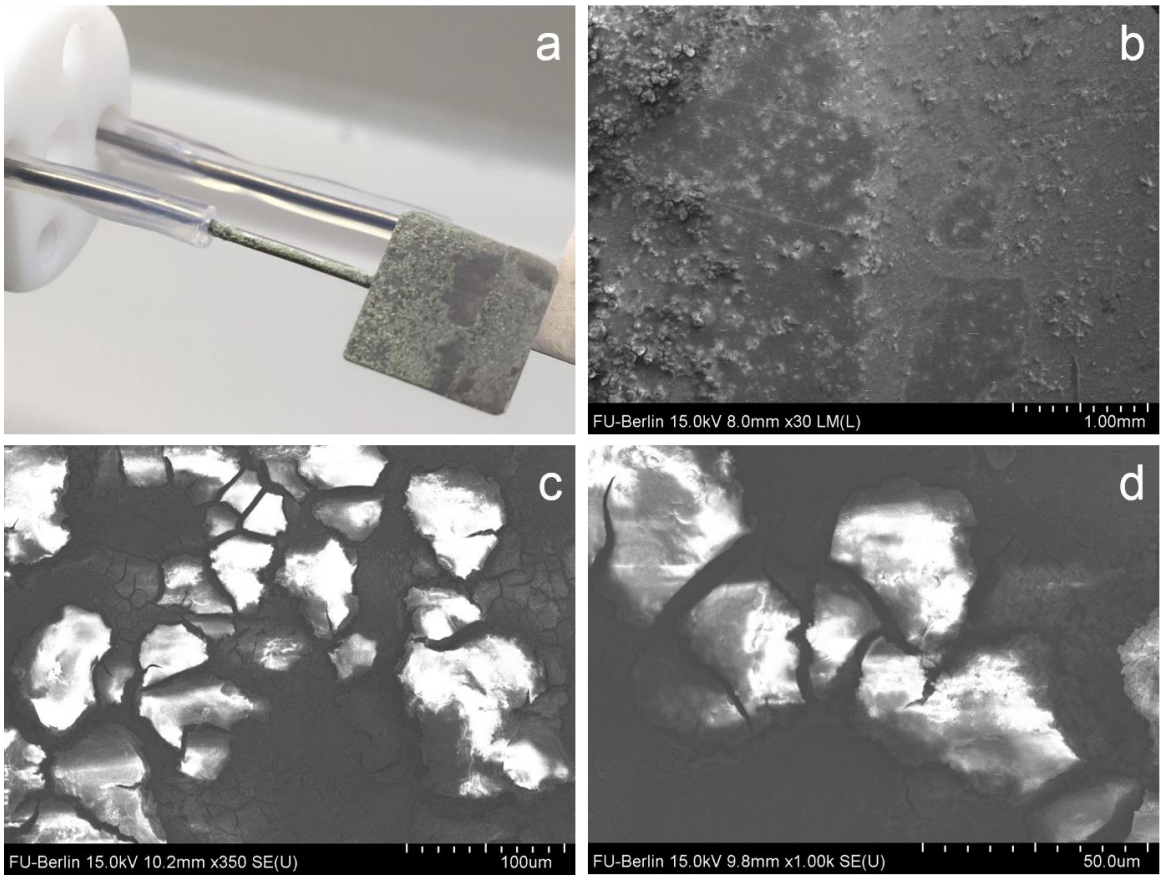

Figure 80: Photo (a) and SEM images (b, c, d) of a nickel electrode that had been anodized at +6.0 V cell voltage for 120 min in liquid *a*HF and decomposed afterwards under open circuit conditions. The SEM images b, c and d depict the 30-, 350- and 1000-fold magnified surface of the electrode, respectively.

The SEM images (Figure 80) revealed particle sizes of 50–100 µm on average, which were found to be sufficiently large to investigate a decomposed anode via XAFS spectroscopy. An analogous sample was therefore prepared and mounted in a 3D-printed sample holder that was covered with a single layer of Kapton® foil for the measurement of XANES spectra in fluorescence (Figure 81).

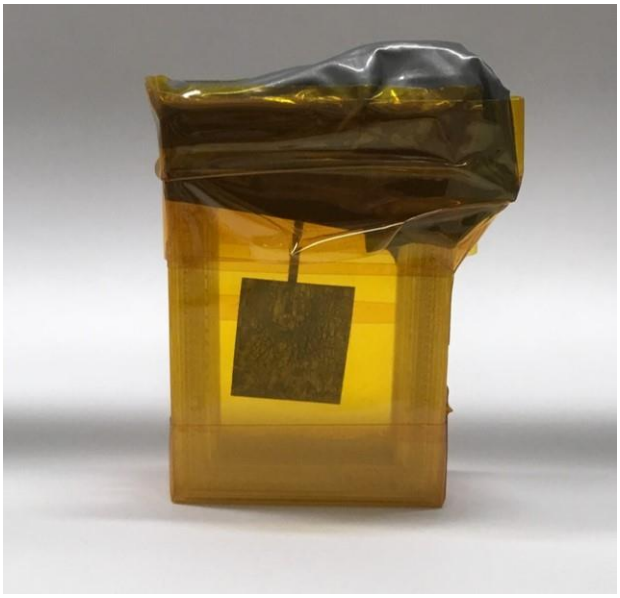

Figure 81: Decomposed anodic film on a nickel plate electrode for the measurement of XANES spectra in fluorescence mounted in a 3D-printed sample holder covered with a single layer of 125 µm-Kapton® foil.

The XANES spectra of the decomposed anodic film revealed contributions of 4.2 % NiF_2 and 95.8 % Ni (Figure 82, full range in Figure 168 in the appendix) resulting from the linear combination of data acquired for the standards Ni and NiF_2 (Figure 169 in the appendix). These values are promising, since the thickness of the anodic black film is assumed to significantly surpass the thickness of the decomposed film in view of the amounts of NiF_2 that are found on the bottom of the cell after decomposition.

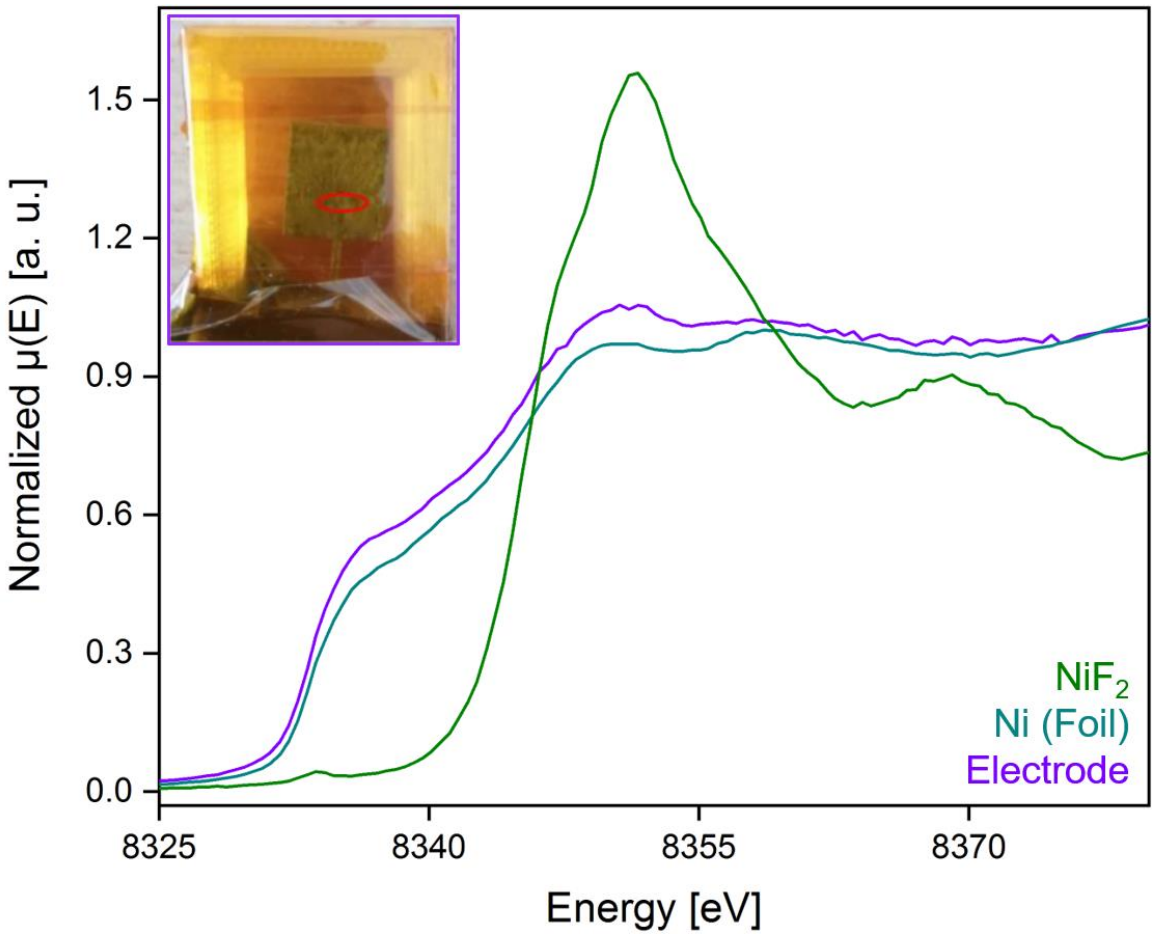

Figure 82: Ni K-edge XANES spectra in the range 8325–8380 eV at a spectral resolution of 0.5 eV of a decomposed nickel electrode (purple, photo with the measurement position highlighted in red) and the standards Ni (foil, transmission measurement, turquoise) and NiF_2 (green).

3.4.2 In-situ Investigations

3.4.2.1 Development of XAFS Cells

The ex-situ investigation of the anodic film formed under the conditions of the Simons process revealed that even a thin film of NiF_2 can be discriminated from underlying Ni bulk material by their XAFS with respect to suitable reference standards (Section 3.4.1). An electrochemical cell to allow for XAFS spectroscopy at the Ni K-edge on samples in liquid *a*HF has not been reported yet. Therefore, an electrochemical cell for the in-situ characterization of the anodic black film had to be developed that fulfills the following requirements:

- resistance to liquid and gaseous *a*HF (cell body, window, seals)
- temperature maintainable at 0 °C (reducing the vapor pressure of *a*HF)
- electrode surface areas sufficiently large to allow for XAFS spectroscopy and photography
- thin window material (Ni K-edge at 8333 eV)
- electrodes closely adjustable to the window (Ni K-edge at 8333 eV)

The latter two points are essential to improve the signal-to-noise ratio, since the absorption length is short at the soft Ni K-edge of 8333 eV,[175,182] even for materials like *a*HF (electrolyte) and fluorinated polymers (suitable window material).

Next to the experimental requirements, the setup must meet the following safety criteria:

- leak proof cell design (*a*HF electrolyte)
- closed but pressure balanced cell design
- chemical deactivation of HF
- transportable setup
- operable without a fume hood

The safety criteria are particularly important, since the electrochemical cell can only be filled with *a*HF in a laboratory with stainless-steel high vacuum equipment to allow for the safe handling of HF (cf. Figure 157 in the appendix). Since there is no corresponding on-site solution at the synchrotron source BESSY II (Berlin) available, the transportability of the setup must be ensured. Any HF exiting the cell via different pathways must be chemically deactivated, which is especially important because no fume hood is available at the beamline.

Nickel absorbs X-rays at 8448 eV (a value above the edge within the measuring range in this work, see below) with 326 $cm^2 \cdot g^{-1}$[512] more strongly than H, C and F with $4.71 \cdot 10^{-3}$, 3.37 and

12.59 $cm^2 \cdot g^{-1}$,[513] respectively. The latter three elements are important for the cell design with respect to the *a*HF electrolyte and a fluoro-plastic like FEP (suitable window material, see below).

Table 29: Selected materials with their densities ρ, linear absorption coefficients μ and absorption lengths μ^{-1}. μ and μ^{-1} are both calculated at 8448 eV.

Species	**ρ [g·cm^{-3}]**	**μ [cm^{-1}]**[a]	**μ^{-1} [µm]**[a]
Ni	8.902 (25 °C)[b]	2897.60	3.45
NiF_2	4.7 (r.t.)[b]	951.86	10.51
FEP ("C_5F_{10}")	2.2[c]	22.83	438.02
HF	1.015 (0 °C)[d]	12.14	823.72

[a] calculated values based on the data taken from references [512,513], [b] data taken from ref. [29], [c] specific gravity ranges from 2.14 to 2.17 g·cm^{-3} according to ref. [514], [d] data taken from reference [2].

Aiming for a value of $\mu \cdot t \leq 3$ above the edge, as recommended in the literature,[175,179] would require the layer thickness of Ni to be lower than 10 µm. Applying high cell potentials on nickel electrodes in *a*HF caused severe corrosion on the anode (cf. Section 3.4.1), yielding NiF_2 particles sized 50–100 µm (cf. Figure 80). Considering these facts, the use of thin nickel foils as electrode materials for the measurement in transmission for the in-situ XAFS cell is precluded. A thick anode is necessary to supply sufficient amounts of elemental nickel for the generation of a black film instead. Moreover, the short absorption lengths around the soft Ni K-edge[175,182] of the materials featured in Table 29 add the demand of thin layers of FEP and *a*HF to the cell design.

According to these requirements, an electrochemical cell for the in-situ characterization of a black anodic film by XAFS spectroscopy in fluorescence was developed (Figure 83). Its functional principle is described in the following and additionally depicted in Figure 162 (exploded assembly drawing), Figure 163 (all parts and materials), Figure 164 (sealing principle) and Figure 165 (HF shield) in the appendix.

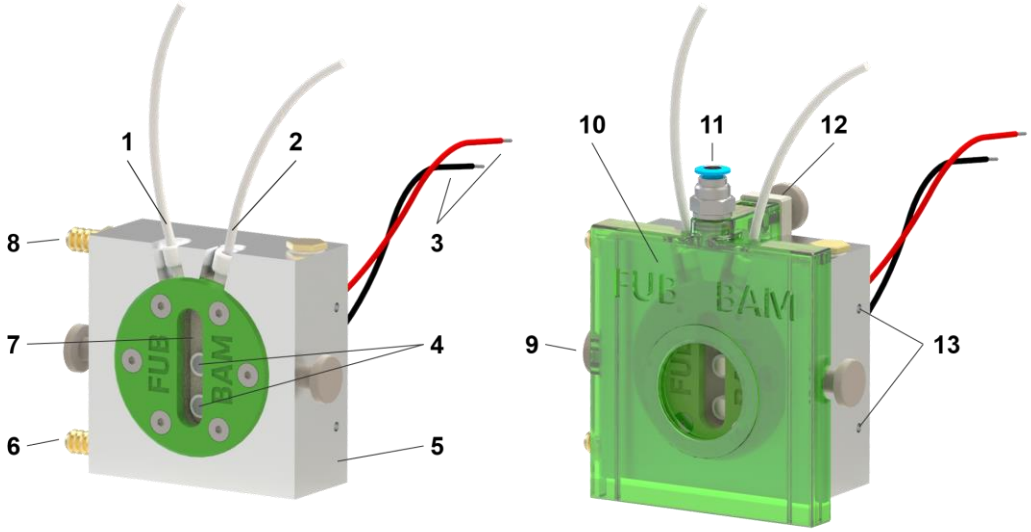

Figure 83: Scheme of the electrochemical in-situ XAFS cell (left) and assembled with an additional HF shield (right) to prevent an impact of HF on the X-ray detector. The cell consists of the following parts: **1**) liquid *a*HF inlet, **2**) exhaust gas (H_2/HF) outlet, **3**) connector cables, **4**) nickel electrodes, **5**) heat sink and cell mount (aluminum), **6**) inlet for coolant (EtOH), **7**) HF reservoir with FEP window (50 µm-foil), **8**) outlet of coolant (EtOH), **9**) fixation screw for fixing the electrochemical cell within **5**, **10**) HF shield with FEP window (25 µm-foil), **11**) inlet for gaseous N_2, **12**) mounting clamp for HF shield, **13**) M6 threads for connecting the setup to a stable mount.[515]

A cylindrical cell body made from PCTFE depicts the center piece of the electrochemical in-situ XAFS cell. It features a central oblong hole representing the reservoir of *a*HF (V_{max} = 3 cm^3) and drilled holes with each a threaded part providing sockets for the HF inlet, exhaust gases outlet and the PTFE coated nickel electrodes. The latter three items are sealed with two FKM O-rings each, and the nickel electrodes thereby become freely adjustable towards the window of the cell. A 50 µm-FEP foil is used as the window material and is press-fitted in the *a*HF reservoir with a circumferential bead of the 3D-printed green cap of the cell. It must be noted that the low surface tension of *a*HF[516,517] (the primary substance for leak testing was water) made it necessary to apply halocarbon wax as an additional sealant. Despite making the cell reliably leakproof, the literature-known (long-term) permeability of fluorinated polymers such as FEP for HF and other molecules,[100] lead to constant HF liberation from the thin-walled window (FEP foil) applied in the in-situ XAFS cell. Consequently, the safe use of this cell outside the fume hood was not possible. Therefore, a shield was developed, which allowed a slight but constant N_2 stream to pass over the window to transport any gaseous HF to the deactivation in a KOH/ice bath in a basin located beneath the cell setup. After its passage through a bubbler filled with perfluorinated hexanes, the exhaust gas stream (H_2/HF) is purified from HF by passing a U-tube filled with soda lime

(NaOH/CaO), which is illustrated in Figure 84. For safety reasons, the quantity of soda lime used was chosen to be double the amount of substance of *a*HF.

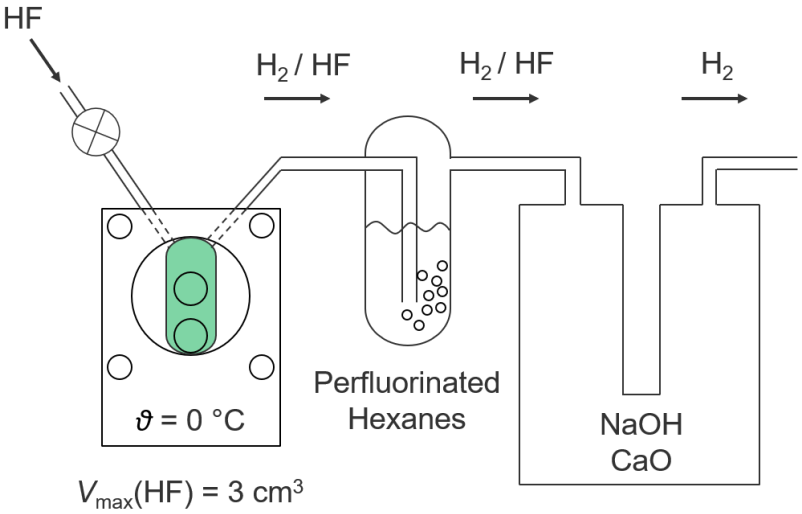

Figure 84: Schematic depiction of an in-situ XAFS cell containing a mobile HF deactivation. The green highlighted area represents the *a*HF container of the electrochemical cell. A photo of the applied setup is found in Figure 166 in the appendix.

The measurement of XAFS spectra of the room temperature stable Ni, NiF_2 and $K_2[NiF_6]$ are facile compared to the desired reference standards NiF_3, and especially NiF_4 since the latter are metastable or even unstable at room temperature, respectively.[126] In addition to that NiF_4 has not been structurally characterized.[269] Therefore, an XAFS cell was developed that provided a clear window while maintaining adequately low temperatures for these samples in a dual-window setup, as depicted in Figure 85. A corresponding cutaway drawing is shown in Figure 167 in the appendix.

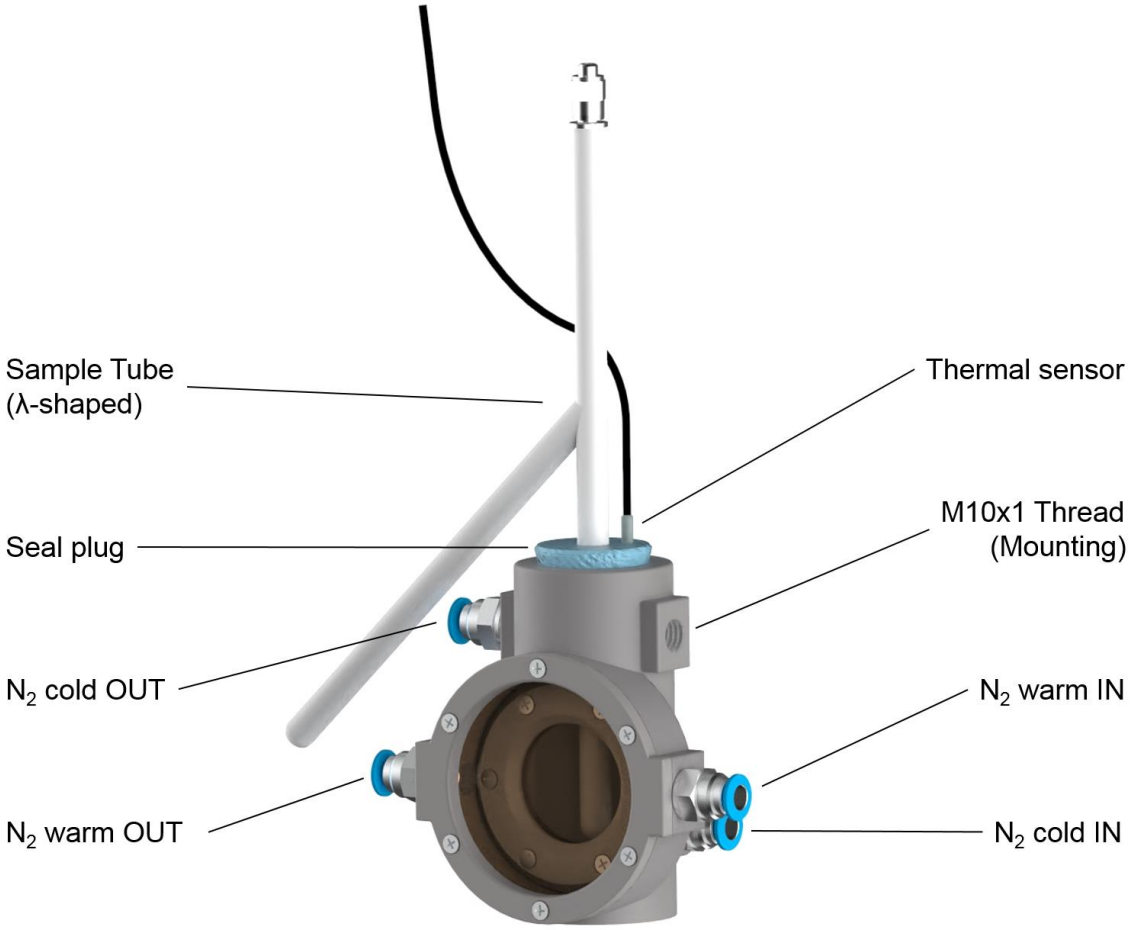

Figure 85: Functional principle of an XAFS cell designed for low temperature ($\vartheta < -60$ °C) reference measurements of NiF_4 and NiF_3 with a coolable inner sample container (cylindrical) and an outer, warm layer ($\vartheta \geq +10$ °C) to prevent icing of the windows.[515]

The dual-window approach allowed for temperatures below −60 °C in the sample compartment by passage of a cold nitrogen stream generated by passing gaseous N_2 through liquid N_2 in a bubbler-like Dewar vessel setup. As the temperature was found to be directly proportional to the gaseous N_2 flow, colder temperatures were achieved at higher flow rates. A warm N_2 stream was passed between the two windows to prevent icing on the outer window. As the temperatures depend on each other, independent flow controlling and temperature sensing for both the warm and the cold N_2 streams were necessary. Due to the large window sizes that are required for collecting the most possible fluorescent light with respect to the detector geometry, an overall higher flow rate is necessary when compared to the 'N_2-consumption' of a test-cell with windows of ½ the size in diameter. During the first cell tests, the condensation of water on the outer FEP layer was observed at temperatures below +10 °C.

3.4.2.2 Electrochemical Characteristics of the In-Situ XAFS Cell

Prior to the in-situ investigations of the black film, the in-situ XAFS cell was studied in terms of its electrochemical characteristics with respect to CV and CA, and the controlled formation of a black film. A cyclic voltammogram (Figure 159 in the appendix) comparable to the preliminary results (cf. Figure 72) was obtained for the in-situ XAFS cell and only one distinct oxidation feature was observed. As a result of the arrangement of the electrodes this feature had its maximum at 5.25 V, which is shifted by +0.7 V compared to earlier findings.[174]

In accordance with these results and the potential dependence of the film thickness (cf. Section 3.4.1), the cell potential for the polarization was chosen to be +8.0 V to ensure the formation of a substantial anodic film in a CA experiment (Figure 86).

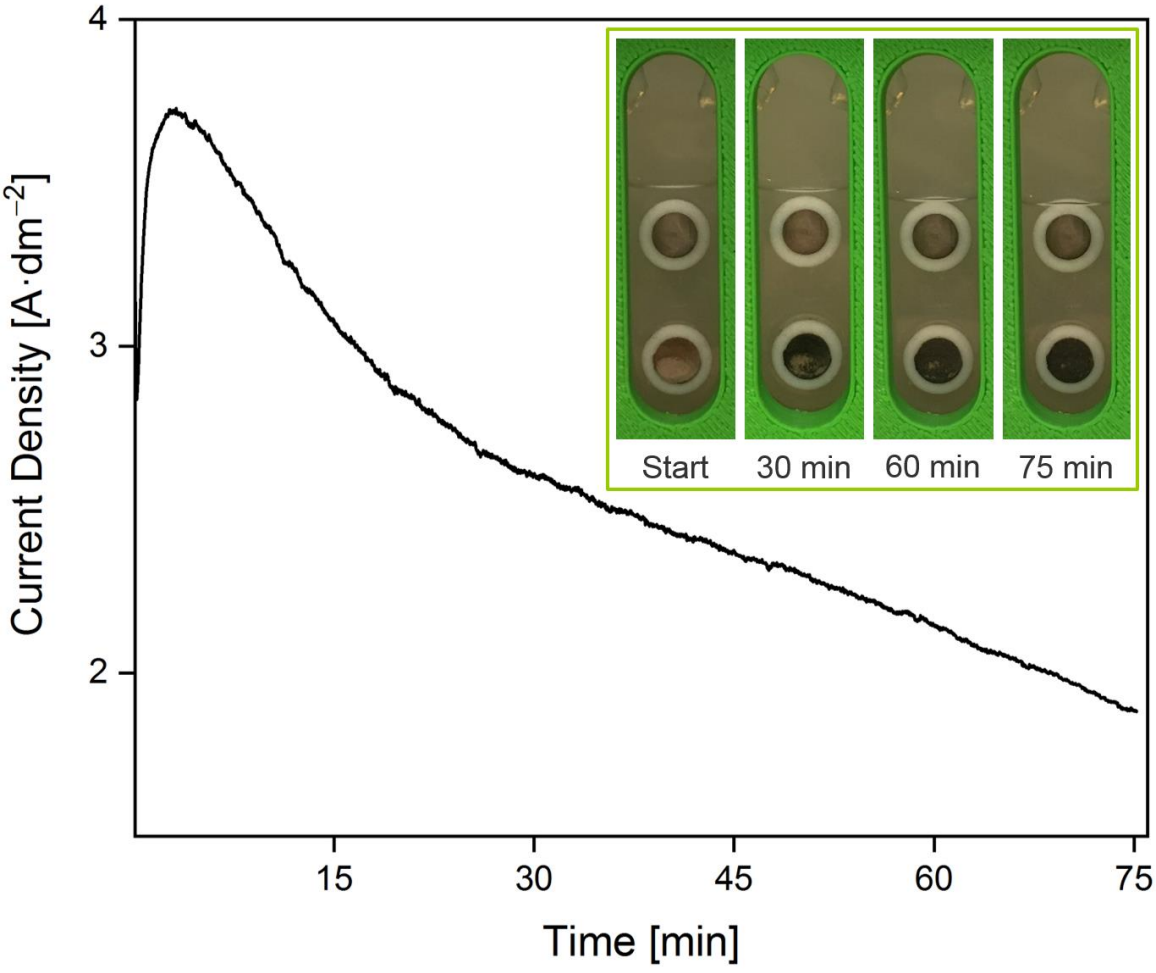

Figure 86: Chronoamperogram of a test polarization for the generation of a black film on the nickel anode at a cell potential of +8.0 V in the in-situ XAFS cell setup, and corresponding photos of the nickel anode (bottom) and cathode (top) in liquid *a*HF.

The formation of the black film on the anode began closer to the cathode and the complete covering of the anode was achieved after 75 min. The greyish shadow on the cathode and the slightly brownish shadow on the anode in the beginning resulted from a previous experiment with a reverse polarization of the electrodes. The decomposition of the black film was studied in a consecutive OCV measurement (Figure 87).

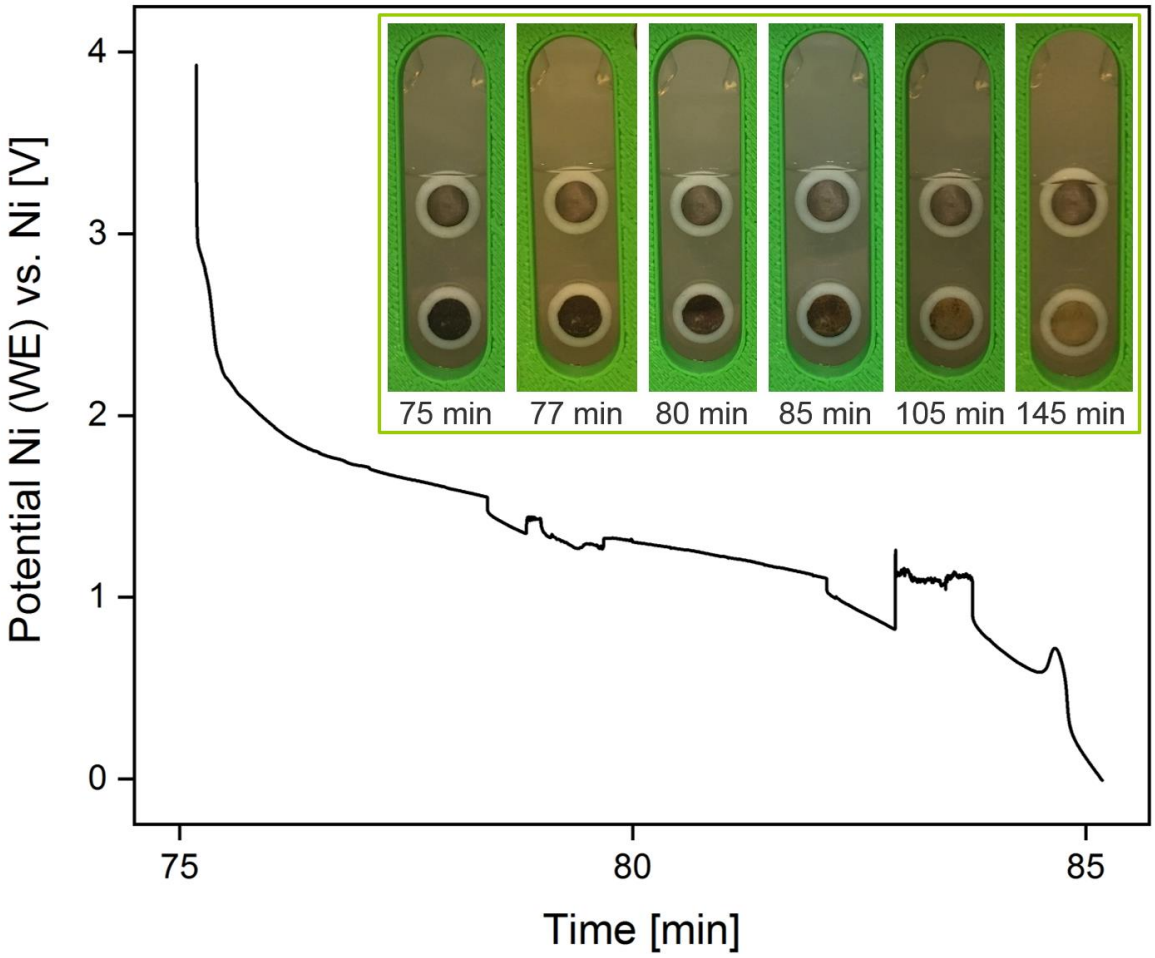

Figure 87: OCV scan until 10 min after the generation of a black film on the nickel anode at a cell potential of +8.0 V in liquid *a*HF and photos of the nickel anode (bottom) and cathode (top). The time scale refers to the absolute run time of the experiment, including CA (Figure 86).

The black color of the anodic film bleached to a brownish film during 10 min under open circuit conditions, which correlates to the loss in residual cell potential, and fully decolorized during further 60 min. The development of the anodic film is thus comparable to the ones observed in several ex-situ experiments in Section 3.4.1 and the observations in reference [142]. Thus, these tests proved the electrochemical in-situ XAFS cell fully functional.

3.4.2.3 In-Situ Characterization of the Black Anodic Film

As discussed in Section 1.4.1.1 and Section 1.5.1, there are mainly two fundamentally different mechanisms that could account for the observations in the Simons process, i.e. the EC_bEC_N and a mediated (presumably by a high valent nickel fluoride) mechanism. The latter mechanism would necessitate an oxidizing agent, namely nickel in an oxidation state higher than +II, to be present on the anode. The method of choice to distinguish between the different oxidation states on the surface of the electrode is XAFS spectroscopy at the Ni K-edge at 8333 eV.[182]

Analogously to the preliminary studies with the electrochemical in-situ XAFS setup, the electrochemical cell was filled with liquid *a*HF and – before applying any potential – the surface of the anode was studied by XAFS spectroscopy. Not surprisingly, the anode was found passivated by a thin layer of NiF_2, which had also been reported in an ex-situ XPS approach by Scherson and coworkers.[167,168] Afterwards, the electrochemical cell was subjected to a non-stop electrochemical program:

1) OCV scan for 10 min
2) CA at +5.5 to +8.9 V (increased in 0.1 V steps every 10 min)
3) CA at +8.7 V for 127 min
4) OCV for 120 min

The consecutive steps of the program are described in the following and an overview of the anodic film development is depicted in Figure 88.

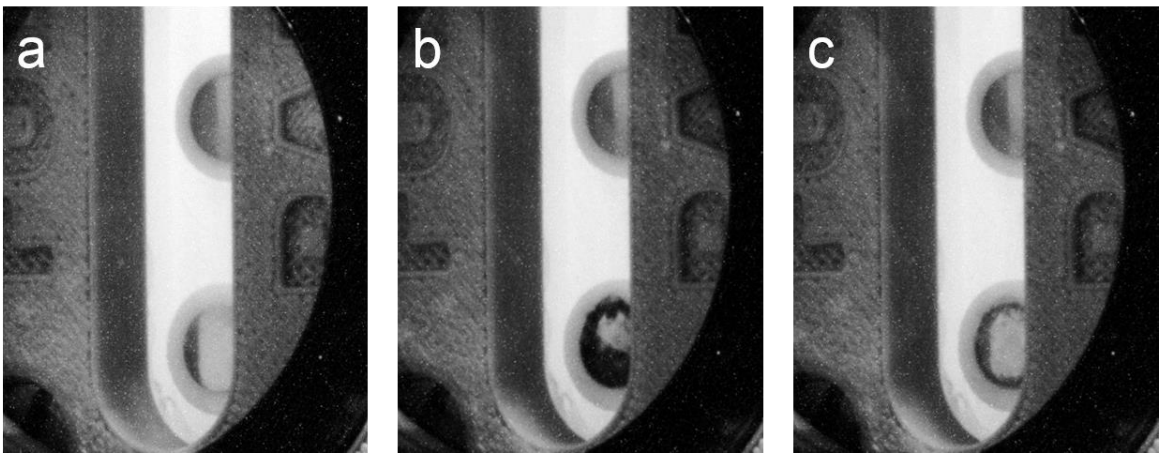

Figure 88: Photos of the electrochemical in-situ XAFS cell with nickel anode (bottom) and cathode (top) in liquid *a*HF at different steps of the electrochemical non-stop program. The anode features a) a metallic luster at 0 V, b) a black film after the complete conditioning period at +8.7 V and c) a bleached film after decomposition under open circuit conditions for 120 min. The cathode remained visibly unchanged during the whole process.

After an initial OCV scan (cf. Figure 160 in the appendix) resulting in an expected cell voltage of ca. 0 V, a potential of +5.5 V, slightly surpassing the maximum of the distinct oxidation feature in a CV scan (cf. Figure 159 in the appendix), was applied for 10 min. This potential was increased stepwise by 0.1 V every 10 min to a maximum of +8.9 V, while a XANES spectrum with an approximate measurement time of 6 min was recorded one minute after each potential change. After each XANES spectrum was recorded a photo of the cell was taken. The formation of the black film on the anode started in a position close to the cathode, grew further around the rim and then towards the central area of the anode. The stepwise development is depicted in Figure 178 in the appendix.

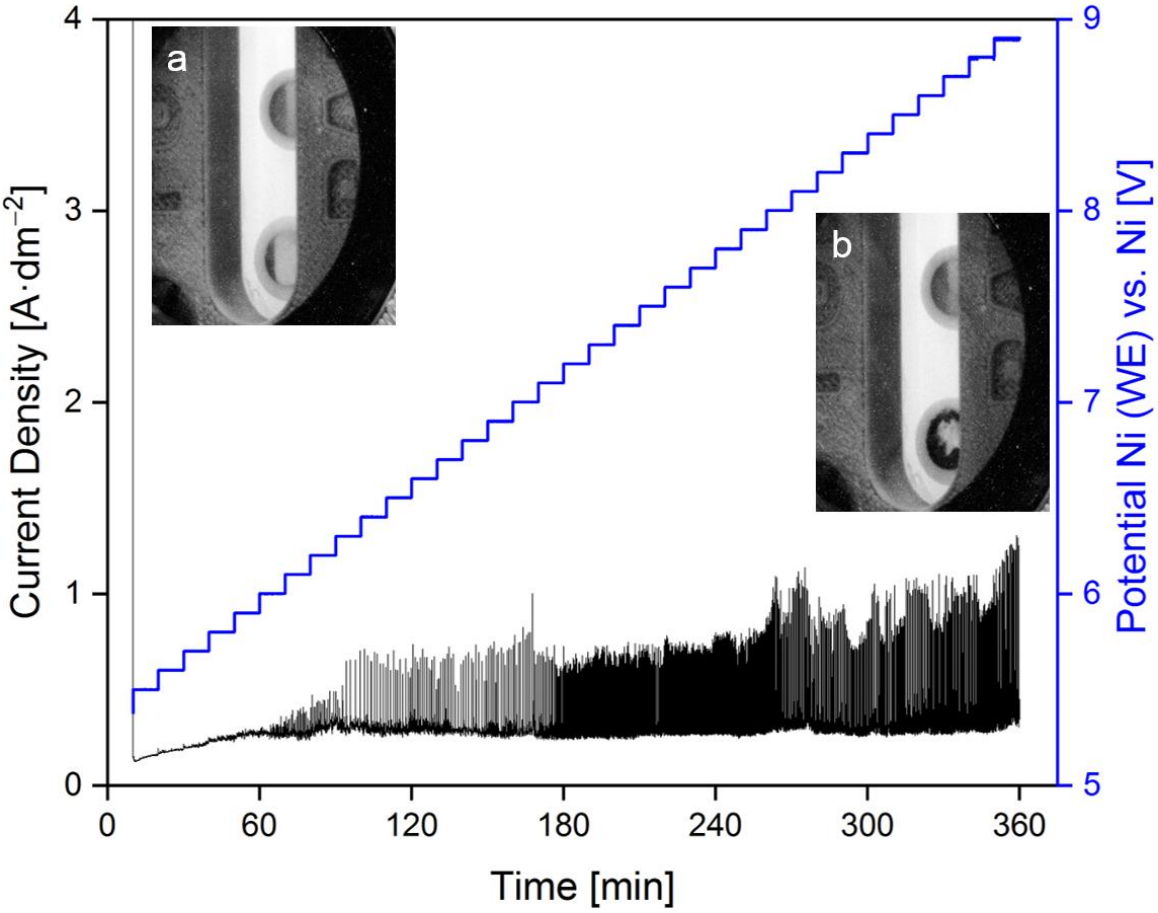

Figure 89: Chronoamperogram (left axis) and potential-time curve (right axis) of the primary conditioning phase with the potential increasing stepwise from +5.5 V to +8.9 V every 10 min. The photos depict the start (a) and end state (b) of nickel anode (bottom) and cathode (top) in liquid *a*HF.

After the primary conditioning phase with stepwise increased cell potentials (Figure 89), a potential of +8.7 V was applied for 127 min to further increase the film thickness (Figure 161 in the appendix). It must be noted that this potential (0.2 V lower than the last step of the primary phase at +8.9 V) was chosen for the prolonged conditioning period, because the electrochemical system appeared to be destabilized with more and stronger peaks in current density at potentials

higher than +8.7 V. After that, the decomposition of the black film was studied during an OCV scan (Figure 90), and photos were taken accordingly (Figure 179 in the appendix). The residual cell potential of about 2 V decreased to ca. 0 V within 90 min. That the final cell potential was found to be slightly negative is seen to be caused by NiF_2 films of different thicknesses of anode (thicker) and cathode (thinner). The cathode remained visibly unchanged during polarization (formation of the black film) and decomposition experiments (Figure 180 in the appendix).

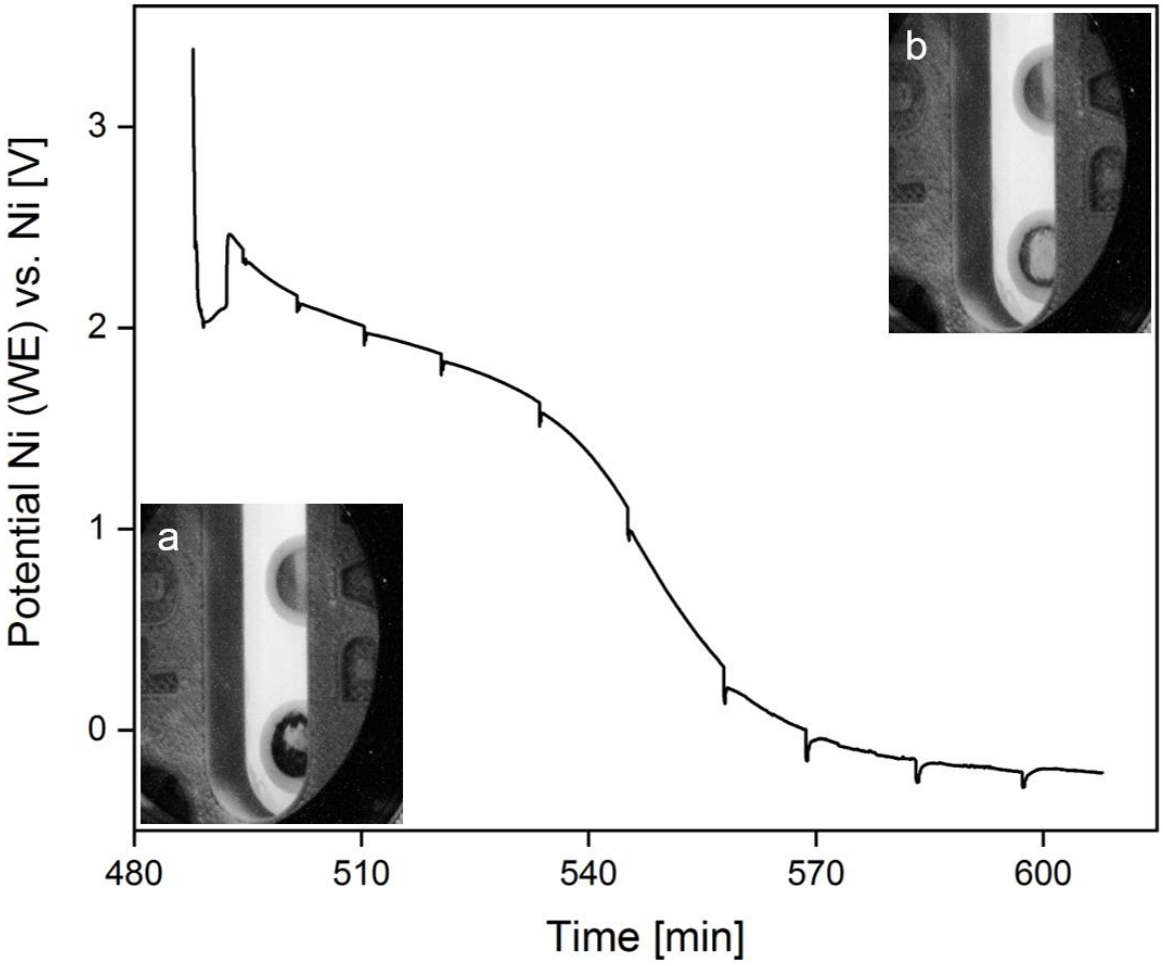

Figure 90: OCV scan during the decomposition of the black film and photos of start (a) and end state (b) of nickel anode (bottom) and cathode (top) in liquid *a*HF. The spikes in potential are associated with vibrations, which are caused by the movement of the detector in-between measurements of the XANES spectra. The time scale refers to the absolute run time of the non-stop electrochemical program.

Despite the applied high potentials, the black film did not fully cover the whole electrode (see the discussion below and Figure 95), especially in the center of the anode, where the Ni K-edge XANES spectra were initially recorded, with the beam spot 2 mm (horizontal) by 1 mm (vertical) focused onto the center of the electrode (Ø = 5 mm). Consequently, the spectra of the incompletely black anode resembled the ones recorded from the Ni electrode before polarization. Therefore, the measurement position was adjusted to the 'blackest region' in the lower left part of the anode (Figure 181 in the appendix) and all subsequent measurements were performed in this region. As

all photos were taken from a fixed angle, the analysis of the photos' colors allowed to follow and picturize the development of the anodic black film, as shown in Figure 91.

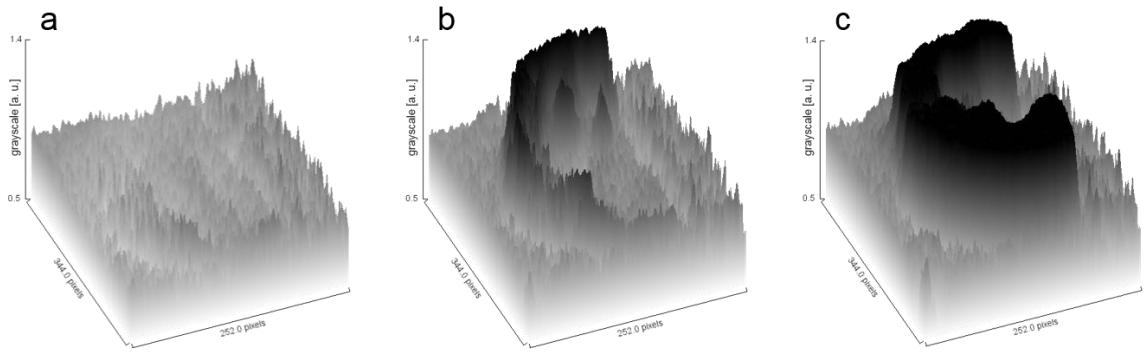

Figure 91: Color development on the nickel anode's surface in the electrochemical in-situ XAFS cell upon polarization at a) 0 V, b) +5.9 V and c) +8.4 V. The figures (a–c) were generated from the color difference of the photo of the anode at the corresponding potential and the photo of the anode before applying an external potential.

The Ni K-edge XANES spectra of the black and decomposed anodic film are compiled with those obtained for the reference substances Ni^0 (bulk anode exposed to *a*HF prior to the application of any external potential), NiF_2, NiF_3, NiF_4 and $K_2[NiF_6]$ in Figure 92 and in combination with their first derivatives in Figure 172 in the appendix. The XANES spectra and their first derivatives obtained from the reference materials are featured in Figure 173 in the appendix. They show the impact of HF on the nickel surface that leads to passivation (increased NiF_2 content) before polarization, and that the reference compounds in high oxidation states have a joint maximum at 8354.6 eV.

Consistent with the CA data (Figure 161 in the appendix), the spectra recorded during the prolonged conditioning phase at a cell potential of +8.7 V (Figure 170, first derivatives in Figure 171 in the appendix) did not show remarkable changes and resembled the one of the black film shown in Figure 92. The Ni K-edge XANES spectrum of the black anodic film revealed a shoulder at 8337.0 eV and two peaks at 8352.5 and 8354.0 eV, the latter representing the maximum of the white line. As it is already evident from the ex-situ characterization (Section 3.4.1), the anodic film is generally thin. This leads to the fact that all spectra of the anode contain elemental nickel, which is also reflected in the first derivatives of the XANES spectra featured in Figure 172 in the appendix. Upon comparison with the spectrum of NiF_2, the peak at 8352.5 eV indicates the presence of Ni^{II} in the black film. The maximum of the white line at 8354.0 eV is indicative for nickel in an oxidation state higher than +II,[166,262] as it can be compared with the coinciding maxima at 8354.6 eV, which were found for the reference compounds NiF_3, NiF_4 and $K_2[NiF_6]$. It must be noted that the measurement of XANES data of NiF_4 required the synthesis, purification, and transport of this sensitive substance at temperatures below −60 °C (see also Section 4.3.3). The present work

unveils the very first spectroscopical data for the elusive NiF_4[126] as a bulk compound (with respect to recent results on matrix-isolated molecular NiF_4).[268] Its Ni K-edge XANES spectrum featured an additional local maximum at 8369.1 eV. This peak was not observed for either NiF_3 or the black film and indicates that NiF_4 is less likely to be present in the anodic film than NiF_3.

Despite the direct assignment of the maxima at 8352.5 and 8354.0 eV to Ni^{II} and Ni^{IV} in terms of a mixed-valent $Ni^{II}[Ni^{IV}F_6]$[166,262] being appealing, it is not unequivocally possible. Since the XANES spectra show an average of the species apparent on the anode's surface,[175] more than one highly oxidized species could be present in the black film. This agrees with the preliminary results in reference [174] on the calculated stabilization of mono-valent NiF_3 (equal Ni–F bond distances) at high potentials. Moreover, most recent quantum-chemical calculations showed comparable energies for structures of mono-valent NiF_3 and mixed-valent $Ni^{II}[Ni^{IV}F_6]$ with longer (Ni^{II}–F) and shorter (Ni^{IV}–F) bond distances.[518]

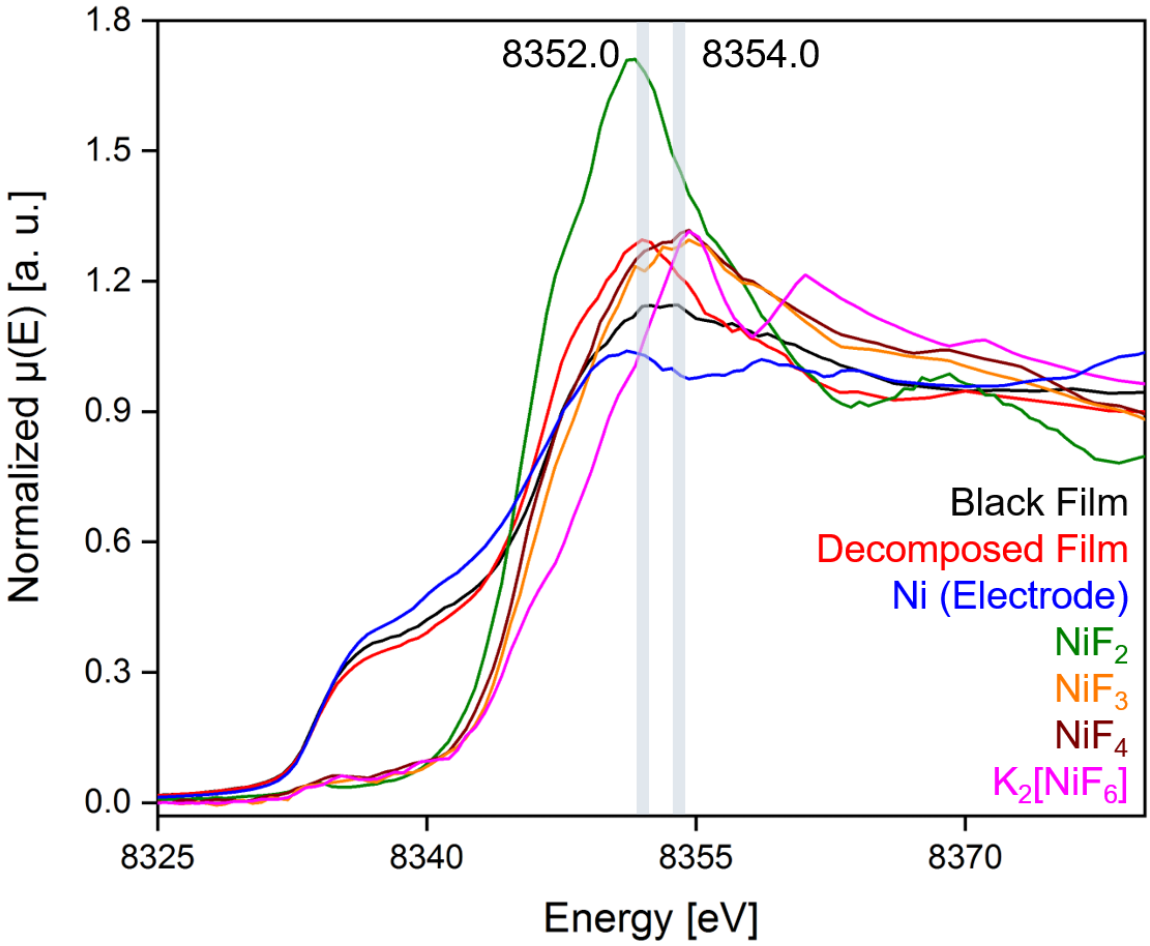

Figure 92: Ni K-edge XANES spectra obtained from an in-situ generated black film on a nickel anode (black trace), after its decomposition (red trace), and from the reference substances Ni (bulk anode that is exposed to liquid *a*HF, blue trace), NiF_2 (green trace), NiF_3 (orange trace) and NiF_4 (brown trace) as well as $K_2[NiF_6]$ (magenta trace). The maxima of the white lines of the black film and the decomposed film have been highlighted at 8354.0 and 8352.0 eV, respectively. A compilation with the corresponding first derivatives is shown in Figure 172 in the appendix.

From the ex-situ investigation, it is known that the black film decomposes below cell potentials of +4.5 V and that only NiF_2 and traces of elemental nickel are found on the surface of the anode after decomposition (cf. Section 3.4.1). In order to follow the decomposition process in-situ by their XANES spectra, applying the +8.7 V cell potential (CA) was discontinued and immediately followed by an OCV scan (Figure 90). Once induced, the decomposition of the black film led to a strong increase of the white line's intensity, a shift of its maximum to 8352.0 eV, and gave rise to a peak at 8370.0 eV. Both positions and their intensities agree well with the spectrum of NiF_2 and therefore the development of the XANES spectra corresponds to an increase of Ni^{II} centers (Figure 93). This process was accompanied by the strongly decreasing cell voltage (Figure 90).

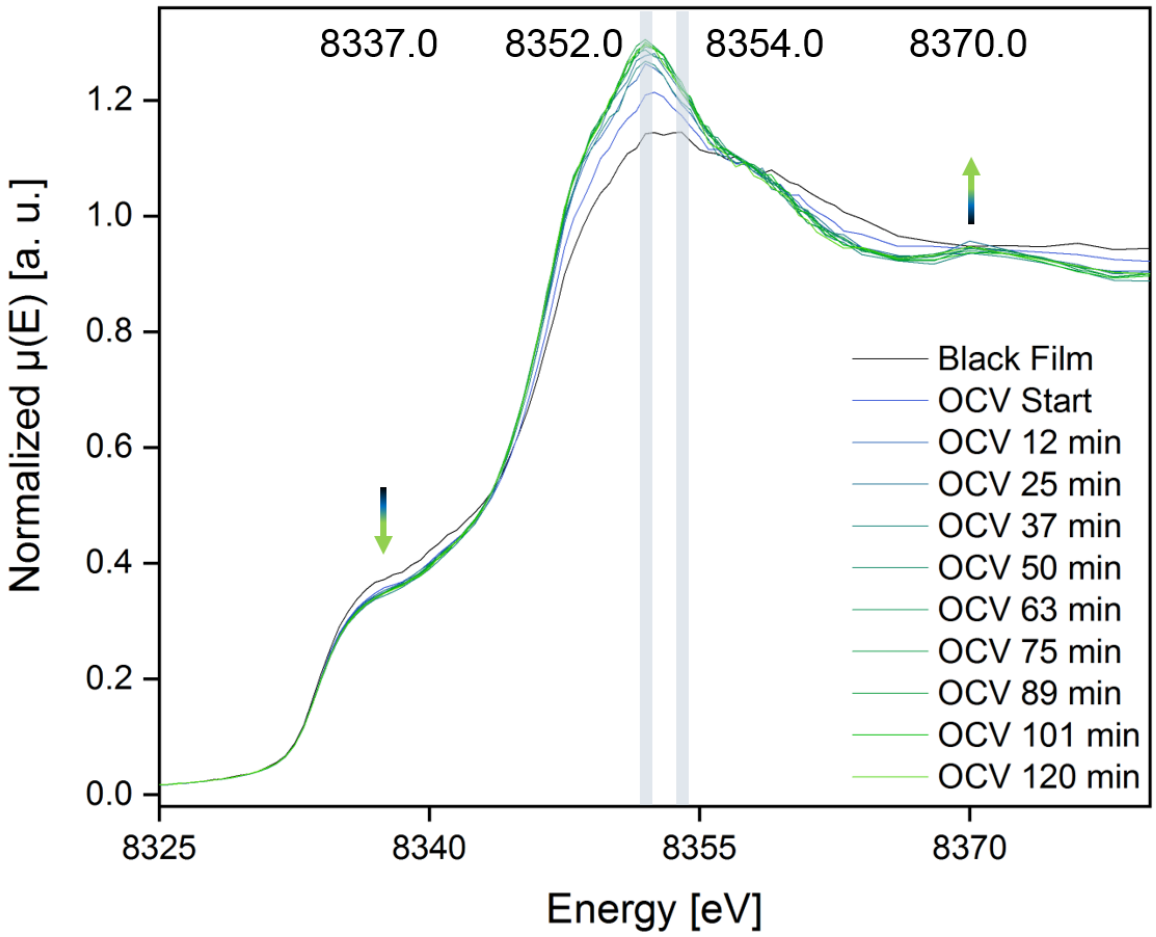

Figure 93: Ni K-edge XANES spectra recorded during the decomposition of the anodic black film (black trace) under open circuit conditions (see also the OCV scan in Figure 90) with the color transitioning from blue (start) to green (120 min). The spectrum after 120 min is identical with the "Decomposed Film" in Figure 92. The positions of the strongest changes have been highlighted for decreasing Ni^0 (8337.0 eV) and increasing NiF_2 (two features at 8352.0 and 8370.0 eV). The weaker features are additionally highlighted with arrows. The first derivatives of these spectra are depicted in Figure 175 and the identical spectra in the range 8300–8540 eV are found in Figure 174 in the appendix.

Just as important, the amount of elemental nickel significantly decreased upon the decomposition of the black film, which is evident from the visual inspection of the spectra in Figure 92 and Figure 93 (see also the first derivatives in Figure 175 and a larger range in Figure 174 in the appendix) with respect to the decreasing shoulder at 8337.0 eV. The linear combination fitting (LCF) of the XANES spectra obtained during the prolonged conditioning phase at +8.7 V (CA) and the decomposition (OCV) of the anode to the spectra of the reference materials Ni^0 (electrode), NiF_2 and NiF_3 shows the correlation between these species and is depicted in Figure 94.

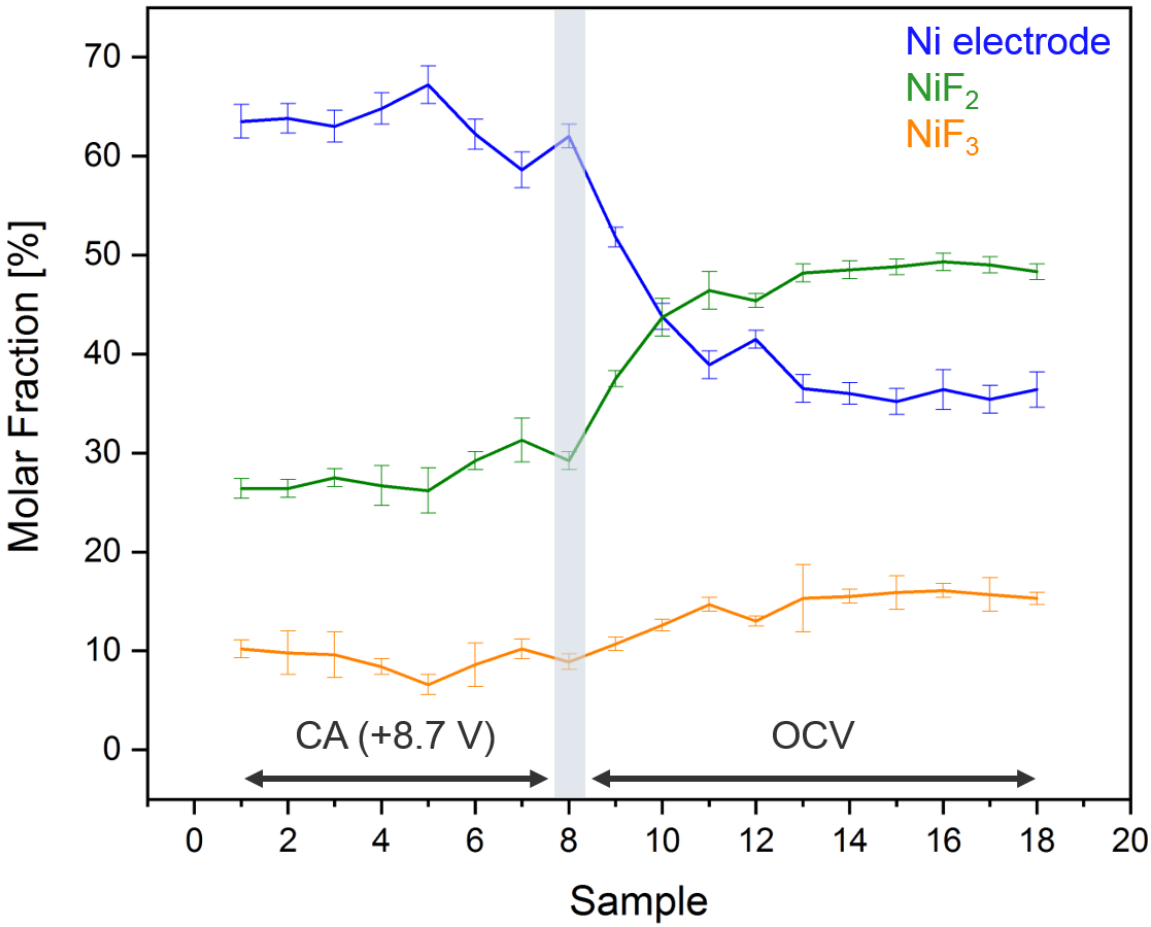

Figure 94: Linear combination fitting of the XANES spectra obtained during the prolonged conditioning of the nickel anode in liquid *a*HF at a cell potential of +8.7 V (samples 1–8, see also Figure 170 in the appendix) and the consecutive decomposition of the anodic film during an OCV scan (samples 9–18, see also Figure 93) to the spectra of the reference materials Ni (bulk anode that is exposed to liquid *a*HF, blue trace), NiF_2 (green trace) and NiF_3 (orange trace).

In accordance with the development of the molar fractions after discontinuing the CA the overall amount of oxidized nickel centers increased. Moreover, the NiF_2:NiF_3 ratio increases from 2.6:1 (during CA) to 3.2:1 after the decomposition (120 min OCV). The decomposition of the anodic black film therefore corresponds to a synproportionation of the reducing agent Ni^0 of the underlying bulk material of the anode with the highly oxidized nickel centers to stable Ni^{II}. Analogous LCF data were processed with the reference spectra of Ni, NiF_2 and NiF_4 (Figure 176 in the appendix) as well as for Ni, NiF_2, NiF_3 and NiF_4 (Figure 177 in the appendix) but were found to poorly describe the observations in the light of larger error bars (the former) and unrealistic development of the fractions of NiF_4 and NiF_3 (the latter).

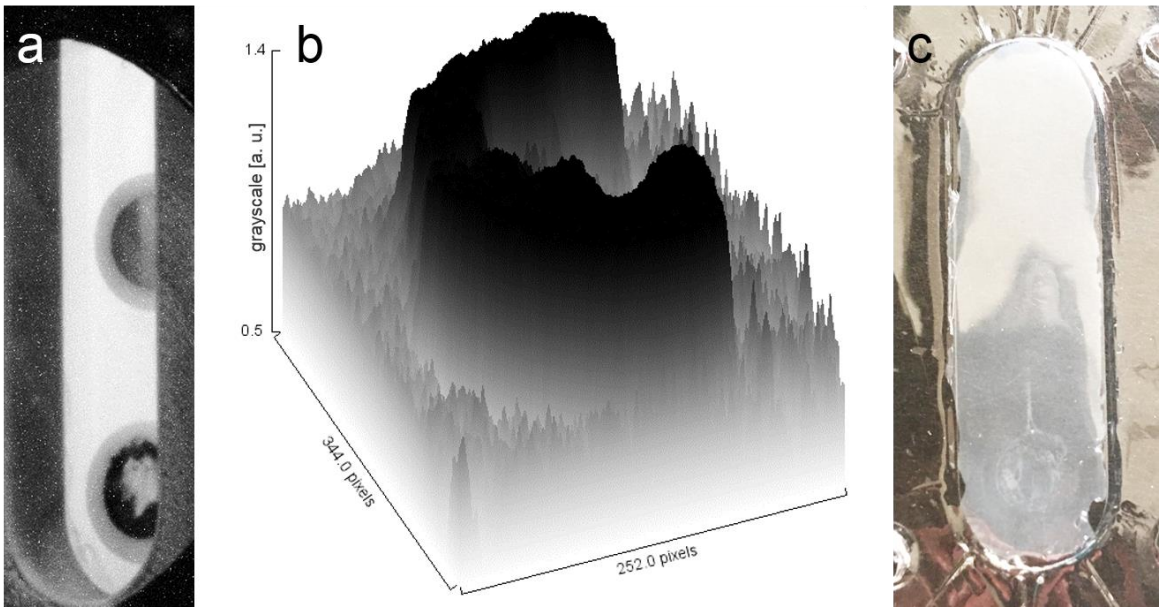

Figure 95: Photo (a) of nickel anode (bottom) and cathode (top) in *a*HF in the electrochemical in-situ XAFS cell at a potential of +8.4 V, the corresponding color difference (b) of the anode at +8.4 V vs. the disconnected case (see also Figure 91), and a photo of the FEP window (c) that is clear in the non-exposed area, opaque in the HF-exposed area and visibly attacked in the area of the black film.

That the center of the electrode was not fully covered by the black film during the in-situ investigation is reasoned by two facts: I) The anode was carefully polished to a mirror finish in advance of the experiments, but was found slightly elevated in its center. II) In order to optimize the signal-to-noise ratio, the layer of *a*HF had to be as thin as possible at the soft Ni K-edge.[175,512,513] Therefore, the anode was adjusted as close as possible to the FEP window. Because of that, the FEP foil, which generally turned opaque upon exposure to *a*HF, was found to be (additionally) visibly attacked by the species apparent on the anode's surface during the experiments (Figure 95). The degraded areas of the FEP foil somewhat resemble the shape of the black film that was observed rather on the rim than in the center of the anode. In accordance, the frequent spikes in current density observed during the CA experiments (Figure 89, and Figure 161 in the appendix), can be tentatively interpreted as the regeneration of the black film upon consumption of the window material.

3.4.2.4 Summary and Outlook

It was shown by chronoamperometric methods that the black film formed on the anode in the Simons process can be stabilized at cell potentials of +4.5 V and above, which agrees well with the literature.[50,123,174] A specifically designed, portable electrochemical cell operable without a fume hood for more than 15 hours, allowed for the characterization of the anodic film in *a*HF in an unprecedented in-situ XAFS study. The maximum of the white line of the black film was found at 8354.0 eV, which is in very good agreement with the maxima of the reference compounds $K_2[NiF_6]$, NiF_3 and NiF_4 at 8354.6 eV. XANES spectra of the meta-stable NiF_3 and – for the first time – the unstable NiF_4 were obtained using a second tailor-made cell for the measurement of XAFS spectra in fluorescence at temperatures below −60 °C.

At cell potentials below +4.5 V, the black film spontaneously decomposes in the sense of a synproportionation of highly oxidized Ni^{x+} centers ($x > 2$) with the underlying Ni metal of the electrode to Ni^{II} centers. This synproportionation takes place even in *a*HF and at temperatures as low as −68 °C, where both NiF_3 and NiF_4 are reported to be stable.[126] Powder X-ray diffractograms of fragments of a decomposed film consequently revealed only NiF_2 and traces of Ni^0. The in-situ decomposition of the anodic film was monitored by OCV measurements, which showed the residual cell voltage to decrease from ca. 2 V to about 0 V within 90 min, and was followed by the simultaneously recorded XANES spectra. The spectra showed an increasing white line that was shifted from 8354.0 to 8352.0 eV, and a feature appearing at 8370.0 eV. The latter two are comparable to the spectrum of NiF_2 and are thus indicative for Ni^{II} centers. The coincidentally decreasing amount of metallic Ni adds further evidence to the synproportionation and therefore to the existence of a high potential oxidizer, i.e. nickel centers in an oxidation state higher than +II, in the black film.

The discovery of highly oxidized nickel centers in the anodic film does not represent a proof of a mediated mechanism, since organic substrates are known to cause changes to the anodic film,[123,152] and more than one mechanism might account for the products observed in the Simons process. However, these results represent the first physical evidence for highly oxidized nickel centers in the black film formed under the conditions of the Simons process.

4 Experimental Part

CAUTION: *The handling of the hazardous substances HF, F_2, BF_3, AsF_5, SbF_5, $Cs[AuF_6]$, PtF_6, HSO_3F and the reportedly explosive MnO_3F[187,215,235,236] requires fluorine/hydrogen fluoride specific safety equipment and trained personnel.*

All volatiles – during synthesis and experiment – were manipulated in fluorine-passivated stainless-steel high vacuum lines and perfluorinated equipment made from FEP, PFA, PCTFE, or PTFE equipped with *Swagelok*® or *FITOK* stainless-steel (needle) valves. The non-volatile compounds were handled in a glovebox under an argon atmosphere.

4.1 Matrix Isolation Experiments

4.1.1 Matrix Sample Preparation and General Procedure

The matrix isolation experiments were performed in custom-made high vacuum chambers ($p_{deposition} \leq 3 \cdot 10^{-6}$ mbar) equipped with each a rotatable cold head with a mounted matrix support, which was cooled to 4 or 5 K by a *Sumitomo Heavy Industries RDK-205D* closed-cycle helium cryocooler with connected compressor unit. These systems differed in the measurement principle (transmission or reflection). For measurements in transmission a CsI window (lowest temperature at 4 K) served as the support. This setup was used for all experiments employing F_2, BF_3, AsF_5, SbF_5 and laser-ablated $Cs[AuF_6]$. For measurements in reflection, which were performed for all combined IR and UV/Vis experiments of MnO_3F and PtF_6, a gold-plated copper mirror (lowest temperature at 5 K) was used as the matrix support. The temperature of the matrix support was maintained by a *Lakeshore 335 Temperature Controller* with a coupled electrical resistance heating during deposition and annealing. The deposition temperature was chosen to be 4 or 5 K in all cases except for MnO_3F. The latter was deposited at 5, 20 and 22 K for neon, nitrogen and argon experiments, respectively. If not stated differently, annealing experiments were performed in a way that the matrix support was heated until the temperature was reached (without ramping) and was immediately cooled to the lowest temperature 4 K (CsI window) or 5 K (gold-plated copper mirror) afterwards.

The samples were prepared in or in combination with a F_2-passivated stainless-steel high vacuum line, which was – accompanied by fluorine passivation – occasionally baked out using heat tapes at temperatures up to 100 °C. Those parts of the deposition unit, which are in direct connection to the vacuum of the high vacuum matrix chamber without an intermediate valve, cannot be

passivated and are thus limited to the 'passivation' by the passage of small amounts of F_2 before the experiments.

All (co-)deposition experiments were performed at flow rates of 0.6, 0.5 or 0.5 mbar·l·min^{-1} on average for neon (99.999 %, *Air Liquide*), argon (99.9999 %, *Sauerstoffwerk Friedrichshafen*) or nitrogen (99.999 %, *Linde*), respectively, while not exceeding a deposition time of 3 hours or 100 mbar·l to prevent a loss of the matrix sample. In advance of the deposition of any reactive species, the matrix support (cesium iodide window or gold-plated copper mirror) was coated with Ne (10 mbar·l) or Ar (5 mbar·l) in order to protect the support material. This is especially important to prevent the oxidation of iodide (CsI) to iodine in experiments employing elemental F_2 as discussed by Brosi et al.[10]

Next to annealing at different temperatures, the matrices were manipulated by irradiation with LEDs and lasers at different wavelengths throughout the visible to the UV spectrum. Quartz (SiO_2) or corundum (Al_2O_3) windows were used for the photolysis experiments. All employed LEDs are soldered to a water-cooled copper-heat sink. The light sources used in this work are summarized with their respective specifications in Table 30.

Table 30: Light sources and their specifications. Wavelengths *λ* are given in nm.

λ	**Type**	**Specification**
730[a]	LED	8.68 W[b]
656[a]	LED	8.68 W[b]
625[a]	LED	8.68 W[b]
617[a]	LED	8.68 W[b]
590[a]	LED	8.68 W[b]
532	Laser	0.8 µJ at 10 kHz[c]
528[a]	LED	8.68 W[b]
470[a]	LED	8.68 W[b]
455[a]	LED	8.68 W[b]
405[d]	LED	3 W
375[d]	LED	3 W
365[d]	LED	3 W
278[e]	LED	100 mW
266	Laser	0.8 µJ at 10 kHz[c]
> 220	Hg lamp	Medium pressure

[a] *OSLON® 80 4+ PowerStar Circular 4 LED Array* [b]at a current of 700 mA, ±10 %; [c] Pulsed Q-switched solid-state laser *CryLas 6FQSS266-Q2-OEM, 266/532 nm*; [d] *Qioptiq ML3 UV LED*; [e] *AMPYR LED33UV278-6060-100*.

For the laser ablation of metals and metal salts a *Continuum Minilite II* pulsed Nd:YAG laser (*λ* = 1064 nm) with a maximum pulse energy of 50 mJ was focused onto the respective rotating target at a maximum repetition rate of 10 Hz.

The purification of the starting materials and the explicit experimental conditions are found in the respective subsections in Section 4.1.3.

4.1.2 Spectral Data Acquisition

IR (and additionally UV/Vis for MnO_3F and PtF_6) spectra were recorded at regular intervals during the deposition of the respective compounds to ensure the formation of a homogenous matrix and after each manipulation step (photolysis or annealing) to monitor the changes.

FTIR spectra of matrix-isolated samples of F_2, BF_3, AsF_5, SbF_5 and laser-ablated $Cs[AuF_6]$ (deposited onto a CsI window) were recorded in transmission on a *Bruker Vertex 70* spectrometer equipped with a KBr beam splitter using a liquid-nitrogen cooled MCT detector (4000–450 cm^{-1}) at a spectral resolution of 0.2 cm^{-1}. The beam path was constantly purged with dry air to suppress atmospheric H_2O.

FTIR spectra of matrix-isolated samples of PtF_6 and MnO_3F (deposited onto a gold-plated copper mirror) were recorded in reflection on a *Bruker Vertex 80v* spectrometer (evacuated beam path) equipped with a KBr beam splitter and transfer optics by using a liquid-nitrogen cooled MCT detector (4000–450 cm^{-1}) at a spectral resolution of 0.2 cm^{-1} (0.5 cm^{-1} for experiments employing MnO_3F).

UV/Vis spectra of matrix-isolated samples of PtF_6 and MnO_3F were measured on a *Perkin Elmer Lambda 850+* UV/Vis Spectrophotometer using quartz optical fiber cables with optics for coupling the beam in and out of the high vacuum chamber at a spectral resolution of 0.5 nm.

4.1.3 Synthesis of Matrix Precursors

4.1.3.1 Platinum Hexafluoride

Platinum hexafluoride was synthesized following the literature instruction by Seppelt and coworkers.[127] Platinum wire (99.99 %, *ChemPur*, *d* = 0.25 mm, *m* = 127 mg, *n* = 0.65 mmol) was coiled to a spiral and connected to the two poles within an autoclave (stainless steel, *V* = 100 ml), of which one was connected to the vessel's wall and the other one to an electrical feedthrough. The autoclave was passivated with elemental fluorine at a pressure of 2 bar overnight. After evacuating the autoclave, it was cooled to −196 °C and elemental F_2 (*n* = 22.2 mmol) was added stepwise to an 11-fold excess. The autoclave was then disconnected from the stainless-steel line, since the outer wall itself represented an electrical pole. To prevent icing and subsequent leakage due to shrinking of the PTFE seal, the top part of the autoclave was warmed by an r.t. air stream. Upon continuous cooling with a liquid nitrogen bath, the Pt wire was electrically heated by the use of a car battery (*U* = 12 V, *I* = 850 A) prompting the ignition of the platinum wire in the fluorine

atmosphere. The reaction took place within a fraction of seconds, yet smoothly while the nitrogen spontaneously started boiling and the main product PtF_6 condensed on the autoclave's wall. At a vapor pressure of ca. 370 mbar at −196 °C, residual fluorine was removed from the reaction mixture in dynamic vacuum. PtF_6 was trapped in a PFA tube equipped with stainless-steel valves.

Since H_2O, O_2 and other small molecules are known to continuously diffuse through the walls of the sample container (PFA) over time,[100] PtF_6 is partially reduced accompanied by the liberation of HF. Therefore, despite the initial removal of HF in high vacuum (p = 1.5·10^{-5} mbar) at a sample temperature of about −80 °C, maintained by a 2-propanol/ethanol cooling bath, a certain amount of HF could not be eliminated and was apparent in all spectra.

PtF_6 was co-condensed with and thereby embedded in solid noble gases by passing neon or argon over a solid sample of PtF_6 maintained at −79 to −78 °C. It was moreover important, to precisely adjust the bath temperature at ±0.1 °C (the accuracy of the Pt-1000 thermometer used), since PtF_6 was found to evaporate rather promptly than smoothly at pressures as low as 1.0·10^{-6} mbar (the usual pressure during co-deposition with Ne). Noteworthy, even when experiments were performed on consecutive days, the 'correct' sample temperature had to be adapted daily (usually at a higher temperature than on the previous day), because the sample got 'purer' within time, accompanied by a lower vapor pressure of PtF_6 at the respective temperature.

4.1.3.2 The Lewis Acids BF_3, AsF_5 and SbF_5

The compounds BF_3, AsF_5 and freshly distilled SbF_5 were provided by Dr. Moritz Malischewski. The samples of BF_3, AsF_5 and SbF_5 were tested for purity by their neon-matrix-isolated IR spectra in accordance with the literature.[351,456,461,470,519] The sampling processes and possible synthetic routes are described in the following.

Boron trifluoride (m.p. = −126.8 °C, b.p. = −101 °C)[29] was transferred by its vapor pressure from the storing stainless-steel cylinder, maintained at −80 °C, to the designated F_2-passivated sampling stainless-steel cylinder.

Arsenic pentafluoride (m.p. = −79.8 °C, b.p. = −52.8 °C)[29] was transferred analogously to BF_3, maintaining the storage cylinder at −50 °C, reducing impurities such as AsF_3.[520]

In a glovebox under argon atmosphere, the highly viscous antimony pentafluoride (m.p. = 8.3 °C, b.p. = 141 °C),[29] was transferred using a syringe equipped with a PFA cannula into a previously flame-dried glass U-tube with by-pass.

The gases BF_3 and AsF_5 were pre-mixed with F_2 diluted in Ne or Ar at room temperature and were subsequently deposited as a gas mixture. The experiments with AsF_5 required a preconditioning period for the deposition capillary (*l* = 100 cm) at a higher concentration of 1.0 % diluted in the respective noble gas at a deposition rate of 0.6 mbar·l·min^{-1} for usually 15 min, depending on the intensity of the AsF_5 bands in the subsequently measured matrix IR spectrum. For the experiments with F_2 the concentration was lowered to the value given in the figure captions. The experiments employing SbF_5 were performed by passing a stream of F_2 diluted in a noble gas over a solid sample of the Lewis acid in a glass U-tube with a by-pass maintained at an optimum of −48.9 to −48.5 °C. Thus, these experiments were conducted using the principle of a single jet setup (all reactants pre-mixed).[73,464,521] A twin or merged jet approach[73,464,521] was not necessary since BF_3, AsF_5 and SbF_5 are unreactive towards F_2.[282]

4.1.3.3 Cs[AuF$_6$]

The room temperature stable cesium hexafluoridoaurate(V)[289] was provided by Marlon Winter and had been synthesized as described in the literature.[455,522]

4.1.3.4 Metal Salt Targets

Metal fluoride targets (NaF, KF, CsF) were prepared from pure alkali metal fluorides, obtained from *Korth Kristalle*, intensely pestled inside a glovebox under argon atmosphere. The powdered metal salts were pressed by the use of a hydraulic laboratory press at up to 12 t to a compact target, which was plugged in or glued onto a corresponding target holder. The mixed salts obtained upon intensely grinding 3 % Cs[AuF_6] and 97 % CsF were pressed at the same conditions as the pure metal fluorides.

A short exposition to air of the metal salt targets could not be circumvented, since the samples had to be transported from the hydraulic lab press to the opened matrix chamber and fixed to the driveshaft on the target motor. The whole process – until the target was mounted and the chamber closed and evacuated – did not exceed a maximum of three minutes. The very hygroscopic CsF appeared in an oily sheen, even after this short amount of time. Upon pumping on the system overnight, the target dried, accompanied by small crystallites forming on the surface, while the target stayed intact. Therefore, the mixed salt target made from Cs[AuF_6] and CsF was seen to be as hygroscopic, but, since the overall structure of the target was not affected, the Cs[AuF_6] (isolated in CsF) was seen to be sufficiently protected at deeper layers of the target.

4.1.3.5 Purification of Elemental Fluorine

Elemental fluorine was obtained from *Solvay Fluor GmbH*. Commercially available elemental fluorine is generally contaminated with small amounts of HF, COF_2, O_2, SiF_4, and CF_4.[10,25] Accordingly, it was purified as follows: In an F_2 passivated (2.5 bar, overnight) and subsequently evacuated system consisting of two stainless-steel gas cylinders equipped with *Swagelok*® or *FITOK* needle valves connected with each other and to the stainless-steel high vacuum line. Cylinder **1** was filled with fluorine at 2.5 bar, closed and cooled to −196 °C for 90 min, while cylinder **2** was evacuated. Afterwards, the connection to the high vacuum line was closed and both cylinders' valves were opened. Cylinder **2**, the designated sample container, was thereby filled at a residual pressure of F_2 (p = 370 mbar) by pressure equilibration and then closed.

The impact of the purity of elemental fluorine used for the co-deposition with different Lewis acids diluted in neon or argon was studied by the IR spectra of the deposits of F_2/Ne mixtures generated from differently purified fluorine and neon (Table 31).

Table 31: Comparison of F_2/Ne mixtures made from differently (in-situ) purified fluorine samples for the deposition onto a matrix support at 4–5 K. The initial quality refers to the purity of F_2 before the connection to the matrix sample line.

$\vartheta(F_2)$	$\vartheta(F_2/Ne$ mixture)	Initial quality	Supplier
r.t.	r.t.	purified by supplier	*MAN* company
r.t.	r.t.	purified at −196 °C[a,b]	*Solvay Fluor GmbH*
−196 °C[a]	r.t.	as received	*Solvay Fluor GmbH*
r.t.	−196 °C[a,c]	as received	*Solvay Fluor GmbH*

[a] The samples were cooled to −196 °C for at least 60 min; [b] see Section 4.1.3.5 [c] the F_2/Ne mixture was cooled to −196 °C throughout the deposition.

The matrix IR spectra of the deposits of the four differently generated F_2/Ne mixtures did not show remarkable differences concerning the purity of the sample.

4.1.4 MnO_3F

In the present work, MnO_3F was synthesized according to Scheme 22 in order to facilitate the separation of the product from the less volatile HSO_3F in vacuo.[235]

$$K[MnO_4] + 2\,HSO_3F \longrightarrow MnO_3F + K[SO_3F] + H_2SO_4$$

Scheme 22: Synthesis of MnO_3F in accordance with reference [235].

The stainless-steel parts of the experimental setup were passivated with elemental fluorine at 1.5 bar overnight and the PFA parts only 60 min prior to the synthesis of MnO_3F. $K[MnO_4]$ (99 %, 1 g, 6.3 mmol, *Merck*) was slowly and stepwise added to freshly distilled, ice cooled HSO_3F (4 ml, 6.9 g, 69 mmol, *Solvay Fluor*), while the crude product was condensed into a PFA trap kept at −78 °C in low vacuum. After the reaction ceased, the crude MnO_3F was warmed to −46 °C and condensed onto $K[MnO_4]$ (4 g, 25.2 mmol) in a PFA trap maintained at −196 °C in static vacuum. Further purification from more volatile residuals (HF and small amounts of a purple sublimable compound)[235] was carefully done in dynamic vacuum at $p = 1 \cdot 10^{-3}$ mbar and up to −87 °C.

Analogous to the deposition of PtF_6 in inert matrices (Section 4.1.3.1), an inert gas stream (Ne, N_2, Ar) was passed over a solid sample of MnO_3F at a sample temperature of −110.3 to −108.5 °C and co-condensed until the intensity of the IR intense bands did not rise significantly.

4.1.5 Experimental Limitations (Matrix)

In the case that a Lewis acid-fluorine adduct had formed upon the discussed co-deposition reactions but is photosensitive towards infrared light, an experimental proof would be impossible with the matrix isolation setup used for these experiments. The matrix support (CsI window) is rotated 45° off the IR beam path in the direction of the deposition unit during deposition of the sample and therefore continuously exposed to the infrared light source of the globar. The unused windows of the matrix chamber had been covered with aluminum foil to prevent light entering in addition to the otherwise dark laboratory.

The passivation of the deposition line with F_2 is crucial and only when the chemical reactions within the deposition line (*l* = 100 cm, *O.D.* 3 mm, stainless-steel) cease, an increased fluorine content can be observed. In the light of the multiple uses of the matrix isolation systems for reactions using for example OF_2, NF_3, hexafluoro-2-propanol (the level of impurity of these gases and the impact on the sample and deposition lines could not be assessed) at varying water amounts, a perfect passivation, at least in the deposition line, is hard to achieve.

Thus, the best trade-off must be found with respect to the reactivity (or inertness) of the compounds and the exact monitoring of the concentration of the deposited species when premixed. For SbF_5, MnO_3F and PtF_6 it was chosen that a constant stream of the matrix host was passed over a solid sample of these compounds, which were positioned 10 (the former) or 20 cm (the latter two) from the matrix support. BF_3 and AsF_5 were premixed with the noble gas or with the noble gas and fluorine at room temperature.

4.2 Computational Details

Except for the calculations of MnO_3F and its derivatives (vide infra), the program package *Turbomole 7.4.1* was used for the molecular structure optimizations and frequency calculations of this work, employing the RI (resolution of identity) approximation in all DFT calculations.[523] The structures of neutral and anionic binary platinum fluorido compounds and ion pairs $M[PtF_6]$ (M = Na, K, Cs) and the Lewis acids BF_3, AsF_5, SbF_5, AuF_5 and the fluorine complexes thereof were calculated at the B3LYP-D4/def2-TZVPP level of theory, with the triple-ζ basis set including a large set of additional polarization functions providing results sufficiently close to the basis set limit.[452,524,525] With respect to the benchmark against CCSD(T)/CBS by Dixon and coworkers,[273] the use of the B3LYP functional is justified in order to describe the free $[PtF_6]^-$ and $[PtF_7]^-$ ions. The Lewis acids BF_3, AsF_5, SbF_5, AuF_5 and the respective fluorine complexes have also been described using the BP86, PBE and SCS-MP2 methods using the def2-TZVPP basis set and the D4 correction.[37,452,525,526] The neutral and ionic platinum fluorine species were calculated in an unrestricted spin approach to account for the open shell systems (see the discussion in Section 3.2.1). The species PtF_6, $[PtF_6]^-$ and $[PtF_7]^-$ (classical and non-classical structures) were calculated based on starting structures taken from the optimized ones from reference [273].

For the heavy elements Pd, Sb, Pt and Au 18, 23, 18 and 19 valence electrons, respectively, were explicitly calculated, the core electrons were treated by the Stuttgart ECP optimized for the applied def2-basis set.[527] The default scaling factors were used at the SCS-MP2 level of theory. All vibrational frequencies have been calculated analytically using the module *aoforce* without applying an empirical scaling factor. For the determination of the electronic ground states, the definitions of the Turbomole output were used by applying the *eiger* program. NPA charges were obtained by population analysis using the *nbo* module.[528] The default convergence criteria have been applied for all calculations (10^{-6} H).

The optimizations of MnO_3F and its derivatives, i.e. all equilibrium and transition structures, were performed at the PBE0-D3(BJ)/def2-QZVPP level of theory,[452,529] as implemented in the *Gaussian16* software package,[530] by Li et al.[453] Thereby, harmonic frequency calculations were carried out at the same level to verify that the minimum structures feature no imaginary frequencies and that the transition structures feature just one imaginary frequency. Connectivities of transition structures to the respective minima were additionally confirmed via intrinsic reaction coordinate calculations.[531] The single point energies were refined using the CCSD(T) method (coupled cluster with singles, doubles, and quasiperturbative triple excitations) using the def2-

QZVPP basis set.[532] Open shell species were treated with the restricted-open-shell (RO-CCSD(T)) formalism.

4.3 Simons Process

4.3.1 Electrochemical Measurements

All electrochemical experiments – open circuit voltage scan (OCV), chronoamperometry (CA) and cyclic voltammetry (CV) – were performed using a *Bio Logic Science Instruments Pvt. Ltd.* SAS model SP-300 potentiostat and the software *EC-Lab® v. 11.0* using two-electrode setups consisting of nickel working and counter electrodes in open (preliminary studies, see Section 3.4.1) or closed cell designs (in-situ XAFS cell, see Section 3.4.2).

4.3.1.1 Ex-Situ Measurements

The nickel plate (99.72 %, *institute's stock*) electrodes for the generation of SEM and ex-situ XANES spectroscopy samples were welded to nickel wires (99.98 %, *ChemPur*), which were insulated in PFA tubing to only allow the contact of liquid *a*HF and to prevent the contact of the electrodes with gaseous HF. The plate electrodes were immersed in nitric acid (65 %) for 1 min, immediately washed with deionized water and dried on air prior to use.

Anhydrous hydrogen fluoride was obtained from *GHC Gerling Holz & Co. Handels GmbH* and used as received for preliminary electrochemical experiments. The required amount of *a*HF (ca. 10 ml) was condensed in a PFA reservoir with a PTFE seal plug with drilled holes for HF inlet and outlet at −196 °C by usage of a stainless-steel high vacuum line. The *a*HF was then transferred via a PFA tubing into the electrochemical cell, a PFA tube (Ø = 2.54 cm, flame-sealed bottom) equipped with a PTFE seal plug with drilled holes for the HF inlet, gas outlet (H_2, HF_{gas}) and the electrodes, by applying a slight overpressure of argon at −80 °C (cf. Figure 157). During the experiments, the temperature of the electrolyte *a*HF was maintained at 0 °C by an ice/water bath.

4.3.1.2 In-Situ Measurements

The planar electrodes used for the in-situ studies were made from nickel rods (Ø = 5 mm, 99.99 %, *ChemPur*) embodied in PTFE (Ø = 10 mm) and were polished to a mirror finish with diamond (1 µm) and alumina (0.05 µm) polishing pastes by using corresponding polishing pads from an electrode polishing kit supplied by *Zimmer & Peacock*, sonicated in a 2-propanol bath for 3 min after each polishing step and dried on air.

The *a*HF was dried over $K_2[NiF_6]$ (99 %, *ABCR*) prior to the experiments employing the in-situ XAFS cell and the production of the NiF_4/NiF_3 samples. The in-situ XAFS cell was filled with *a*HF in analogy to the ex-situ experiments, while the PFA transfer tube was flame sealed after the filling was completed. The in-situ XAFS cell was cooled by a closed-cycle cryostat (coolant: ethanol) with the temperature set at −5 °C. Since the aluminum cooling body of the in-situ XAFS setup was always colder than the electrochemical cell, the water only condensed on the aluminum without impairing the measurement of XANES spectra even after more than ten hours.

4.3.2 Measurement of XANES Spectra

The measurement of XANES spectra were carried out at the Ni K-edge (8333 eV)[182] at the BAM*line*,[533] located at BESSY II (Berlin, Germany). The incident energy was tuned by a double crystal monochromator in a Si(111) arrangement ($\Delta E/E = 2 \cdot 10^{-4}$), in 10 eV steps until 20 eV before the edge, followed by 0.5 eV steps until 30 eV above the edge and 1 eV steps until 200 eV above the edge. The beam size was 2 mm (H) x 1 mm (V). Owed to the irregular sample surface and X-ray thick sample environment,[175,182,534] the measurements were performed in fluorescence mode. Thereby a 4-element silicon drift detector focusing on a point at about 10 mm in front of the detector collects the backscattered signal.

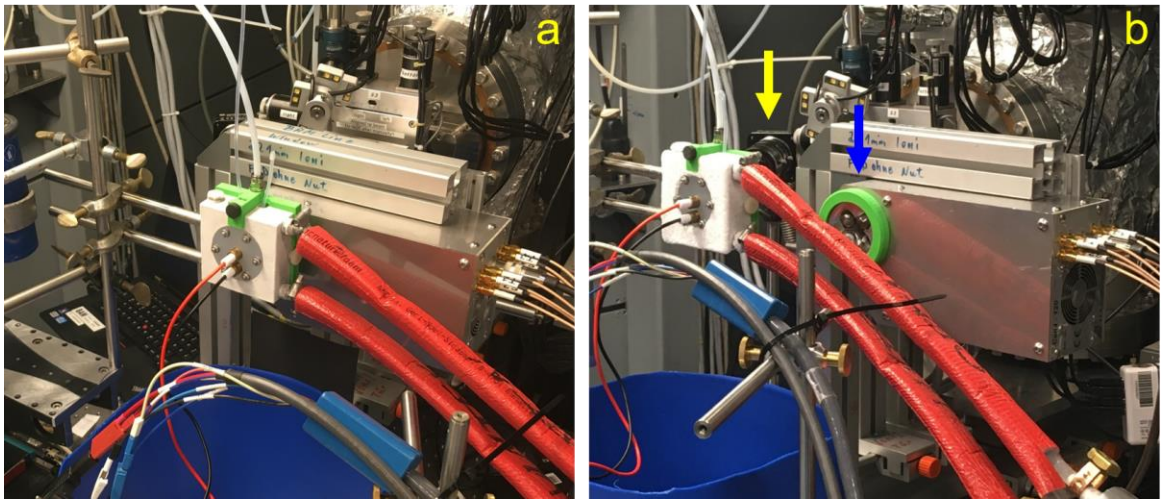

Figure 96: Setup of the in-situ XAFS cell in a) spectroscopy and b) photography positions. The detector was moved after the measurement of each XANES spectrum to take a photo from the cell. The camera (yellow arrow) and detector (blue arrow) were highlighted.

The arrangement of electrochemical in-situ XAFS cell and the detector is shown in Figure 96. XANES spectra were recorded at the specific temperatures where the phases are reported to be stable (Table 32).[126]

Table 32: Sample temperatures during the measurement of the XANES spectra.

Sample	ϑ_{sample}
NiF_4	< −60 °C
In-situ electrode	−5 °C
NiF_3	0 °C
$K_2[NiF_6]$	r. t.
NiF_2	r. t.
Ex-situ electrode	r. t.
Ni foil	r. t.

4.3.3 Reference Substances for the Measurement of XAFS Spectra

Elemental Ni (2 µm-foil, 99.95 %, *Goodfellow*) was used as received. NiF_2 (1.5 mg, 0.016 mmol; 99 %, *ABCR*) was intensely ground with BN (52 mg, 2.1 mmol; 99.5 %, *Alfa Aesar*) and filled in a polycarbonate cell covered with 125 µm-Kapton® foil windows.

NiF_4 was synthesized by dispersing $K_2[NiF_6]$ (0.5 g, 2 mmol; 99 %, *ABCR*) in liquid *a*HF (3 ml) below −65 °C in a selfmade λ-shaped reactor made from FEP tubing (fluorinated ethylene-propylene copolymer; Ø =9 mm, 500 µm wall thickness). A light brown/tan colored precipitate formed instantly as BF_3 (*institute's stock*) was added stepwise at up to 1.5 bar, until the suspension (agitated with a *Mini Vortex Mixer PV-1*) did not absorb further BF_3 and the residual $K_2[NiF_6]$ was converted. The NiF_4 was purified in a procedure adapted from reference [126] by decanting the supernatant solution of $K[BF_4]$ in *a*HF and distilling back the HF to wash the NiF_4 (repeated six times) while maintaining a temperature below −65 °C throughout the experiment. In order to save larger quantities of the NiF_4 sample, the *a*HF was removed under reduced pressure very slowly because of boiling retardation especially at temperatures of −65 °C and below. The dry NiF_4 was transported under an argon atmosphere. The procedure is depicted in Figure 97.

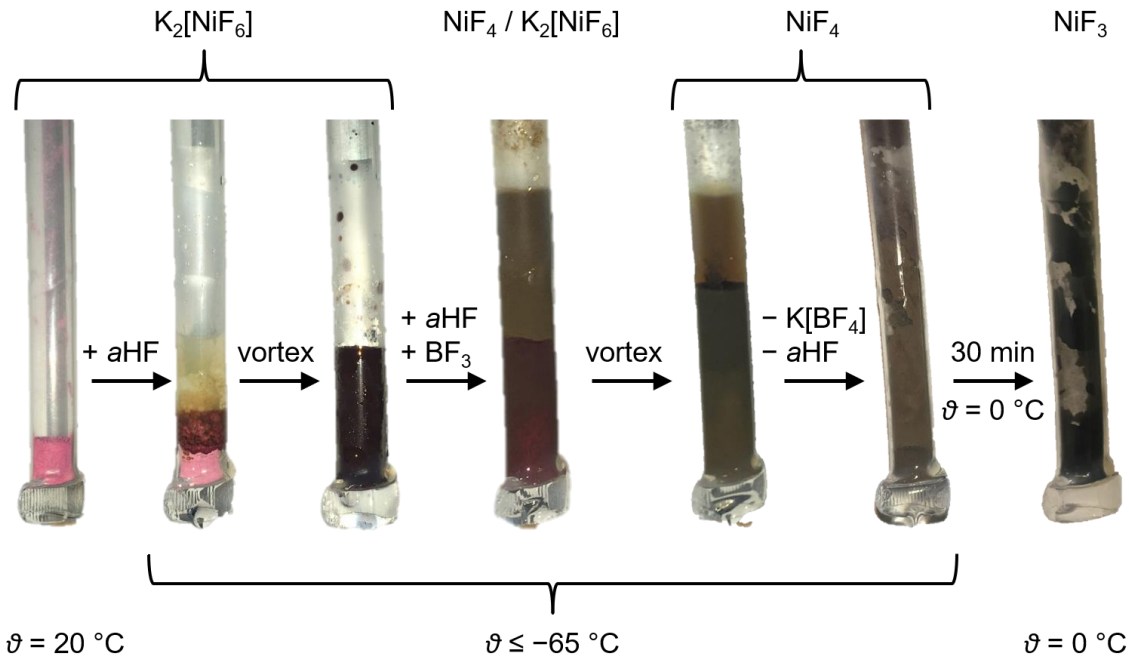

Figure 97: Preparation of an NiF_4 sample and its decomposition to NiF_3 for the measurement of XANES spectra in a selfmade λ-shaped reactor made from FEP tubing with a wall thickness of 500 µm, with only the main arm shown.

The sample of NiF_4 was placed in a specifically designed low-temperature XAFS cell (cf. Section 3.4.2.1) for the measurement of the XANES data (Figure 98). After the data acquisition for NiF_4 was completed, the latter compound was thermally decomposed to NiF_3 by increasing the temperature in the cell from −60 to 0 °C. Any fluorine gas exiting the λ-shaped reactor, was deactivated upon passage over soda lime, while the same mobile deactivation system was used as for the electrochemical in-situ XAFS cell (see Figure 84 and Figure 166 in the appendix).

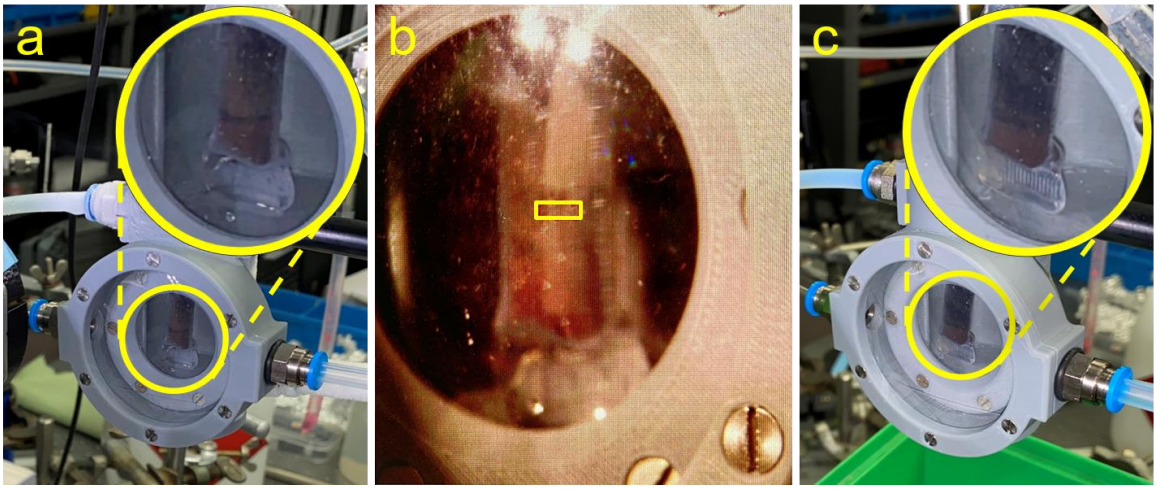

Figure 98: Photographs of NiF_4 (a, ϑ < −60 °C) and NiF_3 (c, ϑ = 0 °C) samples in a cooled FEP tube in the low-temperature XAFS reference cell, and the corresponding beam spot (b, yellow highlighted) during the measurement of the XANES spectra.

4.3.4 PXRD Measurements

Powder X-ray diffractograms were measured on a *Bruker D8 Venture* diffractometer with a *PHOTON II CMOS* detector at 100(1) K using Mo-K_α irradiation at λ = 0.71073 nm via a 360° Phi scan with an exposure time of 60 s and a detector distance of 120 mm. The data were integrated with the *APEX3* program package (*Bruker*).

4.3.5 Surface Morphology (SEM)

The surface morphology was investigated using a *Hitachi SU8030* field emission scanning electron microscope (FE-SEM) at an accelerating voltage (V_{ac}) of 20 kV, a current of 20 µA, and a working distance of 8.5 in. The substrates were sputtered with a 5 nm conductive gold layer prior to the SEM measurements, using a *Safematic CCU-010* sputter machine.

4.3.6 Data Analysis and Manipulation (XANES)

The data analysis was performed in cooperation with Dr. Ana Guilherme Buzanich (BAM) following the procedure described below:[535]

XANES data were evaluated and treated by using the *Athena* program from the *Demeter* package.[536] This includes the background removal, the energy calibration with a Ni metal foil spectrum, as well as the pre- and the post-edge normalization. All phases in the XANES data were quantified by linear combination fitting (LCF) with the reference substances also measured experimentally. The goodness of the fit was based on the χ^2 test and *R*-factor values.

All spectra acquired in fluorescence mode are in most cases affected by a so-called "self-absorption effect". This is when fluorescent radiation created at deeper parts of the sample excites upper layers of the sample when trying to escape, which results in absorption of these photons, hence self-absorption. This hinders the features observed in the XANES curves. However, there are known algorithms that correct this effect, such as the one from Tröger et al.,[183] the so-called self-absorption correction (SA-Fluo). In this algorithm, only an estimated chemical formula of the sample and the geometry of the experiment, with incident and fluorescence angles, need to be introduced. In this work, all XANES spectra are corrected for self-absorption effects using this tool.

4.4 Data Processing and Visualization

FTIR spectra were processed and manipulated with the *OPUS 7.5* software (*Bruker*), the UV/Vis spectra were processed with *WinLab* (*Perkin Elmer*), the electrochemical data with the software *EC-Lab® v. 11.0* (*Bio Logic Science Instruments Pvt. Ltd.*) and the XANES spectra as described in Section 4.3.6.

FTIR, UV/Vis and XANES spectra and linear combination fitting data of the latter, as well as electrochemical data and powder X-ray diffractograms were plotted and manipulated with *Origin Pro 2020*.[537]

The starting structures of molecules, molecular ions and ion pairs for the quantum-chemical calculations were generated with the *Avogadro* software. The optimized structures were visualized with the program *Chemcraft*[538] based on the computed xyz coordinates.

Crystal structures were plotted and visualized using the program *Diamond 4.6.4*.[539] In addition to the visual inspection of the formation of the black film (in-situ investigation of the Simons process), the color development on the anode was analyzed by the program *ImageJ* (*Fiji*) based on color differences on the photos taken. The sample holder for the measurement of XANES spectra of a nickel electrode with a decomposed anodic film was drawn using the program *Fusion 360* (*AutoCAD*).

4.5 Deposition Unit for Combined Laser Ablation and MF_6 Experiments

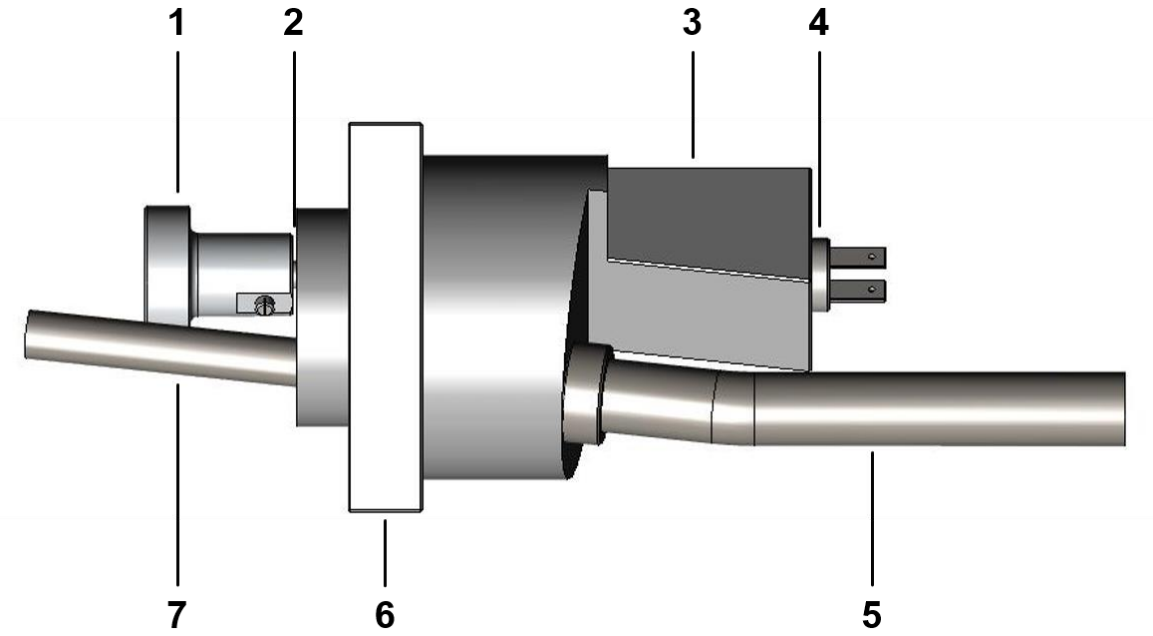

Figure 99: Top view of a high-vacuum adaptable stainless-steel unit for the combined deposition of PtF_6 and laser-ablated metals or metal fluorides with the components and their respective materials: **1**) exchangeable target-holder (aluminum, stainless-steel fixation screws) for compressed metal salt-targets (Ø = 10 mm), **2**) magnetically coupled driveshaft, **3**) socket for the electric motor, **4**) electric motor (Ø = 10 mm, *Faulhaber 1016 M 012 SR* with attachable *Faulhaber 10/1 planetary gears* at 256:1), **5**) reactive gas supply (8 mm stainless-steel tubing) welded to the connector flange and bend for optimized sample placement/alignment, **6**) connector flange for high-vacuum chamber, and **7**) reactive gas supply (stainless-steel tubing, tapered from 8 mm to 6 mm). The resulting plumes of plasma and supplied gas are focused on one point.[444]

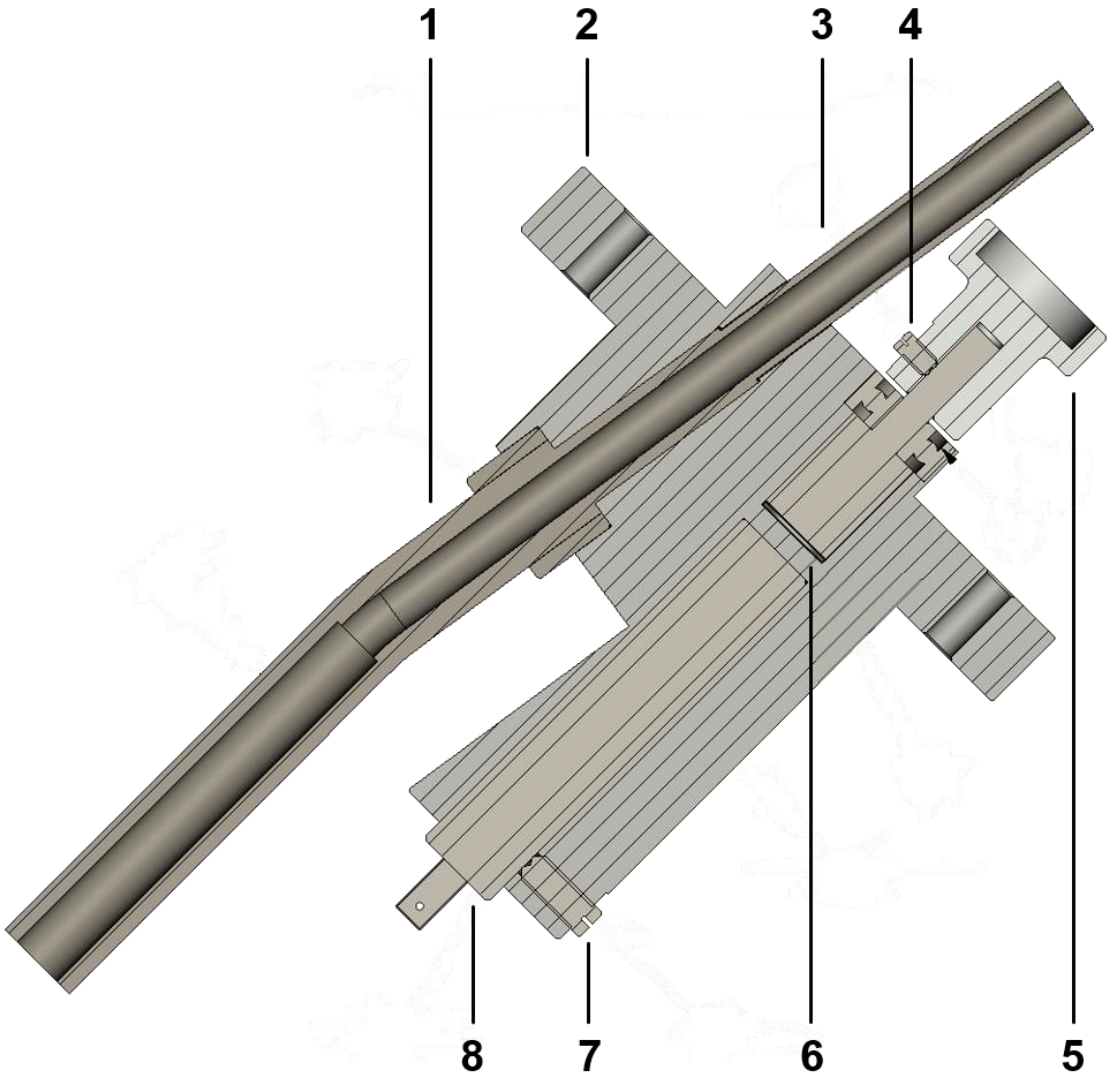

Figure 100: Cutaway drawing of a high-vacuum adaptable stainless-steel unit for the combined deposition of PtF_6 and laser-ablated metals or metal fluorides with the components and their respective materials: **1**) reactive gas supply (8 mm stainless-steel tubing) welded to the connector flange and bend for optimized sample placement/alignment, **2**) connector flange to the high-vacuum chamber, **3**) reactive gas supply (stainless-steel tubing, tapered from 8 mm to 6 mm), **4**) fixation screw (stainless-steel) for the target-holder, **5**) exchangeable target-holder (aluminum) for compressed metal salt-targets (Ø = 10 mm), **6**) magnetic coupling of gears and driveshaft, **7**) fixation screw for the electric motor, and **8**) electric motor (Ø = 10 mm, *Faulhaber 1016 M 012 SR* with attachable *Faulhaber 10/1 planetary gears* at 256:1). The resulting plumes of plasma and supplied gas are focused on one point.[444]

5 Conclusion and Outlook

5.1 Conclusion

The oxidation of Xe with F_2 does not take place without an external activation (e.g. photolysis, heat, electrical discharge),[129] but proceeds mediated by the liquid Lewis acids *a*HF, AsF_5, and SbF_5 in the dark.[130–132] This suggests an increased oxidation power of fluorine by its polarization in a non-classical complex [LA·F_2] featuring a discrete {F_2} unit,[79,273] like in the computed [AuF_5·F_2], as reported by Himmel and Riedel.[195] The F−F fundamental is expected to be sensitive towards the coordination of a Lewis acid.[195] However, the quantum-chemical calculations predict the adducts [BF_3·F_2], [AsF_5·F_2] and [SbF_5·F_2] to be even weaker bound than van der Waals molecules[73,356] and thus likely to be only observed as matrix cage pairs. The calculated trend of a slight redshift of the ν(F−F) in the presence of the Lewis acids BF_3, AsF_5 and SbF_5 hardly corresponds to their acidities[66] and no compelling experimental evidence for distinct [LA·F_2] complexes was found. However, two main positions of the F_2 fundamental were stabilized by these Lewis acids: the bands of solid ($F_{2,s}$) and isolated F_2 ($F_{2,i}$) at 901.3 and 891.7 cm^{-1}, respectively, in neon matrices. The maximum of the latter band was found to be blue-shifted by 1.5 and red-shifted by 1.4 cm^{-1} at the maximum for the Cs[AuF_6]/CsF and AsF_5 experiments, respectively. Due to the band width of about 4 cm^{-1} (FWHM) the single components of the $F_{2,i}$ band were obscured, as was revealed in an experiment with very diluted AsF_5 in neon. A tentatively assigned cage pair [AsF_5·F_2] and the $F_{2,s}$ band decreased during annealing, while the $F_{2,i}$ band increased. In contrast, in experiments with BF_3 only the $F_{2,i}$ band was observed and the impact of the Lewis acid on F_2 was considered small, since BF_3 dimerized upon annealing. Upon the use of SbF_5 the intensity of the $F_{2,s}$ and $F_{2,i}$ bands increased remarkably but no shift of these fluorine bands was observed. AuF_5 was not formed in relevant amounts from laser-ablated Cs[AuF_6] (3 % in CsF) in analogy to reference [455], even with additional F_2 co-deposited, however, the band intensities of the $F_{2,s}$ and $F_{2,i}$ bands could be increased even more than in the SbF_5 experiments while remaining unshifted. This leads to the conclusion that the polarization of fluorine can for some cases be coupled to a redshift of the ν(F−F) band. As the F_2 fundamental itself is IR inactive, the high $F_{2,s}$ and $F_{2,i}$ intensities in the SbF_5 and in the Cs[AuF_6]/CsF cases can only be explained by a strong polarization of the F_2 molecules, which are accordingly IR activated. These observations reflect the catalytic role of AsF_5, SbF_5 and CsF in oxidations with elemental fluorine.[130,131,408,409]

The necessity to pair a Lewis acid and the very weak base fluorine in the same matrix cage to observe a corresponding adduct[73,361] led to a different approach. The fluorine-rich photo-labile precursor PtF_6 represents a source of both the Lewis acid and F_2, as it can be selectively photolyzed

to yield the platinum fluorides PtF_3, PtF_4, and PtF_5.[304] However, despite the constrained fluorine atom mobility in neon matrices and the selective photolysis of PtF_6, a non-classical complex of the type $[PtF_n{\cdot}F_2]$ was not observed.[273,304,499,500] Since fluorine preferably reacts as an electron acceptor, it forms ion pairs of the type $M[F_2]$ with alkali metals under matrix isolation conditions.[374] These species all comprise an $\{[F_2]^-\}$ unit that is more polarizable than elemental fluorine.[74] PtF_6 is known for its extremely high electron affinity. It is easily reduced in the gas phase,[275–277] by electrons from the laser ablation of metals or metal salts.[10] The co-deposition of PtF_6 with the laser-ablated metal fluorides MF (M = Na, K, Cs) or the metals Pd and Pt in solid argon or neon yielded the matrix-isolated ion pairs $M[PtF_6]$ (M = Na, K, Cs) and free $[PtF_6]^-$. The IR bands of the ion pairs were noticeably shifted dependent on the co-deposited alkali metal. The free hexafluoridoplatinate(V) ion was obtained in the highest yield with laser-ablated platinum atoms, allowing for the first time its investigation. Upon laser photolysis at λ = 266 nm all deposits gave rise to a band at 474.4 cm^{-1}, which was assigned to a ν(F–F) band of a polarized $[F_2]^-$ as a part of a non-classical F_2 complex. The highest intensity of this band was also found in the Pt/PtF_6 system in solid neon. Accordingly, the $[F_2]^-$ band is correlated to the free $[PtF_6]^-$. It was found to slightly decrease upon blue light irradiation and regain almost all its intensity by subsequent repeated UV light photolysis. The intensity of the $[F_2]^-$ band remained the same when 0.5 % F_2 was added to the noble gas stream, indicating an intramolecular process. An influence of fluorine atoms on the formation of $[F_2]^-$ cannot be excluded since they might be generated by the plasma upon laser ablation as well as the UV light photolysis.[8–10] Supported by the computed data of the non-classical $[PtF_n{\cdot}F_2]^-$ complexes (n = 3–5) the experimental results did not allow an unambiguous assignment to one of these species. However, the appearance of the band assigned to $[F_2]^-$ at 474.4 cm^{-1} and its correlation to the amount of free $[PtF_6]^-$ represents the first experimental evidence for a non-classical fluoro complex.

MnO_3F was long thought to be the only representative of the oxofluorides of manganese. Only very recently novel oxofluorides of manganese in an oxidation state lower than +VII have been reported. However, a new approach based on the unpublished results of Li et al.[453] revealed that the photolysis of the high-valent permanganyl fluoride MnO_3F yields the previously not accessible end-on $[(\eta^1\text{-OO})Mn^{IV}OF]$ and side-on $[(\eta^2\text{-OO})Mn^{V}OF]$ complexes. The investigation of highly pure MnO_3F and its photolysis products isolated in solid Ne, Ar, and N_2 by IR and UV/Vis spectrocopy provided a robust experimental base for the ongoing in-depth high-level quantum-chemical investigation.[505]

The industrially highly important Simons process is used for the electrochemical fluorination of organic molecules employing nickel electrodes in anhydrous hydrogen fluoride. Ever since its

invention about a century ago,[151] the underlying reactions pose a mystery to fluorine chemists.[50,123] Different mechanisms have been proposed to understand the diverse product spectrum. They fall into two groups:[50,123] I) the electrochemical oxidation of the organic substrate, for example via an EC_bEC_N mechanism, and II) the oxidation of the organic starting material mediated by an electrochemically generated strong oxidizer such as black NiF_3. A black film is actually formed on the anode during the Simons process.[50,142] In order to elucidate the nature of this anodic film an ex-situ investigation was conducted. Based on the preliminary results obtained by electrochemical methods (CV, CA, OCV), PXRD, SEM and XAFS spectroscopy a cell for the unprecedented in-situ characterization of the black film was specifically developed. This electrochemical in-situ XAFS cell (Figure 101) fulfilled the requirements of a coolable, leak-proof and closed cell design, maintaining thin films of window and electrolyte to optimize the signal-to-noise ratio, while being transportable and operable without a fume hood for more than 15 hours despite its highly toxic content.

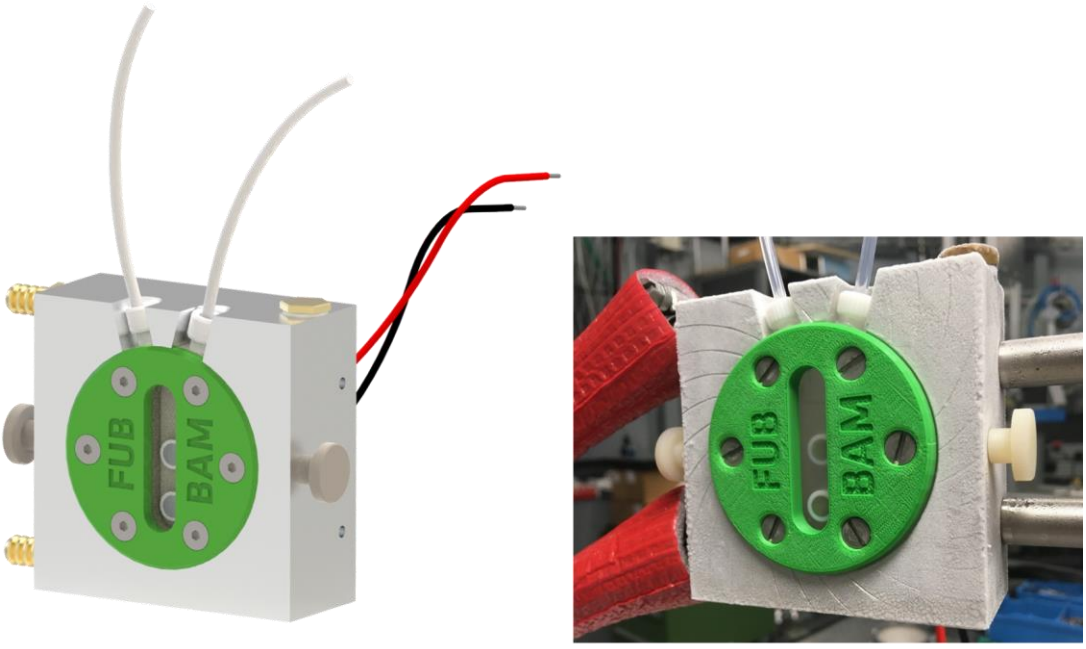

Figure 101: Schematic of the electrochemical in-situ XAFS cell (left)[515] and measurement setup at BESSY II in Berlin (right).

XANES spectra were recorded from an in-situ generated black film and indicated nickel centers in an oxidation state higher than +II. To further support these findings XANES spectra were also recorded from the reference materials Ni, NiF_2 and $K_2[NiF_6]$, as well as meta-stable NiF_3 and, for the first time, the unstable NiF_4. These species were measured in a second tailor-made cell for the measurement of XAFS spectra in fluorescence at temperatures below −60 °C. A higher amount of Ni^{II} and a correspondingly lower amount of Ni^0 were observed upon decomposition of the black

film, resulting from the synproportionation of highly oxidized nickel centers and the underlying Ni^0 of the electrode. This unprecedented in-situ XAFS investigation represents the first experimental evidence for nickel in an oxidation state higher than +II under the conditions of the Simons process.

5.2 Outlook

The co-condensation experiments of different Lewis acids with elemental fluorine diluted in noble gases did not yield compelling experimental evidence for the activation of F_2 by means of distinct [LA·F_2] complexes. However, the FIR regime is worth to be studied in analogous experiments, since the deformation modes should be more significantly shifted, especially for the SbF_5 and AuF_5 cases. Gold pentafluoride is formed as a pyrolysis product from the fluorokryptonium and dioxygenyl hexafluoridoaurates(V),[69,290,291] and could thus be studied as a co-condensate. As a purely experimental approach is not able to explain all observed IR bands, a quantum-chemical modelling of fluorine in noble gas matrices with and without an added Lewis acid could shed light into the structures of the $F_{2,s}$ and $F_{2,i}$ bands with respect to recent publications of Mattsson et al. and Bader et al.[13,495,540]

The first experimental evidence for a non-classical fluoro complex of the type $[PtF_n \cdot F_2]^-$ (n = 3–5) obtained from the free $[PtF_6]^-$ principally opened the gate for the other transition metal hexafluorides to be analogously investigated.

Nickel centers in an oxidation state higher than +II are apparent in the black film formed during the Simons process. At a synchrotron source with more flux than available at BESSY II (Berlin), future in-situ investigations could target the characterization of the black and decomposed films via PXRD, EXAFS or Valence-to-core X-ray emission spectroscopy[176,541] to obtain insight into the coordination environment of these nickel centers. In operando studies via XAFS spectroscopy seem to be too farfetched with respect to the necessity of a continuous HF supply, feed of starting material and product capture. The impact of a simple substrate like CH_3CN on the black film could be studied for instance by a single injection of the organic material into the electrochemical in-situ XAFS cell at a manageable modification of the setup.

6 Appendix

6.1 Lewis Acid-Fluorine Interactions: Additional Data

6.1.1 Optimized Structures of Lewis acids and [LA·F_2] complexes

The optimized structures of the Lewis acids BF_3, AsF_5, SbF_5 and AuF_5 and their F_2 adducts in the following subchapters are given in the form of xyz data in Å.

6.1.1.1 SCS-MP2/def2-TZVPP

BF_3 ($^1A_2'$-D_{3h})

B	-0.0000000	0.0000000	0.0000000
F	0.6568777	-1.1377455	0.0000000
F	0.6568777	1.1377455	0.0000000
F	-1.3137553	0.0000000	0.0000000

[BF_3·F_2] ($^1A''$-C_s)

B	0.1505517	1.0115880	0.0000000
F	1.4649437	1.0195414	0.0000000
F	-0.5061551	1.0167291	1.1378275
F	-0.5061551	1.0167291	-1.1378275
F	-0.9739479	-2.2436871	0.0000000
F	0.3707627	-1.8209006	0.0000000

AsF_5 ($^1E''$-D_{3h})

As	0.0000000	0.0000000	0.0000000
F	0.8378057	-1.4511220	0.0000000
F	0.0000000	0.0000000	-1.6990518
F	0.8378057	1.4511220	0.0000000
F	-1.6756114	0.0000000	0.0000000
F	0.0000000	0.0000000	1.6990518

[AsF_5·F_2] (^1A-C_1)

As	-0.0489807	1.1512604	-0.3790924
F	1.4572806	0.4043851	-0.1323263
F	0.5550111	1.9006539	-1.7521984
F	-1.5548628	1.8922241	-0.6418977
F	-0.7797934	-0.3549869	-0.4479576
F	0.0846215	1.9273040	1.0992227
F	-1.0004191	0.1557595	-3.5275310
F	-1.8450272	-0.9713501	-3.4825694

SbF_5 ($^1A_1'$-D_{3h})
Sb 0.0000000 0.0000000 0.0000000
F 0.0000000 0.0000000 1.8522894
F -0.9210511 1.5953073 0.0000000
F -0.9210511 -1.5953073 0.0000000
F 0.0000000 0.0000000 -1.8522894
F 1.8421022 0.0000000 0.0000000

$[SbF_5 \cdot F_2]$ ($^1A'$-C_s)
Sb 0.8217179 0.1170086 0.0000000
F 0.7203096 0.1168383 1.8493853
F 2.6591391 0.1633975 0.0000000
F 0.0493943 1.7944135 0.0000000
F 0.7203096 0.1168383 -1.8493853
F 0.1348947 -1.5951152 0.0000000
F -2.2289731 0.2693206 0.0000000
F -2.8767920 -0.9827016 0.0000000

AuF_5 (^1E-C_{4v})
Au -0.0000000 0.0000000 -0.2529066
F 0.0000000 1.8921291 -0.3390845
F -1.8921291 0.0000000 -0.3390845
F 0.0000000 -1.8921291 -0.3390845
F 1.8921291 0.0000000 -0.3390845
F 0.0000000 0.0000000 1.6092445

$[AuF_5 \cdot F_2]$ ($^1A''$-C_s)
Au -0.0917379 -0.4285254 0.0000000
F -0.0931783 -0.3798846 1.8984529
F -1.9915186 -0.4517839 0.0000000
F -0.0931783 -0.3798846 -1.8984529
F 1.8020782 -0.2982374 0.0000000
F 0.0167668 -2.2821123 0.0000000
F -0.3980709 1.7792340 0.0000000
F 0.8488390 2.4411943 0.0000000

6.1.1.2 RI-B3LYP-D4/def2-TZVPP

BF_3 ($^1A_2'$-D_{3h})
B -0.0000000 0.0000000 0.0000000
F 0.6579779 -1.1396511 0.0000000
F 0.6579779 1.1396511 0.0000000
F -1.3159558 0.0000000 0.0000000

$[BF_3 \cdot F_2]$ ($^1A''$-C_s)

B	0.1560741	1.0135138	0.0000000
F	1.4723213	1.0443506	0.0000000
F	-0.5018053	1.0069997	1.1397521
F	-0.5018053	1.0069997	-1.1397521
F	-0.9752054	-2.2566747	0.0000000
F	0.3504206	-1.8151889	0.0000000

AsF_5 ($^1E''$-D_{3h})

As	-0.0000000	0.0000000	0.0000000
F	0.8460802	1.4654538	0.0000000
F	0.0000000	-0.0000000	1.7139148
F	0.8460802	-1.4654538	-0.0000000
F	-1.6921603	0.0000000	-0.0000000
F	0.0000000	0.0000000	-1.7139148

$[AsF_5 \cdot F_2]$ (^1A-C_1)

As	-0.0857519	1.1716611	-0.3902552
F	1.3952665	0.3161043	-0.2785180
F	0.4865754	1.9694850	-1.7699510
F	-1.5686452	2.0206276	-0.5216935
F	-0.9216358	-0.2964558	-0.4845064
F	0.1871730	1.8621381	1.1291281
F	-0.9527578	0.1286199	-3.5076717
F	-1.6723942	-1.0669302	-3.4408824

SbF_5 ($^1E''$-D_{3h})

Sb	-0.0000000	0.0000000	-0.0000000
F	-0.0000000	0.0000000	1.8728729
F	1.8637269	0.0000000	0.0000000
F	-0.9318635	1.6140349	0.0000000
F	-0.0000000	0.0000000	-1.8728729
F	-0.9318635	-1.6140349	0.0000000

$[SbF_5 \cdot F_2]$ ($^1A''$-C_s)

Sb	0.8639919	0.1214440	0.0000000
F	0.8124601	0.1216168	1.8724919
F	2.7244291	0.1690077	0.0000000
F	-0.0010304	1.7756710	0.0000000
F	0.8124601	0.1216168	-1.8724919
F	0.0873129	-1.5737121	0.0000000
F	-2.3336011	0.2552810	0.0000000
F	-2.9660225	-0.9909251	0.0000000

AuF_5 ($^1B_2$-C_{4v})
Au 0.0000000 0.0000000 -0.2272706
F -0.0000000 1.8982470 -0.3488344
F -1.8982470 -0.0000000 -0.3488344
F -0.0000000 -1.8982470 -0.3488344
F 1.8982470 0.0000000 -0.3488344
F 0.0000000 0.0000000 1.6356077

$[AuF_5 \cdot F_2]$ ($^1A''$-C_s)
Au -0.0916512 -0.4528033 0.0000000
F -0.0933393 -0.3838698 1.9059889
F -1.9998704 -0.4537081 0.0000000
F -0.0933393 -0.3838698 -1.9059889
F 1.8076045 -0.2883993 0.0000000
F 0.0043475 -2.3082037 0.0000000
F -0.3687402 1.7768271 0.0000000
F 0.8349884 2.4940269 0.0000000

6.1.1.3 RI-BP86-D4/def2-TZVPP

BF_3 ($^1A_2'$-D_{3h})
B -0.0000000 0.0000000 0.0000000
F 0.6628781 -1.1481385 0.0000000
F 0.6628781 1.1481385 0.0000000
F -1.3257562 0.0000000 -0.0000000

$[BF_3 \cdot F_2]$ ($^1A''$-C_s)
B -0.0185295 1.0854755 0.0000000
F 1.2889156 1.3076970 0.0000000
F -0.6731380 0.9822872 1.1482248
F -0.6731380 0.9822872 -1.1482248
F -0.5968272 -2.4914627 0.0000000
F 0.6727172 -1.8662842 0.0000000

AsF_5 ($^1E''$-D_{3h})
As -0.0000000 0.0000000 0.0000000
F 0.8551622 -1.4811843 0.0000000
F 0.0000000 0.0000000 -1.7298453
F 0.8551622 1.4811843 0.0000000
F -1.7103243 0.0000000 -0.0000000
F 0.0000000 0.0000000 1.7298453

$[AsF_5 \cdot F_2]$ (^1A-C_1)

As	-0.0637997	1.2007317	-0.3275437
F	1.4339197	0.3425540	-0.2127272
F	0.5034002	1.9927586	-1.7344403
F	-1.5619445	2.0556744	-0.4563460
F	-0.9051554	-0.2849210	-0.4186048
F	0.2169565	1.9080098	1.2031950
F	-1.0029968	0.0431819	-3.7082184
F	-1.7525499	-1.1527394	-3.6096647

SbF_5 ($^1E''$-D_{3h})

Sb	0.0000000	0.0000000	0.0000000
F	0.0000000	0.0000000	1.8896857
F	-0.9408523	1.6296040	0.0000000
F	-0.9408523	-1.6296040	-0.0000000
F	0.0000000	0.0000000	-1.8896857
F	1.8817046	0.0000000	0.0000000

$[SbF_5 \cdot F_2]$ ($^1A''$-C_s)

Sb	0.7605159	-0.0004582	0.0000000
F	0.5782058	0.0187651	1.8811612
F	2.6279629	-0.1557973	0.0000000
F	0.3155221	1.8384863	0.0000000
F	0.5782058	0.0187651	-1.8811612
F	0.0127710	-1.7322449	0.0000000
F	-1.9949118	0.5616413	0.0000000
F	-2.8782718	-0.5491574	0.0000000

AuF_5 (^1A-C_1)

Au	5.4196186	0.1267787	0.1405138
F	6.5684334	1.6230651	-0.1797658
F	3.9244962	1.3247697	0.0355189
F	4.2923764	-1.4246230	0.0660063
F	6.9193233	-1.0170327	-0.1739809
F	5.0078222	0.1029823	1.9970276

$[AuF_5 \cdot F_2]$ ($^1A''$-C_s)

Au	-0.0593714	-0.4574421	0.0000000
F	-0.0585882	-0.3861912	1.9228633
F	-1.9895231	-0.3459559	0.0000000
F	-0.0585882	-0.3861912	-1.9228633
F	1.8574694	-0.3622160	0.0000000
F	-0.0293229	-2.3337644	0.0000000
F	-0.4087372	1.7012148	0.0000000
F	0.7466617	2.5705461	0.0000000

6.1.1.4 RI-PBE-D4/def2-TZVPP

BF_3 ($^1A_2'$-D_{3h})

B	0.0000000	0.0000000	-0.0000000
F	0.6626902	-1.1478132	0.0000000
F	0.6626902	1.1478132	0.0000000
F	-1.3253805	0.0000000	0.0000000

$[BF_3 \cdot F_2]$ ($^1A''$-C_s)

B	-0.0225730	1.0215232	0.0000000
F	1.2828880	1.2560162	0.0000000
F	-0.6767198	0.9150431	1.1478429
F	-0.6767198	0.9150431	-1.1478429
F	-0.5824222	-2.3765609	0.0000000
F	0.6755467	-1.7310646	0.0000000

AsF_5 ($^1E''$-D_{3h})

As	-0.0000000	0.0000000	-0.0000000
F	0.8553485	1.4815071	0.0000000
F	0.0000000	0.0000000	1.7301601
F	0.8553485	-1.4815071	0.0000000
F	-1.7106970	0.0000000	0.0000000
F	0.0000000	0.0000000	-1.7301601

$[AsF_5 \cdot F_2]$ ($^1A''$-C_s)

As	-0.9254150	-0.1560439	0.0000000
F	-0.0211755	-1.6103394	0.0000000
F	-0.9149418	-0.1573031	-1.7301784
F	-0.1750572	1.3811106	0.0000000
F	-2.6326931	-0.2436637	0.0000000
F	-0.9149418	-0.1573031	1.7301784
F	2.5204066	-0.1807907	0.0000000
F	3.0638177	1.1243333	0.0000000

SbF_5 ($^1E''$-D_{3h})

Sb	0.0000000	0.0000000	0.0000000
F	0.0000000	0.0000000	1.8898310
F	-0.9409452	1.6297648	0.0000000
F	-0.9409452	-1.6297648	-0.0000000
F	0.0000000	-0.0000000	-1.8898310
F	1.8818903	0.0000000	0.0000000

$[SbF_5 \cdot F_2]$ ($^1A''$-C_s)

Sb	0.7482875	0.0009936	0.0000000
F	0.5602095	0.0217526	1.8808287
F	2.6153379	-0.1614402	0.0000000
F	0.3178385	1.8444772	0.0000000
F	0.5602095	0.0217526	-1.8808287
F	0.0001726	-1.7312073	0.0000000
F	-1.9647113	0.5610184	0.0000000
F	-2.8373441	-0.5573468	0.0000000

AuF_5 ($^1A'$-C_s)

Au	0.0666949	0.1755425	0.0000000
F	-1.2560747	0.2938720	1.3842896
F	-1.2560747	0.2938720	-1.3842896
F	1.4094773	0.4549172	-1.3343476
F	1.4094773	0.4549172	1.3343476
F	-0.3734993	-1.6731214	0.0000000

$[AuF_5 \cdot F_2]$ ($^1A''$-C_s)

Au	-0.0589310	-0.4594373	0.0000000
F	-0.0586455	-0.3879728	1.9224965
F	-1.9885693	-0.3388108	0.0000000
F	-0.0586455	-0.3879728	-1.9224965
F	1.8576498	-0.3648726	0.0000000
F	-0.0206839	-2.3353843	0.0000000
F	-0.4153197	1.7066940	0.0000000
F	0.7431450	2.5677567	0.0000000

6.1.2 NPA Charges of [LA·F_2] Adducts

The following tables comprise the NPA charges of the [LA·F_2] adducts obtained at the RI-B3LYP-D4/def2-TZVPP level of theory. The atomic labels are found in Figure 102.

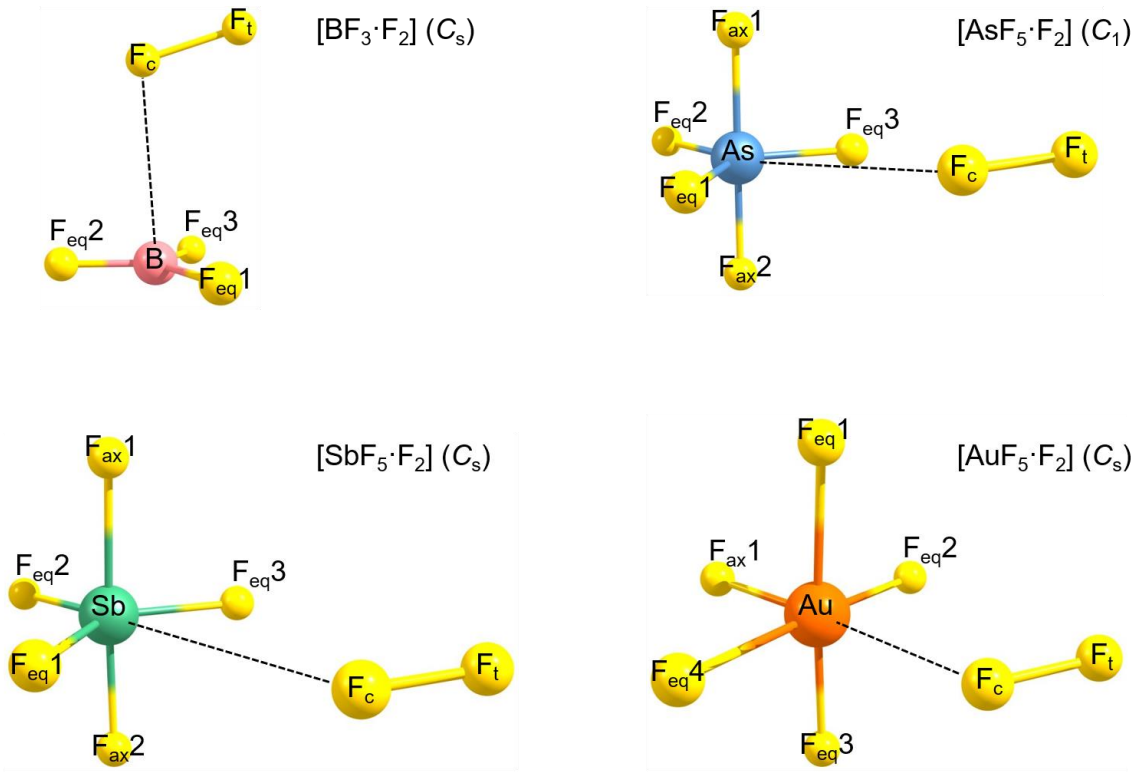

Figure 102: Labelling of [LA·F_2] adducts optimized at the RI-B3LYP-D4/def2-TZVPP level of theory in accordance with the obtained NPA charges. The free Lewis acids are labelled accordingly (with respect to identical axial and equatorial ligands).

Table 33: NPA charges (in e) of the B3LYP structures of [BF_3·F_2] and BF_3.

[BF_3·F_2]		**BF_3**	
Atom	Charge	Atom	Charge
B	1.446	B	1.447
$F_{eq}1$	−0.483	$F_{eq}1$	−0.482
$F_{eq}2$	−0.484	$F_{eq}2$	−0.482
$F_{eq}3$	−0.483	$F_{eq}3$	−0.482
F_c	−0.007		
F_t	0.011		

Table 34: NPA charges (in e) of the B3LYP structures of $[AsF_5 \cdot F_2]$ and AsF_5.

$[AsF_5 \cdot F_2]$		**AsF_5**	
Atom	Charge	Atom	Charge
As	2.834	As	2.832
$F_{ax}1$	−0.582	$F_{ax}1$	−0.582
$F_{ax}2$	−0.582	$F_{ax}2$	−0.582
$F_{eq}1$	−0.557	$F_{eq}1$	−0.556
$F_{eq}2$	−0.557	$F_{eq}2$	−0.556
$F_{eq}3$	−0.556	$F_{eq}3$	−0.556
F_c	−0.007		
F_t	0.008		

Table 35: NPA charges (in e) of the B3LYP structures of $[SbF_5 \cdot F_2]$ and SbF_5.

$[SbF_5 \cdot F_2]$		**SbF_5**	
Atom	Charge	Atom	Charge
Sb	3.114	Sb	3.114
$F_{ax}1$	−0.627	$F_{ax}1$	−0.626
$F_{ax}2$	−0.627	$F_{ax}2$	−0.626
$F_{eq}1$	−0.621	$F_{eq}1$	−0.620
$F_{eq}2$	−0.623	$F_{eq}2$	−0.620
$F_{eq}3$	−0.620	$F_{eq}3$	−0.620
F_c	−0.013		
F_t	0.017		

Table 36: NPA charges (in e) of the B3LYP structures of $[AuF_5 \cdot F_2]$ and AuF_5.

$[AuF_5 \cdot F_2]$		**AuF_5**	
Atom	Charge	Atom	Charge
Au	2.218	Au	2.223
$F_{ax}1$	−0.309	$F_{ax}1$	−0.274
$F_{eq}1$	−0.501	$F_{eq}1$	−0.487
$F_{eq}2$	−0.499	$F_{eq}2$	−0.487
$F_{eq}3$	−0.501	$F_{eq}3$	−0.487
$F_{eq}4$	−0.501	$F_{eq}4$	−0.487
F_c	0.006		
F_t	0.088		

6.1.3 Vibrational Frequencies of $[LA \cdot F_2]$ Adducts

6.1.3.1 RI-B3LYP-D4/def2-TZVPP

The following tables comprise the vibrational frequencies and their respective IR intensities of the Lewis acids BF_3, AsF_5, SbF_5 and AuF_5 together with the corresponding F_2 adducts calculated at the RI-B3LYP-D4/def2-TZVPP level of theory on the basis of the optimized structures described in Section 6.1.1.2.

Table 37: B3LYP vibrational frequencies $\tilde{\nu}$ of $[BF_3 \cdot F_2]$ and BF_3 given in cm^{-1}, their respective symmetries and the corresponding IR intensities *I* given in $km \cdot mol^{-1}$. Degenerate bands have twice the given intensity.

Symmetry	**$\tilde{\nu}$ ($[BF_3 \cdot F_2]$)**	***I*** **($[BF_3 \cdot F_2]$)**	**Symmetry**	**$\tilde{\nu}$ (BF_3)**	***I*** **(BF_3)**	**Description**
a"	18.89	0.007				$\tau BF_3(F_2)$
a'	32.25	0.002				$\omega BF_3(F_2)$
a"	48.50	0.003				$\rho BF_3(F_2)$
a'	53.51	0.06				$\nu B(F_2)$
a'	76.42	0.25				$\delta B(F_2)$
a"	471.73	11.83	e'	472.16	12.44	δBF_3
a'	472.09	11.17				δBF_3
a'	679.64	122.20	a2"	687.38	97.47	$\delta BF_{3,um}$
a'	883.47	0.10	a1'	884.66	0	$\nu_s BF_3$
a'	1046.44	0.18				$\nu F–F$
a'	1455.67	408.37	e'	1458.96	439.72	$\nu_{as} BF_3$
a"	1457.89	424.82				$\nu_{as} BF_3$

Table 38: B3LYP vibrational frequencies $\tilde{\nu}$ of $[AsF_5 \cdot F_2]$ and AsF_5 given in cm^{-1}, their respective symmetries and the corresponding IR intensities *I* given in $km \cdot mol^{-1}$. Degenerate bands have twice the given intensity. Where applicable, the description of the vibrational modes refers to the parent AsF_5 molecule.

Symmetry	$\tilde{\nu}$ ($[AsF_5 \cdot F_2]$)	*I* ($[AsF_5 \cdot F_2]$)	Symmetry	$\tilde{\nu}$ (AsF_5)	*I* (AsF_5)	Description
a	15.21	0.003				$\rho AsF_5(F_2)$
a	26.72	0.004				$\tau AsF_5(F_2)$
a	39.72	0.02				$\omega AsF_5(F_2)$
a	47.30	0.08				$\nu As(F_2)$
a	71.13	0.06				$\delta As(F_2)$
a	125.30	0.50	e'	124.14	0.37	$\delta AsF_{3,eq}$
a	136.53	0.43				$\delta AsF_{3,eq}$
a	355.40	51.63	e'	357.35	46.77	$\delta AsF_{2,ax}$
a	358.95	44.89				$\delta AsF_{2,ax}$
a	370.08	0.13	e''	373.31	0	ρAsF_3
a	376.63	0.005				ρAsF_3
a	388.60	58.59	a2''	388.28	59.94	$\delta AsF_{3,um}$
a	630.00	0.04	a1'	630.34	0	$\nu_s AsF_{5,oop}$
a	710.91	0.09	a1'	711.12	0	$\nu_s AsF_{5,ip}$
a	768.85	173.03	a2''	768.92	175.64	$\nu_{as} AsF_{2,ax}$
a	783.56	132.28	e'	785.29	130.50	$\nu_{as} AsF_{3,eq}$
a	785.51	127.68				$\nu_{as} AsF_{3,eq}$
a	1046.90	0.02				$\nu F{-}F$

Table 39: B3LYP vibrational frequencies $\tilde{\nu}$ of $[SbF_5 \cdot F_2]$ and SbF_5 given in cm^{-1}, their respective symmetries and the corresponding IR intensities *I* given in $km \cdot mol^{-1}$. Where applicable, the description of the vibrational modes refers to the parent SbF_5 molecule.

Symmetry	$\tilde{\nu}$ ($[SbF_5 \cdot F_2]$)	*I* ($[SbF_5 \cdot F_2]$)	Symmetry	$\tilde{\nu}$ (SbF_5)	*I* (SbF_5)	Description
a"	5.78	0.002				$\rho SbF_5(F_2)$
a'	30.21	1.22				$\nu Sb(F_2)$
a"	41.39	0.01				$\tau SbF_5(F_2)$
a'	53.29	0.08				$\omega SbF_5(F_2)$
a'	94.62	0.50	e'	91.32	1.11	$\delta SbF_{3,eq}$
a'	100.05	0.04				$\delta Sb(F_2)$
a'	125.03	1.10	e'	91.32	1.11	$\delta SbF_{3,eq}$
a'	246.18	55.12	e'	252.57	46.19	$\delta SbF_{2,ax}$
a'	256.76	43.96	e'	252.57	46.19	$\delta SbF_{2,ax}$
a"	260.39	3.07	e"	272.18	0	ρSbF_3
a"	274.85	43.48	a2"	272.74	48.26	$\delta SbF_{3,um}$
a"	281.78	0.33	e"	272.18	0	ρSbF_3
a'	612.00	0.12	a1'	613.24	0	$\nu_s SbF_{5,oop}$
a'	653.47	0.68	a1'	654.75	0	$\nu_s SbF_{5,ip}$
a'	698.91	103.16	e'	701.47	102.05	$\nu_{as} SbF_{3,eq}$
a"	699.57	123.33	a2"	700.23	125.14	$\nu_{as} SbF_{2,ax}$
a'	701.53	99.93	e'	701.47	102.05	$\nu_{as} SbF_{3,eq}$
a'	1043.09	0.06				$\nu F{-}F$

Table 40: B3LYP vibrational frequencies $\tilde{\nu}$ of $[AuF_5 \cdot F_2]$ and AuF_5 given in cm^{-1}, their respective symmetries and the corresponding IR intensities *I* given in $km \cdot mol^{-1}$. Degenerate bands have twice the given intensity. Vibrational modes highlighted with an asterisk (*) are out-of-plane. The $\{AuF_4\}$ moiety refers to the basal plane of the parent AuF_5.

Symmetry	$\tilde{\nu}$ ($[AuF_5 \cdot F_2]$)	*I* ($[AuF_5 \cdot F_2]$)	Symmetry	$\tilde{\nu}$ (AuF_5)	*I* (AuF_5)	Description
a"	12.15	0.03				$\tau AuF_5(F_2)$
a'	85.65	0.23				$\omega AuF_5(F_2)$
a"	122.18	0.13				$\rho AuF_5(F_2)$
a'	145.38	1.08				$\delta Au(F_2)$
a'	174.14	1.80	e	58.76	1.74	ρAuF_4
a"	175.24	0.02				ρAuF_4
a"	200.13	0.00002	b2	197.16	0	δAuF_4
a'	200.22	0.006	b1	176.49	0	$\delta AuF_{2,eq,oop}$*
a'	245.63	18.16	a1	230.75	11.77	$\delta AuF_{4,um}$*
a'	251.41	5.28	e	256.87	2.73	$\delta AuF_{2,eq}$
a"	255.10	2.45				$\delta AuF_{2,eq}$
a'	273.07	9.17				$\nu Au(F_2)$
a'	597.21	0.01	b1	604.55	0	$\nu_s AuF_{2,eq,oop}$
a'	601.94	0.02	a1	610.46	0.06	$\nu_s AuF_{2,eq,ip}$
a'	656.71	105.12	e	661.51	107.96	$\nu_{as} AuF_{2,eq}$
a"	657.45	110.34				$\nu_{as} AuF_{2,eq}$
a'	673.75	13.82	a1	660.51	2.35	$\nu Au{-}F$
a'	1003.02	0.67				$\nu F{-}F$

6.1.3.2 SCS-MP2/def2-TZVPP

The following tables comprise the vibrational frequencies and their respective IR intensities of the Lewis acids BF_3, AsF_5, SbF_5 and AuF_5 together with the corresponding $[LA{\cdot}F_2]$ adducts calculated at the SCS-MP2/def2-TZVPP level of theory on the basis of the optimized structures described in Section 6.1.1.1.

Table 41: SCS-MP2 vibrational frequencies $\tilde{\nu}$ of C_s-$[BF_3{\cdot}F_2]$ and D_{3h}-BF_3 given in cm^{-1}, their respective symmetries and the corresponding IR intensities I given in $km{\cdot}mol^{-1}$.

Symmetry	$\tilde{\nu}$ **($[BF_3{\cdot}F_2]$)**	I **($[BF_3{\cdot}F_2]$)**	**Symmetry**	$\tilde{\nu}$ **(BF_3)**	I **(BF_3)**
a"	1491.36	499.77283	e'	1491.73	515.4456
a'	1488.70	470.51838	e'	1491.73	515.4456
a'	980.79	0.37997	a1'	900.78	0
a'	899.82	0.16683	a2"	768.30	149.49759
a'	763.27	176.1131	e'	508.33	14.40485
a'	508.21	12.58456	e'	508.33	14.40485
a"	508.12	13.76991			
a'	269.42	0.23691			
a"	254.16	0.0078			
a'	113.40	0.04439			
a"	108.38	0.00663			
a'	60.74	0.10308			

Table 42: SCS-MP2 vibrational frequencies $\tilde{\nu}$ of C_1-[$AsF_5 \cdot F_2$] and D_{3h}-AsF_5 given in cm^{-1}, their respective symmetries and the corresponding IR intensities I given in $km \cdot mol^{-1}$.

Symmetry	$\tilde{\nu}$ ([$AsF_5 \cdot F_2$])	I ([$AsF_5 \cdot F_2$])	Symmetry	$\tilde{\nu}$ (AsF_5)	I (AsF_5)
a	982.16	0.11129	e'	820.39	159.42688
a	820.58	154.63931	e'	820.39	159.42688
a	818.30	159.522	a2"	799.99	222.79711
a	799.90	220.42659	a1'	759.66	0
a	759.22	0.11347	a1'	643.28	0
a	642.92	0.02729	a2"	439.29	80.92203
a	439.20	79.89752	e"	417.26	0
a	420.07	0.2419	e"	417.26	0
a	414.38	0.11165	e'	410.84	67.08255
a	411.90	64.00613	e'	410.84	67.08255
a	409.42	72.46343	e'	179.51	0.25527
a	273.36	0.08044	e'	179.51	0.25527
a	261.57	0.00867			
a	187.32	0.36178			
a	178.31	0.36649			
a	108.28	0.0047			
a	90.98	0.00258			
a	50.72	0.0668			

Table 43: SCS-MP2 vibrational frequencies $\tilde{\nu}$ of C_s-[$SbF_5 \cdot F_2$] and D_{3h}-SbF_5 given in cm^{-1}, their respective symmetries and the corresponding IR intensities *I* given in $km \cdot mol^{-1}$.

Symmetry	$\tilde{\nu}$ ([$SbF_5 \cdot F_2$])	*I* ([$SbF_5 \cdot F_2$])	Symmetry	$\tilde{\nu}$ (SbF_5)	*I* (SbF_5)
a'	979.75	1.34541	e'	740.58	131.49534
a'	740.66	133.01026	e'	740.58	131.49534
a"	739.55	170.23716	a2"	739.70	173.70262
a'	737.28	121.80204	a1'	710.23	0
a'	707.48	5.08919	a1'	634.46	0
a'	632.23	0.20797	a2"	319.10	69.47505
a"	329.49	0.07167	e"	312.42	0
a"	320.11	63.82544	e"	312.42	0
a'	304.49	64.27124	e'	296.46	70.22986
a'	292.80	60.45201	e'	296.46	70.22986
a"	289.60	3.58072	e'	140.41	0.61856
a'	284.80	24.68558	e'	140.41	0.61856
a"	265.00	0.05366			
a'	182.14	1.04867			
a'	131.07	0.05338			
a'	109.04	0.00682			
a"	74.48	0.00188			
a'	51.08	1.34593			

Table 44: SCS-MP2 vibrational frequencies $\tilde{\nu}$ of C_s-[$AuF_5 \cdot F_2$] and C_{4v}-AuF_5 given in cm^{-1}, their respective symmetries and the corresponding IR intensities *I* given in $km \cdot mol^{-1}$.

Symmetry	$\tilde{\nu}$ ([$AuF_5 \cdot F_2$])	*I* ([$AuF_5 \cdot F_2$])	Symmetry	$\tilde{\nu}$ (AuF_5)	*I* (AuF_5)
a'	964.37	24.83136	e	656.87	209.4275
a'	663.83	8.95589	e	656.87	209.4275
a''	648.70	203.53158	a1	644.24	0.2321
a'	648.25	191.39802	a1	627.31	1.10758
a'	620.35	0.7838	b1	626.26	0
a'	618.68	0.37902	e	307.03	2.02516
a'	349.67	36.93457	e	307.03	2.02516
a'	310.99	23.88565	a1	295.98	22.86811
a''	307.25	1.52069	b2	262.23	0
a'	306.70	1.93258	b1	239.58	0
a''	275.06	0.00688	e	215.57	0.20896
a''	262.14	0.00199	e	215.57	0.20896
a'	257.54	0.311			
a'	251.32	0.63135			
a''	251.08	0.51108			
a'	169.69	4.6892			
a'	143.48	3.67547			
a''	137.89	0.06781			

6.1.3.3 RI-BP86-D4/def2-TZVPP

The following tables comprise the vibrational frequencies and their respective IR intensities of the Lewis acids BF_3, AsF_5, SbF_5 and AuF_5 together with the corresponding F_2 adducts calculated at the RI-BP86-D4/def2-TZVPP level of theory on the basis of the optimized structures described in Section 6.1.1.3.

Table 45: BP86 vibrational frequencies $\tilde{\nu}$ of C_s-[BF_3·F_2] and D_{3h}-BF_3 given in cm^{-1}, their respective symmetries and the corresponding IR intensities I given in $km \cdot mol^{-1}$.

Symmetry	$\tilde{\nu}$ ([BF_3·F_2])	I ([BF_3·F_2])	Symmetry	$\tilde{\nu}$ (BF_3)	I (BF_3)
a"	1416.87	400.70332	e'	1417.93	413.34655
a'	1415.37	386.7503	e'	1417.93	413.34655
a'	994.62	0.08429	a1'	856.88	0
a'	855.95	0.06216	a2"	664.59	80.16623
a'	658.56	97.77446	e'	457.08	10.97589
a'	457.00	9.98107	e'	457.08	10.97589
a"	456.78	10.49257			
a'	55.35	0.08519			
a"	37.89	0.00261			
a'	35.11	0.07913			
a'	28.71	0.01			
a"	19.64	0.00372			

Table 46: BP86 vibrational frequencies $\tilde{\nu}$ of C_1-[$AsF_5 \cdot F_2$] and D_{3h}-AsF_5 given in cm^{-1}, their respective symmetries and the corresponding IR intensities *I* given in $km \cdot mol^{-1}$.

Symmetry	$\tilde{\nu}$ ([$AsF_5 \cdot F_2$])	*I* ([$AsF_5 \cdot F_2$])	Symmetry	$\tilde{\nu}$ (AsF_5)	*I* (AsF_5)
a	995.40	0.00715	e'	745.94	124.13042
a	746.60	121.96945	e'	745.94	124.13042
a	744.79	125.64478	a2"	734.04	163.02824
a	733.97	161.00316	a1'	672.99	0
a	673.05	0.05021	a1'	604.08	0
a	603.88	0.02437	a2"	370.95	50.7688
a	371.55	49.8633	e"	356.23	0
a	358.47	0.0046	e"	356.23	0
a	354.37	0.03269	e'	340.93	38.66147
a	342.07	37.29426	e'	340.93	38.66147
a	339.88	41.7447	e'	115.41	0.31051
a	124.08	0.32303	e'	115.41	0.31051
a	114.97	0.4311			
a	48.84	0.01158			
a	28.86	0.00076			
a	25.35	0.03022			
a	17.62	0.00138			
a	15.18	0.0017			

Table 47: BP86 vibrational frequencies $\tilde{\nu}$ of C_s-[$SbF_5 \cdot F_2$] and D_{3h}-SbF_5 given in cm^{-1}, their respective symmetries and the corresponding IR intensities *I* given in $km \cdot mol^{-1}$.

Symmetry	$\tilde{\nu}$ ([$SbF_5 \cdot F_2$])	*I* ([$SbF_5 \cdot F_2$])	Symmetry	$\tilde{\nu}$ (SbF_5)	*I* (SbF_5)
a'	961.09	3.70039	e'	666.62	94.77499
a'	666.80	89.14446	e'	666.62	94.77499
a"	665.13	109.64988	a2"	666.34	112.41462
a'	660.86	96.18863	a1'	619.23	0
a'	613.29	2.70768	a1'	586.79	0
a'	581.49	0.67811	a2"	259.97	40.23961
a"	283.41	0.06474	e"	259.96	0
a"	263.05	35.67441	e"	259.96	0
a'	254.43	34.63533	e'	241.42	37.95085
a'	230.83	54.31006	e'	241.42	37.95085
a"	223.13	2.2025	e'	84.75	1.09732
a'	161.91	1.84571	e'	84.75	1.09732
a'	136.88	0.58756			
a'	82.62	0.11145			
a"	64.79	0.01755			
a'	62.34	0.04564			
a"	32.84	0.0132			
a'	32.73	1.94074			

Table 48: BP86 vibrational frequencies $\tilde{\nu}$ of C_s-[$AuF_5 \cdot F_2$] and C_1-AuF_5 given in cm^{-1}, their respective symmetries and the corresponding IR intensities *I* given in $km \cdot mol^{-1}$.

Symmetry	$\tilde{\nu}$ ([$AuF_5 \cdot F_2$])	*I* ([$AuF_5 \cdot F_2$])	Symmetry	$\tilde{\nu}$ (AuF_5)	*I* (AuF_5)
a'	770.38	109.74161	a	631.90	74.60128
a'	639.97	16.80561	a	624.98	74.998
a''	625.89	83.42525	a	576.83	2.89862
a'	615.93	67.40283	a	576.32	7.93382
a'	568.94	0.69228	a	560.89	1.32578
a'	562.17	1.73693	a	255.14	2.76096
a'	264.29	2.25688	a	251.25	1.76067
a''	242.62	2.0956	a	237.86	4.10451
a'	240.45	3.96659	a	213.70	0.53044
a'	221.42	5.59568	a	179.75	2.70108
a'	185.71	0.35668	a	90.42	1.69572
a''	183.38	0.00033	a	31.19	1.90687
a'	157.15	0.02544			
a''	153.20	0.61423			
a''	128.00	0.25105			
a'	120.29	1.83424			
a'	54.90	2.05234			
a''	40.10	0.05305			

6.1.3.4 RI-PBE-D4/def2-TZVPP

The following tables comprise the vibrational frequencies and their respective IR intensities of the Lewis acids BF_3, AsF_5, SbF_5 and AuF_5 together with the corresponding F_2 adducts calculated at the RI-PBE-D4/def2-TZVPP level of theory on the basis of the optimized structures described in Section 6.1.1.4.

Table 49: PBE vibrational frequencies $\tilde{\nu}$ of C_s-[BF_3·F_2] and D_{3h}-BF_3 given in cm^{-1}, their respective symmetries and the corresponding IR intensities I given in $km \cdot mol^{-1}$.

Symmetry	$\tilde{\nu}$ ([BF_3·F_2])	I ([BF_3·F_2])	Symmetry	$\tilde{\nu}$ (BF_3)	I (BF_3)
a"	1419.00	392.40335	e'	1420.17	407.28887
a'	1415.85	376.44662	e'	1420.17	407.28887
a'	993.64	0.10442	a1'	858.44	0
a'	856.80	0.11682	a2"	663.48	79.2385
a'	653.94	103.63049	e'	456.94	10.80065
a'	456.88	9.62325	e'	456.94	10.80065
a"	456.38	10.18116			
a'	70.09	0.21687			
a'	57.27	0.09439			
a"	49.12	0.00406			
a'	32.36	0.00270			
a"	19.40	0.00497			

Table 50: PBE vibrational frequencies $\tilde{\nu}$ of C_s-[$AsF_5 \cdot F_2$] and D_{3h}-AsF_5 given in cm^{-1}, their respective symmetries and the corresponding IR intensities *I* given in $km \cdot mol^{-1}$.

Symmetry	$\tilde{\nu}$ ([$AsF_5 \cdot F_2$])	*I* ([$AsF_5 \cdot F_2$])	Symmetry	$\tilde{\nu}$ (AsF_5)	*I* (AsF_5)
a'	993.50	0.02574	e'	746.65	123.11246
a'	746.85	122.35951	e'	746.65	123.11246
a'	744.13	123.96942	a2"	735.01	161.84394
a"	734.91	159.19633	a1'	673.71	0
a'	673.23	0.12892	a1'	604.66	0
a'	604.14	0.06055	a2"	370.38	50.54252
a"	370.86	49.14702	e"	355.80	0
a"	358.73	0.00968	e"	355.80	0
a"	352.39	0.08367	e'	340.50	38.48573
a'	341.78	37.02185	e'	340.50	38.48573
a'	337.79	43.03169	e'	115.10	0.32826
a'	127.76	0.37212	e'	115.10	0.32826
a'	116.66	0.50278			
a'	67.17	0.01518			
a'	42.76	0.06134			
a'	34.47	0.03665			
a"	26.19	0.0033			
a"	5.33	0.00126			

Table 51: PBE vibrational frequencies $\tilde{\nu}$ of C_s-[$SbF_5 \cdot F_2$] and D_{3h}-SbF_5 given in cm^{-1}, their respective symmetries and the corresponding IR intensities *I* given in $km \cdot mol^{-1}$.

Symmetry	$\tilde{\nu}$ ([$SbF_5 \cdot F_2$])	*I* ([$SbF_5 \cdot F_2$])	Symmetry	$\tilde{\nu}$ (SbF_5)	*I* (SbF_5)
a'	956.54	4.72502	e'	667.06	94.43254
a'	667.17	88.6814	e'	667.06	94.43254
a"	665.63	109.42436	a2"	667.05	112.18444
a'	660.40	95.39597	a1'	619.86	0
a'	613.38	2.79399	a1'	587.18	0
a'	581.25	0.78061	a2"	259.43	40.20051
a"	283.15	0.05955	e"	259.30	0
a"	262.71	35.48466	e"	259.30	0
a'	254.32	34.485	e'	241.00	37.99285
a'	230.85	54.94053	e'	241.00	37.99285
a"	221.38	2.24972	e'	85.08	1.09924
a'	165.54	1.99578	e'	85.08	1.09924
a'	141.95	0.61137			
a'	90.05	0.26468			
a"	68.61	0.01904			
a'	67.36	0.07028			
a'	38.63	1.84182			
a"	33.65	0.01367			

Table 52: PBE vibrational frequencies $\tilde{\nu}$ of C_s-[$AuF_5 \cdot F_2$] and C_s-AuF_5 given in cm^{-1}, their respective symmetries and the corresponding IR intensities *I* given in $km \cdot mol^{-1}$.

Symmetry	$\tilde{\nu}$ ([$AuF_5 \cdot F_2$])	*I* ([$AuF_5 \cdot F_2$])	Symmetry	$\tilde{\nu}$ (AuF_5)	*I* (AuF_5)
a'	776.66	102.86019	a'	631.29	73.84685
a'	639.31	17.64877	a"	624.45	74.29709
a"	625.54	83.08119	a'	577.87	10.71219
a'	615.05	66.30119	a'	576.02	0.13847
a'	568.57	0.68723	a"	561.05	1.42323
a'	561.80	2.06278	a'	254.04	2.94784
a'	261.85	1.52947	a"	250.55	1.72919
a"	242.44	2.08256	a'	236.27	4.03301
a'	240.17	3.94379	a"	211.75	0.57775
a'	221.52	6.32126	a'	177.59	2.52593
a'	185.65	0.33398	a'	84.99	1.84621
a"	182.01	0.00198	a"	21.61	1.96492
a'	155.42	0.00766			
a"	152.26	0.59321			
a"	126.44	0.28668			
a'	119.68	1.68315			
a'	54.13	2.16648			
a"	41.13	0.04945			

6.1.4 Structure of F_2 in the Presence of Two {AsF_5} Moieties

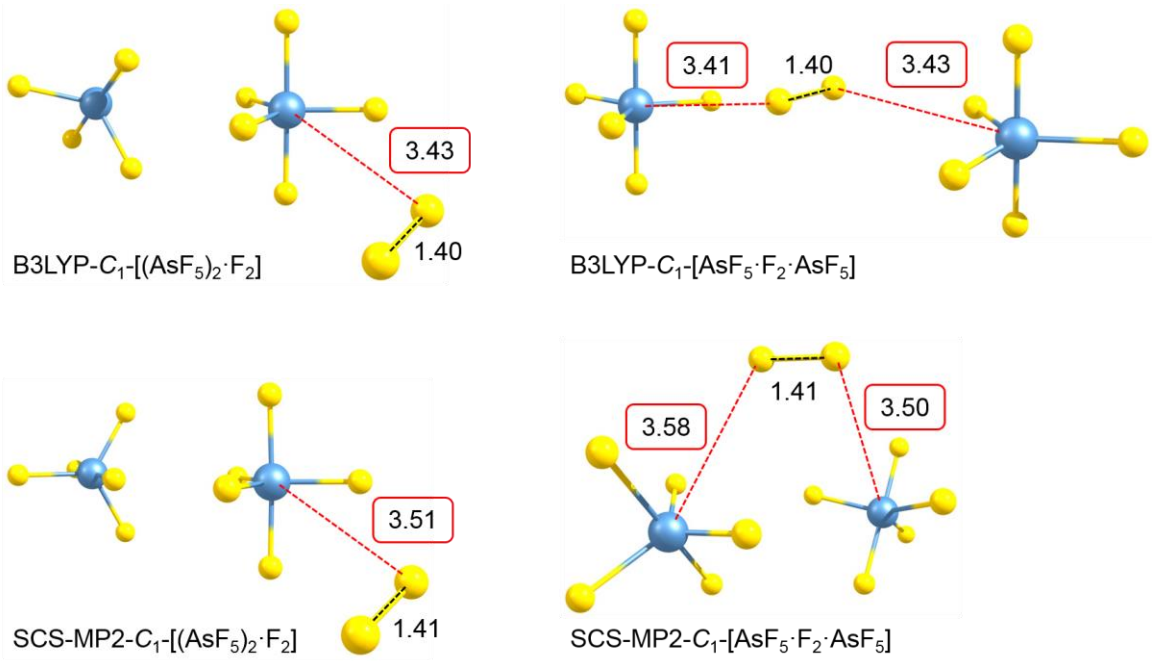

Figure 103: Structures of [$(AsF_5)_2$·F_2] and [AsF_5·F_2·AsF_5] calculated at the RI-B3LYP-D4/def2-TZVPP and SCS-MP2/def2-TZVPP levels of theory. Bond distances are given in Å. The sum of the van der Waals radii of As and F is 3.32 Å, the van der Waals radius of a fluorine atom is 1.47 Å.[457]

Table 53: Properties of [$(AsF_5)_2$·F_2] and [AsF_5·F_2·AsF_5] calculated at the RI-B3LYP-D4/def2-TZVPP and SCS-MP2/def2-TZVPP levels of theory. Calculated ZPE-corrected electronic contributions to the energy of formation ΔE_f are given in kJ·mol^{-1}, vibrational frequencies in cm^{-1}, IR intensities in km·mol^{-1} and bond lengths in Å.

Property	[$(AsF_5)_2$·F_2]		[AsF_5·F_2·AsF_5]	
	B3LYP	SCS-MP2	B3LYP	SCS-MP2
ΔE_f	–3.73	+0.69	–7.86	–3.11
d(F–F)	1.397	1.409	1.397	1.410
$\tilde{\nu}$(vF–F)	1047.32	982.43	1045.85	980.32
I_{IR}(vF–F)	0.02	0.07	0.00	0.00
$\Delta\tilde{\nu}$(vF–F)[a]	–0.7	–1.4	–2.2	–3.5
Charge(F_c, F_t)[b]	–0.006, 0.007	–0.004, 0.005	0.000, 0.001	0.000, 0.002

[a] The shift of the ν(F–F) of the {F_2} moiety in the respective adduct compared to the F_2 fundamental (see Table 11); [b] NPA charges (in e) of coordinated (c) and terminal (t) fluorine atoms of the {F_2} moiety. The labelling for fluorine atoms does not hold for the complexes with a central {F_2} moiety, but the more positively charged atom is considered terminal.

6.1.4.1 Optimized Structures

The optimized structures of F_2 coordinated by two {AsF_5} moieties (cf. Section 6.1.4.1) are given in the form of xyz data in Å.

6.1.4.1.1 RI-B3LYP-D4/def2-TZVPP

$[(AsF_5)_2{\cdot}F_2]$ (^{1}A-C_1)

As	0.6358404	1.6972859	-0.8551146
F	2.0864881	0.8767886	-0.4635647
F	1.0756319	1.7170732	-2.4886045
F	-0.8189144	2.5239918	-1.2255631
F	-0.2627121	0.4048365	-0.2387135
F	1.1220312	3.0081995	0.1067312
F	-1.1372567	2.7493995	2.0676047
As	0.0305920	2.6281520	3.2883456
F	-0.2628412	1.6474848	4.6329164
F	-0.6736746	3.9654527	4.0925993
F	0.7244395	1.2892807	2.4632035
F	1.4983128	3.4570767	3.1767695
F	-1.9090346	-1.0712404	-2.4756724
F	-0.9804822	-0.2714713	-3.1461373

$[AsF_5{\cdot}F_2{\cdot}AsF_5]$ (^{1}A-C_1)

As	-0.0975828	1.0932257	-0.5295109
F	1.4378960	0.3341477	-0.4663584
F	0.3563219	1.8794882	-1.9586624
F	-1.6349918	1.8464010	-0.6084046
F	-0.8428819	-0.4258572	-0.5559019
F	0.2020968	1.8412274	0.9573103
F	-1.1768312	-0.0183252	-3.5886724
F	-1.9223958	-1.1864030	-3.4112789
F	-1.0958044	-1.6229594	-6.3508989
F	-3.4945560	-1.8257187	-6.3666338
As	-2.1787485	-2.9231639	-6.3368822
F	-2.6931142	-3.5904631	-7.8034842
F	-0.8597162	-4.0167955	-6.2942391
F	-2.7554718	-3.5697941	-4.8821725

6.1.4.1.2 SCS-MP2/def2-TZVPP

$[(AsF_5)_2{\cdot}F_2]$ (^1A-C_1)

As	0.4174985	1.4614014	-0.7188846
F	2.0603930	1.1502393	-0.4181306
F	0.6909526	1.4798962	-2.3700615
F	-1.2335114	1.7836072	-0.9528299
F	0.0219303	-0.0025636	-0.0083274
F	0.5725626	2.9362884	0.0739370
F	-0.9394646	-0.9647931	-2.8542308
F	-1.6514671	-1.9125126	-2.0924084
F	-1.1282923	3.6198717	2.6128073
As	0.1069538	2.8804281	3.4665709
F	-0.2639395	1.9389248	4.7995034
F	0.2511144	4.2508691	4.4573459
F	-0.0366597	1.5053730	2.4643171
F	1.7043392	3.0455201	2.9949317

$[AsF_5{\cdot}F_2{\cdot}AsF_5]$ (^1A-C_1)

As	-0.6823245	0.5492578	-1.6775597
F	0.4843117	-0.1753563	-0.6778712
F	0.5356338	1.2179500	-2.6142554
F	-1.8496535	1.2657758	-2.6797320
F	-1.3068480	-0.9674660	-2.0362758
F	-1.2813757	1.3998130	-0.3645465
F	1.5341580	-1.6183053	-3.3111944
F	0.8535647	-2.8492923	-3.4052937
F	-1.0532862	-0.7817637	-5.0016421
F	-3.3403712	-1.1767650	-4.4405612
As	-2.1206790	-2.0571939	-5.2268075
F	-3.0547756	-2.1159561	-6.6164730
F	-0.8963641	-2.9350359	-6.0126945
F	-2.2576504	-3.2744022	-4.0835030

6.1.5 Additional IR Spectra of Matrix-Isolated Lewis Acids and Fluorine

6.1.5.1 Lewis acids and laser-ablated $Cs[AuF_6]$

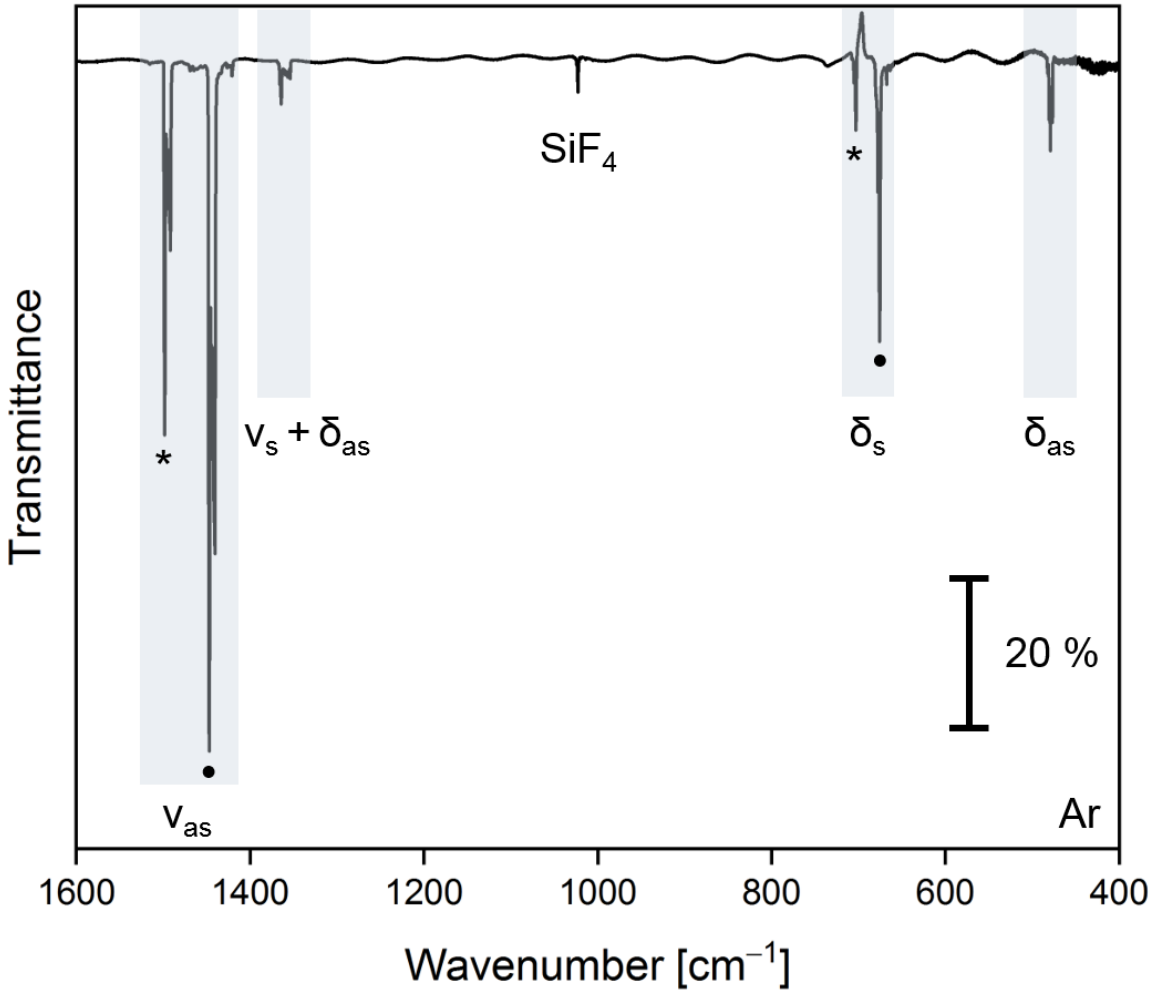

Figure 104: IR spectrum of the fundamentals of BF_3 and a combination band in solid argon. The spectrum was recorded after the deposition of BF_3 (0.1 % in Ar) onto a CsI window at 4 K for 15 min at a deposition rate of 0.5 mbar·l·min^{-1}. The isotopomers $^{11}BF_3$ and $^{10}BF_3$ are marked by an asterisk and bullet, respectively. The isotopic splitting of the antisymmetric deformation mode and the combination band could not be determined with certainty, since they were obscured by the extended site structure in argon. The bands were found to match the reported data from the literature.[456,461,469] A weak band caused by SiF_4 is labelled.[365]

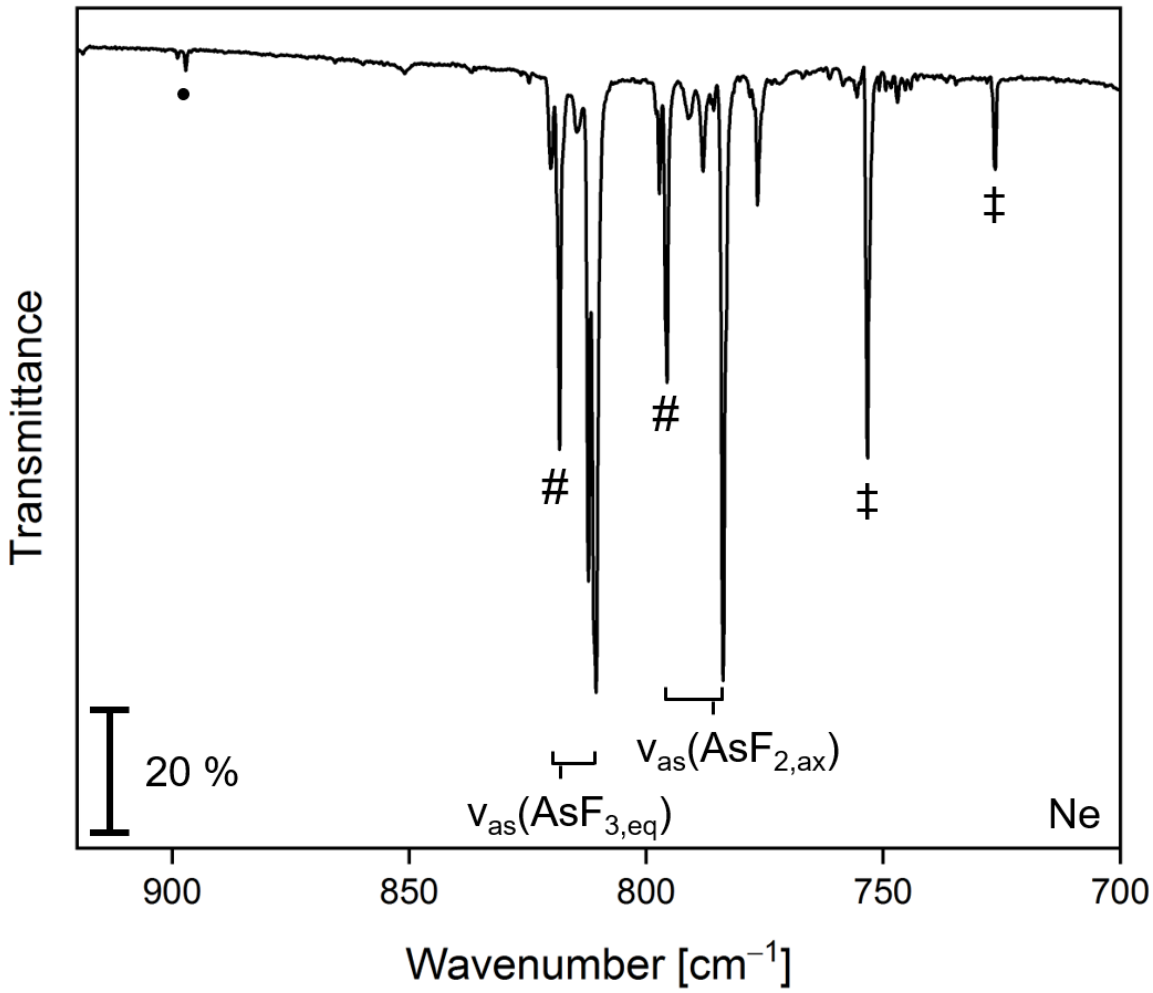

Figure 105: Spectrum of the IR active fundamentals of AsF_5 in the MIR regime in solid neon. Oligomeric absorptions are marked by a hash, unassigned impurity bands by a double dagger. The absorption in the F−F stretching region (marked by a bullet) was found not to be sensitive towards annealing, while no corresponding band was found in Ar (Figure 33). IR spectrum recorded after the deposition of AsF_5 (0.1 % in Ne) onto a CsI window at 4 K for 45 min at a deposition rate of 0.8 mbar·l·min^{-1}. The bands were found to match the reported literature values.[351,461,476,477]

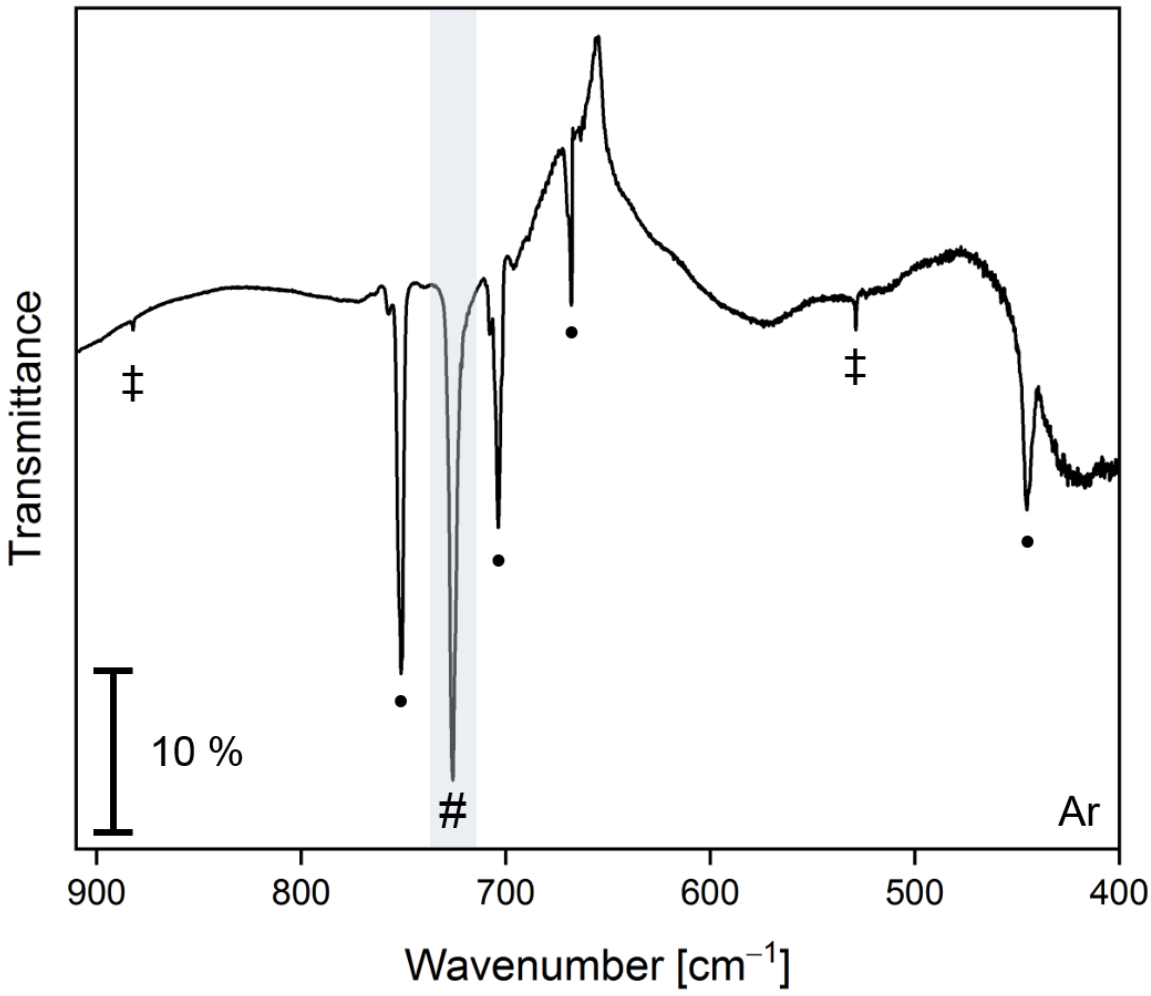

Figure 106: IR spectrum recorded after the deposition of an F_2 stream (1 % in Ar) passed over a solid sample of SbF_5 in a temperature range from −49.2 to −48.7 °C onto a CsI window at 4 K for 30 min at a deposition rate of 0.6 mbar·l·min^{-1}. The bands match the literature values.[351,483–487] The quasi-degenerate $\nu_{as}(SbF_{3,eq})/\nu_{as}(SbF_{2,ax})$ band(s) of monomeric SbF_5 is marked with a hash, the bands of polymeric SbF_5 by a bullet (cf. Table 17 and Table 39). Impurity bands of unknown origin are marked by a double dagger.

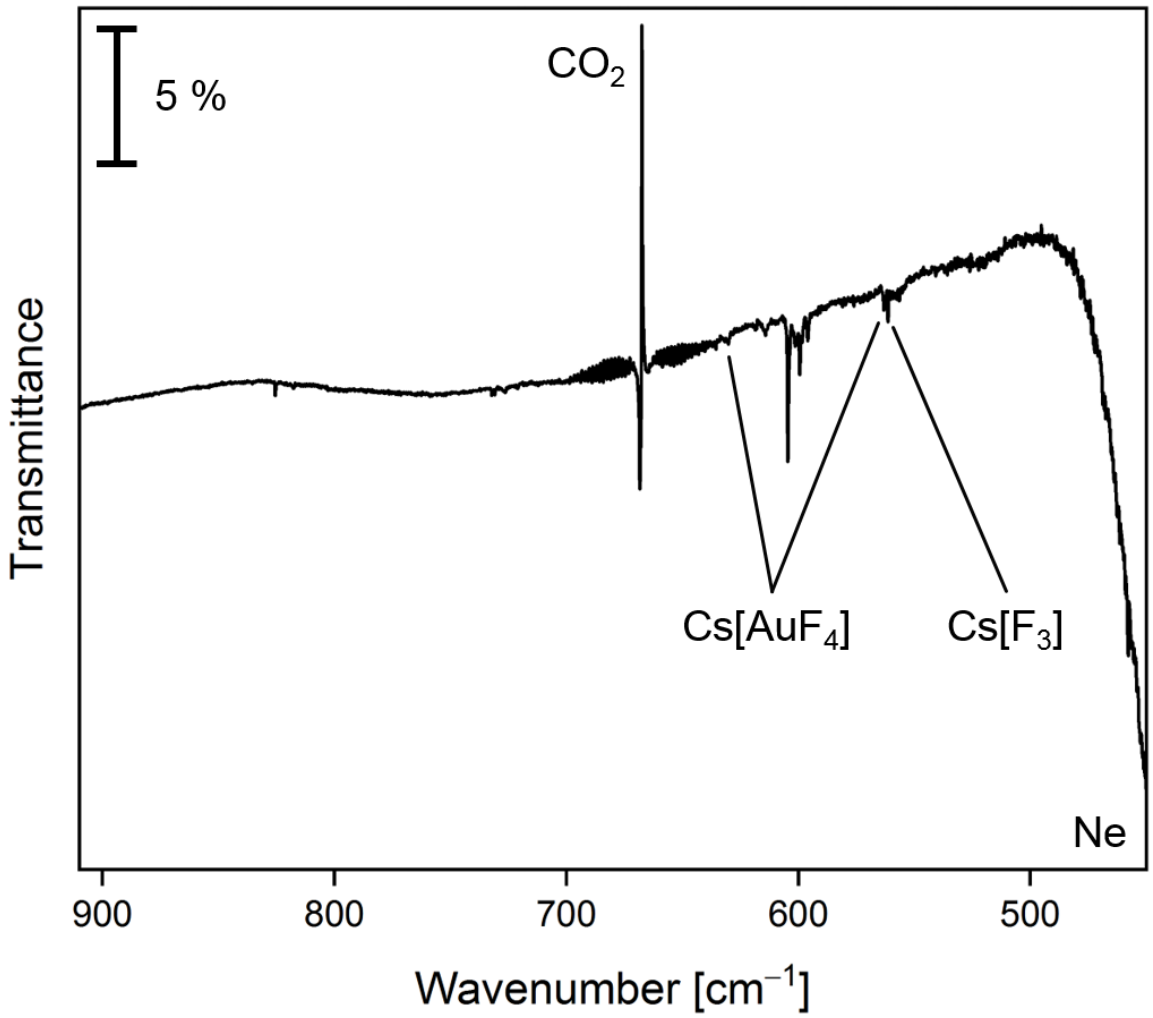

Figure 107: IR spectrum recorded after the deposition of laser-ablated $Cs[AuF_6]$ (3 % in CsF, 3 Hz repetition rate, 30 mJ/pulse) in excess Ne onto a CsI window at 4 K for 180 min at a deposition rate of 0.5 mbar·l·min^{-1}. The band centered at 604.5 cm^{-1} could not be assigned to any of the Au or F containing species.[10,77,434,493] Higher frequency bands of $Cs[AuF_4]$ are most likely obscured by the CO_2 absorptions.[10,455,490]

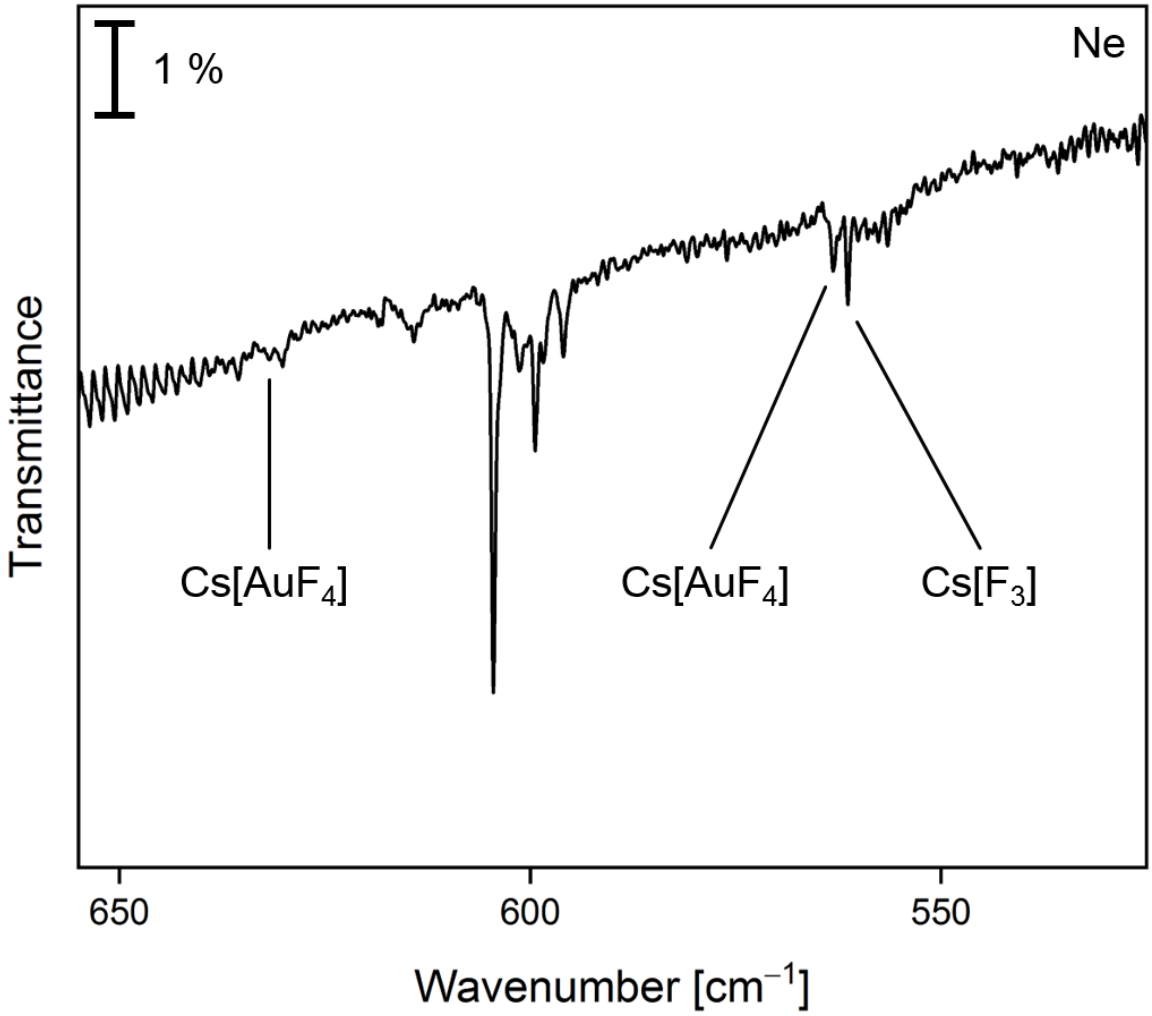

Figure 108: IR spectrum (magnified region of Figure 107) recorded after the deposition of laser-ablated $Cs[AuF_6]$ (3 % in CsF, 3 Hz repetition rate, 30 mJ/pulse) in excess Ne onto a CsI window at 4 K for 180 min at a deposition rate of 0.5 mbar·l·min^{-1}. The band centered at 604.5 cm^{-1} could not be assigned to any of the Au or F containing species.[10,77,434,493] Higher frequency bands of $Cs[AuF_4]$ are most likely obscured by the CO_2 absorptions.[10,455,490]

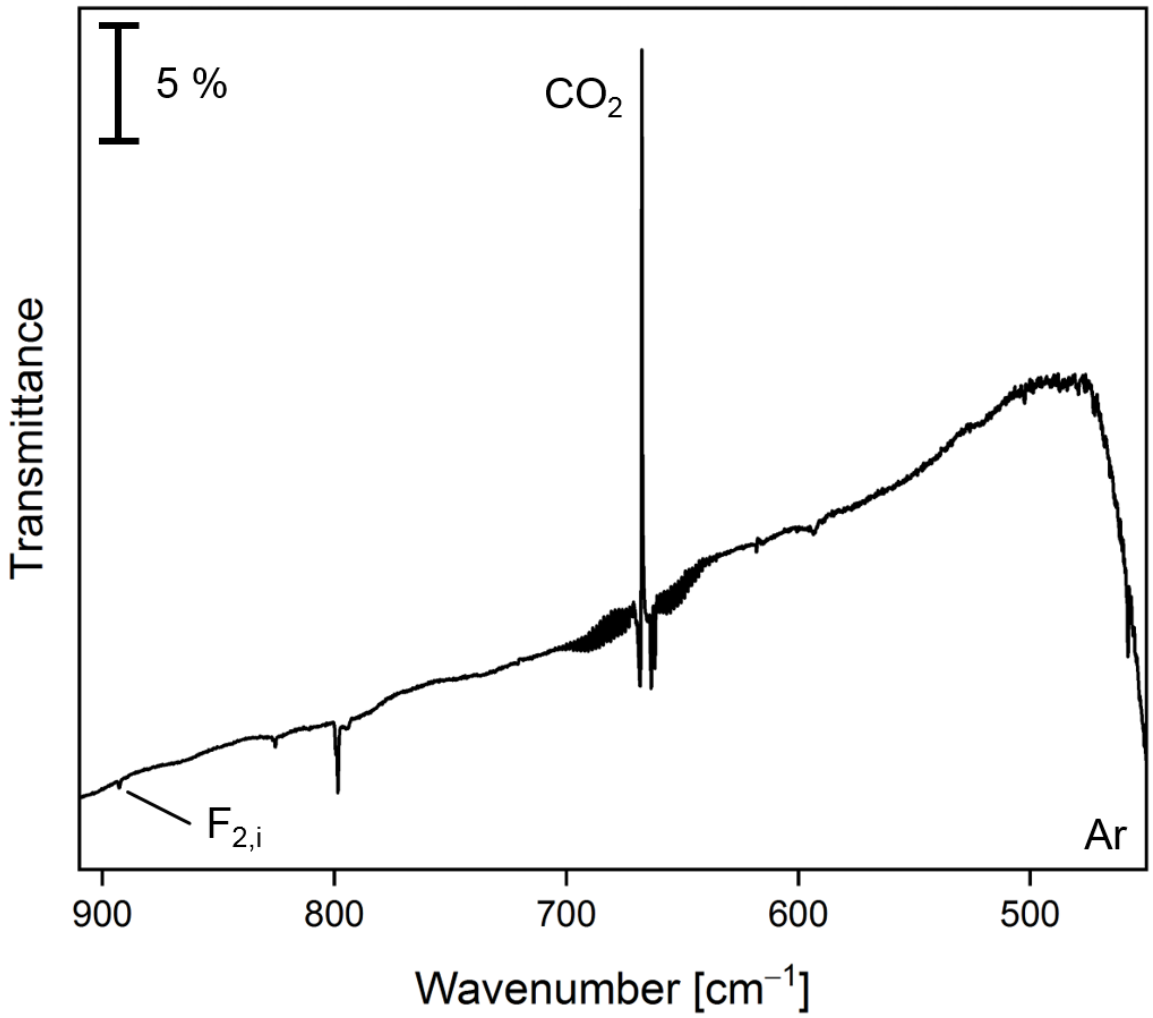

Figure 109: IR spectrum recorded after the deposition of laser-ablated $Cs[AuF_6]$ (1 % in CsF, 2 Hz repetition rate, 35 mJ/pulse) in excess Ar onto a CsI window at 4 K for 98 min at a deposition rate of 0.5 mbar·l·min^{-1}. Next to CO_2, none of the features could be assigned to any of the Au or F containing species of interest.[10,77,434,490,493]

6.1.5.2 Lewis Acid-Fluorine Experiments

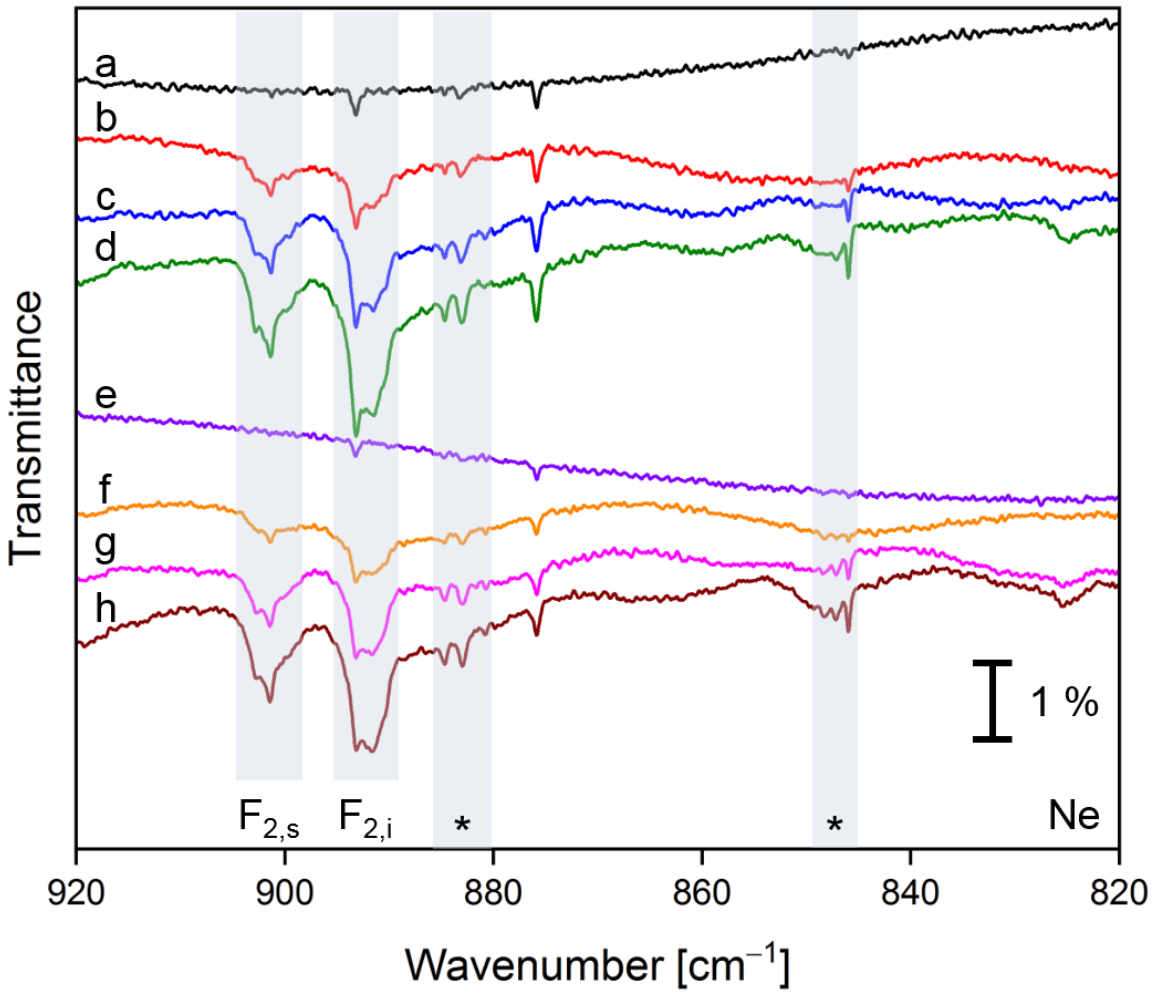

Figure 110: The IR spectra were recorded after the deposition of a)/e) neon for 20 min, and the subsequent deposition of F_2 (3 % diluted in neon) for b)/f) 60 min, c)/g) 120 min and d)/g) 180 min in two independent but consecutive sets of experiments for 180 min each at a deposition rate of 0.6 mbar·l·min^{-1} onto a CsI window at 4 K. The gas mixture was exchanged in between the two sets of experiments. IR active features caused by traces of AsF_5 in combination with F_2 are marked by an asterisk.

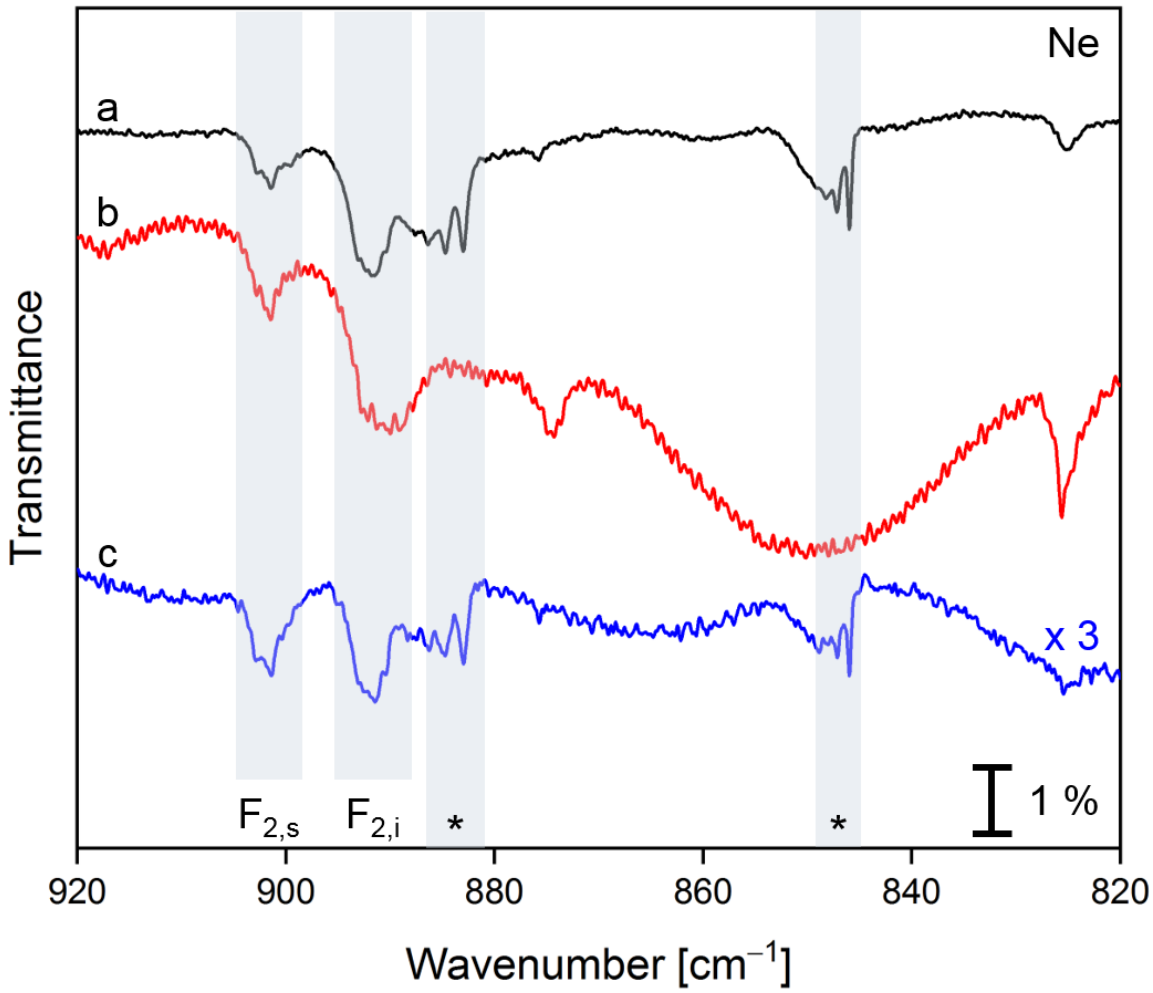

Figure 111: The IR spectra were recorded in independent experiments after the deposition of F_2 (3 % diluted in neon) for a) 180 min at a deposition rate of 0.6 mbar·l·min^{-1} onto a CsI window at 4 K, b) 180 min at a deposition rate of 0.6 mbar·l·min^{-1} onto a gold-plated copper mirror at 5 K, and c) 60 min (magnified for clarity) at a deposition rate of 0.7 mbar·l·min^{-1} onto a CsI window at 4 K. The deposited gas mixture of spectrum c was cooled to 77 K throughout the deposition and 60 min in advance of the deposition. The matrix supports had been coated with neon for 20 min prior to the deposition of the F_2/Ne mixtures. IR active features caused by traces of AsF_5 in combination with F_2 are marked by an asterisk.

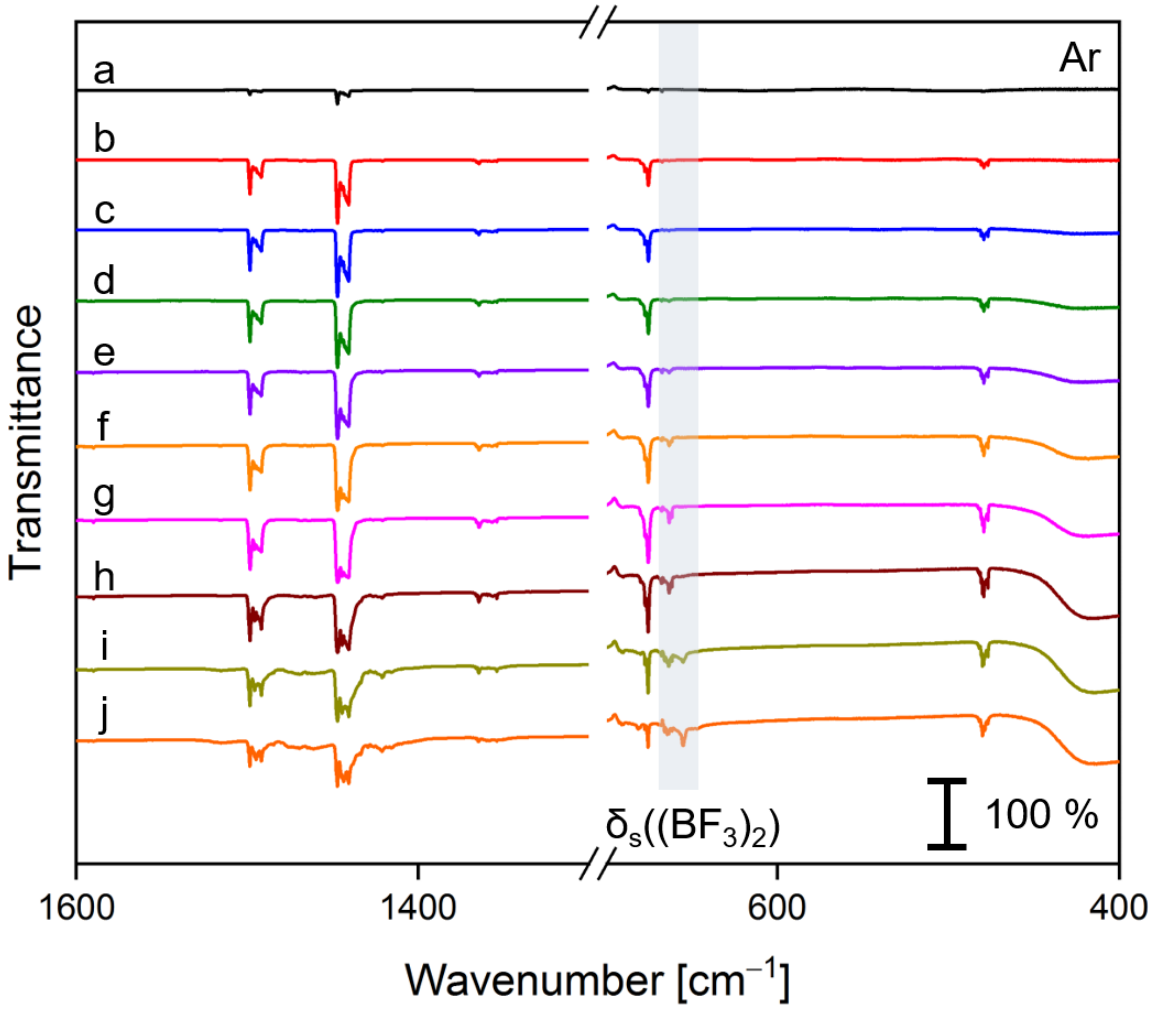

Figure 112: The IR spectra were recorded after the deposition of a) argon for 18 min, b) subsequently BF_3 (0.1 % in excess argon) for 15 min, c) subsequently BF_3 (0.02 % in excess argon) for 16 min, and after the subsequent deposition of BF_3 (0.02 %) and F_2 (1 %), diluted in argon, for d) 16 min, e) 32 min, f) 62 min, and g) 122 min onto a CsI window at 4 K at a deposition rate of 0.5 mbar·l·min^{-1} and after annealing of the matrix to h) 22 K, i) 30 K, and j) 35 K.

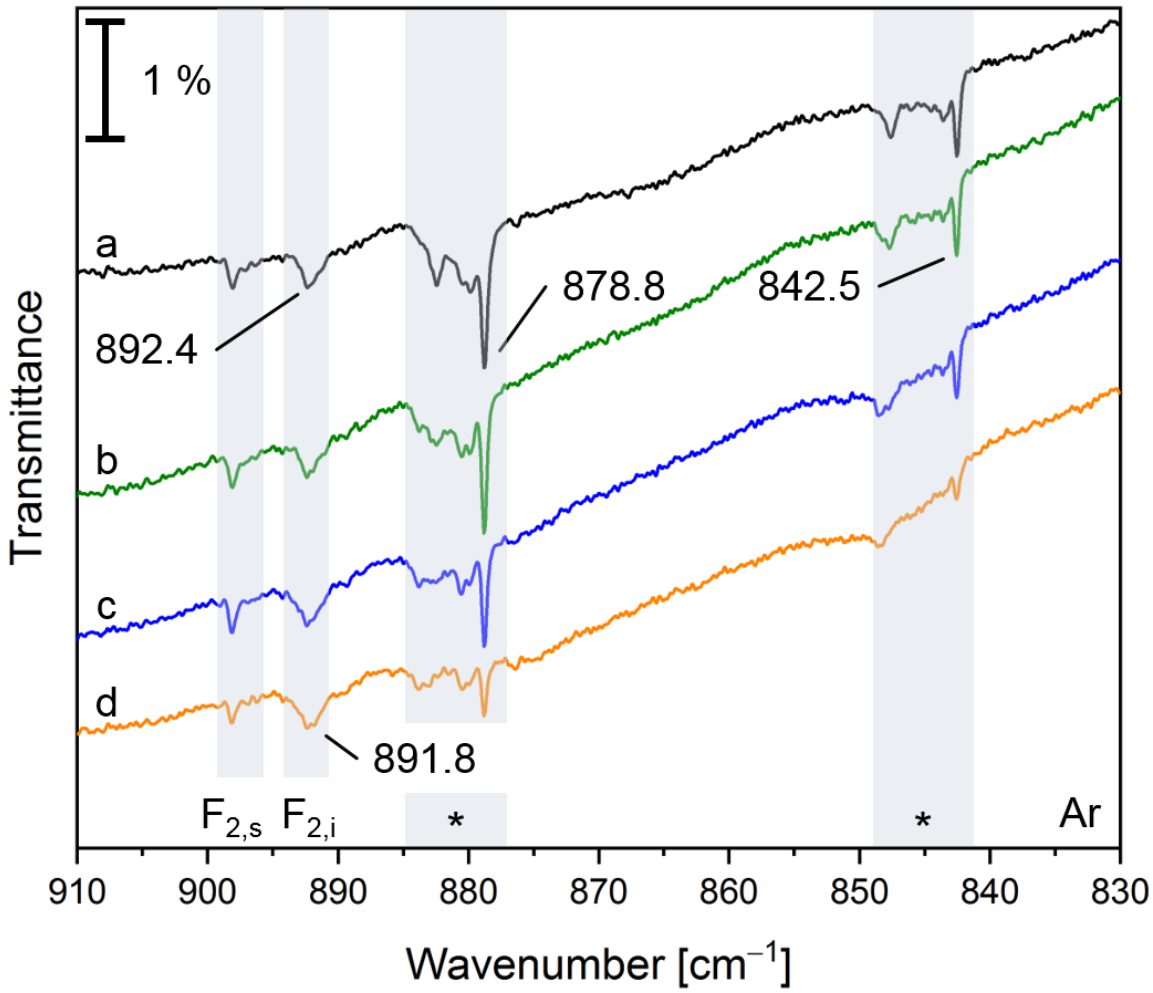

Figure 113: The IR spectra were recorded after the deposition of a) argon for 18 min, subsequently BF_3 (0.1 % in excess argon) for 15 min, subsequently BF_3 (0.02 % in excess argon) for 16 min, and after the subsequent deposition of BF_3 (0.02 %) and F_2 (1 %) diluted in argon onto a CsI window at 4 K for 122 min at a deposition rate of 0.5 mbar·l·min^{-1} and after annealing of the matrix to b) 22 K, c) 30 K, and d) 35 K. IR active features caused by traces of AsF_5 in combination with F_2 are marked by an asterisk.

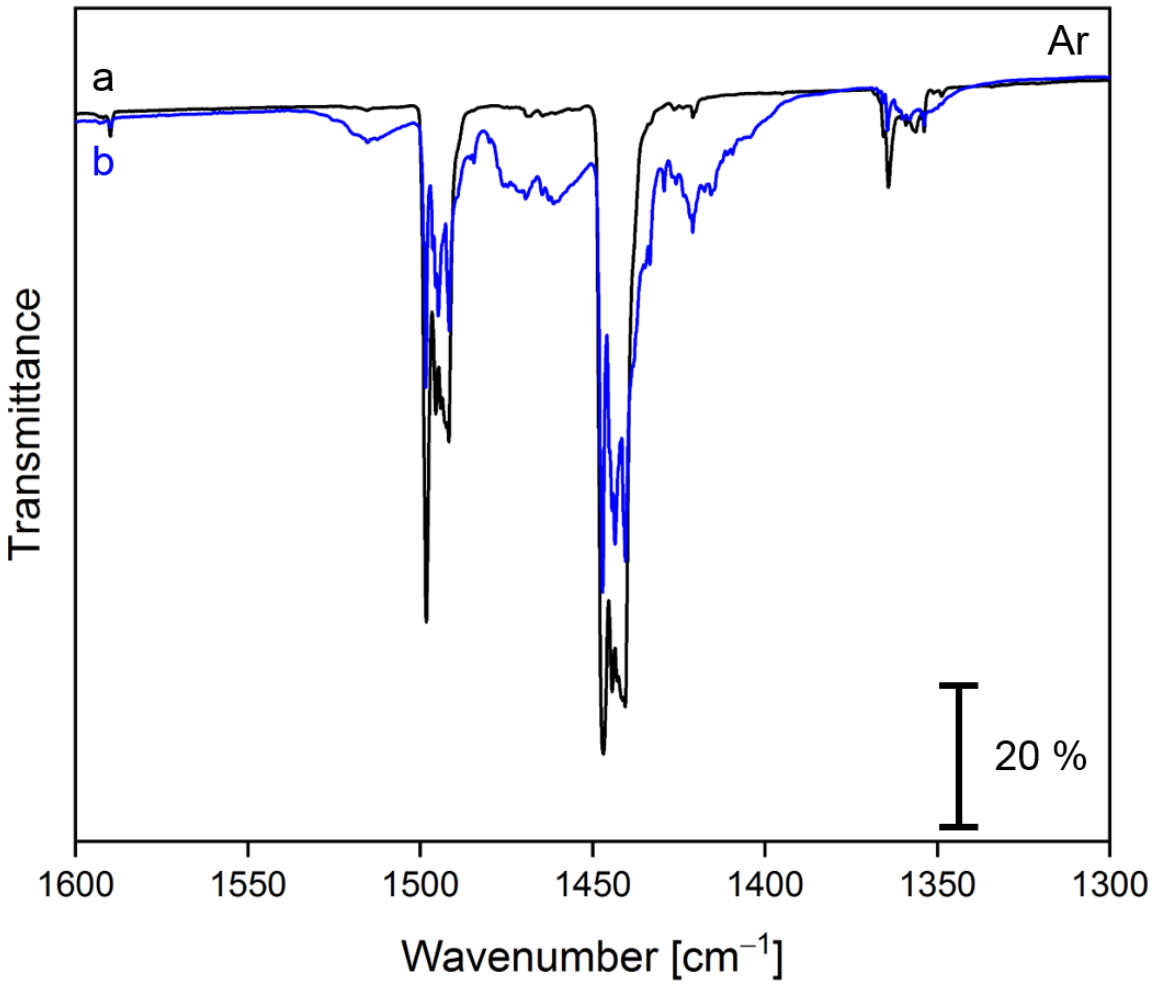

Figure 114: The IR spectra were recorded after the deposition of a) argon for 18 min, subsequently BF_3 (0.1 % in excess argon) for 15 min, subsequently BF_3 (0.02 % in excess argon) for 16 min, and after the subsequent deposition of BF_3 (0.02 %) and F_2 (1 %) diluted in argon onto a CsI window at 4 K for 122 min at a deposition rate of 0.5 mbar·l·min^{-1} and after annealing of the matrix to b) up to 35 K.

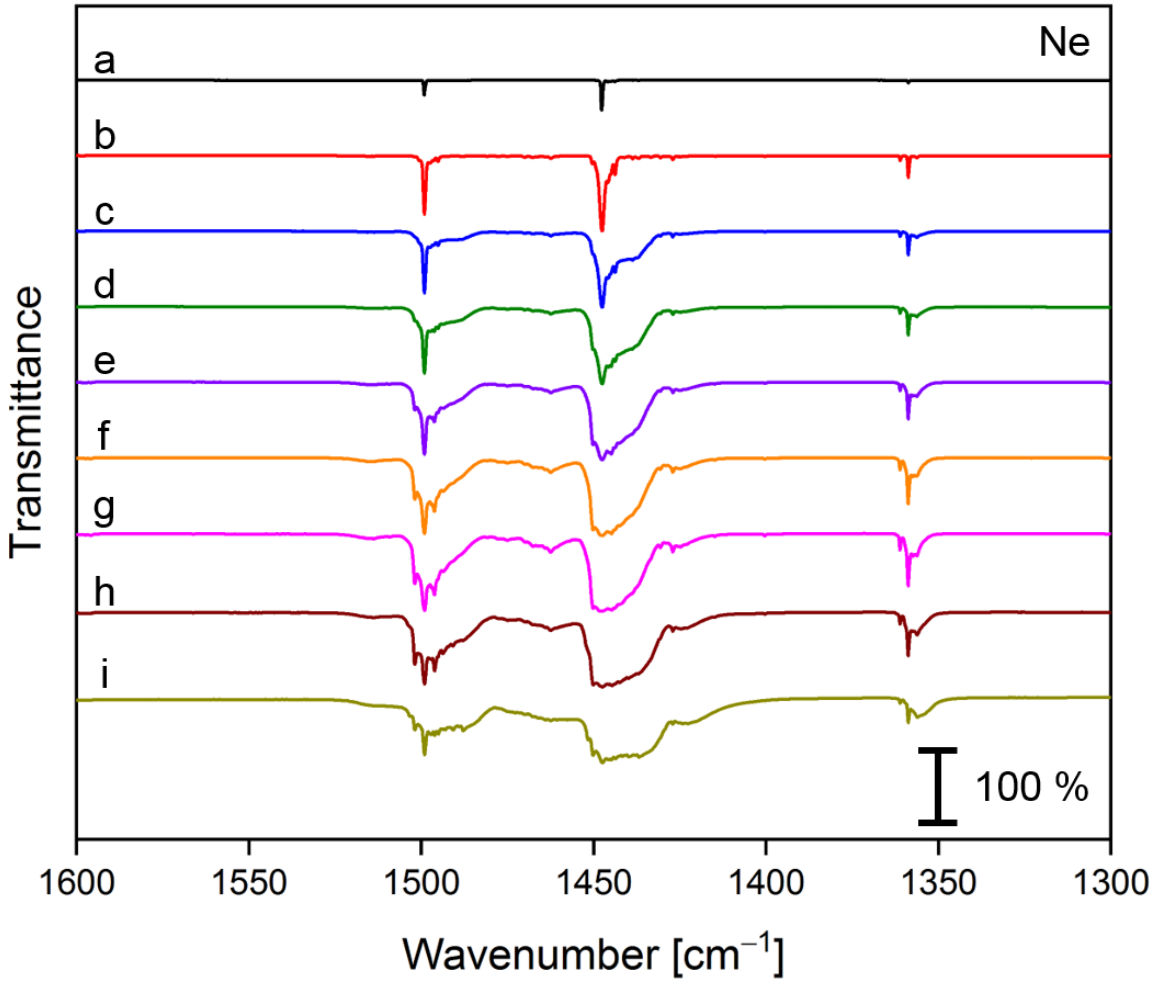

Figure 115: The IR spectra were recorded after the deposition of a) neon for 19 min, b) subsequently BF_3 (0.1 % in excess neon) for 17 min, and after the subsequent deposition of BF_3 (0.1 %) and F_2 (1 %) diluted in neon for c) 16 min, d) 33 min, e) 60 min, f) 91 min and g) 120 min onto a CsI window at 4 K at a deposition rate of 0.6 mbar·l·min^{-1} and after annealing of the matrix to h) 11 K and i) 13 K.

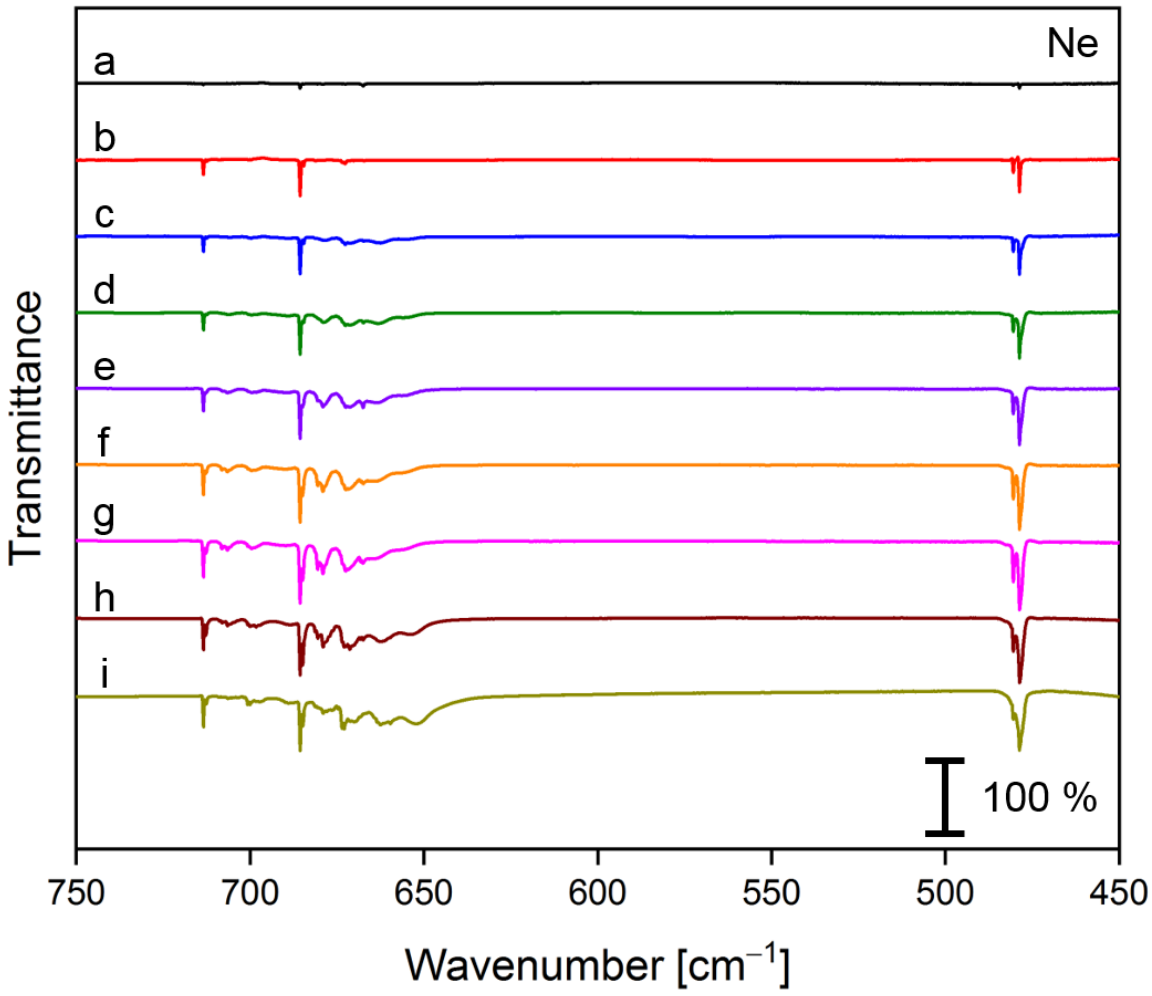

Figure 116: The IR spectra were recorded after the deposition of a) neon for 19 min, b) subsequently BF_3 (0.1 % in excess neon) for 17 min, and after the subsequent deposition of BF_3 (0.1 %) and F_2 (1 %), diluted in neon, for c) 16 min, d) 33 min, e) 60 min, f) 91 min and g) 120 min onto a CsI window at 4 K at a deposition rate of 0.6 mbar·l·min^{-1} and after annealing of the matrix to h) 11 K and i) 13 K.

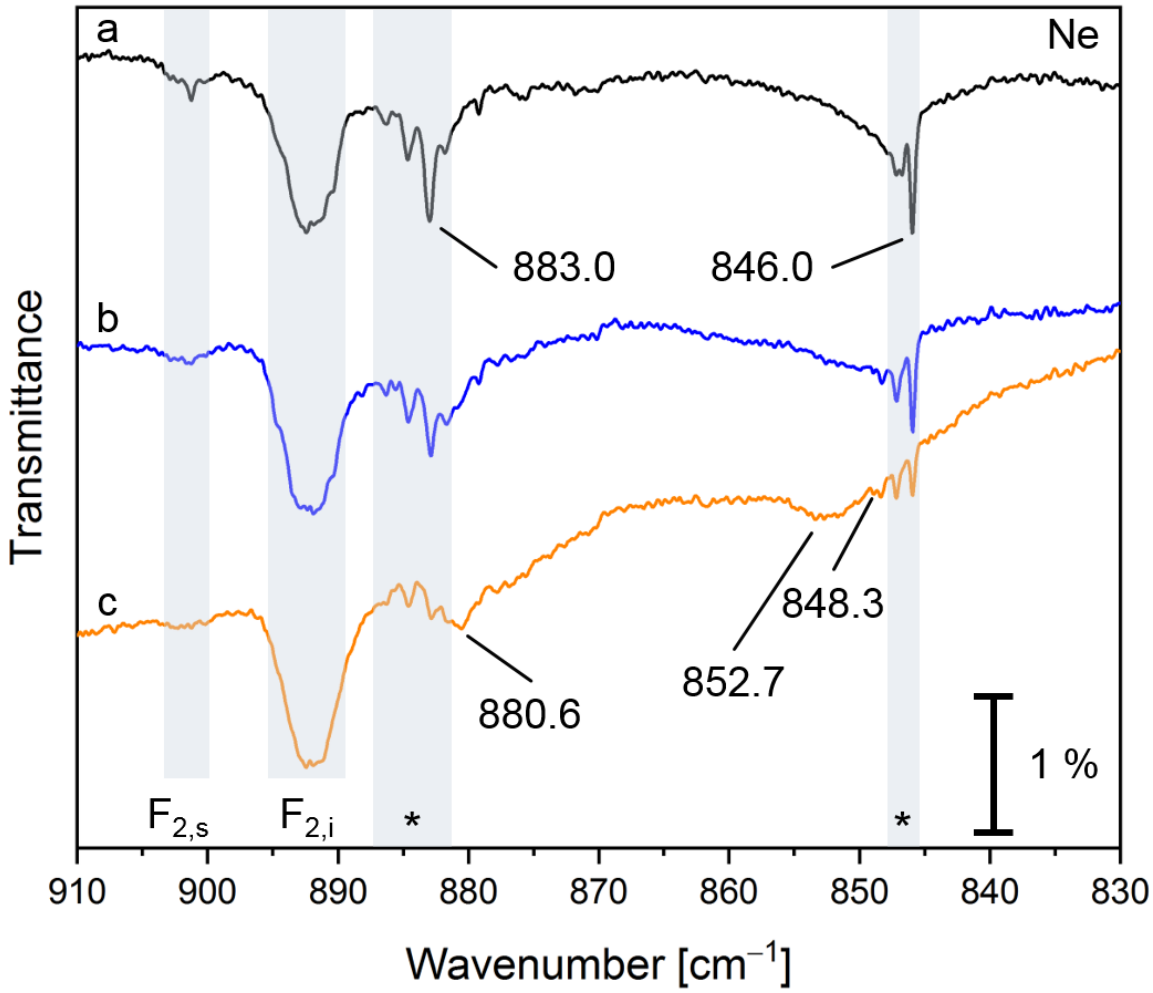

Figure 117: The IR spectra were recorded after the deposition of a) neon for 19 min, subsequently BF_3 (0.1 % in excess neon) for 17 min, and the subsequent deposition of BF_3 (0.1 %) and F_2 (1 %) diluted in neon onto a CsI window at 4 K for 120 min at a deposition rate of 0.6 mbar·l·min^{-1} and after annealing of the matrix to b) 11 and c) 13 K. IR active features caused by traces of AsF_5 in combination with F_2 are marked by an asterisk.

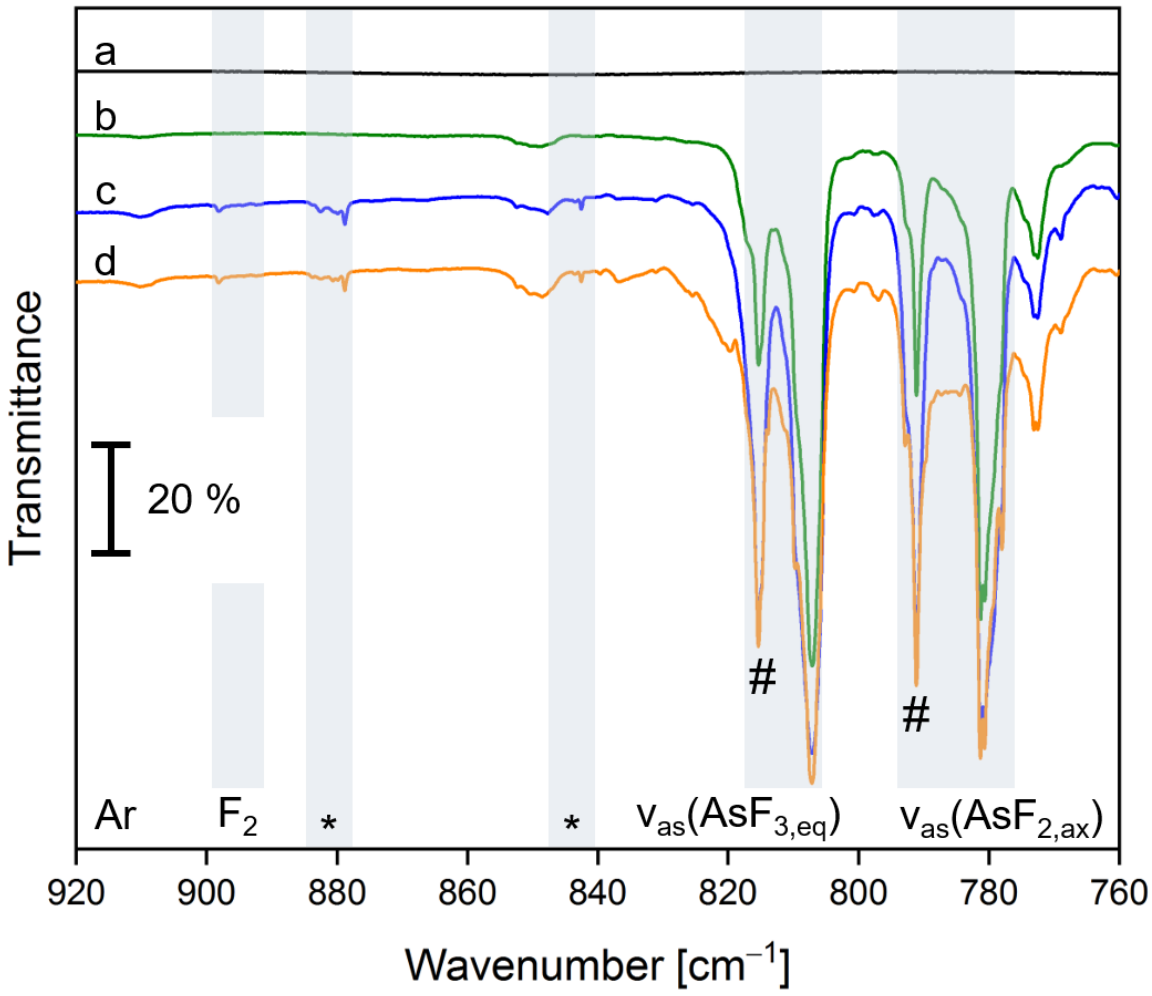

Figure 118: The IR spectra were recorded after the deposition of a) argon for 15 min, b) AsF_5 (1 % in Ar) for 18 min, c) a gas mixture of 0.1 % AsF_5 and 1 % F_2 in excess Ar for 180 min onto a CsI window at 4 K at a deposition rate of 0.6 mbar·l·min^{-1} and d) the subsequent annealing of the matrix to 25 K. Literature-known oligomeric bands[351] are marked by a hash. IR active features caused by AsF_5 in combination with F_2 are marked with an asterisk.

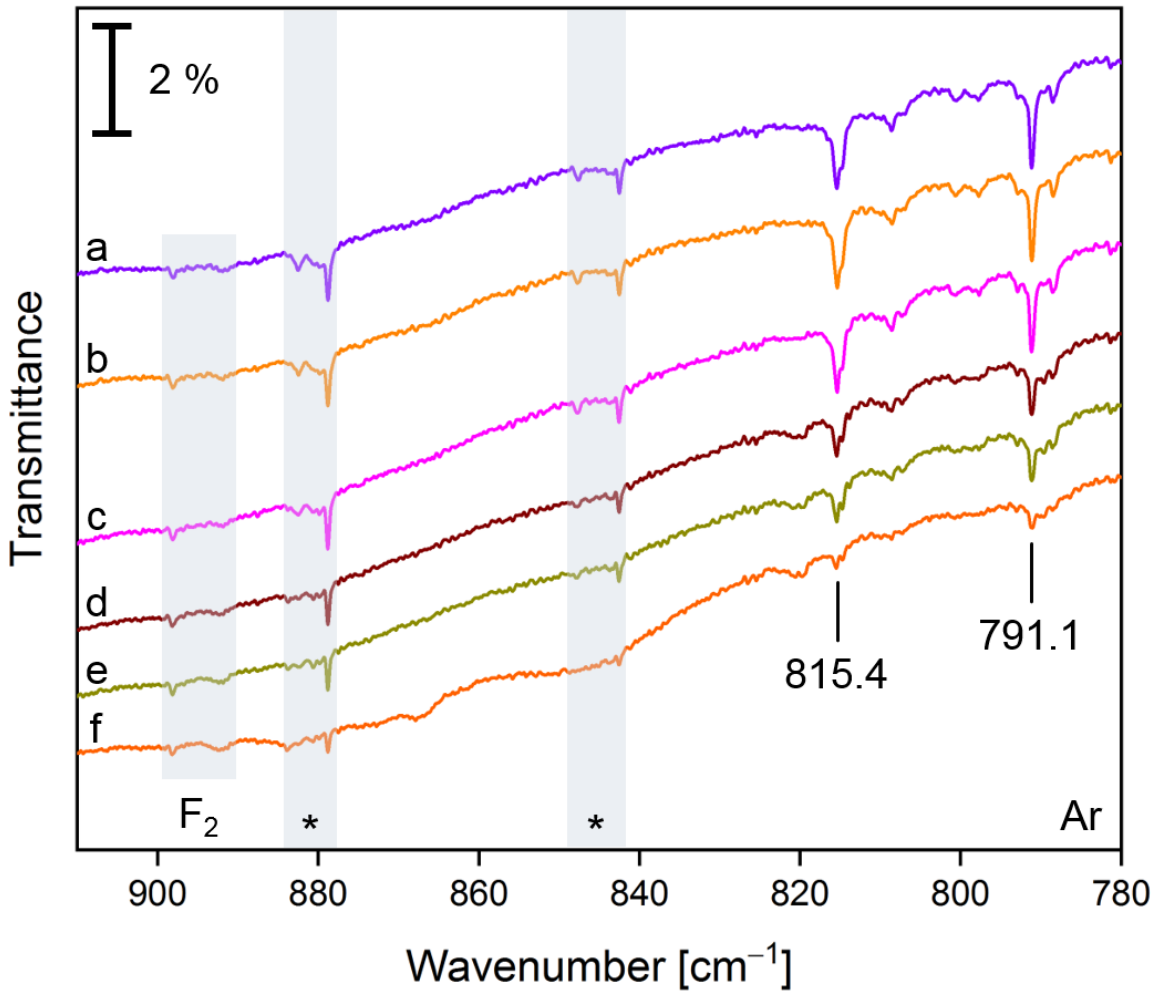

Figure 119: IR spectra recorded after the deposition of a) argon for 20 min and fluorine (1 % in excess argon, accompanied by highly diluted AsF_5) for 180 min onto a CsI window at 4 K at a deposition rate of 0.6 mbar·l·min^{-1} and the subsequent annealing to b) 12 K, c) 20 K, d) 25 K for 5 min, e) 25 K for further 10 min and f) 30 K for 5 min. Absorptions of oligomeric AsF_5 and molecular fluorine were highlighted. IR active features caused by AsF_5 in combination with F_2 are marked by an asterisk.

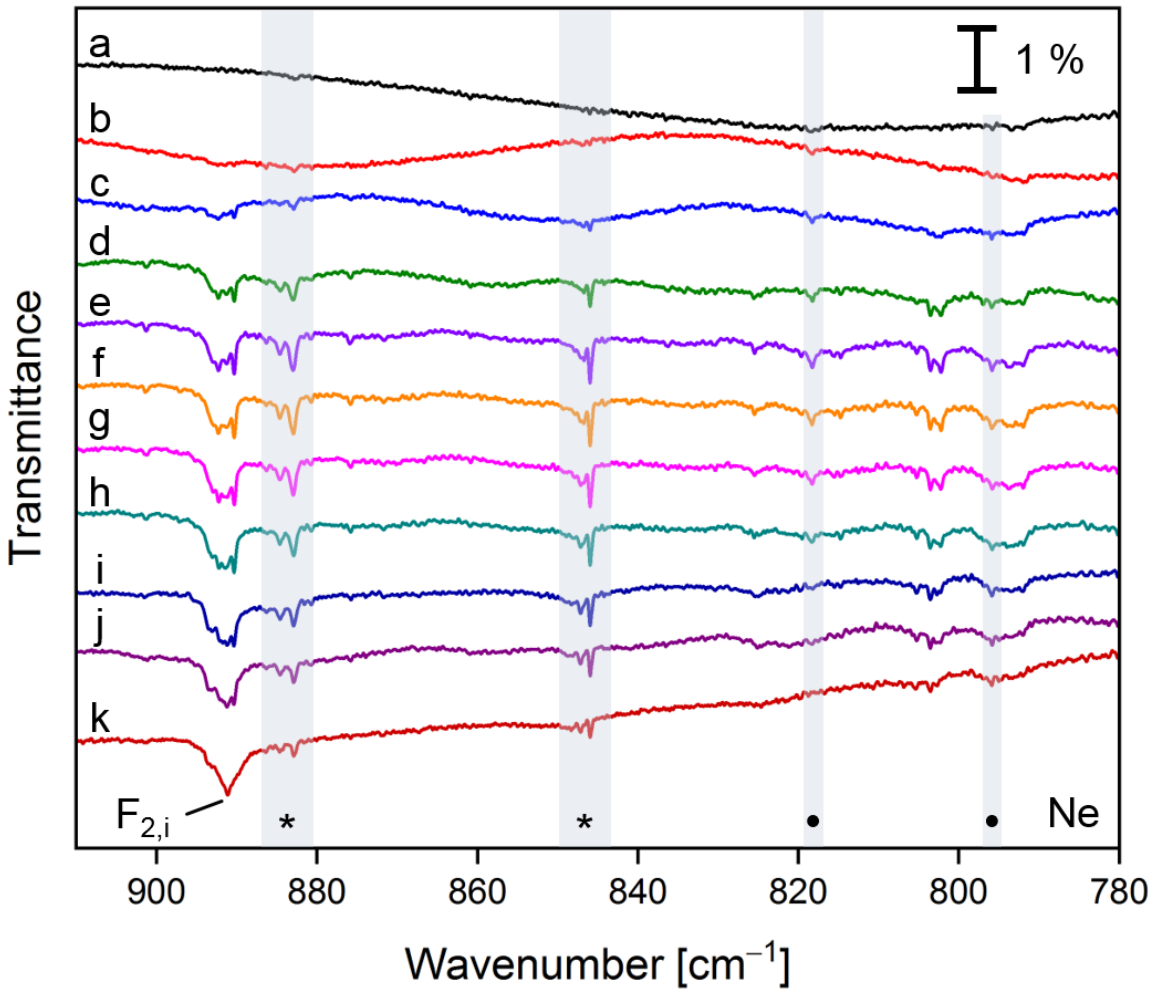

Figure 120: The IR spectra were recorded after the deposition of a) neon for 22 min, and after the subsequent deposition of fluorine (1 % in excess neon, accompanied by highly diluted AsF_5) for b) 20 min, c) 60 min, d) 120 min and e) 180 min onto a CsI window at 4 K at a deposition rate of 0.6 mbar·l·min^{-1} and after annealing of the matrix to f) 8 K, g) 10 K, h) 11 K, i) 11 K (a second time), j) 11.5 K and k) 13 K. IR active features caused by AsF_5 in combination with F_2 are marked by an asterisk, AsF_5 fundamentals by a bullet.

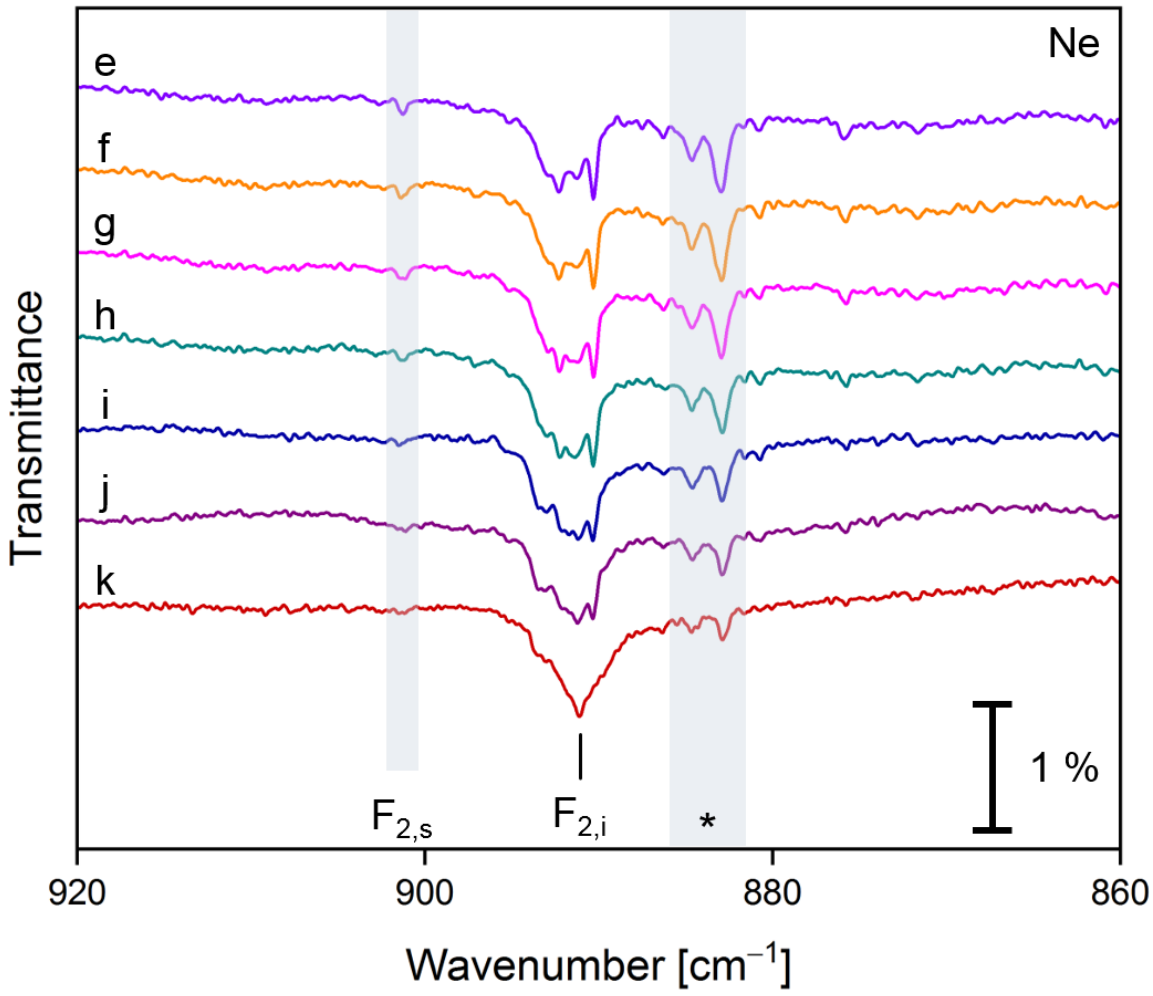

Figure 121: The IR spectra (magnified region of Figure 120) were recorded after e) the deposition of neon for 22 min and the subsequent deposition of fluorine (1 % in excess neon, accompanied by highly diluted AsF_5) onto a CsI window at 4 K for 180 min at a deposition rate of 0.6 mbar·l·min^{-1} and after annealing of the matrix to f) 8 K, g) 10 K, h) 11 K, i) 11 K (a second time), j) 11.5 K and k) 13 K. IR active features caused by AsF_5 in combination with F_2 are marked by an asterisk.

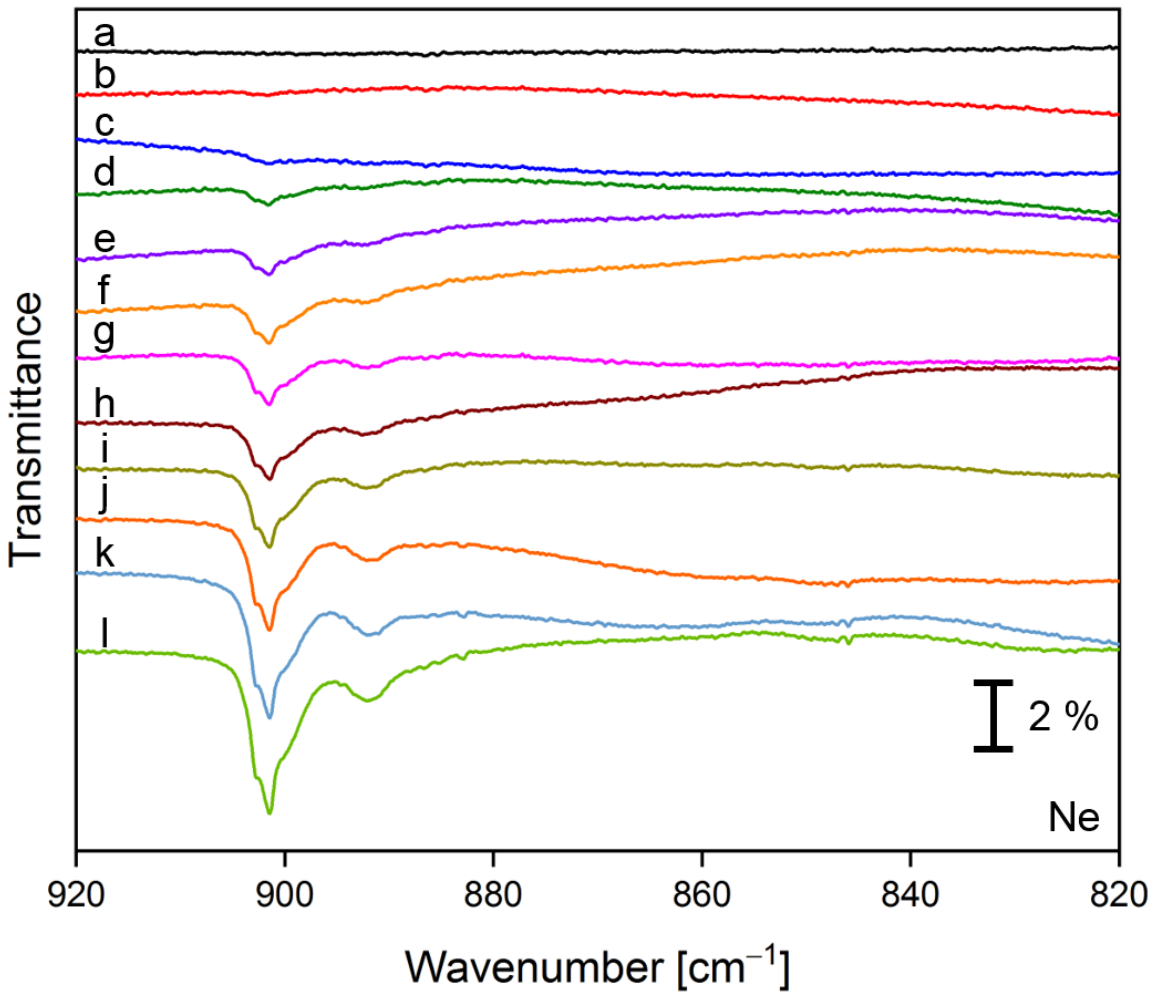

Figure 122: The IR spectra were recorded after the deposition of a) neon for 22 min, and the subsequent deposition of fluorine (3 % in excess neon) passed over a solid sample of SbF_5 maintained at b) −52.3 to −52.2 °C for 10 min, c) −50.3 to −50.1 °C for 11 min, and at −48.9 to −47.8 °C for d) 11 min, e) 31 min, f) 51 min, g) 62 min, h) 70 min, i) 100 min, j) 130 min, k) 160 min and l) 190 min (referring to d–l, when substantial amounts of SbF_5 were deposited) onto a CsI window at 4 K at a deposition rate of 0.6 mbar·l·min^{-1}.

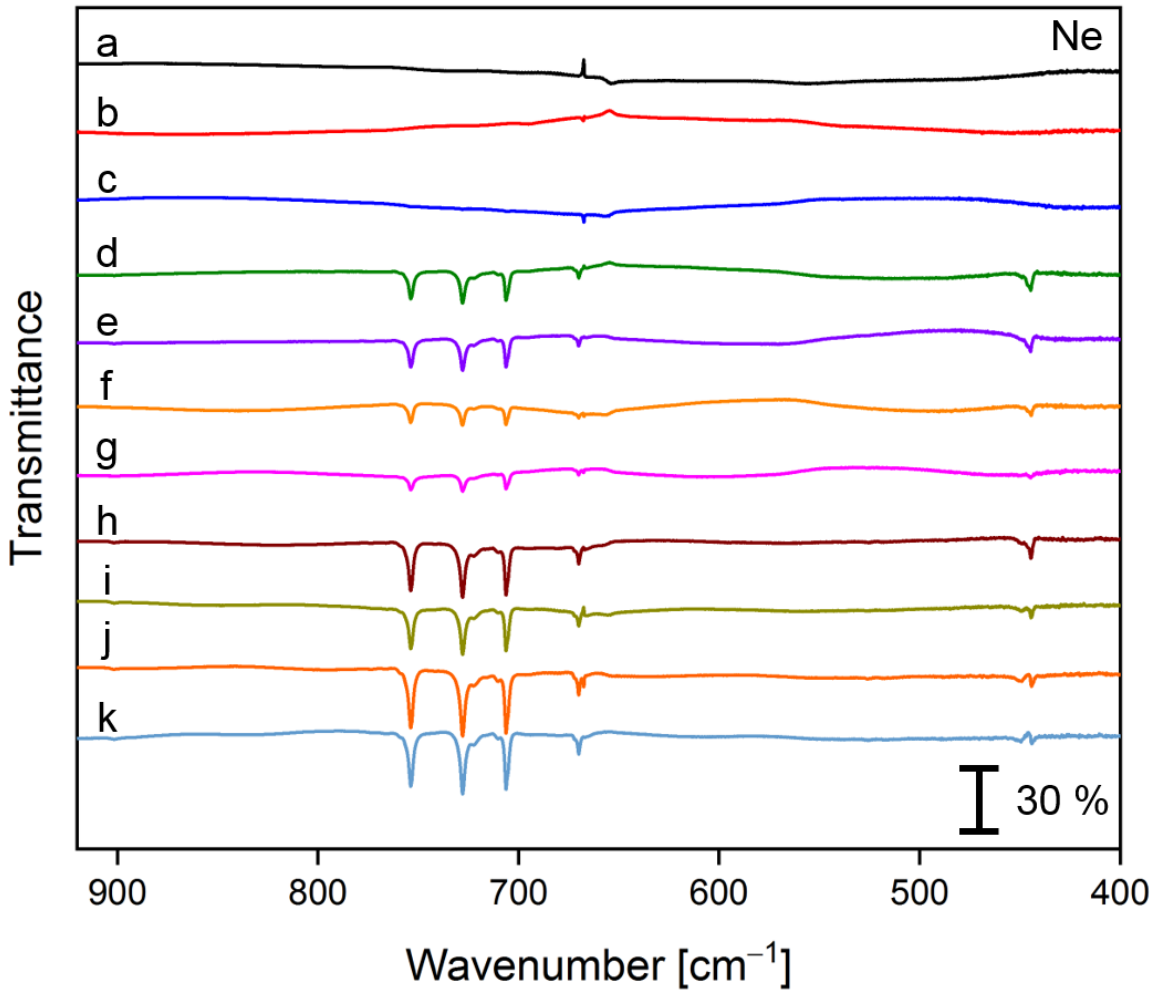

Figure 123: The difference IR spectra show the spectral changes after the deposition of fluorine (3 % in excess neon) passed over a solid sample of SbF_5 maintained at a) −52.3 to −52.2 °C for 10 min, b) −50.3 to −50.1 °C for further 11 min, and at −48.9 to −47.8 °C for c) further 11 min, d) further 20 min, e) further 20 min, f) further 11 min, g) further 8 min, h) further 30 min, i) further 30 min, j) further 30 min and k) further 30 min to a total of 190 min (referring to c–k, when substantial amounts of SbF_5 were deposited) at a deposition rate of 0.6 mbar·l·min^{-1}. Bands pointing downwards are formed at the expense of the bands pointing upwards. The CsI window (matrix support, T = 4 K) was coated with neon for 22 min prior to the deposition of the SbF_5/F_2 sample (spectrum not shown).

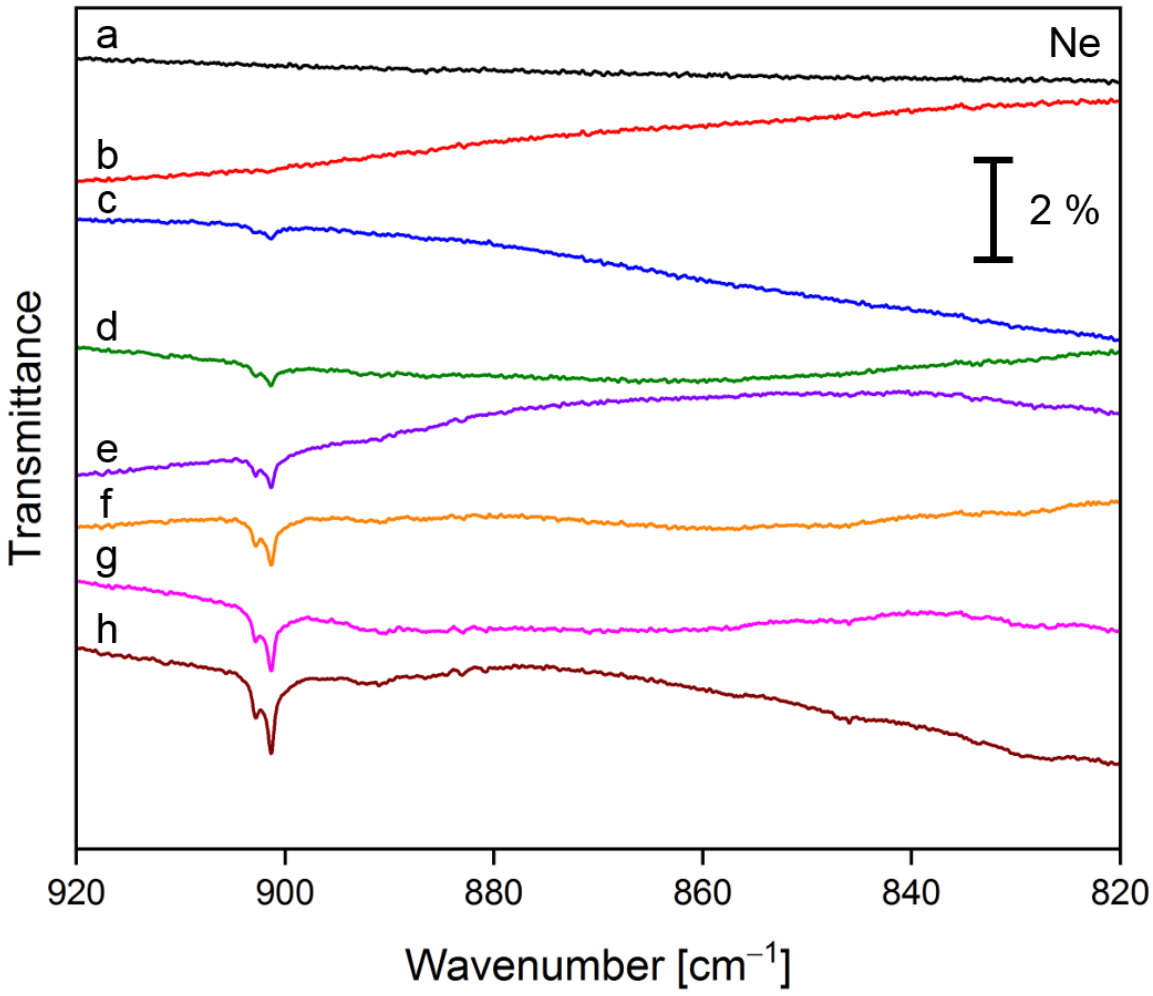

Figure 124: The IR spectra were recorded after the deposition of a) neon for 27 min, and the subsequent deposition of fluorine (1 % diluted in neon) passed over a solid sample of SbF_5 maintained at −49.1 to −48.1 °C for b) 16 min, c) 46 min, d) 60 min, e) 90 min, f) 120 min, g) 150 min, and after h) 180 min onto a CsI window at 4 K at a deposition rate of 0.6 mbar·l·min^{-1}.

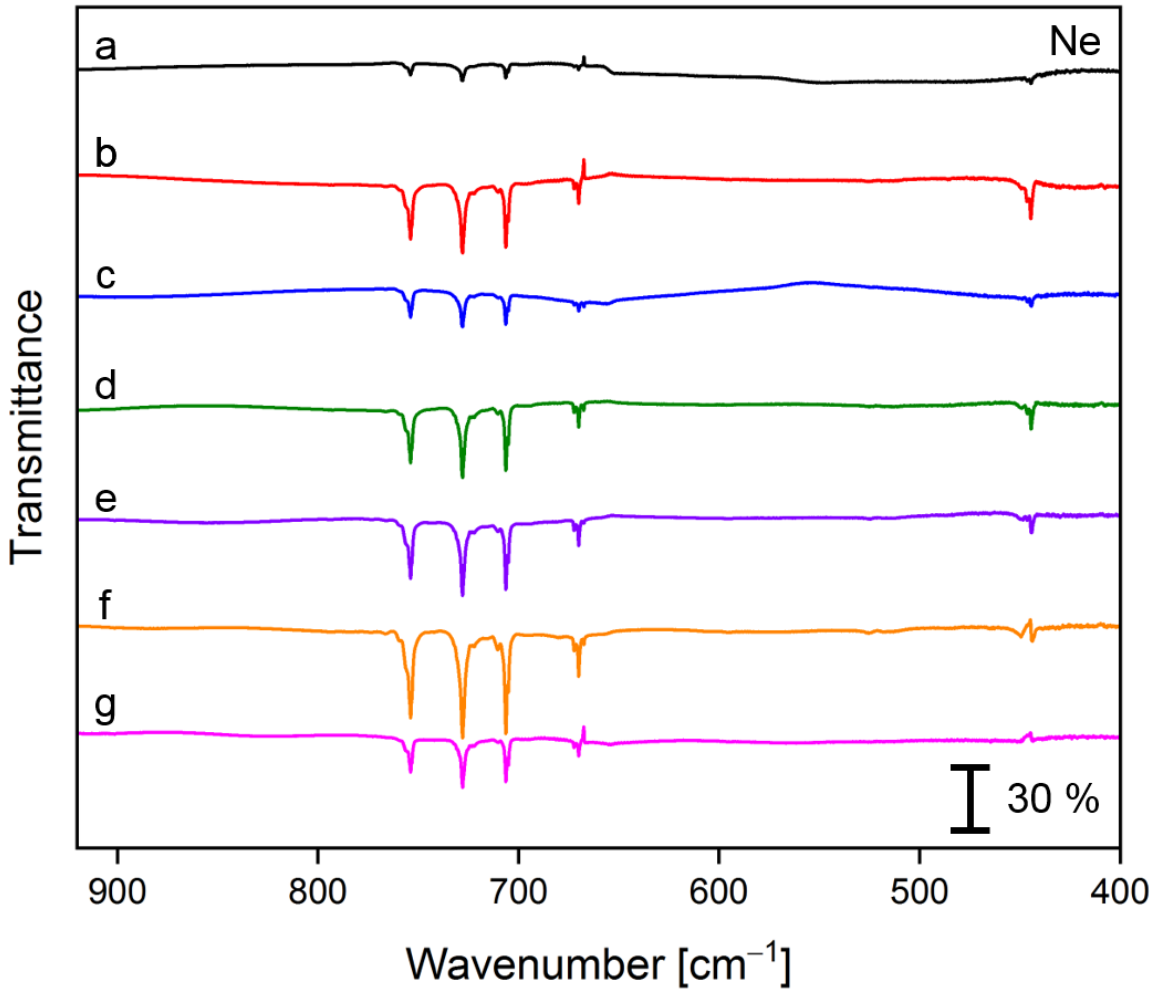

Figure 125: The difference IR spectra show the spectral changes after the deposition of fluorine (1 % diluted in neon) passed over a solid sample of SbF_5 maintained at −49.1 to −48.1 °C for b) 16 min, c) further 30 min, d) further 14 min, e) further 30 min, f) further 30 min, g) further 30 min, and after h) further 30 min to a total of 180 min at a deposition rate of 0.6 mbar·l·min^{-1}. Bands pointing downwards are formed at the expense of the bands pointing upwards. The CsI window (matrix support, T = 4 K) was coated with neon for 27 min prior to the deposition of the SbF_5/F_2 sample (spectrum not shown).

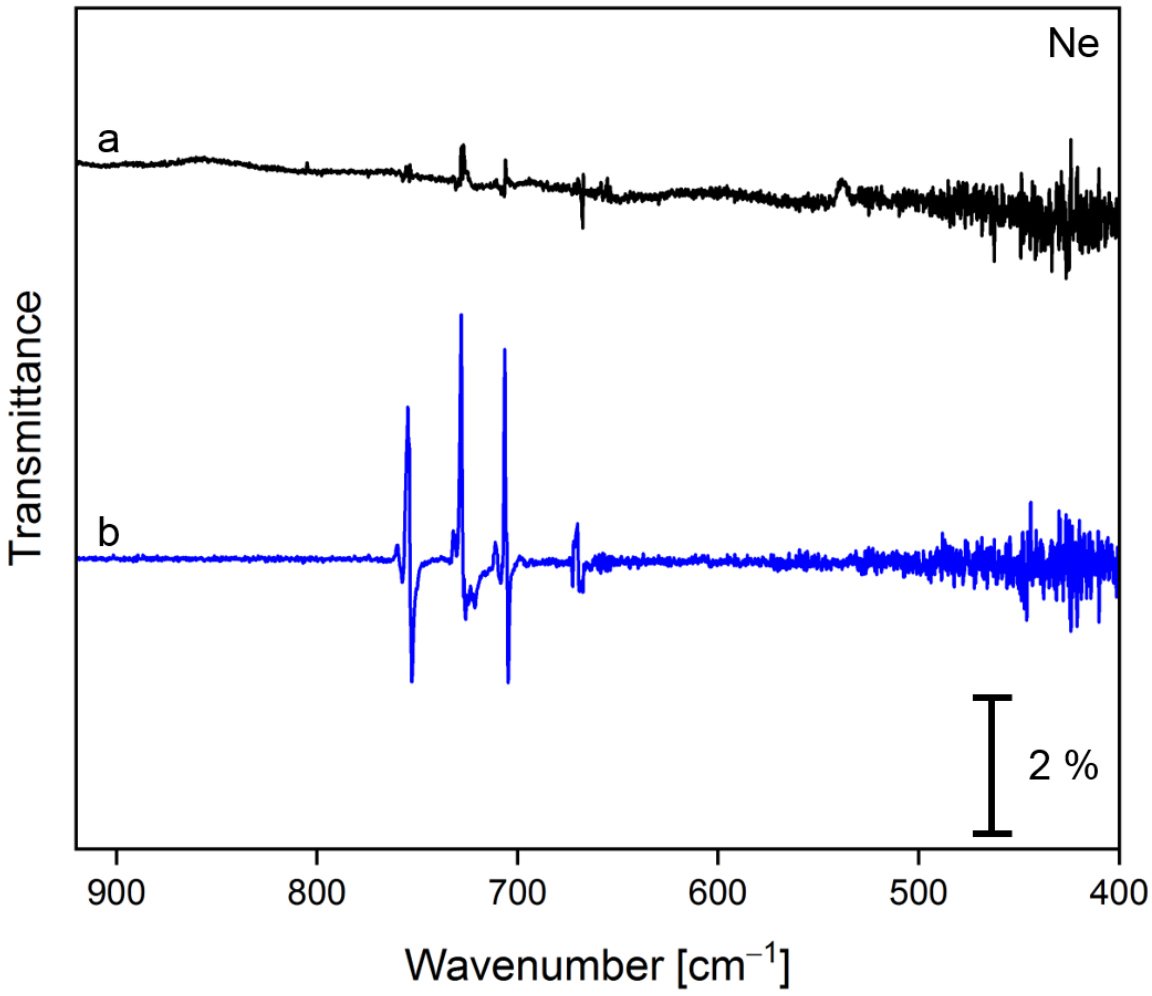

Figure 126: The difference IR spectra show the spectral changes after a) the irradiation of an initial deposit of fluorine (1 % diluted in neon) passed over a solid sample of SbF_5 maintained at −49.1 to −48.1 °C for 180 min at a deposition rate of 0.6 mbar·l·min^{-1} by a full-arc Hg lamp, and b) the subsequent annealing of the matrix to 9 K. The CsI window (matrix support, T = 4 K) was coated with neon for 27 min prior to the deposition of the SbF_5/F_2 sample (spectrum not shown). Bands pointing downwards are formed at the expense of the bands pointing upwards.

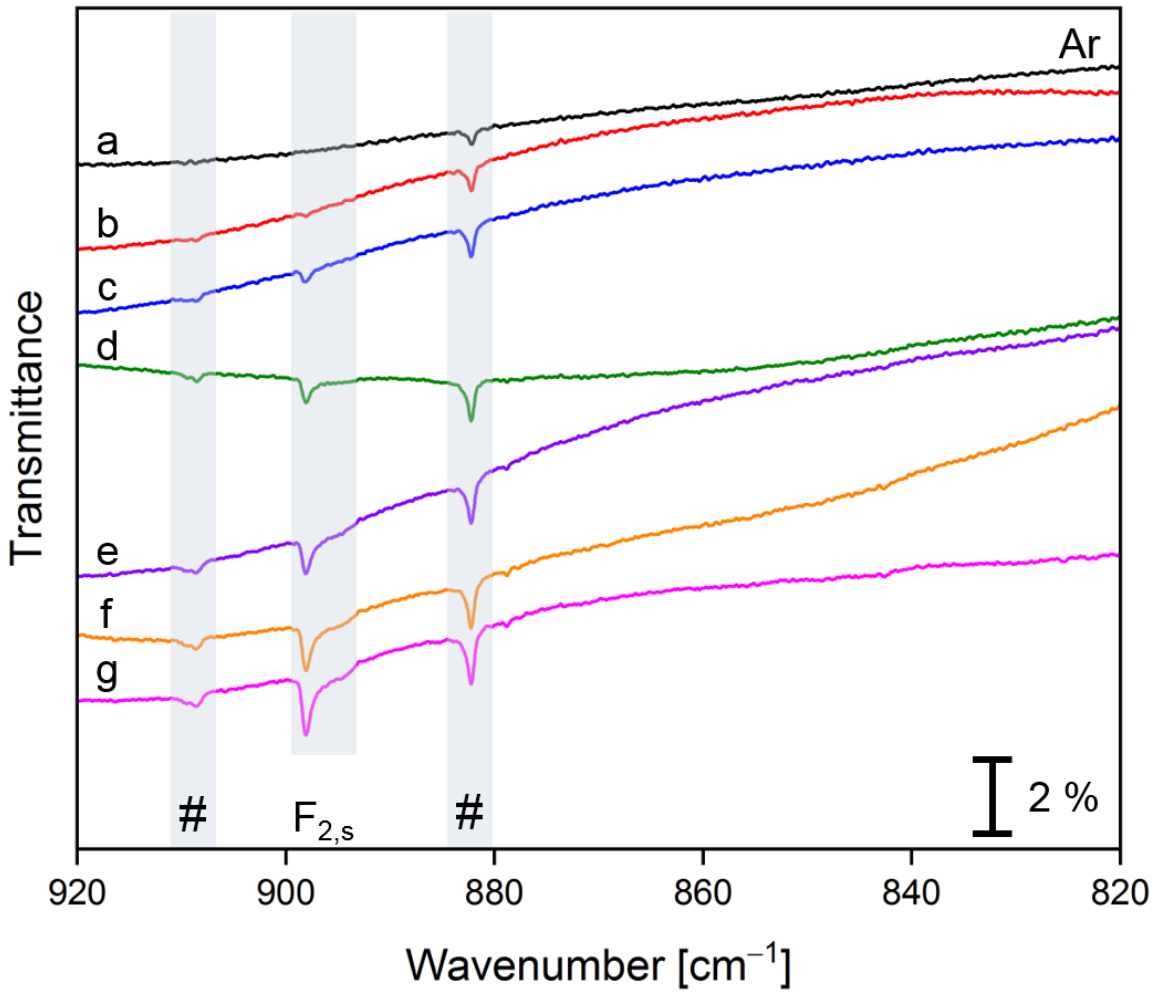

Figure 127: The IR spectra were recorded after the deposition of a) argon for 20 min, and the subsequent deposition of fluorine (1 % diluted in argon) passed over a solid sample of SbF_5 maintained at −49.2 to −48.3 °C for b) 30 min, c) 60 min, d) 90 min, e) 120 min, f) 150 min, and g) 180 min onto a CsI window at 4 K at a deposition rate of 0.5 mbar·l·min^{-1}. Impurity bands of unknown origin are marked by a hash.

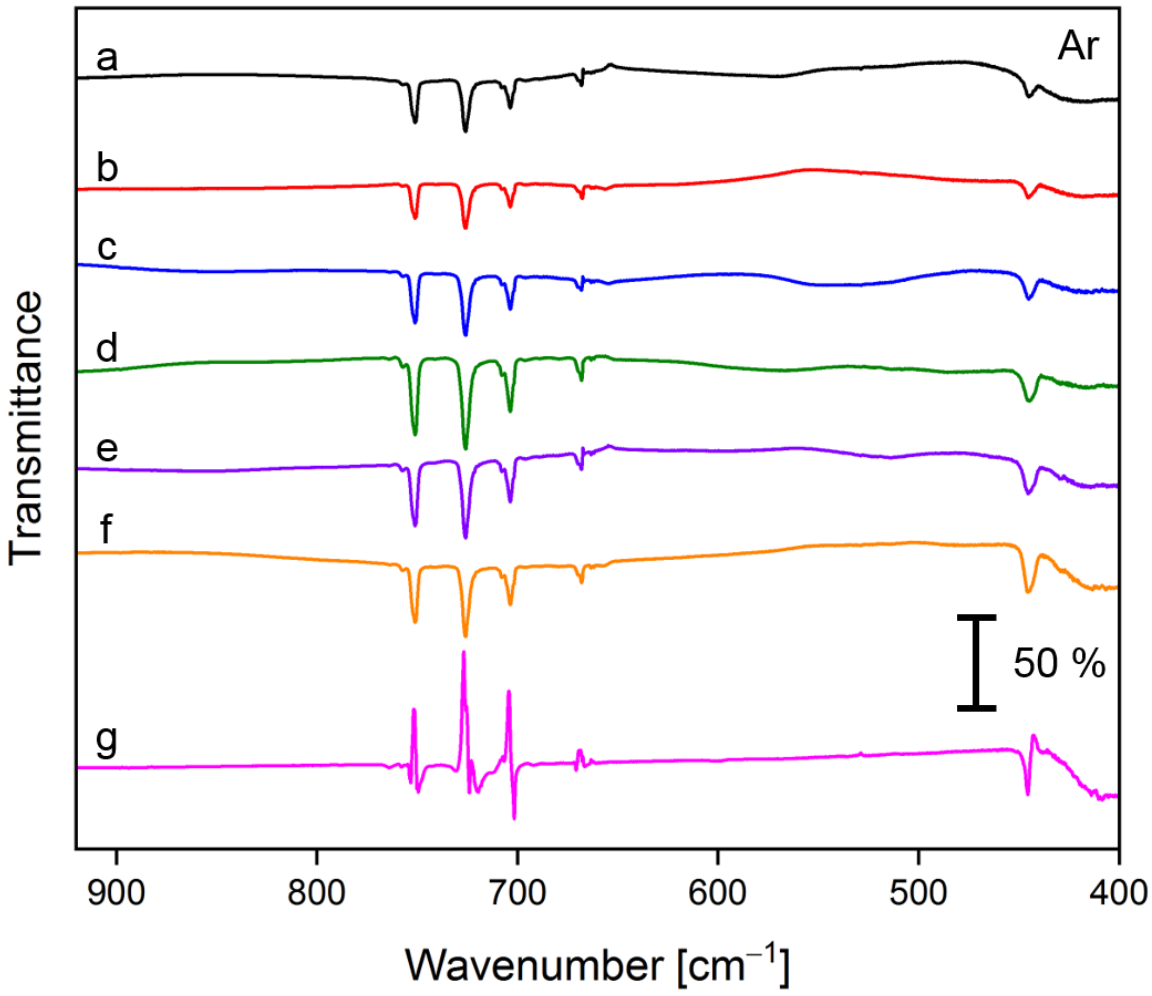

Figure 128: The difference IR spectra show the spectral changes after the deposition of fluorine (1 % diluted in argon) passed over a solid sample of SbF_5 maintained at −49.2 to −48.3 °C for a) 30 min, b) further 30 min, c) further 30 min, d) further 30 min, e) further 30 min, and after f) further 30 min to a total of 180 min at a deposition rate of 0.5 mbar·l·min^{-1}, and g) after the annealing of the matrix to 25 K. Bands pointing downwards are formed at the expense of the bands pointing upwards. The CsI window (matrix support, T = 4 K) was coated with argon for 20 min prior to the deposition of the SbF_5/F_2 sample (spectrum not shown).

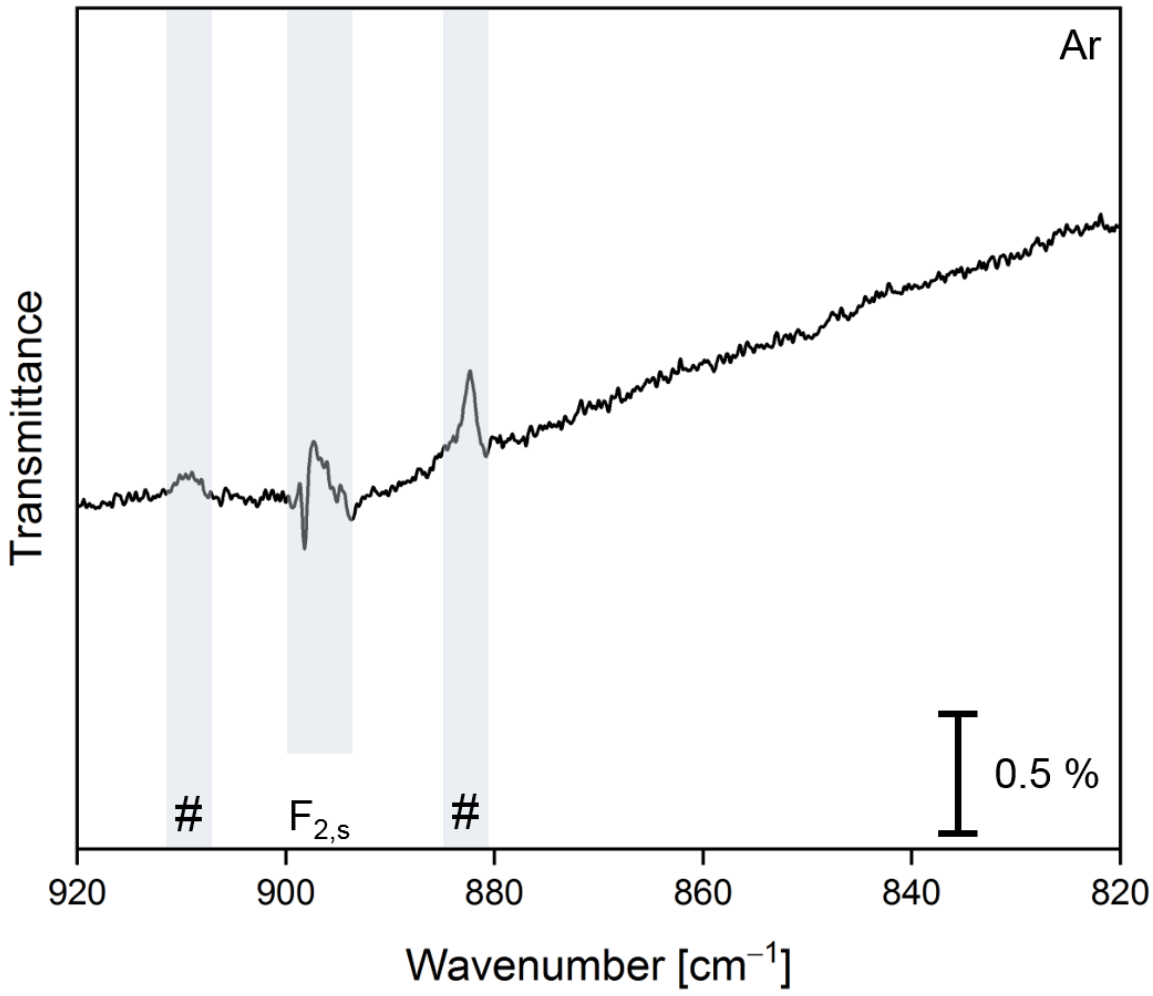

Figure 129: The difference IR spectrum show the spectral changes after the annealing to 25 K of a deposit of fluorine (1 % diluted in argon) passed over a solid sample of SbF_5 maintained at −49.2 to −48.3 °C for 180 min at a deposition rate of 0.5 mbar·l·min^{-1}. Impurity bands of unknown origin are marked by a hash. Bands pointing downwards are formed at the expense of the bands pointing upwards. The CsI window (matrix support, T = 4 K) was coated with argon for 20 min prior to the deposition of the SbF_5/F_2 sample (spectrum not shown).

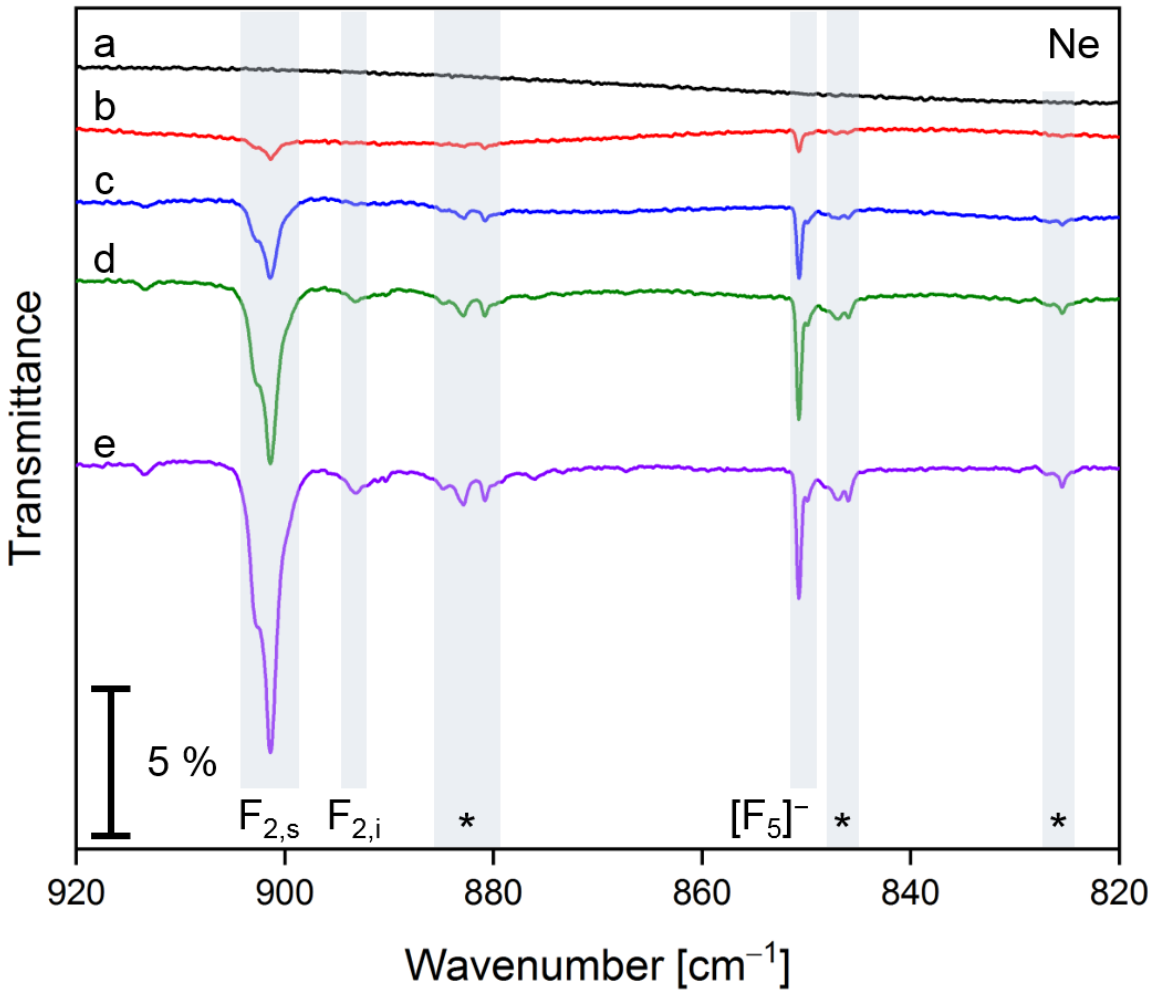

Figure 130: The IR spectra were recorded after the deposition of a) neon for 21 min, and the subsequent co-deposition of fluorine (1 % diluted in neon) and laser-ablated $Cs[AuF_6]$ (3 % diluted in a CsF-target, 3 Hz repetition rate, 30 mJ/pulse) for b) 15 min, c) 60 min, d) 120 min, and e) 180 min onto a CsI window at 4 K at a deposition rate of 0.5 mbar·l·min^{-1}. IR active features caused by traces of AsF_5 in combination with F_2 are marked by an asterisk.

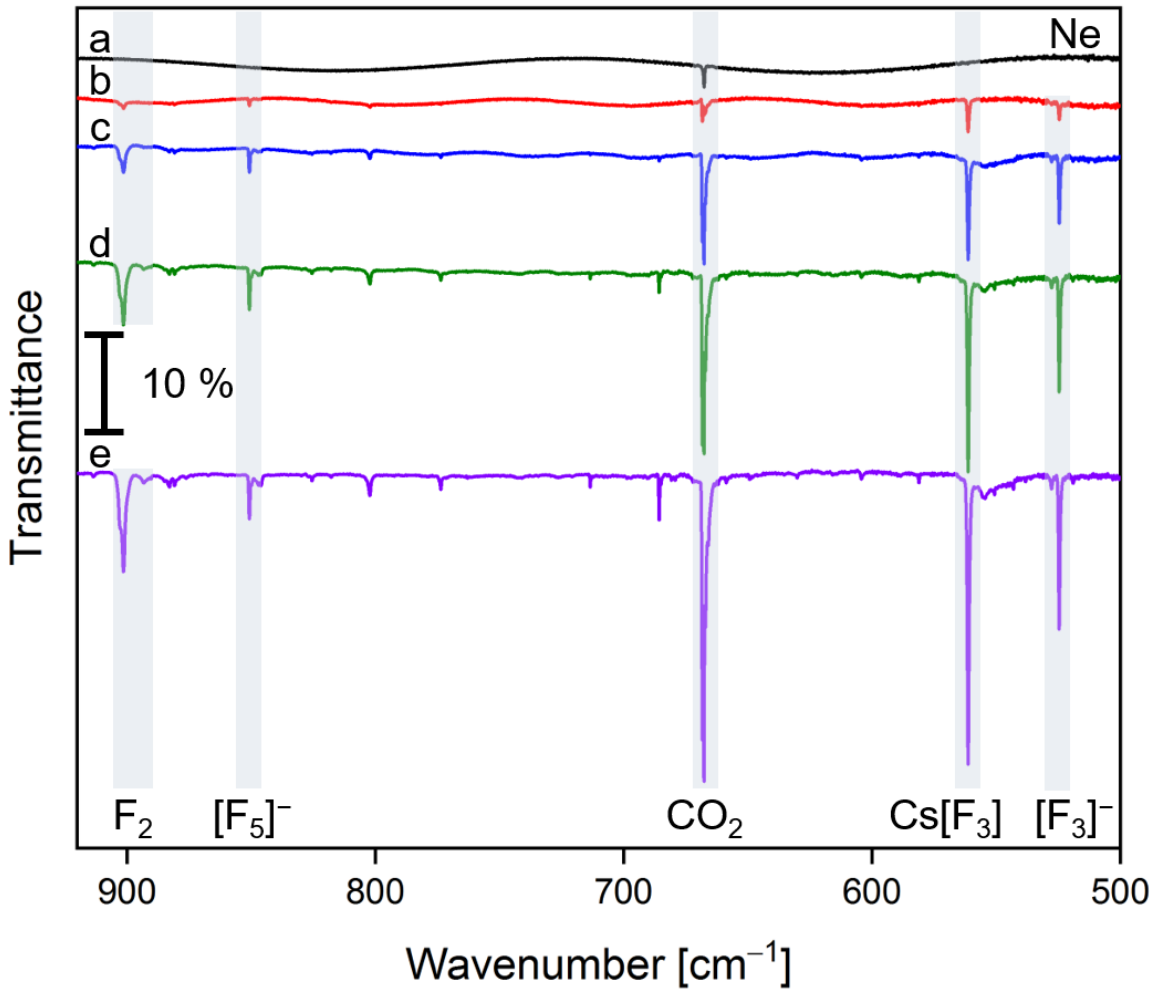

Figure 131: The IR spectra were recorded after the deposition of a) neon for 21 min, and the subsequent co-deposition of fluorine (1 % diluted in neon) and laser-ablated Cs[AuF_6] (3 % diluted in a CsF-target, 3 Hz repetition rate, 30 mJ/pulse) for b) 15 min, c) 60 min, d) 120 min, and e) 180 min onto a CsI window at 4 K at a deposition rate of 0.5 mbar·l·min^{-1}.

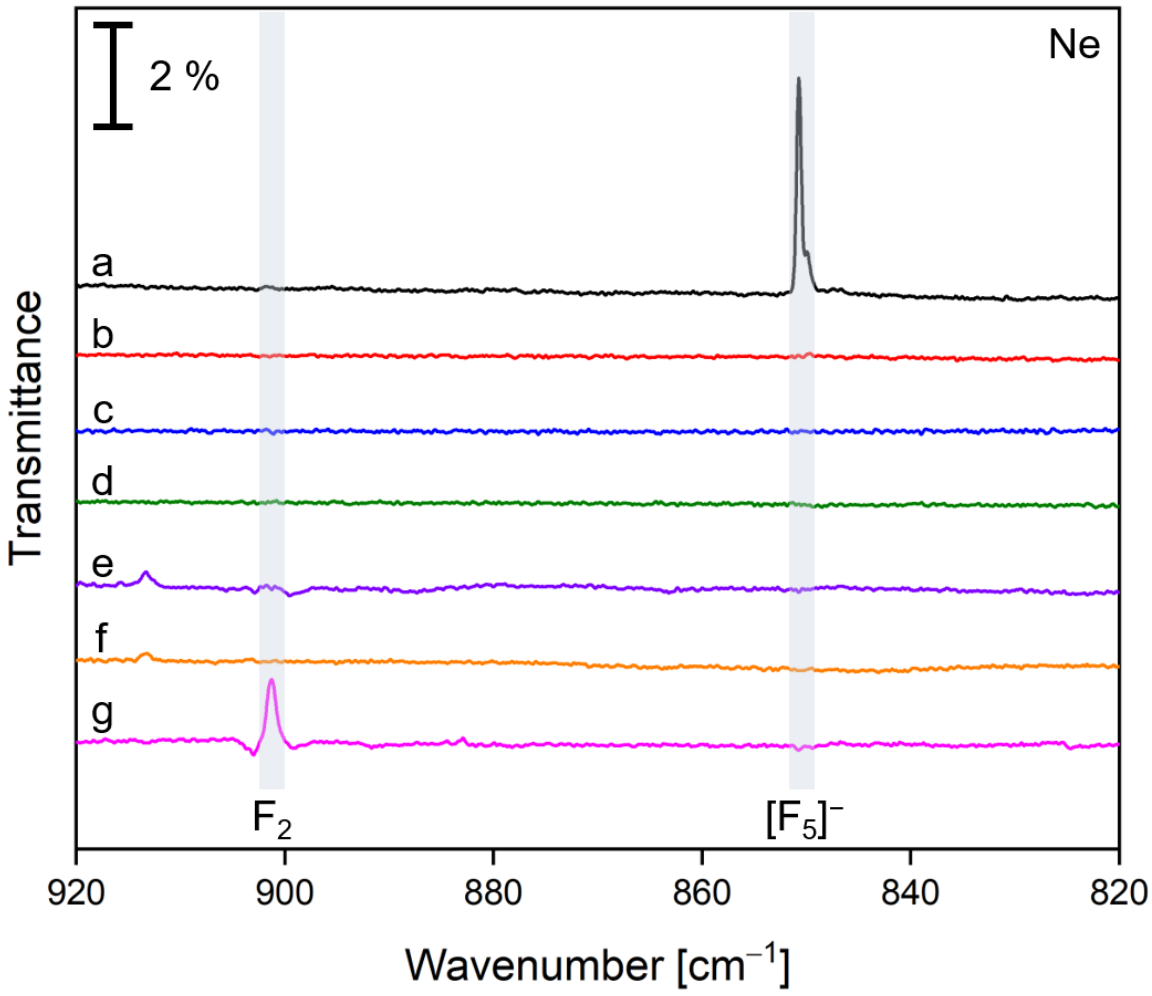

Figure 132: The difference IR spectra show the spectral changes after the irradiation of an initial deposit of fluorine (1 % diluted in neon) and laser-ablated $Cs[AuF_6]$ (3 % diluted in a CsF-target, 3 Hz repetition rate, 30 mJ/pulse) deposited for 180 min at a deposition rate of 0.5 mbar·l·min^{-1} at a) λ = 730 nm (LED), b) λ = 625 nm (LED), c) λ = 596 nm (LED), d) λ = 528 nm (LED), e) λ = 455 nm (LED), f) λ = 278 nm (LED), for 12 min respectively, and after a final annealing step to g) T = 9 K. The CsI window (matrix support, T = 4 K) was coated with neon for 21 min prior to the deposition of the $Cs[AuF_6]/F_2$ sample. The bands pointing downwards are formed at the expense of the bands pointing upwards.

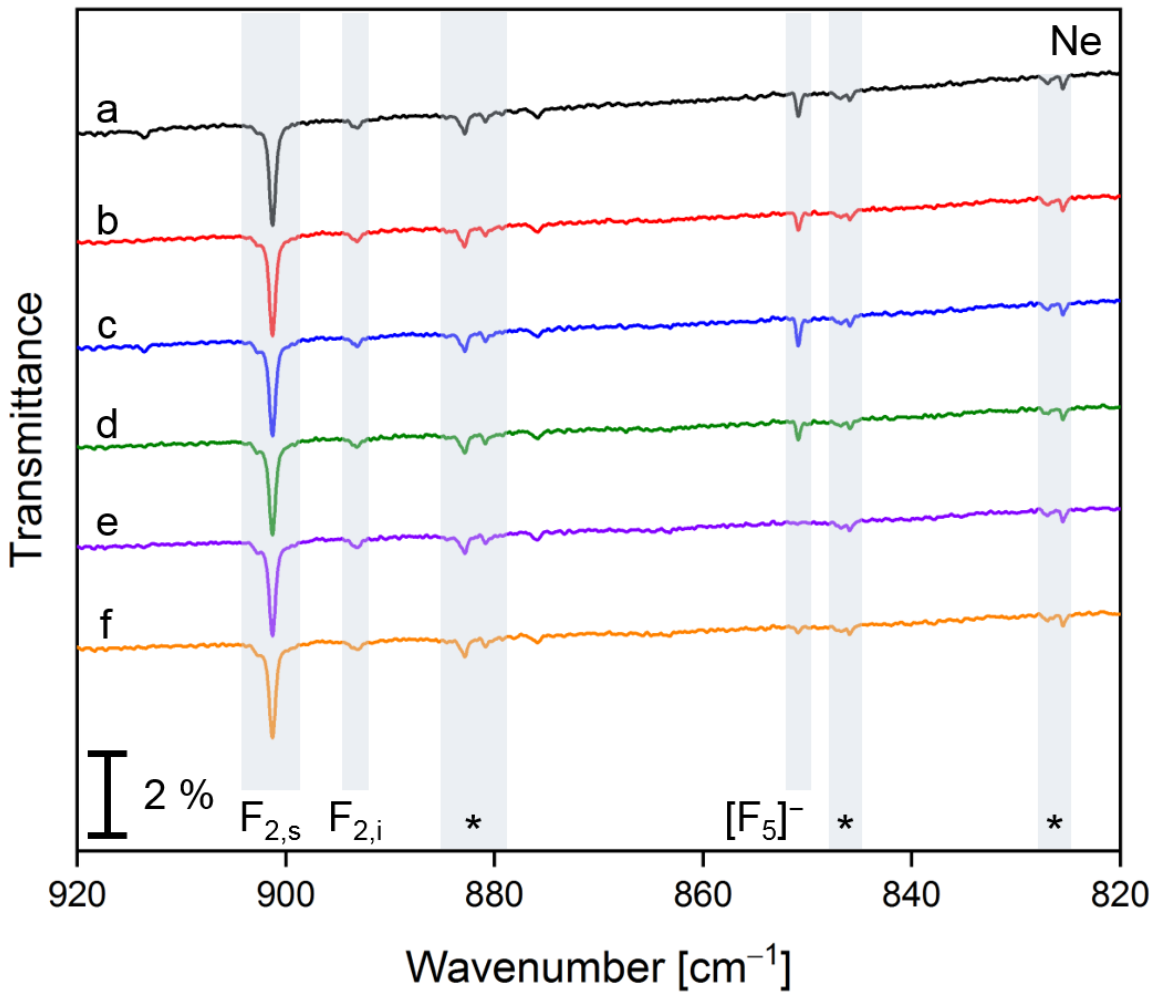

Figure 133: The IR spectra were recorded after a) the deposition of neon for 24 min, and the subsequent co-deposition of fluorine (0.1 % diluted in neon) and laser-ablated $Cs[AuF_6]$ (3 % diluted in a CsF-target, 3 Hz repetition rate, 30 mJ/pulse) onto a CsI window at 4 K for 180 min at a deposition rate of 0.5 mbar·l·min^{-1}, b) the irradiation of the initial deposit λ = 278 nm (LED) for 60 min, c) the annealing of the matrix to 9 K, and the subsequent irradiation at d) λ = 278 nm (LED) for 40 min, e) λ = 730 nm (LED) for 5 min and f) λ = 278 nm (LED) for 20 min. IR active features caused by traces of AsF_5 in combination with F_2 are marked by an asterisk.

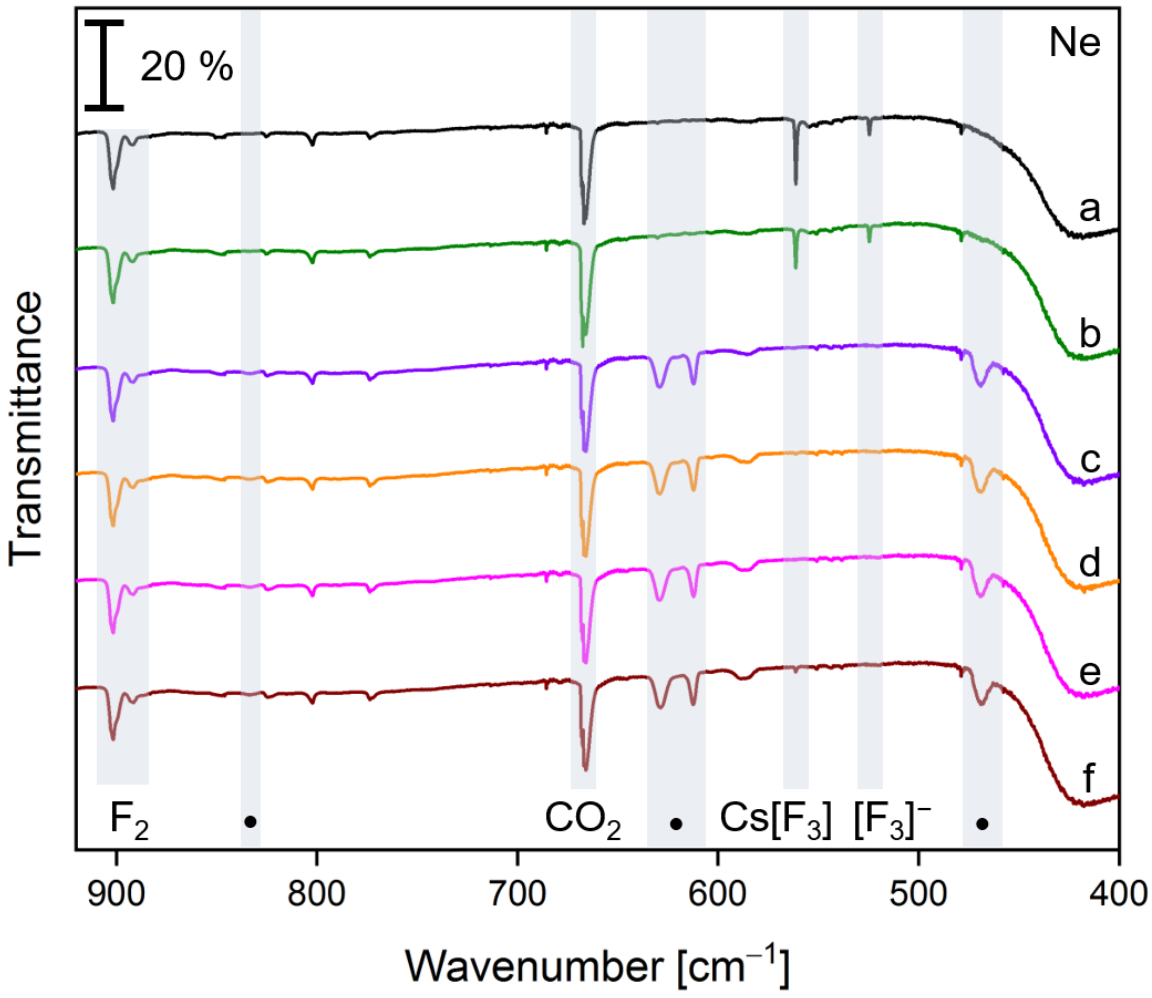

Figure 134: The IR spectra were recorded after (a) the co-deposition of laser-ablated $Cs[AuF_6]$ (3 % diluted in a CsF-target, 3 Hz repetition rate, 30 mJ/pulse) and fluorine at 3.0 % diluted in neon onto a CsI window at 4 K for 180 min at a deposition rate of 0.6 mbar·l·min^{-1}, b) the irradiation of this deposit at λ = 730 nm (LED) for 5 min and annealing of the matrix to 9 K and the consecutive irradiation at λ = 656 nm (LED) for 5 min, λ = 625 nm (LED) for 5 min, λ = 596 nm (LED) for 20 min and λ = 528 nm (LED) for 20 min, and after the subsequent irradiation at c) λ = 455 nm (LED) for 60 min, d) λ = 375 nm (LED) for 20 min, and e) λ = 278 nm (LED) for 10 min and after f) annealing the matrix to 9 K for a second time. New features are marked by a bullet.

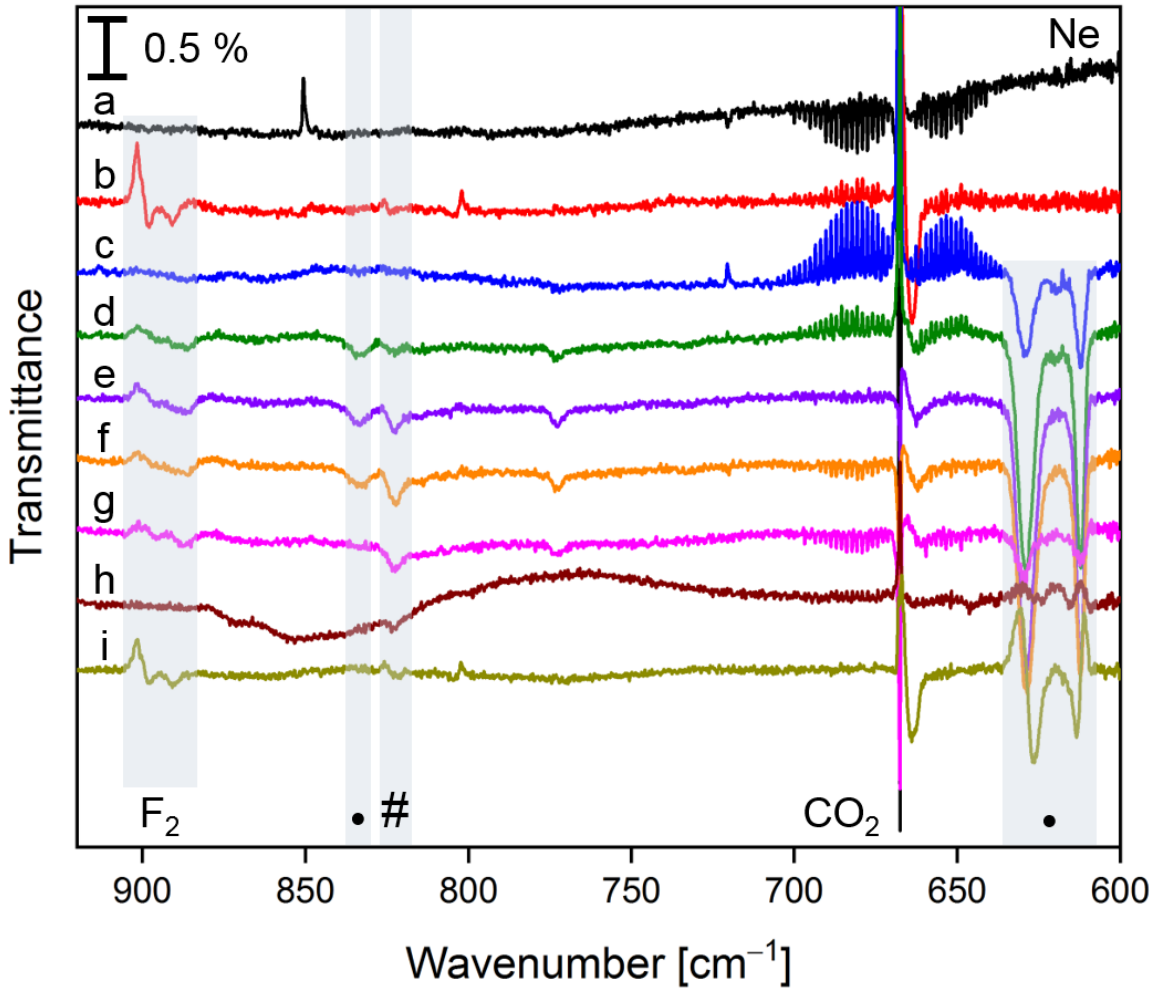

Figure 135: The difference spectra show the spectral changes after consecutive irradiation and annealing steps of an initial deposit of laser-ablated $Cs[AuF_6]$ (3 % diluted in a CsF-target, 3 Hz repetition rate, 30 mJ/pulse) and fluorine (3.0 % diluted in neon) onto a CsI window at 4 K for 180 min at a deposition rate of 0.6 mbar·l·min^{-1}. The matrix was irradiated at a) λ = 730 nm (LED) for 5 min, and b) annealed to 9 K, and irradiated at λ = 455 nm (LED) for c) 5 min, d) further 15 min, e) further 20 min and f) further 20 min. The matrix was subsequently irradiated at g) λ = 375 nm (LED) for 20 min and h) λ = 278 nm (LED) for 10 min and annealed to i) 9 K for a second time. The bands pointing downwards are formed at the expense of the bands pointing upwards. New prominent features are marked by a bullet, a feature at 822.2 cm^{-1} depicts a shoulder of an already existing band in the initial deposit and is marked by a hash.

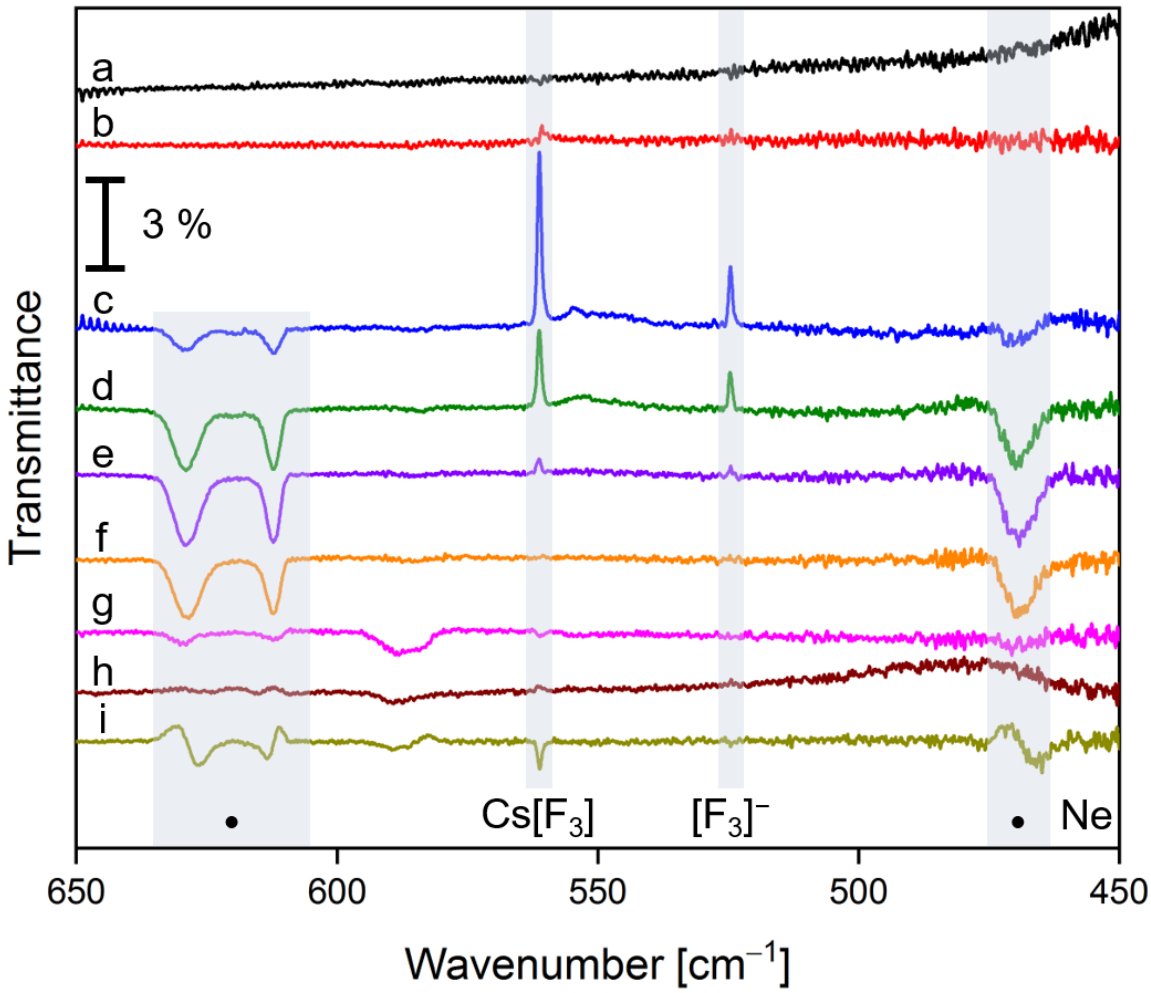

Figure 136: The difference spectra show the spectral changes after consecutive irradiation and annealing steps of an initial deposit of laser-ablated $Cs[AuF_6]$ (3 % diluted in a CsF-target, 3 Hz repetition rate, 30 mJ/pulse) and fluorine (3.0 % diluted in neon) onto a CsI window at 4 K for 180 min at a deposition rate of 0.6 mbar·l·min^{-1}. The matrix was irradiated at a) λ = 730 nm (LED) for 5 min, and b) annealed to 9 K, and irradiated at λ = 455 nm (LED) for c) 5 min, d) further 15 min, e) further 20 min and f) further 20 min. The matrix was subsequently irradiated at g) λ = 375 nm (LED) for 20 min and h) λ = 278 nm (LED) for 10 min and annealed to i) 9 K for a second time. The bands pointing downwards are formed at the expense of the bands pointing upwards. New prominent features are marked by a bullet.

6.2 Additional Data of PtF_6 and its Derivatives

6.2.1 B3LYP Structures of Platinum Fluorido Compounds

The optimized structures of the binary neutral as well as binary and ternary ionic platinum fluorido compounds and M[F_2] (M = Na, K, Cs) in the following subchapters are given in the form of xyz data in Å.

6.2.1.1 Binary Neutral and Anionic Platinum Fluorido Compounds

PtF_6 (^3E_g-D_{4h})

F	0.0000000	0.0000000	1.8458186
F	-1.3246045	1.3246045	0.0000000
F	0.0000000	0.0000000	-1.8458186
F	1.3246045	-1.3246045	0.0000000
F	-1.3246045	-1.3246045	0.0000000
F	1.3246045	1.3246045	0.0000000
Pt	0.0000000	0.0000000	0.0000000

$[PtF_6]^-$ ($^2B_{1g}$-D_{4h})

Pt	0.0000000	0.0000000	0.0000000
F	0.0000000	0.0000000	1.9423102
F	1.3371329	1.3371329	0.0000000
F	1.3371329	-1.3371329	0.0000000
F	-1.3371329	1.3371329	0.0000000
F	-1.3371329	-1.3371329	0.0000000
F	0.0000000	0.0000000	-1.9423102

PtF_4 (^1E_g-D_{4h})

Pt	0.0000000	0.0000000	0.0000000
F	-1.3073839	1.3073839	0.0000000
F	-1.3073839	-1.3073839	0.0000000
F	1.3073839	1.3073839	0.0000000
F	1.3073839	-1.3073839	0.0000000

PtF_4 ($^3B_{2g}$-D_{2h})

Pt	0.0000000	0.0000000	0.0000000
F	1.3402350	-1.2851273	0.0000000
F	1.3402350	1.2851273	0.0000000
F	-1.3402350	-1.2851273	0.0000000
F	-1.3402350	1.2851273	0.0000000

$[PtF_4]^-$ ($^2B_{1g}$-D_{4h})

Pt	0.0000000	0.0000000	0.0000000
F	-1.3559802	1.3559802	0.0000000
F	-1.3559802	-1.3559802	0.0000000
F	1.3559802	1.3559802	0.0000000
F	1.3559802	-1.3559802	0.0000000

$[PtF_4{\cdot}F_2]^-$ ($^2B_1$-C_{4v})

Pt	0.0000000	0.0000000	-0.8264395
F	-1.3441349	-1.3441349	-0.8958859
F	1.3441349	-1.3441349	-0.8958859
F	-1.3441349	1.3441349	-0.8958859
F	1.3441349	1.3441349	-0.8958859
F	0.0000000	0.0000000	3.1405224
F	0.0000000	0.0000000	1.2648658

$[PtF_4{\cdot}F_2]^-$ (^2A-C_1)

Pt	0.2033048	0.6486667	-0.0190613
F	-1.1568605	0.6277098	1.3523164
F	-1.1788180	0.6657173	-1.3840833
F	1.5703023	0.8657832	1.3435177
F	1.5366259	0.9727464	-1.3877988
F	-0.6695357	-2.6276133	1.1332668
F	0.3899610	-1.2204902	-0.0449874

PtF_5 ($^2B_1$-C_{4v})

Pt	-0.0000000	0.0000000	-0.2608324
F	1.3252913	-1.3252913	-0.3352032
F	1.3252913	1.3252913	-0.3352032
F	-1.3252913	-1.3252913	-0.3352032
F	-1.3252913	1.3252913	-0.3352032
F	0.0000000	0.0000000	1.6016454

$[PtF_5]^-$ ($^1B_1$-C_{4v})

Pt	0.0000000	0.0000000	-0.2359659
F	1.3734472	-1.3734472	-0.3519682
F	1.3734472	1.3734472	-0.3519682
F	-1.3734472	-1.3734472	-0.3519682
F	-1.3734472	1.3734472	-0.3519682
F	0.0000000	0.0000000	1.6438388

$[PtF_7]^-$ ($^1E_1''$-D_{5h})

F	-1.5550387	1.1298018	0.0000000
F	0.0000000	0.0000000	1.9372898
F	-1.5550387	-1.1298018	0.0000000
F	0.5939719	-1.8280577	0.0000000
F	1.9221336	0.0000000	0.0000000
F	0.5939719	1.8280577	0.0000000
F	0.0000000	0.0000000	-1.9372898
Pt	-0.0000000	0.0000000	-0.0000000

$[PtF_5{\cdot}F_2]^-$ ($^1A'$-C_s)

F	-0.3706612	1.5057958	0.0000000
F	1.2614821	-0.3012242	-1.3364724
F	-0.1193925	-2.2452327	0.0000000
F	-1.4573427	-0.4660628	1.3690157
F	-1.4573427	-0.4660628	-1.3690157
F	1.2614821	-0.3012242	1.3364724
F	0.9876659	2.6465021	0.0000000
Pt	-0.1060026	-0.3710717	0.0000000

PtF_3 (^2A-C_1)

Pt	0.1513578	-0.2968815	0.1659736
F	1.9569165	0.1835022	0.1055543
F	-1.6098845	-0.9217326	0.2118639
F	-0.4082698	1.4949819	-0.0324717

$[PtF_3{\cdot}F_2]^-$ ($^1A''$-C_s)

F	-1.0303933	-0.9709726	0.0000000
F	1.0632815	2.1480177	0.0000000
F	1.6971173	-0.4796297	0.0000000
F	-1.4718307	1.6268602	0.0000000
F	-0.3514663	-2.8402571	0.0000000
Pt	0.0932915	0.5159815	0.0000000

6.2.1.2 Ternary and Mixed-Valent Platinum Fluorido Compounds

$Na[PtF_6]$ (^2A-C_1)

Na	-2.1993571	1.3185330	1.8557893
F	-0.1523861	-2.1872610	0.3720629
F	1.5562994	-0.1073748	0.5778444
Pt	-0.2915836	-0.3006979	0.3606530
F	-0.1657324	-0.3668285	-1.5054609
F	-0.5475739	-0.1966866	2.2735439
F	-2.2232013	-0.3544350	0.3133499
F	-0.5341181	1.6410336	0.4055324

$K[PtF_6]$ (^2A-C_1)

K	-2.4517627	1.4946986	2.0356646
F	-0.1431487	-2.2024943	0.3731728
F	1.5935493	-0.1342595	0.5413244
Pt	-0.2675649	-0.3191786	0.3451356
F	-0.1379390	-0.3704086	-1.5250082
F	-0.4832216	-0.2350678	2.2590749
F	-2.2000589	-0.3997538	0.2636247
F	-0.4675066	1.6127468	0.3603261

$Cs[PtF_6]$ (^2A-C_1)

Cs	-2.6304049	1.6855744	2.2043386
F	-0.1551565	-2.2278170	0.3543861
F	1.6251149	-0.1924109	0.4897676
Pt	-0.2476766	-0.3438946	0.3249340
F	-0.1411340	-0.3841894	-1.5484696
F	-0.4222245	-0.2674311	2.2392131
F	-2.1830252	-0.4096720	0.2520138
F	-0.4031462	1.5861233	0.3371311

$Pd[PtF_6]$ (^1A-C_1)

Pd	-2.2904639	1.4206114	1.6111693
F	-0.1403891	-2.2185963	0.3648300
F	1.6217336	-0.2344262	0.4424086
Pt	-0.2523060	-0.3443139	0.3990430
F	-0.2135599	-0.3040996	-1.4992441
F	-0.3962503	-0.2936690	2.3296279
F	-2.2987092	-0.2528851	0.4641549
F	-0.5877081	1.6736614	0.5413251

$Pt[PtF_6]$ ($^1A''$-C_s)

Pt	-2.3978779	-0.8157702	0.0000000
F	1.7993838	0.1420656	-1.3331284
F	1.7993838	0.1420656	1.3331284
Pt	0.4799328	0.1477756	0.0000000
F	0.4701801	2.0648511	0.0000000
F	0.2986162	-1.7907588	0.0000000
F	-1.2259802	0.0546705	-1.3058364
F	-1.2259802	0.0546705	1.3058364

6.2.1.3 Alkali Metal Difluorides $M[F_2]$ (M = Na, K, Cs)

$Na[F_2]$ ($^2B_1$-C_{2v})

F	1.0142658	0.0000000	0.5966861
F	-1.0142658	0.0000000	0.5966861
Na	0.0000000	0.0000000	-1.1927263

$K[F_2]$ ($^2B_1$-C_{2v})

F	1.0038472	0.0000000	0.7198924
F	-1.0038472	0.0000000	0.7198924
K	0.0000000	0.0000000	-1.4380814

$Cs[F_2]$ ($^2A'$-C_s)

F	-1.0033916	0.8052000	0.0000000
F	0.9904722	0.8202356	0.0000000
Cs	0.0129194	-1.6254356	0.0000000

6.2.2 NPA Charges of Platinum Fluorido Compounds

The following tables comprise the NPA charges of the binary neutral and anionic as well as ternary ionic platinum fluorido compounds and M[F_2] (M = Na, K, Cs) calculated at the RI-B3LYP-D4/def2-TZVPP level of theory on the basis of the optimized structures described in Section 6.2.1.

The atomic labels are shown in Figure 137 for $[PtF_6]^-$ and M[PtF_6] (M = Na, K, Pd, Cs, Pt) and in Figure 138 for the anionic non-classical $[PtF_n{\cdot}F_2]^-$ (n = 3, 4, 5) and classical $[PtF_7]^-$. The neutral PtF_n (n = 3–6) are labelled analogously to their anionic forms.

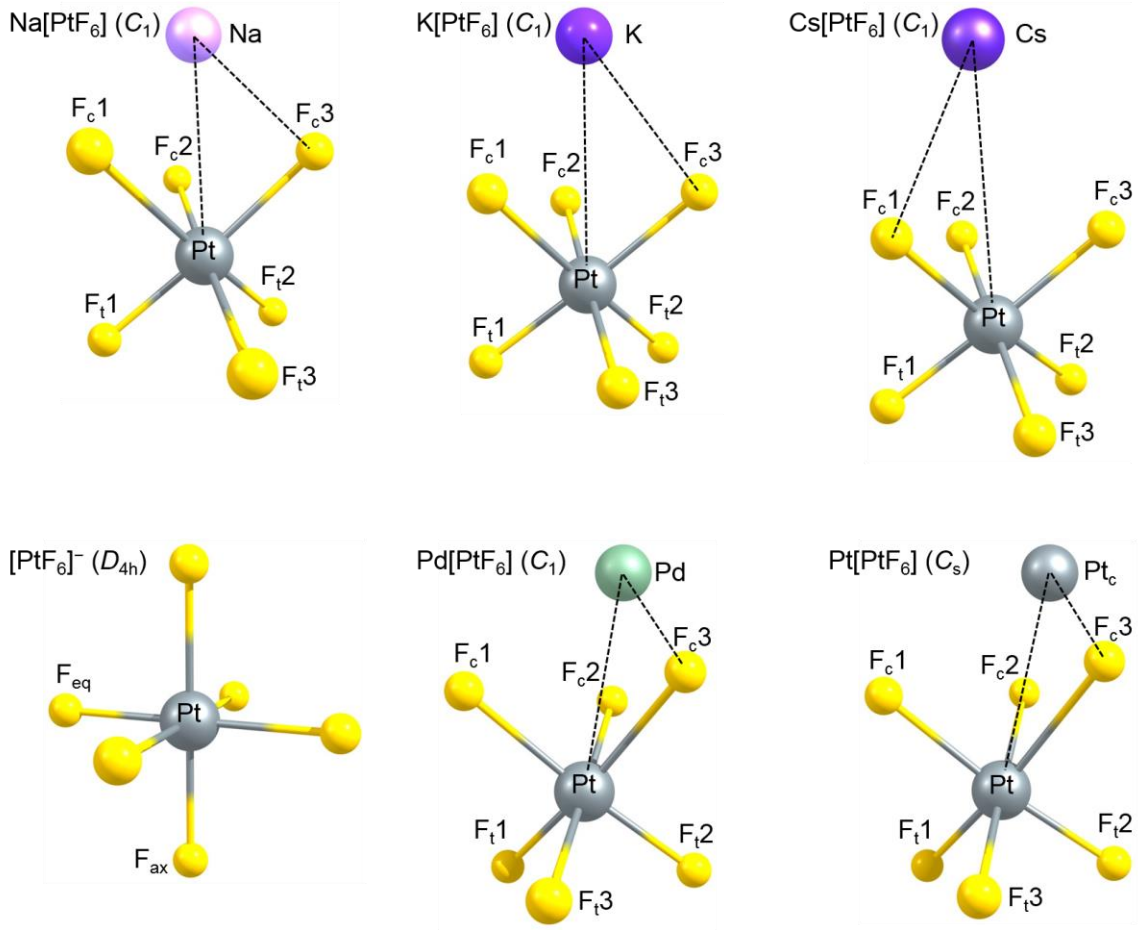

Figure 137: Labelling of M[PtF_6] (M = Na, K, Pd, Cs, Pt) and $[PtF_6]^-$ optimized at the RI-B3LYP-D4/def2-TZVPP level of theory in accordance with the obtained NPA charges.

Table 54: NPA charges (in e) of the B3LYP structures of the ion pairs C_1-M[PtF_6] (M = Na, K, Cs).

Na[PtF_6]		**K[PtF_6]**		**Cs[PtF_6]**	
Atom	Charge	Atom	Charge	Atom	Charge
Na	0.971	K	0.980	Cs	0.983
F_c1	−0.588	F_c1	−0.582	F_c1	−0.600
F_c2	−0.589	F_c2	−0.596	F_c2	−0.597
F_c3	−0.624	F_c3	−0.605	F_c3	−0.576
Pt	2.174	Pt	2.182	Pt	2.187
F_t1	−0.479	F_t1	−0.474	F_t1	−0.453
F_t2	−0.434	F_t2	−0.448	F_t2	−0.473
F_t3	−0.431	F_t3	−0.458	F_t3	−0.473

Table 55: NPA charges (in e) of the B3LYP structures of D_{4h}-$[PtF_6]^-$, C_1-Pd[PtF_6] and C_s-Pt[PtF_6].

$[PtF_6]^-$		**Pd[PtF_6]**		**Pt[PtF_6]**	
Atom	Charge	Atom	Charge	Atom	Charge
Pt	2.200	Pd	1.068	Pt_c	1.140
F_{eq}	−0.503	F_c1	−0.578	F_c1	−0.606
F_{ax}	−0.594	F_c2	−0.544	F_c2	−0.508
		F_c3	−0.543	F_c3	−0.508
		Pt	2.015	Pt	1.937
		F_t1	−0.455	F_t1	−0.449
		F_t2	−0.507	F_t2	−0.558
		F_t3	−0.455	F_t3	−0.449

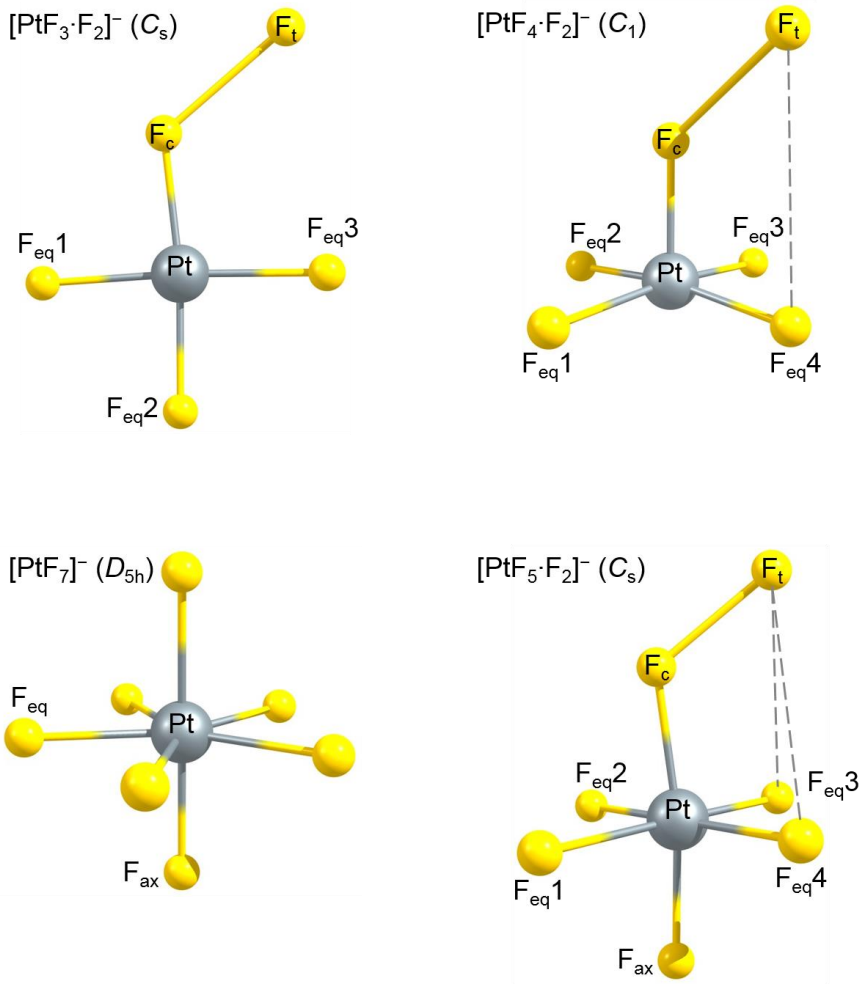

Figure 138: Labelling of anionic non-classical $[PtF_n{\cdot}F_2]^-$ (n = 3, 4, 5) and classical $[PtF_7]^-$ optimized at the RI-B3LYP-D4/def2-TZVPP level of theory in accordance with the obtained NPA charges. The neutral PtF_n (n = 3–6) are labelled accordingly.

Table 56: NPA charges (in e) of the B3LYP structures of D_{4h}-PtF_6 and D_{5h}-$[PtF_7]^-$.

PtF_6		**$[PtF_7]^-$**	
Atom	Charge	Atom	Charge
Pt	2.315	Pt	2.289
F_{eq}	−0.397	F_{eq}	−0.433
F_{ax}	−0.363	F_{ax}	−0.563

Table 57: NPA charges (in e) of the B3LYP structures of C_{4v}-PtF_5, C_{4v}-$[PtF_5]^-$ and C_s-$[PtF_5{\cdot}F_2]^-$.

PtF_5		**$[PtF_5]^-$**		**$[PtF_5{\cdot}F_2]^-$**	
Atom	Charge	Atom	Charge	Atom	Charge
Pt	2.158	Pt	1.937	Pt	2.134
F_{eq}	−0.458	F_{eq}	−0.625	$F_{eq}1$	−0.563
F_{ax}	−0.324	F_{ax}	−0.438	$F_{eq}2$	−0.563
				$F_{eq}3$	−0.533
				$F_{eq}4$	−0. 533
				F_{ax}	−0.471
				F_c	−0.222
				F_t	−0.247

Table 58: NPA charges (in e) of the B3LYP structures of D_{4h}-$[PtF_4]^-$, C_1-$[PtF_4{\cdot}F_2]^-$ and C_{4v}-$[PtF_4{\cdot}F_2]^-$.

D_{4h}-$[PtF_4]^-$		**C_1-$[PtF_4{\cdot}F_2]^-$**		**C_{4v}-$[PtF_4{\cdot}F_2]^-$**	
Atom	Charge	Atom	Charge	Atom	Charge
Pt	1.414	Pt	1.967	Pt	1.889
F	−0.604	$F_{eq}1$	−0.615	F_{eq}	−0.553
		$F_{eq}2$	−0.609		
		$F_{eq}3$	−0.616		
		$F_{eq}4$	−0.594		
		F_c	−0.361	F_c	−0.418
		F_t	−0.172	F_t	−0.261

Table 59: NPA charges (in e) of the B3LYP structures of D_{2h}-PtF_4 and D_{4h}-PtF_4. The D_{2h} isomer is 67 kJ·mol^{-1} lower in energy.

D_{2h}-PtF_4		**D_{4h}-PtF_4**	
Atom	Charge	Atom	Charge
Pt	1.801	Pt	1.676
F	−0.450	F	−0.419

Table 60: NPA charges (in e) of the B3LYP structures of C_1-PtF_3 and C_s-$[PtF_3 \cdot F_2]^-$. PtF_3 is T-shaped and has two 'equatorial' and one 'axial' ligands, with shorter (1.87 Å) and longer (1.89 Å) Pt–F bonds, respectively.

PtF_3		**$[PtF_3 \cdot F_2]^-$**	
Atom	Charge	Atom	Charge
Pt	1.480	Pt	1.450
F_{eq}	−0.512	$F_{eq}1$	−0.591
F_{ax}	−0.456	$F_{eq}2$	−0.562
		$F_{eq}3$	−0.531
		F_c	−0.341
		F_t	−0.424

6.2.3 B3LYP Vibrational Frequencies of Platinum Fluorido Compounds

The following tables comprise the vibrational frequencies and their respective IR intensities of the binary neutral and anionic as well as ternary ionic platinum fluorido compounds and $M[F_2]$ (M = Na, K, Cs) calculated at the RI-B3LYP-D4/def2-TZVPP level of theory on the basis of the optimized structures described in Section 6.2.1.

Table 61: Vibrational frequencies $\tilde{\nu}$ of the all C_1-symmetric ion pairs $M[PtF_6]$ (M = Na, K, Cs) given in cm^{-1} and the corresponding IR intensities *I* given in $km \cdot mol^{-1}$ obtained at the RI-B3LYP-D4/def2-TZVPP level of theory.

$\tilde{\nu}$ (Na[PtF_6])	*I* (Na[PtF_6])	$\tilde{\nu}$ (K[PtF_6])	*I* (K[PtF_6])	$\tilde{\nu}$ (Cs[PtF_6])	*I* (Cs[PtF_6])
665.49	84.55333	660.82	93.80422	657.82	105.84697
643.92	161.11562	634.21	168.204	631.51	161.20478
620.03	170.20621	624.54	172.4599	625.65	166.10317
587.52	100.32565	592.16	101.92494	594.16	110.43366
486.24	7.14174	429.19	0.62447	397.14	1.44185
398.64	0.53599	368.81	0.41531	355.15	1.18967
332.99	49.885	309.21	30.24041	297.71	24.27504
276.00	2.28215	266.72	1.59277	261.39	8.17699
266.35	10.26552	260.85	8.43906	257.94	2.78236
256.51	11.65331	244.76	5.87192	236.64	3.41949
248.79	4.14513	234.20	1.39425	229.42	1.92573
229.41	3.65102	218.87	5.55151	221.38	4.50156
217.62	8.15859	218.38	1.65059	210.80	3.05262
199.98	8.22544	180.82	10.4369	185.47	9.60474
181.94	1.70306	173.13	11.60411	147.79	7.08358
164.76	0.35769	152.55	11.60417	94.99	13.9144
106.67	12.07324	73.54	11.29164	46.77	5.38457
40.34	35.2854	66.36	16.68055	37.72	6.23086

Table 62: B3LYP vibrational frequencies $\tilde{\nu}$ of C_1-Pd[PtF_6] and C_s-Pt[PtF_6] given in cm^{-1}, their symmetries and corresponding IR intensities *I* given in $km \cdot mol^{-1}$.

Symmetry	$\tilde{\nu}$ (Pd[PtF_6])	*I* (Pd[PtF_6])	Symmetry	$\tilde{\nu}$ (Pt[PtF_6])	*I* (Pt[PtF_6])
a	667.90	76.48725	a'	670.52	63.33374
a	645.66	64.81583	a"	660.88	39.91313
a	640.32	110.64282	a'	624.76	112.33376
a	574.10	34.10058	a'	572.03	40.11279
a	484.05	31.27653	a'	502.55	61.71415
a	392.00	38.48986	a"	435.86	32.06249
a	297.84	7.67559	a'	268.64	2.81488
a	269.92	5.49123	a"	241.88	11.88342
a	253.54	5.57012	a'	238.42	0.66624
a	238.86	3.4863	a'	227.28	4.69891
a	227.20	1.42712	a"	226.31	0.00088
a	219.13	1.43101	a'	201.72	0.37585
a	201.62	0.68841	a"	183.86	0.12443
a	199.93	0.26533	a'	177.64	0.23566
a	193.32	0.02451	a"	166.51	0.05192
a	150.99	2.29478	a"	117.82	1.12042
a	136.72	2.77181	a'	117.43	2.44971
a	80.91	1.8137	a'	51.54	1.36445

Table 63: B3LYP vibrational frequencies $\tilde{\nu}$ of D_{4h}-PtF_6 and D_{4h}-$[PtF_6]^-$ given in cm^{-1}, their symmetries and corresponding IR intensities I given in $km \cdot mol^{-1}$.

Symmetry	$\tilde{\nu}$ (PtF_6)	I (PtF_6)	Symmetry	$\tilde{\nu}$ ($[PtF_6]^-$)	I ($[PtF_6]^-$)
a2u	709.90	139.3767	eu	641.43	188.55044
eu	686.12	99.57496	eu	641.43	188.55044
eu	686.12	99.57496	a1g	634.19	0
a1g	663.35	0	a2u	603.73	177.58471
b2g	632.69	0	b2g	581.12	0
a1g	621.69	0	a1g	577.97	0
eu	293.64	7.41722	a2u	292.08	1.35797
eu	293.64	7.41722	eu	259.85	11.51979
a2u	247.82	19.89012	eu	259.85	11.51979
eg	234.44	0	b1g	254.78	0
eg	234.44	0	eg	248.89	0
eu	227.71	3.54577	eg	248.89	0
eu	227.71	3.54577	b1u	243.08	0
b1g	204.11	0	eu	205.65	2.63311
b1u	181.50	0	eu	205.65	2.63311

Table 64: B3LYP vibrational frequencies $\tilde{\nu}$ of D_{5h}-$[PtF_7]^-$ and C_{4v}-$[PtF_5]^-$ given in cm^{-1}, their symmetries and corresponding IR intensities *I* given in $km \cdot mol^{-1}$.

Symmetry	$\tilde{\nu}$ ($[PtF_7]^-$)	*I* ($[PtF_7]^-$)	Symmetry	$\tilde{\nu}$ ($[PtF_5]^-$)	*I* ($[PtF_5]^-$)
a2"	616.64	161.19793	a1	659.01	20.51506
e1'	600.73	102.73331	a1	586.09	2.31814
e1'	600.73	102.73331	e	583.82	206.10508
a1'	599.4	0	e	583.82	206.10508
a1'	580.94	0	b2	572.13	0
e2'	507.85	0	e	248.99	3.67001
e2'	507.85	0	e	248.99	3.67001
e2'	422.71	0	a1	228.83	19.58962
e2'	422.71	0	b1	188.95	0
a2"	303.67	0.83523	b2	178.26	0
e1'	302.37	7.11097	e	73.92	4.04019
e1'	302.37	7.11097	e	73.92	4.04019
e1'	233.33	0.46455			
e1'	233.33	0.46455			
e1"	194.05	0			
e1"	194.05	0			
e2"	89.98	0			
e2"	89.98	0			

Table 65: B3LYP vibrational frequencies $\tilde{\nu}$ of C_s-$[PtF_5 \cdot F_2]^-$ and C_{4v}-PtF_5 given in cm^{-1}, their symmetries and corresponding IR intensities I given in $km \cdot mol^{-1}$.

Symmetry	$\tilde{\nu}$ ($[PtF_5 \cdot F_2]^-$)	I ($[PtF_5 \cdot F_2]^-$)	Symmetry	$\tilde{\nu}$ (PtF_5)	I (PtF_5)
a'	649.73	81.70729	a1	686.01	5.53296
a'	626.09	144.9393	e	679.31	151.81133
a"	619.06	174.29209	e	679.31	151.81133
a'	595.12	20.59228	a1	660.34	0.62609
a"	555.17	0.59342	b2	618.28	0
a'	542.50	10.37711	a1	266.10	10.43347
a'	430.67	184.18834	b1	261.85	0
a'	283.87	23.36588	e	230.60	13.9207
a"	269.49	5.71564	e	230.60	13.9207
a'	254.14	3.7995	b2	203.15	0
a"	250.50	0.00224	e	108.32	0.44973
a"	231.52	0.00185	e	108.32	0.44973
a'	224.40	8.3667			
a'	206.88	13.75531			
a'	193.93	2.85855			
a"	190.17	0.01349			
a'	86.23	1.59388			
a"	39.02	0.20799			

Table 66: B3LYP vibrational frequencies $\tilde{\nu}$ of C_{4v}-$[PtF_4{\cdot}F_2]^-$ and C_1-$[PtF_4{\cdot}F_2]^-$ given in cm^{-1}, their symmetries and corresponding IR intensities *I* given in $km{\cdot}mol^{-1}$.

Symmetry	$\tilde{\nu}$ ($[PtF_4{\cdot}F_2]^-$) (C_{4v})	*I* ($[PtF_4{\cdot}F_2]^-$) (C_{4v})	Symmetry	$\tilde{\nu}$ ($[PtF_4{\cdot}F_2]^-$) (C_1)	*I* ($[PtF_4{\cdot}F_2]^-$) (C_1)
e	626.78	202.45293	a	617.37	4.48156
e	626.78	202.45293	a	597.93	162.65084
a1	621.79	11.13748	a	592.11	197.20045
b2	561.15	0	a	586.64	29.77044
a1	410.41[a]	16.21523	a	571.41	22.15874
a1	273.73	13.32225	a	250.70	4.32421
b1	256.37	0	a	250.60	3.9085
e	220.74	13.08259	a	223.88	11.93912
e	220.74	13.08259	a	205.96[a]	4.28739
a1	209.74	0.10718	a	186.98	0.01064
b2	201.33	0	a	169.08	1.1173
e	130.61	0.29678	a	76.98	2.90454
e	130.61	0.29678	a	58.82	2.93024
e	57.89	0.15621	a	41.15	1.45088
e	57.89	0.15621	a	18.38	0.03735

[a] ν(F–F).

Table 67: B3LYP vibrational frequencies $\tilde{\nu}$ of D_{2h}-PtF_4 and D_{4h}-PtF_4 given in cm^{-1}, their symmetries and corresponding IR intensities *I* given in $km{\cdot}mol^{-1}$.

Symmetry	$\tilde{\nu}$ (D_{2h}-PtF_4)	*I* (D_{2h}-PtF_4)	Symmetry	$\tilde{\nu}$ (D_{4h}-PtF_4)	*I* (D_{4h}-PtF_4)
b3u	705.01	147.02232	eu	697.13	153.23146
b2u	693.63	156.48182	eu	697.13	153.23146
ag	677.47	0	a1g	683.71	0
ag	273.82	0	b2g	615.62	0
b1g	258.74	0	b1g	290.42	0
b3u	254.19	7.26343	a2u	288.10	5.49766
b1u	231.74	10.44198	b1u	218.97	0
b2u	221.27	12.10173	eu	192.08	19.70716
au	159.15	0	eu	192.08	19.70716

Table 68: B3LYP vibrational frequencies $\tilde{\nu}$ of C_s-$[PtF_3{\cdot}F_2]^-$ and C_1-PtF_3 given in cm^{-1}, their symmetries and corresponding IR intensities I given in $km{\cdot}mol^{-1}$.

Symmetry	$\tilde{\nu}$ ($[PtF_3{\cdot}F_2]^-$)	I ($[PtF_3{\cdot}F_2]^-$)	Symmetry	$\tilde{\nu}$ (PtF_3)	I (PtF_3)
a'	644.23	84.92268	a	679.86	167.34014
a'	621.99	95.62829	a	663.99	0.17639
a'	605.74	111.27038	a	629.44	26.77191
a'	563.84	34.62784	a	243.25	5.88507
a'	374.23	63.71944	a	131.57	3.42319
a'	267.65	1.50735	a	109.97	9.97283
a"	252.28	8.04185			
a'	211.94	9.55927			
a'	188.67	49.54855			
a"	172.98	0.07177			
a'	80.26	4.27321			
a"	44.09	4.20753			

Table 69: B3LYP vibrational frequencies $\tilde{\nu}$ of C_1-$[F_2]^-$ ($d_{F-F}([F_2]^-)$ = 2.02 Å), C_{2v}-$Na[F_2]$, C_{2v}-$K[F_2]$ and C_s-$Cs[F_2]$ given in cm^{-1}, their symmetries and corresponding IR intensities I given in $km{\cdot}mol^{-1}$. Superscript 'a' denotes the ν(F−F).

Symmetry	$\tilde{\nu}$ ($[F_2]^-$)	I ($[F_2]^-$)
a	351.57[a]	0
Symmetry	**$\tilde{\nu}$ ($Na[F_2]$)**	**I ($Na[F_2]$)**
a1	453.45[a]	37.32828
b1	316.58	1.70623
a1	308.97	19.64077
Symmetry	**$\tilde{\nu}$ ($K[F_2]$)**	**I ($K[F_2]$)**
a1	391.74[a]	16.52184
a1	294.63	43.01858
b1	247.22	0.78891
Symmetry	**$\tilde{\nu}$ ($Cs[F_2]$)**	**I ($Cs[F_2]$)**
a'	384.47[a]	5.58748
a'	235.17	56.23990
a'	196.72	0.08474

6.2.4 Additional Computed IR Spectra

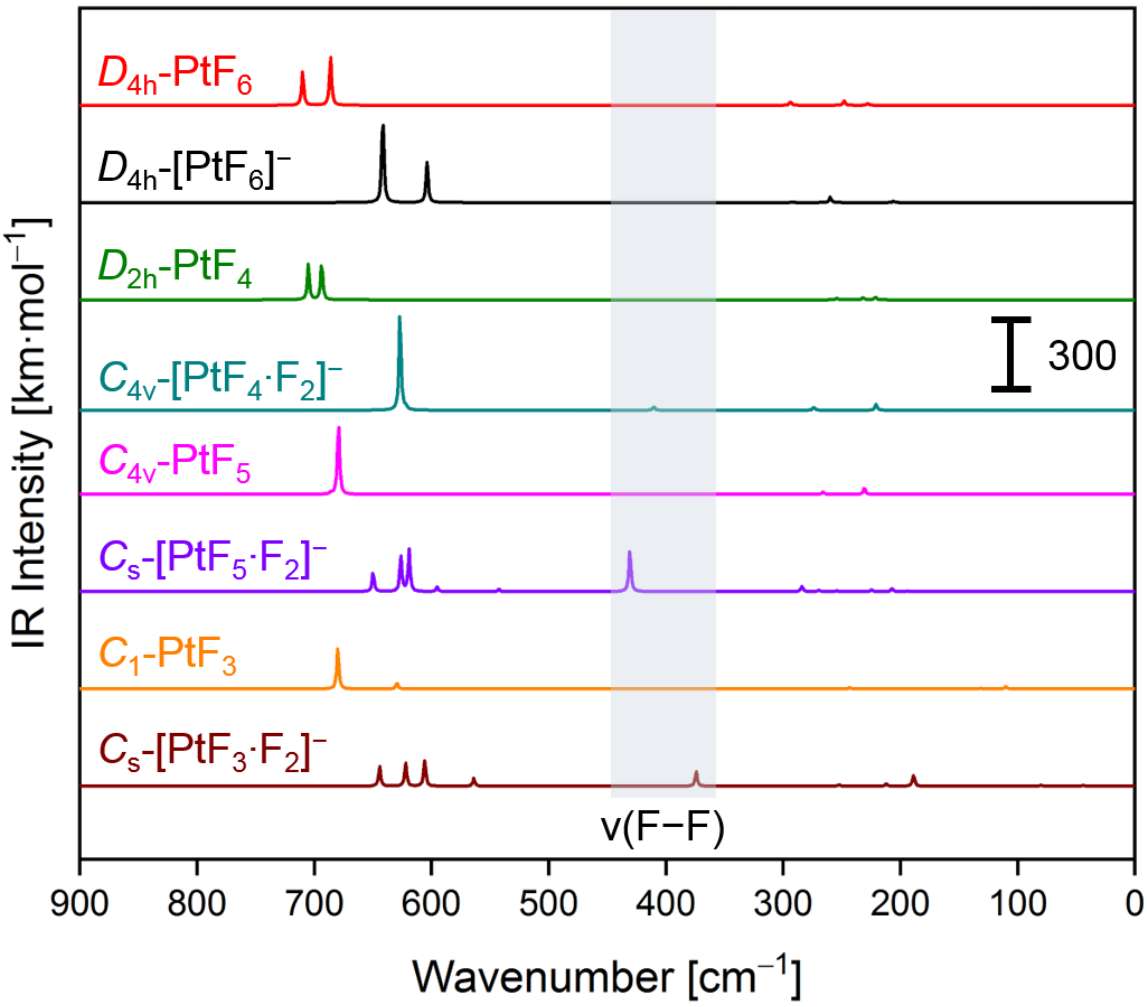

Figure 139: Infrared spectra of binary neutral and anionic platinum-fluorido compounds calculated at the RI-B3LYP-D4/def2-TZVPP level of theory, referring to the minimum structures in Section 3.2.1. Bands associated with a stretching mode of $[F_2]^-$ are highlighted.

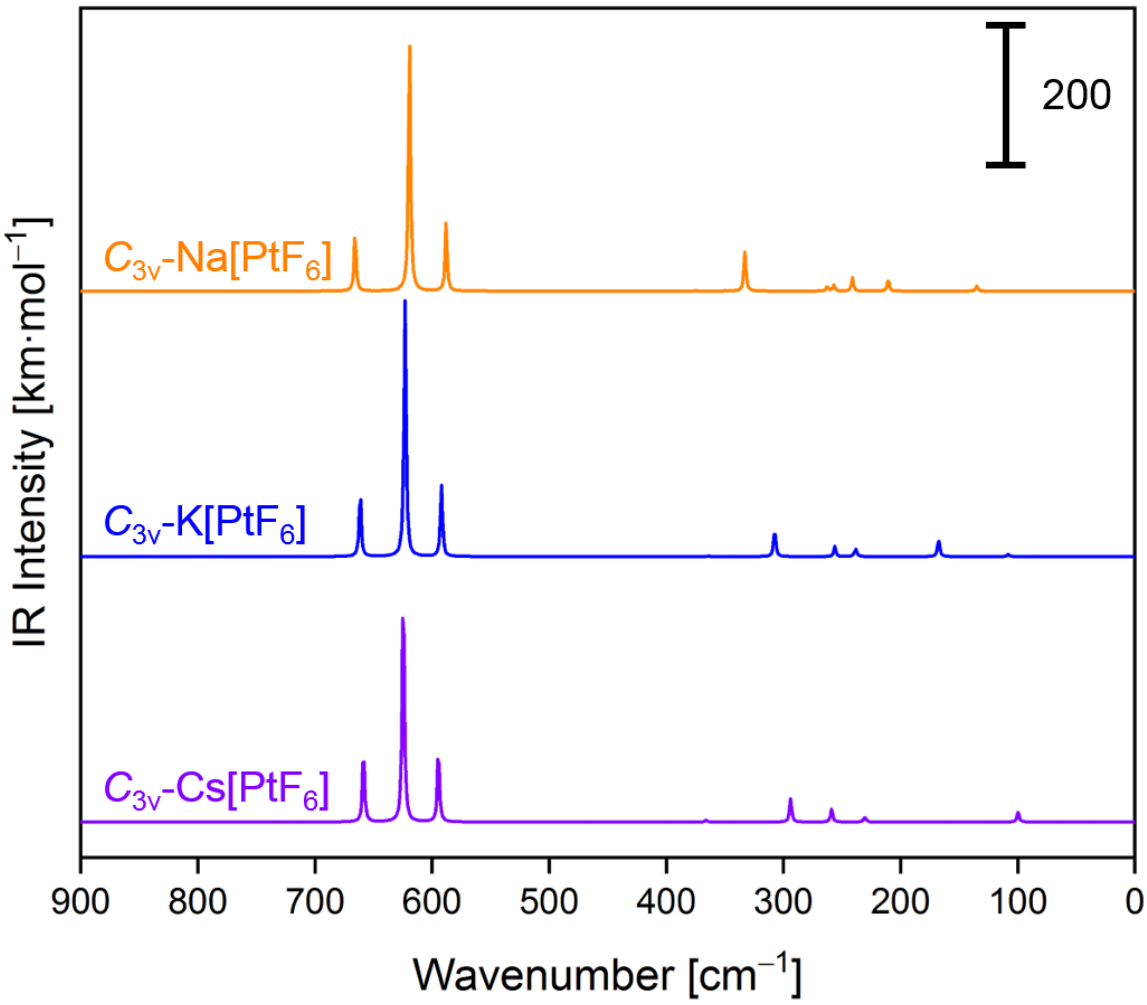

Figure 140: IR spectra of the C_{3v}-symmetric Na[PtF_6], K[PtF_6], and Cs[PtF_6] calculated at the RI-B3LYP-D4/def2-TZVPP level of theory, with the remark that the underlying structures do not represent minimum structures with each twofold degenerate (E) imaginary frequencies at 317.5i, 211.2i and 121.9i cm^{-1}, respectively.

6.2.5 Additional IR Spectra

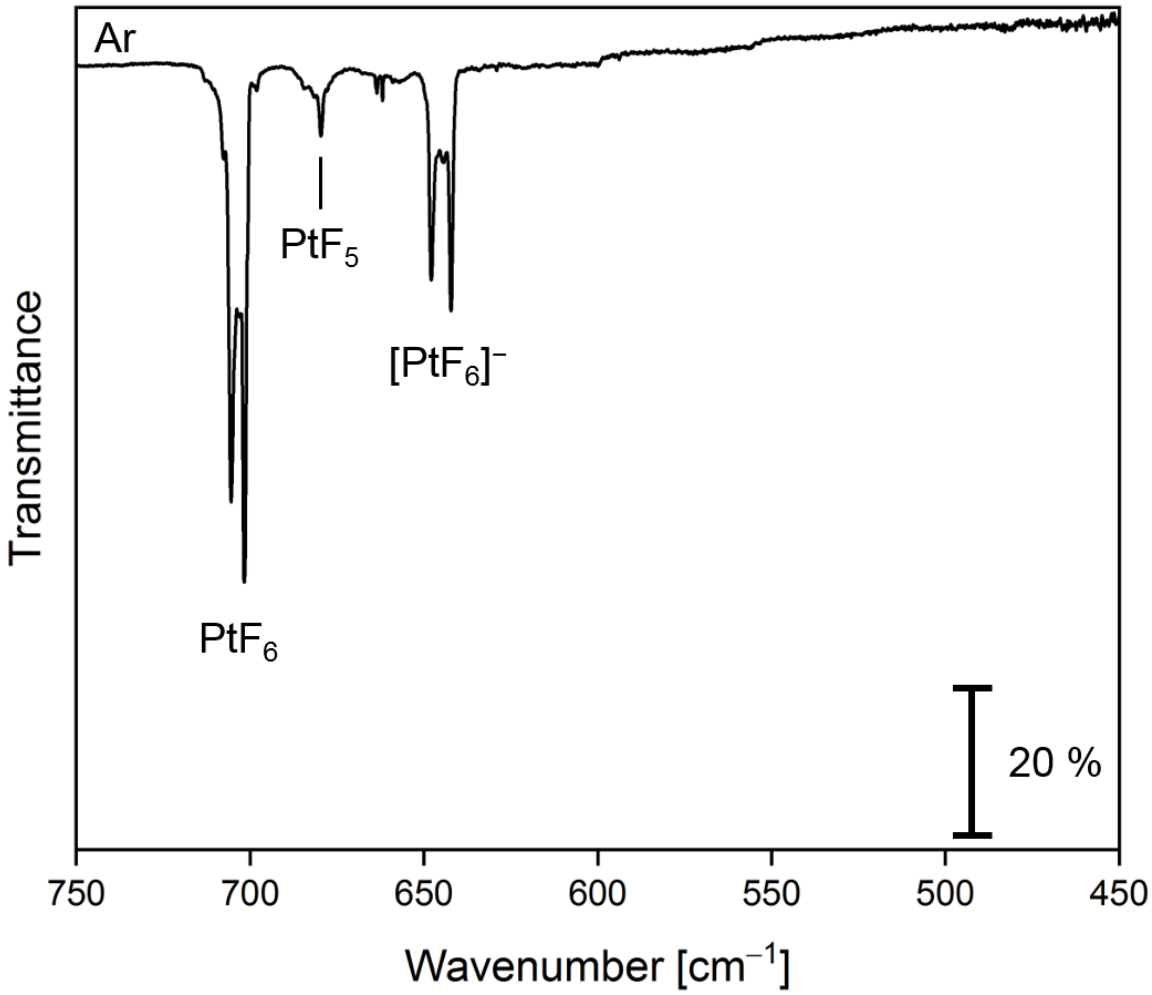

Figure 141: The IR spectrum was recorded after the co-deposition of argon passed over a solid sample of PtF_6 maintained at −77.8 to −76.9 °C and laser-ablated platinum atoms (10 Hz repetition rate, 18 mJ/pulse) onto a gold-plated copper mirror at 5 K for 60 min at a deposition rate of 0.6 mbar·l·min^{-1}. The matrix support had been coated with pure argon for 11 min prior to the co-deposition and the corresponding spectrum served as the background.

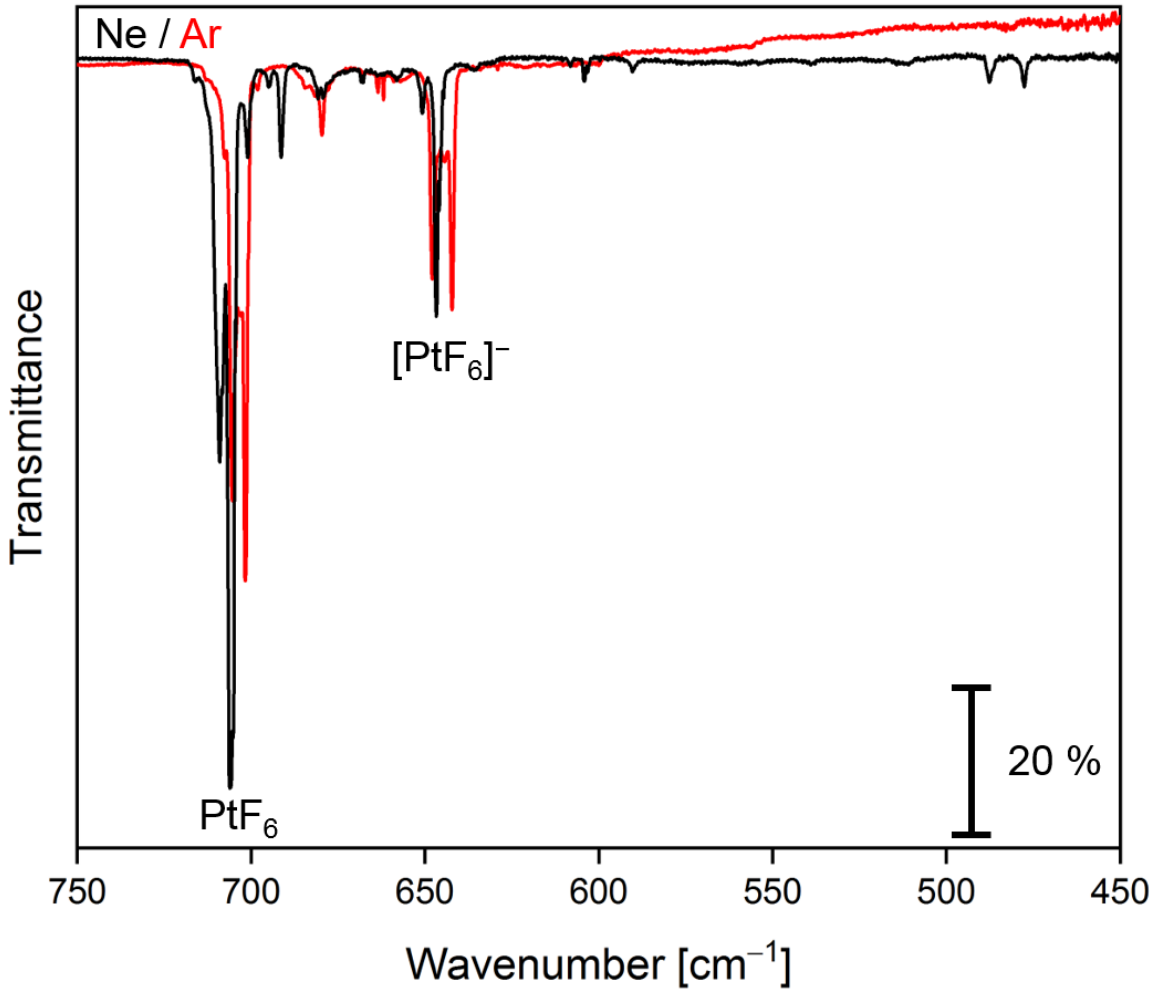

Figure 142: A comparison of IR spectra obtained after the co-deposition of PtF_6 and laser-ablated platinum atoms in neon (black trace, single spectrum in Figure 58) and argon (red trace, single spectrum in Figure 141) for 60 min each.

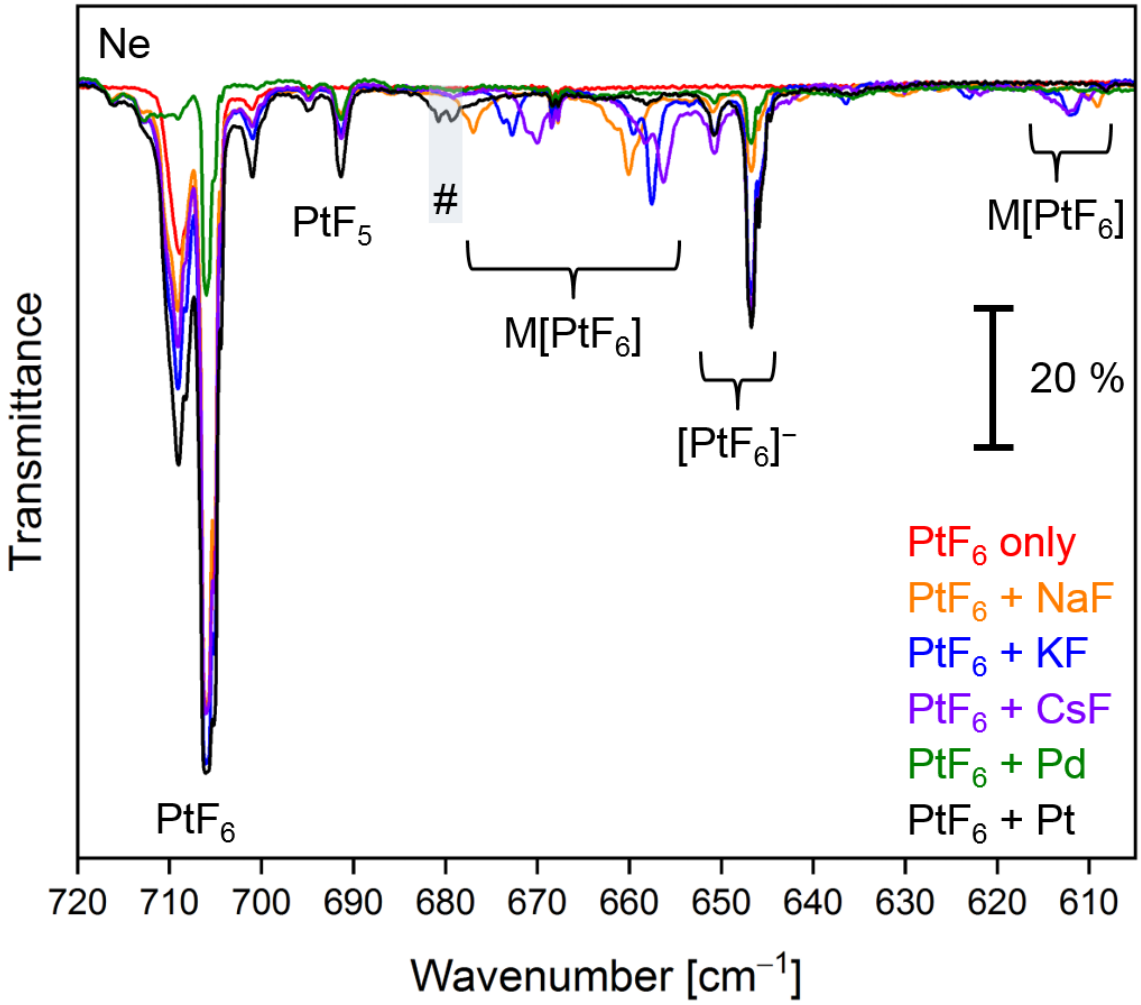

Figure 143: The IR spectra were obtained after the co-deposition of neon passed over a solid sample of PtF_6 maintained at −79 to −78 °C and laser-ablated NaF (orange trace), KF (blue trace) and CsF (purple trace), each at 6 Hz repetition rate and 25 mJ/pulse, and laser-ablated Pd atoms (10 Hz repetition rate, 25 mJ/pulse, green trace) and platinum atoms (10 Hz repetition rate, 18 mJ/pulse, black trace) onto a gold-plated copper mirror at 5 K for 60 min at a deposition rate of 0.5 mbar·l·min^{-1}. The PtF_6 reference spectrum was obtained after 45 min and 0.6 mbar·l·min^{-1}. The feature marked with a hash contains fractions of both PtF_5 and PtF_3. The matrix support had been coated with pure neon for 20 min prior to the co-deposition and the corresponding spectrum served as the background.

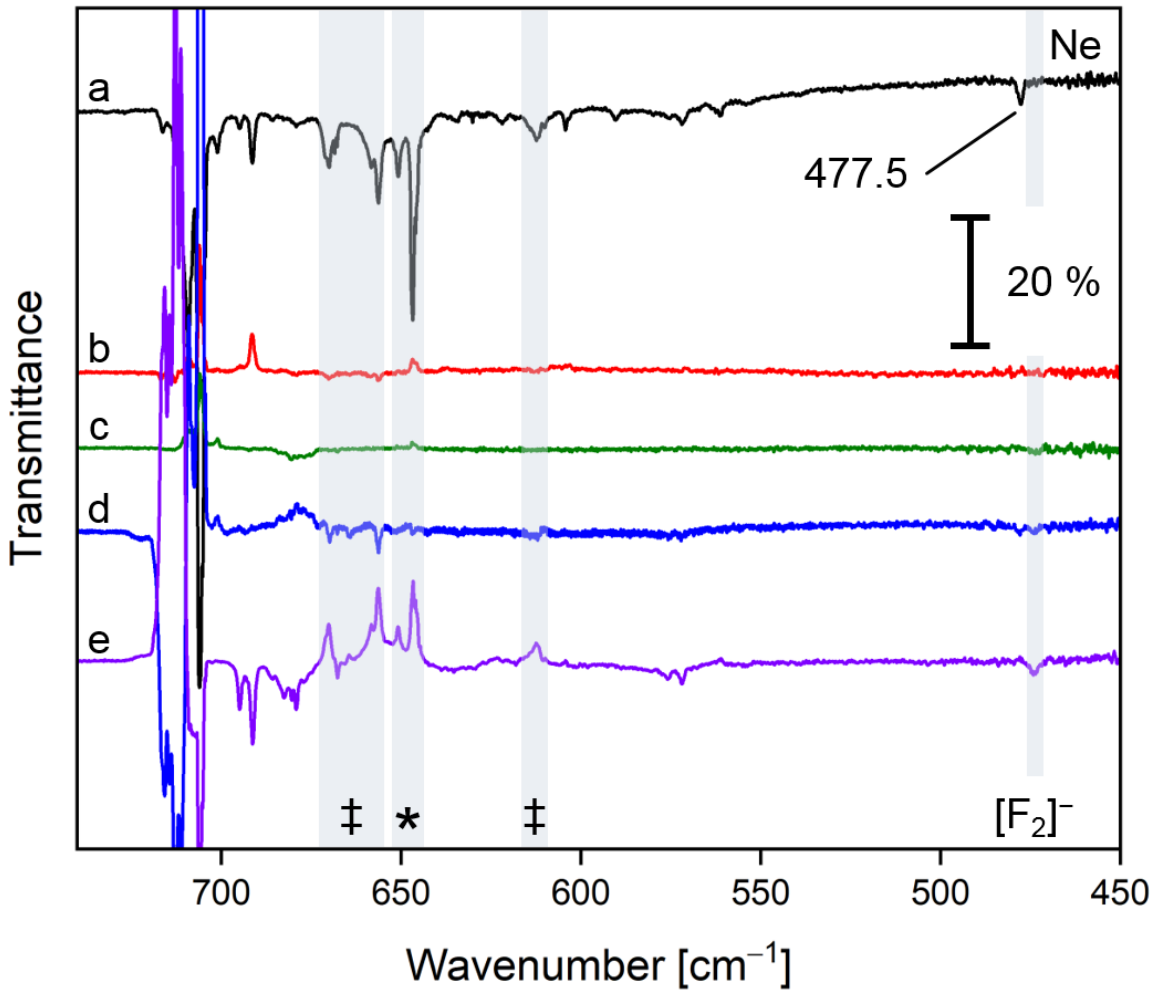

Figure 144: IR spectra were recorded after sequential steps of annealing and irradiation of an initial deposit (spectrum a) of neon passed over a solid sample of PtF_6 maintained at −79 to −78 °C and laser-ablated CsF (6 Hz repetition rate, 25 mJ/pulse) onto a gold-plated copper mirror at 5 K for 60 min at a deposition rate of 0.5 mbar·l·min^{-1}. Only the spectra with the largest changes are shown. The difference IR spectra show the changes after the irradiation of the deposit at b) λ = 656 nm (LED) for 20 min, c) λ = 528 nm (LED) for 8 min, d) λ = 405 nm (LED) for 60 min, and e) λ = 266 nm (LASER) for 90 min. The bands of $Cs[PtF_6]$ are marked with a double dagger, those of free $[PtF_6]^-$ by an asterisk. The assignments of the binary neutral platinum fluorides were omitted for clarity. The band at 477.5 is an impurity band. The matrix support had been coated with pure neon for 20 min prior to the co-deposition and the corresponding spectrum served as the background for (a). The bands pointing downwards are formed at the expense of the bands pointing upwards.

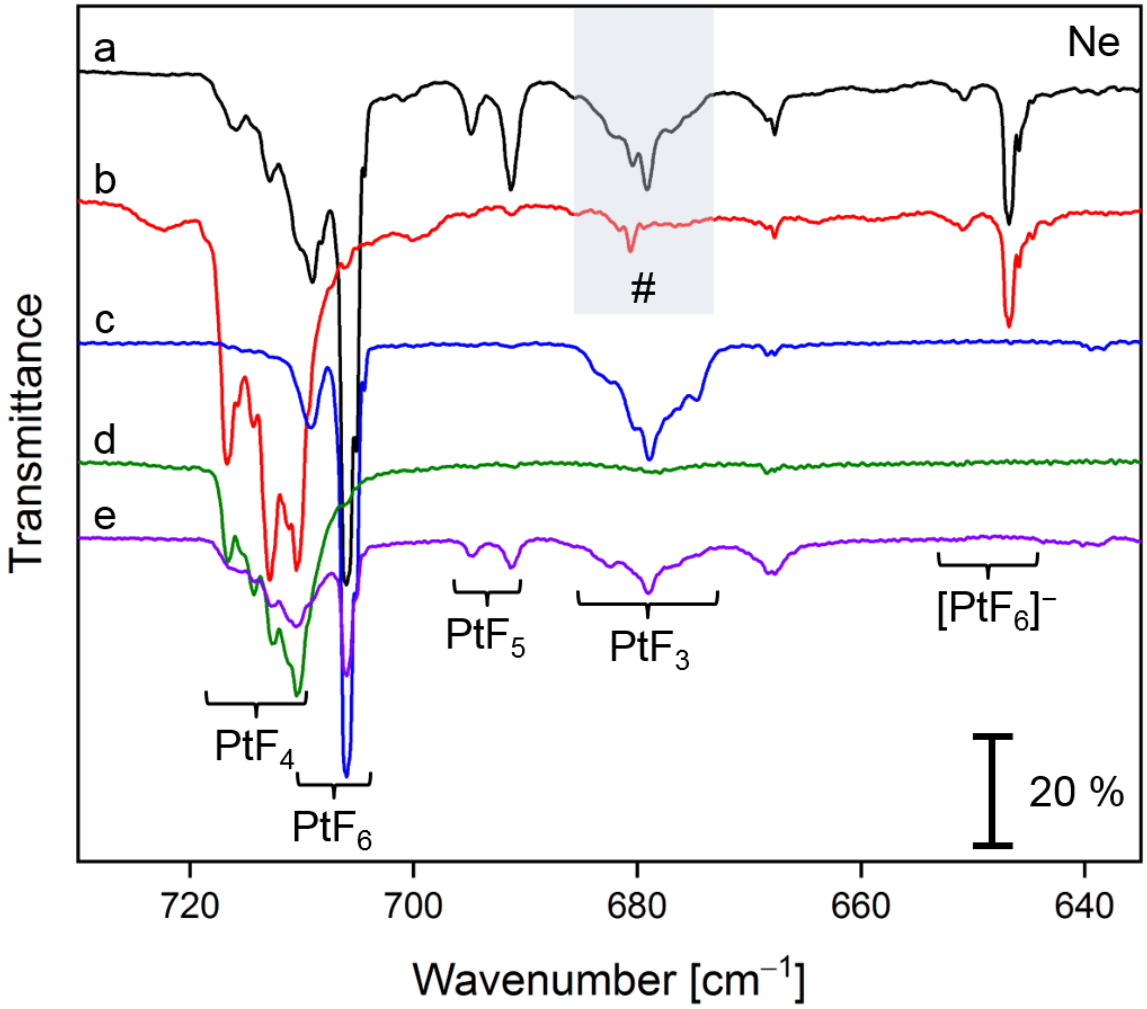

Figure 145: The IR spectra were obtained after the irradiation of an initial co-deposit of neon passed over a solid sample of PtF_6 maintained at −79 to −78 °C and laser-ablated platinum atoms (10 Hz repetition rate, 18 mJ/pulse) onto a gold-plated copper mirror at 5 K for 60 min at a deposition rate of 0.5 mbar·l·min^{-1} at a) λ = 266 nm (LASER) for 90 min and b) λ = 470 nm (LED) for 60 min. The other IR spectra stem from an independent experiment and were recorded after sequential steps of annealing and irradiation of an initial deposit of neon passed over a solid sample of PtF_6 maintained at −79 to −78 °C onto a gold-plated copper mirror at 5 K for 45 min at a deposition rate of 0.6 mbar·l·min^{-1}. Only the spectra with the largest changes are shown. The spectra were recorded after the irradiation of the second deposit at c) λ = 528 nm (LED) for 60 min, d) λ = 470 nm (LED) for 20 min, e) λ = 266 nm (LASER) for 10 min.

6.2.6 UV/Vis Spectra

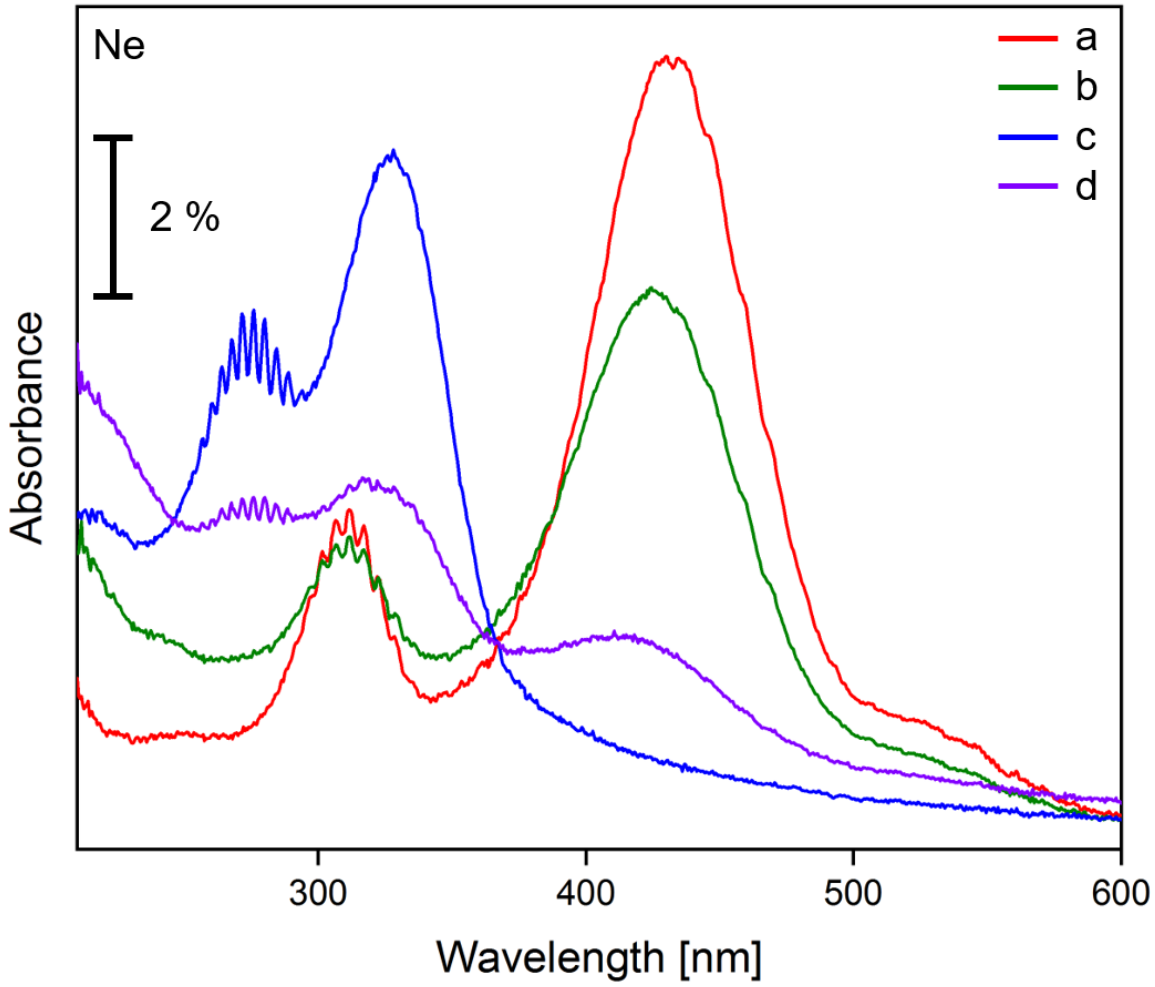

Figure 146: UV/Vis spectra (210–600 nm) were recorded after several sequential steps of annealing and irradiation of an initial deposit of neon passed over a solid sample of PtF_6 maintained at −79 to −78 °C onto a gold-plated copper mirror at 5 K for 45 min at a deposition rate of 0.6 mbar·l·min^{-1}. Only the spectra with the largest changes are shown. The spectra were recorded after a) annealing the primary deposit to 10 K, b) the subsequent irradiation at λ = 656 nm (LED) for 20 min and at λ = 528 nm (LED) for 60 min, c) the subsequent irradiation at λ = 656 nm (LED) for 10 min and at λ = 470 nm (LED) for 20 min and d) the subsequent irradiation at λ = 656 nm (LED) for 7 min, at λ = 528 nm (LED) for 7 min and at λ = 266 nm (LASER) for 10 min. In accordance with reference [304], the spectra resembled the photochemistry of the neutral platinum fluorides.

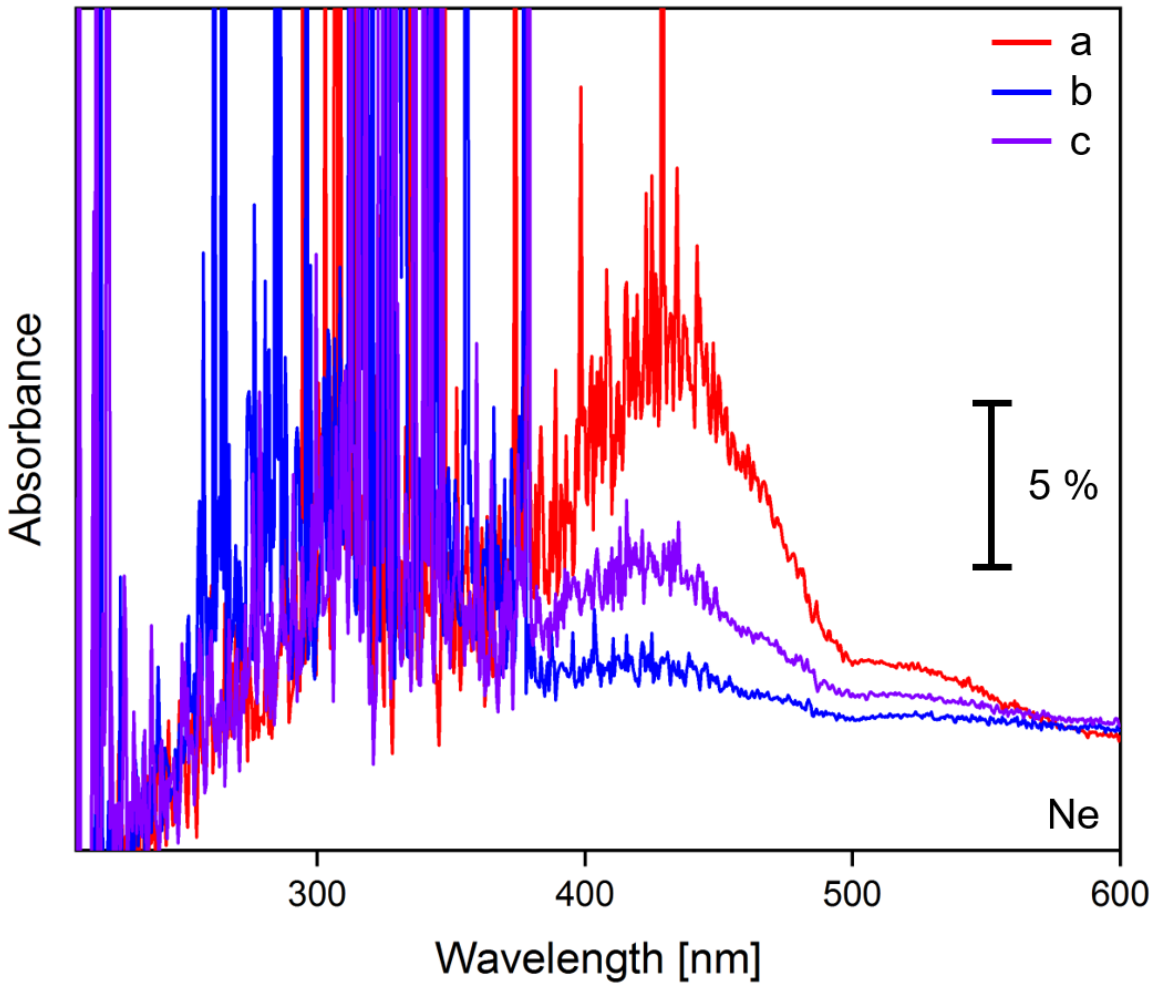

Figure 147: The UV/Vis spectra (210–600 nm) were recorded after a) the co-deposition of neon passed over a solid sample of PtF_6 maintained at −79 to −78 °C and laser-ablated CsF (6 Hz repetition rate, 25 mJ/pulse) onto a gold-plated copper mirror at 5 K for 60 min at a deposition rate of 0.5 mbar·l·min^{-1}, b) the subsequent irradiation at λ = 656 nm (LED) for 20 min, at λ = 532 nm (LASER) for 10 min, at λ = 528 nm (LED) for 8 min and at λ = 405 nm (LED) for 60 min, and c) λ = 266 nm (LASER) for 90 min.

6.3 MnO_3F

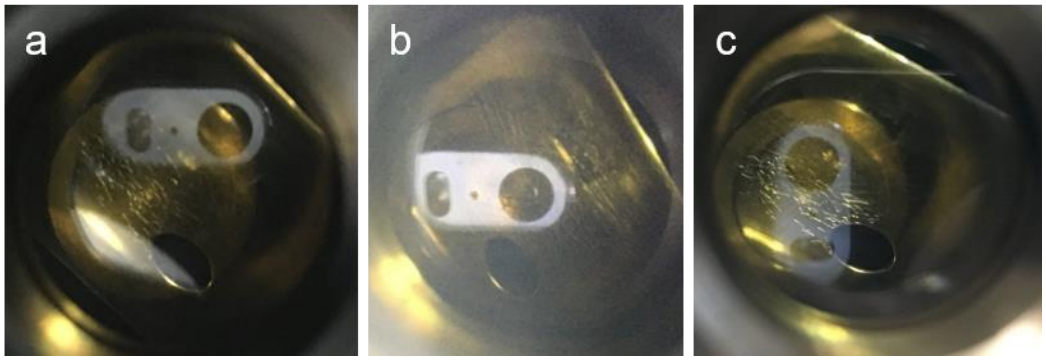

Figure 148: Photos of MnO_3F and its photolysis products embedded in solid Ne. The photos were taken after a) after the deposition of neon passed over a solid sample of MnO_3F maintained at −110.3 to −108.5 °C onto a gold-plated copper mirror at 6 K for 100 min at a deposition rate of 0.6 mbar·l·min^{-1}, b) photolysis of this deposit at λ = 455 nm for 80 min and c) at λ = 365 nm for 40 min and again at λ = 455 nm for 40 min. No change in color was noticed upon visual inspection of the matrix before and after irradiation with λ = 455 nm irradiation, which might be explained by the high dilution of MnO_3F, which appears yellow in a diluted gas phase, on the otherwise golden-yellow color of the matrix support. Secondly, the photolysis products are colorless according to their UV/Vis spectra (Table 28).

6.3.1 PBE0 Structures and Transition States of Manganese Oxofluorides

As outlined in Section 3.3, the structures had been calculated at the PBE0-D3(BJ)/def2-QZVPP level of theory by Li et al.[453] before the present work and are featured in accordance with the manuscript, which is currently in preparation for publication.[505]

Species (A) Oxo, singlet

Mn	0.000000	0.000000	0.062710
O	0.000000	1.464020	0.549034
O	1.267878	-0.732010	0.549034
O	-1.267878	-0.732010	0.549034
F	0.000000	0.000000	-1.638285

TS(oxo-->peroxo), singlet

Mn	0.096462	0.085540	0.015400
O	-0.979474	-0.419970	1.010112
O	0.319282	1.594319	-0.042390
O	-1.300865	-0.425271	-0.899420
F	1.475211	-0.903459	-0.103490

Species (B) Peroxo, singlet

Mn	0.045300	0.212087	0.000000
O	0.045300	-1.379911	0.686032
O	1.380203	0.916415	0.000000
O	0.045300	-1.379911	-0.686032
F	-1.433213	1.049453	0.000000

TS(peroxo-->superoxo), singlet

Mn	-0.309828	0.095355	-0.105082
O	1.103530	-0.824945	0.227829
O	2.090382	-0.090732	-0.106144
O	-0.297223	1.588727	0.158141
F	-1.714201	-0.863141	0.043161

Species (C) Superoxo, singlet

Mn	0.000000	0.408546	0.000000
O	0.042638	-1.222994	0.000000
O	-1.428072	0.942394	0.000000
O	-0.276092	-2.411864	0.000000
F	1.476913	1.258451	0.000000

Species (A) Oxo, triplet

Mn	0.020037	0.061691	-0.071464
O	0.748203	-0.598627	1.336935
O	0.217503	1.586029	-0.017007
O	0.796715	-0.750525	-1.145568
F	-1.622256	-0.381921	0.043524

TS(oxo-->peroxo), triplet

Mn	0.109976	-0.087392	-0.028349
O	-1.275279	0.286397	0.976063
O	-1.167142	0.318705	-0.983266
O	0.571284	-1.548738	0.029471
F	1.357743	1.081543	0.058953

Species (B) Peroxo, triplet

Mn	-0.045726	0.196153	0.000000
O	0.707337	-1.242764	0.695423
O	0.707337	1.537423	0.000000
O	0.707337	-1.242764	-0.695423
F	-1.759215	0.297890	0.000000

TS(peroxo-->superoxo), triplet

Mn	-0.269507	0.077218	0.000072
O	1.167368	-0.856784	0.000949
O	2.063646	0.069320	-0.000872
O	-0.524691	1.613656	0.000223
F	-1.656990	-0.948888	-0.000466

Species (C) Superoxo, triplet

Mn	0.000000	0.377629	0.000000
O	-0.796195	-1.147493	0.000000
O	-0.884455	1.640154	0.000000
O	-0.255313	-2.277779	0.000000
F	1.720856	0.537802	0.000000

6.3.2 Additional IR Spectra

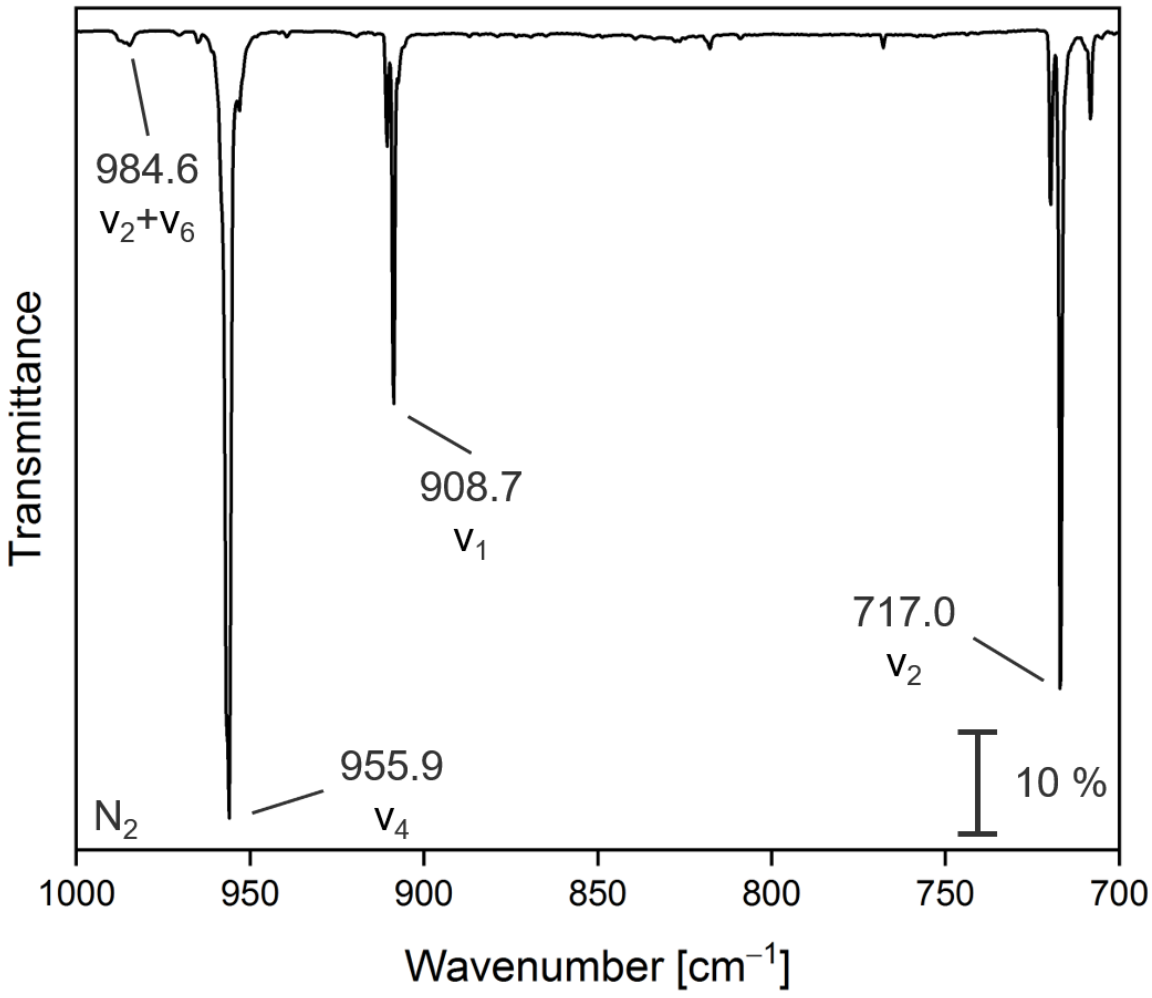

Figure 149: IR spectrum of MnO_3F embedded in solid nitrogen in the Mn–F and Mn=O stretching region. The spectrum was recorded after the deposition of nitrogen passed over a solid sample of MnO_3F maintained at −110.0 to −109.1 °C onto a gold-plated copper mirror at 20 K for 130 min at a deposition rate of 0.5 mbar·l·min^{-1}. A spectrum of pure nitrogen pre-deposited for 27 min served as the background.

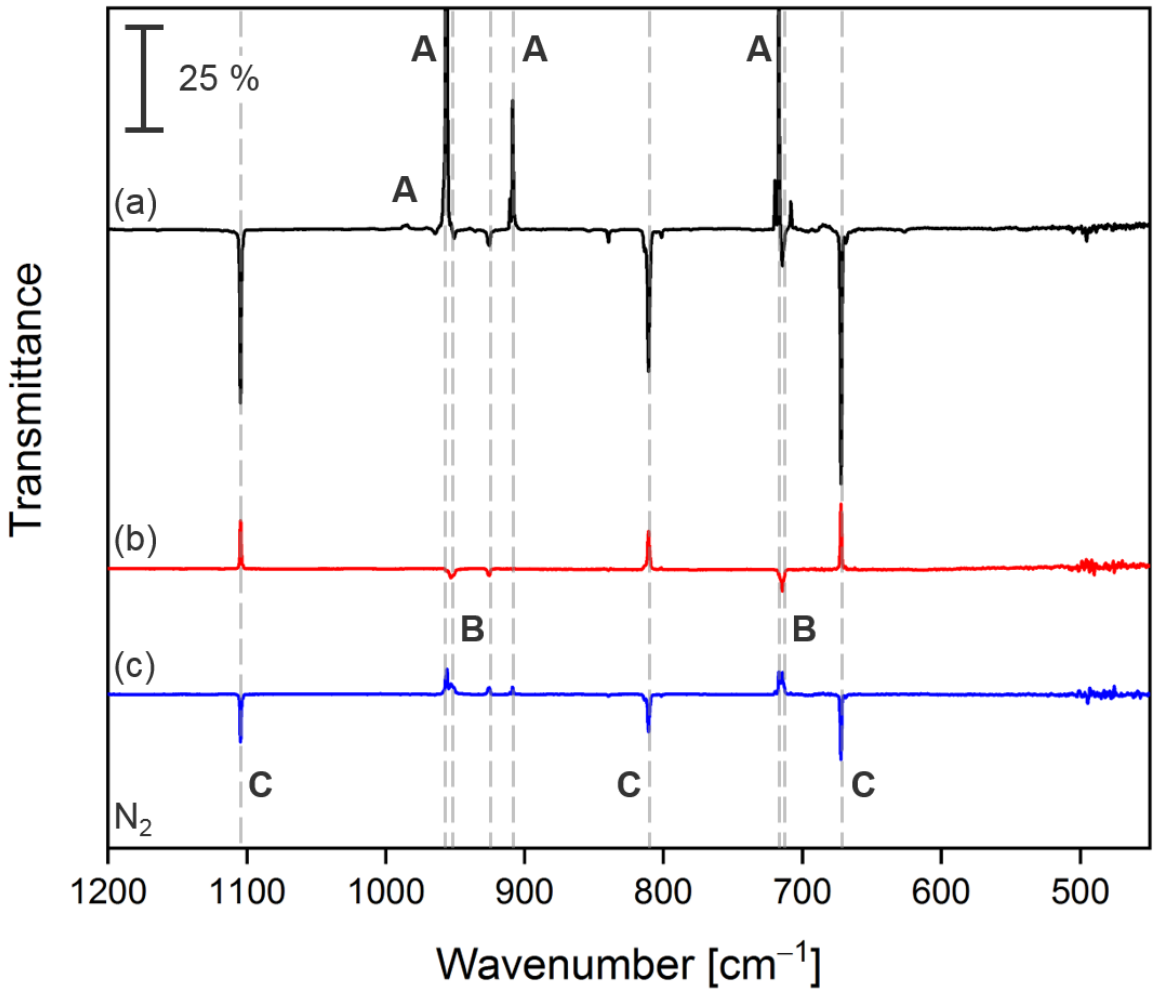

Figure 150: IR difference spectra of N_2 matrix-isolated MnO_3F (**A**), [(η^2-OO)MnOF] (**B**) and [(η^1-OO)MnOF] (**C**). The spectra were recorded after the irradiation of an initial deposit of nitrogen passed over a solid sample of MnO_3F maintained at −110.0 to −109.1 °C onto a gold-plated copper mirror at 20 K for 130 min at a deposition rate of 0.5 mbar·l·min^{-1} at a) λ = 455 nm for 120 min, b) λ = 365 nm for 60 min and c) again at λ = 455 nm for 20 min. The bands pointing downwards are formed at the expense of bands pointing upwards.

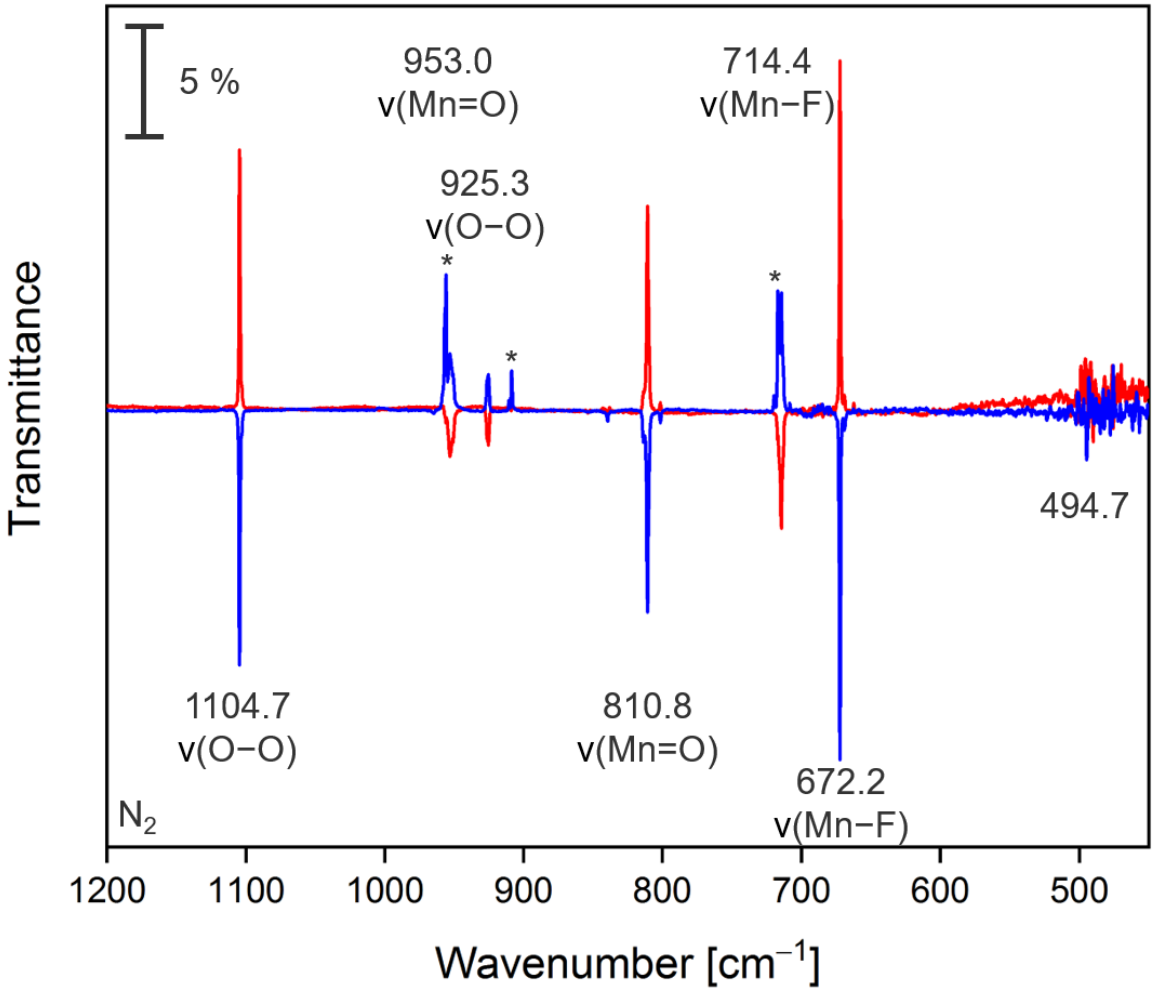

Figure 151: IR difference spectra of [(η^1-OO)MnOF] (**C**) and [(η^2-OO)MnOF] (**B**) in solid N_2 displaying the interconversion of **C** to **B** and **B** to **C** after photolysis at λ = 365 nm for 60 min (red trace) and at λ = 455 nm for 20 min for the second time (blue trace), respectively. The bands pointing downwards are formed at the expense of bands pointing upwards. The bands stemming from the photodecomposition of residual MnO_3F are marked by an asterisk. The spectra are identical with traces b (red) and c (blue) in Figure 150.

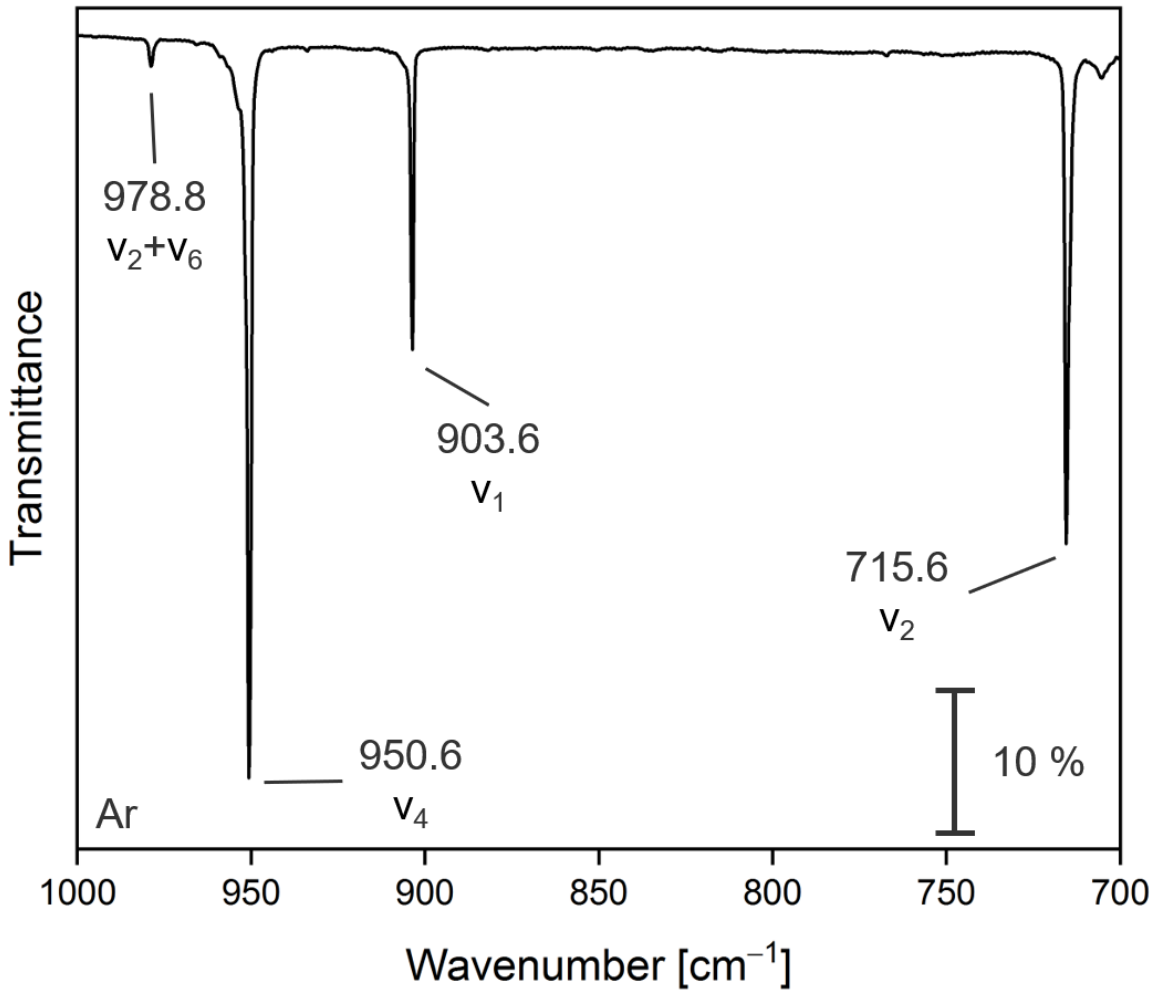

Figure 152: IR spectrum of MnO_3F embedded in solid argon in the Mn–F and Mn=O stretching region. The spectrum was recorded after the deposition of argon passed over a solid sample of MnO_3F maintained at −109.7 to −108.5 °C onto a gold-plated copper mirror at 22 K for 120 min at a deposition rate of 0.7 mbar·l·min^{-1}. A spectrum of pure argon pre-deposited for 23 min served as the background.

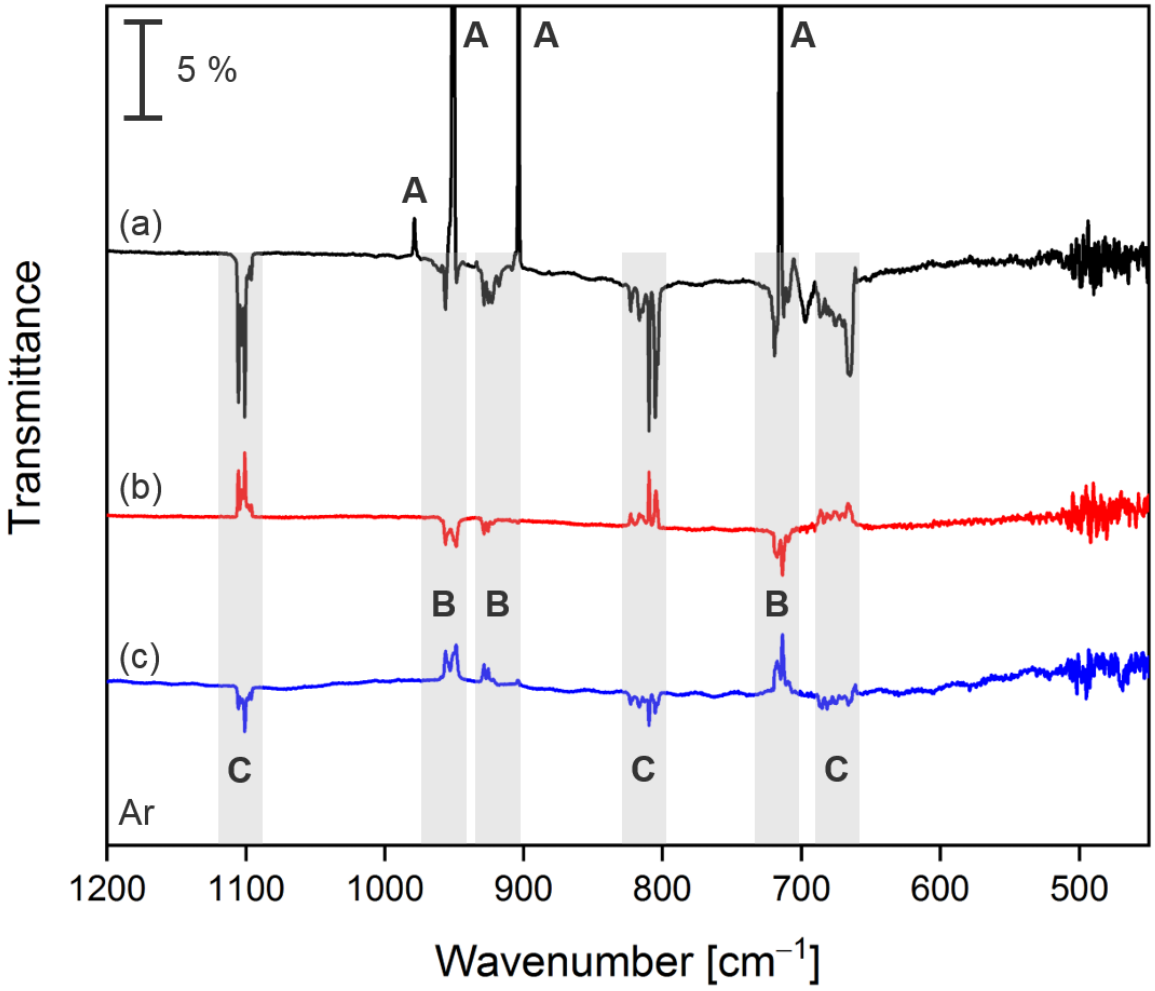

Figure 153: IR difference spectra of Ar matrix-isolated MnO_3F (**A**), [(η^2-OO)MnOF] (**B**) and [(η^1-OO)MnOF] (**C**). The spectra were recorded after the irradiation of a primary deposit of argon passed over a solid sample of MnO_3F maintained at −109.7 to −108.5 °C onto a gold-plated copper mirror at 22 K for 120 min at a deposition rate of 0.7 mbar·l·min^{-1} at a) λ = 455 nm for 120 min, b) λ = 365 nm for 60 min and c) again at λ = 455 nm for 40 min. The bands pointing downwards are formed at the expense of the bands pointing upwards.

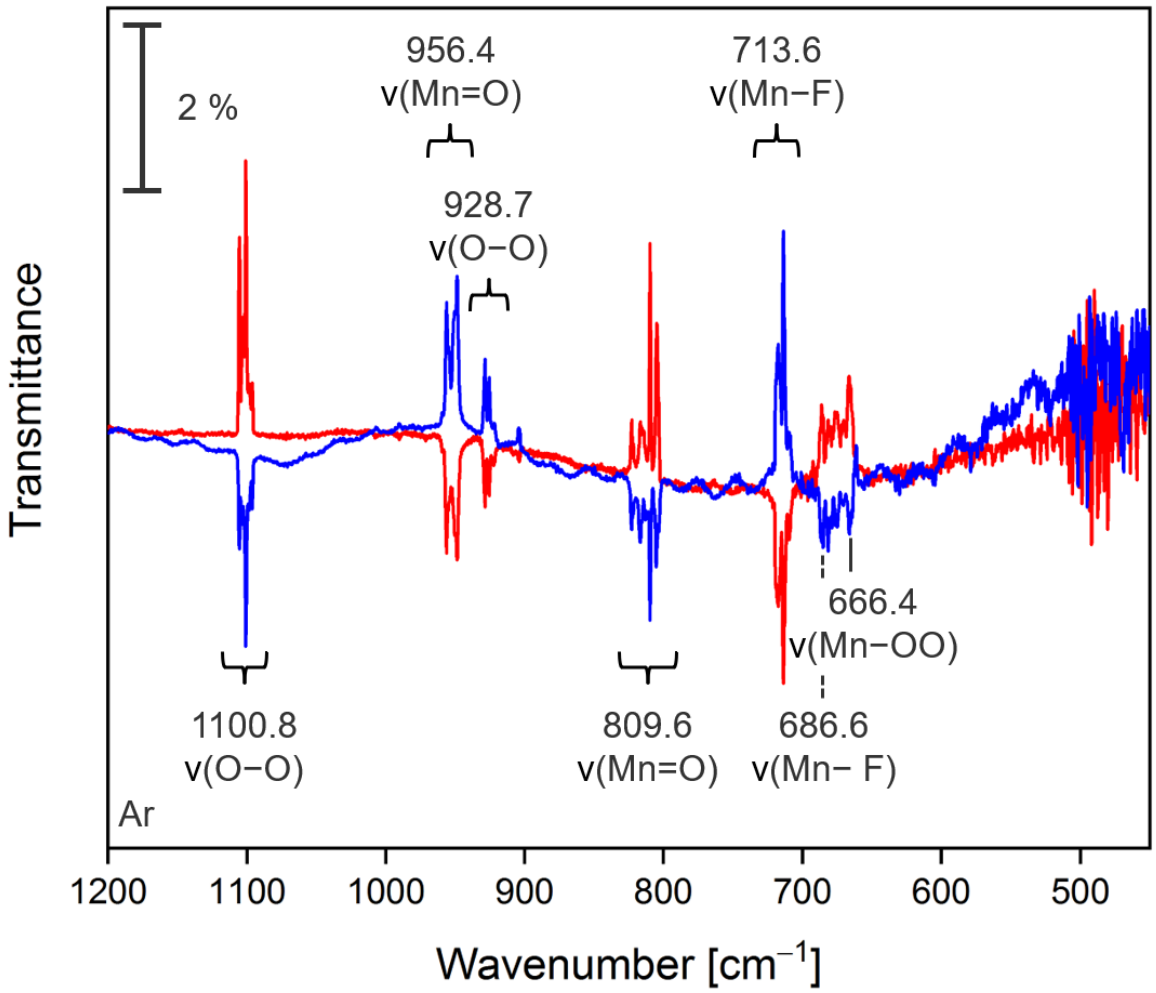

Figure 154: IR difference spectra of [(η^1-OO)MnOF] (**C**) and [(η^2-OO)MnOF] (**B**) in solid Ar displaying the interconversion of **C** to **B** and **B** to **C** after photolysis at λ = 365 nm for 60 min (red trace) and at λ = 455 nm for 40 min for the second time (blue trace), respectively. The bands pointing downwards are formed at the expense of the bands pointing upwards. The spectra are identical with traces b (red) and c (blue) in Figure 153.

6.3.3 Additional UV/Vis Spectra

Only the most intense features in the absorption bands were considered for verifying the identity of the MnO_3F compound. A detailed analysis of all vibrational progressions of the absorption bands can be found in the work of Jasinski et al.[242]

Determining the band positions in the N_2 spectra was difficult, since features of residual MnO_3F influenced the band structure and peak position.

Irradiation of MnO_3F embedded in solid nitrogen (Table 71) with λ = 455 nm for 120 min (red trace) yielded a band centered at 360.5 nm, which is influenced by residual MnO_3F in its structure, as well as a shoulder at 278.5 nm indicative for **C**. Little change in this quite noisy region was observed after photolysis at λ = 365 nm for 60 min (blue trace) and again at λ = 455 nm for 20 min (green trace), making the tentative assignment to **B** difficult. The overall low intensity of the absorption bands of MnO_3F in argon is also reflected in the new features at 276 nm (sh) and 358 nm (sh) after irradiation with λ = 455 nm for 120 min (red trace) indicative for **C**. These features – analogously to the results in nitrogen – only marginally change upon irradiation at λ = 365 nm for 60 min (blue trace) and again at λ = 455 nm for 40 min (green trace) and allow no assignment to **B**.

Table 70: Electronic transitions (λ in nm) and their vibrational spacing ($\Delta\tilde{\nu}$ in cm^{-1}) obtained for MnO_3F (C_{3v}) in solid Ne and N_2 matrices. Absorption maxima are indicated by bold values.

Ne matrix, λ [nm] [a]	**$\Delta\tilde{\nu}$ [cm^{-1}]** [a]	**$\Delta\tilde{\nu}_{av}$ [cm^{-1}]** [a]	**N_2 matrix [cm^{-1}]** [b]
208.5 (47961.6 cm^{-1})		Not resolved	**46200 (216 nm)**
261.0 (38314.2 cm^{-1})		Not resolved	**40000 (250 nm sh; vib. spacing 710 cm^{-1})**
299.5 (33389.0 cm^{-1})		663	**33300 (300 nm; vib. spacing 660 cm^{-1})**
307.0 (32573.3 cm^{-1})	815.7		
312.5 (32000.0 cm^{-1})	573.3		
318.5 (31397.2 cm^{-1})	602.8		
327.5 (30534.4 cm^{-1})	862.8		
334.0 (29940.1 cm^{-1})	594.3		
340.0 (29411.8 cm^{-1})	528.3		
407.0 (24570.0 cm^{-1})		741	
421.5 (23724.8 cm^{-1})	845.2		
431.0 (23201.9 cm^{-1})	522.9		
444.0 (22522.5 cm^{-1})	679.4		**22300 (448 nm; vib. spacing 780 cm^{-1})**
459.5 (21762.8 cm^{-1})	759.7		
475.5 (21030.5 cm^{-1})	732.3		
495.5 (20181.6 cm^{-1})	848.9		
516.0 (19379.8 cm^{-1})	801.8		
596.0 (16778.5 cm^{-1})		851	
629.0 (15898.3 cm^{-1})	880.2		**15500 (645 nm; vib. spacing 830 cm^{-1})**
664.5 (15048.9 cm^{-1})	849.4		
707.5 (14134.3 cm^{-1})	914.6		
753.0 (13280.2 cm^{-1})	854.1		
798.5 (12523.5 cm^{-1})	756.7		

[a] This work, $\Delta\tilde{\nu}_{av}$: mean vibrational spacing; [b] values were taken from reference [187].

Table 71: Electronic transitions (λ in nm) and their vibrational spacing ($\Delta\tilde{\nu}$ in cm^{-1}) obtained for MnO_3F (C_{3v}) embedded in N_2 matrices. Absorption maxima are indicated by bold values.

N_2 matrix, λ [nm] [a]	**$\Delta\tilde{\nu}$ [cm^{-1}] [a]**	**$\Delta\tilde{\nu}_{av}$ [cm^{-1}] [a]**	**N_2 matrix [cm^{-1}] [b]**
207.5 (48192.8 cm^{-1})		Not resolved	**46200 (216 nm)**
252.5 (39604.0 cm^{-1})		Not resolved	**40000 (250 nm sh; vib. spacing 710 cm^{-1})**
293.5 (34071.6 cm^{-1})			
299.5 (33389.0 cm^{-1})	682.6		**33300 (300 nm; vib. spacing 660 cm^{-1})**
304.5 (32840.7 cm^{-1})	548.3		
311.0 (32154.3 cm^{-1})	686.4		
318.0 (31446.5 cm^{-1})	707.8	597	
326.0 (30674.8 cm^{-1})	771.7		
331.0 (30211.5 cm^{-1})	463.3		
338.0 (29585.8 cm^{-1})	625.7		
343.5 (29112.1 cm^{-1})	473.7		
348.5 (28694.4 cm^{-1})	417.7		
403.0 (24813.9 cm^{-1})			
415.5 (24067.4 cm^{-1})	746.5		
430.5 (23228.8 cm^{-1})	838.6		
442.5 (22598.9 cm^{-1})	629.9	763	**22300 (448 nm; vib. spacing 780 cm^{-1})**
458.0 (21834.1 cm^{-1})	764.8		
474.0 (21097.0 cm^{-1})	737.1		
492.5 (20304.6 cm^{-1})	792.4		
513.5 (19474.2 cm^{-1})	830.4		
593.5 (16849.2 cm^{-1})			
622.0 (16077.2 cm^{-1})	772.0	820	**15500 (645 nm; vib. spacing 830 cm^{-1})**
658.5 (15186.0 cm^{-1})	891.2		
695.0 (14388.5 cm^{-1})	797.5		

[a] This work, $\Delta\tilde{\nu}_{av}$: mean vibrational spacing; [b] values were taken from reference [187].

Table 72: Electronic transitions (λ in nm) and their vibrational spacing ($\Delta\tilde{\nu}$ in cm^{-1}) obtained for MnO_3F (C_{3v}) embedded in solid Ar and N_2 matrices. Absorption maxima are indicated by bold values.

Ar matrix, λ [nm] [a]	**$\Delta\tilde{\nu}$ [cm^{-1}]** [a]	**$\Delta\tilde{\nu}_{av}$ [cm^{-1}]** [a]	**N_2 matrix [cm^{-1}]** [b]
211.5 (47281.3 cm^{-1})		Not resolved	**46200 (216 nm)**
246.0 sh (40650.4 cm^{-1})		Not resolved	**40000 (250 nm sh; vib. spacing 710 cm^{-1})**
299.5 sh (33389.0 cm^{-1})		Not resolved	**33300 (300 nm; vib. spacing 660 cm^{-1})**
402.0 (24875.6 cm^{-1})		796	
416.5 (24009.6 cm^{-1})	866.0		
431.5 (23175.0 cm^{-1})	834.6		
446.5 (22396.4 cm^{-1})	778.6		**22300 (448 nm; vib. spacing 780 cm^{-1})**
461.5 (21668.5 cm^{-1})	727.9		
478.0 (20920.5 cm^{-1})	748.0		
496.5 (20141.0 cm^{-1})	779.5		
518.0 (19305.0 cm^{-1})	836.0		
632.5 (15810.3 cm^{-1})		840	
665.5 (15026.3 cm^{-1})	784.0		
708.5 (14114.3 cm^{-1})	912.0		**15500 (645 nm; vib. spacing 830 cm^{-1})**
752.5 (13289.0 cm^{-1})	825.3		

[a] This work, $\Delta\tilde{\nu}_{av}$: mean vibrational spacing; [b] values were taken from reference [187].

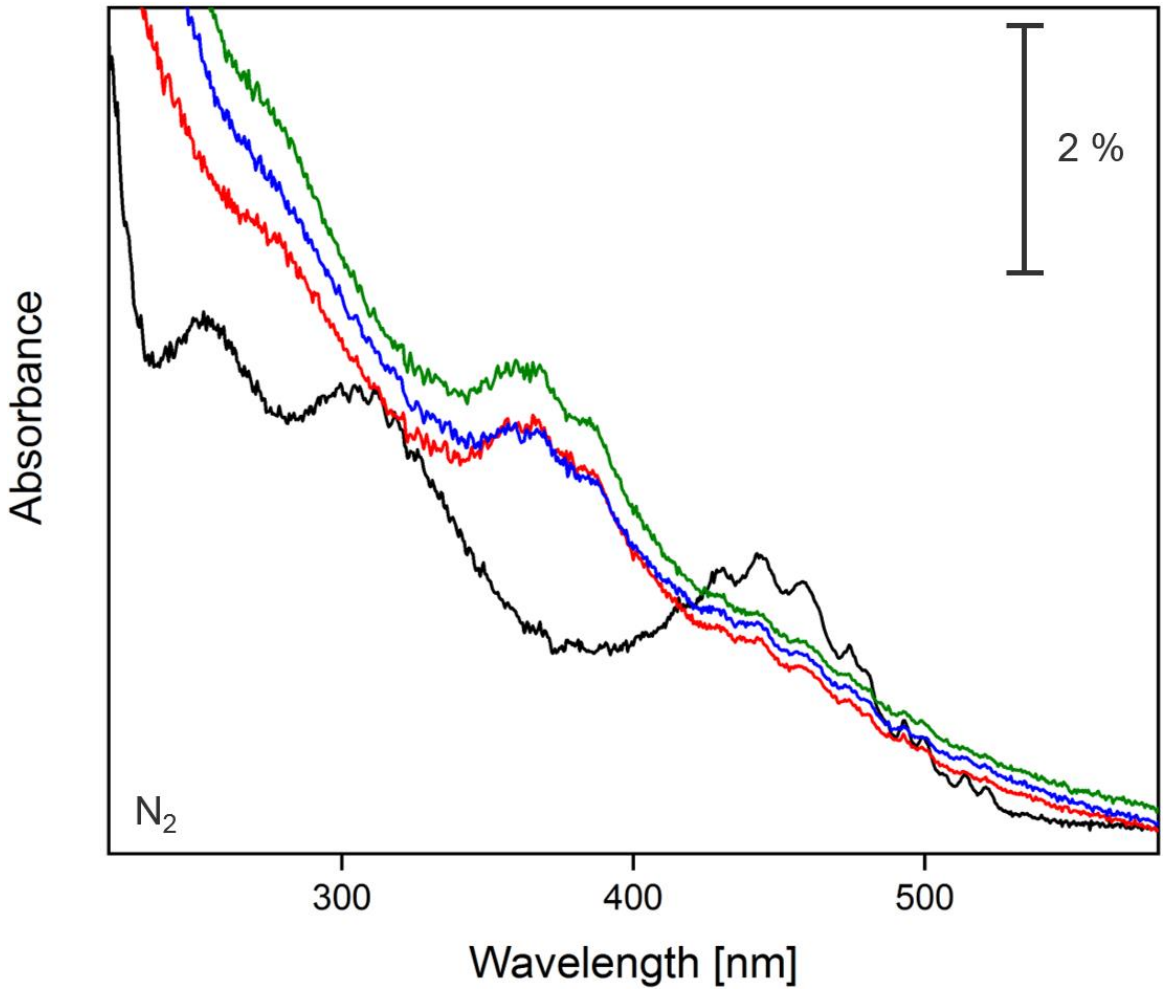

Figure 155: UV/Vis spectra (resolution = 0.5 nm) of MnO_3F (black trace), [(η^1-OO)MnOF] (red trace) and [(η^2-OO)MnOF] (blue trace) in the range from 220 to 580 nm. The spectra were recorded after the deposition of nitrogen passed over a solid sample of MnO_3F maintained at −110.0 to −109.1 °C onto a gold-plated copper mirror at 20 K for 130 min at a deposition rate of 0.5 mbar·l·min^{-1} (black trace) and after the subsequent photolysis of the initially deposited sample at λ = 455 nm for 120 min (red trace), λ = 365 nm for 60 min (blue trace) and again at λ = 455 nm for 20 min (green trace).

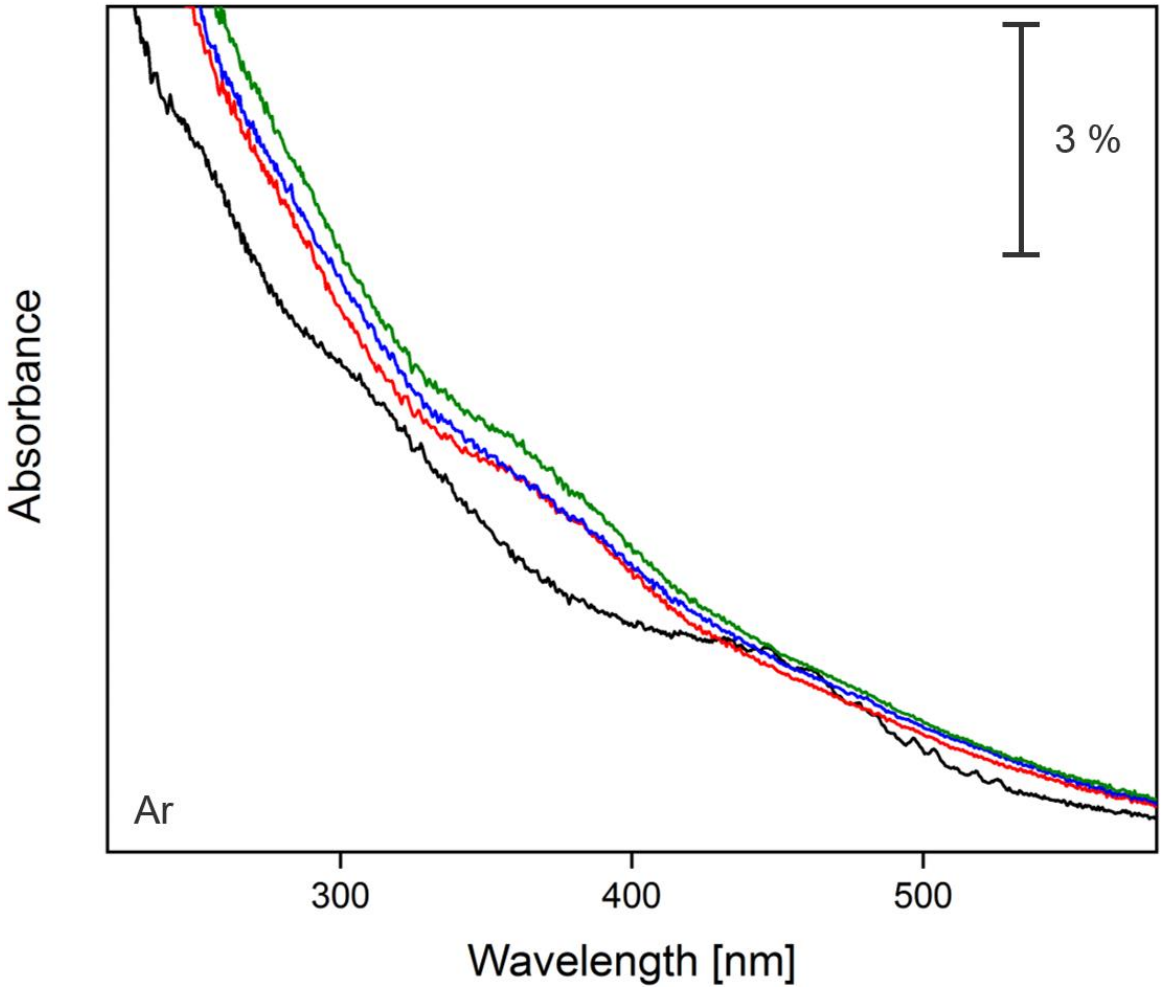

Figure 156: UV/Vis spectra (resolution = 0.5 nm) of MnO_3F (black trace), [(η^1-OO)MnOF] (red trace) and [(η^2-OO)MnOF] (blue trace) in the range from 220 to 580 nm. The spectra were recorded after the deposition of argon passed over a solid sample of MnO_3F maintained at −109.7 to −108.5 °C onto a gold-plated copper mirror at 22 K for 120 min at a deposition rate of 0.7 mbar·l·min^{-1} (black trace) and after the subsequent photolysis of the initially deposited sample at λ = 455 nm for 120 min (red trace), λ = 365 nm for 60 min (blue trace) and again at λ = 455 nm for 40 min (green trace).

6.4 Simons Process

6.4.1 Additional Electrochemical Data

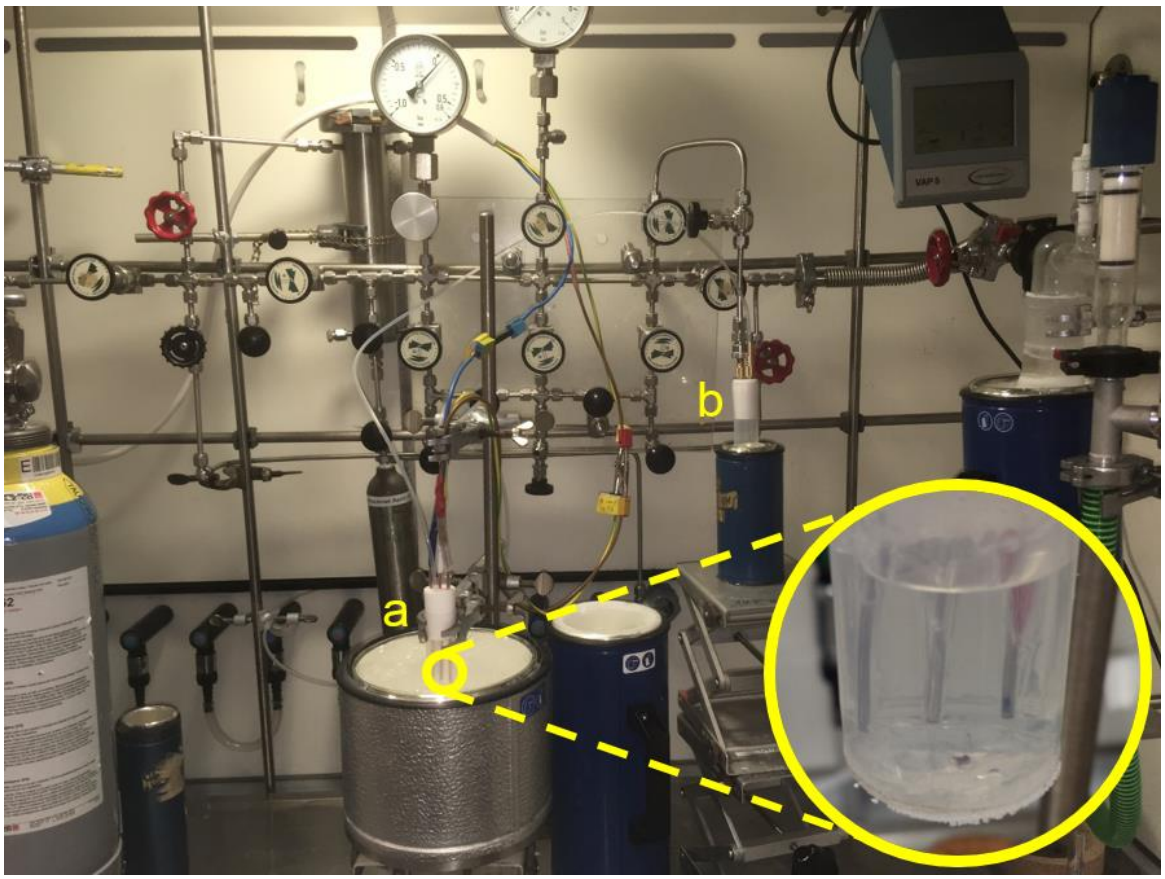

Figure 157: Setup for the electrochemical characterization of the system Ni|NiF_x|HF_l‖HF_l|$H_{2,g}$|Ni ($x \geq 2$) at 0 °C in a fume hood with a stainless-steel high vacuum line that allows the manipulation of HF. The electrochemical cell (a) consists of a PFA tube (Ø = 2.54 cm, flame-sealed bottom) equipped with a PTFE stopper with drilled holes for the electrodes, a liquid *a*HF inlet, and exhaust gas outlet. The Ni anode is depicted right, the Pt quasi reference electrode in central position and the Ni cathode on the left in the magnified area. A PFA container (b) was used for condensing HF and transferring liquid *a*HF via PFA tubing (Ø = 0.32 cm) into the electrochemical cell (a) at a slight argon overpressure.

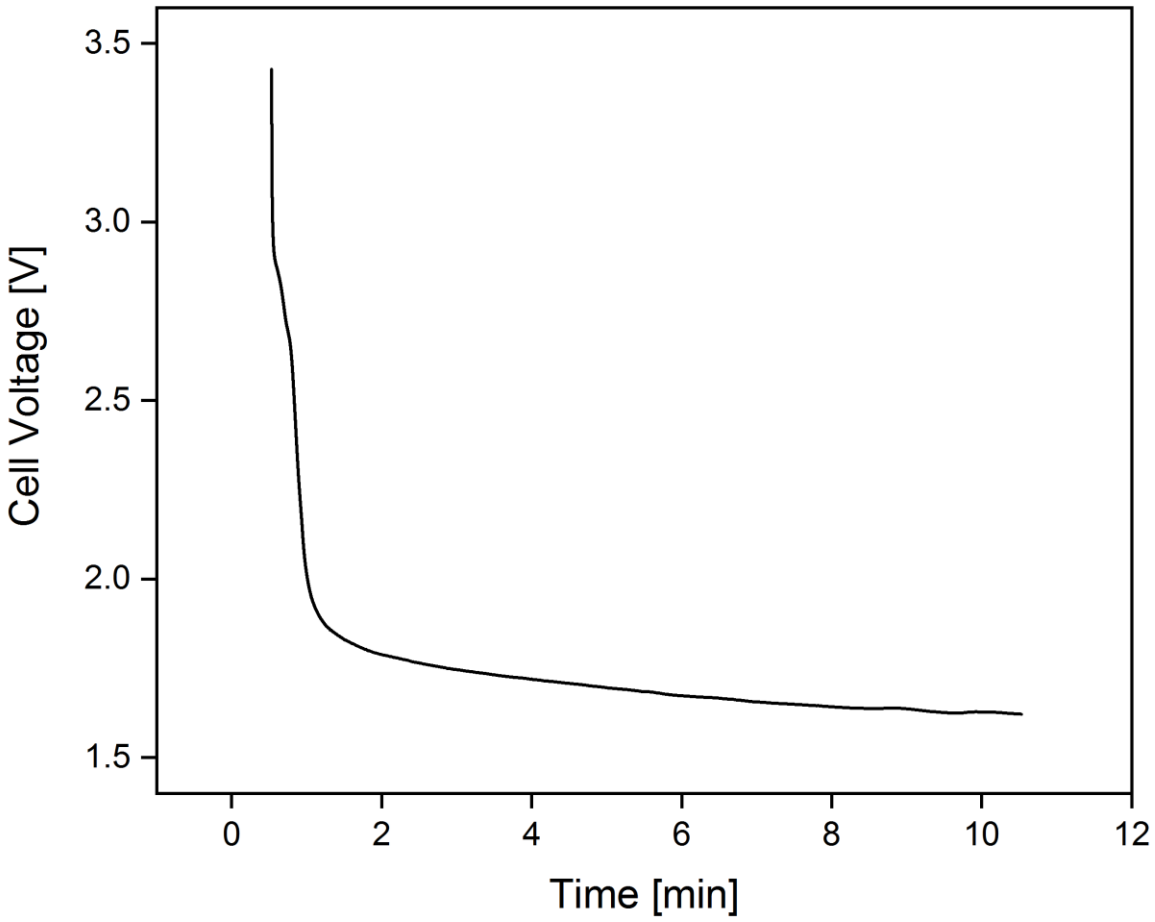

Figure 158: Open circuit voltage (OCV) scan of the system Ni|NiF_x|HF_l‖HF_l|$H_{2,g}$|Ni ($x \geq 2$), which had been conditioned at a potential of +6.0 V vs. Ni for 130 min (Figure 74). The offset of 30 s is subsequently originated by a consecutive set of experiments comprising the steps OCV (30 s), CA (130 min) and OCV (10 min, this figure).

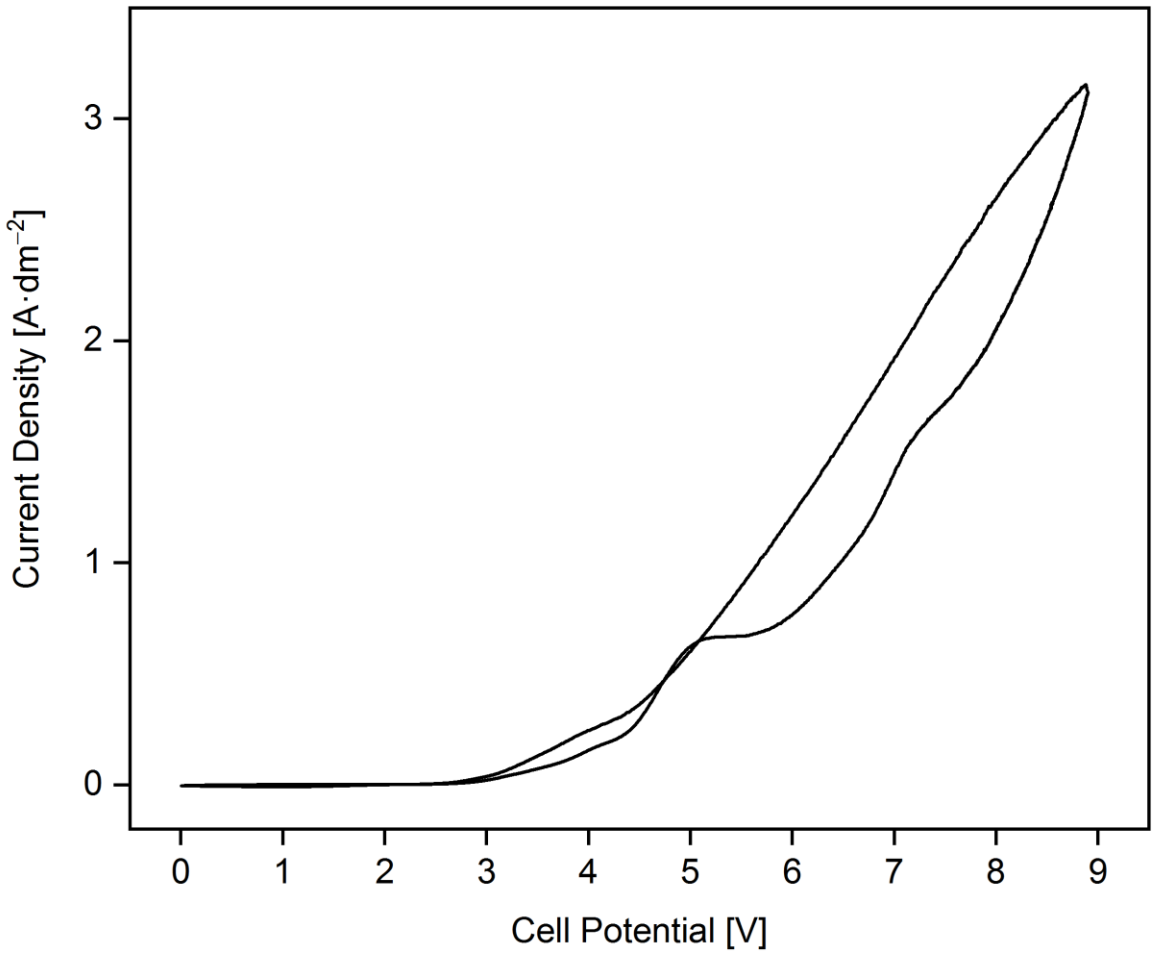

Figure 159: Cyclic voltammogram of nickel anode and cathode in liquid *a*HF in the 2-electrode in-situ XAFS cell in the potential window from 0 to +9.0 V. Only one distinct oxidation feature was observed at a cell voltage of +5.25 V. The electrode arrangement in this setup is seen to cause an increase of the oxidation potential by +0.7 V compared to earlier findings,[174] as well as the crossing of the backward and the forward scan.[172]

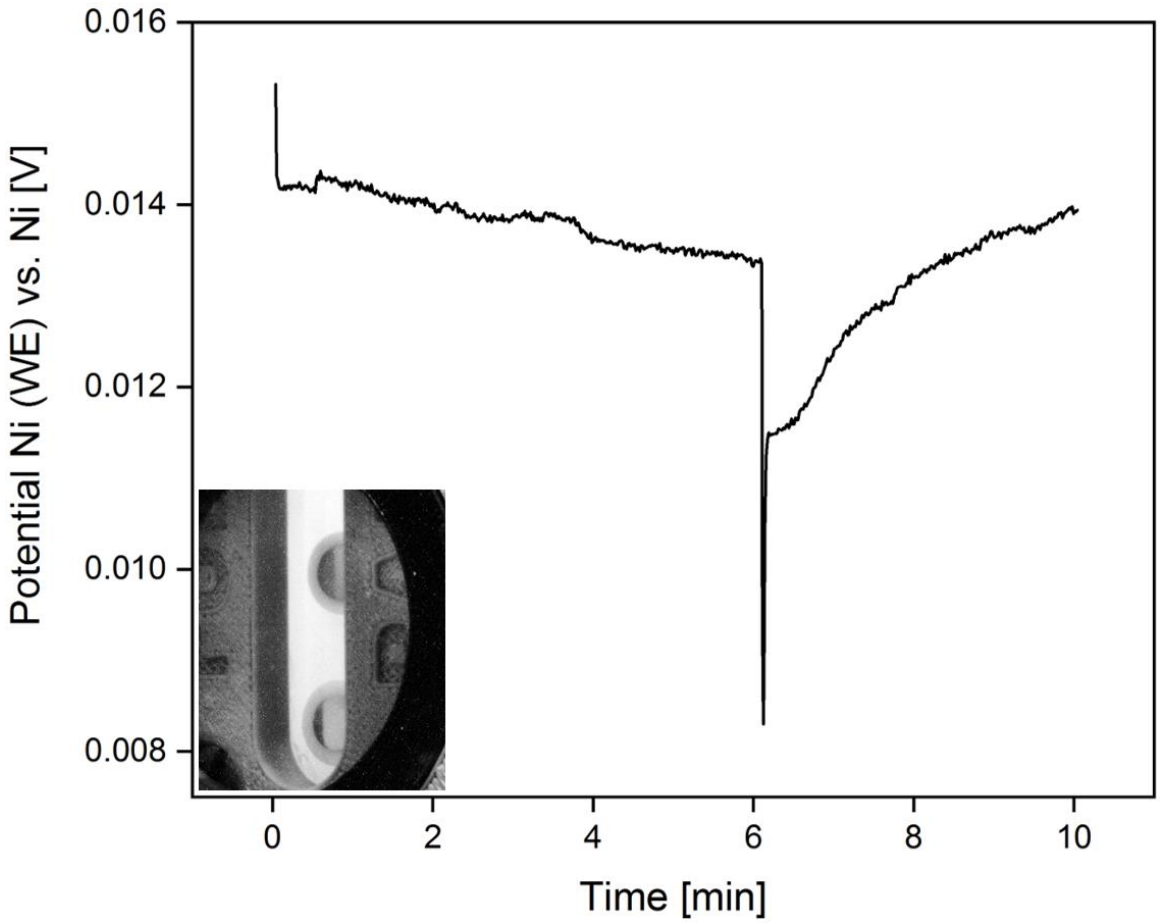

Figure 160: OCV scan before the application of any potential in the electrochemical in-situ XAFS cell. The photo depicts the cell filled with liquid *a*HF with nickel anode (bottom) and cathode (top). The spike in potential accounts for vibrations caused by the movement of the detector.

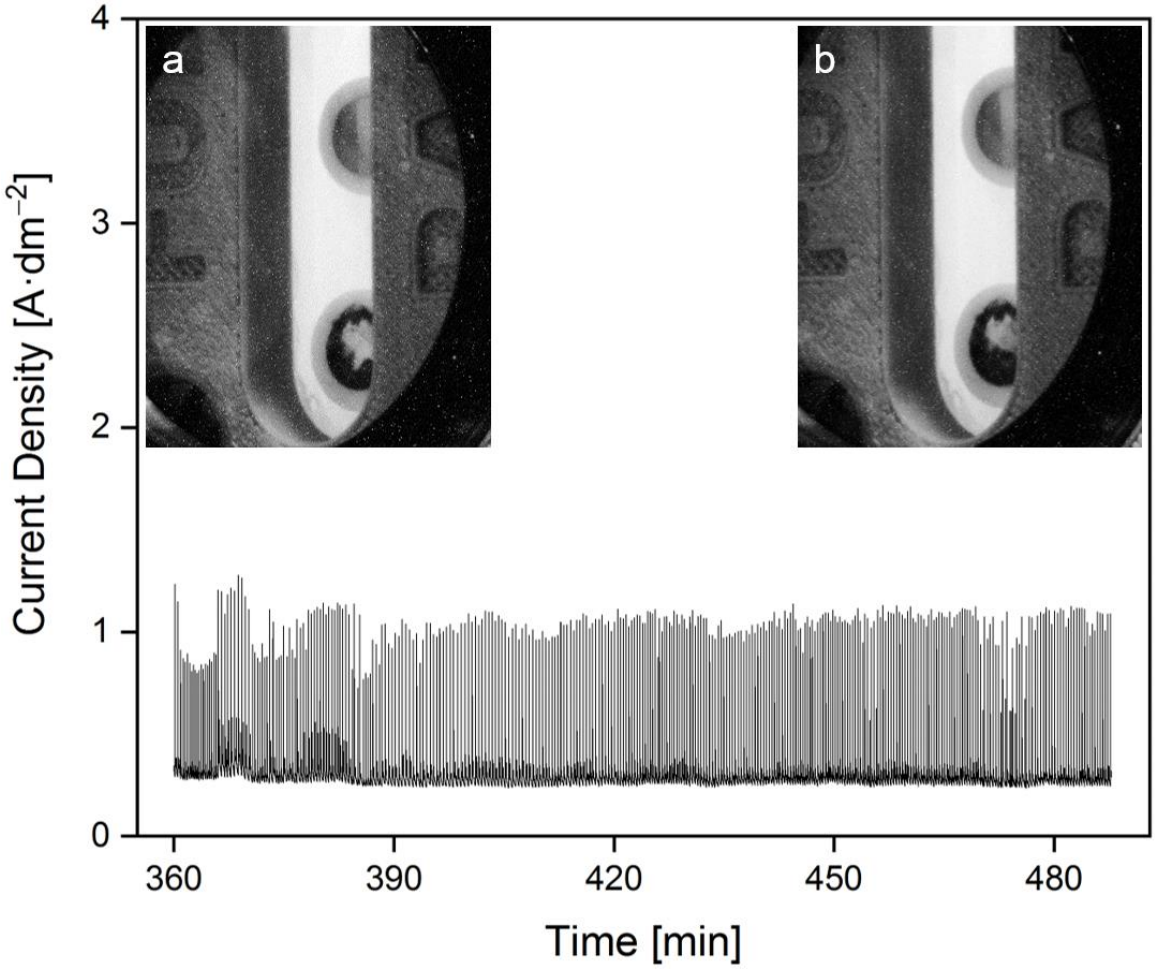

Figure 161: Chronoamperometric scan upon prolonged polarization at +8.7 V. The photos depict the start (a) and end state (b) of nickel anode (bottom) and cathode (top) in liquid *a*HF in the in-situ XAFS cell.

6.4.2 XAFS Cells

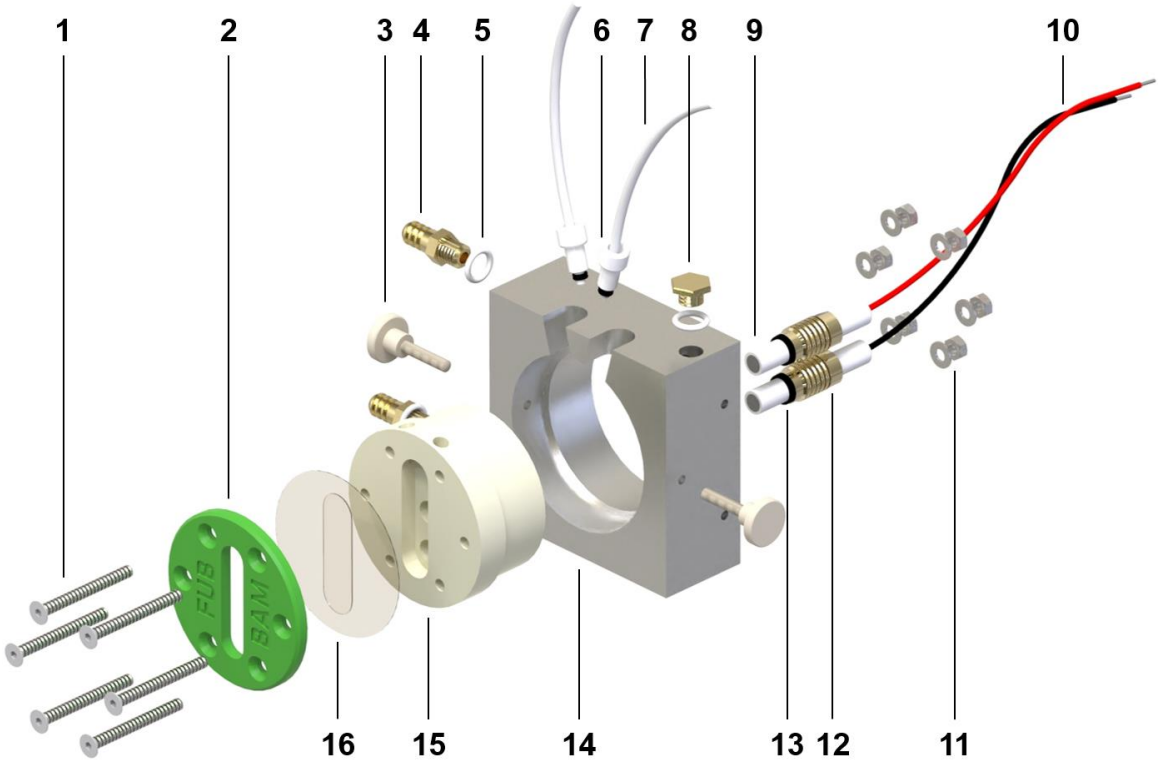

Figure 162: Exploded assembly drawing of the in-situ XAFS cell.[515] Analogous parts have been singly highlighted for clarity: **1**) countersunk bolt DIN 7991 M4 (stainless steel), **2**) cell cap/pressure piece (3D-printed ABS), **3**) knurled-head cell fixation screw (PVC), **4**) hose connector (brass), **5**) flange seal (PTFE), **6**) compression fitting (PTFE), **7**) tubing for *a*HF inlet and exhaust gases (PFA), **8**) seal plug (brass), **9**) planar nickel electrodes (PTFE coated Ni (99.99 %)), **10**) connector cables, **11**) M4 nuts and washers (stainless steel), **12**) compression fitting (brass), **13**) O-rings (FKM), **14**) heat sink and mount (aluminum), **15**) cell body (PCTFE), and **16**) window (FEP, 50 µm). The FEP foil is depicted with the fold edge resulting from mounting the cell cap/pressure piece. For increased safety, two O-rings were used for sealing electrodes as well as *a*HF inlet and exhaust gas tubings.

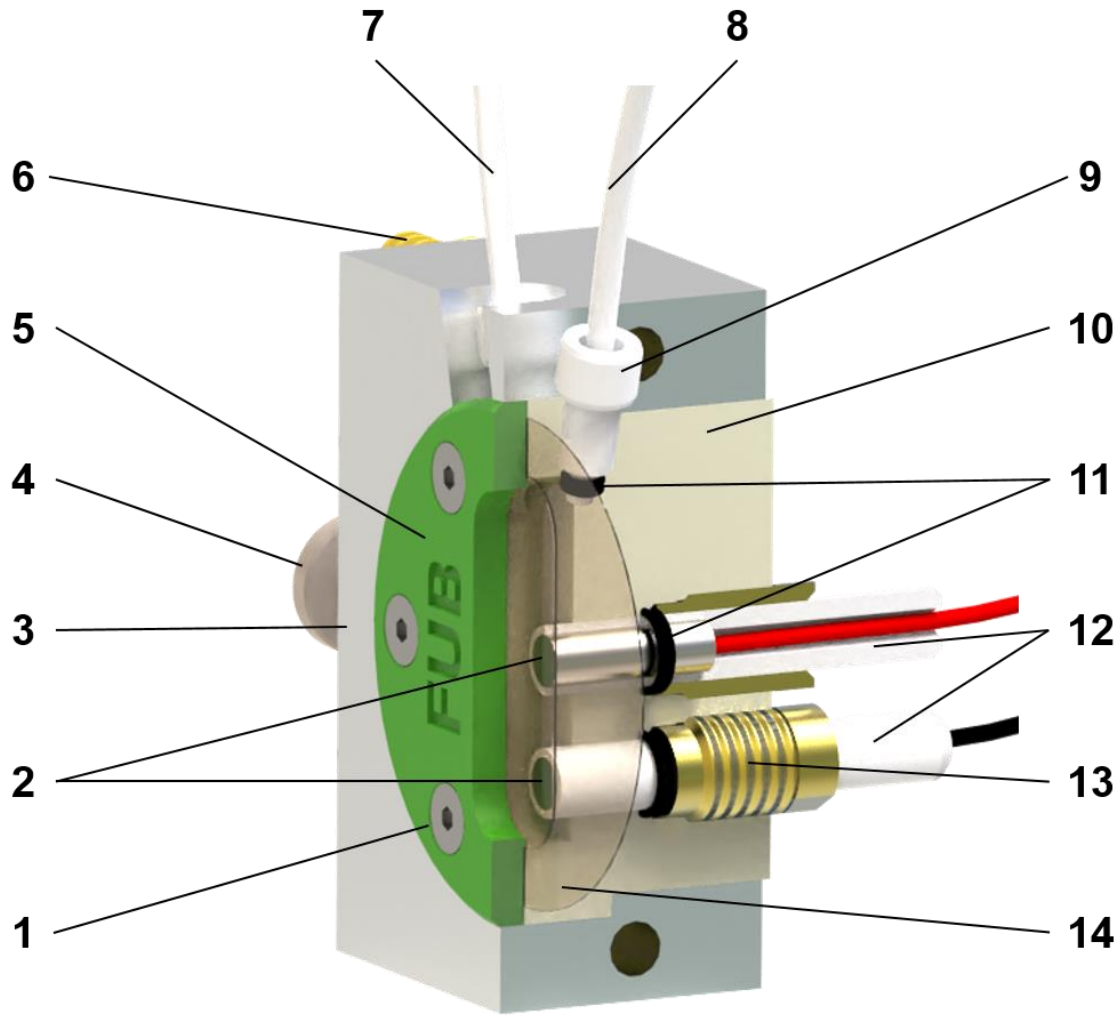

Figure 163: Cutaway drawing of the in-situ XAFS cell with the components and the respective materials (in parentheses):[515] **1**) countersunk bolt DIN 7991 M4 (stainless steel), **2**) planar electrodes (Ni, 99.99 %), **3**) heat sink and mount (aluminum), **4**) knurled-head screw (PVC) for fixation of the cell, **5**) cell cap/pressure piece (3D-printed ABS), **6**) hose connector (brass), **7**) inlet for liquid *a*HF (PFA), **8**) outlet for exhaust gases H_2 and (gaseous) HF (PFA), **9**) compression fitting (PTFE), **10**) cell body (PCTFE), **11**) O-rings (FKM), **12**) coating of the planar electrodes (PTFE), **13**) compression fitting (brass), and **14**) window (FEP, 50 µm). For increased safety, two O-rings were used for sealing electrodes as well as *a*HF inlet and exhaust gas tubings.

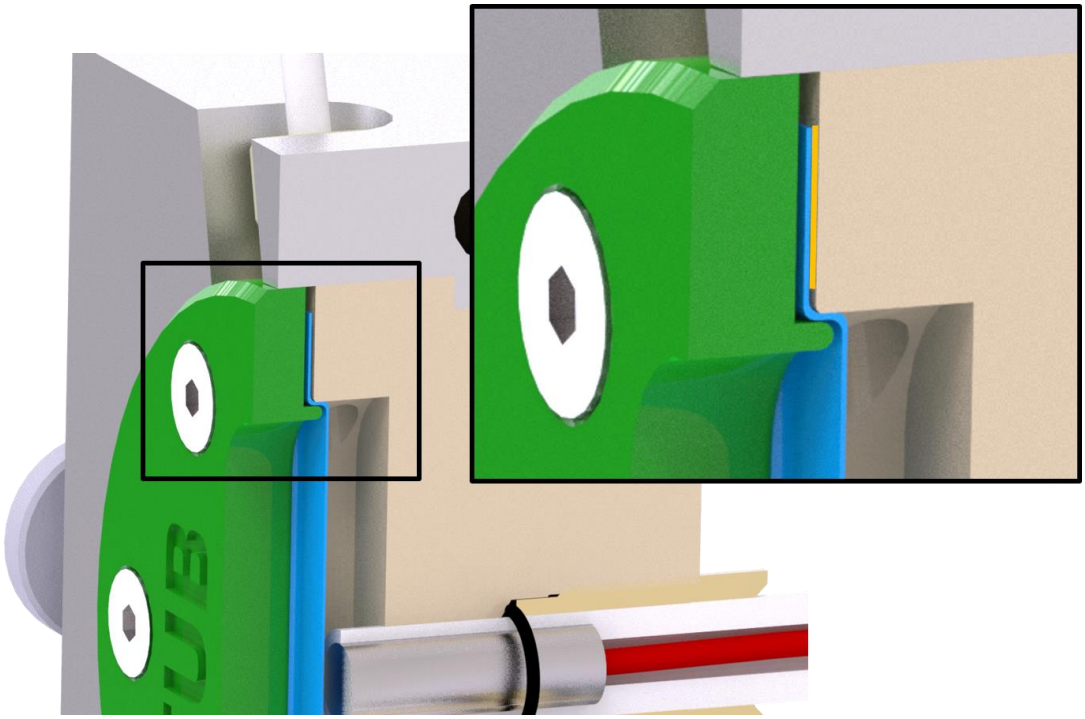

Figure 164: Sealing principle of the in-situ XAFS cell with the FEP foil highlighted blue.[515] By adjusting the 3D-printed green pressure piece to the oblong hole of the liquid *a*HF container of the cell, a tight contact between cell body and FEP foil was achieved and maintained by six M4 screws with corresponding washers and nuts on the backside of the cell (cf. Figure 162). Due to the low surface tension of *a*HF,[516,517] halocarbon wax (25-20M Grease, *Halocarbon*®) was used as an additional sealant on the surrounding contact plane between the FEP foil and the PCTFE cell body (highlighted orange).

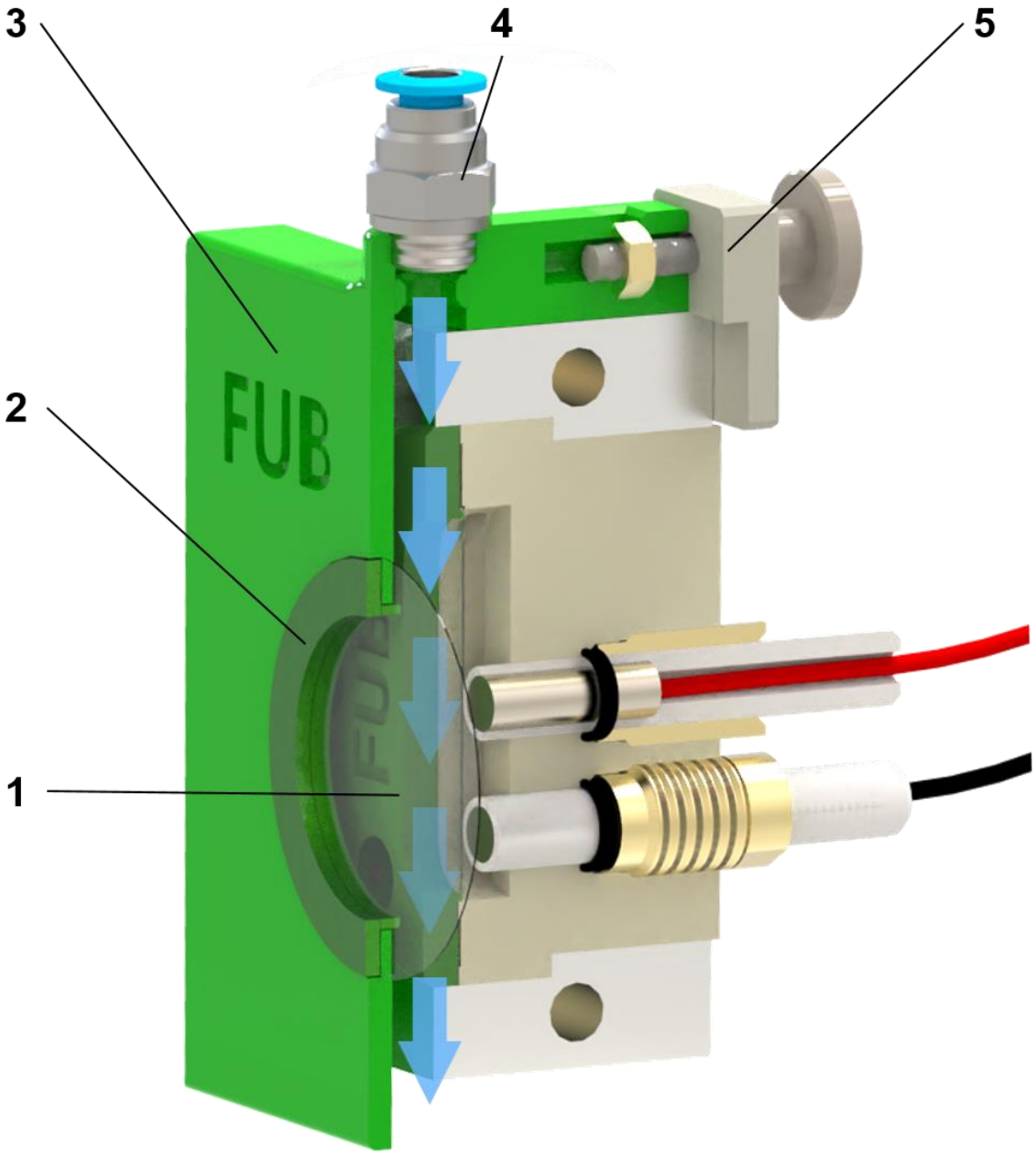

Figure 165: Functional principle of the HF shield employing the following parts:[515] **1**) window (FEP, 25 µm), **2**) foil fixation ring (3D-printed ABS), **3**) HF-shield with applicable N_2 stream (3D-printed ABS), **4**) push-in fitting (Festo QS-G1/8-6 (186096)), and **5**) mounting clamp consisting of screw (M3, stainless steel), knurled screw cap (3D-printed ABS) and nut (M3, stainless steel). The window **1** was glued to the shield **3** with halocarbon wax (25-20M Grease, *Halocarbon*®) and fixed with the fixation ring **2**. The blue arrows depict the direction of the N_2 stream.

Figure 166: Setup of the in-situ XAFS cell with a mobile HF deactivation (brass-colored highlights).I recommend the flame-sealing of the HF inlet after filling of the cell and cooling the bubbler containing the perfluorinated hexanes (98 %, 85 % *n*-isomer, *ABCR*) at ϑ = 0 °C. All parts in contact with HF were made from fluoroplastics or stainless steel. The mobile HF deactivation was used for the low temperature XAFS cell for reference measurements of NiF_4 and NiF_3 as well.

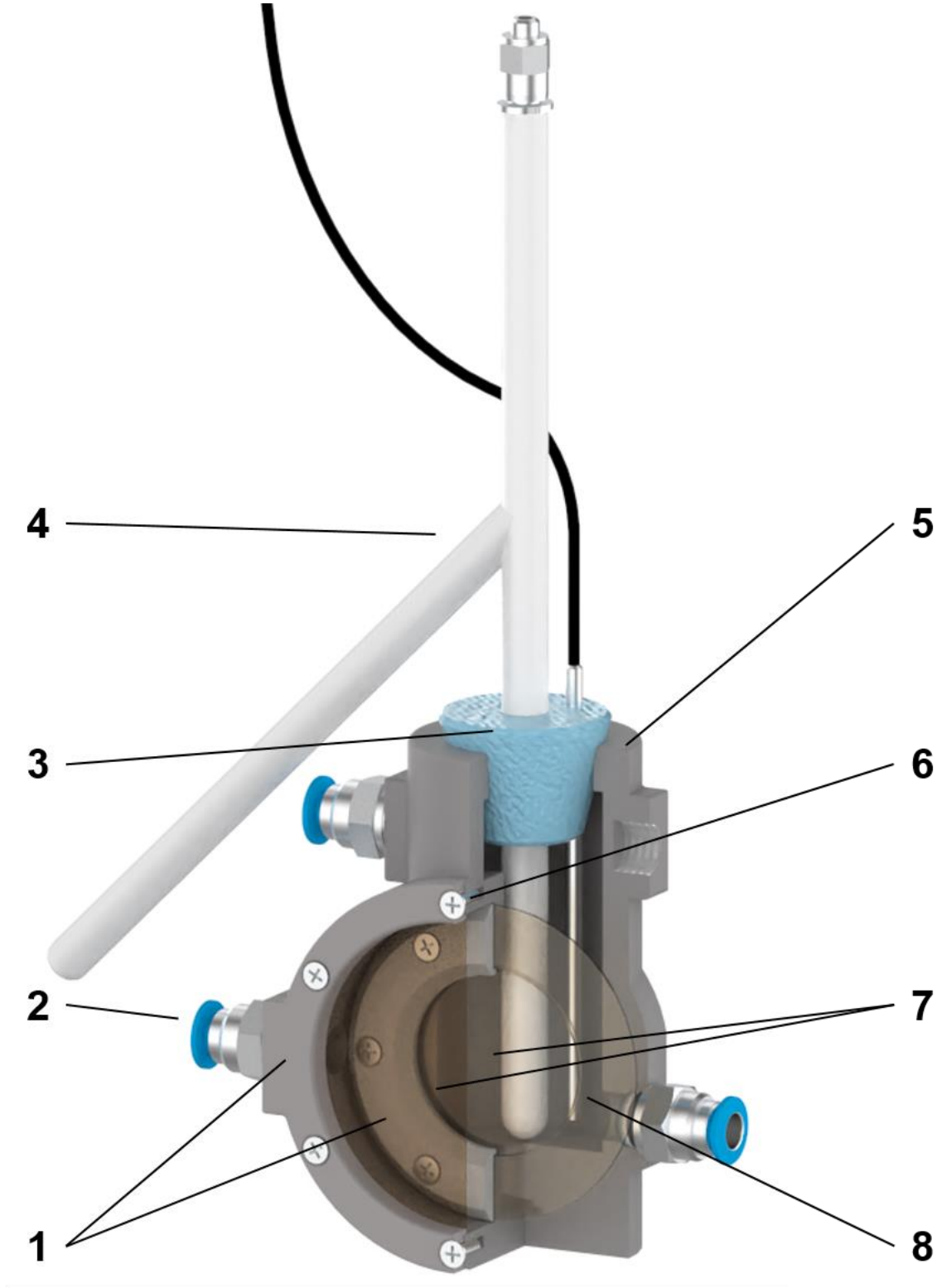

Figure 167: Cutaway drawing of the low temperature XAFS cell for reference measurements of NiF_4 and NiF_3 with a coolable inner sample container with components and their respective materials:[515] **1**) pressure pieces (3D-printed ABS), **2**) push-in fitting (Festo QS-G1/8-6 (186096)), **3**) seal plug with drilled holes for thermal sensor and the sample tube (polystyrene), **4**) sample tube (FEP), **5**) cell body (3D-printed ABS), **6**) countersunk bolt ISO7046-1-M2, 5x6 (stainless steel), **7**) windows (FEP, 25 µm), and **8**) thermal sensor.

6.4.3 Additional XAFS Spectra

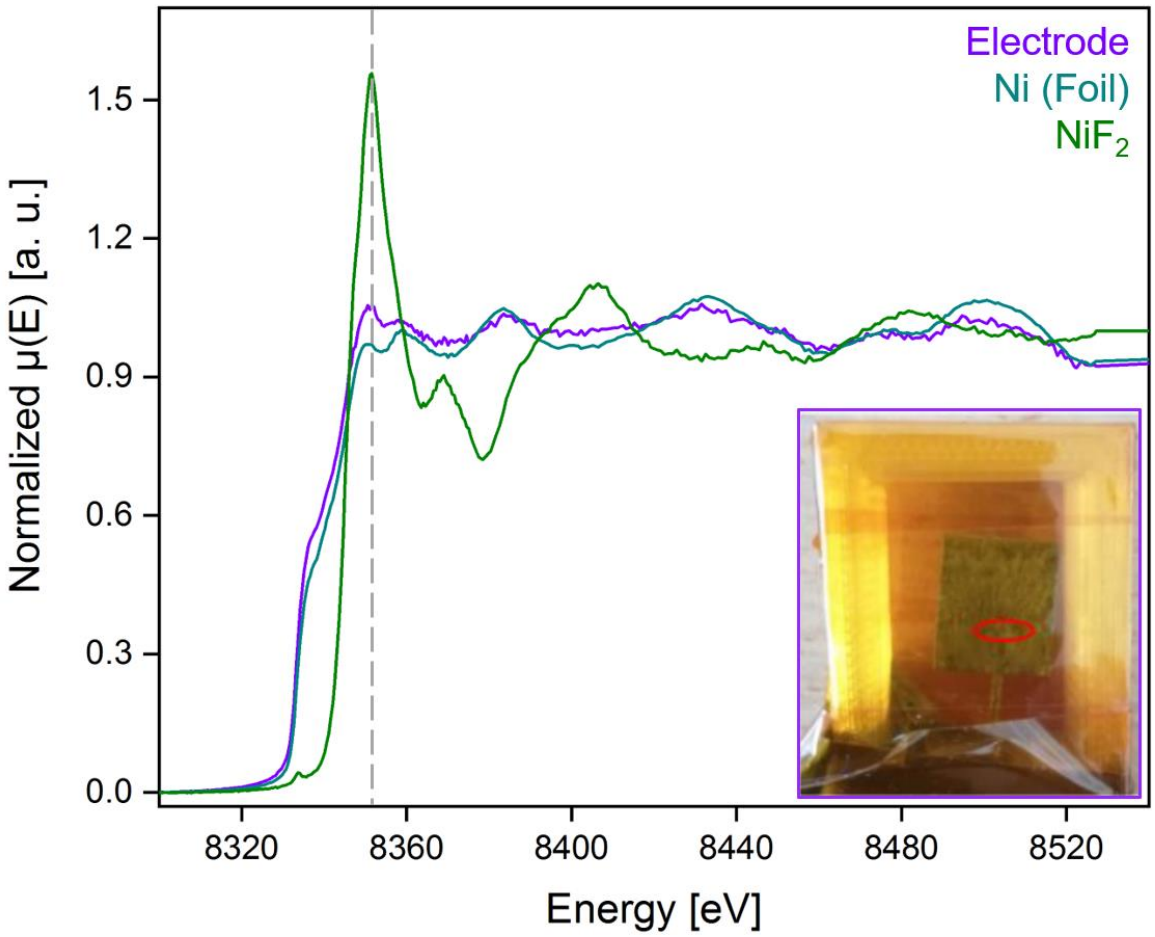

Figure 168: Ni K-edge XANES spectra in the range from 8300–8540 eV at a spectral resolution of 0.5 eV of a decomposed nickel electrode (purple, photo with the measurement position highlighted in red) and the reference standards Ni (foil, transmission measurement, turquoise) and NiF_2 (green). The maximum of absorption of NiF_2 at 8351.6 eV was highlighted with a grey dashed line.

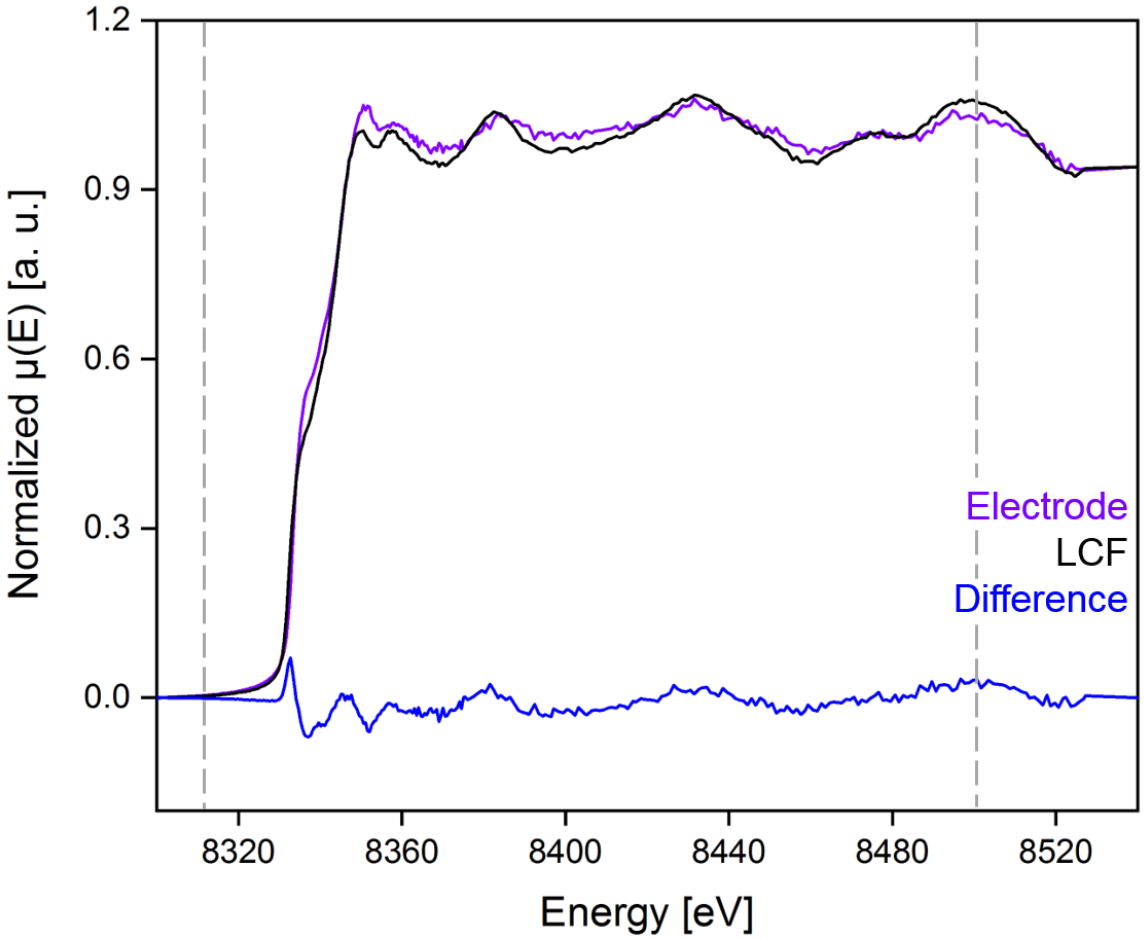

Figure 169: Ni K-edge XANES spectrum of a decomposed nickel electrode (purple) and a linear combination fit using the standards NiF_2 and Ni (black, see also Figure 168) as well as the difference of both (blue) in the range 8300–8540 eV at a spectral resolution of 0.5 eV. The region of the fit (8313.21 to 8503.21 eV) was highlighted (grey dashed lines). The mass fractions were found to be 4.2 % (± 0.9 %) for NiF_2 and 95.8 % (± 0.9 %) for elemental nickel.

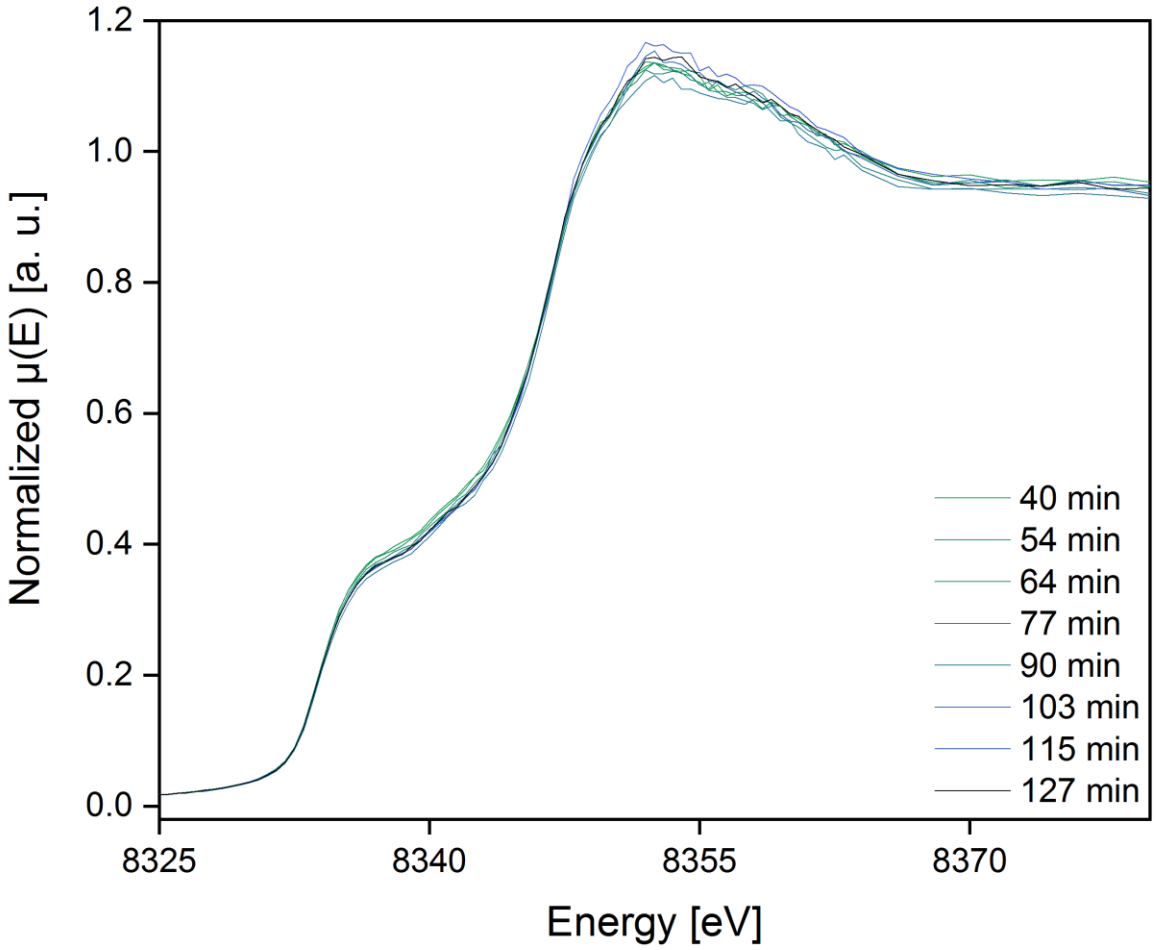

Figure 170: Ni K-edge XANES spectra obtained from a nickel anode in *a*HF during an extended polarization period at a cell voltage of +8.7 V. The spectrum recorded after 127 min is identical with the spectrum of the "Black Film" featured e.g. in Figure 92. Only marginal changes were recorded and therefore reflect the CA data (Figure 161). The corresponding first derivatives are depicted in Figure 171.

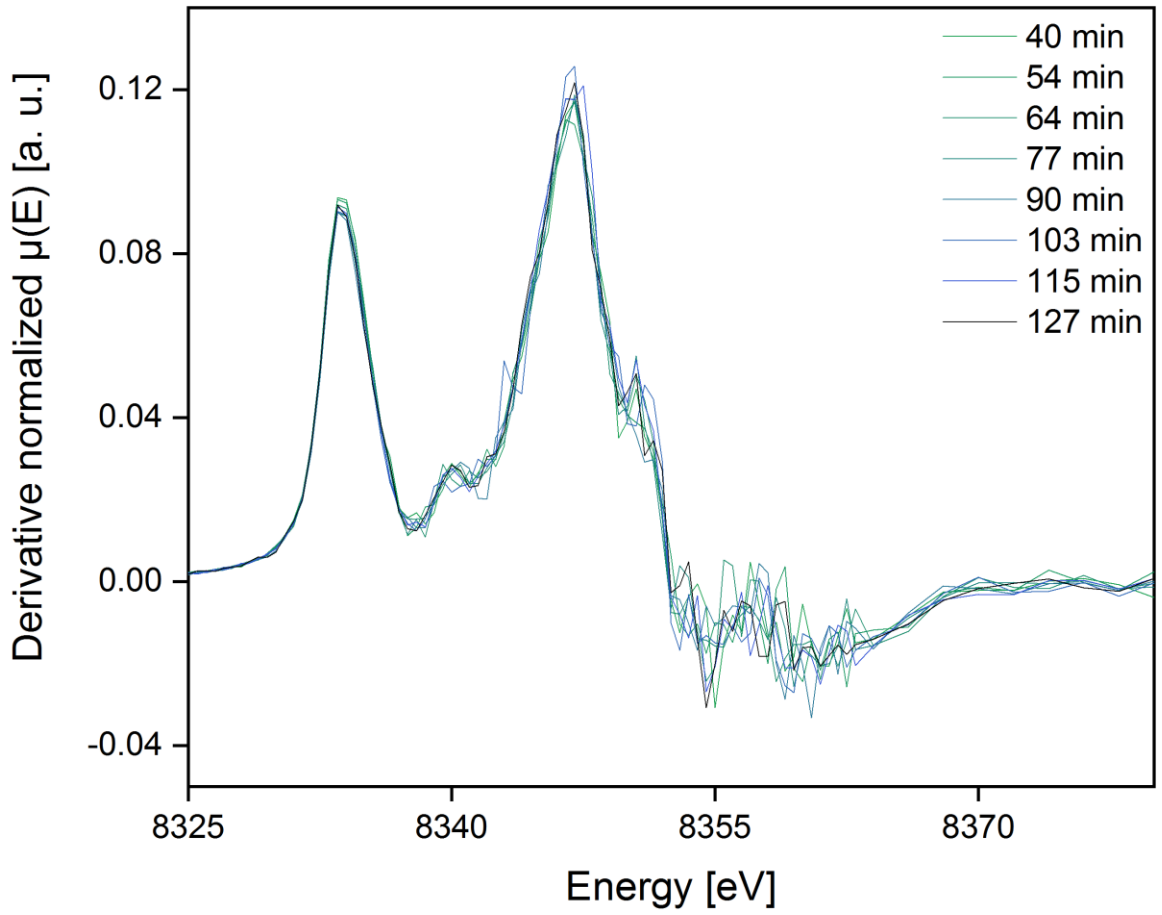

Figure 171: First derivative of Ni K-edge XANES spectra obtained from a nickel anode in *a*HF during an extended polarization period at a cell voltage of +8.7 V. The spectrum recorded after 127 min is identical with the spectrum of the "Black Film" featured e.g. in Figure 92. Only marginal changes were recorded and therefore reflect the CA data (Figure 161). The corresponding XANES spectra are depicted in Figure 170.

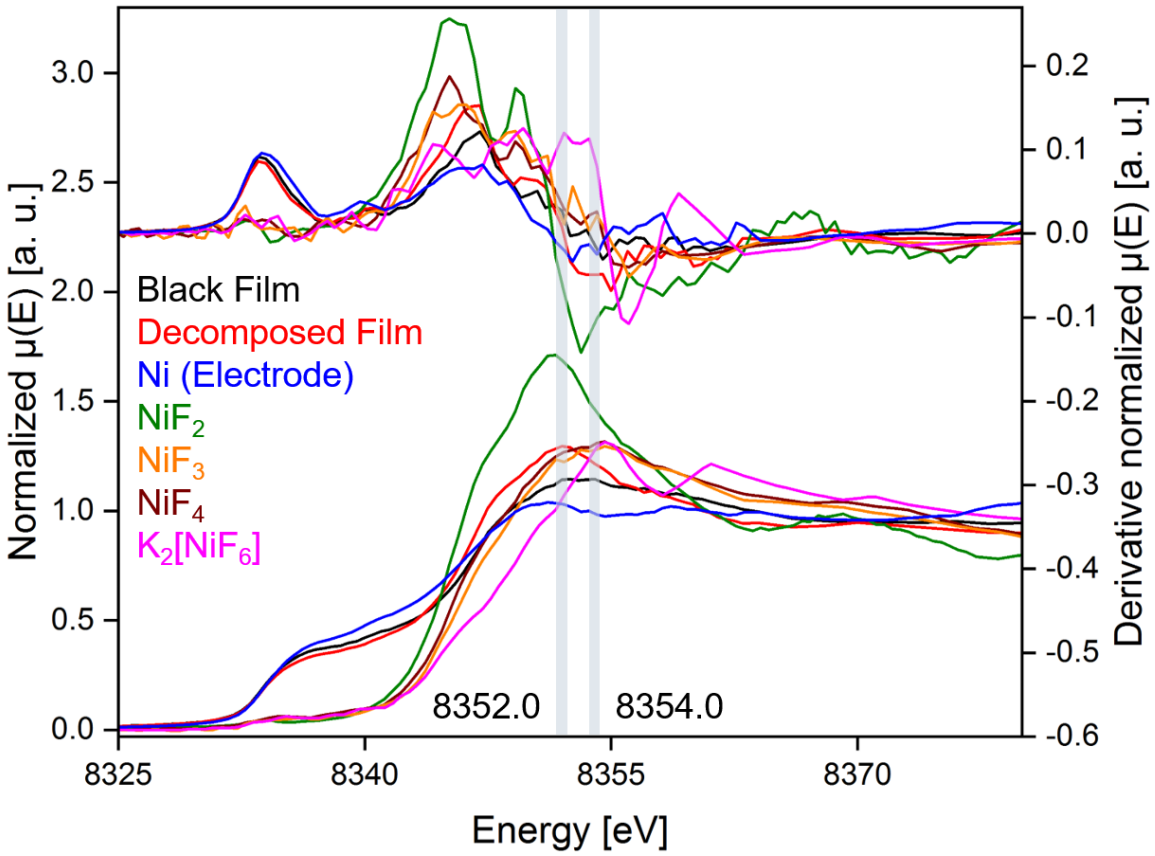

Figure 172: Ni K-edge XANES spectra (left axis, bottom traces) and their first derivatives (right axis, top traces) obtained from an in-situ generated black film on a nickel anode (black traces), after its decomposition (red traces), and from the reference substances Ni (bulk anode that is exposed to liquid *a*HF, blue traces), NiF_2 (green traces), NiF_3 (orange traces) and NiF_4 (brown traces) as well as $K_2[NiF_6]$ (magenta traces). The maxima of the white lines of the black film and the decomposed film have been highlighted at 8354.0 and 8352.0 eV, respectively.

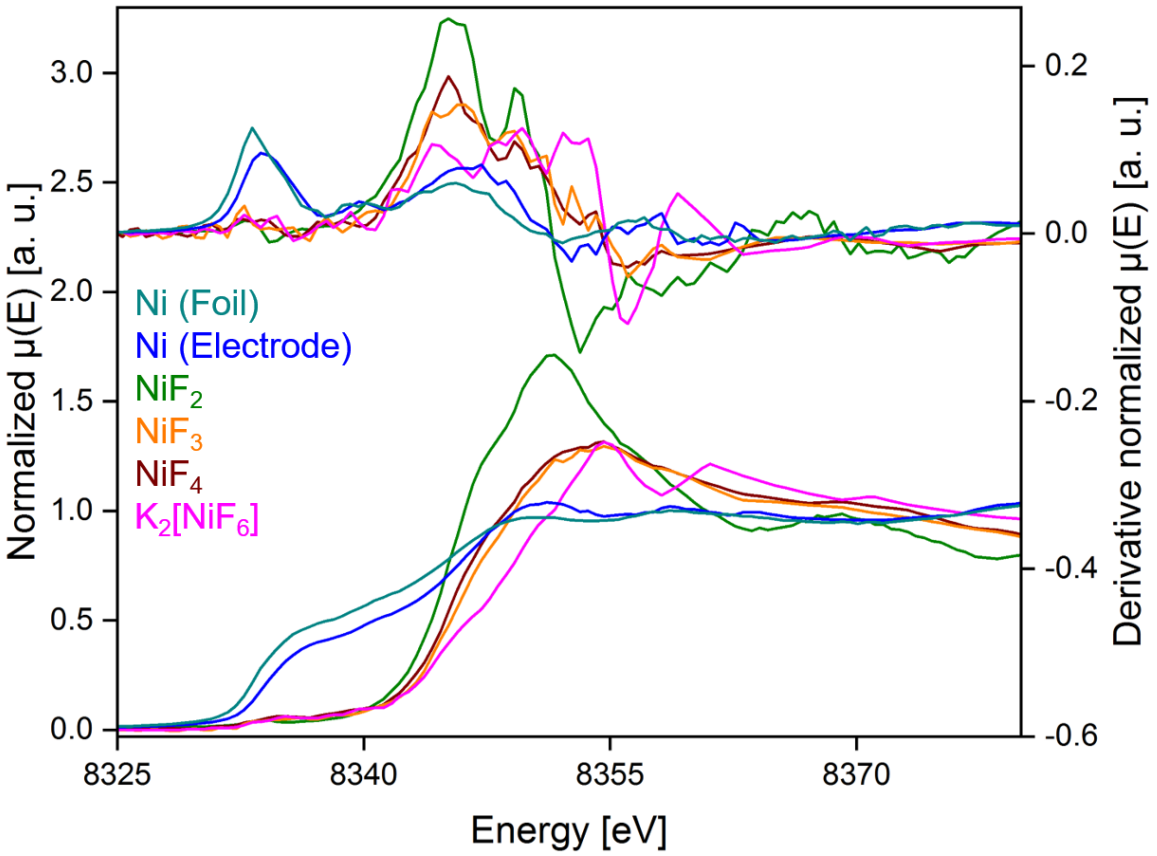

Figure 173: Ni K-edge XANES spectra (left axis, bottom traces) and their first derivatives (right axis, top traces) obtained from the reference substances Ni (foil, turquoise traces), Ni (bulk anode that is exposed to liquid *a*HF, blue traces), NiF_2 (green traces), NiF_3 (orange traces) and NiF_4 (brown traces) as well as $K_2[NiF_6]$ (magenta traces). The spectrum of the Ni foil was measured in transmission, the spectra of the other reference materials were measured in fluorescence.

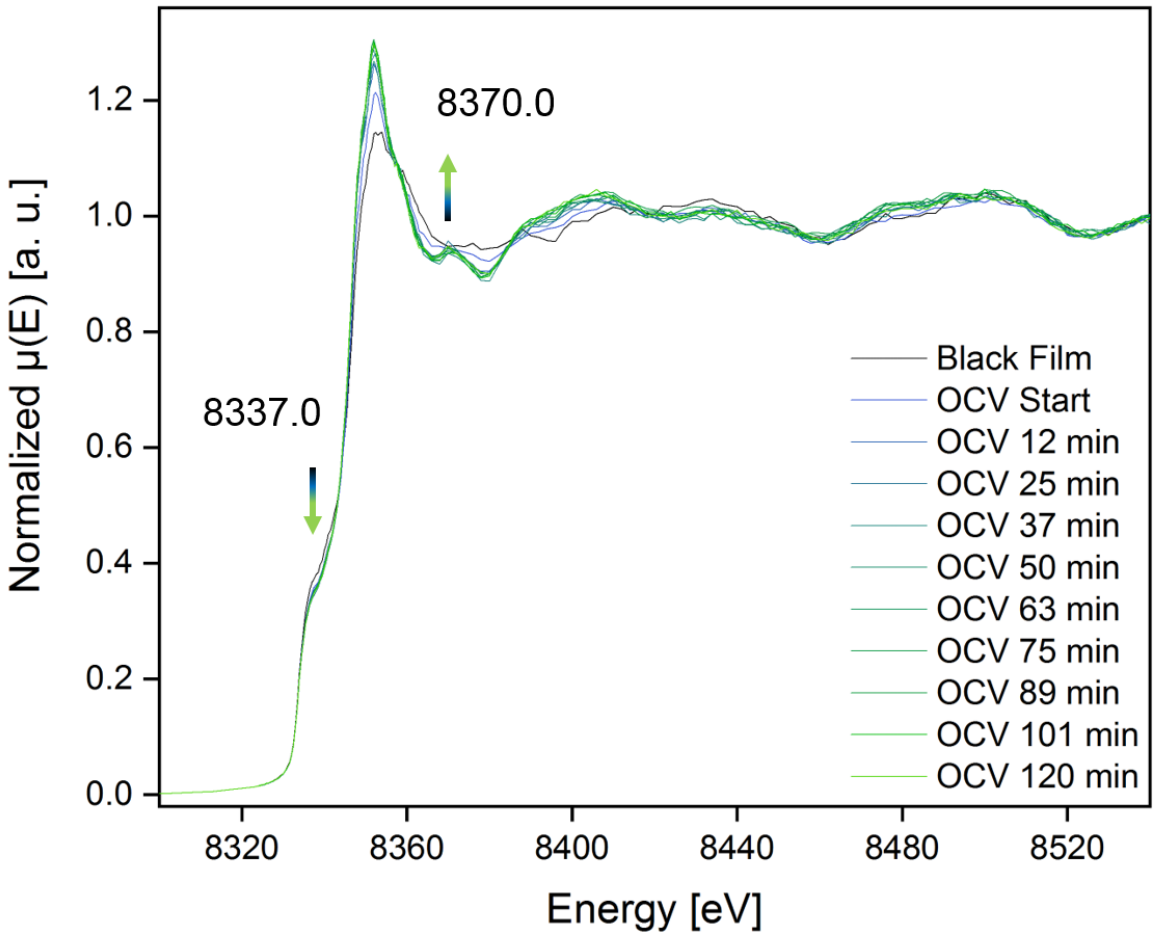

Figure 174: Ni K-edge XANES spectra recorded during the decomposition of the anodic black film (black trace) under open circuit conditions (see also the OCV scan in Figure 90) with the color transitioning from blue (start) to green (120 min). The features of decreasing Ni^0 (8337.0 eV) and increasing NiF_2 (the weaker feature at 8370.0 eV) are additionally highlighted with arrows.

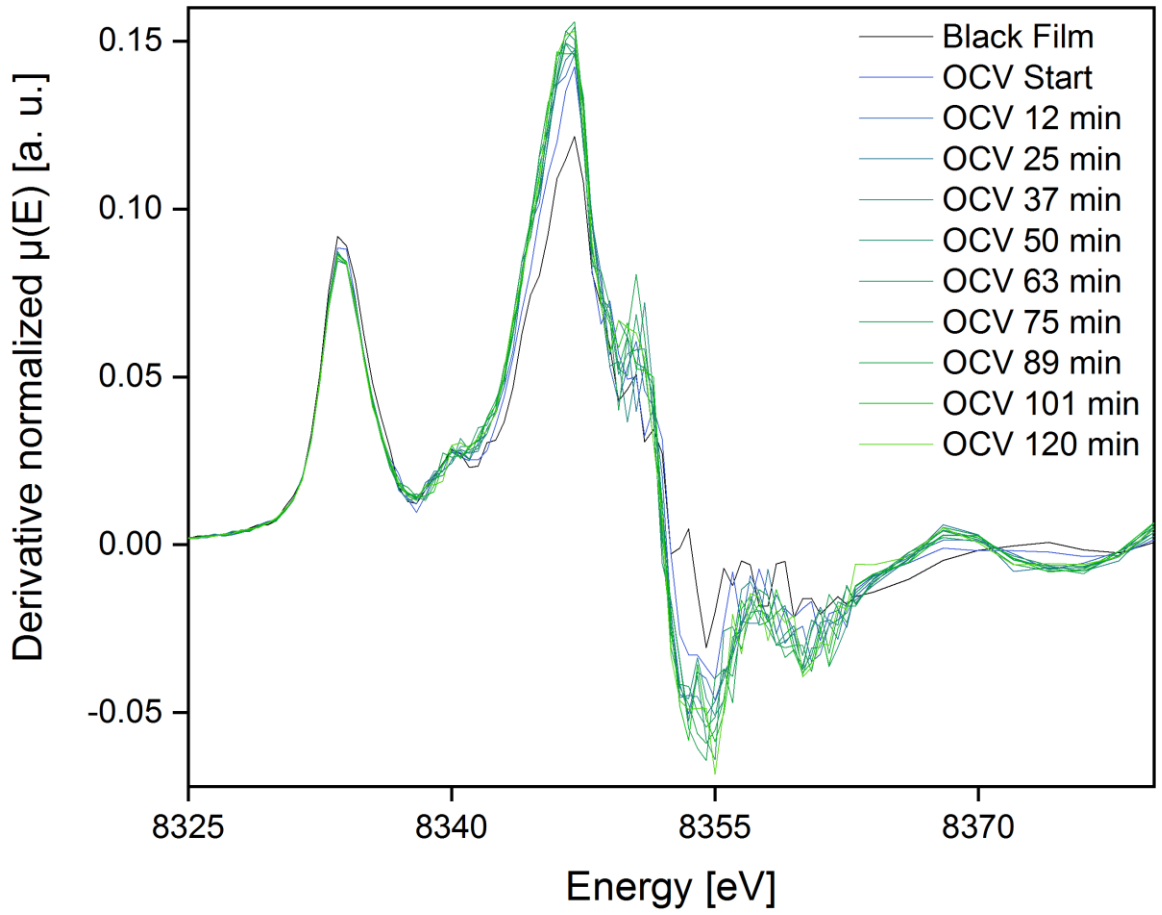

Figure 175: First derivatives of the Ni K-edge XANES spectra recorded during the decomposition of the anodic black film (black trace) under open circuit conditions (see also the OCV scan in Figure 90) with the color transitioning from blue (start) to green (120 min). The spectrum after 120 min corresponds to the "Decomposed Film" in Figure 92. The respective XANES spectra are depicted in Figure 93.

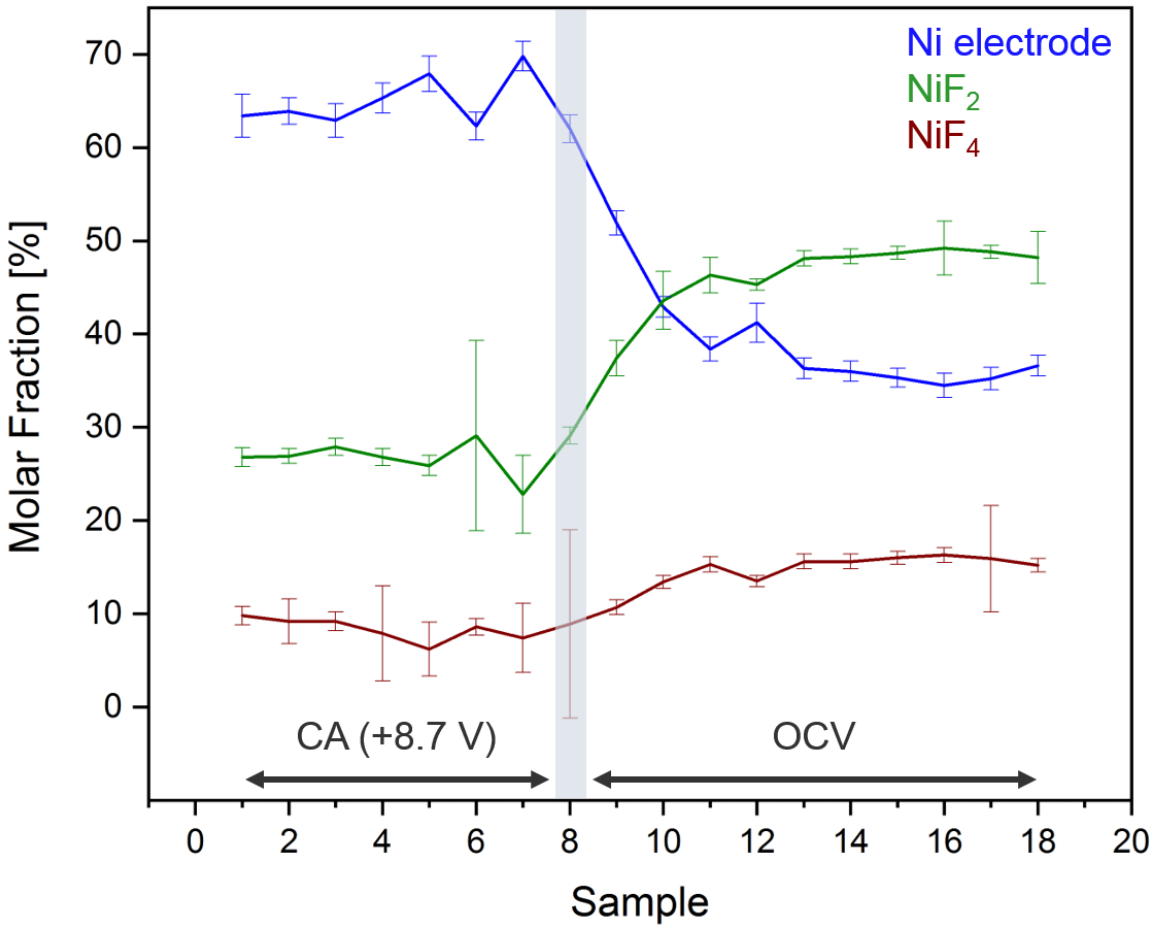

Figure 176: Linear combination fitting of the XANES spectra obtained during the prolonged conditioning of the nickel anode in liquid *a*HF at a cell potential of +8.7 V (samples 1–8, see also Figure 170) and the consecutive decomposition of the anodic film during an OCV scan (samples 9–18, see also Figure 93) to the spectra of the reference materials Ni (bulk anode that is exposed to liquid *a*HF, blue trace), NiF_2 (green trace) and NiF_4 (brown trace).

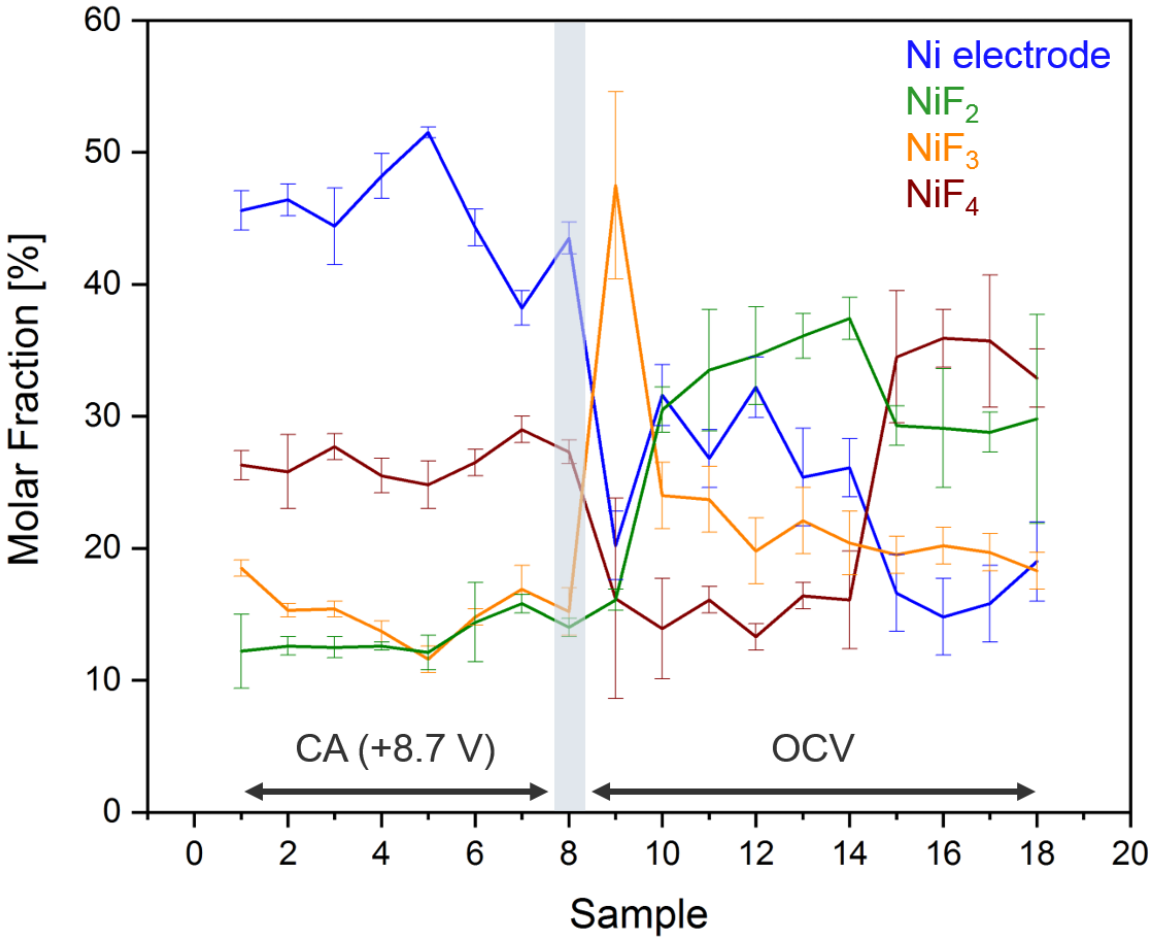

Figure 177: Linear combination fitting of the XANES spectra obtained during the prolonged conditioning of the nickel anode in liquid *a*HF at a cell potential of +8.7 V (samples 1–8, see also Figure 170) and the consecutive decomposition of the anodic film during an OCV scan (samples 9–18, see also Figure 93) to the spectra of the reference materials Ni (bulk anode that is exposed to liquid *a*HF, blue trace), NiF_2 (green trace), NiF_3 (orange trace) and NiF_4 (brown trace).

6.4.4 Photographic Documentation

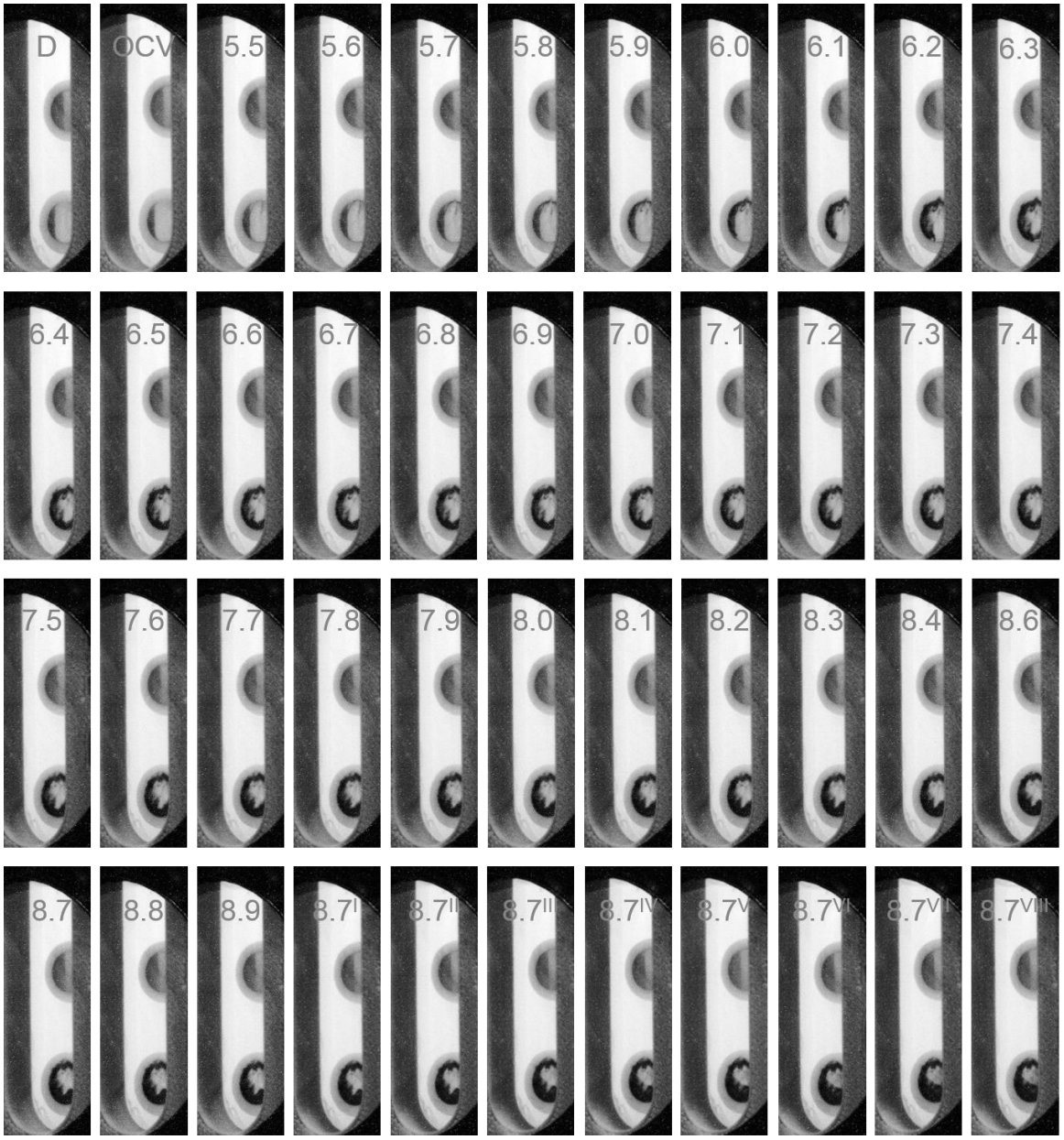

Figure 178: Photos of the electrochemical in-situ XAFS cell with nickel anode (bottom) and cathode (top) in liquid *a*HF were taken between the measurements of the XANES spectra of every potential step. Upon applying stepwise increased potentials from +5.5 V to +8.9 V (all given potentials as the labels of the single photos are positive) every 10 min, the formation of a black film was observed on the anode. The photos labelled 8.7^{I} to 8.7^{VIII} were taken after 40, 54, 64, 77, 90, 103, 115 and 127 min, respectively, during a prolonged conditioning phase at +8.7 V, which led to an increased covering of the anode with the black film. D = disconnected, OCV = open circuit voltage.

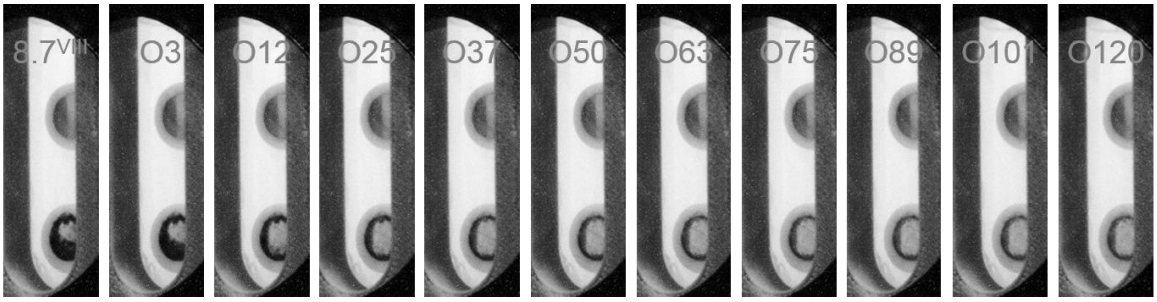

Figure 179: Decomposition of the black film on the nickel anode (bottom) under open circuit conditions. The cathode (top) remained visibly unchanged. The photos were taken at the end of the complete conditioning phase (labelled 8.7^{VIII}, see also Figure 178) and the photos labelled O*N* after *N* = 3, 12, 25, 37, 50, 63, 75, 89, 101 and 120 min, respectively.

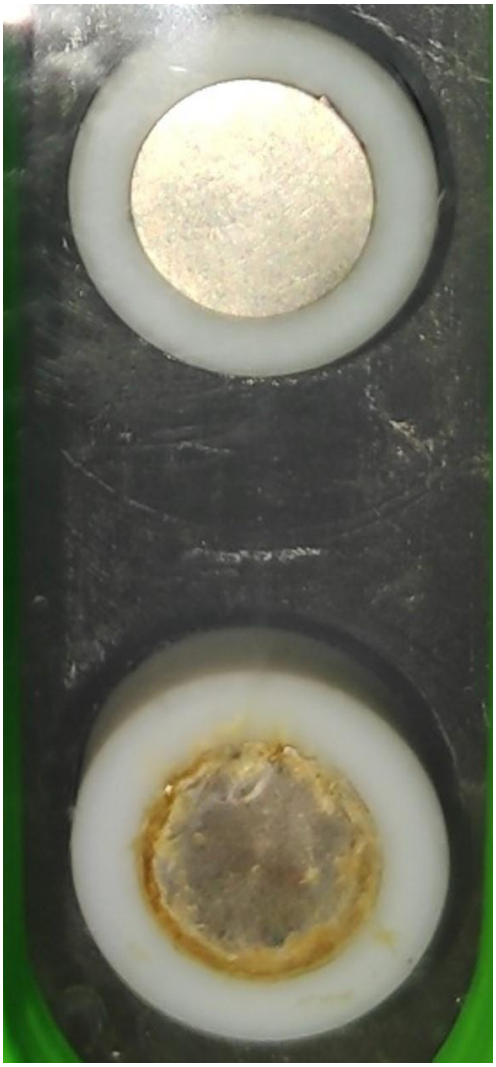

Figure 180: Nickel anode (bottom) and cathode (top) in *a*HF after the decomposition of the black film during an OCV scan for 120 min. The color of the film on the anode ranges from colorless to brownish. The cathode remained visibly unchanged during the formation and decomposition of the black film.

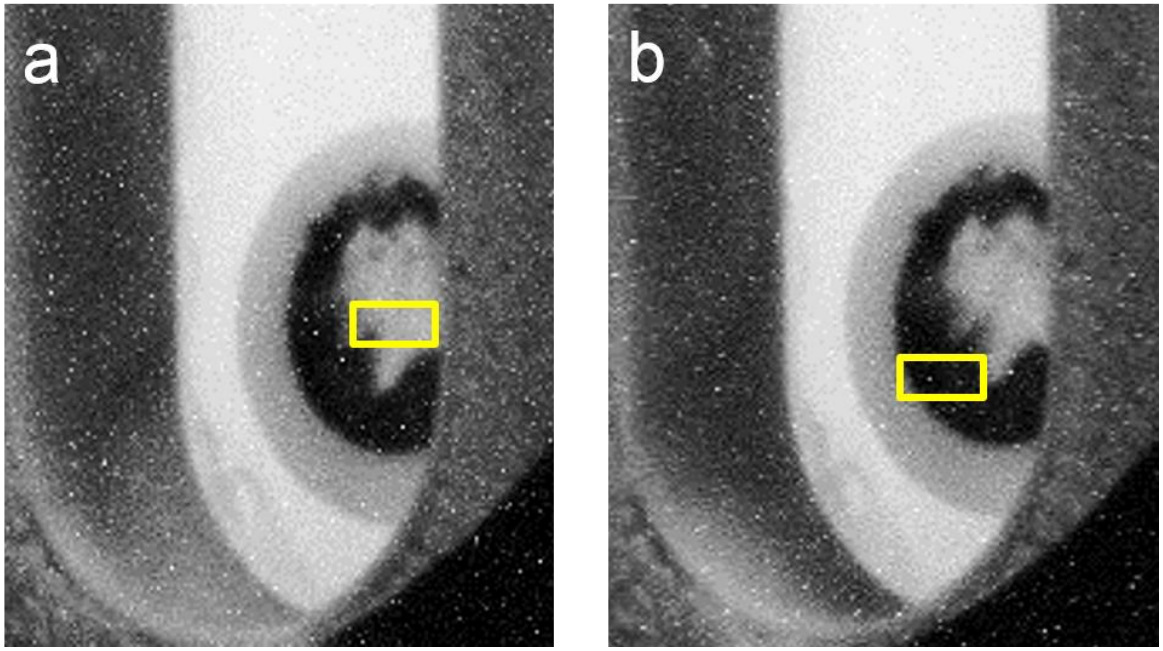

Figure 181: Photos of the nickel anode in *a*HF at a) +8.4 V and b) +8.6 V in the electrochemical in-situ XAFS cell with a) initial (potentials +5.5 V to +8.4 V) and b) optimized (from +8.6 V on) beam spot positions for the measurements of the XANES spectra (yellow-green highlighted areas). The optimization was done during the potential step of +8.5 V and no spectrum was recorded at this potential, accordingly.

7 Publications and Conference Contributions

7.1 Publications

1. S. Mattsson, **G. Senges**, S. Riedel, B. Paulus, *Chem. Eur. J.* **2020**, 26, 10781. (doi.org/10.1002/chem.202000881)
2. **G. Senges**, L. Li, A. Wodyński, H. Beckers, R. Müller, M. Kaupp, S. Riedel, *Chem. Eur. J.* **2021**, 27, 13642. (doi.org/10.1002/chem.202102055)

7.2 Conference Contributions – Oral Presentations

1. **G. Senges**: Simons Process – The Black Film Reinvestigated, *1st Networking Meeting 2019 of the CRC 1349 "Fluorine-Specific Interactions"*, Berlin, Germany, **2019**.
2. **G. Senges**: The Journey to the Active Species in the Simons Process, *Summer School of the CRC 1349 "Fluorine-Specific Interactions"*, Waren (Müritz), Germany, **2019**.
3. L. Li, **G. Senges**, A. Wodyński, R. Müller: New Detection of Historical PtF_6, *2nd Networking Meeting and 6th Colloquium of the CRC 1349 "Fluorine-Specific Interactions"*, Berlin, Germany, **2020**.
4. **G. Senges**: Strong Oxidizers: The Enhancement of the Oxidation Power of Fluorine and New Insights in the Simons Process, *16th WebEx-Seminar of the CRC 1349 "Fluorine-Specific Interactions"*, Berlin, Germany, **2021**.
5. **G. Senges**: Enhancing and Controlling the Oxidation Power of Elemental Fluorine, *Winter Symposium of the CRC 1349 "Fluorine-Specific Interactions"*, Berlin, Germany, **2022**.

7.3 Conference Contributions – Poster Presentations

1. **G. Senges**, T. A. Gully, S. Riedel: The Journey to the Active Species in the Simons Process, *7. Tag der Anorganischen Chemie*, Freie Universität Berlin, Berlin, Germany, **2019**.
2. **G. Senges**, Y. Lu, M. Wen, Z. Zhang, A. Guilherme Buzanich, T. A. Gully, L. Li, Y. A. Tsegaw, M. Radtke, U. Reinholz, B. Röder, G. Thiele, M. Winter, S. Steinhauer, H. Beckers, F. Emmerling, S. Riedel: High Potential Oxidizers Beyond Elemental Fluorine, *International Symposium on Fluorine-Specific Interactions*, Berlin, Germany, **2021**.

3. **G. Senges**, A. Guilherme Buzanich, T. A. Gully, M. Winter, B. Röder, S. Steinhauer, M. Radtke, U. Reinholz, F. Emmerling, S. Riedel: In-Situ XANES: Ni^{IV} involved in the Simons Process, *20th European Symposium on Fluorine Chemistry*, Berlin, Germany, **2022**.

8 Curriculum Vitae

The curriculum vitae is not included for reasons of data protection.

9 References

[1] J. H. Simons, *Chem. Rev.* **1931**, *8*, 213.

[2] P. Kirsch, *Modern fluoroorganic chemistry*. *Synthesis, reactivity, applications*, Wiley-VCH Verlag GmbH & Co. KGaA, Weinheim, **2013**.

[3] A. F. Holleman, N. Wiberg, *Lehrbuch der anorganischen Chemie*, de Gruyter, Berlin, **2007**.

[4] J. E. Huheey, E. A. Keiter, R. L. Keiter, R. Steudel, *Anorganische Chemie*. *Prinzipien von Struktur und Reaktivität*, de Gruyter, Berlin, **2012**.

[5] M. Jaccaud, R. Faron, D. Devilliers, R. Romano, S. Riedel, H. Pernice in *Ullmann's Encyclopedia of Industrial Chemistry 2000*, 1–19.

[6] J. Schmedt auf der Günne, M. Mangstl, F. Kraus, *Angew. Chem. Int. Ed.* **2012**, *51*, 7847.

[7] F. Kraus in *Progress in fluorine science*, *Vol. 6* (Ed.: K. Seppelt), Elsevier, Amsterdam, **2021**, pp. 5–14.

[8] R. Holland, J. L. Lyman, *J. Quant. Spectrosc. Radiat. Transfer* **1987**, *38*, 79.

[9] R. K. Steunenberg, R. C. Vogel, *J. Am. Chem. Soc.* **1956**, *78*, 901.

[10] F. Brosi, T. Vent-Schmidt, S. Kieninger, T. Schlöder, H. Beckers, S. Riedel, *Chem. Eur. J.* **2015**, *21*, 16455.

[11] S. I. Ivlev, K. Gaul, M. Chen, A. J. Karttunen, R. Berger, F. Kraus, *Chem. Eur. J.* **2019**, *25*, 5793.

[12] T. M. Niemcyzk, R. R. Getty, G. E. Leroi, *J. Chem. Phys.* **1973**, *59*, 5600.

[13] S. Mattsson, B. Paulus, F. A. Redeker, H. Beckers, S. Riedel, C. Müller, *Chem. Eur. J.* **2019**, *25*, 3318.

[14] C. S. Garner, D. M. Yost, *J. Am. Chem. Soc.* **1937**, *59*, 2738.

[15] L. Meyer, C. S. Barrett, S. C. Greer, *J. Chem. Phys.* **1968**, *49*, 1902.

[16] S. I. Ivlev, A. J. Karttunen, M. Hoelzel, M. Conrad, F. Kraus, *Chem. Eur. J.* **2019**, *25*, 3310.

[17] M. H. Karimi-Jafari, A. Maghari, *J. Phys. Chem. A* **2007**, *111*, 6077.

[18] S. Riedel, T. Köchner, X. Wang, L. Andrews, *Inorg. Chem.* **2010**, *49*, 7156.

[19] G. Sini, P. Maitre, P. C. Hiberty, S. S. Shaik, *J. Mol. Struct. (Theochem)* **1991**, *229*, 163.

[20] H. Moissan, *C. R. Hebd. Seances Acad. Sci.* **1886**, *102*, 1543.

[21] J. Aigueperse, P. Mollard, D. Devilliers, M. Chemla, R. Faron, R. Romano, J. P. Cuer in *Ullmann's Encyclopedia of Industrial Chemistry (Poly(Vinyl Chloride))* (Eds.: I. Fischer, W. F. Schmitt, H.-C. Porth, M. W. Allsopp, G. Vianello), Wiley-VCH Verlag GmbH & Co. KGaA, Weinheim, **2014**, pp. 397–441.

[22] A. Matsugi, H. Shiina, K. Tsuchiya, A. Miyoshi, *J. Phys. Chem. A* **2013**, *117*, 14042.

[23] J. F. Froning, M. K. Richards, T. W. Stricklin, S. G. Turnbull, *Ind. Eng. Chem.* **1947**, *39*, 275.

[24] U. Seseke-Koyro, P. Garcia-Juan, S. Palsherm, A. Schulz, WO2009074560, **2009**.

[25] L. B. Asprey, *J. Fluorine Chem.* **1976**, *7*, 359.

[26] L. B. Asprey, US3989808, **1976**.

[27] L. Khriachtchev, M. Pettersson, N. Runeberg, J. Lundell, M. Räsänen, *Nature* **2000**, *406*, 874.

[28] J. Simons, J. H. Hildebrand, *J. Am. Chem. Soc.* **1924**, *46*, 2223.

[29] D. R. Lide, *CRC Handbook of Chemistry and Physics*. *A Ready-Reference Book of Chemical and Physical Data*, CRC Press, Boca Raton, FL., London, **2004**.

[30] S. Riedel in *Comprehensive inorganic chemistry II* (Eds.: J. Reedijk, K. R. Poeppelmeier), Elsevier, Amsterdam, **2013**, pp. 187–221.

[31] L. E. Forslund, N. Kaltsoyannis, *New J. Chem.* **2003**, *27*, 1108.

[32] S. Shaik, D. Danovich, W. Wu, P. C. Hiberty, *Nat. Chem.* **2009**, *1*, 443.

[33] S. Shaik, P. Maitre, G. Sini, P. C. Hiberty, *J. Am. Chem. Soc.* **1992**, *114*, 7861.

[34] R. T. Sanderson, *J. Inorg. Nucl. Chem.* **1968**, *30*, 375.

[35] D. Andrychuk, *Can. J. Phys.* **1951**, *29*, 151.

[36] H. H. Claassen, H. Selig, J. Shamir, *Appl. Spectrosc.* **1969**, *23*, 8.

[37] S. Grimme, *J. Chem. Phys.* **2003**, *118*, 9095.

[38] P. Metrangolo, G. Resnati, *Halogen Bonding*, Springer, Berlin, Heidelberg, New York, **2008**.

[39] R. Cipollini, M. E. Crestoni, S. Fornarini, *J. Am. Chem. Soc.* **1997**, *119*, 9499.

[40] a) T. L. Porter, *J. Chem. Phys.* **1968**, *48*, 2071; b) R. P. Tuckett, A. R. Dale, D. M. Jaffey, P. S. Jarrett, T. Kelly, *Mol. Phys.* **1983**, *49*, 475.

[41] a) R. E. Banks, D. W. A. Sharp, J. C. Tatlow, *Fluorine - The first hundred years (1886-1986)*, Elsevier Sequoia, Lausanne, **1986**; b) D. A. Atwood in *Encyclopedia of Inorganic and Bioinorganic Chemistry* (Ed.: R. A. Scott), Wiley, Chichester, **2012**, p. 874; c) S. W. Green, D. S. L. Slinn, R. N. F. Simpson, A. J. Woytek in *Topics in Applied Chemistry* (Eds.: R. E. Banks, B. E. Smart, J. C. Tatlow), Springer US, Boston, MA, s.l., **1994**, pp. 89–119.

[42] J. S. Moilliet in *Topics in Applied Chemistry* (Eds.: R. E. Banks, B. E. Smart, J. C. Tatlow), Springer US, Boston, MA, s.l., **1994**, pp. 195–219.

[43] F. Zeng, H. Li, H. Cheng, J. Tang, Y. Liu, *High Voltage* **2021**, *6*, 955.

[44] F. Y. Chu, *IEEE Trans. Elect. Insul.* **1986**, *EI-21*, 693.

[45] A. Tressaud, E. Durand, C. Labrugère, A. P. Kharitonov, L. N. Kharitonova, *J. Fluorine Chem.* **2007**, *128*, 378.

[46] E. P. Gillis, K. J. Eastman, M. D. Hill, D. J. Donnelly, N. A. Meanwell, *J. Med. Chem.* **2015**, *58*, 8315.

[47] R. Halder, T. Ritter, *J. Org. Chem.* **2021**, *86*, 13873.

[48] N. Ichiishi, A. F. Brooks, J. J. Topczewski, M. E. Rodnick, M. S. Sanford, P. J. H. Scott, *Org. Lett.* **2014**, *16*, 3224.

[49] G. Balz, G. Schiemann, *Chem. Ber.* **1927**, *60*, 1186.

[50] N. V. Ignat'ev in *Modern Synthesis Processes and Reactivity of Fluorinated Compounds*. *Progress in Fluorine Science* (Eds.: H. Groult, F. Leroux, A. Tressaud), Elsevier Science, San Diego, CA, USA, **2016**, pp. 71–123.

[51] E. Bajraktarova-Valjakova, V. Korunoska-Stevkovska, S. Georgieva, K. Ivanovski, C. Bajraktarova-Misevska, A. Mijoska, A. Grozdanov, *Maced. J. Med. Sci.* **2018**, *6*, 2257.

[52] R. E. Banks, J. C. Tatlow in *Topics in Applied Chemistry* (Eds.: R. E. Banks, B. E. Smart, J. C. Tatlow), Springer US, Boston, MA, s.l., **1994**, pp. 1–24.

[53] E. Riedel, C. Janiak, *Anorganische Chemie*, de Gruyter, Berlin, Boston, **2015**.

[54] M. W. Johnson, E. Sándor, E. Arzi, *Acta Cryst. B* **1975**, *31*, 1998.

[55] S. E. McLain, C. J. Benmore, J. E. Siewenie, J. Urquidi, J. F. C. Turner, *Angew. Chem. Int. Ed.* **2004**, *43*, 1952.

[56] J. Janzen, L. S. Bartell, *J. Chem. Phys.* **1969**, *50*, 3611.

[57] J. W. Larson, T. B. McMahon, *J. Am. Chem. Soc.* **1983**, *105*, 2944.

[58] F. G. Drakesmith, D. A. Hughes, *J. Fluorine Chem.* **1986**, *32*, 103.

[59] N. V. Ignat'ev, personal communication, **2019**.

[60] G. A. Olah, G. K. Surya Prakash, Á. Molnár, J. Sommer, *Superacid Chemistry*, John Wiley & Sons, Inc, Hoboken, NJ, USA, **2009**.

[61] J. H. Simons, *J. Electrochem. Soc.* **1949**, *95*, 47.

[62] J. H. Simons, R. D. Dresdner, *J. Electrochem. Soc.* **1949**, *95*, 64.

[63] J. H. Simons, H. T. Francis, J. A. Hogg, *J. Electrochem. Soc.* **1949**, *95*, 53.

[64] J. H. Simons, W. J. Harland, *J. Electrochem. Soc.* **1949**, *95*, 55.

[65] J. H. Simons, W. H. Pearlson, T. J. Brice, W. A. Wilson, R. D. Dresdner, *J. Electrochem. Soc.* **1949**, *95*, 59.

[66] K. O. Christe, D. A. Dixon, D. McLemore, W. W. Wilson, J. A. Sheehy, J. A. Boatz, *J. Fluorine Chem.* **2000**, *101*, 151.

[67] N. Bartlett, *J. Fluorine Chem.* **2006**, *127*, 1285.

[68] a) G. Oláh, S. Kuhn, J. Oláh, *J. Chem. Soc.* **1957**, 2174; b) V. P. Reddy, Prakash, G. K. Surya in *Kirk-Othmer Encyclopedia of Chemical Technology* (Ed.: I. John Wiley & Sons), Wiley, **2000**.

[69] I.-C. Hwang, K. Seppelt, *Angew. Chem. Int. Ed.* **2001**, *40*, 3690.

[70] N. Bartlett, *Proc. Chem. Soc.* **1962**, 218.

[71] N. Bartlett, D. H. Lohmann, *Proc. Chem. Soc.* **1962**, 115.

[72] A. B. Lindstrom, M. J. Strynar, E. L. Libelo, *Environ. Sci. Technol.* **2011**, *45*, 7954.

[73] N. A. Young, *Coord. Chem. Rev.* **2013**, *257*, 956.

[74] W. F. Howard, L. Andrews, *J. Am. Chem. Soc.* **1973**, *95*, 3045.

[75] B. S. Ault, L. Andrews, *J. Am. Chem. Soc.* **1976**, *98*, 1591.

[76] B. S. Ault, L. Andrews, *Inorg. Chem.* **1977**, *16*, 2024.

[77] T. Vent-Schmidt, F. Brosi, J. Metzger, T. Schlöder, X. Wang, L. Andrews, C. Müller, H. Beckers, S. Riedel, *Angew. Chem. Int. Ed.* **2015**, *54*, 8279.

[78] K. F. Hoffmann, A. Wiesner, C. Müller, S. Steinhauer, H. Beckers, M. Kazim, C. R. Pitts, T. Lectka, S. Riedel, *Nat. Commun.* **2021**, *12*, 5275.

[79] K. Seppelt, *Chem. Rev.* **2015**, *115*, 1296.

[80] a) P. Tomar, T. Braun, E. Kemnitz, *Chem. Commun.* **2018**, *54*, 9753; b) D. Dirican, N. Pfister, M. Wozniak, T. Braun, *Chem. Eur. J.* **2020**, *26*, 6945.

[81] D. Lentz, K. Seppelt, *Angew. Chem. Int. Ed.* **1979**, *18*, 66.

[82] A. Wiesner, T. W. Gries, S. Steinhauer, H. Beckers, S. Riedel, *Angew. Chem. Int. Ed.* **2017**, *56*, 8263.

[83] K. F. Hoffmann, A. Wiesner, S. Steinhauer, S. Riedel, *Chem. Eur. J.* **2022**, e202201958.

[84] J. L. Kyzer, M. Martens, *Chem. Res. Toxicol.* **2021**, *34*, 678.

[85] a) R. A. Peters, *Endeavour* **1954**, *13*, 147; b) K. Seppelt in *Progress in fluorine science*, *Vol. 6* (Ed.: K. Seppelt), Elsevier, Amsterdam, **2021**, pp. 1–4.

[86] a) M. Schlosser, *Angew. Chem. Int. Ed.* **1998**, *37*, 1496; b) B. E. Smart, *J. Fluorine Chem.* **2001**, *109*, 3.

[87] T. Honda, I. Ojima in *Progress in fluorine science*, *Vol. 6* (Ed.: K. Seppelt), Elsevier, Amsterdam, **2021**, pp. 241–276.

[88] a) Q. A. Huchet, B. Kuhn, B. Wagner, N. A. Kratochwil, H. Fischer, M. Kansy, D. Zimmerli, E. M. Carreira, K. Müller, *J. Med. Chem.* **2015**, *58*, 9041; b) F.-L. Qing, X.-H. Xu in *Modern Synthesis Processes and Reactivity of Fluorinated Compounds*. *Progress in Fluorine Science* (Eds.: H. Groult, F. Leroux, A. Tressaud), Elsevier Science, San Diego, CA, USA, **2016**, pp. 201–222.

[89] X. Liu, C. Xu, M. Wang, Q. Liu, *Chem. Rev.* **2015**, *115*, 683.

[90] J. H. Nissen, T. Stüker, T. Drews, S. Steinhauer, H. Beckers, S. Riedel, *Angew. Chem. Int. Ed.* **2019**, *58*, 3584.

[91] S. Dix, P. Golz, J. R. Schmid, S. Riedel, M. N. Hopkinson, *Chem. Eur. J.* **2021**, *27*, 11554.

[92] I. M. Riddlestone, A. Kraft, J. Schaefer, I. Krossing, *Angew. Chem. Int. Ed.* **2018**, *57*, 13982.

[93] S. Kotsyuda, A. N. Toraman, P. Voßnacker, M. A. Ellwanger, S. Steinhauer, C. Müller, S. Riedel, *Chem. Eur. J.* **2022**, e202202749.

[94] P. A. Albrecht, S. M. Rupf, M. Sellin, J. Schlögl, S. Riedel, M. Malischewski, *Chem. Commun.* **2022**, *58*, 4958.

[95] B. A. Shainyan, L. L. Tolstikova, *Chem. Rev.* **2013**, *113*, 699.

[96] L. Suo, O. Borodin, T. Gao, M. Olguin, J. Ho, X. Fan, C. Luo, C. Wang, K. Xu, *Science* **2015**, *350*, 938.

[97] H. Sakaguchi, K. Fujii, S. Sakai, Y. Kobayashi, Y. Kita, DE19533711A1, **1996**.

[98] A. Parekh, *Front. Energy Res.* **2022**, *10*, 101536.

[99] W. G. Grot in *Electrochemistry in Industry*. *New Directions* (Eds.: U. Landau, E. Yeager, D. Kortan), Springer US, Boston, MA, **1982**, pp. 73–87.

[100] Z. Mazej, E. A. Goreshnik, *J. Fluorine Chem.* **2017**, *196*, 3.

[101] M. K. Björnsdotter, W. F. Hartz, R. Kallenborn, I. Ericson Jogsten, J. D. Humby, A. Kärrman, L. W. Y. Yeung, *Environ. Sci. Technol.* **2021**, *55*, 15853.

[102] R. Renner, *Environ. Sci. Technol.* **2006**, *40*, 12.

[103] R. C. Buck, J. Franklin, U. Berger, J. M. Conder, I. T. Cousins, P. de Voogt, A. A. Jensen, K. Kannan, S. A. Mabury, S. P. J. van Leeuwen, *Integr. Environ. Assess. Manage.* **2011**, *7*, 513.

[104] OECD, *Results of the 2006 Survey on Production and Use of PFOS, PFAS, PFOA, PFCA, their Related Substances and Products/Mixtures Containing these Substances*, **2006**.

[105] OECD, *Synthesis paper on per- and polyfluorinated chemicals (PFCs), Environment, Health and Safety, Environment Directorate*, **2013**.

[106] OECD, *Toward a new comprehensive global database of per- and polyfluoroalkyl substances (PFASs): Summary report on updating the OECD 2007 list of per- and polyfluoroalkyl substances (PFASs)*, **2018**.

[107] a) M. Peschka, N. Fichtner, W. Hierse, P. Kirsch, E. Montenegro, M. Seidel, R. D. Wilken, T. P. Knepper, *Chemosphere* **2008**, *72*, 1534; b) M. Rabnawaz, G. Liu, H. Hu, *Angew. Chem. Int. Ed.* **2015**, *54*, 12722; c) M. Rabnawaz, G. Liu, H. Hu, *Angew. Chem.* **2015**, *127*, 12913.

[108] OECD, *OECD Hazard Assessment of Perflurooctane Sulphonate (PFOS) and its Salts*, **2002**.

[109] a) *Directive 2002/95/EC of the European Parliament and of the Council of 27 January 2003 on the restriction of the use of certain hazardous substances in electrical and electronic equipment*, **2003**; b) K. Sonnenberg, L. Mann, F. A. Redeker, B. Schmidt, S. Riedel, *Angew. Chem.* **2020**, *132*, 5506; c) B. Xu, G. Yang, A. Lehmann, S. Riedel, M. C. Rillig, *Soil Ecol. Lett.* **2023**, *5*, 108; d) J. T. Thompson, B. Chen, J. A. Bowden, T. G. Townsend, *Environ. Sci. Technol. Lett.* **2023**, *10*, 234; e) I. A. Titaley, F. B. de La Cruz, M. A. Barlaz, J. A. Field, *Environ.*

Sci. Technol. Lett. **2023**, *10*, 214; f) *Directive 2003/11/EC of the European Parliament and of the Council of 6 February 2003 amending for the 24th time Council Directive 76/769/EEC relating to restrictions on the marketing and use of certain dangerous substances and preparations (pentabromodiphenyl ether, octabromodiphenyl ether)*, **2003**.

[110] K. Sonnenberg, L. Mann, F. A. Redeker, B. Schmidt, S. Riedel, *Angew. Chem. Int. Ed.* **2020**, *59*, 5464.

[111] J. M. Whalen, L. C. Chacon, N. Bartlett in *Proceedings*, *v. 97-15* (Eds.: W. V. Childs, T. Fuchigami), Electrochemical Society, Pennington, NJ, **1997**, pp. 1–12.

[112] E. Hollitzer, P. Sartori, *Chem. Ing. Tech.* **1986**, *58*, 31.

[113] a) A. Studer, *Angew. Chem. Int. Ed.* **2012**, *51*, 8950; b) J. Charpentier, N. Früh, A. Togni, *Chem. Rev.* **2015**, *115*, 650; c) H. Xiao, Z. Zhang, Y. Fang, L. Zhu, C. Li, *Chem. Soc. Rev.* **2021**, *50*, 6308.

[114] S. Barata-Vallejo, S. M. Bonesi, A. Postigo, *Chem. Eur. J.* **2022**, *28*, e202201776.

[115] a) X.-H. Xu, K. Matsuzaki, N. Shibata, *Chem. Rev.* **2015**, *115*, 731; b) C. Xu, S. Wang, Q. Shen, *ACS Sustainable Chem. Eng.* **2022**, *10*, 6889.

[116] D. P. Cox, J. Terpinski, W. Lawrynowicz, *J. Org. Chem.* **1984**, *49*, 3216.

[117] a) G. A. Olah, J. T. Welch, Y. D. Vankar, M. Nojima, I. Kerekes, J. A. Olah, *J. Org. Chem.* **1979**, *44*, 3872; b) N. Yoneda, *Tetrahedron* **1991**, *47*, 5329.

[118] O. E. Okoromoba, J. Han, G. B. Hammond, B. Xu, *J. Am. Chem. Soc.* **2014**, *136*, 14381.

[119] M. Döbele, S. Vanderheiden, N. Jung, S. Bräse, *Angew. Chem. Int. Ed.* **2010**, *49*, 5986.

[120] H. G. Lee, P. J. Milner, S. L. Buchwald, *J. Am. Chem. Soc.* **2014**, *136*, 3792.

[121] K. O. Christe, *Inorg. Chem.* **1986**, *25*, 3721.

[122] T. Schlöder, F. Kraus, S. Riedel, *Encyclopedia of Inorganic and Bioinorganic Chemistry* **2014**, 1.

[123] Y. W. Alsmeyer, W. V. Childs, R. M. Flynn, G. G. I. Moore, J. C. Smeltzer in *Topics in Applied Chemistry* (Eds.: R. E. Banks, B. E. Smart, J. C. Tatlow), Springer US, Boston, MA, s.l., **1994**, pp. 121–143.

[124] R. Fowler, H. Anderson, J. J. Hamilton, W. Burford III, A. Spadetti, S. Bitterlich, I. Litant, *Ind. Eng. Chem.* **1947**, *39*, 343.

[125] J. Burdon, I. W. Parsons, J. C. Tatlow, *Tetrahedron* **1972**, *28*, 43.

[126] B. Žemva, K. Lutar, L. Chacón, M. Fele-Beuermann, J. Allman, C. Shen, N. Bartlett, *J. Am. Chem. Soc.* **1995**, *117*, 10025.

[127] T. Drews, J. Supel, A. Hagenbach, K. Seppelt, *Inorg. Chem.* **2006**, *45*, 3782.

[128] D. R. Aris, C. Knapp, J. Passmore, X. Wang, *J. Fluorine Chem.* **2005**, *126*, 1368.

[129] M. Tramšek, B. Žemva, *Acta Chim. Slov.* **2006**, *53*, 105.

[130] C. Shen, R. Hagiwara, T. E. Mallouk, N. Bartlett, *ACS Symp. Ser.* **1994**, *555*, 26.

[131] L. Stein, *J. Fluorine Chem.* **1982**, *20*, 65.

[132] U. Breddemann, J. R. DeBackere, G. J. Schrobilgen in *Efficient Preparations of Fluorine Compounds* (Ed.: H. W. Roesky), John Wiley & Sons, Hoboken, NJ, USA, **2012**, pp. 11–15.

[133] A. F. Janzen, *Coord. Chem. Rev.* **1994**, *130*, 355.

[134] J. Haner, G. J. Schrobilgen, *Chem. Rev.* **2015**, *115*, 1255.

[135] L. Conte, G. Gambaretto, *J. Fluorine Chem.* **2004**, *125*, 139.

[136] W. H. Pearlson, *J. Fluorine Chem.* **1986**, *32*, 29.

[137] W. H. Pearlson, US3274081A, **1962**.

[138] A. Tasaka, M. Yamanaka, T. Osada, T. Kawagoe in *Proceedings*, *v. 97-15* (Eds.: W. V. Childs, T. Fuchigami), Electrochemical Society, Pennington, NJ, **1997**, pp. 144–157.

[139] I. N. Rozhkov, *Russ. Chem. Rev.* **1976**, *45*, 615.

[140] A. Konno, T. Fuchigami in *Proceedings*, *v. 97-15* (Eds.: W. V. Childs, T. Fuchigami), Electrochemical Society, Pennington, NJ, **1997**, pp. 101–105.

[141] K. J. M. Noel, *Bull. Electrochem.* **2001**, *17*, 227.

[142] N. V. Ignat'ev, U. Welz-Biermann, U. Heider, A. Kucheryna, S. von Ahsen, W. Habel, P. Sartori, H. Willner, *J. Fluorine Chem.* **2003**, *124*, 21.

[143] P. Sartori, N. Ignat'ev, *J. Fluorine Chem.* **1998**, *87*, 157.

[144] N. S. Rao, B. E. Baker in *Topics in Applied Chemistry* (Eds.: R. E. Banks, B. E. Smart, J. C. Tatlow), Springer US, Boston, MA, s.l., **1994**, pp. 321–338.

[145] a) K. C. Lowe in *Topics in Applied Chemistry* (Eds.: R. E. Banks, B. E. Smart, J. C. Tatlow), Springer US, Boston, MA, s.l., **1994**, pp. 555–577; b) C. Wakselman, A. Lantz in *Topics in Applied Chemistry* (Eds.: R. E. Banks, B. E. Smart, J. C. Tatlow), Springer US, Boston, MA, s.l., **1994**, pp. 177–194.

[146] United Nations, United Nations Environment Programme (UNEP) Ozone Secretariat, *Stockholm Convention on Persistent Organic Pollutants (POPs)*, **2009**.

[147] ECHA (Ed.) *Inclusion of substances of very high concern in the Candidate List for eventual inclusion in Annex XIV*, **2020**.

[148] R. D. Howells, J. D. Mc Cown, *Chem. Rev.* **1977**, *77*, 69.

[149] M. Schmeisser, P. Sartori, *Chem. Ing. Tech.* **1964**, *36*, 9.

[150] J. H. Simons, US2519983A, **1950**.

[151] J. H. Simons in *Fluorine chemistry*. *Volume V* (Ed.: J. H. Simons), Academic Press, New York, London, **1964**, pp. 1–131.

[152] A. Dimitrov, D. Pfeifer, U. Jonethal, St. Rüdiger, K. Seppelt, *J. Fluorine Chem.* **1997**, *82*, 143.

[153] A. Dimitrov, H. Stewig, St. Rüdiger, L. Kolditz, *J. Fluorine Chem.* **1990**, *47*, 13.

[154] P. Sartori, N. Ignat'ev, S. Datsenko, *J. Fluorine Chem.* **1995**, *75*, 157.

[155] U. Groß, S. Rüdiger, A. Dimitrov, *J. Fluorine Chem.* **1996**, *76*, 139.

[156] I. Krossing, personal communication, translated from German, **2022**.

[157] G. P. Gambaretto, M. Napoli, L. Conte, A. Scipioni, R. Armelli, *J. Fluorine Chem.* **1985**, *27*, 149.

[158] H. Schmidt, H. Meinert, *Angew. Chem.* **1960**, *72*, 109.

[159] T. M. Rangarajan, S. Sathyamoorthi, D. Velayutham, M. Noel, R. P. Singh, R. Brahma, *J. Fluorine Chem.* **2011**, *132*, 107.

[160] H. Meinert, J. Mader, W. Röhlke, U. Thewalt, T. Debaerdemaeker, *J. Fluorine Chem.* **1994**, *67*, 235.

[161] a) S. Rüdiger, A. Dimitrov, K. Hottmann, *J. Fluorine Chem.* **1996**, *76*, 155; b) N. Ignat'ev, P. Sartori, *J. Fluorine Chem.* **2000**, *103*, 57; c) N. Ignat'ev, P. Sartori, *J. Fluorine Chem.* **2000**, *101*, 203; d) R. N. Haszeldine, F. Nyman, *J. Chem. Soc.* **1956**, 2684.

[162] A. Dimitrov, S. Rüdiger, N. V. Ignat'ev, S. Datsenko, *J. Fluorine Chem.* **1990**, *50*, 197.

[163] H. Meinert, R. Fackler, J. Mader, P. Reuter, W. Röhlke, *J. Fluorine Chem.* **1992**, *59*, 351.

[164] J. A. Gervasi, M. Brown, L. A. Bigelow, *J. Am. Chem. Soc.* **1956**, *78*, 1679.

[165] N. Bartlett, R. D. Chambers, A. J. Roche, R. C. H. Spink, L. Chacón, J. M. Whalen, *Chem. Commun.* **1996**, 1049.

[166] C. Shen, L. C. Chacón, N. Rosov, S. H. Elder, J. C. Allman, N. Bartlett, *C. R. Acad. Sci., Paris, Ser. II C* **1999**, *2*, 557.

[167] G. G. Totir, G. S. Chottiner, C. L. Gross, D. A. Scherson, *J. Electrochem. Soc.* **2001**, *148*, E262-E266.

[168] G. G. Totir, G. S. Chottiner, C. L. Gross, W. Ves Childs, D. A. Scherson, *J. Electrochem. Soc.* **2000**, *147*, 4212.

[169] L. Stein, J. M. Neil, G. R. Alms, *Inorg. Chem.* **1969**, *8*, 2472.

[170] a) A. Tasaka, T. Kawagoe, A. Takuwa, M. Yamanaka, T. Tojo, M. Aritsuka, *J. Electrochem. Soc.* **1998**, *145*, 1160; b) J. A. Donohue, A. Zletz, R. J. Flannery, *J. Electrochem. Soc.* **1968**, *115*, 1042; c) B. Chang, H. Yanase, K. Nakanishi, N. Watanabe, *Electrochim. Acta* **1971**, *16*, 1179; d) B. Chang, N. Watanabe, K. Nakanishi, *Electrochim. Acta* **1972**, *17*, 1317; e) M. Haruta, N. Watanabe, *J. Fluorine Chem.* **1976**, *7*, 159; f) N. Watanabe, M. Haruta, *Electrochim. Acta* **1980**, *25*, 461; g) D. Lines, H. Sutcliffe, *J. Fluorine Chem.* **1981**, *17*, 423; h)

D. J. Wasser, P. S. Johnson, F. W. Klink, F. Kucera, C.-C. Liu, *J. Fluorine Chem.* **1987**, *35*, 557; i) M. Noel, *Bull. Electrochem.* **1999**, *15*, 466.

[171] N. Hackerman, E. S. Snavely, L. D. Fiel, *Electrochim. Acta* **1967**, *12*, 535.

[172] N. Watanabe, *J. Fluorine Chem.* **1983**, *22*, 205.

[173] a) S. Mattsson, B. Paulus, *Phys. Chem. Chem. Phys.* **2020**, *22*, 4407; b) S. Mattsson, B. Paulus, *Chem. Phys.* **2022**, *557*, 111469.

[174] S. Mattsson, G. Senges, S. Riedel, B. Paulus, *Chem. Eur. J.* **2020**, *26*, 10781.

[175] G. Bunker, *Introduction to XAFS*. *A practical guide to x-ray absorption fine structure spectroscopy*, Cambridge University Press, Cambridge, **2010**.

[176] Z. Mathe, D. A. Pantazis, H. B. Lee, R. Gnewkow, B. E. van Kuiken, T. Agapie, S. DeBeer, *Inorg. Chem.* **2019**, *58*, 16292.

[177] Y. Yang, Y. Wang, Y. Xiong, X. Huang, L. Shen, R. Huang, H. Wang, J. P. Pastore, S.-H. Yu, L. Xiao, J. D. Brock, L. Zhuang, H. D. Abruña, *J. Am. Chem. Soc.* **2019**, *141*, 1463.

[178] J. M. Hollas, *Modern spectroscopy*, Wiley, Chichester, **2004**.

[179] M. Newville, *Fundamentals of XAFS*, Consortium for Advanced Radiation Sources, University of Chicago, Chicago, IL, **2004**.

[180] J. F. Rooms, A. V. Wilson, I. Harvey, A. J. Bridgeman, N. A. Young, *Phys. Chem. Chem. Phys.* **2008**, *10*, 4594.

[181] A. Guilherme Buzanich, *X-Ray Spectrom.* **2022**, *51*, 294.

[182] A. C. Thompson (Ed.) *X-ray Data Booklet*, Lawrence Berkeley National Laboratory, Berkeley, CA, **2009**.

[183] L. Tröger, D. Arvanitis, K. Baberschke, H. Michaelis, U. Grimm, E. Zschech, *Phys. Rev. B* **1992**, *46*, 3283.

[184] A. Guilherme Buzanich, personal communication, **2023**.

[185] B. Žemva, L. Chacon, K. Lutar, C. Shen, J. Allman, N. Bartlett, *J. Fluorine Chem.* **1995**, *71*, 195.

[186] T. Stüker, X. Xia, H. Beckers, S. Riedel, *Chem. Eur. J.* **2021**, *27*, 11693.

[187] A. K. Brisdon, J. H. Holloway, E. G. Hope, P. J. Townson, W. Levason, J. S. Ogden, *J. Chem. Soc., Dalton Trans.* **1991**, 3127.

[188] S. Riedel, M. Kaupp, *Coord. Chem. Rev.* **2009**, *253*, 606.

[189] a) P. J. Chirik, K. Wieghardt, *Science* **2010**, *327*, 794; b) S. A. Pattenaude, K. C. Mullane, E. J. Schelter, M. G. Ferrier, B. W. Stein, S. E. Bone, J. S. Lezama Pacheco, S. A. Kozimor, P. E. Fanwick, M. Zeller, S. C. Bart, *Inorg. Chem.* **2018**, *57*, 6530; c) W. Kaim, B. Schwederski,

Coord. Chem. Rev. **2010**, *254*, 1580; d) M. D. Ward, J. A. McCleverty, *J. Chem. Soc., Dalton Trans.* **2002**, 275.

[190] G. Wang, M. Zhou, J. T. Goettel, G. J. Schrobilgen, J. Su, J. Li, T. Schlöder, S. Riedel, *Nature* **2014**, *514*, 475.

[191] M. Da Silva Santos, T. Stüker, M. Flach, O. S. Ablyasova, M. Timm, B. von Issendorff, K. Hirsch, V. Zamudio-Bayer, S. Riedel, J. T. Lau, *Angew. Chem. Int. Ed.* **2022**, *61*, e202207688.

[192] S. Riedel, M. Kaupp, *Inorg. Chem.* **2006**, *45*, 10497.

[193] A. Higelin, S. Riedel in *Modern Synthesis Processes and Reactivity of Fluorinated Compounds*. *Progress in Fluorine Science* (Eds.: H. Groult, F. Leroux, A. Tressaud), Elsevier Science, San Diego, CA, USA, **2016**, pp. 561–586.

[194] C. K. Jørgensen, *Z. Anorg. Allg. Chem.* **1986**, *540-541*, 91.

[195] D. Himmel, S. Riedel, *Inorg. Chem.* **2007**, *46*, 5338.

[196] M. Kaupp, Schleyer, P. v. R., *J. Am. Chem. Soc.* **1993**, *115*, 1061.

[197] a) C. Remenyi, M. Kaupp, *J. Am. Chem. Soc.* **2005**, *127*, 11399; b) M. Kaupp, H. G. von Schnering, *Angew. Chem. Int. Ed.* **1995**, *34*, 986; c) M. Kaupp, H. G. von Schnering, *Angew. Chem.* **1995**, *107*, 1076.

[198] M. Kaupp, *J. Comput. Chem.* **2007**, *28*, 320.

[199] T. Schloeder, F. Brosi, B. J. Freyh, T. Vent-Schmidt, S. Riedel, *Inorg. Chem.* **2014**, *53*, 5820.

[200] O. Glemser, H. Roesky, K. H. Hellberg, *Angew. Chem. Int. Ed.* **1963**, *2*, 266.

[201] S. Riedel, M. Renz, M. Kaupp, *Inorg. Chem.* **2007**, *46*, 5734.

[202] J. Lin, Q. Yang, X. Li, X. Zhang, F. Li, G. Yang, *Phys. Chem. Chem. Phys.* **2022**, *24*, 1736.

[203] J. Lin, X. Du, M. Rahm, H. Yu, H. Xu, G. Yang, *Angew. Chem. Int. Ed.* **2020**, *59*, 9155.

[204] S. X. Hu, W. L. Li, J. B. Lu, J. L. Bao, H. S. Yu, D. G. Truhlar, J. K. Gibson, J. Marçalo, M. Zhou, S. Riedel, W. H. E. Schwarz, J. Li, *Angew. Chem. Int. Ed.* **2018**, *57*, 3242.

[205] H. S. Yu, D. G. Truhlar, *Angew. Chem. Int. Ed.* **2016**, *55*, 9004.

[206] Ł. Wolański, M. A. Domański, W. Grochala, P. Szarek, *Chem. Commun.* **2020**, *56*, 13137.

[207] a) X. Wang, L. Andrews, S. Riedel, M. Kaupp, *Angew. Chem. Int. Ed.* **2007**, *46*, 8371; b) X. Wang, L. Andrews, S. Riedel, M. Kaupp, *Angew. Chem.* **2007**, *119*, 8523.

[208] T. Schlöder, S. Riedel in *Comprehensive inorganic chemistry II* (Eds.: J. Reedijk, K. R. Poeppelmeier), Elsevier, Amsterdam, **2013**, pp. 227–243.

[209] R. Wei, Z. T. Fang, M. Vasiliu, D. A. Dixon, L. Andrews, Y. Gong, *Inorg. Chem.* **2019**, *58*, 9796.

[210] L. Li, T. Stüker, S. Kieninger, D. Andrae, T. Schlöder, Y. Gong, L. Andrews, H. Beckers, S. Riedel, *Nat. Commun.* **2018**, *9*, 1267.

[211] L. Li, H. Beckers, T. Stüker, T. Lindič, T. Schlöder, D. Andrae, S. Riedel, *Inorg. Chem. Front.* **2021**, *8*, 1215.

[212] L. Andrews, X. Wang, Y. Gong, T. Schlöder, S. Riedel, M. J. Franger, *Angew. Chem. Int. Ed.* **2012**, *51*, 8235.

[213] a) J. M. Mayer, *Comments Inorg. Chem.* **1988**, *8*, 125; b) J. R. Winkler, H. B. Gray in *Molecular Electronic Structures of Transition Metal Complexes I* (Eds.: D. M. P. Mingos, P. Day, J. P. Dahl), Springer, Berlin, Germany, **2012**, pp. 17–28.

[214] Lin Li, *PhD Thesis*, Freie Universität Berlin, Berlin, **2021**.

[215] A. K. Brisdon, J. H. Holloway, E. G. Hope, *J. Fluorine Chem.* **1998**, *89*, 35.

[216] I. R. Beattie, C. J. Marsden, J. S. Ogden, *J. Chem. Soc., Dalton Trans.* **1980**, 535.

[217] a) E. G. Hope, P. J. Jones, W. Levason, J. S. Ogden, M. Tajik, J. W. Turff, *J. Chem. Soc., Dalton Trans.* **1985**, 529; b) D. Turnbull, P. Chaudhary, D. Leenstra, P. Hazendonk, S. D. Wetmore, M. Gerken, *Inorg. Chem.* **2020**, *59*, 17544.

[218] N. Bartlett, *Angew. Chem. Int. Ed.* **1968**, *7*, 433.

[219] Y. Gong, M. Zhou, L. Andrews, *Chem. Rev.* **2009**, *109*, 6765.

[220] a) V. A. Larson, B. Battistella, K. Ray, N. Lehnert, W. Nam, *Nat. Rev. Chem.* **2020**, *4*, 404; b) M. M. Najafpour, G. Renger, M. Hołyńska, A. N. Moghaddam, E.-M. Aro, R. Carpentier, H. Nishihara, J. J. Eaton-Rye, J.-R. Shen, S. I. Allakhverdiev, *Chem. Rev.* **2016**, *116*, 2886; c) J. R. Carney, B. R. Dillon, S. P. Thomas, *Eur. J. Org. Chem.* **2016**, *2016*, 3912; d) Y. Umena, K. Kawakami, J.-R. Shen, N. Kamiya, *Nature* **2011**, *473*, 55; e) G. R. Patzke, Y. Zhou, R. Kontic, F. Conrad, *Angew. Chem. Int. Ed.* **2011**, *50*, 826; f) L. Gan, L. Ye, M. Liu, S. Tao, K. Xie, *RSC Adv.* **2016**, *6*, 641.

[221] H. Schmidbaur, Schwarz, W. H. Eugen, *Chem. Eur. J.* **2021**, *27*, 6848.

[222] W. Levason, C. A. McAuliffe, *Coord. Chem. Rev.* **1972**, *7*, 353.

[223] F. Brosi, T. Schlöder, A. Schmidt, H. Beckers, S. Riedel, *Dalton Trans.* **2016**, *45*, 5038.

[224] H. Bürger, P. Weinrath, S. Dressler, T. Hansen, W. Thiel, *J. Mol. Spectrosc.* **1997**, *183*, 139.

[225] H. Selig, J. G. Malm, *J. Inorg. Nucl. Chem.* **1963**, *25*, 349.

[226] X.-L. Jiang, C.-Q. Xu, J.-B. Lu, C.-S. Cao, H. Schmidbaur, Schwarz, W. H. Eugen, J. Li, *Inorg. Chem.* **2021**, *60*, 9504.

[227] A. K. Srivastava, N. Misra, *Mol. Phys.* **2014**, *112*, 2820.

[228] G. L. Gutsev, A. I. Boldyrev, *Chem. Phys.* **1981**, *56*, 277.

[229] G. Balducci, M. Campodonico, G. Gigli, G. Meloni, S. N. Cesaro, *J. Chem. Phys.* **2002**, *117*, 10613.

[230] T. Huang, L. Zhao, X. Jiang, W. Yu, B. Xu, X. Wang, W. H. E. Schwarz, J. Li, *Inorg. Chem.* **2021**, *60*, 7687.

[231] D. Schilter, *Nat. Rev. Chem.* **2021**, *5*, 445.

[232] Y. Gong, M. Zhou, L. Andrews, T. Schlöder, S. Riedel, *Theor. Chem. Acc.* **2011**, *129*, 667.

[233] Y. Gong, M. Zhou, M. Kaupp, S. Riedel, *Angew. Chem. Int. Ed.* **2009**, *48*, 7879.

[234] a) F. Wöhler, *Ann. Chim. Phys.* **1828**, *37*, 101; b) F. Wöhler, *Ann. Miner.* **1828**, *3*, 163.

[235] A. Engelbrecht, A. V. Grosse, *J. Am. Chem. Soc.* **1954**, *76*, 2042.

[236] J. Spandl, J. Supeł, T. Drews, K. Seppelt, *Z. Anorg. Allg. Chem.* **2006**, *632*, 2222.

[237] W. Levason, J. S. Ogden, A. K. Saad, N. A. Young, A. K. Brisdon, P. J. Holliman, J. H. Holloway, E. G. Hope, *J. Fluorine Chem.* **1991**, *53*, 43.

[238] E. L. Varetti, R. R. Filgueira, A. Müller, *Spectrochim. Acta, Part A* **1981**, *37*, 369.

[239] E. L. Varetti, A. Mueller, *Z. Anorg. Allg. Chem.* **1978**, *442*, 230.

[240] A. Mueller, K. H. Schmidt, E. Ahlborn, C. J. L. Lock, *Spectrochim. Acta, Part A* **1973**, *29*, 1773.

[241] P. J. Aymonino, H. Schulze, A. Müller, *Z. Naturforsch. B* **1969**, *24*, 1508.

[242] J. P. Jasinski, S. L. Holt, J. H. Wood, J. W. Moskowitz, *J. Chem. Phys.* **1975**, *63*, 1429.

[243] W. Levason, J. S. Ogden, J. W. Turff, *J. Chem. Soc., Dalton Trans.* **1983**, 2699.

[244] M. J. Reisfeld, L. B. Asprey, N. A. Matwiyoff, *Spectrochim. Acta, Part A* **1971**, *27*, 765.

[245] A. Javan, A. Engelbrecht, *Phys. Rev.* **1954**, *96*, 649.

[246] E. Diemann, E. L. Varetti, A. Müller, *Chem. Phys. Lett.* **1977**, *51*, 460.

[247] M. Lein, A. Hammerl, H. L. Hermann, P. Schwerdtfeger, *Polyhedron* **2007**, *26*, 486.

[248] R. J. Gillespie, G. J. Schrobilgen, *Inorg. Chem.* **1976**, *15*, 22.

[249] L. O. Müller, D. Himmel, J. Stauffer, G. Steinfeld, J. Slattery, G. Santiso-Quiñones, V. Brecht, I. Krossing, *Angew. Chem. Int. Ed.* **2008**, *47*, 7659.

[250] H. Henkel, R. Hoppe, *Z. Anorg. Allg. Chem.* **1969**, *364*, 253.

[251] G. C. Allen, K. D. Warren, *Inorg. Chem.* **1969**, *8*, 1895.

[252] H. Bode, E. Voss, *Z. Anorg. Allgem. Chem.* **1957**, *290*, 1.

[253] W. Klemm, E. Huss, *Z. Anorg. Allgem. Chem.* **1949**, *258*, 221.

[254] a) J. C. Taylor, P. W. Wilson, *J. Inorg. Nucl. Chem.* **1974**, *36*, 1561; b) H. Bode, E. Voss, *Z. Anorg. Allg. Chem.* **1956**, *286*, 136.

[255] J. M. Whalen, G. M. Lucier, L. Chacón, N. Bartlett, *J. Fluorine Chem.* **1998**, *88*, 107.

[256] M. M. R. Costa, J. A. Paixão, M. J. M. de Almeida, L. C. R. Andrade, *Acta Cryst. B* **1993**, *49*, 591.

[257] W. Jauch, A. Palmer, A. J. Schultz, *Acta Cryst. B* **1993**, *49*, 984.

[258] B. Zemva, K. Lutar, A. Jesih, W. J. Casteel, N. Bartlett, *J. Chem. Soc., Chem. Commun.* **1989**, 346.

[259] W. Biltz, *Z. Anorg. Allg. Chem.* **1927**, *166*, 275.

[260] B. Žemva, L. Chacon, K. Lutar, C. Shen, J. Allman, N. Bartlett, *J. Fluorine Chem.* **1995**, *71*, 195.

[261] B. Žemva in *Advanced Inorganic Fluorides; Synthesis, Characterization and Applications* (Eds.: T. Nakajima, B. Žemva, A. Tressaud), Elsevier Science S.A., Lausanne, Switzerland, **2000**, pp. 79–115.

[262] A. L. Hector, E. G. Hope, W. Levason, M. T. Weller, *Z. Anorg. Allg. Chem.* **1998**, *624*, 1982.

[263] A. Tressaud, F. Pintchovski, L. Lozano, A. Wold, P. Hagenmuller, *Mater. Res. Bull.* **1976**, *11*, 689.

[264] M. Tramšek, B. Žemva, *Acta Chim. Slov.* **2002**, *49*, 209.

[265] a) N. Bartlett, G. Lucier, C. Shen, W. J. Casteel, L. Chacón, J. Munzenberg, B. Žemva, *J. Fluorine Chem.* **1995**, *71*, 163; b) M. G. Fete, Z. Havlas, J. Michl, *J. Am. Chem. Soc.* **2011**, *133*, 4123.

[266] G. Lucier, C. Shen, W. J. Casteel, L. Chacón, N. Bartlett, *J. Fluorine Chem.* **1995**, *72*, 157.

[267] O. Graudejus, A. P. Wilkinson, L. C. Chacon, N. Bartlett, *Inorg. Chem.* **2000**, *39*, 2794.

[268] L. Li, A. K. Sakr, T. Schlöder, S. Klein, H. Beckers, M.-P. Kitsaras, H. V. Snelling, N. A. Young, D. Andrae, S. Riedel, *Angew. Chem. Int. Ed.* **2021**, *60*, 6391.

[269] T. Lindič, A. Schulz, B. Paulus, *Crystals* **2022**, *12*, 1640.

[270] T. Vogt, A. N. Fitch, J. K. Cockcroft, *Science* **1994**, *263*, 1265.

[271] M. Hargittai, *Chem. Rev.* **2000**, *100*, 2233.

[272] K. O. Christe, D. A. Dixon, *J. Am. Chem. Soc.* **1992**, *114*, 2978.

[273] R. Craciun, D. Picone, R. T. Long, S. Li, D. A. Dixon, K. A. Peterson, K. O. Christe, *Inorg. Chem.* **2010**, *49*, 1056.

[274] J. C. Rienstra-Kiracofe, G. S. Tschumper, H. F. Schaefer, S. Nandi, G. B. Ellison, *Chem. Rev.* **2002**, *102*, 231.

[275] R. N. Compton, P. W. Reinhardt, C. D. Cooper, *J. Chem. Phys.* **1978**, *68*, 2023.

[276] D. Smith, P. Španěl, *Adv. At., Mol., Opt. Phys.* **1994**, *32*, 307.

[277] J. F. Friedman, A. E. Stevens, T. M. Miller, A. A. Viggiano, *J. Chem. Phys.* **2006**, *124*, 224306.

[278] E. B. Rudnyi, E. A. Kaibicheva, L. N. Sidorov, *Rapid Commun. Mass Spectrom.* **1992**, *6*, 356.

[279] S. V. Kuznetsov, M. V. Korobov, L. N. Sidorov, L. N. Savinova, V. A. Shipachev, V. N. Mit'kin, *Int. J. Mass Spectrom. Ion Processes* **1989**, *87*, 1.

[280] R. Wesendrup, P. Schwerdtfeger, *Inorg. Chem.* **2001**, *40*, 3351.

[281] S. Riedel, *J. Fluorine Chem.* **2007**, *128*, 938.

[282] K. O. Christe, R. Haiges, M. Vasiliu, D. A. Dixon, *Angew. Chem. Int. Ed.* **2017**, *56*, 7924.

[283] R. Craciun, R. T. Long, D. A. Dixon, K. O. Christe, *J. Phys. Chem. A* **2010**, *114*, 7571.

[284] Gutsev, G. L., Boldyrev, A. I., *Adv. Chem. Phys.* **1985**, *61*, 169.

[285] P. Botkovitz, G. M. Lucier, R. P. Rao, N. Bartlett, *Acta Chim. Slov.* **1999**, *46*, 141.

[286] L. Graham, O. Graudejus, N. K. Jha, N. Bartlett, *Coord. Chem. Rev.* **2000**, *197*, 321.

[287] A. V. Wilson, T. Nguyen, F. Brosi, X. Wang, L. Andrews, S. Riedel, A. J. Bridgeman, N. A. Young, *Inorg. Chem.* **2016**, *55*, 1108.

[288] Z. Mazej, E. Goreshnik, *Inorg. Chem.* **2022**, *61*, 10587.

[289] K. Leary, N. Bartlett, *J. Chem. Soc., Chem. Commun.* **1972**, 903.

[290] M. J. Vasile, T. J. Richardson, F. A. Stevie, W. E. Falconer, *J. Chem. Soc., Dalton Trans.* **1976**, 351.

[291] J. H. Holloway, G. J. Schrobilgen, *J. Chem. Soc., Chem. Commun.* **1975**, 623.

[292] A. A. Timakov, V. N. Prusakov, Y. V. Drobyshevskii, *Dokl. Akad. Nauk SSSR* **1986**, *291*, 125.

[293] S. Riedel, M. Kaupp, *Inorg. Chem.* **2006**, *45*, 1228.

[294] S. Siegel, D. A. Northrop, *Inorg. Chem.* **1966**, *5*, 2187.

[295] B. Weinstock, H. H. Claassen, J. G. Malm, *J. Am. Chem. Soc.* **1957**, *79*, 5832.

[296] S. S. Rudel, F. Kraus, *Z. Anorg. Allg. Chem.* **2015**, *641*, 2404.

[297] B. Weinstock, H. H. Claassen, J. G. Malm, *J. Chem. Phys.* **1960**, *32*, 181.

[298] J. H. Holloway, G. Stanger, E. G. Hope, W. Levason, J. S. Ogden, *J. Chem. Soc., Dalton Trans.* **1988**, 1341.

[299] B. Weinstock, G. L. Goodman in *Advances in Chemical Physics,. Volume 9* (Ed.: I. Prigogine), John Wiley & Sons, Inc, Hoboken, NJ, USA, **1965**, pp. 169–319.

[300] M. J. Molski, K. Seppelt, *Dalton Trans.* **2009**, 3379.

[301] H. H. Claassen, H. Selig, *Isr. J. Chem.* **1969**, *7*, 499.

[302] W. Moffitt, G. L. Goodman, M. Fred, B. Weinstock, *Mol. Phys.* **1959**, *2*, 109.

[303] A. D. Richardson, K. Hedberg, G. M. Lucier, *Inorg. Chem.* **2000**, *39*, 2787.

[304] G. Senges, L. Li, A. Wodyński, H. Beckers, R. Müller, M. Kaupp, S. Riedel, *Chem. Eur. J.* **2021**, *27*, 13642.

[305] K. O. Christe, W. W. Wilson, R. D. Wilson, *Inorg. Chem.* **1984**, *23*, 2058.

[306] a) K. O. Christe, *Inorg. Chem.* **1973**, *12*, 1580; b) K. O. Christe, *Inorg. Nucl. Chem. Lett.* **1972**, *8*, 741.

[307] M. Broschag, T. M. Klapoetke, I. C. Tornieporth-Oetting, *J. Chem. Soc., Chem. Commun.* **1992**, 446.

[308] G. M. Lucier, C. Shen, S. H. Elder, N. Bartlett, *Inorg. Chem.* **1998**, *37*, 3829.

[309] N. Bartlett, D. H. Lohmann, *J. Chem. Soc.* **1962**, 5253.

[310] M. Bork, R. Hoppe, *Z. Anorg. Allg. Chem.* **1996**, *622*, 417.

[311] S. S. Rudel, T. G. Müller, F. Kraus, *Z. Anorg. Allg. Chem.* **2015**, *641*, 298.

[312] A. K. Brisdon, J. H. Holloway, E. G. Hope, W. Levason, J. S. Ogden, A. K. Saad, *J. Chem. Soc., Dalton Trans.* **1992**, 139.

[313] I. R. Beattie, K. R. Millington, *J. Chem. Soc., Dalton Trans.* **1987**, 1521.

[314] S. A. Arthers, I. R. Beattie, P. J. Jones, *J. Chem. Soc., Dalton Trans.* **1984**, 711.

[315] I. R. Beattie, *Angew. Chem. Int. Ed.* **1999**, *38*, 3294.

[316] a) E. G. Hope, *Polyhedron* **1993**, *12*, 2977; b) F. Q. Roberto, G. Mamantov, *Inorg. Chim. Acta* **1968**, *2*, 317; c) A. A. Ischenko, *J. Mol. Struct.* **2017**, *1132*, 109.

[317] N. Bartlett, D. H. Lohmann, *J. Chem. Soc.* **1964**, 619.

[318] W. A. Sunder, A. L. Wayda, D. Distefano, W. E. Falconer, J. E. Griffiths, *J. Fluorine Chem.* **1979**, *14*, 299.

[319] F. O'Donnell, D. Turnbull, S. D. Wetmore, M. Gerken, *Chem. Eur. J.* **2021**, *27*, 16334.

[320] A. V. Dzhalavyan, E. G. Rakov, A. S. Dudin, *Russ. Chem. Rev.* **1983**, *52*, 960.

[321] N. Bartlett, F. Einstein, D. F. Stewart, J. Trotter, *Chem. Commun.* **1966**, 550.

[322] A. G. Sharpe, *J. Chem. Soc.* **1950**, 3444.

[323] B. G. Mueller, M. Serafin, *Eur. J. Solid State Inorg. Chem.* **1992**, *29*, 625.

[324] J. E. Griffiths, W. A. Sunder, *J. Fluorine Chem.* **1975**, *6*, 533.

[325] J. Slivnik, B. Žemva, B. Družina, *J. Fluorine Chem.* **1980**, *15*, 351.

[326] a) M. V. Korobov, A. A. Bondarenko, L. N. Sidorov, V. V. Nikilin, *High Temp. Sci.* **1983**, *16*, 411; b) A. A. Bondarenko, M. V. Korobov, V. N. Mitkin, L. N. Sidorov, *J. Chem. Thermodyn.* **1988**, *20*, 299; c) M. I. Nikitin, E. N. Karpukhina, *Russ. J. Inorg. Chem.* **2007**, *52*, 334; d) M. I. Nikitin, E. V. Karpukhina, *Russ. J. Inorg. Chem.* **2007**, *52*, 475; e) M. I. Nikitin, *Russ. J. Inorg. Chem.* **2008**, *53*, 1292; f) K. G. G. Hopkins, P. G. Nelson, *J. Chem. Soc., Dalton Trans.* **1984**, 1393.

[327] Y. Lu, Y. A. Tsegaw, A. Wodyński, L. Li, H. Beckers, M. Kaupp, S. Riedel, *Chem. Eur. J.* **2022**, *28*, e202104005.

[328] A. K. Sakr, H. V. Snelling, N. A. Young, *New J. Chem.* **2022**, *46*, 9666.

[329] P. Pyykkö, *Ann. Rev. Phys. Chem.* **2012**, *63*, 45.

[330] J. Lin, S. Zhang, W. Guan, G. Yang, Y. Ma, *J. Am. Chem. Soc.* **2018**, *140*, 9545.

[331] J. N. Brönsted, *Recl. Trav. Chim. Pays-Bas* **1923**, *42*, 718.

[332] T. M. Lowry, *J. Chem. Technol. Biotechnol.* **1923**, *42*, 43.

[333] G. N. Lewis, *Valence and the Structure of Atoms and Molecules*, The Chemical Catalog Company, Inc., New York, **1923**.

[334] H. Yamamoto, *Lewis Acids in Organic Synthesis*, Wiley-VCH Verlag GmbH, Weinheim, Germany, **2000**.

[335] A. Corma, H. García, *Chem. Rev.* **2003**, *103*, 4307.

[336] A. Corma, H. García, *Chem. Rev.* **2002**, *102*, 3837.

[337] D. W. Stephan, G. Erker, *Angew. Chem. Int. Ed.* **2010**, *49*, 46.

[338] R. G. Pearson, *J. Am. Chem. Soc.* **1963**, *85*, 3533.

[339] P. Erdmann, L. Greb, *Angew. Chem. Int. Ed.* **2022**, *61*, e202114550.

[340] M. Winter, N. Peshkur, M. A. Ellwanger, A. Pérez-Bitrián, P. Voßnacker, S. Steinhauer, S. Riedel, *Chem. Eur. J.* **2023**, *29*, e202203634.

[341] a) U. Mayer, V. Gutmann, W. Gerger, *Monatsh. Chem.* **1975**, *106*, 1235; b) M. A. Beckett, G. C. Strickland, J. R. Holland, K. Sukumar Varma, *Polymer* **1996**, *37*, 4629.

[342] L. Greb, *Chem. Eur. J.* **2018**, *24*, 17881.

[343] I. Krossing, I. Raabe, *Chem. Eur. J.* **2004**, *10*, 5017.

[344] L. P. Hammett, A. J. Deyrup, *J. Am. Chem. Soc.* **1932**, *54*, 2721.

[345] T. E. Mallouk, G. L. Rosenthal, G. Mueller, R. Brusasco, N. Bartlett, *Inorg. Chem.* **1984**, *23*, 3167.

[346] H. D. B. Jenkins, I. Krossing, J. Passmore, I. Raabe, *J. Fluorine Chem.* **2004**, *125*, 1585.

[347] a) K. F. Hoffmann, A. Wiesner, N. Subat, S. Steinhauer, S. Riedel, *Z. Anorg. Allg. Chem.* **2018**, *644*, 1344; b) A. Wiesner, S. Steinhauer, H. Beckers, C. Müller, S. Riedel, *Chem. Sci.* **2018**, *9*, 7169.

[348] H. Lynton, J. Passmore, *Can. J. Chem.* **1971**, *49*, 2539.

[349] S. Seidel, K. Seppelt, *Science* **2000**, *290*, 117.

[350] M. Malischewski, K. Seppelt, *Angew. Chem. Int. Ed.* **2017**, *56*, 368.

[351] A. L. K. Aljibury, R. L. Redington, *J. Chem. Phys.* **1970**, *52*, 453.

[352] C. S. Sass, B. S. Ault, *J. Phys. Chem.* **1987**, *91*, 551.

[353] N. P. Machara, B. S. Ault, *J. Phys. Chem.* **1987**, *91*, 2046.

[354] B. S. Ault, *Rev. Chem. Intermed.* **1988**, *9*, 233.

[355] L. Andrews in *Chemistry and physics of matrix-isolated species* (Eds.: L. Andrews, M. Moskovits), North-Holland, Amsterdam, **1989**, pp. 15–46.

[356] V. Jonas, G. Frenking, M. T. Reetz, *J. Am. Chem. Soc.* **1994**, *116*, 8741.

[357] K. R. Leopold, M. Canagaratna, J. A. Phillips, *Acc. Chem. Res.* **1997**, *30*, 57.

[358] K. C. Janda, L. S. Bernstein, J. M. Steed, S. E. Novick, W. Klemperer, *J. Am. Chem. Soc.* **1978**, *100*, 8074.

[359] J. L. Hoard, S. Geller, W. M. Cashin, *Acta Cryst.* **1951**, *4*, 396.

[360] D. J. Hankinson, J. Almlöf, K. R. Leopold, *J. Phys. Chem.* **1996**, *100*, 6904.

[361] E. P. L. Hunter, S. G. Lias, *J. Phys. Chem. Ref. Data* **1998**, *27*, 413.

[362] M. E. Jacox, *J. Mol. Spectrosc.* **1980**, *80*, 257.

[363] M. E. Jacox, *J. Mol. Spectrosc.* **1980**, *84*, 74.

[364] R. D. Hunt, L. Andrews, *J. Phys. Chem.* **1988**, *92*, 3769.

[365] B. S. Ault, *J. Am. Chem. Soc.* **1983**, *105*, 5742.

[366] K. O. Christe, R. Bau, D. Zhao, *Z. Anorg. Allg. Chem.* **1991**, *593*, 46.

[367] R. J. Gillespie, B. Landa, *Inorg. Chem.* **1973**, *12*, 1383.

[368] K. O. Christe, R. D. Wilson, W. Sawodny, *J. Mol. Struct.* **1971**, *8*, 245.

[369] H. Haller, S. Riedel, *Z. Anorg. Allg. Chem.* **2014**, *640*, 1281.

[370] P. H. Svensson, L. Kloo, *Chem. Rev.* **2003**, *103*, 1649.

[371] H. Haller, personal communication, **2014**.

[372] a) M. Wolff, J. Meyer, C. Feldmann, *Angew. Chem. Int. Ed.* **2011**, *50*, 4970; b) M. Wolff, A. Okrut, C. Feldmann, *Inorg. Chem.* **2011**, *50*, 11683; c) K. Sonnenberg, P. Pröhm, N. Schwarze, C. Müller, H. Beckers, S. Riedel, *Angew. Chem. Int. Ed.* **2018**, *57*, 9136.

[373] a) B. Schmidt, K. Sonnenberg, H. Beckers, S. Steinhauer, S. Riedel, *Angew. Chem. Int. Ed.* **2018**, *57*, 9141; b) B. Schmidt, B. Schröder, K. Sonnenberg, S. Steinhauer, S. Riedel, *Angew. Chem. Int. Ed.* **2019**, *58*, 10340.

[374] W. F. Howard, L. Andrews, *Inorg. Chem.* **1975**, *14*, 409.

[375] L. Andrews, *J. Am. Chem. Soc.* **1976**, *98*, 2147.

[376] A. A. Tuinman, A. A. Gakh, R. J. Hinde, R. N. Compton, *J. Am. Chem. Soc.* **1999**, *121*, 8397.

[377] F. A. Redeker, H. Beckers, S. Riedel, *RSC Adv.* **2015**, *5*, 106568.

[378] Frenio A. Redeker, *PhD Thesis*, Freie Universität Berlin, Berlin, **2019**.

[379] G. L. Gutsev, R. J. Bartlett, A. I. Boldyrev, J. Simons, *J. Chem. Phys.* **1997**, *107*, 3867.

[380] W. Känzig, *Phys. Rev.* **1955**, *99*, 1890.

[381] F. B. Otto, O. R. Gilliam, *Phys. Rev.* **1967**, *154*, 244.

[382] T. P. P. Hall, *Br. J. Appl. Phys.* **1966**, *17*, 1011.

[383] L. B. Knight Jr., E. Earl, A. R. Ligon, D. P. Cobranchi, *J. Chem. Phys.* **1986**, *85*, 1228.

[384] L. B. Knight Jr. in *Chemistry and physics of matrix-isolated species* (Eds.: L. Andrews, M. Moskovits), North-Holland, Amsterdam, **1989**, pp. 167–202.

[385] T. R. Burkholder, L. Andrews, *J. Chem. Phys.* **1991**, *95*, 8697.

[386] G. V. Chertihin, A. Citra, L. Andrews, C. W. Bauschlicher Jr., *J. Phys. Chem. A* **1997**, *101*, 8793.

[387] R. C. Spiker, L. Andrews, *J. Chem. Phys.* **1973**, *59*, 1851.

[388] M. E. Jacox, *Chem. Soc. Rev.* **2002**, *31*, 108.

[389] A. Karpfen, *J. Phys. Chem. A* **2001**, *105*, 2064.

[390] L. Andrews, R. Lascola, *J. Am. Chem. Soc.* **1987**, *109*, 6243.

[391] J. A. Gómez Castaño, A. L. Picone, R. M. Romano, H. Willner, C. O. Della Védova, *Chem. Eur. J.* **2007**, *13*, 9355.

[392] A. M. Sapse, *J. Chem. Phys.* **1983**, *78*, 5733.

[393] T. C. McInnis, L. Andrews, *J. Phys. Chem.* **1992**, *96*, 2051.

[394] S. A. Cooke, G. Cotti, J. H. Holloway, A. C. Legon, *Angew. Chem. Int. Ed.* **1997**, *36*, 129.

[395] A. Karpfen, *Chem. Phys. Lett.* **2000**, *316*, 483.

[396] a) A. Karpfen, *J. Phys. Chem. A* **2000**, *104*, 6871; b) A. V. Akimov, I. U. Goldschleger, E. Y. Misochko, C. A. Wight, *J. Phys. Chem. A* **2002**, *106*, 9756; c) H. I. Bloemink, K. Hinds, J. H. Holloway, A. C. Legon, *Chem. Phys. Lett.* **1995**, *245*, 598; d) L. Andrews, T. C. McInnis, *Inorg. Chem.* **1991**, *30*, 2990.

[397] E. Y. Misochko, I. U. Goldschleger, A. V. Akimov, C. A. Wight, *Low Temp. Phys.* **2000**, *26*, 727.

[398] L. Andrews, T. C. McInnis, Y. Hannachi, *J. Phys. Chem.* **1992**, *96*, 4248.

[399] G. Cotti, C. M. Evans, J. H. Holloway, A. C. Legon, *Chem. Phys. Lett.* **1997**, *264*, 513.

[400] G. Cotti, S. A. Cooke, C. M. Evans, J. H. Holloway, A. C. Legon, *Chem. Phys. Lett.* **1996**, *260*, 388.

[401] a) R. D. Hunt, L. Andrews, *Inorg. Chem.* **1987**, *26*, 3051; b) S. A. Cooke, G. Cotti, C. M. Evans, J. H. Holloway, A. C. Legon, *Chem. Phys. Lett.* **1996**, *262*, 308.

[402] C. M. Evans, J. H. Holloway, A. C. Legon, *Chem. Phys. Lett.* **1997**, *267*, 281.

[403] X.-F. Wang, L. Andrews, *J. Am. Chem. Soc.* **2011**, *133*, 3768.

[404] A. E. Reed, F. Weinhold, L. A. Curtiss, D. J. Pochatko, *J. Chem. Phys.* **1986**, *84*, 5687.

[405] A. C. Legon, *Chem. Commun.* **1998**, 2737.

[406] D. Andrychuk, *J. Chem. Phys.* **1950**, *18*, 233.

[407] K. O. Christe, *J. Fluorine Chem.* **1995**, *71*, 149.

[408] F. A. Hohorst, J. M. Shreeve, *J. Am. Chem. Soc.* **1967**, *89*, 1809.

[409] R. L. Cauble, G. H. Cady, *J. Am. Chem. Soc.* **1967**, *89*, 1962.

[410] M. Miao, *Nat. Chem.* **2013**, *5*, 846.

[411] A. Y. Rogachev, M. Miao, G. Merino, R. Hoffmann, *Angew. Chem. Int. Ed.* **2015**, *54*, 8275.

[412] T. Bally in *Reactive intermediate chemistry* (Eds.: R. A. Moss, M. Platz, M. Jones), Wiley-Interscience, Hoboken, N.J., **2004**.

[413] M. Beaurepaire, B. Daunois, *Phys. Rev. Lett.* **1996**, *76*, 4250.

[414] T. Elsaesser, *Chem. Rev.* **2017**, *117*, 10621.

[415] E. Whittle, D. A. Dows, G. C. Pimentel, *J. Chem. Phys.* **1954**, *22*, 1943.

[416] E. D. Becker, G. C. Pimentel, *J. Chem. Phys.* **1956**, *25*, 224.

[417] D. A. Dows, E. Whittle, G. C. Pimentel, *J. Chem. Phys.* **1955**, *23*, 1475.

[418] R. N. Perutz, *Chem. Rev.* **1985**, *85*, 77.

[419] R. N. Perutz, *Chem. Rev.* **1985**, *85*, 97.

[420] V. E. Bondybey in *Chemistry and physics of matrix-isolated species* (Eds.: L. Andrews, M. Moskovits), North-Holland, Amsterdam, **1989**, pp. 107–138.

[421] L. Andrews, M. Moskovits in *Chemistry and physics of matrix-isolated species* (Eds.: L. Andrews, M. Moskovits), North-Holland, Amsterdam, **1989**, pp. 1–14.

[422] M. E. Jacox in *Chemistry and physics of matrix-isolated species* (Eds.: L. Andrews, M. Moskovits), North-Holland, Amsterdam, **1989**, pp. 75–106.

[423] P. A. Giguère, *Dokl. Akad. Nauk SSSR* **1954**, *22*, 2085.

[424] I. Norman, G. Porter, *Nature* **1954**, *174*, 508.

[425] M. Zhou, L. Andrews, C. W. Bauschlicher, *Chem. Rev.* **2001**, *101*, 1931.

[426] B. S. Ault in *Frontiers and Advances in Molecular Spectroscopy* (Ed.: J. Laane), Elsevier, **2018**, pp. 667–712.

[427] a) L. Li, T. Stüker, L. Andrews, H. Beckers, S. Riedel, *Chem. Eur. J.* **2019**, *25*, 1795; b) J. M. Grzybowski, L. Andrews, *J. Chem. Phys.* **1978**, *68*, 4540.

[428] I. R. Dunkin in *Chemistry and physics of matrix-isolated species* (Eds.: L. Andrews, M. Moskovits), North-Holland, Amsterdam, **1989**, pp. 203–238.

[429] O. Hübner, H.-J. Himmel, *Chem. Eur. J.* **2018**, *24*, 8941.

[430] G. Karir, K. S. Viswanathan in *Encyclopedia of Analytical Chemistry* (Ed.: R. A. Meyers), Wiley, **2006**, pp. 1–17.

[431] Y. A. Tsegaw, *PhD Thesis*, Ruhr-Universität Bochum, Bochum, **2018**.

[432] V. I. Feldman, S. V. Ryazantsev, S. V. Kameneva, *Russ. Chem. Rev.* **2021**, *90*, 1142.

[433] M. E. Jacox, D. E. Milligan, *J. Chem. Phys.* **1968**, *48*, 4040.

[434] X. Wang, L. Andrews, K. Willmann, F. Brosi, S. Riedel, *Angew. Chem. Int. Ed.* **2012**, *51*, 10628.

[435] L. Andrews, M. Moskovits (Eds.) *Chemistry and physics of matrix-isolated species*, North-Holland, Amsterdam, **1989**.

[436] R. N. Perutz in *Chemistry and physics of matrix-isolated species* (Eds.: L. Andrews, M. Moskovits), North-Holland, Amsterdam, **1989**, pp. 239–276.

[437] V. E. Bondybey, A. M. Smith, J. Agreiter, *Chem. Rev.* **1996**, *96*, 2113.

[438] R. T. Paine, R. S. McDowell, L. B. Asprey, L. H. Jones, *J. Chem. Phys.* **1976**, *64*, 3081.

[439] O. M. Wilkin, N. Harris, J. F. Rooms, E. L. Dixon, A. J. Bridgeman, N. A. Young, *J. Phys. Chem. A* **2018**, *122*, 1994.

[440] a) M. S. Gudipati, *J. Phys. Chem. A* **2004**, *108*, 4412; b) T. Momose, H. Hoshina, M. Fushitani, H. Katsuki, *Vib. Spectrosc.* **2004**, *34*, 95.

[441] Y. A. Tsegaw, H. Li, L. Andrews, H.-G. Cho, P. Voßnacker, H. Beckers, S. Riedel, *Chem. Eur. J.* **2022**, *28*, e202103142.

[442] J. E. Willard, *Cryogenics* **1982**, *22*, 359.

[443] M. E. Jacox, *Rev. Chem. Intermed.* **1985**, *6*, 77.

[444] F. Totzauer, technical drawing, **2022**.

[445] S. S. Harilal, C. V. Bindhu, M. S. Tillack, F. Najmabadi, A. C. Gaeris, *J. Appl. Phys.* **2003**, *93*, 2380.

[446] A. Kornath, A. Kaufmann, M. Torheyden, *J. Chem. Phys.* **2002**, *116*, 3323.

[447] M. Moskovits in *Chemistry and physics of matrix-isolated species* (Eds.: L. Andrews, M. Moskovits), North-Holland, Amsterdam, **1989**, pp. 47–74.

[448] a) N. Harris, A. K. Sakr, H. V. Snelling, N. A. Young, *J. Mol. Struct.* **2018**, *1172*, 80; b) N. A. Young, *Coord. Chem. Rev.* **2014**, *277-278*, 224.

[449] a) H. Beckers, P. Garcia, H. Willner, G. A. Argüello, C. J. Cobos, J. S. Francisco, *Angew. Chem. Int. Ed.* **2007**, *46*, 3754; b) K. O. Patten, L. Andrews, *J. Chem. Phys.* **1986**, *84*, 2898.

[450] W. Koch, M. C. Holthausen, *A chemist's guide to density functional theory*, Wiley-VCH, Weinheim, New York, **2001**.

[451] P. Hohenberg, W. Kohn, *Phys. Rev. B* **1964**, *136*, 864.

[452] F. Weigend, R. Ahlrichs, *Phys. Chem. Chem. Phys.* **2005**, *7*, 3297.

[453] L. Li, S. Helle, R. Hahn, F. Brosi, H. Beckers, A. Karton, S. Riedel, Unpublished Results.

[454] F. Claus, R. Minkwitz, *J. Fluorine Chem.* **1982**, *19*, 243.

[455] F. A. Redeker, M. A. Ellwanger, H. Beckers, S. Riedel, *Chem. Eur. J.* **2019**, *25*, 15059.

[456] L. M. Nxumalo, T. A. Ford, *Vib. Spectrosc.* **1994**, *6*, 333.

[457] A. Bondi, *J. Phys. Chem.* **1964**, *68*, 441.

[458] M. Mantina, A. C. Chamberlin, R. Valero, C. J. Cramer, D. G. Truhlar, *J. Phys. Chem. A* **2009**, *113*, 5806.

[459] S. S. Batsanov, *Inorg. Mater.* **2001**, *37*, 871.

[460] L. Goerigk, S. Grimme, *Phys. Chem. Chem. Phys.* **2011**, *13*, 6670.

[461] T. Shimanouchi, *J. Phys. Chem. Ref. Data* **1977**, *6*, 993.

[462] G. V. Chertihin, L. Andrews, *J. Phys. Chem.* **1993**, *97*, 10295.

[463] M. J. Vasile, W. E. Falconer, *Inorg. Chem.* **1972**, *11*, 2282.

[464] J. D. Carpenter, B. S. Ault, *J. Phys. Chem.* **1991**, *95*, 3502.

[465] E. Jacob, J. Goubeau, *Ber. Bunsenges. Phys. Chem.* **1970**, *74*, 992.

[466] R. Z. Martinez, D. Bermejo, J. Santos, P. Cancio, *J. Mol. Spectrosc.* **1994**, *168*, 343.

[467] D. Schiferl, S. Kinkead, R. C. Hanson, D. A. Pinnick, *J. Chem. Phys.* **1987**, *87*, 3016.

[468] D. Forney, M. E. Jacox, W. E. Thompson, *J. Mol. Spectrosc.* **1993**, *157*, 479.

[469] M. E. Jacox, K. K. Irikura, W. E. Thompson, *J. Chem. Phys.* **2000**, *113*, 5705.

[470] M. E. Jacox, W. E. Thompson, *J. Chem. Phys.* **1995**, *102*, 4747.

[471] L. M. Nxumalo, M. Andrzejak, T. A. Ford, *J. Chem. Inf. Comput. Sci.* **1996**, *36*, 377.

[472] J. Gebicki, J. Liang, *J. Mol. Struct.* **1984**, *117*, 283.

[473] L. M. Nxumalo, T. A. Ford, *S. Afr. J. Chem.* **1995**, *48*, 30.

[474] E. J. Sluyts, B. J. van der Veken, *J. Am. Chem. Soc.* **1996**, *118*, 440.

[475] V. M. Rayón, J. A. Sordo, *J. Phys. Chem. A* **1997**, *101*, 7414.

[476] L. C. Hoskins, C. N. Perng, *J. Chem. Phys.* **1971**, *55*, 5063.

[477] L. C. Hoskins, R. C. Lord, *J. Chem. Phys.* **1967**, *46*, 2402.

[478] A. J. Downs, G. P. Gaskill, S. B. Saville, *Inorg. Chem.* **1982**, *21*, 3385.

[479] X. Wang, J. T. Lyon, L. Andrews, *Inorg. Chem.* **2009**, *48*, 6297.

[480] X. Wang, L. Andrews, M. Knitter, P.-A. Malmqvist, B. O. Roos, *J. Phys. Chem. A* **2009**, *113*, 6064.

[481] J. M. Parnis, G. A. Ozin, *J. Phys. Chem.* **1989**, *93*, 1215.

[482] W. E. Falconer, G. R. Jones, W. A. Sunder, M. J. Vasile, A. A. Muenter, T. R. Dyke, W. Klemperer, *J. Fluorine Chem.* **1974**, *4*, 213.

[483] I. Beattie, R. Crocombe, A. German, P. Jones, C. Marsden, G. van Schalkwyk, A. Bukovszky, *J. Chem. Soc., Dalton Trans.* **1976**, 1380.

[484] L. E. Alexander, I. R. Beattie, *J. Chem. Phys.* **1972**, *56*, 5829.

[485] J. Breidung, W. Thiel, *J. Comput. Chem.* **1992**, *13*, 165.

[486] L. E. Alexander, *Inorg. Nucl. Chem. Lett.* **1970**, *7*, 1053.

[487] C. J. Adams, A. J. Downs, *J. Chem. Soc., A* **1971**, 1534.

[488] R. R. Holmes, *Acc. Chem. Res.* **1972**, *5*, 296.

[489] G. S. H. Chen, J. Passmore, P. Taylor, T. K. Whidden, P. S. White, *J. Chem. Soc., Dalton Trans.* **1985**, 9.

[490] T. Shimanouchi in *National standard reference data series* (Ed.: United States National Bureau of Standards), **1972**, pp. 1–160.

[491] S. E. McLain, A. K. Soper, J. J. Molaison, C. J. Benmore, M. R. Dolgos, J. L. Yarger, J. Turner, *J. Mol. Liq.* **2007**, *131-132*, 239.

[492] a) I. R. Beattie, K. M. S. Livingston, G. A. Ozin, D. J. Reynolds, *J. Chem. Soc. A* **1969**, 958; b) A. J. Edwards, P. Taylor, *J. Chem. Soc. D* **1971**, 1376.

[493] X. Wang, L. Andrews, F. Brosi, S. Riedel, *Chem. Eur. J.* **2013**, *19*, 1397.

[494] S. G. Lias, J. E. Bartmess, J. F. Liebman, J. L. Holmes, R. D. Levin, N. G. Mallard, *J. Phys. Chem. Ref. Data, Suppl. 1* **1988**, *17*.

[495] F. Bader, J. C. Tremblay, B. Paulus, *Phys. Chem. Chem. Phys.* **2022**, *24*, 3555.

[496] L. Alvarez-Thon, J. David, R. Arratia-Pérez, K. Seppelt, *Phys. Rev. A* **2008**, *77*, 34502.

[497] R. W. Jotham, S. Kettle, *Inorg. Chim. Acta* **1971**, *5*, 183.

[498] a) J. David, D. Guerra, A. Restrepo, *Inorg. Chem.* **2011**, *50*, 1480; b) J. David, P. Fuentealba, A. Restrepo, *Chem. Phys. Lett.* **2008**, *457*, 42.

[499] V. A. Apkarian, N. Schwentner, *Chem. Rev.* **1999**, *99*, 1481.

[500] R. Alimi, R. B. Gerber, V. A. Apkarian, *J. Chem. Phys.* **1990**, *92*, 3551.

[501] H. Böhrer, N. Trapp, D. Himmel, M. Schleep, I. Krossing, *Dalton Trans.* **2015**, *44*, 7489.

[502] P. Erdmann, J. Leitner, J. Schwarz, L. Greb, *ChemPhysChem* **2020**, *21*, 987.

[503] N. Bartlett, S. P. Beaton, N. K. Jha, *Chem. Commun.* **1966**, 168.

[504] Z. Mazej in *Modern Synthesis Processes and Reactivity of Fluorinated Compounds*. *Progress in Fluorine Science* (Eds.: H. Groult, F. Leroux, A. Tressaud), Elsevier Science, San Diego, CA, USA, **2016**, pp. 587–607.

[505] G. Senges, C. J. Schattenberg, Y. A. Tsegaw, L. Li, S. Helle, R. Hahn, F. Brosi, H. Beckers, A. Karton, M. Kaupp, S. Riedel, manuscript in preparation.

[506] M. K. Kesharwani, B. Brauer, J. M. L. Martin, *J. Phys. Chem. A* **2015**, *119*, 1701.

[507] M. L. Laury, S. E. Boesch, I. Haken, P. Sinha, R. A. Wheeler, A. K. Wilson, *J. Comput. Chem.* **2011**, *32*, 2339.

[508] A. Dimitrov, S. Rüdiger, N. V. Ignatyev, S. Datcenko, *J. Fluorine Chem.* **1990**, *50*, 197.

[509] N. Elgrishi, K. J. Rountree, B. D. McCarthy, E. S. Rountree, T. T. Eisenhart, J. L. Dempsey, *J. Chem. Educ.* **2018**, *95*, 197.

[510] F. G. Drakesmith, D. A. Hughes, *J. Appl. Electrochem.* **1976**, *6*, 23.

[511] E. R. Jette, F. Foote, *J. Chem. Phys.* **1935**, *3*, 605.

[512] B. R. Roy, P. Rajput, S. N. Jha, A. S. Nageswara Rao, *Radiat. Phys. Chem.* **2015**, *114*, 38.

[513] C. T. Chantler, *J. Phys. Chem. Ref. Data* **1995**, *24*, 71.

[514] K. Hintzer, T. Zipplies, D. P. Carlson, W. Schmiegel in *Ullmann's Encyclopedia of Industrial Chemistry (Poly(Vinyl Chloride))* (Eds.: I. Fischer, W. F. Schmitt, H.-C. Porth, M. W. Allsopp, G. Vianello), Wiley-VCH Verlag GmbH & Co. KGaA, Weinheim, **2014**, pp. 1–55.

[515] B. Röder, technical drawing, **2022**.

[516] J. H. Simons, J. W. Bouknight, *J. Am. Chem. Soc.* **1932**, *54*, 129.

[517] J. J. Jasper, *J. Phys. Chem. Ref. Data* **1972**, *1*, 841.

[518] T. Lindič, B. Paulus, Unpublished Results.

[519] L. M. Nxumalo, T. A. Ford, *Comput. Theor. Chem.* **1991**, *236*, 135.

[520] A. A. Emara, J. F. Lehmann, G. J. Schrobilgen, *J. Fluorine Chem.* **2005**, *126*, 1373.

[521] P. Varma, B. S. Ault, *J. Phys. Chem. A* **2008**, *112*, 5613.

[522] M. A. Ellwanger, S. Steinhauer, P. Golz, H. Beckers, A. Wiesner, B. Braun-Cula, T. Braun, S. Riedel, *Chem. Eur. J.* **2017**, *23*, 13501.

[523] a) *Turbomole 7.4.1 ed., a development of University of Karlsruhe and Forschungszentrum Karlsruhe GmbH, 1989-2007, TURBOMOLE GmbH, since 2007*, Karlsruhe, **2019**; b) K. Eichkorn, O. Treutler, H. Öhm, M. Häser, R. Ahlrichs, *Chem. Phys. Lett.* **1995**, *242*, 652; c) O. Treutler, R. Ahlrichs, *J. Chem. Phys.* **1995**, *102*, 346; d) M. v. Arnim, R. Ahlrichs, *J. Comput. Chem.* **1998**, *19*, 1746; e) K. Eichkorn, O. Treutler, H. Öhm, M. Häser, R. Ahlrichs, *Chem. Phys. Lett.* **1995**, *240*, 283; f) K. Eichkorn, F. Weigend, O. Treutler, R. Ahlrichs, *Theor. Chem. Acc.* **1997**, *97*, 119; g) R. Ahlrichs, M. Bär, M. Häser, H. Horn, C. Kölmel, *Chem. Phys. Lett.* **1989**, *162*, 165; h) F. Weigend, *Phys. Chem. Chem. Phys.* **2006**, *8*, 1057; i) M. Sierka, A. Hogekamp, R. Ahlrichs, *J. Chem. Phys.* **2003**, *118*, 9136; j) F. Weigend, *Phys. Chem. Chem. Phys.* **2002**, *4*, 4285; k) M. K. Armbruster, F. Weigend, C. van Wüllen, W. Klopper, *Phys. Chem. Chem. Phys.* **2008**, *10*, 1748; l) D. Peng, N. Middendorf, F. Weigend, M. Reiher, *J. Phys. Chem.* **2013**, *138*, 184105.

[524] a) A. D. Becke, *J. Chem. Phys.* **1993**, *98*, 5648; b) C. Lee, W. Yang, R. G. Parr, *Phys. Rev. B* **1988**, *37*, 785; c) P. J. Stephens, F. J. Devlin, C. F. Chabalowski, M. J. Frisch, *J. Phys. Chem.* **1994**, *98*, 11623; d) S. H. Vosko, L. Wilk, M. Nusair, *Can. J. Phys.* **1980**, *58*, 1200.

[525] E. Caldeweyher, C. Bannwarth, S. Grimme, *J. Chem. Phys.* **2017**, *147*, 34112.

[526] a) J. P. Perdew, *Phys. Rev. B* **1986**, *33*, 8822; b) A. D. Becke, *Phys. Rev. A* **1988**, *38*, 3098; c) J. P. Perdew, K. Burke, M. Ernzerhof, *Phys. Rev. Lett.* **1996**, *77*, 3865; d) J. P. Perdew, K. Burke, M. Ernzerhof, *Phys. Rev. Lett.* **1997**, *78*, 1396.

[527] a) B. Metz, H. Stoll, M. Dolg, *J. Chem. Phys.* **2000**, *113*, 2563; b) D. Andrae, U. Häußermann, M. Dolg, H. Stoll, H. Preuß, *Theor. Chim. Acta* **1990**, *77*, 123.

[528] A. E. Reed, R. B. Weinstock, F. Weinhold, *J. Chem. Phys.* **1985**, *83*, 735.

[529] a) C. Adamo, V. Barone, *J. Chem. Phys.* **1999**, *110*, 6158; b) S. Grimme, S. Ehrlich, L. Goerigk, *J. Comput. Chem.* **2011**, *32*, 1456.

[530] M. J. Frisch, G. W. Trucks, H. B. Schlegel, G. E. Scuseria, M. A. Robb, J. R. Cheeseman, G. Scalmani, V. Barone, G. A. Petersson, H. Nakatsuji, X. Li, M. Caricato, A. V. Marenich, J. Bloino, B. G. Janesko, R. Gomperts, B. Mennucci, H. P. Hratchian, J. V. Ortiz, A. F. Izmaylov, J. L. Sonnenberg, D. Williams-Young, F. Ding, F. Lipparini, F. Egidi, J. Goings, B. Peng, A. Petrone, T. Henderson, D. Ranasinghe, V. G. Zakrzewski, J. Gao, N. Rega, G. Zheng, W. Liang, M. Hada, M. Ehara, K. Toyota, R. Fukuda, J. Hasegawa, M. Ishida, T. Nakajima, Y. Honda, O. Kitao, H. Nakai, T. Vreven, K. Throssell, J. A. Montgomery, Jr., J. E. Peralta, F. Ogliaro, M. J. Bearpark, J. J. Heyd, E. N. Brothers, K. N. Kudin, V. N. Staroverov, T. A. Keith, R. Kobayashi, J. Normand, K. Raghavachari, A. P. Rendell, J. C. Burant, S. S. Iyengar, J. Tomasi, M. Cossi, J. M. Millam, M. Klene, C. Adamo, R. Cammi, J. W. Ochterski, R. L. Martin, K. Morokuma, O. Farkas, J. B. Foresman, and D. J. Fox, *Gaussian 16*, Gaussian, Inc., Wallingford CT, **2016**.

[531] C. Gonzalez, H. B. Schlegel, *J. Chem. Phys.* **1989**, *90*, 2154.

[532] K. Raghavachari, G. W. Trucks, J. A. Pople, M. Head-Gordon, *Chem. Phys. Lett.* **1989**, *157*, 479.

[533] H. Riesemeier, K. Ecker, W. Görner, B. R. Müller, M. Radtke, M. Krumrey, *X-Ray Spectrom.* **2005**, *34*, 160.

[534] B. L. Henke, E. M. Gullikson, J. C. Davis, *At. Data Nucl. Data Tables* **1993**, *54*, 181.

[535] G. Senges, A. Guilherme Buzanich, T. Lindič, T. A. Gully, M. Winter, M. Radtke, Reinholz, B. Röder, S. Steinhauer, B. Paulus, F. Emmerling, S. Riedel, manuscript in preparation.

[536] B. Ravel, M. Newville, *J. Synchrotron Rad.* **2005**, *12*, 537.

[537] OriginLab Corporation, *Origin(Pro), Version 2020*, Northhampton, MA, USA.

[538] G. A. Zhurko, *Chemcraft - graphical program for visualization of quantum chemistry computations. https://www.chemcraftprog.com*, Ivanovo (Russia), **2005**.

[539] H. Putz, K. Brandenburg, *DIAMOND*, Crystal Impact GbR, Bonn, **2020**.

[540] F. Bader, S. Riedel, H. Beckers, C. Müller, J. C. Tremblay, B. Paulus, *J. Phys. Chem. A* **2021**, *125*, 6221.

[541] G. E. Cutsail, N. L. Gagnon, A. D. Spaeth, W. B. Tolman, S. DeBeer, *Angew. Chem. Int. Ed.* **2019**, *58*, 9114.